



Bitlis Eren Üniversitesi
Fen Bilimleri Dergisi

Bitlis Eren University
Journal of Science

ISSN : 2147-3129
e-ISSN : 2147-3188

Cilt / Volume: 12

Sayı / Number: 2

Yıl / Year: 2023

Yazışma Adresi

Bitlis Eren Üniversitesi
Lisansüstü Eğitim Enstitüsü
13000, Merkez, Bitlis/TÜRKİYE
Tel: 0 (434) 2220071

<https://dergipark.org.tr/tr/pub/bitlisfen>



BEU FBD

Bitlis Eren Üniversitesi Fen Bilimler Dergisi

Bitlis Eren University Journal of Science

Yıl/Year: 2023 - Cilt/Volume: 12 - Sayı/Number: 1

Sahibi / Owner

Prof. Dr. Necmettin ELMASTAŞ

Sorumlu Müdür / Director

Doç. Dr. Mehmet Bakır ŞENGÜL

Baş Editör / Editor in Chief

Doç. Dr. Engin YILMAZ

Editörler / Editors

Doç. Dr. Kesran AKIN

Dr. Öğr. Üyesi Ufuk KAYA

Dr. Öğr. Üyesi Yunus SAYAN

Dr. Öğr. Üyesi Fatih AVCIL

Arş. Gör. Dr. Mehmet Akif YERLİKAYA

Dil Editörleri / Language Editors

Öğr. Gör. Murat ÇAN (İngilizce)

Dizgi / Typographic

Doç. Dr. Engin YILMAZ

Dergi Sekreteri / Journal Secretary

Ahmet UĞUR

Editör (Yayın) Kurulu / Editorial Board

Prof. Dr. Zekeriya YERLİKAYA	Kastamonu Üniversitesi
Doç. Dr. Ali ÇAKMAK	Bitlis Eren Üniversitesi
Doç. Dr. Yunus Levent EKİNCİ	Bitlis Eren Üniversitesi
Doç. Dr. Engin YILMAZ	Bitlis Eren Üniversitesi
Doç. Dr. Kesran AKIN	Bitlis Eren Üniversitesi
Doç. Dr. Tuncay TUNÇ	Mersin Üniversitesi
Doç. Dr. Ayşegül Demir YETİŞ	Bitlis Eren Üniversitesi
Doç. Dr. Ramazan KATIRCI	Sivas Bilim ve Teknoloji Üniversitesi
Dr. Sajad KHORSANDROO	North Carolina Agricultural and Technical State University
Dr. Öğr. Üyesi Zehra Nur KULUÖZTÜRK	Bitlis Eren Üniversitesi
Dr. Öğr. Üyesi Halil YETGİN	Bitlis Eren Üniversitesi
Dr. Öğr. Üyesi Erdal AKIN	Bitlis Eren Üniversitesi
Dr. Öğr. Üyesi Faruk ORAL	Bitlis Eren Üniversitesi
Dr. Öğr. Üyesi Necla ÖZDEMİR	Bitlis Eren Üniversitesi
Dr. Nadjet LAOUE	Constantine 1 University
Arş. Gör. Dr. İsmet SÖYLEMEZ	Abdullah Gül Üniversitesi

Danışma Kurulu / Advisory Board

Prof. Dr. Atilla ARSLAN	Selçuk Üniversitesi
Prof. Dr. Nurtaç ÖZ	Sakarya Üniversitesi
Prof. Dr. Saim ÖZDEMİR	Sakarya Üniversitesi
Prof. Dr. Soner ÖZGEN	Fırat Üniversitesi
Prof. Dr. Hasan SEVGİLİ	Ordu Üniversitesi
Prof. Dr. Mahmut BÖYÜKATA	Kırıkkale Üniversitesi
Prof. Dr. Esvet AKBAŞ	Van Yüzüncü Yıl Üniversitesi
Prof. Dr. Mikail ET	Fırat Üniversitesi
Prof. Dr. Özdemir ADIZEL	Van Yüzüncü Yıl Üniversitesi
Prof. Dr. Orhan Taner CAN	Bursa Teknik Üniversitesi
Doç. Dr. Bayram GÜNDÜZ	Malatya Turgut Özal Üniversitesi
Doç. Dr. Sait İZGİ	Siirt Üniversitesi
Doç. Dr. Murat ÇELTEK	Trakya Üniversitesi
Doç. Dr. Cem KOŞAR	Gaziantep Üniversitesi
Doç. Dr. Tarkan YORULMAZ	Çankırı Karatekin Üniversitesi
Dr. Öğr. Üyesi Serhat Berat EFE	Bandırma Onyediy Eylül Üniversitesi
Dr. Öğr. Üyesi Mehmet Can BALCI	Batman Üniversitesi

Bitlis Eren Üniversitesi Fen Bilimleri Dergisi, mühendislik ve temel bilimler alanlarındaki gelişmeleri ve yenilikleri takip etmek, meslek kuruluşlarının, araştırmacıların ve bireylerin ulusal ve uluslararası gelişmelerine katkıda bulunmak ve bu alanlarda elektronik bir kaynak oluşturmak amacıyla yayımlanmaktadır. Derginin yazım dili Türkçe veya İngilizcedir. Fen Bilimleri Dergisi, Bitlis Eren Üniversitesi Lisansüstü Eğitim Enstitüsü yayını olup, 2012 yılından bu yana ücretsiz ve açık erişimli olarak yayın hayatına devam etmektedir. Mühendislik ve temel bilimlerin bilgi tabanına ve teknolojik gelişmelere ışık tutması amacıyla bu alanlarda yapılmış deneysel ve teorik ilerlemeleri konu alan özgün araştırma makalelerine yer verilmektedir. Dergiye gönderilen çalışmaların benzerlik oranı %25'i geçmemelidir. Yazım kurallarına uymayan makaleler, hakemlere gönderilmeden önce düzeltilmek üzere yazara geri gönderilir. Bu nedenle, derginin yazım kuralları dikkate alınmalıdır. Ayrıca, editörlerden yazarlara iletilen düzeltmelere veya taleplere 30 gün içerisinde cevap verilmediği takdirde ilgili makaleler reddedilir. Makaleler şekiller ve tablolar dâhil 20 sayfayı geçmemelidir. Dergiye yayın için gönderilen makaleler en az iki hakem tarafından değerlendirilir. Yazarlardan hakem önerisi talep edilmemektedir. Makalelerin dergide yayımlanabilmesi için hakemler tarafından olumlu görüş bildirilmesi gerekmektedir. Dergi Editör Kurulu, hakem raporlarını (*en aziki hakemin değerlendirmeleri geldikten sonra*) dikkate alarak makalelerin yayımlanmak üzere kabul edilip edilmemesine karar verir. Fen Bilimleri Dergisi, yılda dört defa (*Mart, Haziran, Eylül, Aralık*) yayımlanmaktadır. **Dergimiz Tübitak-Ulakbim Mühendislik ve Temel Bilimler Veri Tabanı Dergi Listesinde taranmaktadır.**

B.E.Ü. Fen Bilimleri Dergisi 12(2), 2023 / B.E.U. Journal of Science 12(2), 2023
İÇİNDEKİLER / CONTENTS

1. **Examination of the Potential Effect of Corrosion Current Density of Ship Hulls on the Sacrificial Anode Cathodic Protection** 292-298
K. Yiğit, M. Adanur
2. **Determining The Number of Principal Components with Schur's Theorem in Principal Component Analysis** 299-306
İ. H. Gümüş, C. Karakuzulu, S. Güldal, M. Yavaş
3. **Co(II) Adsorption onto Ferrous Chloride and Thermally Modified Diatomite: Surface Properties and Adsorption Mechanism** 307-319
E. Gökırmak Söğüt, M. Çelebi
4. **Electrospun TiO₂ Nanofibers in the Presence of Avocado Seed Extract** 320-328
M. Çapkın Yurtsever, K. Temiz
5. **Antioxidant and Antibacterial Activities of Salen-type Schiff Base and Metal Complexes** 329-336
S. Göycincık, H. Danahaliloğlu
6. **On the Coefficient Bound Estimates and Fekete-Szegö Problem** 337-343
S. Korkmaz, N. Mustafa
7. **Predicting the Work-Life Balance of Employees Based on the Ensemble Learning Method** 344-353
V. Tümen, A. S. Sunar
8. **Dry Ice Blasting Method as a Descaling** 354-359
E. A. Güven, M. Uçkan, R. Uzun
9. **A Study on Changes in Some Physicochemical Properties, Volatile Compounds, Sugar, and Organic Acid Contents of Grape Juice During Molasses Production** 360-368
A. Korkmaz
10. **Astrophysical Parameters of the Open Cluster Berkeley 6** 369-375
S. Koç, T. Yontan
11. **The Effect of The Bearing Capacity of Sub-Grade Soil on The Thickness and Cost of The Superstructure of Chip Seals** 376-386
M. Tanyıldızı, M. Çınar
12. **Investigation of The Effect of Cr₂O₃ Particles on Al-Si Matrix Composites Produced by Powder Metallurgy** 387-395
S. Özel, K. Aslan
13. **Comparison Of Anomalous Higgs Couplings at the Large Hadron Collider and at Proton-Proton Collider with 100 TeV Energy** 396-401
G. Akkaya Selçin
14. **An Optimization Approach for a Biogas Supply Chain using Goal Programming and Mixed Integer Linear Programming** 402-411
O. Derse, E. Göçmen Polat
15. **Sentiment Analyzing from Tweet Data's Using Bag of Words and Word2Vec** 412-417
Y. Aydın

16. **Carbon Dioxide Absorption Using Different Solvents (MEA, NaOH, KOH and Mg(OH)₂) in Bubble Column Reactor** 418-427
A.Gul, U. Tezcan Un
17. **NMR Spectroscopy in the Earth's Magnetic Field** 428-434
H. Engin Kırımlı, C. Akay
18. **Investigation of Pyrolysis of Walnut Shells and Pyrolysis Oil Quality** 435-444
E. Gonel, F. Oral, R. Behçet
19. **Performance Optimization of Auxetic Structures on Energy Absorption of Cylindrical Sandwich Using Taguchi and ANOVA Methods** 445-454
O. Kaya, A. H. Bademlioglu, C. Kaboglu
20. **An Approach to Determine of the Formation Stages of Volcanism Using Natural Gamma-Ray Spectrometer from Geophysical Methods (Example of Gölcük Volcanism)** 455-464
N. A. Uyanık
21. **Analysis of Intrusion Detection Systems in UNSW-NB15 and NSL-KDD Datasets with Machine Learning Algorithms** 465-477
F. Türk
22. **Recycling Wastewater with Membrane Technology and The Case of Singapore** 478-484
M. Yeniçeri, K. Tortum Yeniçeri
23. **Lichens as Biomonitors of Air Pollutants Deposition: Strategically Important Element Pollution** 485-495
E. I. Arslan Topal, M. Topal, E. Öbek, A. Aslan
24. **Determination of MIC and MBC Values Using Different Extraction Methods in Plants of Nigella Sativa, Cuminum Cyminum and Pimpinella Anisum L. Samples from Kırıkkale Region** 496-500
E. Böke, B. Kaçmaz, A. Ergene
25. **Investigation of Post-weld Heat Treatment of Laser Welded Ti6Al4V Materials** 501-507
K. Aydın, M. Karamolla
26. **Bioecology and Systematic of Scorpions in Southwestern Anatolia Region (Arachnida: Scorpiones)** 508-523
F. Yeşilyurt, İ. Albayrak
27. **Application of Intuitionistic Fuzzy Topological Operators in Spatial Objects Modeling** 524-530
S. Yılmaz Tarsuslu
28. **Identification of Walnut Variety from The Leaves Using Deep Learning Algorithms** 531-543
A.T. Karadeniz, E. Başaran, Y. Çelik
29. **Assessing Seismic Crack Performance of Diyarbakır Çüngüş Masonry Stone Bridge Considering 2023 Kahramanmaraş, Hatay, Malatya, Gaziantep Earthquakes** 544-556
M. Çavuşlu
30. **An Application of an (R, S) Inventory Management Model for a Construction Materials Manufacturing Company by Using Simulation** 557-567
D. H. Utku
31. **Synthesis, Solvatochromic Analysis and Theoretical Studies of 3-((1H-benzo[d][1,2,3]triazole-1-yl)methyl)-4-phenylethyl-1H-1,2,4-triazole-5(4H)-thione** 568-577
M. Genç, Z. Karagöz Genç, U. İ. Oğuz

- 32 **Estimating The Location of a Buried Body from Magnetic Anomaly Through Normalized Full Gradient: A Case Study from The Sapinuwa Ancient City, Turkey** 578-590
Ş. Özyalın, Z. Akçığ
-

Examination of the Potential Effect of Corrosion Current Density of Ship Hulls on the Sacrificial Anode Cathodic Protection

Kenan YİĞİT^{1*}, Mustafa ADANUR¹

¹*Yıldız Technical University, Faculty of Naval Architecture and Maritime, Marine Engineering Department, Istanbul, Turkey*
(ORCID: [0000-0002-4165-4081](https://orcid.org/0000-0002-4165-4081)) (ORCID: [0000-0003-3698-9490](https://orcid.org/0000-0003-3698-9490))



Keywords: Ship corrosion, Cathodic protection, Sacrificial anode, Electrical current density.

Abstract

In this study, the sacrificial anode cathodic protection system, which is one of the electrical protection methods in the prevention of corrosion in ships, was examined. Within the scope of the study, the potential effects of corrosion current density, which is an important parameter for cathodic protection design, were studied. The study includes cathodic protection calculations for a bulker with a protected hull area of 9406 m² and a general cargo ship with a protected hull area of 1770 m². As a result, it was estimated that each 1 mA/m² change in the electric current density parameter changes the anode usage amount by 64 kg in bulker and 12 kg in general cargo, depending on the reference parameters such as protected hull area, anode type, and design life. It can be stated that the evaluation of the corrosion current density parameter, taking into account the operating conditions of each ship, will be beneficial in terms of optimizing the sacrificial anode consumption.

1. Introduction

Cathodic protection is an electrical control method that protects metallic structures in contact with soil or water from corrosion [1]. In the Earth's atmosphere, most alloys and metals have an unstable structure. As a result, it will always be undefended against corrosion as it will decompose into a lower-energy inorganic compound [2]. Corrosion can be defined as the damage to metallic structures as a result of chemical or electrochemical interactions with their environment [3]. Depending on the characteristics of the deterioration in the metallic structure, corrosion is divided into various classes, such as intergranular corrosion, crevice corrosion, and pitting corrosion. However, methods such as coating, alloying, anodic protection, and cathodic protection are used to minimize the formation of corrosion in the metal [4]. Although the effect of corrosion is limited in an individual sense, it causes serious costs in a global sense. Globally, the cost of corrosion is approximately US\$4 trillion per year [5]. Therefore,

many industries, such as oil, gas, and maritime, work hard to control corrosion.

When the subject is observed from a maritime perspective, seawater causes an aggressive environment on ships and offshore structures due to its high oxygen content and high electrical conductivity [6]. In addition to offshore structures, the protection of ships from corrosion is one of the industry's main priorities. Also, the most vulnerable area of a ship to corrosion is the hull [7]. In general, the ship hull is protected against corrosion by both passive (coating) and active (cathodic) protection. In addition to factors such as chlorine ions, chlorine compounds, humidity, and oxygen content in the marine environment, interactions arising from frictional resistance increase the importance and role of cathodic protection [8]. The sacrificial anode cathodic protection system is one of the most widely used cathodic protection methods on ships [9]. In the literature, cathodic protection systems used to prevent corrosion on ships have been discussed from different perspectives. Kim et al. [10] investigated the effect of anode amount and location on underwater electric

*Corresponding author: kyigit@yildiz.edu.tr

Received: 21.06.2022, Accepted: 19.06.2023

fields for cathodic protection of ship hulls. Koli et al. [11] suggested the aluminum-based (Al-based) sacrificial anode alloy to improve the cathodic protection quality of ship hulls. Kalovelonis et al. [12] designed the impressed current cathodic protection system to protect a container ship from corrosion using the boundary element method. Kramar et al. [13] developed a cathodic protection model for ship hull structures using neural network technology. Clematis et al. [14] analyzed the sacrificial anode cathodic protection system for ships, compared it to the ISO (International Organization for Standardization), and actually implemented corrosion protection schemes. Yiğit and Adanur [15] compared the potential economic effects of Al and zinc (Zn) anodes, which are preferred for sacrificial anode cathodic protection for a cruise ship.

As can be seen in the literature, various studies have been carried out on corrosion and cathodic protection in ships. While some studies focus on passive protection systems to prevent corrosion, others emphasize the importance of active protection systems. It can be said that sacrificial anode cathodic protection is one of the most common methods used for active protection on ships. At this point, the choice of parameters necessary for the ship's cathodic protection design will affect the amount of sacrificial anode. One of the most important parameters affecting cathodic protection is the electrical current density of the structure. To the best of the authors' knowledge, although various cathodic protection designs have been made in the literature, the impact of corrosion current density on the amount of sacrificial anode has not been adequately studied. For this reason, in this study, the effect of corrosion current density on the design of a sacrificial anode cathodic protection system for ship hulls has been analyzed. The aim of this study is to examine and compare the impact of corrosion current density on the sacrificial anode consumption rate of Al during cathodic protection of steel hulls.

2. Material and Method

The technique of eliminating anodic currents from a metal surface by converting the metal to be protected into the cathode of the electrochemical cell to be constructed is known as cathodic protection. The metal can be protected by applying an external current to it or by connecting it to a more active metal, such as a sacrificial anode [16]. In this study, the effect of the corrosion current density parameter on the sacrificial anode cathodic protection design in ship hulls was examined. In the cathodic protection design,

first the total net anode weight needed on the ship was defined. The total net anode weight can be calculated using Equation 1 [17].

$$W = \frac{A \times i \times C \times T}{1000} \quad (1)$$

Here, W is the total net anode weight (kg), A is the protected area of the ship (m²), i is the corrosion current density of the structure (mA/m²), C is the sacrificial anode consumption rate (kg/A/y), and T is the design life of the system (year).

In this study, two different hull areas were considered for cathodic protection design. The protected areas for a bulker and a general cargo were taken as 9406 m² and 1770 m², respectively. These values reflect the average wetted surface areas for the two different ship types [18]. Some metals, such as Al, Zn, and magnesium (Mg), can be preferred as sacrificial anodes in cathodic protection. However, the Mg anode is not recommended for use in ship hulls due to the high release of hydrogen gas during corrosion in seawater (saline or brackish water) environments. In addition, it has been stated that the use of Al anodes in the ship's hull provides an economic advantage over the use of Zn anodes [17], [19]. Therefore, it is assumed that an Al anode alloy is used in the design. For the consumption rate, the value of 3.39 kg/A/y given by the supplier was taken [17]. In general, the design life of the system varies between one and four years [20]. A two-year design life was determined for this study. The required current density of the ship's hull structure depends on different parameters, such as coating specifications, seawater characteristics, and flow conditions. For this reason, evaluations were made, considering different current density values for different situations in the literature. Within the scope of this study, current density values that can be used for cathodic protection of coated ship hulls were explored as far as can be obtained from the literature. The current density values expressed in various studies are shown in Figure 1 [17], [20-23].

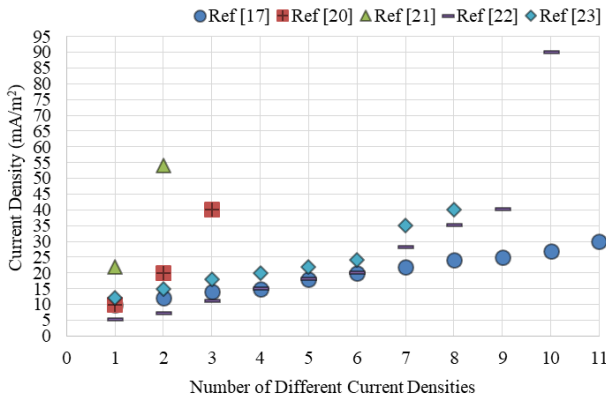


Figure 1. Electrical current density range required for coated ship hulls.

As seen in Figure 1, it can be said that the required current density values for the whole wetted surface area vary between 5 mA/m² and 90 mA/m² according to different situations. The frequency of the current density values expressed in the studies can also be seen in Figure 2.

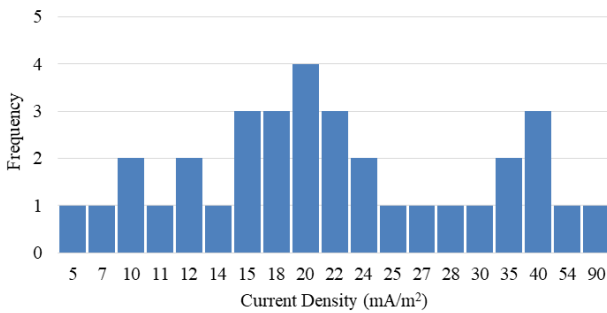


Figure 2. Distribution by current density.

Figure 2 shows that the most common electric current density reference value for a coated hull is 20 mA/m². Figure 1 and Figure 2 also show that the current density requirement of the material to be protected can significantly affect the cathodic protection design. It is therefore critical to obtain as much information as possible about the average current density of each ship's hull. This situation may not mean much for a single ship. However, considering the world maritime fleet, a significant increase in efficiency can be achieved in the use of sacrificial anodes in the process of protecting ships from corrosion. Therefore, in this study, the impact of the corrosion current density parameter on sacrificial anode cathodic protection design has been estimated in terms of two different ship models. Thus, the potential effect of sacrificial anode consumption on ships, depending on the current density parameter, is emphasized.

3. Results and Discussion

In order to show the effect of corrosion current density in the sacrificial anode cathodic protection design, two different ship models are considered. In the cathodic protection calculation, it is assumed that the required corrosion current density value for each ship hull varies between 5 mA/m² and 90 mA/m². In this case, the total net Al anode alloy weight required for cathodic protection is calculated for two ship models and shown in Figure 3.

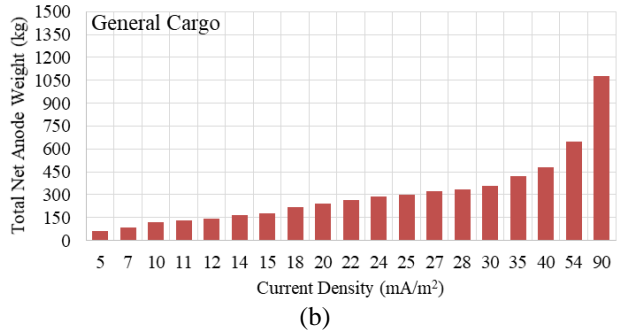
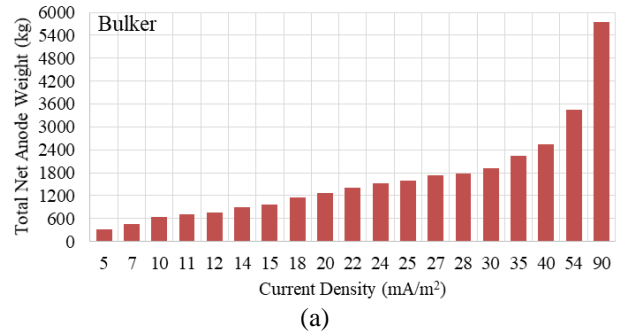


Figure 3. Total net anode weight depending on current density.

Figure 3(a) shows that the total net anode weight required to protect the hull of the bulker is calculated as 319 kg if the corrosion current density is taken as 5 mA/m². When the corrosion current density is taken as 90 mA/m², this amount is 5740 kg. Figure 3(b) shows that if the corrosion current density varies between 5 mA/m² and 90 mA/m² on the general cargo, the total net anode requirement is between 60 kg and 1080 kg. The difference between these two extreme corrosion current densities gives remarkable results in terms of efficiency. For this reason, a calculation to be made over the corrosion current density value (20 mA/m²), which was determined to be emphasized more as a result of the literature study, may give more reasonable results. If the corrosion current density is taken as 20 mA/m², the total net amount of anode required for bulker and general cargo is 1275 kg and 240 kg, respectively.

The percent change in total net anode weight for different corrosion current densities compared to 20 mA/m² in cathodic protection calculations is shown in Figure 4.

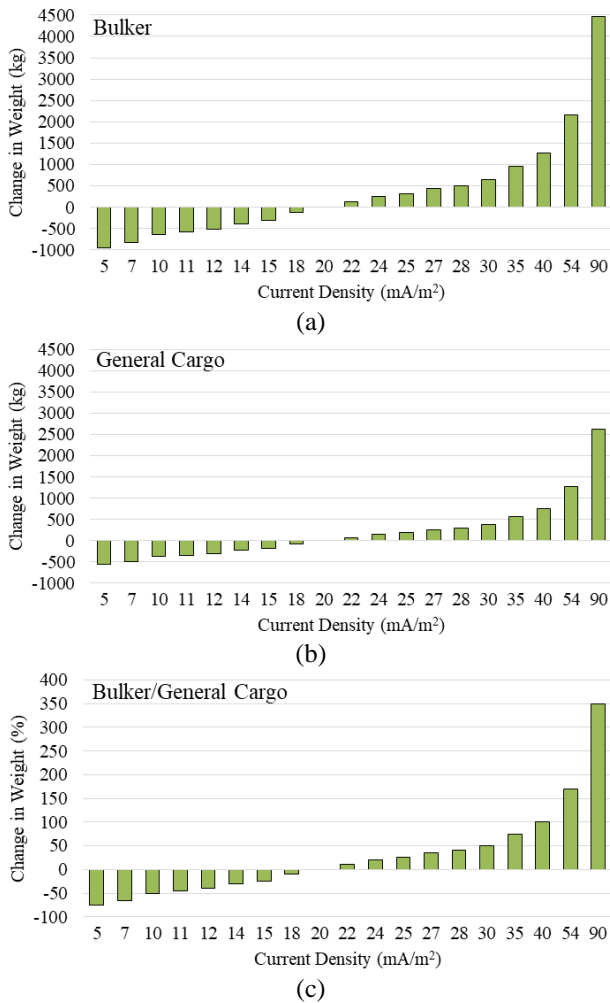


Figure 4. Change in anode use for different corrosion current densities compared to 20 mA/m².

Figures 4(a) and (b) show that choosing a corrosion current density of less than 20 mA/m² in the cathodic protection calculation reduces the total amount of anode required for the bulker and general cargo hulls. In the opposite case, the amount of sacrificial anode required will increase. As seen in Figure 4(c), this means that the amount of sacrificial anode to be used is reduced by 75% when the corrosion current density drops from 20 mA/m² to 5 mA/m² for both ship types. If the corrosion current density rises from 20 mA/m² to 90 mA/m², the increase in the amount of sacrificial anode will be 350%.

In this study, the effect of corrosion current density change on anode consumption is tried to be explained by taking average bulker and general cargo ship hulls as a reference. Thus, the effect of this

parameter, which is used in the calculation of sacrificial anode cathodic protection in ships, on anode consumption is emphasized. As seen in Figure 1, the corrosion current density of the ship hull may vary depending on different parameters such as sea water, material, and environment. Also, Figure 3 shows that the change in this parameter significantly changes the sacrificial anode consumption. Here, it is possible to say that while some studies emphasize generally accepted values, in others, more specific values are emphasized according to ship types. Therefore, in order to determine the average Al anode alloy consumption values for these two ships, [23] can also be taken into account. In other words, if the corrosion current density is taken as 15 mA/m², the total net amount of anode required for bulker and general cargo is 959 kg and 181 kg, respectively. Moreover, each 1 mA/m² change in the corrosion current density parameter will decrease or increase the amount of anode used in selected bulker and general cargo hulls by 64 kg and 12 kg, respectively.

In the design of sacrificial anode cathodic protection for ships, attention should be paid to the anode distribution in the hulls as well as the amount of sacrificial anode. The anodes should be distributed symmetrically on both sides of the wetted surface area to protect the entire ship and obtain good current distribution. Placing a large number of small anodes evenly spaced along the hull can also further increase efficiency. The anodes are placed on the hull at intervals of about 6 m. About 25–30% of the anodes to be used are also placed on the stern. In the hull, flat anodes should be preferred to minimize flow resistance [20], [22]. To summarize, the corrosion of the ship's hull and the design and application examples of sacrificial anode cathodic protection to prevent this corrosion are illustrated, respectively, in Figure 5 [24]-[26].

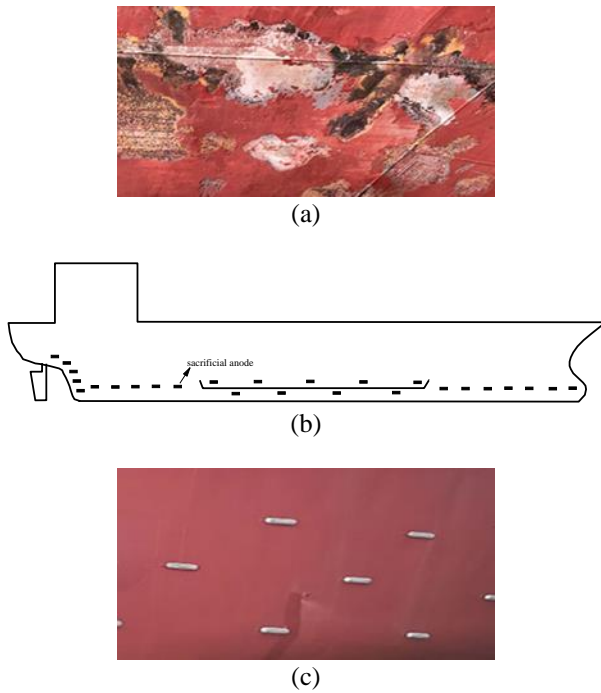


Figure 5. Ship hull corrosion and sacrificial anode cathodic protection.

As a result, corrosion-related deterioration in ship hulls is highly dependent on environmental factors, seawater compositions, and the protection quality of steel structures. Many parameters, such as deterioration in the protective layer of the ship's hull in contact with seawater, changes in the temperature, flow rate, and chemical components of seawater, can affect the rate of corrosion. The uncertainties in these parameters make it difficult to determine the amount of anode to be used in the design of the sacrificial anode cathodic protection system on board. There are international organizations that have published specifications that address these variables, and they may offer slightly different values. Therefore, it may not be appropriate to state whether the specified characteristics are strictly true or false, as the methods for collecting the calculated data may differ [27]. As a result of shipyards' long years of experience, adaptation of previous cathodic protection systems to similar ships may also affect sacrificial anode consumption [14]. Such reasons may indirectly cause the calculated amount of sacrificial anode to be less or more. Obviously, the corrosion current density values specified in the literature for different situations make a great contribution to reducing such errors. To minimize these errors, various solutions can also be evaluated. e.g., for cathodic protection optimization, physical modeling technique and computational simulation techniques such as boundary element, finite difference, and finite

element methods can be used [28], [29]. Since electrochemical protection techniques depend on the nature of the material and ambient conditions, the cathodic protection design can be supported by experimental studies that take into account the operating conditions of the ship [30]. Thus, it can contribute to reducing the global effects of corrosion.

4. Conclusion and Suggestions

In this study, the impact of the corrosion current density parameter on sacrificial anode cathodic protection design in ships was investigated. For the calculation of cathodic protection, a bulker model with a 9406 m² hull to be protected and a general cargo model with a 1770 m² hull to be protected were considered. Then, the amount of Al alloy anode to be used for each ship model was calculated if the electrical current density of the coated hull changed between 5 and 90 mA/m². As a result, for the 5–90 mA/m² range, the amount of sacrificial anode used in the bulker and general cargo over the two-year design life is expected to range between 319–5740 kg and 60–1080 kg, respectively. In addition, it was concluded that each 1 mA/m² change in current density will change the anode usage amount by 64 kg in bulker and 12 kg in general cargo.

It can be stated that the evaluation of the corrosion current density parameter for each ship as much as possible in the cathodic protection design will contribute to the increase in efficiency in this area. In this context, increasing experimental studies as well as computational simulation techniques can contribute to the improvement of reference parameters. In addition, examining the historical navigation plans of existing ships can also reduce the error in the cathodic protection calculation. Because if the ship is constantly navigating the same route, cathodic protection parameters can be determined by considering the environmental conditions of that route. In this way, a clearer approach can be presented for the reference value of the corrosion current density parameter to be considered during the replacement phase of the sacrificial anodes on the ship. For new ships under construction, estimating the corrosion current parameters for the conditions of that area may be a more efficient approach if the ship is to be operated on a particular course. Thus, the anode consumption in the cathodic protection design can be optimized, and the negative effects of corrosion can be reduced further.

Acknowledgment

This work has been supported by Yildiz Technical University Scientific Research Projects Coordination Unit under project number FLO-2021-4656

Contributions of the authors

All authors contributed equally to the study.

Conflict of Interest Statement

There is no conflict of interest between the authors.

Statement of Research and Publication Ethics

The study is complied with research and publication ethics

References

- [1] M. Hashim, K. Mohammed, and N. Hamadi, "Modeling and control of impressed current cathodic protection (ICCP) system," *Iraqi Journal for Electrical and Electronic Engineering*, vol. 10, no. 2, pp. 80–88, 2014.
- [2] C. M. Hansson, "The impact of corrosion on society," *Metallurgical and Materials Transactions A*, vol. 42, no. 10, pp. 2952–2962, 2011.
- [3] T. Koyun and Ş. Y. Güven, "Galvanik korozyon ve alüminyum-bakır üzerine deneysel bir çalışma," *Mühendislik Bilimleri ve Tasarım Dergisi*, vol. 5, no. 1, 2017.
- [4] A. Kadhim, A. A. Al-Amiery, R. Alazawi, M. K. S. Al-Ghezi, and R. H. Abass, "Corrosion inhibitors. A review," *International Journal of Corrosion and Scale Inhibition*, vol. 10, no. 2, pp. 54-67, 2021.
- [5] X. Li, D. Zhang, Z. Liu, Z. Li, C. Du, and C. Dong, "Materials science: Share corrosion data," *Nature*, vol. 527, no. 7579, pp. 441–442, 2015.
- [6] M. Shehadeh and I. Hassan, "Study of sacrificial cathodic protection on marine structures in sea and fresh water in relation to flow conditions," *Ships and Offshore Structures*, vol. 8, no. 1, pp. 102–110, 2013.
- [7] Ş. Şanlıer, "Gemilerde korozyon ve korozyondan korunma yöntemleri," *GAP Matematik, Mühendislik, Fen ve Sağlık Bilimleri Kongresi*, Şanlıurfa, Türkiye, pp.1-10, 2018.
- [8] H. Elçiçek, A. C. Karaoğlanlı, and B. Demirel, "Gemicilik endüstrisinde korozyon problemi ve katodik koruma uygulamaları," *In 6th International Advanced Technologies Symposium*, pp. 16-18, 2011.
- [9] S. Sutrisno, A. Bastari, and O. S. Suharyo, "The comparison study of cathodic protection system of victim anoda between Zink anoda (Zn) and Aluminum anoda (Al)," *International Journal of Progressive Sciences and Technologies*, vol. 24, no. 1, pp. 183-193, 2021.
- [10] Y.-S. Kim, S. K. Lee, and J.-G. Kim, "Influence of anode location and quantity for the reduction of underwater electric fields under Cathodic protection," *Ocean Engineering*, vol. 163, pp. 476–482, 2018.
- [11] P. M. Koli, A. K. Satapathy, G. S. Ambre, and G. Gunasekaran, "Eco-friendly sacrificial anode for corrosion mitigation of steel and aluminium alloy based ship hull", *CORCON, 23rd–26th September*, Mumbai, India, pp. 1-5, 2019.
- [12] D. T. Kalovelonis, D. C. Rodopoulos, T. V. Gortsas, D. Polyzos, and S. V. Tsinopoulos, "Cathodic protection of a container ship using a detailed BEM model," *Journal of Marine Science and Engineering*, vol. 8, no. 5, p. 359, 2020.
- [13] V. Kramar, A. Rodkina, O. Ivanova, S. Chernyi, and A. Zinchenko, "Analysis Technology and cathodic protection for hull structures of ships and floating facilities," *Inventions*, vol. 6, no. 4, p. 74, 2021.
- [14] D. Clematis, A. Marroccu, M. Panizza, and A. Barbucci, "A critical analysis on the current design criteria for cathodic protection of ships and superyachts," *Materials*, vol. 15, no. 7, p. 2645, 2022.
- [15] K. Yiğit and M. Adanur, "Comparison of the potential effects of using aluminum and zinc anode in galvanic anode cathodic protection design for a cruise ship," *In 2. International Mediterranean Scientific Research and Innovation Congress*, Girne, K.K.T.C., pp. 954, 2022.
- [16] E. Karataş and L. Seyfi, "Afyon bölgesinde yer alan doğalgaz boru hattı üzerindeki AC enterferans seviyelerinin ölçülmesi ve AC korozyon ihtimalinin değerlendirilmesi," *Uluslararası Bilimsel Çalışmalarda Yenilikçi Yaklaşımlar Sempozyumu*, Samsun, Türkiye, pp. 645-649, 2018.
- [17] T. Tezdogan and Y. K. Demirel, "An overview of marine corrosion protection with a focus on cathodic protection and coatings," *Brodogradnja: Teorija I Praksa Brodogradnje I Pomorske Tehnike*, vol. 65, no. 2, pp. 49-59, 2014.

- [18] C. S. Moser, T. P. Wier, J. F. Grant, M. R. First, M. N. Tamburri, G. M. Ruiz, A. W. Miller, and L. A. Drake, "Quantifying the total wetted surface area of the World Fleet: A first step in determining the potential extent of ships' biofouling," *Biological Invasions*, vol. 18, no. 1, pp. 265–277, 2015.
- [19] L. Yan, G.-L. Song, and D. Zheng, "Magnesium alloy anode as a smart corrosivity detector and intelligent sacrificial anode protector for reinforced concrete," *Corrosion Science*, vol. 155, pp. 13–28, 2019.
- [20] A. Bahadori, "Design considerations on cathodic protection for buried pipelines and marine structures, cathodic corrosion protection systems. A guide for oil and gas industries," *USA: Gulf Professional Publishing*, 2014.
- [21] U.S. Naval Academy, "Appendix: Cathodic Protection Design – 1," 1996.
- [22] American Bureau of Shipping, "Guidance notes on cathodic protection of ships," 2017.
- [23] Netherlands National Water Board, "Sacrificial anodes, merchant shipping and fisheries," 2008.
- [24] C. Georgios, T. Iason, and K. Konstantinos, "MaVeCoDD dataset: Marine vessel hull corrosion in dry-dock images", *Mendeley Data VI*, 2021.
- [25] Marine Cathodic Protection Systems, "Galvanic anode cathodic protection design," 2023. [Online]. Available: <http://www.z-guard.co.uk/anodeplan.html>. [Accessed: Mar. 9, 2023].
- [26] Altın Çıpa Denizcilik, "Galvanic anode cathodic protection application," 2023. [Online]. Available: <https://altincipa.com.tr/galeri/>. [Accessed: Mar. 9, 2023].
- [27] R. Singh, "Corrosion control for offshore structures: Cathodic protection and high-efficiency coating," *Gulf Professional Publishing*, 2014.
- [28] L. Xu, Y. Xin, L. Ma, H. Zhang, Z. Lin, and X. Li, "Challenges and solutions of cathodic protection for marine ships," *Corrosion Communications*, vol. 2, pp. 33–40, 2021.
- [29] I. Gurrappa, I. V. Yashwanth, and I. Mounika, "Cathodic protection technology for protection of naval structures against corrosion," *Proceedings of the National Academy of Sciences, India Section A: Physical Sciences*, vol. 85, no. 1, pp. 1–18, 2014.
- [30] A. S. Oryshchenko and Y. L. Kuzmin, "Development of electrochemical cathodic protection against corrosion of ships, vessels, and offshore structures," *Inorganic Materials: Applied Research*, vol. 6, no. 6, pp. 612–625, 2015.



Determining The Number of Principal Components with Schur's Theorem in Principal Component Analysis

Cihan KARAKUZULU¹, İbrahim Halil GÜMÜŞ^{2*}, Serkan GÜLDAL³,
Mustafa YAVAŞ⁴



¹Adiyaman University, Graduate Education Institute, Department of Mathematics, Adiyaman

²Adiyaman University, Faculty of Arts and Sciences, Department of Mathematics, Adiyaman

³Adiyaman University, Graduate Education Institute, Department of Physics, Adiyaman

⁴Adiyaman University, Vocational School of Technical Sciences, Department of Computer Technologies, Adiyaman
(ORCID: 0000-0002-3027-6927) (ORCID: 0000-0002-3071-1159) (ORCID: 0000-0002-4247-0786)
(ORCID: 0000-0002-9111-9095)

Keywords: Principal component analysis, Majorization theory, Schur's theorem, Positive semidefinite matrices, Eigenvalues.

Abstract

Principal Component Analysis is a method for reducing the dimensionality of datasets while also limiting information loss. It accomplishes this by producing uncorrelated variables that maximize variance one after the other. The accepted criterion for evaluating a Principal Component's (PC) performance is $\frac{\lambda_j}{tr(S)}$ where $tr(S)$ indicates the trace of the covariance matrix S . It is standard procedure to determine how many PCs should be maintained using a specified total variance. In this study, the diagonal elements of the covariance matrix are used instead of the eigenvalues to determine how many PCs need to be considered to obtain the defined threshold of the total variance. For this, an approach which uses one of the important theorems of majorization theory is proposed. Based on the tests, this approach lowers computational costs.

1. Introduction

In many disciplines, high-dimensional datasets are becoming more common. Although researchers intend to collect more detailed information with every added dimension, higher dimensional datasets have several drawbacks. They require more sophisticated methods to analyze, interpret, and visualize. Even processing is impractical or impossible in some cases. Additionally, storing the data and related costs, such as maintenance and security, are more expensive. However, these drawbacks are avoidable with no considerable information lost. One of the solutions is the reorganization of the dataset (a.k.a. dimension reduction). Thus, the dimensions can be described by a linear combination of newly defined dimensions since in high-dimensional data, dimensions are generally correlated and the data has a lower dimensional structure in essence.

Dimension reduction, taking the correlation of dimensions into account, is the process of obtaining a representation of the data that has lower dimensions. Dimensionality can be reduced by using the Principal Component Analysis (PCA) algorithm, which is suggested by [1] and [2]. Although more than 100 years have passed, it is still a widely used data reduction method. Its objective is to preserve as much variability as possible while lessening the dataset's dimensionality [3]. Namely, PCA extracts new variables that are linear functions of the variables in the original dataset for maximized variance. These new variables are called Principal Components (PCs). The spectral decomposition of the covariance matrix, which defines the PCs' variance by their eigenvalues and their directions by their eigenvectors, is the key to PCA. In other words, the process of obtaining PCs is mathematically an eigenvalue/eigenvector problem. Since the covariance matrix's eigenvectors and eigenvalues are used to define PCA, many matrix

*Corresponding author: igumus@adiyaman.edu.tr

Received: 17.07.2022, Accepted: 23.02.2023

analysis methods can be used to improve the quality of the newly defined dataset.

Despite being frequently used for unsupervised linear dimensionality reduction and visualization, PCA has also been employed to solve statistical problems like regression, clustering, and nonlinear dimensionality reduction [4-6]. Because the utility of PCA has been discovered in many different scientific fields, it is called by many different names today. In numerical analysis and matrix analysis, it is known as Singular Value Decomposition, Karhunen-Loève transforms in signal processing, and characteristic vector analysis in the physical sciences. Thurstone and other psychologists pioneered the development of Factor Analysis (FA) in the 1930s [7]. This is worth mentioning because FA and PCA are very related, and these two methods are sometimes confused. Incorrectly, these two names are used interchangeably.

In recent years, important research has been done using PCA. In [8], a method for investigating systematic co-variation of vowels has been presented by using PCA. In [9], an application of principal component analysis has been obtained to reduce the dimensionality of variables representing the speech signal. The obtained results have been used for the disturbed and fluent speech recognition processes. In [10], a new combination strategy based on PCA to increase the predictability of crude oil futures market returns has been proposed. In [11], the status of PCA in the area of ECG signal processing has been reviewed. The use of PCA for spectral data reduction and colorant estimation has been illustrated in [12]. For interested readers, there are many excellent works investigating the various facets of PCA [13-16]. In addition, there are works in the literature examining how many principal components should be in PCA. For example, see [17-20] and the references therein.

In this study, a method is proposed to help select the right number of dimensions in the newly defined dataset quickly and efficiently. In section 2, the method and its theoretical basis are given. In section 3, the proposed method is tested for various datasets and extreme cases. In the last section, concluding remarks and future works are presented.

2. Material and Method

As a data analysis tool, PCA involves a dataset with observations on p features for n samples. These data values define an $n \times p$ data matrix \mathbf{X} . The j^{th} column of \mathbf{X} is the vector \mathbf{x}_j of observations on the j^{th} feature. The purpose of PCA is to find a linear combination of the columns of the matrix \mathbf{X} that has the optimal variance. These linear combinations are

obtained by $\mathbf{X}\mathbf{a}$ such that $\mathbf{a} = [a_1, a_2, \dots, a_p]^T$ is a $p \times 1$ vector where T stands for transpose. Finding the linear combination which has the optimal variance is equivalent to the computation of a p -dimensional vector that maximizes the $\mathbf{a}^T \mathbf{S} \mathbf{a}$ where \mathbf{S} is data covariance matrix, namely $Var(\mathbf{X}\mathbf{a}) = \mathbf{a}^T \mathbf{S} \mathbf{a}$. It is worth noting that increasing the magnitude of the vector arbitrarily increases variance. Therefore, $\|\mathbf{a}\| = 1$ is taken, resulting in a constrained optimization problem in which we look for the data in the most variable direction. This constrained optimization problem can be written in the following form

$$\begin{aligned} \max_{\mathbf{a}} \mathbf{a}^T \mathbf{S} \mathbf{a} \\ \text{s. t. } \|\mathbf{a}\|^2 = 1 \end{aligned} \tag{1}$$

For solving this optimization problem, we write the Lagrangian

$$L = \mathbf{a}^T \mathbf{S} \mathbf{a} + \lambda(1 - \mathbf{a}^T \mathbf{a}) \tag{2}$$

By computing the partial derivative of L with respect to \mathbf{a} and λ and equating these partial derivatives to $\mathbf{0}$, we get

$$\begin{aligned} \mathbf{S} \mathbf{a} &= \lambda \mathbf{a} \\ \mathbf{a}^T \mathbf{a} &= 1. \end{aligned} \tag{3}$$

So, the Lagrange multiplier acts as the corresponding eigenvalue and must be an eigenvector of the data covariance matrix \mathbf{S} . By multiplying both sides of $\mathbf{S} \mathbf{a} = \lambda \mathbf{a}$ with \mathbf{a}^T from the left side, the following equation is obtained.

$$Var(\mathbf{X}\mathbf{a}) = \mathbf{a}^T \mathbf{S} \mathbf{a} = \mathbf{a}^T \lambda \mathbf{a} = \lambda \tag{4}$$

This means that the eigenvalue associated with the basis vector that spans this subspace is equal to the variance of the data projected onto a one-dimensional subspace. As a result, the selected basis was related to the greatest eigenvalue of the data covariance matrix to optimize the variance of the low-dimensional representation. Since \mathbf{S} is a symmetric matrix, it has exactly p real eigenvalues. The eigenvectors corresponding to these eigenvalues can be constructed to create an orthonormal set of vectors. By adding restrictions of orthogonality of different coefficient vectors on the Lagrange multipliers method, we can obtain all eigenvectors of \mathbf{S} . These answers to the problem of producing up to p new linear combinations $\mathbf{X}\mathbf{a}_k = \sum_{j=1}^p a_{jk} \mathbf{x}_j$ and maximizing variance that is uncorrelated with earlier linear combinations [3].

The linear combinations $\mathbf{X}\mathbf{a}_k$ are the Principal Components (PCs) of the dataset. Sometimes, many researchers also use the term PCs when mentioning to the eigenvectors \mathbf{a}_k . The variance associated with the set of retained PCs can be used to assess the quality of any q -dimensional subspace. The trace of the covariance matrix \mathbf{S} is the sum of variances of the p original variables. It is simple to prove that this value is exactly the sum of the variances of all PCs. As a result, the accepted gauge of a PC's quality is $\frac{\lambda_j}{tr(\mathbf{S})}$ where $tr(\mathbf{S})$ denotes the trace of matrix \mathbf{S} . Determination of how many PCs should be preserved is usual practice to utilize a predetermined percentage of the total variance. This predetermined percentage is commonly 70% [21]. As noticed, in order to obtain the predetermined percentage of the total variance, we need to find all the eigenvalues of the matrix. Then, it is necessary to identify the $\frac{\lambda_j}{tr(\mathbf{S})}$ values whose sum exceeds this predetermined percentage of the total variance.

It is known that the eigenvalues of a matrix are obtained by finding the roots of the characteristic polynomial of that matrix. It is not possible to obtain these roots analytically for matrices larger than 4×4 . Based on the Abel-Ruffini theorem, for polynomials of degree 5 or more, there is no algebraic solution. As a result, eigenvalues are obtained by using numerical methods. However, this means extra time for a data analyst who decides how many PCs to take based on finding the $\frac{\lambda_j}{tr(\mathbf{S})}$.

Now let's introduce the concept of majorization, which allows us to compare two vectors and observe which has "less spread out" components. Comparison of two vectors frequently leads to inequalities that can be expressed as majorization relations. Let $z = (z_1, z_2, \dots, z_n) \in \mathbb{R}^n$ and z^\downarrow be the vector obtained by repositioning the coordinates of z in decreasing order. Thus if $z^\downarrow = (z_1^\downarrow, z_2^\downarrow, \dots, z_n^\downarrow) \in \mathbb{R}^n$, then $z_n^\downarrow \leq \dots \leq z_2^\downarrow \leq z_1^\downarrow$. For $x, y \in \mathbb{R}^n$, y majorizes x (or x is majorized by y), written as $x < y$, if

$$\sum_{j=1}^k x_j^\downarrow \leq \sum_{j=1}^k y_j^\downarrow \quad (5)$$

for $1 \leq k < n$ and

$$\sum_{j=1}^n x_j^\downarrow = \sum_{j=1}^n y_j^\downarrow. \quad (6)$$

If inequality is put in place of the equality

$$\sum_{j=1}^n x_j^\downarrow \leq \sum_{j=1}^n y_j^\downarrow, \quad (7)$$

we state that y weakly majorizes x , and is indicated by $x <_w y$.

Majorization theory is a crucial tool that enables us to solve problems in various disciplines. One of these disciplines is matrix theory. Let's write the diagonal elements and eigenvalues of a $n \times n$ symmetric matrix \mathbf{X} as vectors, respectively, by

$$d(\mathbf{X}) = (d_1(\mathbf{X}), d_2(\mathbf{X}), \dots, d_n(\mathbf{X})) \quad (8)$$

and

$$\lambda(\mathbf{X}) = (\lambda_1(\mathbf{X}), \lambda_2(\mathbf{X}), \dots, \lambda_n(\mathbf{X})) \quad (9)$$

Note that the components of these vectors are always arranged in decreasing order throughout the paper. The following theorem which is known as Schur's Theorem has a key role in our study, which can be found in [22].

Theorem: Let \mathbf{X} be a $n \times n$ symmetric matrix. Then

$$d(\mathbf{X}) < \lambda(\mathbf{X}). \quad (10)$$

This theorem says that

$$\begin{aligned} d_1(\mathbf{X}) &\leq \lambda_1(\mathbf{X}) \\ d_1(\mathbf{X}) + d_2(\mathbf{X}) &\leq \lambda_1(\mathbf{X}) + \lambda_2(\mathbf{X}) \\ d_1(\mathbf{X}) + d_2(\mathbf{X}) + \dots + d_n(\mathbf{X}) &= \lambda_1(\mathbf{X}) + \lambda_2(\mathbf{X}) \\ &+ \dots + \lambda_n(\mathbf{X}) \\ &= tr(\mathbf{X}) \end{aligned} \quad (11)$$

for symmetric matrix \mathbf{X} . Namely, the total of the largest k eigenvalues of a symmetric matrix is bounded below by the total of the largest k diagonal elements of that matrix. Considering the fact that the covariance matrix is a symmetric matrix, if we want to use a predetermined percentage of the total variance, instead of calculating the total of the k largest eigenvalues of the covariance matrix that exceed this value, it will be sufficient to calculate the total of the k largest diagonal elements of the covariance matrix that exceeds this value. Using diagonal elements instead of calculating eigenvalues will provide us processing speed and convenience.

In this study, the diagonal elements of the covariance matrix are used instead of the eigenvalues. For this, we will make use of the majorization theory, which is commonly used to obtain inequalities. Thus, before starting the PCA process, the predetermined

percentage of the total variance will be obtained more quickly with the help of the diagonal elements. The approach is validated by numerical simulations (See

Hata! Başvuru kaynağı bulunamadı.) Let's illustrate this fact with examples in the following section.

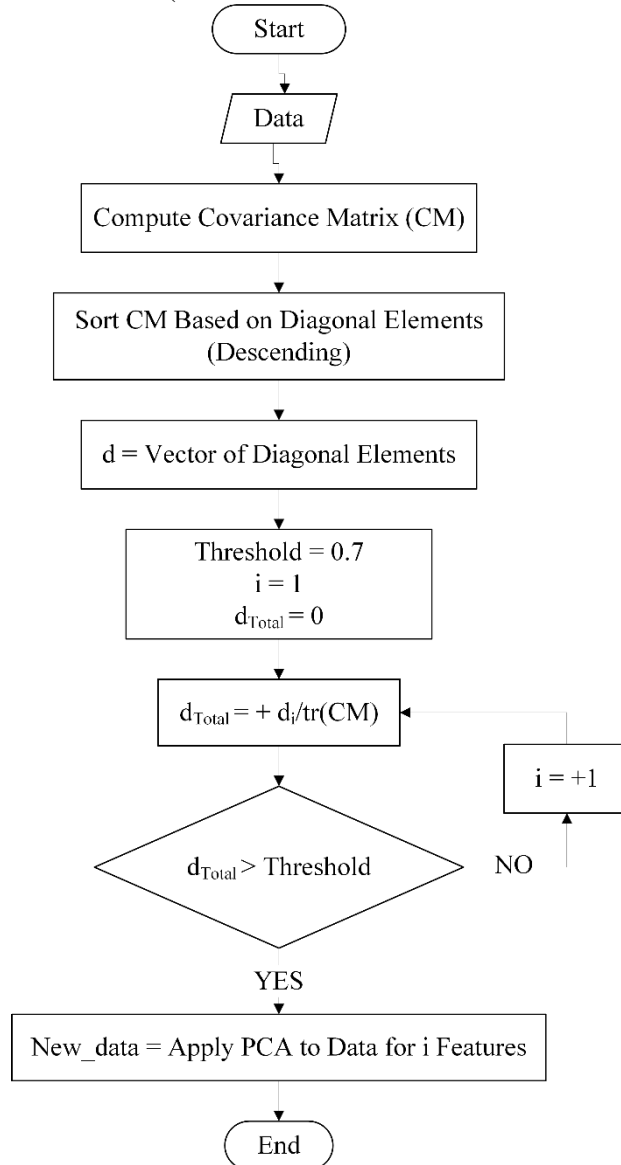


Figure 1. Flowchart of the proposed approach

3. Results and Discussion

The proposed approach is tested for 5 different datasets. Also, the method is tested for symmetric

matrices up to 100×100 . Yeast dataset is selected to exemplify the approach [23, 24]. Since this dataset has 8 features, the covariance matrix is an 8×8 which is obtained as

$$Y = \begin{pmatrix} 355.953 & 82.8840 & -21.243 & 21.7097 & 0.44443 & -0.8670 & 4.14396 & -17.0248 \\ 82.8840 & 325.978 & -14.622 & 22.9344 & 0.33581 & -4.3622 & 7.31506 & -7.0348 \\ -21.243 & -14.622 & 258.660 & -0.8992 & -0.1108 & -2.1924 & -2.49194 & 3.07863 \\ 21.7097 & 22.9344 & -0.8992 & 206.712 & -0.0527 & -0.8870 & -10.7392 & -2.3823 \\ 0.44443 & 0.33581 & -0.1108 & -0.0527 & 0.23378 & -0.0296 & 0.34835 & -0.2966 \\ -0.8670 & -4.3622 & -2.1924 & -0.8870 & -0.0296 & 50.7703 & -1.0152 & -1.6376 \\ 4.14396 & 7.31506 & -2.4919 & -10.739 & 0.34835 & -1.0152 & 227.085 & 8.58366 \\ -17.024 & -7.0348 & 3.07863 & -2.3823 & -0.2966 & -1.6376 & 8.58366 & 117.485 \end{pmatrix}$$

When we computed the components of the diagonal elements and eigenvalues of this covariance matrix in descending order, we get the following two vectors

$$d(\mathbf{Y}) = (355.953, 325.978, 258.660, 227.085, 206.712, 117.485, 50.7703, 0.23378) \quad (12)$$

and

$$\lambda(\mathbf{Y}) = (434.575, 259.07, 253.696, 231.774, 197.33, 115.579, 50.6234, 0.231774) \quad (13)$$

As noticed,

$$355.953 \leq 434.575$$

$$355.953 + 325.978 \leq 434.575 + 259.07$$

$$355.953 + 325.978 + 258.660 \leq 434.575 + 259.07 + 253.696 \quad (14)$$

⋮

$$\begin{aligned} & 355.953 + 325.978 + 258.660 + 227.085 + 206.712 + 117.485 + 50.7703 \\ & \quad + 0.23378 \\ & = 434.575 + 259.07 + 253.696 + 231.774 + 197.33 + 115.579 + 50.6234 \\ & \quad + 0.231774 \end{aligned}$$

Both sides of the last equality give us the trace of the covariance matrix, $tr(\mathbf{Y}) = 1542,879$. Cumulative percentage values of sums of $\frac{\lambda_j(\mathbf{Y})}{tr(\mathbf{Y})}$ and $\frac{d_j(\mathbf{Y})}{tr(\mathbf{Y})}$ for $j = 1, 2, \dots, 8$ are depicted in **Hata! Başvuru kaynağı bulunamadı..**

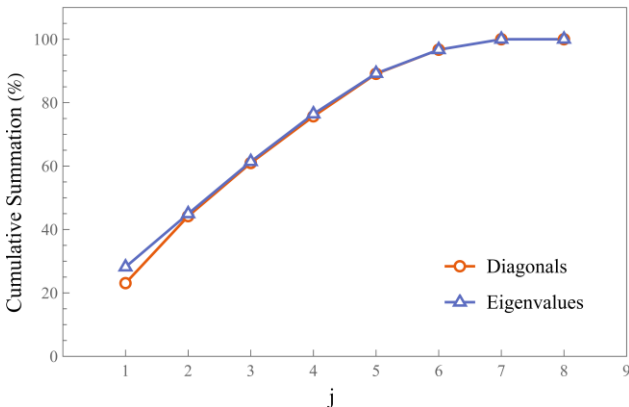


Figure 2. Cumulative summation of eigenvalues and diagonals are shown in percentage for Yeast dataset.

It is observed that the cumulative sums of eigenvalues and diagonals are almost the same. In the specified example, the ratio of the sum of the four largest eigenvalues to the trace of the covariance matrix is approximately 76% which is higher than 70%. This result shows that the first 4 largest eigenvalues (i.e. 4 PCs) should be taken for no considerable information lost. Additionally, corresponding diagonal values are

approximately 76%. Therefore, instead of computing how many eigenvalues provide the predetermined percentage of the total variance (70%), as claimed in the previous sections, we can utilize the information from the diagonal elements of the covariance matrix.

To highlight the value of the proposed approach, computational times of eigenvalue and diagonal calculations are compared for 5 datasets. The list of datasets is given in Table 1. Here, Yeast is a medical dataset and consists of a protein-protein network [23, 24]. Accelerometer is used to estimate the engine failure time. Data obtained from the vibrations of the cooling fan with weights on its blades. It can be used for classification and other purposes for situations requiring vibration analysis [25]. Breast Cancer Coimbra is a medical dataset, anthropometric data and parameters that can be collected in routine blood analysis. These data indicate the presence and absence of cancer and are all quantitative data [26]. Cardiotocography is also a medical dataset, consisting of measurements of fetal heart rate and uterine contraction properties in cardiotocograms. This dataset is classified and labeled by expert obstetricians [27]. Combined Cycle Power Plant dataset is the data collected from a power plant operating at full load for six years. It is aimed to estimate the hourly net electrical energy output of the facility from the hourly average Temperature, Ambient Pressure, Relative Humidity and Exhaust

Vacuum characteristics [28, 29]. All features of datasets consist of numeric values. They are frequently used in machine learning classification and regression studies. The datasets are collected from different fields. Variation in the number of features requires different computation times. The

computation efforts are shown in Figure 1. The results show the computation with eigenvalues requires more time than diagonals in every case. This difference is as great as 30 times for Cardiocography datasets at maximum because of the higher number of features.

Table 1. 5 different datasets are selected from various subjects

Datasets	Number of features	Number of samples
Yeast [23, 24]	8	1484
Accelerometer [25]	5	153000
Breast Cancer Coimbra [26]	10	116
Cardiotocography [27]	23	2126
Combined Cycle Power Plant [28, 29]	4	9568

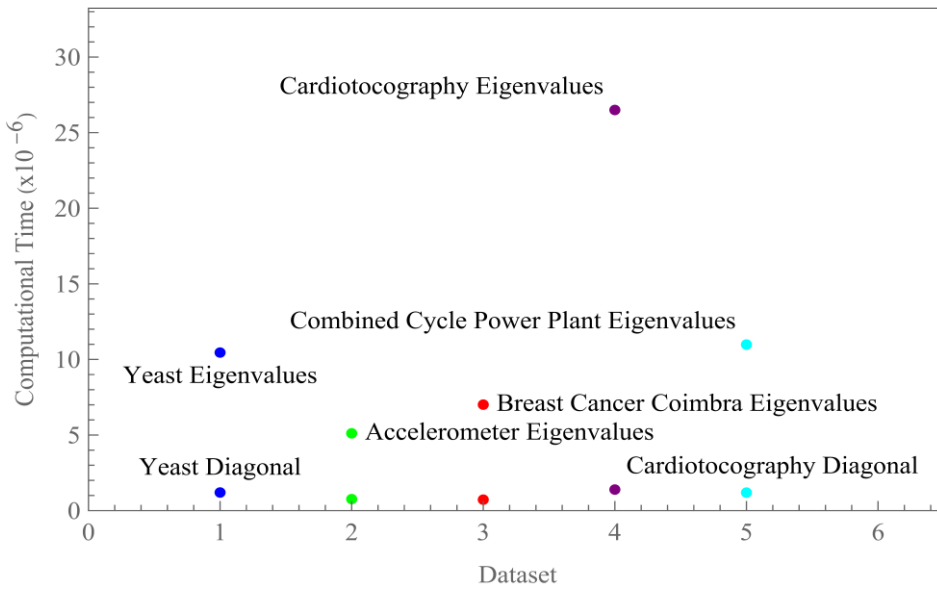


Figure 1. Computation time varieties for datasets, but the computation of eigenvalues requires more time than the computation of diagonal elements.

The covariance matrix of the listed datasets changes from 4×4 to 25×25 . Computation of eigenvalues is relatively efficient. However, it is a known fact that increasing the size of the matrices will complicate the calculation of their eigenvalues. To illustrate this situation, let's take a randomly chosen

positive semi-definite matrix (for an $n \times n$ matrix M , $M^T M$ is always positive semidefinite, and elements in [1,5]). Increment in the size of this matrix regularly up to 100×100 shows that computation with diagonals has linear complexity and eigenvalues have exponential complexity.

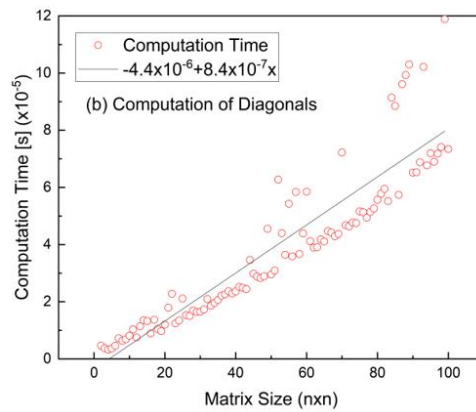
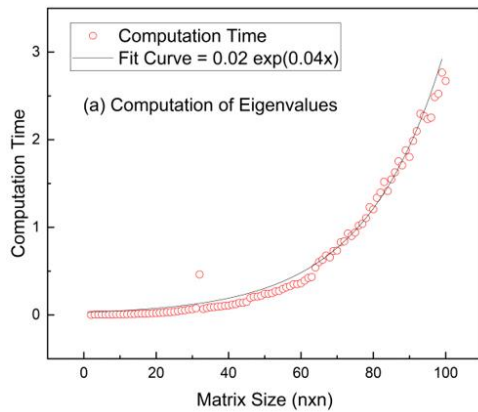


Figure 2. Required computational time is shown for eigenvalues (a), and diagonals (b).

4. Conclusion

In Principal Component Analysis, it is a standard procedure to determine how many Principal Components should be retained using a predetermined percentage of the total variance. For this, it is necessary to calculate all the eigenvalues of the covariance matrix. Then the necessary step is to identify how many of the largest eigenvalues we need so that the cumulative sum of the $\frac{\lambda_j}{tr(S)}$ exceeds the specified threshold. However, calculating the eigenvalues of the covariance matrix brings a computational cost. In this study, this process was done by using the diagonal elements of the covariance matrix instead of the eigenvalues of the covariance matrix. For this, Schur's theorem, which is well known in majorization theory, was used. The time savings of using diagonal elements was demonstrated using five different datasets. In addition, the increase

in time required for computations as a result of increasing the matrix size is illustrated using randomly taken positive semi-definite matrices. As a result, it is seen that it is advantageous to use diagonal elements instead of calculating eigenvalues.

Contributions of the Authors

The authors confirm that the contribution is equally for this paper.

Conflict of Interest Statement

There is no conflict of interest between the authors of the article.

Statement of Research and Publication Ethics

The study complies with research and publication ethics.

References

- [1] K. Pearson, "LIII. On lines and planes of closest fit to systems of points in space," *The London, Edinburgh, and Dublin philosophical magazine and journal of science*, vol. 2, no. 11, pp. 559-572, 1901.
- [2] H. Hotelling, "Analysis of a complex of statistical variables into principal components," *Journal of educational psychology*, vol. 24, no. 6, p. 417, 1933.
- [3] I. T. Jolliffe, "Graphical representation of data using principal components," *Principal component analysis*, pp. 78-110, 2002.
- [4] T. Hastie, R. Tibshirani, and J. Friedman, "Unsupervised learning," in *The elements of statistical learning*: Springer, pp. 485-585, 2009.
- [5] C. Hafemeister and R. Satija, "Normalization and variance stabilization of single-cell RNA-seq data using regularized negative binomial regression," *Genome biology*, vol. 20, no. 1, pp. 1-15, 2019.
- [6] L. McInnes, J. Healy, and J. Melville, "Umap: Uniform manifold approximation and projection for dimension reduction," *arXiv preprint arXiv:1802.03426*, 2018.
- [7] M. P. Deisenroth, A. A. Faisal, and C. S. Ong, *Mathematics for machine learning*. Cambridge University Press, 2020.
- [8] J. Wilson Black, J. Brand, J. Hay, and L. Clark, "Using principal component analysis to explore co-variation of vowels," *Language and Linguistics Compass*, vol. 17, no. 1, p. e12479, 2023.
- [9] I. Świetlicka, W. Kuniszyk-Józkowiak, and M. Świetlicki, "Artificial Neural Networks Combined with the Principal Component Analysis for Non-Fluent Speech Recognition," *Sensors*, vol. 22, no. 1, p. 321, 2022.
- [10] Y. Zhang and Y. Wang, "Forecasting crude oil futures market returns: A principal component analysis combination approach," *International Journal of Forecasting*, vol. 39, no. 2, pp. 659-673, 2023.
- [11] F. Castells, P. Laguna, L. Sörnmo, A. Bollmann, and J. M. Roig, "Principal Component Analysis in ECG Signal Processing," *EURASIP Journal on Advances in Signal Processing*, vol. 2007, no. 1, p. 074580, 2007.
- [12] D.-Y. Tzeng and R. S. Berns, "A review of principal component analysis and its applications to color technology," *Color Research & Application*, vol. 30, no. 2, pp. 84-98, 2005.
- [13] O. H. J. Christie, "Introduction to multivariate methodology, an alternative way?," *Chemometrics and Intelligent Laboratory Systems*, vol. 29, no. 2, pp. 177-188, 1995.

- [14] M. Ghil *et al.*, "Advanced Spectral Methods for Climatic Time Series," *Reviews of Geophysics*, vol. 40, no. 1, pp. 3-1-3-41, 2002.
- [15] J. Hwang *et al.*, "Fast and sensitive recognition of various explosive compounds using Raman spectroscopy and principal component analysis," *Journal of Molecular Structure*, vol. 1039, pp. 130-136, 2013.
- [16] P. Federolf, R. Reid, M. Gilgien, P. Haugen, and G. Smith, "The application of principal component analysis to quantify technique in sports," *Scandinavian Journal of Medicine & Science in Sports*, vol. 24, no. 3, pp. 491-499, 2014.
- [17] L. Ferré, "Selection of components in principal component analysis: A comparison of methods," *Computational Statistics & Data Analysis*, vol. 19, no. 6, pp. 669-682, 1995.
- [18] E. Saccenti and J. Camacho, "Determining the number of components in principal components analysis: A comparison of statistical, crossvalidation and approximated methods," *Chemometrics and Intelligent Laboratory Systems*, vol. 149, pp. 99-116, 2015.
- [19] P. R. Peres-Neto, D. A. Jackson, and K. M. Somers, "How many principal components? stopping rules for determining the number of non-trivial axes revisited," *Computational Statistics & Data Analysis*, vol. 49, no. 4, pp. 974-997, 2005.
- [20] D. A. Jackson, "Stopping Rules in Principal Components Analysis: A Comparison of Heuristical and Statistical Approaches," *Ecology*, vol. 74, no. 8, pp. 2204-2214, 1993.
- [21] I. T. Jolliffe and J. Cadima, "Principal component analysis: a review and recent developments," *Philosophical Transactions of the Royal Society A: Mathematical, Physical and Engineering Sciences*, vol. 374, no. 2065, p. 20150202, 2016.
- [22] F. Zhang, *Matrix theory: basic results and techniques*. Springer, 2011.
- [23] K. Nakai and M. Kanehisa, "Expert system for predicting protein localization sites in gram-negative bacteria," (in eng), *Proteins*, vol. 11, no. 2, pp. 95-110, 1991.
- [24] K. Nakai and M. Kanehisa, "A knowledge base for predicting protein localization sites in eukaryotic cells," (in eng), *Genomics*, vol. 14, no. 4, pp. 897-911, Dec 1992.
- [25] G. Scalabrini Sampaio, A. R. d. A. Vallim Filho, L. Santos da Silva, and L. Augusto da Silva, "Prediction of Motor Failure Time Using An Artificial Neural Network," *Sensors*, vol. 19, no. 19, p. 4342, 2019.
- [26] M. Patrício *et al.*, "Using Resistin, glucose, age and BMI to predict the presence of breast cancer," *BMC Cancer*, vol. 18, no. 1, p. 29, 2018.
- [27] D. Ayres-de Campos, J. Bernardes, A. Garrido, J. Marques-de-Sá, and L. Pereira-Leite, "SisPorto 2.0: a program for automated analysis of cardiocograms," (in eng), *J Matern Fetal Med*, vol. 9, no. 5, pp. 311-8, Sep-Oct 2000.
- [28] P. Tüfekci, "Prediction of full load electrical power output of a base load operated combined cycle power plant using machine learning methods," *International Journal of Electrical Power & Energy Systems*, vol. 60, pp. 126-140, 2014.
- [29] H. Kaya and P. Tufekci, *Local and Global Learning Methods for Predicting Power of a Combined Gas & Steam Turbine*. 2012.

Co(II) Adsorption onto Ferrous Chloride and Thermally Modified Diatomite: Surface Properties and Adsorption Mechanism

Eda GÖKIRMAK SÖĞÜT^{1*}, Metin ÇELEBİ¹

¹Van Güvenlik Meslek Yüksekokulu, Van Yüziüncü Yıl Üniversitesi, 65080 Van, Turkey

(ORCID: 0000-0002-7707-3924) (ORCID: 0000-0003-1475-8878)



Keywords: Adsorption, Co (II), Ferrous chloride, Isotherms, Mechanism, Thermal treatment.

Abstract

As a potential alternative for heavy metal removal, adsorption using various low-cost materials is one of the most effective methods. This study presents the efficiency of local diatomite modified by ferrous chloride and heat treatment in removing Co(II) from an aqueous solution. The samples were characterized by ICP, XRD, TG-DTA, FTIR, SEM, and BET analyses and the adsorption efficiency of the samples for Co(II) ions was investigated under different factors such as contact time and pH. The adsorption equilibrium was well described by the Langmuir isotherm model, with the maximum adsorption capacities of D_A , D_M , $D_{M-550^\circ C}$ and $D_{M-850^\circ C}$ at about 18.18 mg L⁻¹, 28.65 mg L⁻¹, 48.30 mg L⁻¹, and 66.22 mg L⁻¹, respectively. The kinetic data were best fitted to the pseudo-second-order model. In addition, ion exchange and electrostatic surface complexation were predicted to play dominant roles in the adsorption mechanism. The results showed that the selected modification methods were effective in removing heavy metals from aqueous solutions, making the samples potentially cost-effective adsorbents to remove the water pollution problem.

1. Introduction

The advantages of developing technology to facilitate life lead to irreversible damage. Threats from numerous fields such as solid fuel consumption, exhaust emissions, domestic waste, mining and uncontrolled industrialization, rechargeable batteries, military, strategic, and critical industrial applications have started to provide negative notifications, especially for the natural environment [1], [2]. In particular, the pollution of water resources causes the waste to decompose during movement, causing irreversible damage to the environment and living beings [3]. It is a well-known fact that the concentration of heavy metals in wastewater, when the concentration significantly exceeds the limit of mg L⁻¹, has a toxic effect on all living things [1]. Among these heavy metals, the removal of cobalt (II) ions, which leads to the production of new-generation materials, is crucial for the future [2]. Cobalt and its salts are used in nuclear medicine, enamels, and semiconductors, in the coloring of glass and

porcelain, in the hygrometer and electroplating, in the manufacture of vitamin B12, as a desiccant for lacquers, varnishes and dyes and as a catalyst for organic chemical reactions. Also, exposure to ionizing radiation is associated with an increased risk of developing cancer. The uncontrolled concentration of cobalt negatively affects all living species. It can cause paralysis, diarrhea, lung irritation, bone defects, and genetic changes in living cells [4]–[8]. Conventional methods such as membrane filtration [9], chemical precipitation [10], ion exchange [11], and adsorption [12] have been used to remove heavy metals from wastewater. Adsorption is the most widely used method with practical, economical, and recyclable properties. Industrial raw materials are widely used for adsorption applications [13], [14]. The main reason for this is the cheaper cost of industrial raw materials compared to production adsorbents and the financial contribution to the region [15], [16]. Among these industrial raw materials, fine-grained, physically and chemically inert diatomite, 80–90% of the pores consist mainly of amorphous

*Corresponding author: edagokirmak@yyu.edu.tr

Received: 08.09.2022, Accepted: 08.06.2023

silica ($\text{SiO}_2 \cdot n\text{H}_2\text{O}$), which consists of diatom shells. The diatomite surface has many active sites due to the silanol groups dispersed in the silica matrix [17]. These functional groups play a very active role in removing contaminants from the aqueous solution. Additionally, many modification processes are used to further functionalize the diatomite to increase its adsorption capacity. Modification methods are used, such as modification with transition metals, heat treatment, treatment with acids or bases, and organosilane. This leads to more attractive surfaces for adsorption [18], [19].

In this study, diatomite samples were first prepared by washing them with an acid solution for modification. In this study, environmentally harmless iron oxide was selected for surface modification of local diatomite. Iron oxide occurs naturally in several primary forms: ferrihydrite, hematite, goethite, lepidocrocite, and maghemite [20]. Ferrihydrite would be an optimal structure of iron oxide to modify diatomite due to its relatively high solubility in water for adsorption. In the ferrihydrite conversion process, a stable ferrihydrite should be preferred for the diatomite modification so that the adsorbed impurities are not released back into the solution over time. More Fe^{3+} vacancies caused by chemically absorbed Si^{4+} loosen the crystal lattice and inhibit the maturation and accumulation of Si^{4+} Fe-oxide particles. For this reason, stable ferrihydrite could be formed by Fe^{+2} oxidation in the presence of dissolved silica (Si). Dissolved silica could be prepared by treating crude diatomite with NaOH. Consequently, the dissolved Si provided by the diatomite contributes to the formation of stable ferrihydrite from the oxidation of Fe(II) [21], [22]. In the next step, ferrihydrite-modified diatomite samples were thermally treated at 550 °C and 850 °C. The samples with enriched surface properties were characterized. Its effectiveness in the removal of heavy metals from aqueous solutions was

investigated, and its possible mechanism was interpreted.

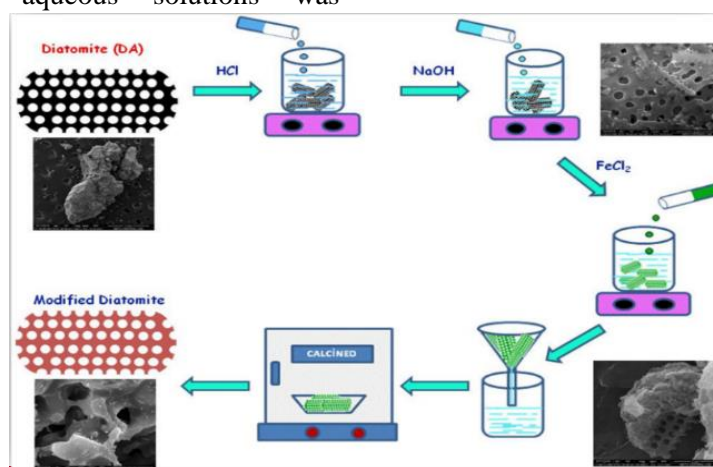
2. Materials and Method

2.1. Materials

Raw diatomite samples obtained from the Çaldıran-Van region were ground and sieved to 350 mesh particle size, washed with distilled water, and then dried at 100 °C. The chemical composition of diatomite is mainly SiO_2 (69.70%) [18]. All the chemicals (Ferrous chloride (FeCl_2) 98%, NaOH 98%, HCl %37, AgNO_3 99%, KNO_3 99%, HNO_3 70%, and $\text{Co}(\text{NO}_3)_2 \cdot 6\text{H}_2\text{O}$) were purchased from Sigma Aldrich, and no purification was performed.

2.2. Preparation of adsorbents

The diatomite sample was stirred with a 2 M HCl solution at 105° C for 4 hours. At the end of this process, it was washed several times to ensure Cl^- (tested by AgNO_3) was removed and named as D_A . 90° C was dried in the oven and stored in a clear glass jar with a lid. Then, in step 15, g of D_A were mixed with 6 M NaOH at 80° C for 2 hours. The mixture was added to 1 M FeCl_2 by keeping the pH between 1 and 2 using HCl, and stirring was continued at room temperature for 10 hours. To increase the rate of formation of iron (II) hydroxide, the sample was treated again with 6 M NaOH at room temperature for 6 h, filtered, washed several times with distilled water, and dried in a drying oven at 105 °C. The resulting sample was named as D_M and stored in a clear glass jar with a lid. In the final step, the D_M sample was thermally treated at 550 °C and 850 °C for 3 hours. These samples were named as $D_{M-550^\circ\text{C}}$ and $D_{M-850^\circ\text{C}}$ and kept for later use in a clear glass jar (Scheme 1).



Scheme 1. Scheme of the process for the preparation of modified diatomite.

2.3. Preparation of Co (II) ion solutions

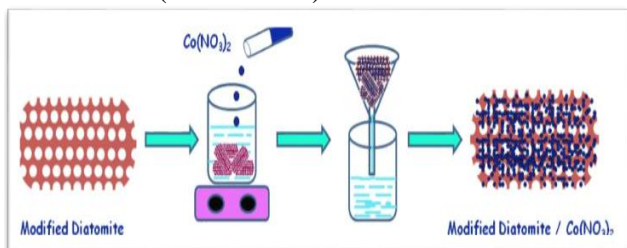
A $\text{Co}(\text{NO}_3)_2 \cdot 6\text{H}_2\text{O}$ stock solution (1000 mg L^{-1}) was prepared with distilled water. It was diluted at different concentrations in the range of $10\text{-}50 \text{ mg L}^{-1}$.

2.4. Characterization of the adsorbents

D_A , D_M , $D_{M-550^\circ\text{C}}$, and $D_{M-850^\circ\text{C}}$ materials were characterized by Inductively Coupled Plasma Optical Emission Spectrometer (ICP-OES, Perkin Elmer Optima 4300DV), X-ray diffraction analysis (XRD, Philips PW 1830-40 with Cu-K radiation), Thermal analysis using a thermal analyzer (TG-DTA, Rigaku 2.22E1), Fourier transform infrared measurement (FT-IR, Bio-Rad Win-IR spectrometer at a resolution of 2 cm^{-1} in KBr pellet at room temperature), and Scanning Electron Microscopy (SEM), Multi-point BET Analysis (Quantachrome Nova 2200E Surface Area & Pore Size Analyzer), and Mastersizer analysis (Malvern) the zero point of charge (pH_{zpc}) of adsorbents were obtained by mass titration [18].

2.5. Batch Adsorption Experiments

The adsorption nature of the samples, the effects of changing contact times (1-120 min.), concentration, and pH (2-9) change were observed. The effect of pH was examined dropwise by adding 0.1 M NaOH or 0.1 M HCl solutions. Experiments were performed on a thermal shaker at a controlled temperature (298 K) using 20 ml glass vials containing 0.1 mg adsorbent and 10 mL of different concentrations ($10\text{-}50 \text{ mg L}^{-1}$) of adsorbent (in Scheme 2).



Scheme 2. Schematic illustration of Co (II) adsorption process.

In the last step, the adsorbents were removed by centrifugation. In the analysis of adsorption data, the percentage of removal (% Removal) was calculated according to Eq. 1;

$$\%R = \frac{C_0 - C_e}{C_0} \times 100\% \quad (1)$$

The adsorption capacity (q_e) (mg g^{-1}) was calculated using Eq. 2;

$$q_e = \frac{(C_0 - C_e)V}{m} \quad (2)$$

where q_e (mg L^{-1}) is the equilibrium adsorption capacity of the adsorbent, C_0 and C_e (mg L^{-1}) are the initial and final concentrations of the Co (II) ions quantity in solution, V (mL) is the volume of solution and m (mg) is the mass of D_A , D_M , $D_{M-550^\circ\text{C}}$, and $D_{M-850^\circ\text{C}}$ used.

Equilibrium data were applied to Langmuir, Freundlich, and Dubinin-Radushkevich isotherm models. Pseudo-first-order (PFO) and second-order (PSO) models, intraparticle diffusion models, and the Boyd model were applied to define adsorption behavior. The equations for all models are presented in Tables S1-2.

3. Results and Discussion

3.1. Characterizations of Adsorbents

The change in percentages of diatomite compounds in different regions depends on geological effects. The rates of diatomite obtained in the Van-Çaldıran region are presented in a previous study [18]. The compound percentages of the D_A , D_M , $D_{M-550^\circ\text{C}}$, and $D_{M-850^\circ\text{C}}$ samples obtained are presented in Table 1.

Table 1. Oxide Content (% weight) in D_A , D_M , $D_{M-550^\circ\text{C}}$ and $D_{M-850^\circ\text{C}}$

Chemical Composition	D_A	D_M	$D_{M-550^\circ\text{C}}$	$D_{M-850^\circ\text{C}}$
SiO_2	71.44	49.82	59.57	56.82
Fe_2O_3	6.22	18.20	20.30	20.72
Na_2O	2.61	7.64	8.44	8.31
Al_2O_3	1.64	8.46	9.21	9.59
K_2O	0.37	0.85	0.96	1.04
TiO_2	0.30	0.35	0.39	0.40
% LOI	17.42	14.68	1.13	3.12

The increased amount (71.44%) in the D_A sample showed the effect of acid washing. In addition, changes in the ratios of other compounds (Fe_2O_3 , Na_2O , Al_2O_3 , K_2O , and TiO_2) are observed. Since the diatomite samples consist of very different-sized particles, after acid treatment, they were transformed from the destroyed/broken oxide particles into crystallite/oxide complex compounds [23].

It was observed that ferrous chloride modified diatomite (D_M , $D_{M-550^\circ\text{C}}$, and $D_{M-850^\circ\text{C}}$) samples decreased SiO_2 contents (49.82%, 59.57%, and 56.82%, respectively). This could be explained

because the SiO_2 compound in the material composition produces sodium silicate (Na_2SiO_3) with NaOH since a 6 M NaOH solution is used during the modification process [24], [25]. Furthermore, the increase in Fe_2O_3 ratio (18.20%, 20.30%, and 20.72%, respectively) of D_M , $D_{M-550^\circ\text{C}}$ and $D_{M-850^\circ\text{C}}$ samples supports the modification process. In addition, especially after heat treatment, the loss of ignition rate is reduced. The volatile substances lost are usually hydrates, unstable hydroxy compounds, and carbon dioxide from carbonates. The new materials obtained with this decrease became more stable [26].

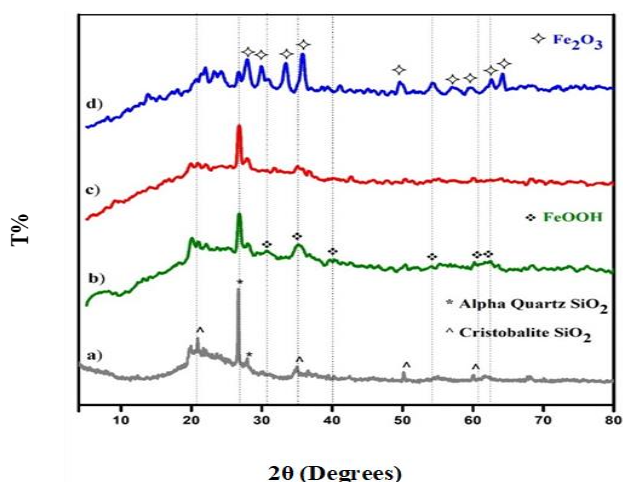


Figure 1. XRD patterns of a) D_A , b) D_M , c) $D_{M-550^\circ\text{C}}$ and d) $D_{M-850^\circ\text{C}}$.

The wide range of $2\theta = 5-8^\circ$, $2\theta = 18-28^\circ$, and at $2\theta = 36^\circ$ in the XRD pattern of the D_A sample indicated amorphous structure in Figure 1. A characteristic quartz peak of D_M , $D_{M-550^\circ\text{C}}$, and $D_{M-850^\circ\text{C}}$ were observed at $2\theta = 26.72^\circ$, 26.84° , and 26.72° , respectively. Table S3. shows that the quartz structure maintains its dominance. However, in the data of D_M , $D_{M-550^\circ\text{C}}$ and especially $D_{M-850^\circ\text{C}}$, Fe_xO_y density increased, and again, the intensity of the characteristic quartz peak decreased in $D_{M-850^\circ\text{C}}$. The obtained data are compatible with the studies presented in Table S3, and it was observed that the magnetic structures in the structure increased with modification, especially in the $D_{M-850^\circ\text{C}}$ sample.

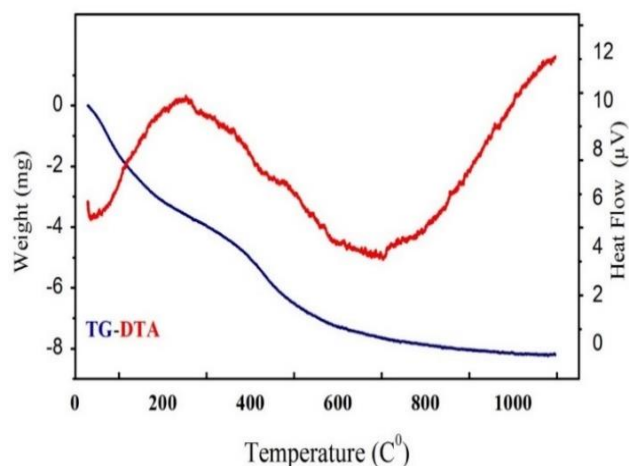


Figure 2. TG-DTA plots of D_A sample.

Thermogravimetric analysis (TG-DTA) was performed to determine the thermal degradation behavior and investigate the absolute stability. Only the TG-DTA thermogram of the D_A sample was obtained between the samples prepared in the 25-1100 $^\circ\text{C}$ temperature range (Fig. 2). A three-step characteristic mass loss of diatomite is observed as the TG plot is examined. The dramatic mass loss (2.7%) between 25-100 $^\circ\text{C}$ was associated with mechanically trapped or physically adsorbed water. This peak depends, for example, on its morphological properties, such as surface area and particle size, rather than its chemical structure. Partially slow mass loss of between 120 and 360 $^\circ\text{C}$ (2.5%) was related to the nature of the opal phase, the hydrous silica with an irregular and amorphous structure, the main component of diatomite. The mass loss of 360- 920 $^\circ\text{C}$ (3.3%) was expressed by the decomposition of alkali metal and alkaline earth metal carbonates of diatomite. The sample did not decrease in weight upon further heating after 900 $^\circ\text{C}$, indicating that the oxygenolysis process or decomposition reaction was complete. DTA curves were observed (Fig. 2), showing that two endothermic peaks appearing at 40 and 690 $^\circ\text{C}$ could be identified by dehydroxylation of silanol groups absorbed on diatomite and the outer surface of diatomite, respectively. Furthermore, at 260 $^\circ\text{C}$, there was a solid exothermic peak due to the oxidation reactions of organic matter in the diatomite [27].

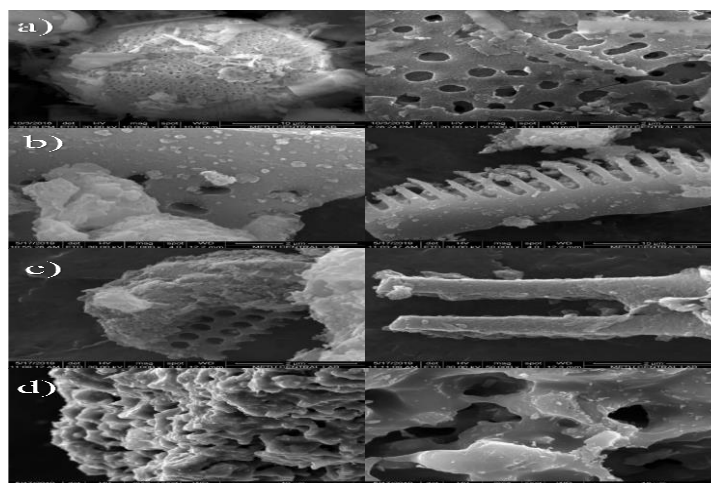


Figure 3. SEM micrographs of the D_A (a), D_M (b), $D_{M-550^\circ C}$ (c) and $D_{M-850^\circ C}$ (d).

In Figure 3, SEM morphologies of samples confirmed that diatomite particles consist of various morphologies such as a sphere, capsule, disc, and bilaterally symmetrical structure. The acid-washed (D_A) diatomite sample was compared with the SEM image of the crude diatomite sample obtained in previous studies, and it was observed that the impurities accumulated in the pores were removed [16]. The SEM image of the ferrous chloride modified sample showed that the pores are enlarged and that some pores of the diatomite are filled and the rest are adsorbed on the surface of the diatomite. Following this treatment, in the $550^\circ C$ heat treated diatomite sample ($D_{M-550^\circ C}$), the diatomite retained its partially skeletal structure; some pores were still open. Furthermore, it was seen that metallic salts are also agglomerated on the surface by the effect of the modification. It could be seen that the skeletal structure of the $850^\circ C$ heat treated diatomite ($D_{M-850^\circ C}$) had completely changed and the spaces in the system had increased, as seen from the visual [28].

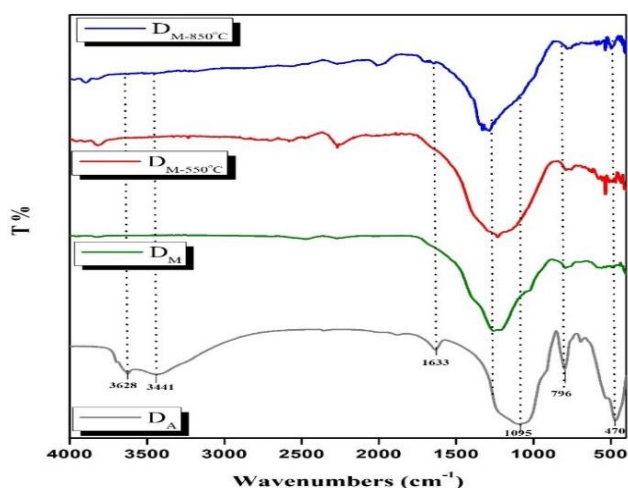


Figure 4. FTIR analysis of the D_A , D_M , $D_{M-550^\circ C}$, and $D_{M-850^\circ C}$.

The FTIR of the D_A sample is presented in Figure 4. The characteristic vibrational peaks of smectite were at 3628 cm^{-1} (O-H stretch), and the broadband centered at 3441 cm^{-1} and 1633 cm^{-1} was attributed to the -OH vibrational mode of physically adsorbed H_2O [29]. The peaks at 470 and 1095 cm^{-1} were from the asymmetric stress modes of Si-O-Si bonds; the weak absorption peaks at 695 cm^{-1} , and 796 cm^{-1} were probably due to Si-O deformation and Al-O stretching; and the peak at 800 cm^{-1} could be due to the stretching vibration of Al-O-Si [30], [31]. According to the FTIR results of the $D_{M-550^\circ C}$ sample, the wide $\sim 3400\text{ cm}^{-1}$ band disappeared when the sample temperature was increased to about $550^\circ C$. The narrow band at $\sim 3700\text{ cm}^{-1}$ was assigned to the strain mode of the free surface OH groups bound as Si-O-H [32].

The 3726 cm^{-1} shoulder band became denser after thermal treatment at $550^\circ C$ (Figure 4). At $850^\circ C$ (Figure 4), the band shifted to a lower wave number at 3780 cm^{-1} with increased symmetry and a significant decrease in intensity [33]. After thermal treatment, the density of the bands increased with water desorption and exposure to more silanol [34]. The results of the BET surface area analysis were summarized in Table S4; the BET surface area of the D_A sample increased by 12.5% compared to the original diatomite sample previously used. This increase could be due to cleaning the blocked pores by opening siloxane bridges with acid treatment [35]. The surface area of the D_M sample increased by 20.8%. The surface area increased with the removal of impurities and the opening of micropore areas due to the effect of the modification. The micropore areas ($83.39\text{ m}^2\text{ g}^{-1}$) presented in Table S4 also support this. In the $D_{M-550^\circ C}$ and $D_{M-850^\circ C}$ samples, microporous walls could be destroyed by the effect of heat, and micro-pore width increased ($37,12\text{ \AA}$ and $58,84\text{ \AA}$)

and surface area decreased by 29% and 96%, respectively. The pore diameters obtained after the modification are presented in Table S4, and it was observed that the mesoporous (pore diameters in the range of 2-50 nm) structure dominates. The morphology analysis expected that the sample's surface area and pore volume would increase due to the porous structure [36]. However, during the thermal treatment at 850 °C, the blocked pores on the surface of the diatomite pores could not be determined by the BET N₂ adsorption method. Therefore, very low surface pore volume values were recorded with low surface area [37]. The data obtained from Mastersizer analysis of samples with a wide variety of shapes are presented in Table S5, and the graphs are shown in Figure S1. In Figure S1, the size distribution of the D_A particles widened from 0.2 to 90 μm, and D (0.5) 32.01 μm was obtained. After the modification, the D_{M-850°C} expanded as the size range (10 to 900 μm in Figure S1) increased as D (0.5): 135.1 μm and the main peak shifted to the right. D (0.5), median, diameter distribution and surface area, and volume width were highest at D_{M-850°C}, while specific surface area was lowest. This reduction in the specific surface area and the increased pore-size diameter after heating could be demonstrated by sintering [38].

3.2. Adsorption experiments

3.2.1. Effect of pH

The effect of pH on the adsorption of Co(II) by D_A, D_M, D_{M-550°C}, and D_{M-850°C} is shown in Figure 5.

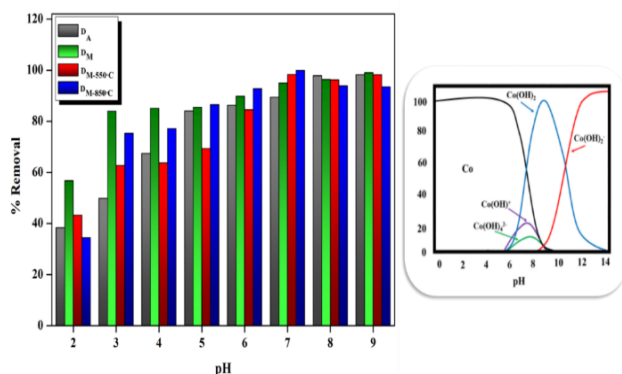


Figure 5. Effect of pH on the adsorption of Co(II) onto D_A, D_M, D_{M-550°C} and D_{M-850°C}.

Another important factor affecting the adsorption capacity of the adsorbent is the pH of the solution. Therefore, the adsorption experiments for

Co(II) were carried out under the conditions of C₀ = 30 mg L⁻¹ and 298 K, ranging from pH 2 to 9. It increased between pH=4-8, as shown in Figure 5. The C=O and OH groups on the surface of the sample are more easily protonated under acidic conditions (< pH=7). It reduces the binding sites of the sample by causing them to bind with H⁺ in the solution and prevents the adsorption of Co⁺². It is conceivable that as the pH of the solution increases from 4 to 8, more negative charges could be used for adsorption. At pH values > 8, Co⁺² ions begin to precipitate as ions [39]. Therefore, a higher Co(II) adsorption capacity was obtained under pH=7 conditions.

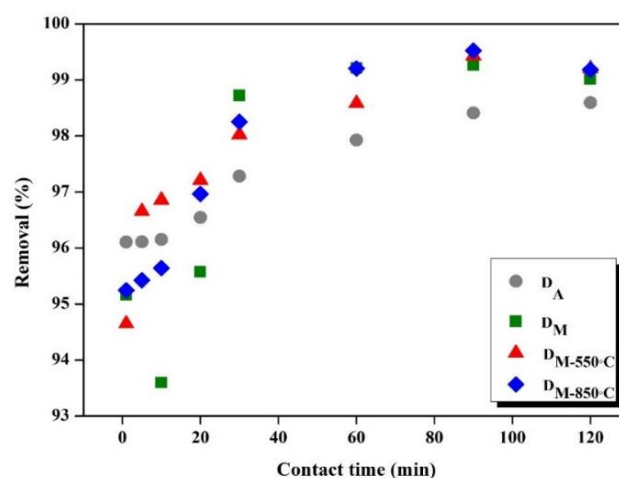


Figure 6. Effect of contact time on the adsorption of Co(II) onto D_A, D_M, D_{M-550°C}, and D_{M-850°C}.

The effect of contact time on the adsorption of Co(II) from aqueous solutions D_A, D_M, D_{M-550°C} and D_{M-850°C} samples was investigated. Figure 6 shows that the ion adsorption rate is constant due to a greater interaction with the vacant adsorption sites on the upper surface of the adsorbent, and then saturation occurs [40]. The removal of Co(II) ions from D_{M-550°C} reached 94% at 10 minutes and its maximum (99.6%) after 90 minutes. Then the adsorption slowed down and reached equilibrium due to the reduced surface area that could be occupied by the adsorbate molecules.

3.3. Adsorption isotherm studies

Isotherm models (Langmuir, Freundlich, and Dubinin-Radushkevich) were used to describe the equilibrium between adsorbate and adsorbent systems (Figure 7), and correlation coefficients were calculated to assess the best fit (Table 2).

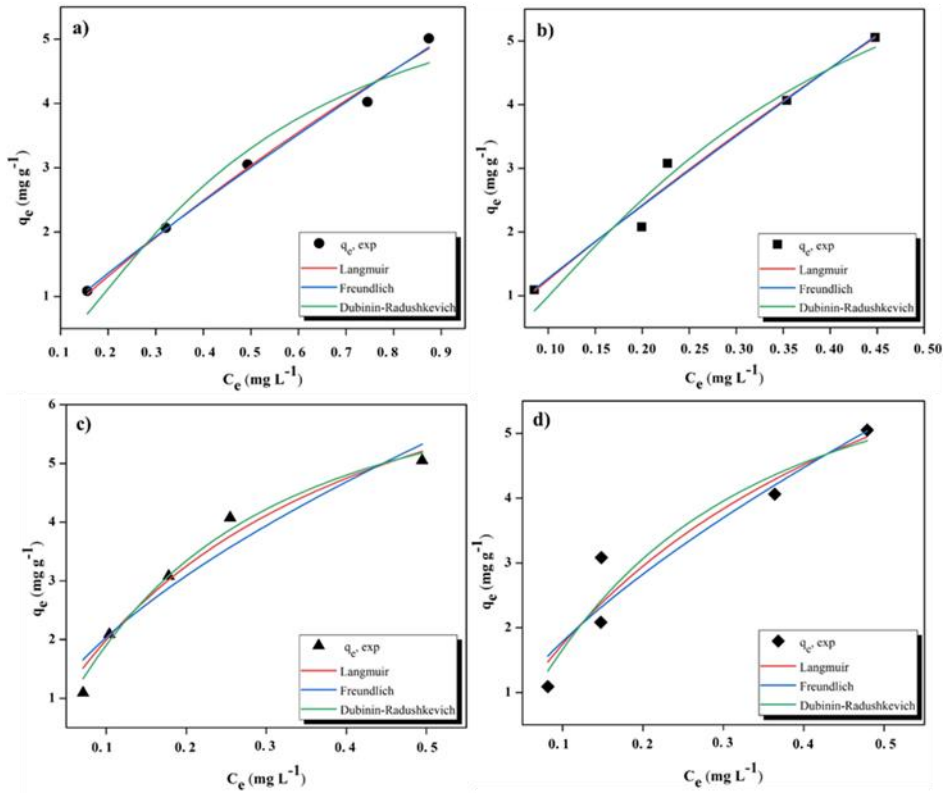


Figure 7. Adsorption nonlinear isotherm model for the D_A (a), D_M (b), $D_{M-550^\circ C}$ (c) and $D_{M-850^\circ C}$ (d).

Table 2. Isotherm parameters obtained by nonlinear fitting for the D_A (a), D_M (b), $D_{M-550^\circ C}$ (c) and $D_{M-850^\circ C}$ (d)

Isotherm/Model		D_A	SE	D_M	SE	$D_{M-550^\circ C}$	SE	$D_{M-850^\circ C}$	SE
Langmuir	q_M (mg g ⁻¹)	18.18	1.1581	28.65	0.5287	48.30	1.5358	66.22	0.3382
	K_L	0.4041	0.1622	0.4586	0.4492	0.3545	0.9333	0.2211	1.335
	R_L	0.1984		0.1790		0.2200		0.3114	
	R^2	0.9992		0.9813		0.9396		0.9091	
	X^2	0.0285		0.0791		0.1030		0.2632	
Freundlich	K_F	5.4853	0.1677	10.7920	1.2798	10.1953	1.1735	9.5214	1.4017
	$1/n$	0.8690	0.0766	0.9371	0.1345	0.7624	0.2941	0.7803	0.3156
	R^2	0.9969		0.9749		0.9146		0.8742	
	X^2	0.0247		0.0805		0.2295		0.2931	
Dubinin-Radushkevich	q_M (mg g ⁻¹)	11.7190	0.6261	15.5897	1.0058	16.2665	0.3546	18.5100	0.8197
	K_{D-R}	0.0005	0.0953	0.0005	0.0582	0.0004	0.0181	0.0004	0.0476
	E_{D-R}	0.3162		0.3162		0.3536		0.3536	
	R^2	0.9941		0.9726		0.9376		0.8903	
	X^2	0.1313		0.1246		0.0435		0.2400	

The data for four nonlinear isotherm models are shown in Table 2. The values showed the fit of the Langmuir model to the experimental data, as it had higher R^2 values. In this study, the maximum adsorption capacities of D_A , D_M , $D_{M-550^\circ C}$, and $D_{M-850^\circ C}$ were 18.18 mg L⁻¹, 28.65 mg L⁻¹, 48.30 mg L⁻¹, and

66.22 mg L⁻¹, respectively. The constant K_L , separation factor R_L values related to the binding energy of the adsorption system, the best fit of the models to the experimental data, chi-square (χ^2), and error analysis (SE) are presented in Table 2. The Freundlich model shows a surface characterized by

multilayer inhomogeneous adsorption on the adsorbent surface. K_F (mg L⁻¹) defines the amount of metal ions adsorbed on the adsorbent at equilibrium, while n measures the adsorption density or surface heterogeneity. The Freundlich model showed poor agreement with the experimental data for Co(II) metal ion at D_A , D_M , $D_{M-550^\circ C}$, and $D_{M-850^\circ C}$ (Fig. 7 A–D). The $1/n < 1$ values of the Freundlich model indicated that the adsorption levels were excellent. In this study, the n values are 0.8690 for D_A , 0.9371 for D_M , 0.7624 for $D_{M-550^\circ C}$, and 0.7803 for $D_{M-850^\circ C}$, which means proper adsorption. The Freundlich isotherm provided a less reasonable fit to the experimental data compared to the Langmuir models. On the other hand, the E values generated using the Dubinin–Radushkevich (D–R) model ($E < 8$ kJ mol⁻¹, 298 K) were the values of samples that confirmed the physical adsorption behaviour (Table 2).

3.4. Adsorption kinetics studies

Kinetic models were used to test the experimental data to investigate the mechanism of adsorption of Co(II) to modified D_A , D_M , $D_{M-550^\circ C}$, and $D_{M-850^\circ C}$ and potential rate control steps such as mass transfer and chemical reactions. The adsorption kinetic model is usually defined by one of the following models: pseudo-first-order, pseudo-second-order, intraparticle diffusion model, and Boyd model.

Table 3. Kinetic parameters obtained using pseudo-first-order and pseudo-second-order kinetic models

Kinetic Models	D_A	D_M	$D_{M-550^\circ C}$	$D_{M-850^\circ C}$
q_e (exp) (mg g⁻¹)	3.0495	3.0761	3.0810	3.084
Pseudo-first order				
q _e (cal) (mg g ⁻¹)	0.1230	0.2586	0.1086	0.1353
k ₁ (min ⁻¹)	0.0519	0.0807	0.0234	0.0907
R ²	0.8846	0.9199	0.9205	0.8753
Pseudo-second order				
q _e (cal) (mg g ⁻¹)	3.0581	3.0807	3.0303	3.0845
k ₂ (g mg ⁻¹ min ⁻¹)	0.0093	0.0121	0.0095	0.0097
R ²	1	1	1	1

Adsorption data were fitted using pseudo-first-order and pseudo-second-order kinetic models in Table 3. This fitting demonstrates that the pseudo-second-order kinetic model successfully describes the kinetics of Co(II) adsorption onto D_A , D_M , $D_{M-550^\circ C}$, and $D_{M-850^\circ C}$. Moreover, the q_e value was close to the experimental data calculated using the pseudo-first-order kinetic model, confirming that the studied adsorption systems belong to the pseudo-second-order kinetic model.

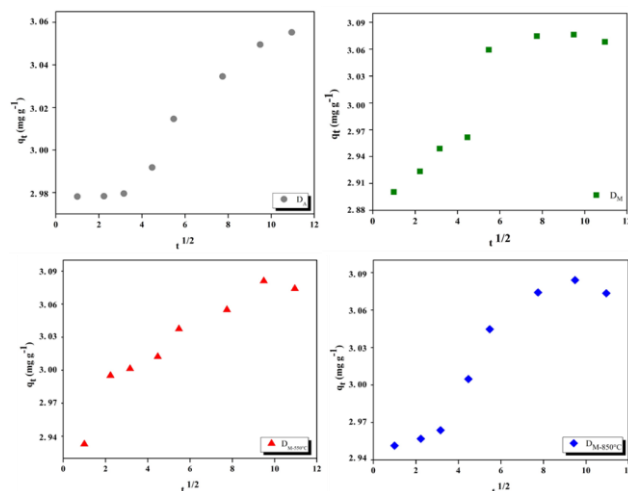


Figure 8. Intraparticle diffusion model for Co(II) adsorption onto the D_A , D_M , $D_{M-550^\circ C}$ and $D_{M-850^\circ C}$ samples.

Table 4. Intraparticle diffusion model data of Co(II) adsorption onto the D_A , D_M , $D_{M-550^\circ C}$ and $D_{M-850^\circ C}$ samples

Intraparticle Diffusion Model	Intraparticle Diffusion Model			
	D_A	D_M	$D_{M-550^\circ C}$	$D_{M-850^\circ C}$
k _i (mg L ⁻¹ min ^{-1(1/2)})	0.0123	0.03	0.0122	0.024
C (mg L ⁻¹)	2.9409	2.8545	2.963	2.8964
R ²	0.9351	0.8001	0.947	0.939

Figure 8 shows that the plot of q_t versus $t^{0.5}$ is an intraparticle diffusion model, indicating that three steps occurred. The boundary layer diffusion controlled the adsorption to some extent; as the drawing did not pass through the origin, it could be assumed that intraparticle diffusion was not the sole mechanism that controlled the adsorption. It could be concluded that three processes control the rate of adsorption of molecules, but only one was rate-limiting at any given time interval. The first process could be attributed to the diffusion of the bulk adsorbent to the outer surface, while the second process could be attributed to the diffusion into the mesopores. The third part was attributed to the equilibrium stage, where diffusion within the particles began to slow down due to the low concentration of chromium in the solution. The slope of the second linear section was defined as a velocity parameter (k_{in}) [41]. This range was characteristic of the adsorption rate, with intraparticle diffusion reported as the rate-limiting factor and the R^2 value ranging between 0.8001 and 0.9470 (Table 4).

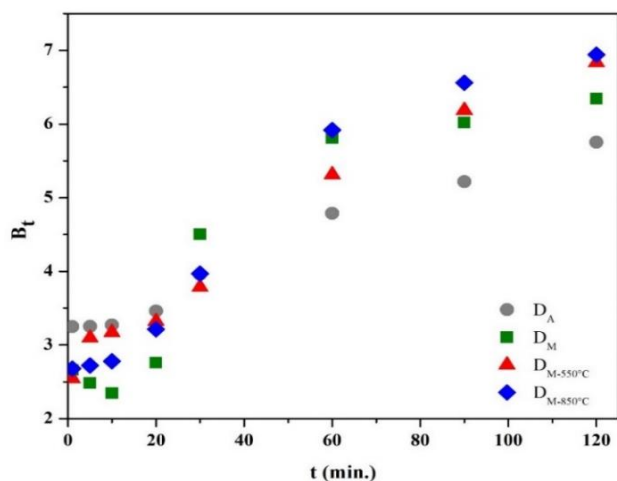


Figure 9. Boyd models of for Co(II) adsorption onto the D_A , D_M , $D_{M-550^\circ C}$ and $D_{M-850^\circ C}$ samples.

The plot of B_t versus t is called a Boyd plot in Figure 9, where a straight line through the origin means that the adsorption process is driven by diffusion within the particles. Otherwise, the adsorption process is controlled by either diffusion in the film or diffusion within the particles [42], [43]. From Figure 9, the plot did not pass through the origin, suggesting that film diffusion dominated the adsorption process.

3.7. Comparison with other adsorbents

Fu-qiang et al. (2013) investigated whether fly ash modified with ferrous chloride is an effective adsorbent in the removal of Mo(VI) from aqueous solutions. The adsorption equilibrium data agreed well with the Langmuir model, and the Langmuir adsorption capacity (Q_0) is 17.83 mg L^{-1} . They reported that the method is inexpensive, effective, and simple compared to existing treatment technologies [44]. Salmani et al. (2016), prepared activated carbon from pomegranate peel (PPC), modified it with FeCl_3 (Fe^{3+}PPC) and FeCl_2 (Fe^{2+}PPC) solutions, and studied the removal of Pb^{+2} from the aqueous solution. The maximum adsorption capacity estimated by the Langmuir model was 34.5 and 17.8 mg L^{-1} for Fe^{2+}PPC and Fe^{3+}PPC for Pb (II) ions, respectively. This was interpreted by the presence of chelating functional groups such as carboxyl, phenol, and OH on the Fe^{2+}PPC surface, which has a high affinity for removing Pb(II) ions [45]. Chunhui et al. (2018), obtained biochar (BC) using yak dung and modified

it with FeCl_2 (Fe-BC3). Adsorption results showed that the maximum adsorption capacities of F^- and As (V) on Fe-BC3 were 3.928 mg L^{-1} and 2.926 mg L^{-1} , respectively [46]. Qi et al. (2020) studied how FeCl_2 was dissolved in anhydrous ethanol and further impregnated cotton textile waste (CTW) to prepare activated carbons (ACs) by pyrolysis. Afterwards, the physicochemical properties for ACs and adsorption capacities of Cr(VI) were evaluated. The maximum adsorption amount of AC-AE was $137.289 \text{ mg L}^{-1}$ for Cr(VI). Also, in this study, it was emphasized that FeCl_2 exhibited better impregnation on raw materials compared to FeCl_3 [47].

3.8. Predicting mechanism of adsorption

Adsorption processes result in different adsorption interactions due to the various designs of adsorbents and consequent changing surface properties. It is explained by physical mechanisms such as van der Waals forces, hydrogen bonding, stacking, electrostatic interaction, and hydrophobic interaction. The chemical adsorption mechanism with more pronounced forces can also be effective due to the development of chemical bonds between the adsorbent and the adsorbate through electron sharing [48]. The more effective adsorption capacity of the modified samples may be the result of some important changes. In physisorption, the pore-filling effect may dominate due to the wide pore size distribution of heavy metals [49]. The adsorption of heavy metals on the surface of the adsorption material can cause a surface reaction. The pH of the aqueous solution is an important factor affecting the heavy metal species, the protonation of functional groups, the electric double layer on the surface, and the adsorption process. Its important effect on the heavy metal adsorption process is the protonation and deprotonation of hydroxyl groups in materials. According to the experimental results of pH change, electrostatic interactions could occur between positively charged adsorbates (Co(II)) and negatively charged functional groups containing residual oxygen [50]. Also, different fractions of Co(II) species could be an effective factor in pH environments. Surface complexation, including coordination and chelation, was an important mechanism for the removal of ionic species, mainly metal ions, from samples (in Figure 10).

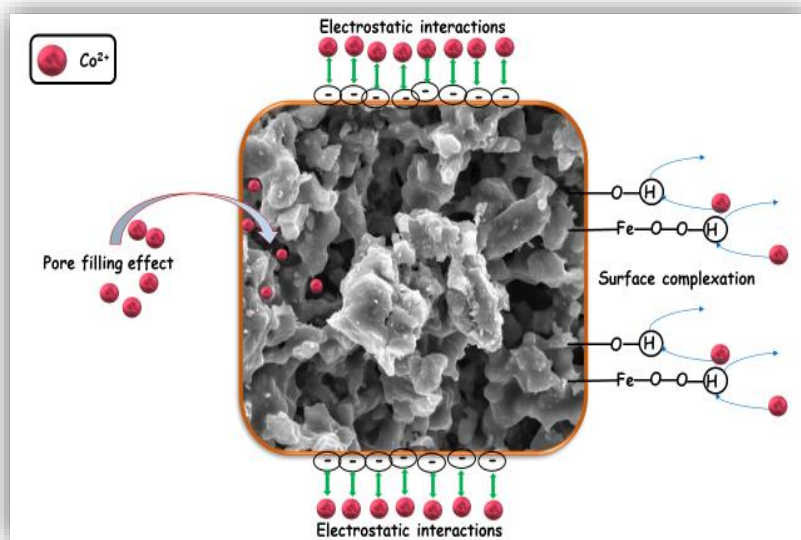


Figure 10. Plausible adsorption mechanism of Co (II) ions onto the D_A , D_M , $D_{M-550^\circ C}$ and $D_{M-850^\circ C}$ samples.

In the adsorption processes, the complex formation is strongly influenced by the pH of the solution, as it could involve the uptake/release of hydrogen ions [51]. The adsorption study showed that monolayer adsorption took place on the homogeneous surfaces of the samples. It could largely contribute to the adsorption behavior due to the domains provided by the oxygen-containing functional groups [52].

4. Conclusion

The aim of this study was to functionalize the surface of the adsorbent, which is a very effective method for removing waste from aqueous solutions. In this context, inspired by the previous work [18], it was modified with transition metal oxides, taking into account the high efficiency of the active groups on the surface, with ferrous chloride, and thermal treatment at two different temperatures (550 °C and 850 °C). In the elemental analysis, it was observed that the content of ferrous chloride ($FeCl_2$) compounds increased and became more stable as a result of the reduction of ignition rate loss with thermal treatment. It was noticed that the Fe_xO_y density increased with the modification according to the XRD pattern. It appeared that there were significant changes in pore structure and surface shape with modification, according to the SEM image. The change in samples with modification was supported by FTIR peaks. The results of the BET analysis and the Mastersizer analysis showed clear changes in the pore structure and the pore size distribution due to the effect of the modification. The pH of a solution is an important parameter affecting adsorption of metal ions on adsorbents. The adsorption capacities were measured

at different pH values and pH=7 was found to be the most suitable for Co(II). The effect of time on the adsorption capacity was studied, and it was observed to reach equilibrium in approximately 90 minutes. From the correlation coefficients of the adsorption isotherms, the type of adsorption was more consistent with the Langmuir isotherm ($R^2 > 0.9$). Also, it was found that $D_{M-850^\circ C}$ adsorbed approximately 3.6 times better than D_A according to the adsorption capacities obtained from the Langmuir isotherm. It was found to be more compatible with the pseudo-second-order kinetics model using kinetic calculations. The adsorption processes of Co(II) on D_A , D_M , $D_{M-550^\circ C}$, and $D_{M-850^\circ C}$ samples were controlled by its monolayer and homogeneous surface, and physical adsorption, ion exchange, and electrostatic surface complexation were predicted to play a dominant role. It was concluded that ferrous chloride and thermally modified diatomite samples could be used as an effective, low-cost, and environmentally friendly adsorbent for the removal of Co(II) from an aqueous solution.

Contributions of the authors

Eda GÖKIRMAK SÖĞÜT: Conceptualization, methodology, investigation, writing-review&editing.

Metin ÇELEBİ: Conceptualization, methodology, investigation, visualization, writing-review&editing.

Data Availability Statement

The data that support the findings of this study are available in the supplementary material of this article.

Conflict of Interest Statement

There is no conflict of interest between the authors.

Statement of Research and Publication Ethics

The study is complied with research and publication ethics.

References

- [1] M. Ferri, S. Campisi, and A. Gervasini, "Nickel and cobalt adsorption on hydroxyapatite: a study for the de-metalation of electronic industrial wastewaters," *Adsorption*, vol. 25, no. 3, pp. 649–660, Mar. 2019.
- [2] L. P. Lingamdinne, J. R. Koduru, H. Roh, Y. L. Choi, Y. Y. Chang, and J. K. Yang, "Adsorption removal of Co(II) from waste-water using graphene oxide," *Hydrometallurgy*, vol. 165, pp. 90–96, Oct. 2016.
- [3] Y. V. Hete, S. B. Gholase, and R. U. Khope, "Adsorption Study of Cobalt on Treated Granular Activated Carbon" *E-Journal Chem.*, vol. 9, no. 1, pp. 335–339, 2012.
- [4] Y. Aşçı and Ş. Kaya, "Removal of cobalt ions from water by ion-exchange method" *New pub Balaban*, vol. 52, no. 1–3, pp. 267–273, 2014.
- [5] F. L. Becker, D. Rodríguez, and M. Schwab, "Magnetic Removal of Cobalt from Waste Water by Ferrite Co-precipitation," *Procedia Mater. Sci.*, vol. 1, pp. 644–650, Jan. 2012.
- [6] B. S. Thaçi and S. T. Gashi, "Reverse Osmosis Removal of Heavy Metals from Wastewater Effluents Using Biowaste Materials Pretreatment," *Polish J. Environ. Stud.*, vol. 28, no. 1, pp. 337–341, Nov. 2018.
- [7] N. Tzanetakis, W. M. Taama, K. Scott, R. J. J. Jachuck, R. S. Slade, and J. Varcoe, "Comparative performance of ion exchange membranes for electro dialysis of nickel and cobalt," *Sep. Purif. Technol.*, vol. 30, no. 2, pp. 113–127, Feb. 2003.
- [8] Ö. Yavuz, Y. Altunkaynak, and F. Güzel, "Removal of copper, nickel, cobalt and manganese from aqueous solution by kaolinite," *Water Res.*, vol. 37, no. 4, pp. 948–952, Feb. 2003.
- [9] N. Abdullah, N. Yusof, W. J. Lau, J. Jaafar, and A. F. Ismail, "Recent trends of heavy metal removal from water/wastewater by membrane technologies," *J. Ind. Eng. Chem.*, vol. 76, pp. 17–38, Aug. 2019.
- [10] S. A. Mirbagheri and S. N. Hosseini, "Pilot plant investigation on petrochemical wastewater treatment for the removal of copper and chromium with the objective of reuse," *Desalination*, vol. 171, no. 1, pp. 85–93, Jan. 2005.
- [11] Y. Huang, X. Zeng, L. Guo, J. Lan, L. Zhang, and D. Cao, "Heavy metal ion removal of wastewater by zeolite-imidazolate frameworks," *Sep. Purif. Technol.*, vol. 194, pp. 462–469, Apr. 2018.
- [12] M. Çelebi and E. Gökırmak Söğüt, "High-efficiency removal of cationic dye and heavy metal ions from aqueous solution using amino-functionalized graphene oxide, adsorption isotherms, kinetics studies, and mechanism," *Turkish J. Chem.*, vol. 46, no. 5, pp. 1577–1593, Jan. 2022.
- [13] H. Peng and J. Guo, "Removal of chromium from wastewater by membrane filtration, chemical precipitation, ion exchange, adsorption electrocoagulation, electrochemical reduction, electro dialysis, electrodeionization, photocatalysis and nanotechnology: a review," *Environ. Chem. Lett.* 186, vol. 18, no. 6, pp. 2055–2068, Jul. 2020.
- [14] E. S. Gokırmak and N. K. Caliskan, "Removal of lead, copper and cadmium ions from aqueous solution using raw and thermally modified diatomite," *Desalin. Water Treat.*, vol. 58, pp. 154–167, Jan. 2017.
- [15] Y. Fu, X. Xu, Y. Huang, J. Hu, Q. Chen, and Y. Wu, "Preparation of new diatomite–chitosan composite materials and their adsorption properties and mechanism of Hg(II)," *R. Soc. Open Sci.*, vol. 4, no. 12, Dec. 2017.
- [16] E. S. Gökırmak and N. K. Çalışkan, "Isotherm and Kinetic Studies of Pb(II) Adsorption on Raw And Modified Diatomite By Using Non-Linear Regression Method," *Fresenius Environ. Bull.*, vol. 26, no. 4, pp. 2720–2728, 2017.
- [17] M. Šljivić, I. Smičiklas, S. Pejanović, and I. Plećaš, "Comparative study of Cu²⁺ adsorption on a zeolite, a clay and a diatomite from Serbia," *Appl. Clay Sci.*, vol. 43, no. 1, pp. 33–40, Jan. 2009.
- [18] N. K. Çalışkan, A. R. Kul, S. Alkan, E. S. Gökırmak, and I. Alacabey, "Adsorption of Zinc(II) on diatomite and manganese-oxide-modified diatomite: A kinetic and equilibrium study," *J. Hazard. Mater.*, vol. 193, pp. 27–36, Oct. 2011.
- [19] E. S. Gökırmak and N. K. Çalışkan, "Equilibrium and Kinetic Studies of a Cationic Dye Adsorption onto Raw Clay," *J. Turk. Chem. Soc. Sect. Chem.*, vol. 7, no. 3, pp. 713–720, 2020.

- [20] S. By and W. Xiong, "Development and application of ferrihydrite-modified diatomite and gypsum for phosphorus control in lakes and reservoirs," 2009.
- [21] W. Xiong and J. Peng, "Development and characterization of ferrihydrite-modified diatomite as a phosphorus adsorbent," *Water Res.*, vol. 42, no. 19, pp. 4869–4877, Dec. 2008.
- [22] W. Xiong, J. Peng, Y. Hu, W. Xiong, J. Peng, and Y. Hu, "Chemical analysis for optimal synthesis of ferrihydrite-modified diatomite using soft X-ray absorption near-edge structure spectroscopy," *PCM*, vol. 36, no. 10, pp. 557–566, Dec. 2009.
- [23] R. Goren, T. Baykara, and M. Marsoglu, "A study on the purification of diatomite in hydrochloric acid," *Scand. J. Metall.*, vol. 31, no. 2, pp. 115–119, Apr. 2002.
- [24] M. K. Faizi, A. B. Shahrman, M. S. A Majid, al -, K. Progo, and Y. Fahmiati, "Characteristics of Iron Sand Magnetic Material from Bugel Beach, Kulon Progo, Yogyakarta," *IOP Conf. Ser. Mater. Sci. Eng.*, vol. 172, no. 1, p. 012020, Feb. 2017.
- [25] J. M. Rimsza, R. E. Jones, and L. J. Criscenti, "Interaction of NaOH solutions with silica surfaces," *J. Colloid Interface Sci.*, vol. 516, pp. 128–137, Apr. 2018.
- [26] O. Heiri, A. F. Lotter, and G. Lemcke, "Loss on ignition as a method for estimating organic and carbonate content in sediments: reproducibility and comparability of results," *J. Paleolimnol.* 2001 251, vol. 25, no. 1, pp. 101–110, 2001.
- [27] R. Zheng, Z. Ren, H. Gao, A. Zhang, and Z. Bian, "Effects of calcination on silica phase transition in diatomite," *J. Alloys Compd.*, vol. 757, pp. 364–371, Aug. 2018.
- [28] Q. Zhang, T. Zhang, T. He, and L. Chen, "Removal of crystal violet by clay/PNIPAm nanocomposite hydrogels with various clay contents," *Appl. Clay Sci.*, vol. 90, pp. 1–5, Mar. 2014.
- [29] J. Madejová, W. P. Gates, and S. Petit, "IR Spectra of Clay Minerals," *Dev. Clay Sci.*, vol. 8, pp. 107–149, Jan. 2017.
- [30] H. Aguiar, J. Serra, P. González, and B. León, "Structural study of sol–gel silicate glasses by IR and Raman spectroscopies," *J. Non. Cryst. Solids*, vol. 355, no. 8, pp. 475–480, Apr. 2009.
- [31] B. B. Zviagina, V. A. Drits, and O. V. Dorzhieva, "Distinguishing Features and Identification Criteria for K-Dioctahedral 1M Micaceous (Illite-Aluminoceladonite and Illite-Glaucanite-Celadonite Series) from Middle-Infrared Spectroscopy Data," *Miner.* 2020, Vol. 10, Page 153, vol. 10, no. 2, p. 153, Feb. 2020.
- [32] B. A. Gawel, A. Ulvensøen, K. Łukaszuk, A. M. F. Muggerud, and A. Erbe, "In situ high temperature spectroscopic study of liquid inclusions and hydroxyl groups in high purity natural quartz," *Miner. Eng.*, vol. 174, p. 107238, Dec. 2021.
- [33] K. Khivantsev, N. R. Jaegers, L. Kovarik, M. A. Derewinski, J. H. Kwak, and J. Szanyi, "On the Nature of Extra-Framework Aluminum Species and Improved Catalytic Properties in Steamed Zeolites," *Mol.* 2022, Vol. 27, Page 2352, vol. 27, no. 7, p. 2352, Apr. 2022.
- [34] L. T. Zhuravlev, "The surface chemistry of amorphous silica. Zhuravlev model," *Colloids Surfaces A Physicochem. Eng. Asp.*, vol. 173, no. 1–3, pp. 1–38, Nov. 2000.
- [35] C. E. Fowler, C. Buchber, B. Lebeau, J. Patarin, C. Delacôte, and A. Walcarius, "An aqueous route to organically functionalized silica diatom skeletons," *Appl. Surf. Sci.*, vol. 253, no. 12, pp. 5485–5493, Apr. 2007.
- [36] X. Ye *et al.*, "Modified natural diatomite and its enhanced immobilization of lead, copper and cadmium in simulated contaminated soils," *J. Hazard. Mater.*, vol. 289, pp. 210–218, May 2015.
- [37] M. Aivalioti, I. Vamvasakis, and E. Gidarakos, "BTEX and MTBE adsorption onto raw and thermally modified diatomite," *J. Hazard. Mater.*, vol. 178, no. 1–3, pp. 136–143, Jun. 2010.
- [38] S. M. Glasauer, P. Hug, P. G. Weidler, and A. U. Gehring, "Inhibition of Sintering by Si During the Conversion of Si-Rich Ferrihydrite to Hematite," *Clays Clay Miner.* 2000 481, vol. 48, no. 1, pp. 51–56, Feb. 2000.
- [39] Ç. Üzüm, T. Shahwan, A. E. Eroğlu, I. Lieberwirth, T. B. Scott, and K. R. Hallam, "Application of zero-valent iron nanoparticles for the removal of aqueous Co²⁺ ions under various experimental conditions," *Chem. Eng. J.*, vol. 144, no. 2, pp. 213–220, Oct. 2008.
- [40] V. Srivastava and M. Sillanpää, "Synthesis of malachite@clay nanocomposite for rapid scavenging of cationic and anionic dyes from synthetic wastewater," *J. Environ. Sci.*, vol. 51, pp. 97–110, Jan. 2017.
- [41] Y. H. Magdy and H. Altaher, "Kinetic analysis of the adsorption of dyes from high strength wastewater on cement kiln dust," *J. Environ. Chem. Eng.*, vol. 6, no. 1, pp. 834–841, Feb. 2018.
- [42] C. Yao and T. Chen, "A film-diffusion-based adsorption kinetic equation and its application," *Chem. Eng. Res. Des.*, vol. 119, pp. 87–92, Mar. 2017.

- [43] K. K. H. Choy, D. C. K. Ko, C. W. Cheung, J. F. Porter, and G. McKay, "Film and intraparticle mass transfer during the adsorption of metal ions onto bone char," *J. Colloid Interface Sci.*, vol. 271, no. 2, pp. 284–295, Mar. 2004.
- [44] W. Fu-Qiang, L. Jian-Jun, and Z. Yi-Min, "Batch and column study: adsorption of Mo(VI) from aqueous solutions using FeCl₂-modified fly ash," *New pub Balaban*, vol. 51, no. 28–30, pp. 5727–5734, 2013.
- [45] M. H. Salmani, M. Abedi, and S. A. Mozaffari, "Adsorption Efficiency of Iron Modified Carbons for Removal of Pb(II) Ions from Aqueous Solution," *J. Community Heal. Res.*, vol. 5, no. 2, pp. 140–148, 2016.
- [46] L. Chunhui, T. Jin, Z. Puli, Z. Bin, B. Duo, and L. Xuebin, "Simultaneous removal of fluoride and arsenic in geothermal water in Tibet using modified yak dung biochar as an adsorbent," *R. Soc. Open Sci.*, vol. 5, no. 11, Nov. 2018.
- [47] R. Qi *et al.*, "Effect of dispersant on the synthesis of cotton textile waste-based activated carbon by FeCl₂ activation: characterization and adsorption properties," *Environ. Sci. Pollut. Res.*, vol. 27, no. 36, pp. 45175–45188, Dec. 2020.
- [48] C. E. R. Barquilha and M. C. B. Braga, "Adsorption of organic and inorganic pollutants onto biochars: Challenges, operating conditions, and mechanisms," *Bioresour. Technol. Reports*, vol. 15, p. 100728, Sep. 2021.
- [49] M. Choudhary, R. Kumar, and S. Neogi, "Activated biochar derived from *Opuntia ficus-indica* for the efficient adsorption of malachite green dye, Cu⁺² and Ni⁺² from water," *J. Hazard. Mater.*, vol. 392, p. 122441, Jun. 2020.
- [50] B. Zhao, X. Xu, R. Zhang, and M. Cui, "Remediation of Cu(II) and its adsorption mechanism in aqueous system by novel magnetic biochar derived from co-pyrolysis of sewage sludge and biomass," *Environ. Sci. Pollut. Res.*, vol. 28, no. 13, pp. 16408–16419, Apr. 2021.
- [51] X. Zhao, H. Feng, P. Jia, Q. An, and M. Ma, "Removal of Cr(VI) from aqueous solution by a novel ZnO-sludge biochar composite," *Environ. Sci. Pollut. Res.*, vol. 1, pp. 1–15, Jun. 2022.
- [52] E. Gökırmak Sögüt, "Effect of Chemical and Thermal Treatment Priority on Physicochemical Properties and Removal of Crystal Violet Dye from Aqueous Solution," *Chemistry Select*, vol. 7, no. 19, p. e202200262, May 2022.

Electrospun TiO₂ Nanofibers in the Presence of Avocado Seed Extract

Kübra TEMİZ¹, Merve ÇAPKIN YURTSEVER^{1*}

¹Adana Alparslan Türkeş Science and Technology University, Faculty of Engineering, Department of Bioengineering, Adana, Türkiye
(ORCID: [0000-0002-3660-3204](https://orcid.org/0000-0002-3660-3204)) (ORCID: [0000-0001-7874-4016](https://orcid.org/0000-0001-7874-4016))



Keywords: TiO₂, Avocado seed extract, Polyvinylpyrrolidone, Electrospinning, Nanofibers.

Abstract

Plant extracts are efficient reducing agents for the synthesis of oxide materials and can regulate fiber diameter, pore size, and phase structure in these materials because of their high organic macromolecule content. In this study, titanium tetraisopropoxide (TTIP) was used as a TiO₂ precursor, and PVP polymer was used as the carrier polymer for electrospinning. Avocado seed extract (ASE), which is a new and valuable source of phenolic compounds, was used for the coordination and reduction of TTIP. ASE was obtained by methanol-water extraction. The total phenolic content of ASE was calculated to be 0.16 g GAE / g dry ASE, and the total dissolved protein amount of ASE was calculated to be equivalent to 0.78 g BSA / g dry ASE. TiO₂-PVP-Avocado seed extract (T/P/A) composite nanofibers were produced at different voltages, distances, and polymer concentrations. Crystalline TiO₂ formation was not observed in as-spun nanofibers; thus, selected nanofibers were heat treated at 500 °C for 3 h. Smooth and integrated TiO₂ nanofibers prepared by using 5 w% PVP at 15 kV and 15 cm distance with or without ASE were imaged by Scanning Electron Microscopy (SEM). X-ray Diffraction (XRD) patterns of heat treated TiO₂ nanofibers prepared in the presence of ASE crystallized mainly in anatase form. However, both anatase and rutile phases were detected in the crystalline structure of TiO₂ nanofibers when ASE was not used. ASE incorporation affected the phase transformation of TiO₂ nanofibers, indicating that the anatase-rutile ratio of TiO₂ nanofibers may also be controlled by the presence of ASE.

1. Introduction

Electrospinning is a method that utilizes electrostatic force to form polymer fibers from a wide variety of materials that contain polymers, metals, composites, and ceramics [1], [2]. Electrospinning is a cheap and sophisticated method to form nano and micro-scale fibers [3], [4]. Electrospun nanofibers have high surface area to volume ratios, and their pore sizes and diameters can easily be modified by changing the spinning parameters [5]–[7]. Electrospun nanofibers are widely used in different areas such as tissue engineering, cosmetics, filtration processes, nano-sensors, military protective clothing [8], wound healing dressings, nanocatalysts, pharmaceuticals, and probiotic encapsulation [5], [7].

Titanium dioxide has antimicrobial, photocatalytic, self-cleaning, and biocompatible

properties. Commercially pure titanium is a biologically compatible metallic material due to its surface properties, resulting in the self-deposition of stable and inert titanium dioxide [9]. Titanium tetra isopropoxide (an organic titanium precursor), TTIP, is often mixed with polyvinyl pyrrolidone (PVP) as the carrier polymer in order to synthesize TiO₂ nanofibers via electrospinning [10], [11]. PVP is also widely used in food additives, personal care products, pharmaceutical technology, drug delivery systems, and bioactive packaging applications [12]. In a study, TiO₂ nanofibers were obtained by electrospinning PVP solutions at 3 different TTIP concentrations. Smooth TiO₂ fibers were obtained after calcination of the electrospun nanofibrous membranes at 600 °C [13]. In another study, a water soluble form of Ti-precursor, titanium (IV) bis (ammonium lactato)

*Corresponding author: mcyurtserver@atu.edu.tr

Received: 30.09.2022, Accepted: 08.05.2023

dihydroxide (TiBALDH), was used to obtain TiO₂ nanofibers in the presence of PVP. The electrospun nanofibers were heat treated up to 600 °C. After heat treatment, the TiO₂ nanofibers preserved their integrity and showed smaller fiber diameters when compared to the diameters of as-spun nanofibers [14]. The formation of crystalline TiO₂ nanoparticles often requires high temperatures, starting at 400 °C. However, crystalline TiO₂ nanoparticles can be synthesized at low temperatures without requiring heat treatment. For this long-term aging process [15], concentrated acid solutions [16] and water soluble titanium precursors or biomolecules are used [17], [18].

The green synthesis of crystalline TiO₂ nanoparticles has been studied in the presence of different types of plant extracts and microorganisms. These biological samples include many types of polyphenols, flavonoids, proteins, etc., which may behave as reducing agents [19]. This environment-friendly approach both reduces the undesired effects of chemical methods and may play an important role either in the structure of TiO₂ nanoparticles or in their properties such as antimicrobial and photocatalytic activity [20]. In a recent study, TiO₂ nanoparticles were obtained at room temperature in the presence of *L. acutangula* leaf extract. Titanium sulfate was used as a precursor, and the synthesis was conducted in a water environment without a calcination step. The green synthesized nanoparticles showed very good antimicrobial activity across a wide-spectrum [21]. In addition, the beneficial effects of TiO₂ nanoparticles as a growth regulator and nanofertilizer-like agent on plant growth have been well described in the studies [19], [22]. The properties of green synthesized TiO₂ nanoparticles have been discussed in many studies; however, this study emphasizes the effects of avocado seed extract (ASE) on the morphology and crystallinity of green synthesized TiO₂ electrospun nanofibers for the first time.

Avocado, with its rich nutritional value, is a fruit that is frequently found on dining tables today and is also grown in Türkiye. The effects of extracts from leaves, ripe and unripe fruits, or seeds of different avocado species on microorganisms and mammalian cells, as well as their effects on nanoparticle production, were studied [23]. Avocado fruit and leaf extracts have been investigated for many years; however, ASE has recently been studied in the literature [24]. Avocado seed extracts show antioxidant, anticarcinogenic, and antimicrobial properties that make avocado seed a precious source for obtaining valuable extracts from plant waste [25], [26]. The effectiveness of the surface-active properties of polyols from ASE was examined in a

self-emulsifying drug delivery system. It was stated that the encapsulation efficiency of drugs with low water solubility, naproxen, and curcumin, was increased in the presence of ASE [27]. In another study, phospholipids obtained from avocado seeds were used to form a stable oil-in-water emulsion [28]. In the literature, no study was found in which ASE was used in the production of TiO₂ nanofibers.

In this study, electrospun TiO₂ nanofibers were synthesized in the presence of ASE. The morphology of the as-spun and heat-treated nanofibers was characterized by SEM analysis. Crystalline and chemical structures were determined by XRD and FTIR analysis, respectively.

2. Material and Method

2.1. Preparation of Avocado Seed Extract

A bacon type avocado was purchased from the commercial market. The seeds were separated from the fruit, and their shells were peeled off. Then, they were cut into small pieces. Approximately 150 g of avocado seed pieces were homogenized in a blender with 500 mL of deionized water. 500 mL of methanol was added to the blended seeds, and they were stirred at 500 rpm at room temperature (RT) for 2 h. Then, the mixture was centrifuged at 8000 rpm for 10 minutes, 3 times. The supernatant was collected and methanol was removed from the rotary evaporator at 50 °C. Water remaining in the samples was removed by freeze-drying at -80 °C (Labconco, FreeZone 2.5 Liter Benchtop Freeze Dryers). The freeze-dried ASE was stored at RT for further use.

2.2. Total Phenolic and Protein Content of Avocado Seed Extract

Folin Ciocalteu reagent (FC, Sigma, Germany) was used to determine the total phenolic content of ASE. Gallic acid (GA, Sigma, Germany) was used as the standard to express the phenolic content of ASE as g GA equivalent / dry weight of avocado seed extract (g GAE / g dry ASE). ASE samples were dissolved in a methanol/water (1:1) mixture at 1mg/mL concentration. The working solution for FC was prepared in ultra-pure water (UPW, 1:10 dilution). 7.5 w% Na₂CO₃ solution was prepared in UPW. All reagents were prepared freshly just before use. Analysis was performed in triplicate on a 96-well plate. 10 µL sample or control without ASE was added to the wells. 100 µL FC working solution was added and waited for 3 min at RT. Then, 90 µL of 7.5 w% Na₂CO₃ solution

was added, and the absorbance values of the resulting solutions were recorded at 765 nm after 1 h of incubation by a spectrophotometer (BMG Labtech, SPECTROstar Nano, Germany).

The total protein amount of ASE was determined by the Lowry protein assay. Bovine serum albumin (BSA) was used as the standard protein. A solution of 0.1 mg/mL ASE was prepared in UPW. 77 μ L of samples with or without ASE were added to the wells. Then, 108 μ L Lowry solution (it was modified from [29]) and 15 μ L FC solution (1:10 dilution in UPW) were mixed with the samples, respectively. Absorbance values were recorded at 750 nm after 1 h of incubation at RT in the dark.

2.3. Preparation of Electrospinning Solutions

Polyvinylpyrrolidone was supplied from Sigma (Mw 360,000 g/mol). Other chemicals were obtained from Sigma, unless stated. 0.25 g and 0.3 g of PVP were dissolved in 3.12 mL of absolute ethanol under stirring at RT overnight. 1.25 mL of acetic acid and 0.62 mL of TTIP were added to the PVP solutions, respectively, and stirred for 1.5 hours to obtain a homogeneous mixture. It is frequently seen in the literature that acetic acid is generally used to dissolve TTIP and trigger its coordination [27]–[29]. Then, 0.9 mg of ASE was added to the PVP/TTIP mixture and sonicated for 5 min at RT for a complete dissolution of the extract in the solution. The solution, including TTIP, PVP, and ASE, was taken into a 5 mL syringe with a blunt end 21-gauge needle. Electrospinning conditions are given in Table 1 and a photograph of the electrospinning apparatus is given in Figure 1 (Fytronix, electrospinning apparatus). Random nanofibers were collected for 30 min for each sample and they were dried overnight at RT. Then they were kept at RT for further analysis. The selected samples were heat treated at 500 °C for 3h (Carbolite, RHF1400). The heating ramp was 5°C/min. Nanofibers without ASE were used as control nanofibers.

2.4. Characterization of Electrospun Nanofibers

The surface morphology of as-spun and heat-treated nanofibers was analyzed by Scanning Electron Microscopy (SEM, FEI, Quanta 650 Field Emission).

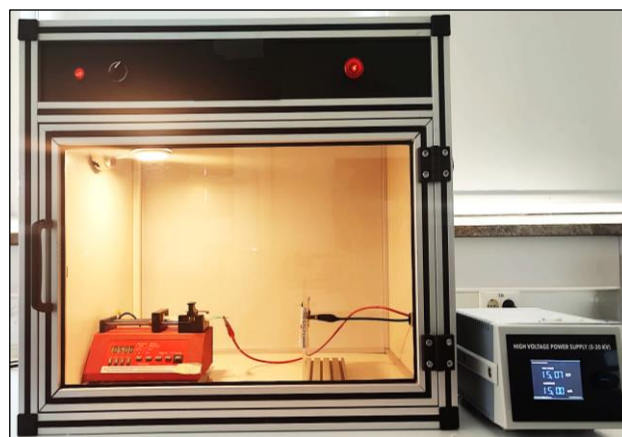


Figure 1. Photograph of electrospinning apparatus.

The electrospun nanofibers were sputtered with gold before imaging. The crystalline structure of TiO₂ was characterized by X-ray Diffraction (XRD, Rigaku MiniFlex 600) analysis. XRD patterns were fitted with the Pseudo-Voigt function. The crystallized size was calculated by using Scherrer's equation (Equation 1) by using (101) reflection of anatase, and the rutile weight percent was calculated by using (101) reflection of anatase and (110) reflection of rutile (Equation 2) [30].

$$d = \frac{k\lambda}{\beta \cdot \cos\theta} \quad (1)$$

where d is the average crystallite size (nm), k is a constant (0.9), λ is the X-ray wavelength (nm), β is the full width half maximum and θ is the Bragg's angle.

$$x_R = 1 - \left(1 + 1.26 \frac{I_R}{I_A}\right)^{-1} \quad (2)$$

where x_R is the rutile weight fraction, I_R and I_A are the intensities of the rutile (110) peak and anatase (101) peak, respectively.

Chemical characterization was carried out by the Fourier Transform Infrared Spectroscopy (FTIR, Perkin Elmer Spectrum 2). Fiber diameters were calculated by the Image J software (NIH, USA). Statistical analysis was carried out using GraphPad Prism 9, USA. Unpaired t test was selected to compare the difference within fiber diameters.

Table 1. Electrospinning parameters

Polymer Concentration (w/v%)	TTIP (mL)	Ethanol (mL)	Acetic Acid (mL)	ASE/PVP (w/w%)	ASE/TTIP (w/w%)	Voltage (kV)	Distance (cm)	Flow rate (mL/h)
5 / 6	0.62	3.12	1.25	0.36 / 0.30	0.15	15 / 17	15 / 20	0.5

3. Results and Discussion

ASE is a precious source due to its rich nutritional and phenolic content [31], as was also demonstrated in this study. The total phenolic content of ASE was calculated to be 0.16 g GAE / g dry ASE. Total dissolved protein amount of ASE was calculated to be equivalent to 0.78 g BSA / g dry ASE. These values were within the range of the literature [24]. The effects of PVP concentration, the presence of ASE, electrospinning voltage, and the distance from the tip of the needle to the surface of the collection plate on the morphology of nanofibers were investigated. Two different polymer concentrations were selected. Uniform and homogeneously distributed nanofibers were obtained at a 5 w% PVP concentration, as shown in the SEM images (Figure 2).

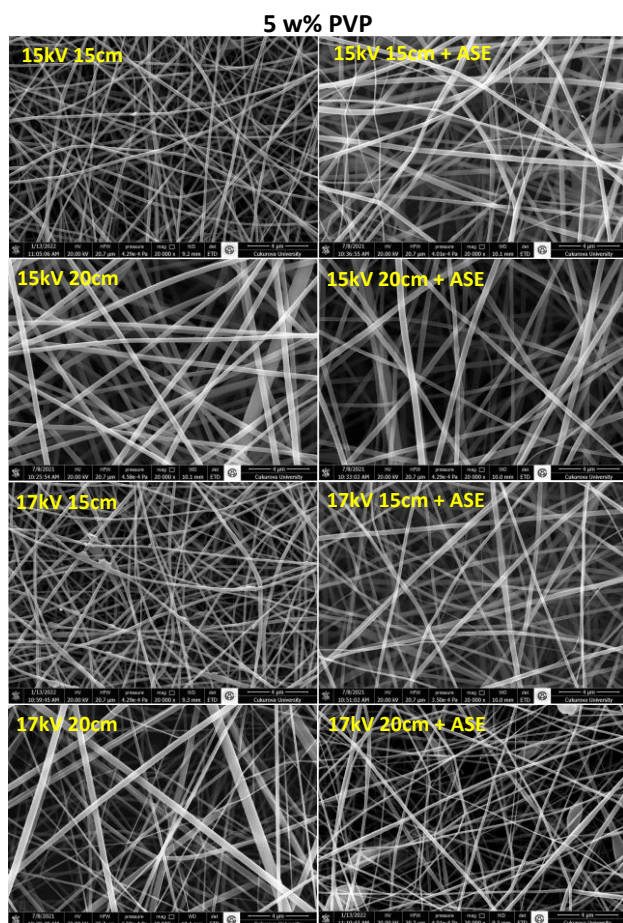


Figure 2. SEM images of as-spun nanofibers obtained with 5w% PVP solution, magnification: 20.000x.

Different voltage and distance values were studied for 6 a w% PVP concentration for only the fibers prepared in the presence of ASE. Wavy and non-homogenous nanofibers were obtained for the selected conditions, as seen in Figure 3. Further studies were carried out with electrospun nanofibers

prepared using a 5 w% PVP concentration. PVP polymers with different molecular weights have been used as carriers to obtain TiO₂ nanofibers [28], [30]. The selected concentration of carrier polymer and the solvent for electrospinning can change according to their Mw. Here, PVP with an Mw:360,000 g/mol was used at 5 w% as a carrier polymer. In the literature, high molecular weight 1,300,000 g/mol PVP was generally used for electrospinning [32], however, in a study, electrospun TiO₂/PVP nanofibers were successfully obtained by using PVP with a relatively lower Mw (360,000 g/mol) [33]. Here we successfully obtained homogeneous TiO₂ / PVP nanofibers with PVP having Mw 360,000 g/mol.

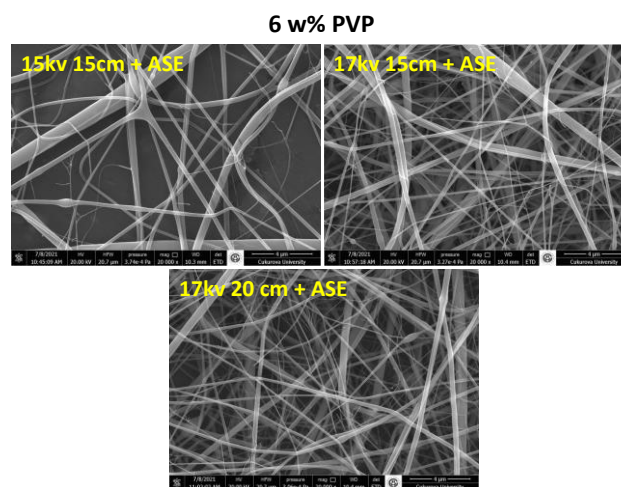


Figure 3. SEM images of as-spun nanofibers obtained with 6w% PVP solution, magnification: 20.000x.

Nanofibers with ASE showed different fiber morphology when compared to the control nanofibers. The average nanofiber diameter was increased; however, there were some thinner nanofibers in the structure of ASE, including groups, resulting in increased standard deviations in the nanofiber diameters. Nanofiber diameters are given in Table 2.

TiO₂ has three main crystalline phases named anatase, rutile, and brookite. Anatase and brookite are metastable forms that have tetragonal and orthorhombic crystalline phase structures, respectively. Rutile is the stable form of TiO₂, which has a tetragonal phase structure [34]. No diffraction peaks of the crystalline phases of TiO₂ were observed in the XRD patterns (not shown) of the as-spun nanofibers. This result was expected for a control group without any plant extract when compared to the literature [35]. In addition, crystal growth of TiO₂ did not occur in the presence of ASE for the electrospinning conditions given in Table 1.

Table 2. Average diameters of as-spun TiO₂ nanofibers

Condition	Average Fiber Diameter (nm)	Condition	Average Fiber Diameter (nm)	Condition	Average Fiber Diameter (nm)
5 w% PVP - ASE		5 w% PVP + ASE		6 w% PVP + ASE	
15kV, 15cm	163.4 ± 45.6	15kV, 15cm	214.7 ± 83.6	15kV, 15cm	257.5 ± 184.4
15kV, 20cm	297.4 ± 69.4	15kV, 20cm	274.9 ± 83.5	17kV, 15cm	215.1 ± 101.3
17kV, 15cm	149.6 ± 48.5	17kV, 15cm	195.1 ± 68.9	17kV, 20cm	178.9 ± 77.9
17kV, 20cm	189.6 ± 16.2	17kV, 20cm	167.4 ± 58.6		

The formation of crystalline phases of TiO₂ in a mild environment depends on the precursor of TiO₂. It was shown that anatase TiO₂ can be obtained from TTIP in the presence of acetic acid and water at RT after one week of aging [36]. Here, electrospinning solutions were prepared just before use to prevent precipitation. The interaction time between ASE and TTIP may not be enough to start the crystallization of TiO₂ at RT.

The selected nanofibers (15 kv, 15 cm, 5 w% PVP) were heat-treated at 500 °C for 3 hours in order to crystallize TiO₂. The heat-treated nanofibers retained their integrity, as seen in the SEM images (Figure 4). PVP polymer (Mw:360,000) loses more than 95% of its weight below 500 °C heat treatment [36], thus these nanofibers may be referred to as TiO₂ nanofibers as the new structure is nearly 100% TiO₂.

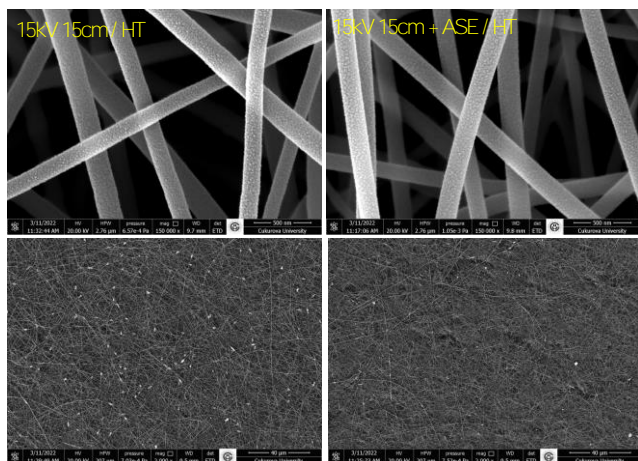


Figure 4. SEM images of heat treated (HT) nanofibers obtained with the electrospinning of 5 w% PVP including solution. Magnifications of the images are 150,000x and 2,000x.

There was less beading formation in TiO₂ nanofibers when they were obtained in the presence of ASE. The distribution of fiber diameter was changed after heat treatment. TiO₂ nanofibers with

ASE showed smaller diameter and narrower size distribution, 181 ± 2 nm, when compared to the

diameters of control TiO₂ nanofibers without ASE, 203 ± 4 nm ($p < 0.01$, **).

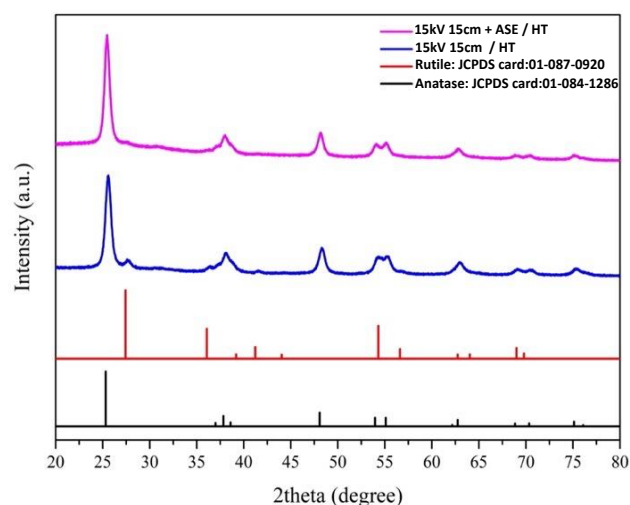


Figure 5. XRD patterns of nanofibers with or without ASE (15 kV, 15 cm, 5 w% PVP) heat treated at 500 °C for 3 hours.

The crystalline properties of the heat-treated nanofibers were determined by XRD analysis. Figure 5 shows the XRD patterns of selected composite nanofibers at the specified conditions. In the presence of ASE, the main phase was found to be anatase with trace amounts of rutile phase (corresponding to the JCPDS cards given in the figure; JCPDS: Joint Committee on Powder Diffraction Standards). However, without ASE, the crystalline structure is still dominated by the anatase phase, but with relatively higher amounts of the rutile phase (about 9 w%). This finding indicated that ASE has a significant effect on the phase evolution of TiO₂. The phase transformation from anatase to rutile could possibly be hindered by organic molecules in the ASE [30]. The crystallite sizes for the control and ASE-containing samples were determined to be 11.6 and 12.6 nm, respectively. It is known that anatase is more

photocatalytically active than rutile, whereas rutile absorbs light in a wider wavelength range than anatase. Therefore, the presence of both anatase and rutile phases in the nanostructure may contribute to the photocatalytic activity. The XRD patterns of the heat-treated nanofibers revealed that an optimization in the anatase-rutile ratio in the nanostructure can be realized by the modification of the ASE amount in the as-spun nanofibers along with the heat treatment temperature, as discussed for metal dopants in the literature [37].

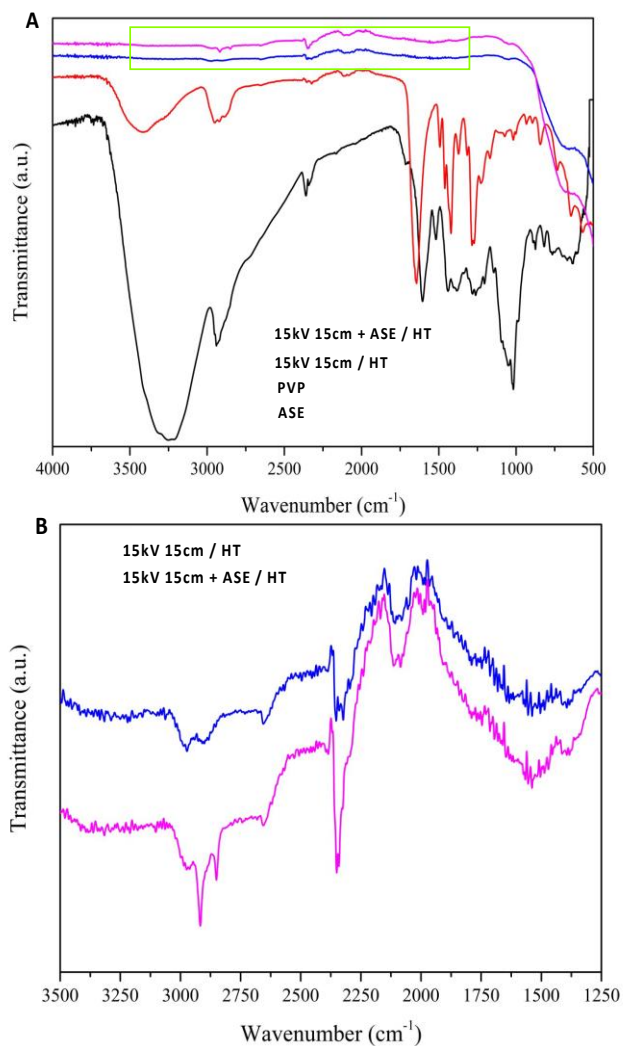


Figure 6. A) FTIR spectra of PVP, ASE and nanofibers heat treated (HT) at 500°C for 3 hours. B) The magnified image of FTIR spectra between 1250-3500 cm^{-1} .

The bending vibration of Ti-O-Ti bonds in the TiO_2 lattice was observed in the range of 500-600 cm^{-1} [39] by FTIR analysis, as seen in Figure 6. Characteristic bands of PVP at 1644 cm^{-1} and 1345 cm^{-1} were attributed to the vibration of the C=O bond and the stretching vibration of the C-N bond, respectively [40]. The strong peak at 1025 cm^{-1} in

ASE was attributed to the vibrations of C-O stretching in ester groups. The wide peak at 3414 cm^{-1} was attributed to the O-H stretching [41]. Here, it was expected for the polymer to burn completely; however, there are still some peaks that may be related to PVP, ASE, or TiO_2 interaction. These peaks were between 2250-3000 cm^{-1} and the intensities of the peaks were higher for nanofibers with ASE when compared to the control nanofibers. ASE is an organic mixture of plants, so it was also expected to burn after heat treatment. However, the peaks between 2250-3000 cm^{-1} may be an indication that organic molecules are not completely burned. On the other hand, specific bonds for PVP and ASE mostly disappeared after heat treatment.

4. Conclusion and Suggestions

Pure TiO_2 nanofiber networks can be prepared by the electrospinning method. Herein, the green synthesis and characterization of electrospun TiO_2 nanofibers in the presence of avocado seed extract (ASE) were performed. As-spun TiO_2 nanofibers with or without ASE were amorphous, whereas crystalline nanofibers were obtained after heat treatment. ASE has a significant effect on the phase evolution of heat-treated TiO_2 nanofibers. Anatase is the main phase in the crystalline structure of TiO_2 nanofibers with or without ASE. However, 9 w% rutile phase was detected in TiO_2 nanofibers without ASE which was at trace amounts in TiO_2 nanofibers with ASE. In addition, smaller diameter fibers were obtained in the presence of ASE. Fiber diameter and crystalline structure are important parameters that may affect the photocatalytic activity, antimicrobial, and biocompatibility properties of the synthesized material. Further studies are needed to show how ASE will affect the functional properties of TiO_2 nanofibers.

Acknowledgement

This study was supported by The Scientific and Technological Research Council of Türkiye (TÜBİTAK) in context of the project TÜBİTAK 2209A/ 1919B012000903.

Contributions of the authors

Kübra Temiz contributed to the literature review, experiments, evaluation of data and article writing, while Merve Çapkın Yurtsever contributed to the formation of ideas, evaluation of the data, article writing and editing.

Statement of Research and Publication Ethics

The study is complied with research and publication ethics.

Conflict of Interest Statement

There is no conflict of interest between the authors.

References

- [1] N. Z. A. Al-Hazeem, “Nanofibers and Electrospinning Method,” in *Novel Nanomaterials - Synthesis and Applications*, InTech, 2018. doi: 10.5772/intechopen.72060.
- [2] A. ElenaOprea, A. Ficai, and E. Andronescu, “Electrospun nanofibers for tissue engineering applications,” in *Materials for Biomedical Engineering: Nanobiomaterials in Tissue Engineering*, 2019, pp. 77–95. doi: 10.1016/B978-0-12-816909-4.00004-X.
- [3] A. Luzio, E. V. Canesi, C. Bertarelli, and M. Caironi, “Electrospun polymer fibers for electronic applications,” *Materials*, vol. 7, no. 2. pp. 906–947, 2014. doi: 10.3390/ma7020906.
- [4] R. S. Bhattarai, R. D. Bachu, S. H. S. Boddu, and S. Bhaduri, “Biomedical applications of electrospun nanofibers: Drug and nanoparticle delivery,” *Pharmaceutics*, vol. 11, no. 1. MDPI AG, Jan. 01, 2019. doi: 10.3390/pharmaceutics11010005.
- [5] N. Bhardwaj and S. C. Kundu, “Electrospinning: A fascinating fiber fabrication technique,” *Biotechnology Advances*, vol. 28, no. 3. pp. 325–347, May 2010. doi: 10.1016/j.biotechadv.2010.01.004.
- [6] M. Rahmati *et al.*, “Electrospinning for tissue engineering applications,” *Progress in Materials Science*, vol. 117. Elsevier Ltd, Apr. 01, 2021. doi: 10.1016/j.pmatsci.2020.100721.
- [7] H. Yu, W. Liu, D. Li, C. Liu, Z. Feng, and B. Jiang, “Targeting delivery system for *Lactobacillus plantarum* based on functionalized electrospun nanofibers,” *Polymers (Basel)*, vol. 12, no. 7, pp. 1–12, Jul. 2020, doi: 10.3390/polym12071565.
- [8] Z. M. Huang, Y. Z. Zhang, M. Kotaki, and S. Ramakrishna, “A review on polymer nanofibers by electrospinning and their applications in nanocomposites,” *Compos Sci Technol*, vol. 63, no. 15, pp. 2223–2253, 2003, doi: 10.1016/S0266-3538(03)00178-7.
- [9] C. N. , Elias, J. H. C. , Lima, and R. et al. Valiev, “Biomedical applications of titanium and its alloys,” *JOM*, vol. 60, pp. 46–49, 2008.
- [10] O. Kéri, P. Bárdos, S. Boyadjiev, T. Igricz, Z. K. Nagy, and I. M. Szilágyi, “Thermal properties of electrospun polyvinylpyrrolidone/titanium tetraisopropoxide composite nanofibers,” *J Therm Anal Calorim*, vol. 137, no. 4, pp. 1249–1254, Aug. 2019, doi: 10.1007/s10973-019-08030-0.
- [11] K. Ghosal, C. Agatemor, Z. Špitálsky, S. Thomas, and E. Kny, “Electrospinning tissue engineering and wound dressing scaffolds from polymer-titanium dioxide nanocomposites,” *Chemical Engineering Journal*, vol. 358, pp. 1262–1278, Feb. 15, 2019. doi: 10.1016/j.cej.2018.10.117.
- [12] F. Çalloğlu C and Kesici Güler H, “Çevreci Çözücüler ile Polivinilpirolidon Nanolif Üretimi,” *Süleyman Demirel Üniversitesi Fen Edebiyat Fakültesi Fen Dergisi*, pp. 352–366, Nov. 2019, doi: 10.29233/sdufeffd.589516.
- [13] S. Kiennork, R. Nakh Wong, R. Chueachot, and U. Tipparach, “Preparation and Characterization of Electrospun TiO₂ Nanofibers via Electrospinning,” in *Integrated Ferroelectrics*, Sep. 2015, vol. 165, no. 1, pp. 131–137. doi: 10.1080/10584587.2015.1063915.
- [14] O. V. Otieno *et al.*, “Synthesis of TiO₂ nanofibers by electrospinning using water-soluble Ti-precursor,” *J Therm Anal Calorim*, vol. 139, no. 1, pp. 57–66, Jan. 2020, doi: 10.1007/s10973-019-08398-z.
- [15] K. Qi and J. H. Xin, “Room-temperature synthesis of single-phase anatase TiO₂ by aging and its self-cleaning properties,” *ACS Appl Mater Interfaces*, vol. 2, no. 12, pp. 3479–3485, Dec. 2010, doi: 10.1021/am1005892.
- [16] K. Fischer *et al.*, “Low-temperature synthesis of anatase/rutile/brookite TiO₂ nanoparticles on a polymer membrane for photocatalysis,” *Catalysts*, vol. 7, no. 7, Jul. 2017, doi: 10.3390/catal7070209.
- [17] M. Taran, M. Rad, and M. Alavi, “Biosynthesis of TiO₂ and ZnO nanoparticles by *Halomonas elongata* IBRC-M 10214 in different conditions of medium,” *BioImpacts*, vol. 8, no. 2, pp. 81–89, 2018, doi: 10.15171/bi.2018.10.

- [18] Rajakumar G *et al.*, “Solanum trilobatum extract-mediated synthesis of titanium dioxide nanoparticles to control *Pediculus humanus capitis*, *Hyalomma anatolicum anatolicum* and *Anopheles subpictus*,” *Parasitol Res*, vol. 113, no. 2, pp. 469–479, 2014, doi: 10.1007/s00436-013-3676-9.
- [19] P. K. Dikshit *et al.*, “Green synthesis of metallic nanoparticles: Applications and limitations,” *Catalysts*, vol. 11, no. 8, Aug. 01, 2021. doi: 10.3390/catal11080902.
- [20] M. Nadeem *et al.*, “The current trends in the green syntheses of titanium oxide nanoparticles and their applications,” *Green Chem Lett Rev*, vol. 11, no. 4, pp. 492–502, Oct. 2018, doi: 10.1080/17518253.2018.1538430.
- [21] D. Anbumani *et al.*, “Green synthesis and antimicrobial efficacy of titanium dioxide nanoparticles using *Luffa acutangula* leaf extract,” *J King Saud Univ Sci*, vol. 34, no. 3, Apr. 2022, doi: 10.1016/j.jksus.2022.101896.
- [22] V. Rodríguez-González, C. Terashima, and A. Fujishima, “Applications of photocatalytic titanium dioxide-based nanomaterials in sustainable agriculture,” *Journal of Photochemistry and Photobiology C: Photochemistry Reviews*, vol. 40, pp. 49–67, Sep. 01, 2019. doi: 10.1016/j.jphotochemrev.2019.06.001.
- [23] B. R. Athaydes *et al.*, “Avocado seeds (*Persea americana* Mill.) prevents indomethacin-induced gastric ulcer in mice,” *Food Research International*, vol. 119, pp. 751–760, May 2019, doi: 10.1016/j.foodres.2018.10.057.
- [24] F. J. Segovia, G. I. Hidalgo, J. Villasante, X. Ramis, and M. P. Almajano, “Avocado seed: A comparative study of antioxidant content and capacity in protecting oil models from oxidation,” *Molecules*, vol. 23, no. 10, Sep. 2018, doi: 10.3390/molecules23102421.
- [25] A. Ochoa-Zarzosa *et al.*, “Bioactive Molecules From Native Mexican Avocado Fruit (*Persea americana* var. *drymifolia*): A Review”, doi: 10.1007/s11130-021-00887-7/Published.
- [26] J. E. Pineda-Lozano, A. G. Martínez-Moreno, and C. A. Virgen-Carrillo, “The Effects of Avocado Waste and Its Functional Compounds in Animal Models on Dyslipidemia Parameters,” *Frontiers in Nutrition*, vol. 8, Feb. 16, 2021. doi: 10.3389/fnut.2021.637183.
- [27] N. Ahmed *et al.*, “Avocado-derived polyols for use as novel co-surfactants in low energy self-emulsifying microemulsions,” *Sci Rep*, vol. 10, no. 1, Dec. 2020, doi: 10.1038/s41598-020-62334-y.
- [28] L. C. B. Züge, H. A. Maieves, J. L. M. Silveira, V. R. da Silva, and A. de P. Scheer, “Use of avocado phospholipids as emulsifier,” *LWT - Food Science and Technology*, vol. 79, pp. 42–51, Jun. 2017, doi: 10.1016/j.lwt.2017.01.013.
- [29] O. H. Lowry, N. J. Rosebrough, A. L. Farr, and R. J. Randall, “Protein measurement with the Folin phenol reagent*”, *J Biol Chem*. 1951 Nov;193(1):265-75.
- [30] H. A. Yurtsever and M. Çiftçioglu, “The effect of rare earth element doping on the microstructural evolution of sol-gel titania powders,” *J Alloys Compd*, vol. 695, pp. 1336–1353, Feb. 2017, doi: 10.1016/j.jallcom.2016.10.275.
- [31] L. Henry, L. N. Henry, U. Yonah Mtaita, and C. C. Kimaro, “Nutritional efficacy of avocado seeds”, *Global Journal of Food Science and Technology*, vol. 3, pp. 192-196, August, 2015.
- [32] Z. S. Tang, N. Bolong, I. Saad, and J. L. Ayog, “The Morphology of Electrospun Titanium Dioxide Nanofibers and Its Influencing Factors” *MATEC Web Conf.*, vol. 47, p. 01020 doi: 10.1051/mateconf/20164701020.
- [33] S. Mirmohammad Sadeghi, M. Vaezi, A. Kazemzadeh, and R. Jamjah, “Morphology enhancement of TiO₂/PVP composite nanofibers based on solution viscosity and processing parameters of electrospinning method,” *J Appl Polym Sci*, vol. 135, no. 23, Jun. 2018, doi: 10.1002/app.46337.
- [34] L. E. Oi, M. Y. Choo, H. V. Lee, H. C. Ong, S. B. A. Hamid, and J. C. Juan, “Recent advances of titanium dioxide (TiO₂) for green organic synthesis,” *RSC Advances*, vol. 6, no. 110., pp. 108741-108754, 2016. doi: 10.1039/c6ra22894a.
- [35] T. Soitong and S. Wongsanmai, “Characteristic and preparation of TiO₂/PVP nanofiber using electrospinning technique,” in *Key Engineering Materials*, 2019, vol. 798 KEM, pp. 223–228. doi: 10.4028/www.scientific.net/KEM.798.223.
- [36] K. Qi and J. H. Xin, “Room-temperature synthesis of single-phase anatase TiO₂ by aging and its self-cleaning properties,” *ACS Appl Mater Interfaces*, vol. 2, no. 12, pp. 3479–3485, Dec. 2010, doi: 10.1021/am1005892.

- [37] H. A. Yurtsever and M. Çiftçioğlu, “The effect of powder preparation method on the artificial photosynthesis activities of neodymium doped titania powders,” *Int J Hydrogen Energy*, vol. 43, no. 44, pp. 20162–20175, Nov. 2018, doi: 10.1016/j.ijhydene.2018.08.185.
- [38] S. Huang, L. Zhou, M. C. Li, Q. Wu, Y. Kojima, and D. Zhou, “Preparation and properties of electrospun poly (vinyl pyrrolidone)/cellulose nanocrystal/silver nanoparticle composite fibers,” *Materials*, vol. 9, no. 7, Jul. 2016, doi: 10.3390/ma9070523.
- [39] S. Al-Taweel, H. Saud, S. S. Al-Taweel, and H. R. Saud, “New route for synthesis of pure anatase TiO₂ nanoparticles via ultrasound-assisted sol-gel method,” *Available online www.jocpr.com Journal of Chemical and Pharmaceutical Research*, vol. 8, no. 2, pp. 620–626, 2016, [Online]. Available: www.jocpr.com
- [40] Y. C. Hung, S. C. Hsieh, S. R. Hou, J. Y. Kung, C. M. Tang, and C. J. Chang, “In vivo evaluation of pvp-gelatin-chitosan composite blended with egg-yolk oil for radiodermatitis,” *Applied Sciences*, vol. 11, no. 21, Nov. 2021, doi: 10.3390/app112110290.
- [41] Kamaruddin, D. Edikresnha, I. Sriyanti, M. M. Munir, and Khairurrijal, “Synthesis of Polyvinylpyrrolidone (PVP)-Green Tea Extract Composite Nanostructures using Electrohydrodynamic Spraying Technique,” in *IOP Conference Series: Materials Science and Engineering*, May 2017, vol. 202, no. 1. doi: 10.1088/1757-899X/202/1/012043.

Antioxidant and Antibacterial Activities of Salen-type Schiff Base and Metal Complexes

Sezer GÖYCINCIK^{1*}, Hatice DANAHALILOĞLU¹

¹Hatay Mustafa Kemal University, Altınözü Vocational School of Agricultural Sciences, Hatay/Turkey
(ORCID: 0000-0002-9128-949X) (ORCID: 0000-0002-5060-1205)



Keywords: Schiff base, Metal complexes, FRAP, DPPH, CUPRAC, Antibacterial activity.

Abstract

2-Aminobenzylamine derived Schiff base and its Cu(II), Ni(II),Co(II) and Fe(III) metal complexes were researched in terms of their antioxidant and antibacterial activities in this study. 1,1-Diphenyl-2-picrylhydrazyl radical scavenging (DPPH) method, ferric reducing antioxidant power (FRAP) method and cupric reducing antioxidant capacity (CUPRAC) method were carried out for determination of antioxidant effects of compounds. The antioxidant activity of the compounds was compared with the standard antioxidants butylated hydroxyanisole (BHA) and butylated hydroxytoluene (BHT). Fe, Ni and Cu complexes exhibited more scavenging activity than BHT. All compounds exhibit lower ferric reducing activity than BHA and BHT. Fe complex, Ni complex and the ligand have more antioxidant capacity than corresponding to BHT according to CUPRAC method. These assays showed that all compounds researched can use as synthetic antioxidants. Antibacterial effects of Schiff base and its metal complexes were investigated by agar disc diffusion method. Antibacterial studies of the compounds were achieved against some gram-positive and gram-negative bacteria. *Enterococcus faecium*, *Pseudomonas aeruginosa*, *Klebsiella pneumoniae* and *Escherichia coli* were used as bacterial strains. The beneficial datas were acquired.

1. Introduction

Schiff bases are obtained from the reaction of aldehydes and ketones with primary amines. Then, these synthesized Schiff bases form complex compounds with transition metal ions [1]. In addition, Schiff bases are useful ligands and employed in biochemistry field such as effects of antioxidants to oxidative stress damage of cells [2]. Therefore, they have been researched for their antioxidant, antibacterial and antifungal effects [3-5]. Similarly, Schiff bases and their metal complexes show important biological activity and they have been considered because of these properties recently [6-11].

Various properties of metal complexes are effected by the structure of the metal ion and the ligand. Metal ions increase the activity of the ligand due to the synergistic effect. Accordingly, metal complexes of salen-type Schiff bases are found to

have antioxidant effects [12]. Moreover salen-type Schiff bases show antimicrobial activity as they have donor O and N atoms [13].

After the COVID-19 epidemic, which effected the whole world, studies on new antioxidant and antibacterial agents has increased. Because, antioxidant substances make the body more resistant to diseases, while antibacterial substances are seen as an important factor in preventing the further spread of this epidemic. As a result, Schiff bases and metal complexes appear as alternative substances that can be investigated with their antioxidant and antibacterial properties. For that reason, 2-Aminobenzylamine derived Schiff base and its Cu(II), Ni(II), Co(II) and Fe(III) metal complexes were investigated in terms of their antioxidant and antibacterial activities in this study. Different methods were used for antioxidant analysis of the compounds. Antibacterial effects of Schiff base and

*Corresponding author: sezersav@gmail.com

Received: 06.10.2022, Accepted: 08.06.2023

its metal complexes were investigated by agar disc diffusion method.

2. Material and Method

2.1. Material

Schiff base and its metal complexes were prepared according to reported method [14]. Structures of the compounds are shown in Figure 1. 1 represents Schiff base structure. 2 represents general formulas of the

metal complexes of Schiff base which M indicates Cu(II), Ni(II), Co(II) and Fe(III) separately. Other chemicals were bought from Sigma Aldrich. Bacterial strains were obtained from Hatay Mustafa Kemal University Research Hospital Microbiology Laboratory. Antioxidant effects of samples were examined in spectrophotometer. Antibacterial studies were carried out with incubator. Autoclave was used for sterilization of tools. The assays were achieved in triplicate.

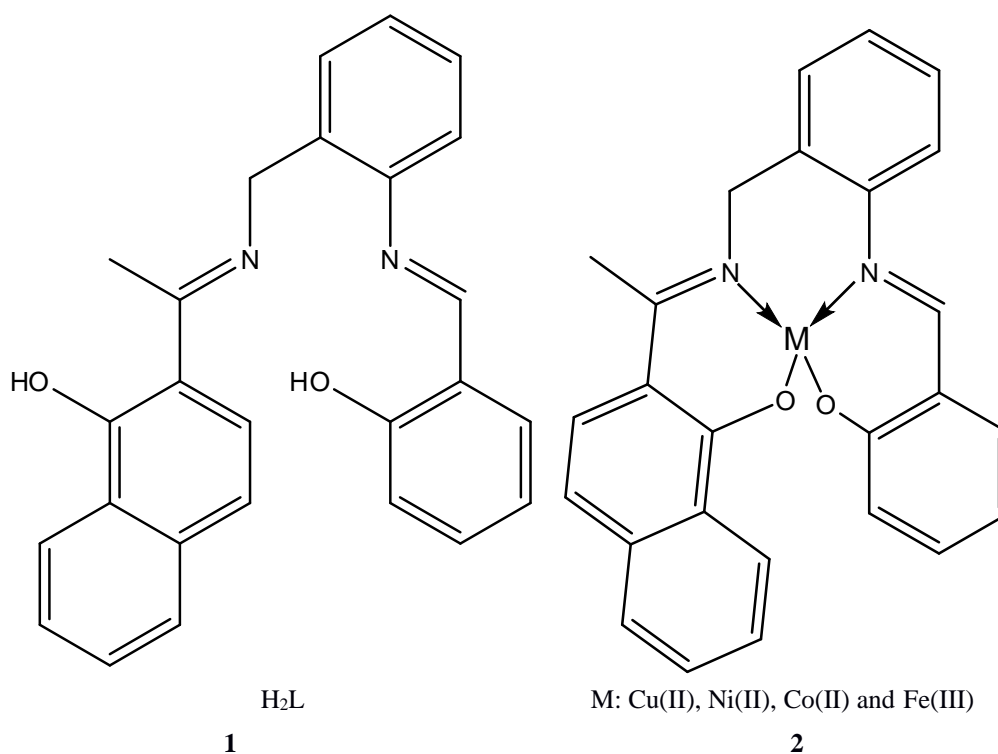


Figure 1. Structures of the compounds

1: FT-IR (U-ATR, cm^{-1}): 3062 cm^{-1} (Ar-H), 2978–2850 cm^{-1} (CH_2), 1611 cm^{-1} ($CH=N$).

1H NMR ($CDCl_3$ as solvent, δ in ppm): 16.0 (s, OH), 12.9 (s, OH), 8.6 (s, $CH=N$), 8.5–6.7 (m, Ar-H), 4.9 (s, CH_2), and 2.5 ppm (s, $-CH_3$).

^{13}C NMR ($CDCl_3$ as solvent, δ in ppm): 175 ($C=N$), 172 ($CH=N$), 163 ($C-OH$), 144–109 (Ar), 45 ($-CH_2-$), and 15 ppm ($-CH_3$).

[CuL]; FT-IR (U-ATR, cm^{-1}): 3442 (O-H), 3047 (Ar,C-H), 2926 (C-H), 1608 ($C=N$), 1258 (C-O), 549 (Cu-O), 459 (Cu-N).

[NiL]; FT-IR (U-ATR, cm^{-1}): 3045 (Ar,C-H), 2997 (C-H), 1608 ($C=N$), 1255 (C-O), 556 (Ni-O), 465 (Ni-N).

[CoL]; FT-IR (U-ATR, cm^{-1}): 3300 (O-H), 3049 (Ar, C-H), 2950 (C-H), 1594 ($C=N$), 1259 (C-O), 582 (Co-O), 462 (Co-N).

[FeL]; FT-IR (U-ATR, cm^{-1}): 3048 (Ar, C-H), 2920 (C-H), 1609 ($C=N$), 1251 (C-O), 574 (Fe-O), 477 (Fe-N).

2.2. Methods

2.2.1. Antioxidant Activity

2.2.1.1. Free Radical Scavenging (DPPH) Assay

2,2-diphenyl-1-picrylhydrazyl (DPPH) was used to determine radical scavenging activities of samples. The method was modified by Brand-Williams [15] and used by Blois firstly [16]. 3.75 mL of 0.06 mM DPPH in methanol was added into various concentrations (1.25 mL) of DMSO solutions of compounds. Absorbances of solutions were observed at 517 nm by spectrophotometrically. BHA and BHT were used as standards. Percentage inhibition was calculated by using the following formula:

$$\% \text{ Inhibition} = [(A_{\text{control}} - A_{\text{sample}}) / A_{\text{control}}] \times 100 \quad (1)$$

A_{control} : DPPH absorbance only, A_{sample} : DPPH absorbance with an antioxidant.

Furthermore, IC_{50} values mean that concentrations of antioxidants cause 50 % scavenging of DPPH radical were calculated.

2.2.1.2. Ferric Reducing Antioxidant Power (FRAP) Assay

Reducing activities of compounds were investigated according to the FRAP method [17]. DMSO solutions of samples in various concentrations added to phosphate buffer. Then, the mixtures were incubated at 50 °C for 20 min. After addition of potassium ferricyanide (1.0 mL, 1.0%). Trichloroacetic acid (10%) was added, and the mixtures were utilized for 10 min. centrifugation. 1.0 mL of the supernatants were mixed with $FeCl_3$ and the absorbances were measured at 700 nm. FRAP values were calculated for the compounds as the ratio of compounds' molar absorptivities to ascorbic acid's molar absorptivity.

2.2.1.3. CUPRAC Antioxidant Capacity Assay

The antioxidant effects of the compounds were investigated by CUPRAC method [18]. $CuCl_2 \cdot 2H_2O$, Nc, ammonium acetate buffer solution and sample solution were mixed. Mixtures were incubated at 25°C for 30 min., and the absorbances were measured at 450 nm. The ratio of each compound's molar absorptivity to molar absorptivity of trolox were calculated as TEAC values (trolox equivalent antioxidant capacity).

2.2.2. Antibacterial Activity

Antibacterial effects of Schiff base and its metal complexes were investigated by agar disc diffusion method [19]. *Enterococcus faecium*, *Pseudomonas aeruginosa*, *Klebsiella pneumoniae* and *Escherichia coli* were used as bacterial strains. Besides, chloramphenicol was used as standard antibacterial agent. The bacteria were cultured at 37 °C. The bacterial suspensions were transferred to sterile Petri plates covered by Muller Hinton agar medium. Filter paper disks were placed on to sterile Petri plates. Solutions of the compounds were dissolved in DMSO. The disks were saturated with 30 μ L of the samples. Incubation was applied to plates at 37 °C. Diameter of the inhibition zones were measured for determination of antibacterial activity of compounds [20].

3. Results and Discussion

3.1. Synthesis

The 1H NMR and ^{13}C NMR spectra of Schiff base are given in Figure 2 and Figure 3, respectively. The observation of peaks in the 1H NMR spectrum at 8.6 ppm and 12.9 ppm attributed to the formation of $CH=N$ and OH , respectively, are the most important evidences of the formation of 1. In addition, the multiplets in the 6.5–8.5 ppm range can be attributed to the protons of benzene rings of H_2L . Also, the $-CH_2-$ protons of these compounds were observed in the 4.9–5.2 ppm region. In the ^{13}C NMR spectrum of H_2L , a band observed at 170 ppm due to $CH=N$ carbon atom. In addition, in the ^{13}C NMR spectrum of this compound, the peaks of the carbon atoms of $-CH_3$ and $-CH_2-$ are observed at 15 ppm and 45 ppm, respectively.

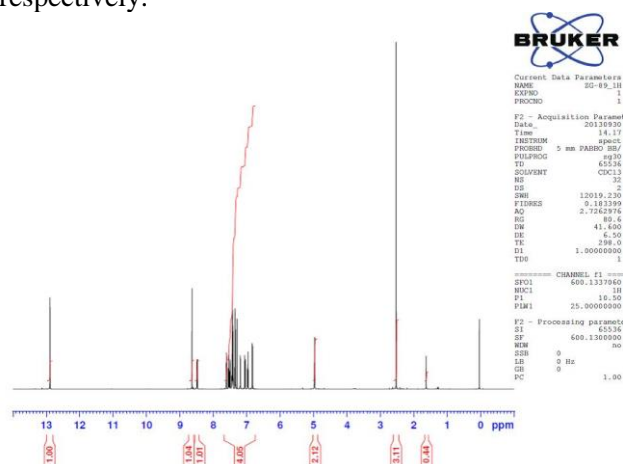


Figure 2. The 1H -NMR spectrum of 1.

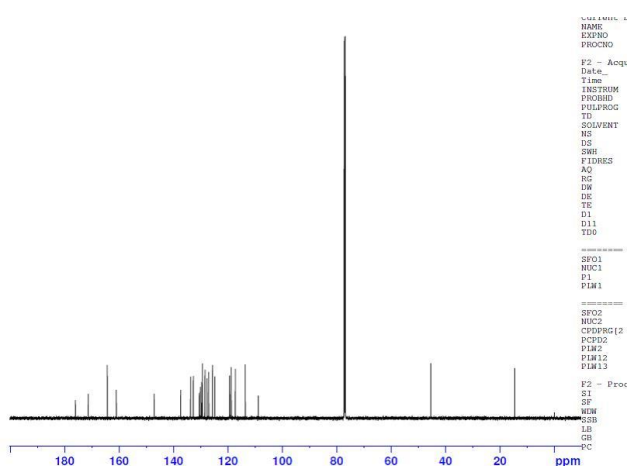


Figure 3. The ^{13}C -NMR spectrum of **1**.

The FT-IR spectra of the ligand and its metal complexes are given in Figure 4. The FT-IR spectrum Schiff base ligand, H_2L , exhibit strong band 1611 cm^{-1}

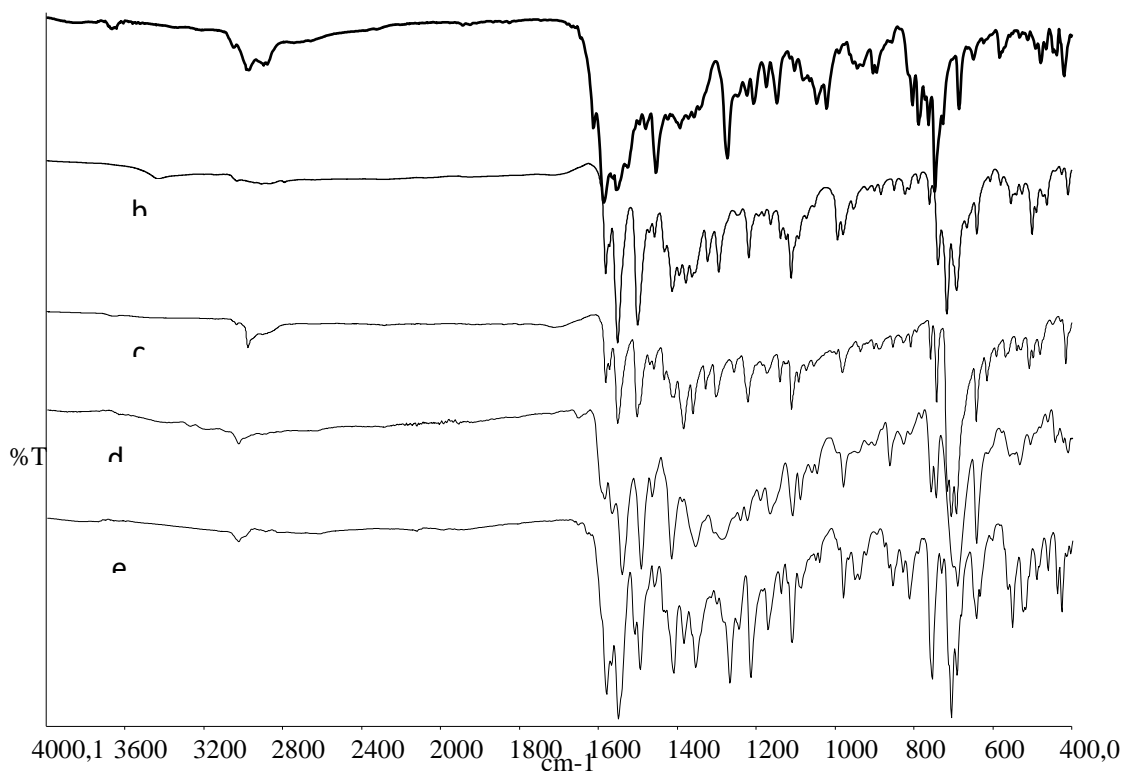


Figure 4. The FT-IR spectra of H_2L (a), $[\text{CuL}]$ (b), $[\text{NiL}]$ (c), $[\text{CoL}]$ (d) and $[\text{FeL}]$ (e).

3.2. Antioxidant Activity

3.2.1. Free Radical Scavenging (DPPH) Assay

1 , attributed to the characteristic peak of $\text{CH}=\text{N}$ stretching vibration frequency. The spectrum also shows several weak bands for the aliphatic and aromatic $\text{C}-\text{H}$ stretching vibration frequencies at the region of $2845\text{--}3070\text{ cm}^{-1}$ and strong bands. The band at 1205 cm^{-1} for H_2L is ascribed to the phenolic $\text{C}-\text{O}$ stretching vibration.

The FT-IR spectra of the metal complexes also showed new bands in the $582\text{--}549$ and $477\text{--}459\text{ cm}^{-1}$ regions, which are probably due to the formation of $\text{M}-\text{O}$ and $\text{M}-\text{N}$ bonds, respectively. The peak observed in the FTIR spectra of metal complexes at around 1600 cm^{-1} , partially differ from the ligand. This can be explained by the formation of a coordination bond between the $\text{C}=\text{N}$ group of the ligand and the metal ion.

Radical scavenging activity of the samples and standards were determined by DPPH assay. IC₅₀ values (amount of antioxidant that scavenged 50% of DPPH radical) were given in Table 1. Low IC₅₀ value represents more scavenging activity. Therefore, BHA is the best antioxidant in Table 1. According to free radical scavenging (DPPH) assay results the metal complexes showed more scavenging activity than the ligand because of chelation theory [21-24]. Ni complex with the lowest IC₅₀ value has the highest scavenging activity among the all metal complexes and the ligand has the lowest scavenging activity because of the highest IC₅₀ value. Furthermore, Fe, Ni and Cu complexes exhibited more scavenging activity than BHT.

Table 1. IC₅₀ values of compounds and standards

Compounds	IC ₅₀
Fe complex	0.265 ± 0.056 (mg/mL)
Co complex	0.430 ± 0.018 (mg/mL)
Ni complex	0.050 ± 0.006 (mg/mL)
Cu complex	0.067 ± 0.008 (mg/mL)
Ligand	0.477 ± 0.079 (mg/mL)
BHA	7.335 ± 0.870 (µg/mL)
BHT	0.359 ± 0.013 (mg/mL)

3.2.2. Ferric Reducing Antioxidant Power (FRAP) Assay

Reducing power of the samples and standards were determined by FRAP assay. FRAP values for FRAP assay were given in Table 2. High FRAP value means high activity whereas low FRAP value means low activity. For that reason, the metal complexes showed more reducing activity than the ligand as FRAP assay results [25]. Even if all of the metal complexes have similar reducing activity, it is observed that Cu complex has the most reducing activity. Fe complex comes after Cu complex. Besides, ligand has the lowest reducing activity.

Both metal complexes and ligand exhibit lower reducing activity than BHA and BHT.

Table 2. FRAP values of compounds and standards

Compounds	FRAP values
Fe complex	0.153 ± 0.07
Co complex	0.110 ± 0.001
Ni complex	0.103 ± 0.006
Cu complex	0.158 ± 0.002
Ligand	0.015 ± 0.005
BHA	2.695 ± 0.311
BHT	1.479 ± 0.234

3.2.3. CUPRAC Antioxidant Capacity Assay

Cupric reducing antioxidant activity of the Schiff base ligand, its metal complexes and standards were determined by CUPRAC assay. TEAC values for CUPRAC assay were given in Table 3. High TEAC value shows more antioxidant capacity. In accordance with CUPRAC assay results, the metal complexes exhibited less antioxidant activity than the ligand due to donor phenolic hydroxyl groups [26, 27]. Ligand has the most antioxidant capacity. Among the metal complexes, Co complex has the lowest antioxidant capacity while Ni complex has the highest antioxidant capacity. Additionally, Fe complex, Ni complex and the ligand have more antioxidant capacity than corresponding to BHT.

Table 3. TEAC values of compounds and standards

Compounds	TEAC values
Fe complex	1.573 ± 0.119
Co complex	0.997 ± 0.036
Ni complex	2.210 ± 0.031
Cu complex	1.235 ± 0.064
Ligand	2.437 ± 0.026
BHA	3.928 ± 0.181
BHT	1.412 ± 0.248

3.3. Antibacterial Activity

In vitro antibacterial activity of compounds was investigated against *Enterococcus faecium*, *Pseudomonas aeruginosa*, *Klebsiella pneumoniae* and *Escherichia coli* strains by agar disc diffusion

method. Zone of inhibition data was given in Table 4. Accordingly, chloramphenicol performed more antibacterial activity on each bacterium than the other compounds. Fe complex showed antibacterial effect to all bacteria except *Klebsiella pneumoniae*. Co and Cu complexes inhibited the growth of *Pseudomonas aeruginosa* and *Escherichia coli* only. Ni complex exhibited antibacterial effect against to all bacteria except to *Enterococcus faecium*. Finally, ligand showed antibacterial effect to all bacteria.

Chloramphenicol

Compounds	Zone of inhibition (mm)		
	<i>E. faecium</i>	<i>P. aeruginosa</i>	<i>K. pneumoniae</i>
Fe complex	13	9	-
Co complex	-	12	-
Ni complex	-	10	12
Cu complex	-	13	-
Ligand	15	10	11
Chloramphenicol	35	25	30

Table 4. Antibacterial activity values of compounds

4. Conclusion and Suggestions

In this study, 2-Aminobenzylamine derived Schiff base and its Cu(II), Ni(II), Co(II) and Fe(III) metal complexes were investigated in terms of their antioxidant and antibacterial activities. Different methods were used for antioxidant analysis of the compounds. According to the results, all of the compounds can be utilized as antioxidant. Likewise, all of the compounds exhibited important antibacterial activities.

Acknowledgment

The authors gratefully acknowledge the support of Prof. Dr. Cahit Demetgül, Department of Chemistry, Faculty of Arts and Sciences, Hatay Mustafa Kemal University, Hatay, Turkey. This research was

financially supported by Hatay Mustafa Kemal University Research foundation (Project No. 18. YL. 032).

Contributions of the authors

The contribution of the authors is equal.

Conflict of Interest Statement

There is no conflict of interest between the author.

Statement of Research and Publication Ethics

The study is complied with research and publication ethics

References

- [1] I. Gonul, M. Kose, G. Ceyhan, and S. Serin, "Methoxy group containing bidentate Schiff base ligands and their transition metal complexes: Synthesis, structural characterisation, photoluminescence,

- antioxidant capacity and superoxide dismutase activity studies”, *Inorganica Chimica Acta*, vol. 453, pp. 522–530, 2016.
- [2] A.A. Al-Amiery, “Synthesis and antioxidant, antimicrobial evaluation, DFT studies of novel metal complexes derivate from Schiff base”, *Res. Chem. Intermed.*, vol.,38, pp. 745–759, 2012.
- [3] C. Demetgül, M. Karakaplan, S. Serin, and M. Diğrak, “Synthesis, characterization, and biological properties of Ni(II), Co(II), and Cu(II) complexes of Schiff bases derived from 4-aminobenzylamine”, *J. Coord. Chem.*, vol.62, pp. 3544–3551, 2009.
- [4] A.A. Al-Amiery, A. A. H. Kadhum, M. Shamel, M. Satar, Y. Khalid, and A. B. Mohamad, “Antioxidant and antimicrobial activities of novel quinazolinones”, *Med. Chem. Res.*, vol. 23, pp. 236–242, 2014.
- [5] S. Saha, A. Das, K. Acharjee, and B. Sinha, “Synthesis, characterization and antibacterial studies of Mn(II) and Co(II) complexes of an ionic liquid tagged Schiff base”, *J. Serb. Chem. Soc.*, vol. 81, pp. 1151–1159, 2016.
- [6] M. S. Refat, “Complexes of uranyl(II), vanadyl(II) and zirconyl(II) with orotic acid “vitamin B13”: Synthesis, spectroscopic, thermal studies and antibacterial activity”, *J. Mol. Struct.*, vol. 842, pp. 24–37, 2007.
- [7] M. A. Neelakantan, F. Rusalraj, J. Dharmaraja, S. Johnsonraja, T. Jeyakumar, and M. S. Pillai, “Spectral characterization, cyclic voltammetry, morphology, biological activities and DNA cleaving studies of amino acid Schiff base metal(II) complexes”, *Spectrochim. Acta A*, vol. 71, pp. 1599–1609, 2008.
- [8] H. F. Abd El-Halim, M. M. Omar, and G. G. Mohamed, “Synthesis, structural, thermal studies and biological activity of a tridentate Schiff base ligand and their transition metal complexes”, *Spectrochim. Acta A*, vol. 78, pp. 36–44, 2011.
- [9] M. B. Halli, and R. B. Sumathi, “Synthesis, spectroscopic, antimicrobial and DNA cleavage studies of new Co(II), Ni(II), Cu(II), Cd(II), Zn(II) and Hg(II) complexes with naphthofuran-2-carbohydrazide Schiff base”, *J. Mol. Struct.*, vol. 1022, pp. 130–138, 2012.
- [10] M. Şahin, N. Koçak, D. Erdenay, and U. Arslan, “Zn(II), Ni(II), Cu(II) and Pb(II) complexes of tridentate asymmetrical Schiff base ligands: Synthesis, characterization, properties and biological activity”, *Spectrochim. Acta A*, vol. 103, pp. 400–408, 2013.
- [11] O. A. M. Ali, “Synthesis, spectroscopic, fluorescence properties and biological evaluation of novel Pd(II) and Cd(II) complexes of NOON tetradentate Schiff bases”, *Spectrochim. Acta A*, vol. 121, pp. 188–195, 2014.
- [12] Q. Hasi, Y. Fan, X. Yao, D. Hu, and J. Liu, “Synthesis, characterization, antioxidant and antimicrobial activities of a bidentate Schiff base ligand and its metal complexes”, *Polyhedron*, vol. 109, pp. 75–80, 2016.
- [13] M. I. Sundararajan, T. Jeyakumar, J. Anandakumaran, and B. K. Selvan, “Synthesis of metal complexes involving Schiff base ligand with methylenedioxy moiety: Spectral, thermal, XRD and antimicrobial

- studies”, *Spectrochimica Acta Part A: Molecular and Biomolecular Spectroscopy*, vol. 131, pp. 82-93, 2014.
- [14] D. Çakmak, S. Çakran, S. Yalçinkaya, and C. Demetgül, “Synthesis of salen-type Schiff base metal complexes, electropolymerization on graphite electrode surface and investigation of electrocatalytic effects”, *Journal of Electroanalytical Chemistry*, vol. 808, pp. 65-74, 2018.
- [15] U. K. Sharma, S. Sood, N. Sharma, P. Rahi, R. Kumar, A. K. Sinha, and A. Gulati, “Synthesis and SAR investigation of natural phenylpropenederived methoxylated cinnamaldehydes and their novel Schiff bases as potent antimicrobial and antioxidant agents”, *Med. Chem. Res.*, vol. 22, pp. 5129–5140, 2013.
- [16] B. B. Sokmen, N. Gumrukcuoglu, S. Ugras, H. Sahin, Y. Sagkal, and H. I. Ugras, “Synthesis, antibacterial, antiurease, and antioxidant activities of some new 1,2,4-triazole Schiff base and amine derivatives”, *Appl. Biochem. Biotechnol.*, vol. 175, pp. 705–714, 2015.
- [17] M. Silinsin, and E. Bursal, “UHPLC-MS/MS phenolic profiling and in vitro antioxidant activities of *Inula graveolens* (L.) Desf.”, *Nat. Prod. Res.*, vol. 32, no. 12, pp. 1467-1471, 2018.
- [18] R. Apak, K. Güçlü, M. Özyürek, and S. E. Karademir, “Novel total antioxidant capacity index for dietary polyphenols and vitamins C and E, using their cupric ion reducing capability in the presence of neocuproine: CUPRAC method”, *J. Agric. Food Chem.*, vol. 52, no. 26, pp.7970-7981, 2004.
- [19] A. Rehman, M. I. Choudhary, and W. J. Thomsen, *Bioassay Techniques for Drug Development*, Amsterdam, The Netherlands, Harwood Academic Publishers, pp. 9, 2001.
- [20] R. S. Varma, Z. K. Khan, and A. P. Singh, “Antifungal agents: past, present and future prospects”, *National Academy of Chemistry and Biology*, India, Lucknow, pp. 55, 1998.
- [21] S. B. Bukhari, S. Memon, M. Mahroof-Tahir, and M. I. Bhangar, “Synthesis, characterization and antioxidant activity copper-quercetin complex”, *Spectrochim. Acta A*, vol.71, no. 5, pp., 2009.
- [22] M. R. Karekal, V. Biradar, and M. B. H. Mathada, “Synthesis, characterization, antimicrobial, DNA cleavage, and antioxidant studies of some metal complexes derived from Schiff base containing indole and quinoline moieties”, *Bioinorg. Chem. Appl. Res.*, doi: 10.1155/2013/315972, 2013.
- [23] H. A. R. Pramanik, P. C. Paul, P. Mondal, C. R. Bhattacharjee, “Mixed ligand complexes of cobalt(III) and iron (III) containing N₂O₂-chelating Schiff Base: Synthesis, characterization, antimicrobial activity, antioxidant and DFT study”, *J. Mol. Struct.*, vol. 1100, pp. 496-505, 2015.
- [24] R. A. Ammar, A. M. A. Alaghaz, M. E. Zayed, and L. A. Al-Bedair, “Synthesis, spectroscopic, molecular structure, antioxidant, antimicrobial and antitumor behavior of Mn(II), Co(II), Ni(II), Cu(II) and Zn(II) complexes of O₂N type tridentate chromone-2-carboxaldehyde Schiff’s base ligand”, *J. Mol. Struct.*, vol. 1141, pp. 368-381, 2017.
- [25] M. Gaber, H. A. El-Ghamry, S. K. Fathalla, and M. A. Mansour, “Synthesis, spectroscopic, thermal and molecular modeling studies of Zn²⁺, Cd²⁺ and UO₂²⁺ complexes of Schiff bases containing triazole moiety. Antimicrobial, anticancer, antioxidant and DNA binding studies”, *Mater. Sci. Eng.*, vol. 83, pp. 78-89, 2018.
- [26] T. Bal-Demirci, M. Şahin, E. Kondakçı, M. Özyürek, B. Ülküseven, and R. Apak, “Synthesis and antioxidant activities of transition metal complexes based 3-hydroxysalicylaldehyde-S-methylthiosemicarbazone”, *Spectrochim. Acta A*, vol. 138, pp. 866-872, 2015.
- [27] W. Al Zoubi, A. A. S. Al-Hamdani, and M. Kaseem, “Synthesis and antioxidant activities of Schiff bases and their complexes: a review”, *Appl. Organometal Chem.*, vol. 30, pp. 810-817, 2016.



On the Coefficient Bound Estimates and Fekete-Szegö Problem

Nizami MUSTAFA¹, Semra KORKMAZ^{2*}



Kafkas Üniversitesi, Fen Edebiyat Fakültesi, Matematik Bölümü, Kars
(ORCID: 0000-0002-2758-0274) (ORCID: 0000-0002-7846-9779)

Keywords:

Coefficient estimates, Fekete-Szegö problem, Analytic function.

Abstract

In this study, we introduce and examine a certain subclass of analytic functions in the open unit disk in the complex plane. Here, we give coefficient bound estimates and investigate the Fekete-Szegö problem for the introduced class. Some interesting special cases of the results obtained here are also discussed.

1. Introduction

In the study, by A we denote the class of all complex valued functions f which are analytic in the open unit disk $\mathcal{A} = \{t \in \mathbb{C} : |t| < 1\}$ in the complex plane \mathbb{C} and written in the form

$$f(t) = t + a_2 t^2 + \dots + a_n t^n + \dots$$

$$= t + \sum_{n=2}^{\infty} a_n t^n, t \in \mathbb{C}. \quad (1)$$

Then, the family of all univalent functions in A is denoted by S . Next, let $\alpha \in [0, 1)$ then, $S^*(\alpha)$ denotes the starlike function classes of order α and $C(\alpha)$ denotes the convex function classes of order α in A . By definition, we have

$$S^*(\alpha) = \left\{ f \in S : \operatorname{Re} \left(\frac{t f'(t)}{f(t)} \right) > \alpha, t \in \mathcal{A} \right\} \text{ and}$$

$$C(\alpha) = \left\{ f \in S : \operatorname{Re} \left(1 + \frac{t f''(t)}{f'(t)} \right) > \alpha, t \in \mathcal{A} \right\}.$$

Moreover, if f and g are analytic functions in A , then we say that f is subordinate to g and denote this condition by $f(t) \prec g(t)$ when an analytic

function ω can be found such that it satisfies the conditions

$$\omega(0) = 0, |\omega(t)| < 1 \text{ and } f(t) = g(\omega(t)).$$

The researchers agree that the coefficient problem is one of the crucial subjects of the geometric function theory. Many different and interesting subclasses of analytic functions have been defined and investigated by many researchers and some estimates on the first two coefficients for the functions of these classes have been found by them (see [2, 3, 10, 15, 19, 22]).

In the literature, the functional $H_2(1) = a_3 - a_2^2$ is known as the Fekete-Szegö functional. Actually, the further generalized functional $H_2(1) = a_3 - \mu a_2^2$ for real or complex number μ is known as the Fekete-Szegö functional in analytic functions theory (see [7]). In this theory, the Fekete-Szegö problem is to estimate the upper bound of $|a_3 - \mu a_2^2|$. Many researchers have investigated this problem for different subclasses of analytic functions (see [12, 13, 21]). Very recently, the Fekete-Szegö problem for the subclass of bi-univalent functions in relation with a shell shaped region was studied by Mustafa and Mrugusundaramoorthy in [14] and associated with a nephroid domain in [20]. Also, the Fekete-Szegö problem is investigated for subclasses of bi-univalent functions with respect to the symmetric points defined by Bernoulli polynomials in [1], for bi-univalent

*Corresponding author: korkmazsemra36@outlook.com

Received: 26.10.2022, Accepted: 13.01.2023

functions related to the Legendre polynomials in [4], for m-fold symmetric bi-univalent functions in [16].

In [18] for the function $f \in \mathcal{A}$, the following differential operator was introduced by Sălăgean and is known in the literature as the Sălăgean operator

$$S^0 f(t) = f(t), S^1 f(t) = tSf(t) = tf'(t),$$

$$S^2 f(t) = tS(Sf(t)) = tf''(t), \dots,$$

$$S^n f(t) = tS(S^{n-1} f(t)),$$

$$n = 1, 2, \dots .$$

From this definition, it can be clearly seen that

$$S^n f(t) = t + \sum_{k=2}^{\infty} k^n a_k t^k, t \in \mathcal{A}, n \in \mathbb{N}_0 = \mathbb{N} \cup \{0\}.$$

Sălăgean differential operator is used in recent research related to Janowski type p -harmonic functions [11], meromorphic harmonic functions [5] and starlike functions [9].

Now, we define some new subclasses of analytic and univalent functions as follows.

Definition 1.1. We will say a function $f \in \mathcal{S}$ is in the class $S^*(n, \varphi)$ if it satisfies

$$\frac{z(S^n f(t))'}{S^n f(t)} \prec \varphi(t), t \in \mathcal{A}$$

for $n = 0, 1, 2, \dots$.

In the case $n = 0$, we have the subclass $S^*(\varphi) = S^*(0, \varphi)$.

In the Definition 1.1, $\varphi(t) = t + \sqrt{1+t^2}$ and the branch of the square root is chosen with the initial value $\varphi(0) = 1$. It can be clearly seen that by $\varphi(t) = t + \sqrt{1+t^2}$, the unit disc \mathcal{A} is mapped onto a shell shaped region on the right half plane and φ is univalent and analytic in \mathcal{A} . Respect to real axis, the range $\varphi(\mathcal{A})$ is symmetric and φ has positive real

part in \mathcal{A} such that $\varphi(0) = \varphi'(0) = 1$. Furthermore, with respect to point $\varphi(0) = 1$, $\varphi(\mathcal{A})$ is a starlike domain.

Let, \mathcal{P} be the set of the functions $k(t)$ analytic in \mathcal{A} and satisfying $\operatorname{Re}(k(t)) > 0, t \in \mathcal{A}$ and $k(0) = 1$ with power series

$$k(t) = 1 + k_1 t + k_2 t^2 + k_3 t^3 + \dots + k_n t^n + \dots$$

$$= 1 + \sum_{n=1}^{\infty} k_n t^n, t \in \mathcal{A}$$

We will need the lemmas below (see [6, 8]) for the functions with positive real part so that we can show our main results.

Lemma 1.2. Let $k \in \mathcal{P}$, then $|k_n| \leq 2$ for $n = 1, 2, \dots$ and

$$\left| k_2 - \frac{c}{2} k_1^2 \right| \leq 2 \cdot \max \{1, |c-1|\}$$

$$= 2 \cdot \begin{cases} 1 & \text{if } c \in [0, 2], \\ |c-1| & \text{elsewhere.} \end{cases}$$

Lemma 1.3. Let $k \in \mathcal{P}$, then $|k_n| \leq 2$ for each $n = 1, 2, \dots$ and

$$2k_2 = k_1^2 + (4 - k_1^2)x,$$

$$4k_3 = k_1^3 + 2(4 - k_1^2)k_1 x - 2(4 - k_1^2)k_1 x^2$$

$$+ 2(4 - k_1^2)(1 - |x|^2)z$$

for some x and z with $|x| < 1$ and $|z| < 1$.

Lemma 1.4. Let $k \in \mathcal{P}$, $b \in [0, 1]$ and $b(2b-1) \leq d \leq b$. Then,

$$|k_3 - 2bk_1 k_2 + dk_1^3| \leq 2.$$

Remark 1.5. As can be seen from the serial expansion the function φ given in Definition 1.1, belong to the class P.

In this paper, we give coefficient bound estimates and solve the Fekete-Szegö problem for the class $S^*(n, \varphi)$.

2. Main Results

In this section, firstly we present the below theorem on the coefficient bound estimates for the class $S^*(n, \varphi)$. In the study of bi-univalent functions, estimates on the first two Taylor–Maclaurin coefficients are usually given. We go further in the present paper and bounds of the first three coefficients as seen also in paper [17].

Theorem 2.1. Let the function f given by (1) be in the class $S^*(n, \varphi)$. Then,

$$|a_2| \leq \frac{1}{2^n}, \quad |a_3| \leq \frac{1}{4 \cdot 3^{n-1}} \quad \text{and} \quad |a_4| \leq \frac{5}{6 \cdot 4^n}.$$

Proof. Let $f \in S^*(n, \varphi)$. Then, according to Definition 1.1 there is an analytic function $\omega: \mathcal{A} \rightarrow \mathcal{A}$ with $\omega(0) = 0$ and $|\omega(t)| < 1$ satisfying the following condition

$$\begin{aligned} \frac{t(S^n f(t))'}{S^n f(t)} &= \varphi(\omega(t)) \\ &= \omega(t) + \sqrt{1 + \omega^2(t)}, \quad t \in \mathcal{A} \end{aligned} \tag{2}$$

Let, we define the function $t \in \mathcal{P}$ as follows

$$\begin{aligned} k(t) &= \frac{1 + \omega(t)}{1 - \omega(t)} \\ &= 1 + k_1 t + k_2 t^2 + k_3 t^3 + \dots + k_n t^n + \dots \\ &= 1 + \sum_{n=1}^{\infty} k_n t^n, \quad t \in \mathcal{A} \end{aligned}$$

It follows from that

$$\begin{aligned} \omega(t) &= \frac{k(t) - 1}{k(t) + 1} \\ &= \frac{1}{2} \left[k_1 t + \left(k_2 - \frac{k_1^2}{2} \right) t^2 + \left(k_3 - k_1 k_2 + \frac{k_1^3}{4} \right) t^3 + \dots \right], \tag{3} \\ &t \in \mathcal{A}. \end{aligned}$$

Changing the formulation of the function ω in (2) with formulation in (3), we get

$$\begin{aligned} \frac{t(S^n f(t))'}{S^n f(t)} &= 1 + \frac{k_1}{2} t + \left(\frac{k_2}{2} - \frac{k_1^2}{8} \right) t^2 + \left(\frac{k_3}{2} - \frac{k_1 k_2}{4} \right) t^3 + \dots, \tag{4} \\ &t \in \mathcal{A} \end{aligned}$$

If necessary derivative operations and simplifications are made to the left-hand side of (4), we get

$$\begin{aligned} &1 + 2^n a_2 t + (2 \cdot 3^n a_3 - 4^n a_2^2) t^2 \\ &+ (3 \cdot 4^n a_4 - 3 \cdot 6^n a_2 a_3 + 8^n a_2^3) t^3 + \dots \\ &= 1 + \frac{k_1}{2} t + \left(\frac{k_2}{2} - \frac{k_1^2}{8} \right) t^2 + \left(\frac{k_3}{2} - \frac{k_1 k_2}{4} \right) t^3 + \dots, \tag{5} \\ &t \in \mathcal{A} \end{aligned}$$

Then, by equalizing the coefficients of the terms of the same degree, are obtained the following equalities for a_2, a_3 and a_4

$$\begin{aligned} 2^n a_2 &= \frac{k_1}{2}, \quad 2 \cdot 3^n a_3 - 4^n a_2^2 = \frac{k_2}{2} - \frac{k_1^2}{8}, \\ 3 \cdot 4^n a_4 - 3 \cdot 6^n a_2 a_3 + 8^n a_2^3 &= \frac{k_3}{2} - \frac{k_1 k_2}{4}; \end{aligned}$$

that is,

$$a_2 = \frac{k_1}{2^{n+1}}, \tag{6}$$

$$a_3 = \frac{1}{2} \left(\frac{4}{3} \right)^n a_2^2 + \frac{1}{4 \cdot 3^n} \left(k_2 - \frac{k_1^2}{4} \right), \tag{7}$$

$$a_4 = \left(\frac{3}{2}\right)^n a_2 a_3 - \frac{2^n}{3} a_2^3 + \frac{1}{6 \cdot 4^n} \left(k_3 - \frac{k_1 k_2}{2}\right). \quad (8)$$

By applying the Lemma 1.2 to the equality (6), immediately obtained first result of theorem.

Now, considering equality (6) and applying the Lemma 1.3, then applying triangle inequality and Lemma 1.2 to the equality (7), we get the following inequality as

$$|a_3| \leq \frac{3}{16 \cdot 3^n} z^2 + \frac{4-z^2}{8 \cdot 3^n} \xi, \quad \xi \in (0,1), \quad (9)$$

with $z = |k_1|$, $\xi = |x| < 1$. If we maximize the right-hand side of the inequality (9) respect to the parameter ξ , we obtain

$$|a_3| \leq \frac{3}{16 \cdot 3^n} z^2 + \frac{4-z^2}{8 \cdot 3^n}, \quad z \in [0,2];$$

that is,

$$|a_3| \leq \frac{1}{3^n} \left(\frac{z^2}{16} + \frac{1}{2}\right), \quad z \in [0,2].$$

From the last inequality obtained the second result of theorem.

Finally, let's find an upper bound estimate for the coefficient a_4 . From the equalities (6)-(8), we write

$$a_4 = \frac{k_1}{2^{2n+3}} \left(k_2 - \frac{k_1^2}{4}\right) + \frac{1}{6 \cdot 4^n} \left(k_3 - \frac{k_1 k_2}{2} + \frac{k_1^3}{8}\right)$$

that is,

$$a_4 = \frac{k_1}{2^{2n+3}} \left(k_2 - \frac{c}{2} k_1^2\right) + \frac{1}{6 \cdot 4^n} (k_3 - 2bk_1 k_2 + dk_1^3),$$

with $c = \frac{1}{2}$, $b = \frac{1}{4}$ and $d = \frac{1}{8}$. Using triangle inequality to the last equality, we get

$$|a_4| \leq \frac{|k_1|}{2^{2n+3}} \left|k_2 - \frac{c}{2} k_1^2\right| + \frac{1}{6 \cdot 4^n} |k_3 - 2bk_1 k_2 + dk_1^3|.$$

Also, since

$$|k_1| \leq 2, \quad \left|k_2 - \frac{c}{2} k_1^2\right| \leq 2 \quad \text{and} \\ |k_3 - 2bk_1 k_2 + dk_1^3| \leq 2,$$

according to Lemma 1.2 and Lemma 1.4, respectively, we obtain desired estimate for $|a_4|$.

Therefore, the proof of Theorem 2.1 is done.

In the case $n = 0$, from the Theorem 2.1 obtained the following result.

Corollary 2.2. Assume that f given by (1) is in the class $S^*(\varphi)$. Then,

$$|a_2| \leq 1, \quad |a_3| \leq \frac{3}{4} \quad \text{and} \quad |a_4| \leq \frac{5}{6}.$$

Now, we give the following theorem on the Fekete-Szegő problem for the class $S^*(n, \varphi)$.

Theorem 2.2. Assume that f given by (1) is in the class $S^*(n, \varphi)$ and $\mu \in \square$. Then,

$$|a_3 - \mu a_2^2| \leq \frac{1}{4 \cdot 3^n} \cdot \begin{cases} 2 & \text{if } 2 \left| \left(\frac{4}{3}\right)^n - 2\mu \right| \leq \left(\frac{4}{3}\right)^n, \\ 2 \left| \left(\frac{4}{3}\right)^n - 2\mu \right| \left(\frac{3}{4}\right)^n + 1 & \text{if } 2 \left| \left(\frac{4}{3}\right)^n - 2\mu \right| > \left(\frac{4}{3}\right)^n. \end{cases}$$

Proof. Let $f \in S^*(n, \varphi)$ and $\mu \in \square$. Then, from the expressions for the coefficients a_2 and a_3 in the equalities (6) and (7), we can write

$$a_3 - \mu a_2^2 = \frac{1}{2} \left[\left(\frac{4}{3}\right)^n - 2\mu \right] a_2^2 + \frac{1}{4 \cdot 3^n} \left(k_2 - \frac{k_1^2}{4}\right).$$

Considering equality (6) and applying Lemma 1.3, we write the following equality

$$a_3 - \mu a_2^2 = \frac{1}{8} \left\{ \left[\left(\frac{4}{3} \right)^n - 2\mu \right] \frac{k_1^2}{4^n} + \frac{1}{3^n} \left(\frac{k_1^2}{2} + (4 - k_1^2)x \right) \right\}$$

for some x with $|x| < 1$. From this, using triangle inequality we obtain

$$|a_3 - \mu a_2^2| \leq \frac{1}{8} \left\{ \left[\left(\frac{4}{3} \right)^n - 2\mu \right] \frac{1}{4^n} + \frac{1}{2 \cdot 3^n} \right\} z^2 + \frac{4 - z^2}{3^n} \xi, \quad \xi \in (0,1)$$

with $z = |k_1|$, $\xi = |x|$. If we maximize the right-hand side of this inequality with respect to the parameter ξ , we get

$$|a_3 - \mu a_2^2| \leq \frac{1}{8 \cdot 3^n} \left\{ \left[\left(\frac{4}{3} \right)^n - 2\mu \right] \left(\frac{3}{4} \right)^n - \frac{1}{2} \right\} z^2 + 4, \quad z \in [0,2]. \tag{10}$$

Now, we define the function $\sigma : [0,2] \rightarrow \mathbb{R}$ as follows

$$\sigma(z) = \left[\left(\frac{4}{3} \right)^n - 2\mu \right] \left(\frac{3}{4} \right)^n - \frac{1}{2} z^2 + 4, \quad z \in [0,2].$$

It is clear that the function σ is a decreasing function if

$$2 \left| \left(\frac{4}{3} \right)^n - 2\mu \right| \leq \left(\frac{4}{3} \right)^n$$

and

$$\max \{ \sigma(z) : z \in [0,2] \} = \sigma(0) = 4. \tag{11}$$

Additionally, the function σ is an increasing function if

$$2 \left| \left(\frac{4}{3} \right)^n - 2\mu \right| > \left(\frac{4}{3} \right)^n$$

and

$$\max \{ \sigma(z) : z \in [0,2] \} = \sigma(2) = 4 \left| \left(\frac{4}{3} \right)^n - 2\mu \right| \left(\frac{3}{4} \right)^n + 2. \tag{12}$$

Considering (11) and (12) in the inequality (10), we arrive at the result.

That is, the proof of Theorem 2.2 is done.

In the cases $n = 0$ and $\mu = 0$, respectively from the Theorem 2.2, the following results are obtained.

Corollary 2.3. Let $f \in S^*(\varphi)$ and $\mu \in \mathbb{R}$, then

$$|a_3 - \mu a_2^2| \leq \frac{1}{4} \cdot \begin{cases} 2 & \text{if } 2|1 - 2\mu| \leq 1, \\ 2|1 - 2\mu| + 1 & \text{if } 2|1 - 2\mu| > 1. \end{cases}$$

Corollary 2.4. Let $f \in S^*(n, \varphi)$, then

$$|a_3| \leq \frac{1}{4 \cdot 3^{n-1}}.$$

Corollary 2.5. Let $f \in S^*(n, \varphi)$, then

$$|a_3 - a_2^2| \leq \frac{1}{4 \cdot 3^n} \cdot \begin{cases} 2 & \text{if } 2 \left| \left(\frac{4}{3} \right)^n - 2 \right| \leq \left(\frac{4}{3} \right)^n, \\ 2 \left| \left(\frac{4}{3} \right)^n - 2 \right| \left(\frac{3}{4} \right)^n + 1 & \text{if } 2 \left| \left(\frac{4}{3} \right)^n - 2 \right| > \left(\frac{4}{3} \right)^n. \end{cases}$$

Remark 2.6. Result obtained in the Corollary 2.4 confirm the second inequality obtained in Theorem 2.1.

Statement of Research and Publication Ethics

The study is complied with research and publication ethics.

References

- [1] M. Buyankara, M. Çağlar, L.-I. Cotîrlă, “New subclasses of bi-univalent functions with respect to the symmetric points defined by bernoulli polynomials”, *Axioms*, vol.11, no.11, pp. 652-660, 2022.
- [2] D. A. Brannan and J. Clunie, “Aspects of Contemporary Complex Analysis”, *Academic Press*, London and New York, USA, 1980.
- [3] D. A. Brannan and T. S. Taha, “On Some Classes of Bi-univalent Functions”, *Studia Univ. Babeş-Bolyai Mathematics*, vol. 31, pp.70-77, 1986.
- [4] Y. Cheng, R. Srivastava, J. L. Liu, “Applications of the q-derivative operator to new families of bi-univalent functions related to the Legendre Polynomials”, *Axioms*, vol. 11, no.11, pp. 595-607, 2022.
- [5] J. Dziok, “Classes of meromorphic harmonic functions defined by Sălăgean operator”, *Revista de la Real Academia de Ciencias Exactas, Físicay Naturales. Serie A. Matemáticas*, vol. 116, no.4, pp.1-16, 2022.
- [6] P. L. Duren, “Univalent Functions”, In: *Grundlehren der Mathematischen Wissenschaften*, Band 259, New- York, Berlin, Heidelberg and Tokyo, Springer-Verlag, 1983.
- [7] M. Fekete and G. Szegő, “Eine Bemerkung über ungerade schlichte funktionen”, *Journal of the London Mathematical Society*, vol.8, pp.85-89, 1993.
- [8] U. Grenander and G. Szegő, “Toeplitz form and their applications”, *California Monographs in Mathematical Sciences*, University California Press, Berkeley, 1958.
- [9] H.Ö. Güney, G.I. Oros, S. Owa, “An Application of Sălăgean operator concerning starlike functions”, *Axioms*, vol. 11, no.2, pp. 50-59, 2022.
- [10] M. Lewin, “On a coefficient problem for bi-univalent functions”, *Proceedings of the American Mathematical Society*, vol.18, pp.63-68, 1967.
- [11] S. Li, L. Ma, H. Tang, “On Janowski type p-harmonic functions associated with generalized Sălăgean operator”, *AIMS Mathematics*, vol. 6, no.1, pp.569-583, 2021.
- [12] N. Mustafa, “Fekete- Szegő problem for certain subclass of analytic and bi-univalent functions”, *Journal of Scientific and Engineering Research*, vol.4, no.8, pp.30-400, 2017.
- [13] N. Mustafa and M. C. Gündüz, “The Fekete-Szegő problem for certain class of analytic and univalent functions”, *Journal of Scientific and Engineering Research*, vol.6, no.5, pp.232-239, 2019.
- [14] N. Mustafa and G. Murugusundaramoorthy, “Second Hankel for mocanu type bi-starlike functions related to shell shaped region”, *Turkish Journal of Mathematics*, vol.45, pp.1270-1286, 2021.
- [15] E. Netanyahu, “The minimal distance of the image boundary from the origin and the second coefficient of a univalent function”, *Archive for Rational Mechanics and Analysis*, vol.32, pp.100-112, 1969.
- [16] G.I. Oros, L.-I. Cotîrlă, “Coefficient Estimates and the Fekete–Szegő problem for new classes of m-fold symmetric bi-univalent functions”, *Mathematics*, vol. 10, pp. 129-141, 2022. <https://doi.org/10.3390/math10010129>
- [17] Á.O. Páll-Szabó, G. I. Oros, “Coefficient related studies for new classes of bi-univalent functions”, *Mathematics*, vol. 8, no.7, pp. 1110-1123, 2020.
- [18] G. S. Sălăgean, “Subclasses of univalent functions”, *Complex Analysis*, vol.103, pp.362-372, 1983.

- [19] H. M. Srivastava, A. K. Mishra and P. Gochhayat, "Certain subclasses of analytic and bi-univalent functions", *Applied Mathematics Letters*, vol.23, pp.1188-1192, 2010.
- [20] H. M. Srivastava, G. Murugusundaramoorthy, T. Bulboacă, "The second Hankel determinant for subclasses of bi-univalent functions associated with a nephroid domain", *Revista de la Real Academia de Ciencias Exactas, Físicas y Naturales. Serie A. Matemáticas*, vol. 116, no.4, 1-21, 2022.
- [21] P. Zaprawa, "On the Fekete-Szegő problem for the classes of bi-univalent functions", *Bulletin of the Belgain Mathematical Society*, vol.21, pp.169-178, 2014.
- [22] Q. H. Xu, G. Xiao and H. M. Srivastava, "A certain general subclass of analytic and bi-univalent functions and associated coefficient estimate problems", *Applied Mathematics and Computation*, vol. 218, pp.11461-11465, 2012.

Predicting the Work-Life Balance of Employees Based on the Ensemble Learning Method

Vedat TÜMEN^{1*}, Ayşe Saliha SUNAR¹

¹Bitlis Eren University, Faculty of Engineering and Architecture, Department of Computer Engineering (ORCID: 0000-0003-0271-216X) (ORCID: 0000-0002-0836-5616)



Keyword: Work Life Balance, Ensemble learning, Extreme Gradient Boosting, Random forest.

Abstract

Working life has a great impact on other areas of people's lives. Efforts made at work lead to attrition, exhaustion, and health problems. Employers need to take the necessary steps to keep employees motivated by helping them balance work and personal lives. Employers can use many different techniques to measure and analyse the work-life balance of their employees, such as questionnaires and machine learning techniques. This research was conducted to group workers based on turnover levels using effort and work-life balance parameters. Machine learning, including ensemble learning techniques, is used to achieve this. One ensemble learning algorithm, Random Forest, performed almost as well as Support Vector Machine with the highest score of 95%. Almost all algorithms, regardless of whether they are part of ensemble learning or not, achieved an f-score of 86%. However, one of the ensemble learning models, xGBoost, performed poorly with the lowest f-score of 69%. All algorithms predicted the lowest and highest work-life balance scores but were confused when predicting the middle scores (class 2 and class 3).

1. Introduction

While it is a challenge in the labour market to find a suitable job or a competent employee, one of the biggest problems after recruitment is the attrition rate. This problem affects both employees and employers, and it is not a sector-specific problem. Whether it is government or private institutions in various sectors, from medicine [1] to education [2, 3] to engineering [4], attrition rate is considered a problem. Researchers therefore examined the problem from different angles, e.g. private government institutions [5], employee age [6, 7], maternity leave [8], and so on.

Evidence from the literature shows that many factors can lead to a high attrition rate. For example, researchers from India found that for engineers, salary is the most important factor affecting attrition rates, while for non-engineers, the most important factor is the boss, which is made up of boss, stress and salary factors [9]. In [10], the causes of turnover were analysed in depth using both contextual factors (gender, generation, tenure) and 12 human resource

factors, including better career opportunities, enriching work content, reward and recognition, and work-life balance. The authors also found that gender and work-life balance are positively correlated. This is also noted by [4] in their study. The respondents identified the problem of work-life balance and categorised it into lack of personal life, long working hours and work pressure, shift hours and night shifts, and insufficient holidays and lack of national holidays. Nevertheless, work-life balance is becoming more and more important in our lives, as one of the consequences of the COVID -19 pandemic is remote working with flexible working hours, which could make it more difficult to balance private and professional life [11-13].

These identified characteristics, including work-life balance, help researchers predict attrition before it occurs so employers can be aware of the problem to make preventative decisions. Machine learning techniques are often used to predict attrition [14]. Some research uses regression or tree-based models to determine which features best predict

*Corresponding Author: vtumen@beu.edu.tr

Received: 31.10.2022, Accepted: 17.04.2023

turnover. For example, [15] uses XGBoost and [16] uses a regression model. Apart from that, [17] compares a number of machine learning algorithms and finds that the decision tree model has the best predictive model.

In this study, ensemble learning algorithms were used to evaluate, compare and optimise performance metrics. This method, in which predictions are made by using many different model algorithms, has been widely used in the field of artificial intelligence for a variety of applications in recent years [18]. Ensemble learning algorithms produce successful results in various machine learning systems, such as feature extraction, confidence estimation, error correction, unbalanced data, and learning the variance in non-stationary distributions. Ensemble learning is a method of combining multiple models and usually improves the predictive performance of the model and increases confidence in the decision to be made [19].

The ensemble learning method has led to successful results in many different fields. For example, in health science, machine learning techniques were used to diagnose Alzheimer's disease [20], and in sports science, machine learning techniques were used to determine a position based on the performance of football players [21], and high success was achieved. To predict the presence of salmonella in agricultural surface waters [22], a study [23] was conducted to estimate how many sensor nodes are needed to install sensors in the field of wireless sensor networks and how large the distance between nodes should be examined [24].

How machine learning can predict effective work schedules and patterns that increase worker productivity. Estimation results were evaluated using the Random Forest Classifier, SVM, and Naïve Bayes algorithms. The algorithms estimated WLB with a best accuracy of 71.5%. The selectKbest algorithm

was used to examine the factors that influence the subjective feeling of work-life balance of 800 workers in a country. In the tests, it predicted WLB with 81% accuracy based on the prepared data set and the selected characteristics [25].

While these studies predict turnover based on parameters that include work-life balance, in this study we predict work-life balance values based on some indicative characteristics from the data collected from the workers at IBM. The aim of this study is to use ensemble learning to predict the work-life balance of employees in a company.

2. Dataset

The dataset used is a freely available Kaggle dataset, namely the IBM HR Analytics Employee Attrition & Performance Dataset (<https://www.kaggle.com/datasets/pavansubhasht/ibm-hr-analytics-attrition-dataset> IBM HR Analytics Employee Attrition & Performance Dataset). As it is a freely available, anonymous dataset provided by IBM and Kaggle, it is also used as a trusted resource by other researchers for the implementation of the developed models [16].

There are 35 non-null features derived from the responses of the 1470 employees of IBM. The information collected consists of data on demographics, position, salary, and promotion status in the company, as well as personal opinions on job satisfaction and work-life balance. The parameters that impact work-life balance in this 35-attribute database include the attributes of education, satisfaction with work environment, job engagement, job satisfaction, performance evaluation, satisfaction with relationship, and work-life balance, as shown in Table 1.

Table 1. Possible flood flow rates of E26A010 AGI.

Education	Environment Satisfaction	Job Involvement	Job Satisfaction	Performance Rating	Relationship Satisfaction	Work Life Balance
Below College	Low /	Low /	Low /	Low /	Low /	bad / good / better / the best
College	Medium /	Medium /	Medium /	Medium /	Medium /	
Bachelor	High / Very	High / Very	High / Very	High / Very	High / Very	
Master	High	High	High	High	High	
Doctor						

3. Methodology

This study takes a quantitative research approach to quantitatively analyse the results of the IBM employee survey by applying machine learning techniques to predict work-life balance. To perform

the basic machine learning and ensemble learning algorithms, the Python language and its libraries were used.

The questionnaire asks employees to rank their work-life balance in one of four categories: bad, good, better, and best. Apart from these questions, the

IBM survey asks employees about demographic information, income, distance from home, job satisfaction, environment satisfaction, business travel, working hours, etc.

The algorithms used are divided into two sets: 80% for training and 20% for testing. They are trained on the parameters contained in the answers to the questions in order to categorize workers based on the answers to the work-life balance question.



Figure 1. Methodological approach taken.

3.1. Ensemble Learning

Researchers and developers are searching for the most appropriate algorithm to achieve more accurate prediction results for classification and regression problems. One of the approaches in this search is ensemble learning, which combines the predictions of multiple machine learning models to achieve

better predictive performance. Ensemble learning aims to create multiple classifiers with similar bias (a systematic error that occurs due to incorrect assumptions in the ML process) and reduce the variance by combining their results [18]. Although an unlimited number of ensemble learning models can be developed, there are three main families of ensemble learning methods: Bagging, Stacking and Boosting [19].

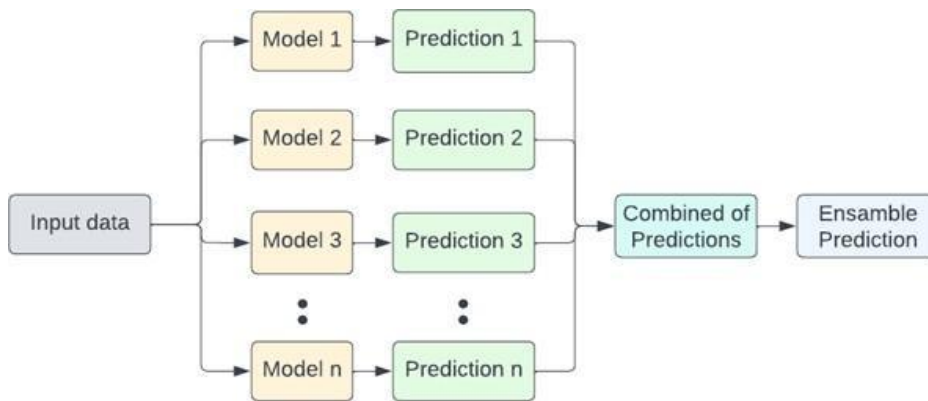


Figure 2. Proposed Ensemble Learning Method.

Bagging fits many decision trees to different samples of the same data set and averages the predictions, i.e., packed decision trees, Random Forest [26]. Stacking applies many different models to the same data and uses a different model for learning to find the best combination of predictions, i.e. voting, weighted average. Boosting uses the prediction errors of the previous models and adds models to the ensemble one by one so that the last model corrects the predictions of the previous models and outputs a weighted average of the predictions [26], e.g., AdaBoost, XGBoost.

decision tree (DT) and support vector machine (SVM) models as non-ensemble learning techniques.

4. Analysis and Result

Since the aim of the study is to predict work-life balance using ensemble learning models, Figure 4 shows the distribution of workers according to the degree of work-life balance. The classification was divided into four categories. The classification parameters obtained are shown in Table 2.

In this study, we used the ensemble learning techniques k-nearest neighbours (kNN), random forest (RF), gradient boosting (GB), and extreme gradient boosting (XGBoost) in comparison to the

Table 2. Classification results.

Classes	Precision	Recall	F1-score	Accuracy	Data Size
Bad	0.96	1.00	0.98	0.87	173
Good	0.79	0.89	0.84		184
Better	0.84	0.56	0.67		168
Best	0.88	1.00	0.94		190

Table 2 shows that the average accuracy value is 0.87. It can be seen that the highest success parameters are in the "Poor" category (Precision:0.96, Recall:1.00, f-score:0.98). The lowest results were obtained in the "Better" class with 168 data.

The results of the ensemble model are shown in the rest of the section, and then they are compared at the end.

4.1. Imbalanced Data Problem

The distribution of employees according to work-life balance classes is uneven. Class 3 has the highest proportion at over 60.75%, while Class 1 has the lowest proportion at almost 5.44%. This may result in the minority class being left out. To solve this problem, we need to balance the data. We used the random oversampling method [27] as one of the methods to manipulate the data. In this method, the minority class data is duplicated until the distribution of the classes is balanced. After redistribution of the data, the data is split into a test and a training data set at a rate of 20% and 80%, respectively.

4.2. k-Nearest Neighbor Method

The kNN algorithm classifies similar things in close proximity. It is an ensemble learning algorithm on a single basis. k stands for the distance between neighbors. The calculation of the distance can vary, but Euclidean distance is the most commonly used method. To determine the number k, we plotted the test error rate. The kNN algorithm is one of the sample-based classification methods based on the different distance measures (Euclidean distance, Manhattan distance, and Minkowski distance) of the samples in the known class dataset. It is usually calculated using the Euclidean distance given in Equation (1):

$$\sqrt{\sum_{i=1}^n (x_i - y_i)^2} \tag{1}$$

Figure 3 shows the k in the range 1 to 30 and the error rate. The k for this model is determined as 1.

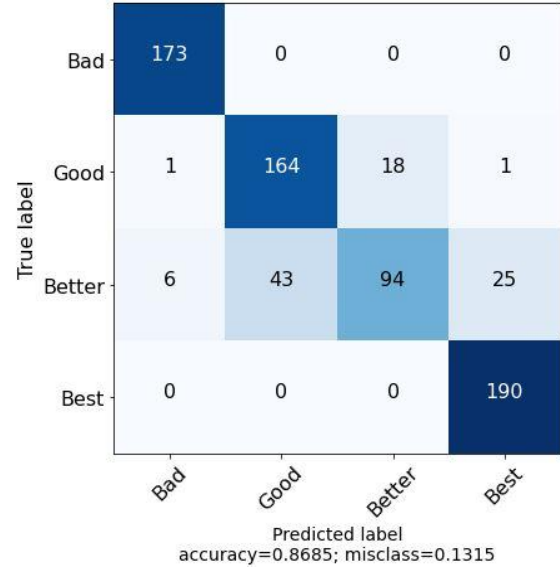


Figure 3. The result confusion matrix of kNN.

Figure 3 shows the heat map of the predicted and true labels. The figure shows that the algorithm correctly classifies between "bad" and "best" in most cases, but confuses some between "good" and "better". The accuracy rate of the kNN algorithm was found to be 86.85%.

4.3. Support Vector Machine Method

Founded in 1963 by Vladimir Vapnik and Alexey Chervonenkis, the Support Vector Machine (SVM) is one of the supervised learning methods generally used in classification problems. The SVM algorithm draws a line to separate points lying on a plane by linear or non-linear methods. It is an ensemble learning algorithm on a single basis. These separations are to achieve the maximum distance between the points of the two classes [28]. The goal of the SVM algorithm is to maximize the distance between the data to be separated. Figure 3 shows the operating principle of the SVM algorithm.

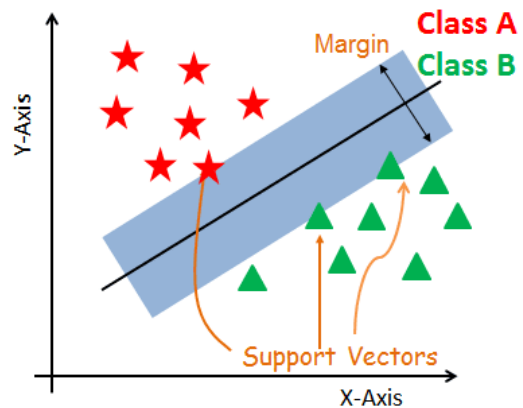


Figure 4. The goal of the SVM algorithm [29].

Looking at Figure 4, the lines are drawn using linear or non-linear methods based on the furthest data in the clustered data with different values. By optimizing these lines, the most distant lines and the lines closest to the data are selected and a new line is drawn over which the average is taken and the separation process is performed. Parameters of the SVM algorithm: The gamma value was set at 0.001 and the class number at 4. The result of the classification process with the SVM algorithm is shown in Figure 5 as a confusion matrix.

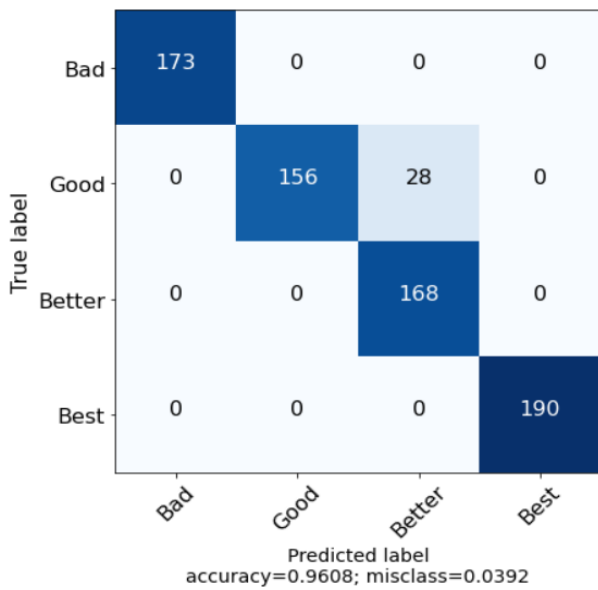


Figure 5. The confusion matrix result of SVM algorithm.

Figure 5 shows that all the data in the 'Bad', 'Better', and 'Best' classes were correctly classified, while 28 of the 'Good' data were incorrectly classified as 'Better'. Figure 5 shows the heat map of the predicted and true labels. The accuracy rate of the SVM algorithm was found to be 96.08%.

4.4. Random Forest

The RF model is one of the most widely used ensemble learning methods that use a set of decision trees and find the most optimal combination from the results of the decision trees. The RF method consists of compilations of the classification tree or the RF tree, depending on the purpose, as many as the number of trees to be created. Therefore, one of the most commonly used algorithms among ensemble methods is RF [30]. In Random Forest, the estimator is 100 and the random value is 101. In addition, the value for the maximum features is set to auto. Since the algorithm randomly selects estimators, the accuracy of the model is higher because less

correlation is achieved between the relationships formed in a data set [31].

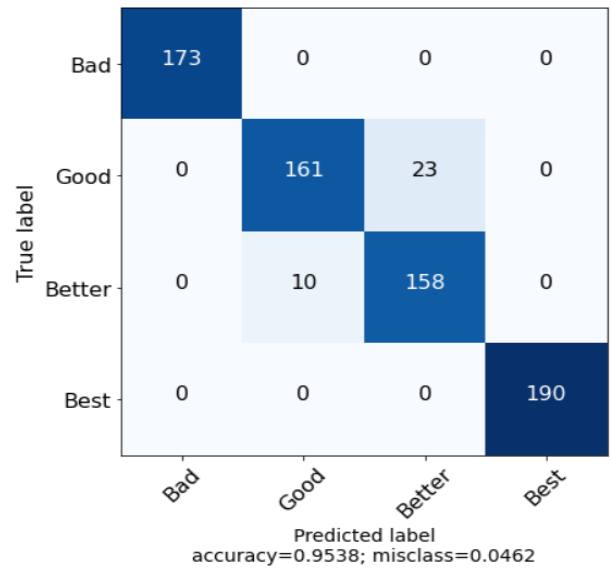


Figure 6. The confusion matrix result of Random Forest method.

Figure 6 shows that the model predicts 'bad' and 'best' perfectly but confuses "good" and "better". The accuracy rate of the random forest method was found to be 95.38%.

4.5. Decision Tree Algorithm

Results were obtained using the Decision tree method, and the comparison matrix is shown in Figure 7.

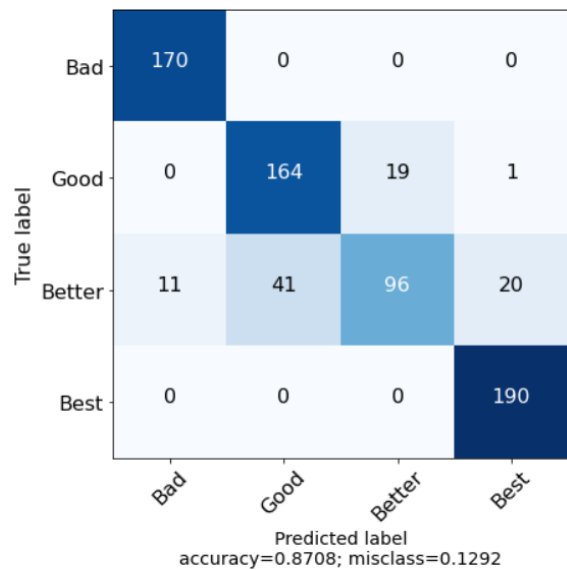


Figure 7. The confusion matrix result of Decision Tree method.

Figure 7 shows that the model predicts 'bad' and 'best' perfectly but confuses "good" and "better". For the "better" data, the model DT showed high mixing (error). The accuracy rate of the decision tree method was found to be 87.08%.

4.6. Gradient Boosting

The gradient boosting method (GBM) is a technique used to solve classification and regression problems and it is a very successful model used to combine several models whose individual performance can be considered poor [32]. The GBM is one of the very popular boosting examples for ensemble learning models. It uses Loss functions, weak learners (decision trees), and an additive model to improve performance over basic algorithms. The parameters of Gradient Boosting are listed in Table 3.

Table 3. The parameters of Gradient Boosting.

Parameters	Value
Number of estimators	100
Max features	0.9
Learning rate	0.3
Depth	4
Minimum samples leaf	2
Sub sample	1

Figure 8 shows the predictions made by the Gradient Boosting method.

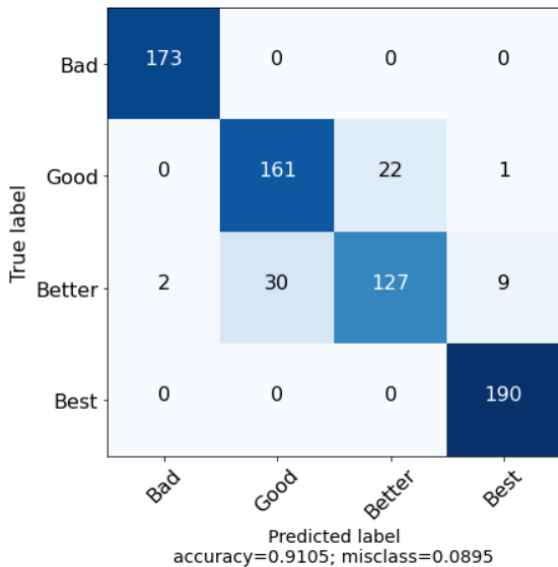


Figure 8. The confusion matrix result of Gradient Boosting method.

4.7. Light Gradient Boosting

Light Gradient Boosting (LGBost) is a based algorithm that offers leaf-shaped growth with depth constraints to speed up the training process and reduce memory consumption. The structure produces a histogram of width k by separating k bins of continuous floating point eigenvalues. The parameters of LGBost are set to the values 0.9 for the bagging portion, 0.9 for the feature portion, and 0.2 for the reg lambda [33]. Figure 9 shows the predictions made by the Light Gradient Boosting method.

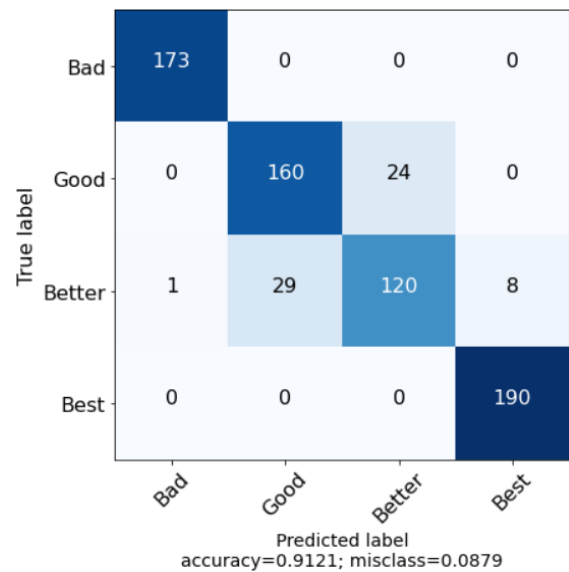


Figure 9. The confusion matrix result of Light Gradient Boosting.

4.8. Comparison of the Results

Table 4 shows the precision, recall, f-score, and accuracy of each algorithm, including the decision tree algorithm and the support vector machine model, for comparison with the models without ensemble learning. DT models propose a tree-like model of decisions with conditional control statements. The SVM algorithm finds a hyperplane in a dimensional space that provides a unique classification of the data. The dimension is the number of features. The algorithm is quite successful in terms of accuracy, misclassifying only some class 2 members as class 3.

Table 4. Classification performance results of algorithms.

Models	Precision	Recall	f-Score	Accuracy
Decision Tree	0.87	0.87	0.86	0.87
SVM	0.97	0.96	0.96	0.96
kNN	0.87	0.86	0.86	0.87
RF	0.96	0.95	0.95	0.95
GBM	0.91	0.91	0.91	0.91
LightGBM	0.91	0.91	0.91	0.91
Average	0.92	0.91	0.91	0.91

To evaluate the performance of a classification algorithm, there are a number of metrics. Among them, accuracy and f-score are the most commonly used. Accuracy simply calculates the proportion of correctly categorised examples out of the total number of examples [34]. However, it does not take into account the unbalanced categories or the false negative and false positive examples. On the other hand, the f-score is calculated as the harmonic mean of the precision and recall of the model, which takes into account the proportion of false-positive and false-negative examples. All performance values of the algorithms used in this study are listed in Table 3. Shown are the average performance values of the algorithms used in the study. The average accuracy is 91%.

5. Discussion

In this study, the SVM algorithm achieved the best result, while the k-NN and DT algorithms achieved the worst result. While the RF method achieved high success with an accuracy of 0.95, the ensemble models studied showed lower success. Although the performance values of the models differed fundamentally, their results were close to each other and showed similarity.

5.1. Benefits of Proposed Study

In this proposed study, information about the work-life balance of employees at a workplace was analyzed using machine learning techniques, and conclusions were drawn. This result can be used to evaluate employee satisfaction in any workplace. In addition, other benefits are mentioned below.

- With the help of artificial intelligence techniques, it has been possible to determine work-life balance with great success.
- The proposed method can be used to determine employee satisfaction in a workplace with high efficiency without manager intervention.

- The managers of workplaces can increase the efficiency of their employees by considering the results of this method.
- Considering this study, the performance of monthly or yearly employees can be measured again with this study and the changes can be evaluated.
- With an account to be opened at Google Colab, the results of this study can be accessed free of charge by providing the data.

6. Conclusion

The random forest model as an ensemble of decision trees outperforms the decision tree model by 9%. RF also provides the best results among the ensemble models. Furthermore, the boosting ensemble models (GBM, LightGBM) show relatively poor performance. The reasons for these results are the small number of data, the inconsistency of some relationships between values, and the large imbalance between classes. Table 5 shows the average result of this study and the results of similar studies in the literature.

Table 5. Comparison of own method with the literature.

Models	Accuracy
Radha et al.[24]	71.50
Pawlicka et al. [25]	81.00
Toğaçar [36]	87.76
Mansor [37]	84.59
Our Method	91.05%

In the [24] study, a total of 12,756 individuals' work-life balance data were used with different machine learning techniques, and the highest success rate (SVM algorithm) was 71.50%. In the [25] study, the artificial neural network method was used to measure the work-life balance of 800 people (Male: 389, Female: 411) in a workplace, and a success rate of 81.00% was achieved. The average success rate of this study was found to be 91.05%. There are many similar studies in the literature. A large amount of data was used in these studies. The study examined in [36] found 87.66% success for work-life balance, while [37] found 84.59% success. Although we used a small number of data in our study, better results were obtained. Although the amount of data was insufficient and had low quality features, the method we proposed was quite successful.

Contributions of the Authors

There is no conflict of interest between the authors.

The authors confirm that the contribution is equally for this paper.

Statement of Research and Publication Ethics

The study is complied with research and publication ethics.

Conflict of Interest Statement

References

- [1] S. M. Crow, S. A. Smith, and S. J. Hartman, "Attrition in nursing: Perspectives from the national survey of college graduates," *Health Care Manag. (Frederick)*, vol. 24, no. 4, pp. 336–346, 2005.
- [2] W. P. Durow and B. Brock, "The retention and attrition of catholic school principals," *Journal of Catholic Education*, vol. 8, no. 2, 2004.
- [3] P. Weldon, "Early career teacher attrition in Australia: evidence, definition, classification and measurement," *Aust. J. Educ.*, vol. 62, no. 1, pp. 61–78, 2018.
- [4] N. Pandey and G. Kaur, "Factors influencing employee attrition in Indian ITeS call centres," *Int. J. Indian Cult. Bus. Manage.*, vol. 4, no. 4, p. 419, 2011.
- [5] L. Kanteh and A. Gibba, "A study on employees' attrition in public and private institutions in the Gambia, 2007-2017," *Arabian J Bus Manager Review*, 2007.
- [6] D. Kennedy, "Attrition rates of mature engineers," *Eng. Manag. J.*, vol. 18, no. 3, pp. 36–40, 2006.
- [7] C. Marcelo, *Does Employee Training and Development Programs Mitigate Attrition in the Millennial Workforce?* 2022.
- [8] N. Aariya, "A study on the impact of maternity benefit on teacher's career and increase in post maternity attrition rate in India," *Journal for Educators, Teachers and Trainers*, vol. 13, no. 2, pp. 207–214, 2022.
- [9] S. Bhardwaj and A. Singh, "Factors affecting employee attrition among engineers and non-engineers in manufacturing industry," *Bus. IT*, vol. VII, no. 2, pp. 26–34, 2017.
- [10] S. Barpanda and S. Athira, "Cause of Attrition in an Information Technology-Enabled Services Company: A Triangulation Approach," *International Journal of Human Capital and Information Technology Professionals (IJHCITP)*, vol. 13, no. 1, pp. 1–22, 2022.
- [11] D. Ayar, M. A. Karaman, and R. Karaman, "Work-life balance and mental health needs of health professionals during COVID-19 pandemic in turkey," *Int. J. Ment. Health Addict.*, vol. 20, no. 1, pp. 639–655, 2022.
- [12] C. Calderwood, R. Breaux, L. L. Ten Brummelhuis, T. Mitropoulos, and C. S. Swanson, "When daily challenges become too much during COVID-19: Implications of family and work demands for work-life balance among parents of children with special needs," *J. Occup. Health Psychol.*, vol. 27, no. 5, pp. 516–527, 2022.
- [13] L. Vyas, "New normal" at work in a post-COVID world: work-life balance and labor markets," *Policy and Society*, vol. 41, no. 1, pp. 155–167, 2022.
- [14] K. K. Mohbey, "Employee's attrition prediction using machine learning approaches," in *Machine Learning and Deep Learning in Real-Time Applications*, IGI Global, 2020, pp. 121–128.
- [15] R. Jain and A. Nayyar, "Predicting employee attrition using XGBoost machine learning approach," in *2018 International Conference on System Modeling & Advancement in Research Trends (SMART)*, 2018.

- [16] S. Najafi-Zangeneh, N. Shams-Gharneh, A. Arjomandi-Nezhad, and S. Hashemkhani Zolfani, “An improved machine learning-based employees attrition prediction framework with emphasis on feature selection,” *Mathematics*, vol. 9, no. 11, p. 1226, 2021.
- [17] N. El-Rayes, M. Fang, M. Smith, and S. M. Taylor, “Predicting employee attrition using tree-based models,” *Int. J. Organ. Anal.*, vol. ahead-of-print, no. ahead-of-print, 2020.
- [18] C. Zhang and Y. Ma, Eds., *Ensemble machine learning: methods and applications*. Springer Science & Business Media, 2012.
- [19] R. Polikar, “Ensemble Learning,” in *Ensemble Machine Learning*, Boston, MA: Springer US, 2012, pp. 1–34.
- [20] S. Buyrukoglu, “Improvement of Machine Learning Models’ Performances based on Ensemble Learning for the detection of Alzheimer Disease,” in *2021 6th International Conference on Computer Science and Engineering (UBMK)*, 2021.
- [21] S. Buyrukoğlu and S. Savaş, “Stacked-based ensemble machine learning model for positioning footballer,” *Arab. J. Sci. Eng.*, 2022.
- [22] S. Buyrukoğlu, “New hybrid data mining model for prediction of Salmonella presence in agricultural waters based on ensemble feature selection and machine learning algorithms,” *J. Food Saf.*, vol. 41, no. 4, 2021.
- [23] A. Akbas and S. Buyrukoglu, “Stacking Ensemble Learning-Based Wireless Sensor Network Deployment Parameter Estimation,” *Arabian Journal for Science and Engineering*, pp. 1–10, 2022.
- [24] K. Radha and M. Rohith, “An experimental analysis of work-life balance among the employees using machine learning classifiers,” *Int. J. Comput. Trends Technol.*, vol. 69, no. 4, pp. 39–48, 2021.
- [25] A. Pawlicka, M. Pawlicki, R. Tomaszewska, M. Choraś, and R. Gerlach, “Innovative machine learning approach and evaluation campaign for predicting the subjective feeling of work-life balance among employees,” *PLoS One*, vol. 15, no. 5, p. e0232771, 2020.
- [26] J. Brownlee, “Ensemble Learning Algorithms With Python: Make Better Prediction with Bagging, Boosting, and Stacking,” *Machine Learning Mastery*, 2021.
- [27] J. Brownlee, “A Gentle Introduction to Ensemble Learning Algorithms,” *Machine Learning Mastery*, 2021.
- [28] X. Wang, B. Yu, A. Ma, C. Chen, B. Liu, and Q. Ma, “Protein-protein interaction sites prediction by ensemble random forests with synthetic minority oversampling technique,” *Bioinformatics*, vol. 35, no. 14, pp. 2395–2402, 2019.
- [29] A. Navlani, “Support vector machine classification in scikit-learn,” *Medium*, 16-Aug-2020. [Online]. Available: <https://avinashnavlani.medium.com/support-vector-machine-classification-in-scikit-learn-3800bc4979ce>. [Accessed: 05-Mar-2023].
- [30] S. Suthaharan, “Big Data Essentials,” in *Machine Learning Models and Algorithms for Big Data Classification*, Boston, MA: Springer US, 2016, pp. 17–29.
- [31] M. Pal, “Random forest classifier for remote sensing classification,” *Int. J. Remote Sens.*, vol. 26, no. 1, pp. 217–222, 2005.
- [32] B. Suchetana, B. Rajagopalan, and J. Silverstein, “Assessment of wastewater treatment facility compliance with decreasing ammonia discharge limits using a regression tree model,” *Sci. Total Environ.*, vol. 598, pp. 249–257, 2017.
- [33] A. Natekin and A. Knoll, “Gradient boosting machines, a tutorial,” *Front. Neurobot.*, vol. 7, 2013.

- [34] D. Chakraborty, H. Elhegazy, H. Elzarka, and L. Gutierrez, “A novel construction cost prediction model using hybrid natural and light gradient boosting,” *Adv. Eng. Inform.*, vol. 46, no. 101201, p. 101201, 2020.
- [35] M. Toğaçar, B. Ergen, and V. Tümen, “Use of dominant activations obtained by processing OCT images with the CNNs and slime mold method in retinal disease detection,” *Biocybern. Biomed. Eng.*, vol. 42, no. 2, pp. 646–666, 2022.
- [36] N. Mansor, N. S. Sani, and M. Aliff, “Machine learning for predicting employee attrition,” *Int. J. Adv. Comput. Sci. Appl.*, vol. 12, no. 11, 2021.
- [37] N. Darapaneni *et al.*, “A detailed analysis of AI models for predicting employee attrition risk,” in *2022 IEEE 10th Region 10 Humanitarian Technology Conference (R10-HTC)*, 2022.



Dry Ice Blasting Method as a Descaling

Ersin Asım GÜVEN^{1*}, Mehmet UÇKAN², Ramazan UZUN³

¹ Kocaeli Üniversitesi Makine Müh. Böl. Umuttepe Yerleşkesi 41001, İzmit/KOCAELİ

² Türk Havacılık ve Uzay Sanayii A.Ş. 06980, Kahramankazan/ANKARA

³ Ereğli Demir ve Çelik Fabrikaları T.A.Ş AR-GE Merkezi 67302, Karadeniz Ereğli/ZONGULDAK
(ORCID: 0000-0003-0153-6774) (ORCID: 0000-0001-8967-9248) (ORCID: 0000-0002-7148-4044)



Keywords: Dry Ice Blasting, Eco-friendly, Pickling, Scale.

Abstract

The scale removing process with acid, generally called as the pickling process, is accepted by the steel producers and applied satisfactorily. However, most of the producers tend to develop scale removing process without acid due to the environmental regulations. In the related literature, some methods were studied for finding eco-friendly solutions. Although these studies seem to be promising, pickling process is still dominant as a descaling process before cold rolling applications. In this study, efficient surface cleaning method which is called as dry ice blasting method was used under different parameters on the carbon steel surface as it might be used instead of pickling process. Results of the experiments were studied by observing cross-sectional microstructure of samples. In addition, before destroying samples for hot mounting application, the surface topographies were measured by non-contact device. Finally, surface roughness values of the samples were showed on figures.

1. Introduction

The formation of the scale is a natural process in which surface of the hot steel alloy is faced with air. While the magnetite and hematite are formed in steel below temperature of 570 °C, at above this temperature, wustite, magnetite and hematite appear on the surface of metal alloy [1]. The chemical composition of the material is less effective in the formation of scale, but the temperature and cooling rate of the material are more effective [2].

The scale layer on the steel is an undesired shell because of the quality requirements. Therefore, it should be cleared before cold rolling and coating processes. The scale removal process is called as pickling process and it needs to use acid for cleaning of carb on steels [3]. Pickling process is the chemical or electrochemical reaction process that cleans surface of metal by etching [4]. The HCl and H₂SO₄ acid is used for carbon steel pickling process while HF and HNO₃ acid is used for stainless steel [5]. However, HCl acid is widely used by steel producers located in Europe generally [2]. HCl acid is preferred due to three ma

in reasons: its low cost, swift pickling process and getting better surface quality after pickling [5].

The most important problem in pickling process with acid is waste of liquor. The waste of this media is hazardous for the environment. Therefore, most of the countries have limit values for discharge of waste [6]. Although the pickling process has been accepted by iron-steel producers, the environmental regulations as well as the operation and maintenance costs of this process urge steel producers to find eco-friendly solutions. For this purpose, gas reduction and slurry blast methods have been developed [7].

Gas reduction method is a chemical process reducing iron oxide under heated atmosphere. There are many studies in the related literature about iron oxide reduction. However, there is limited research on the scale surface on hot rolled steel sheet. The first experiment on hot rolled sample was conducted by Robert M. Hudson. He kept the samples in stainless steel box under the H₂ or H₂-N₂ mixture atmosphere whose temperature was 635 °C throughout 24 hours. Due to the beneficial results of gas reduction method which is published in academic papers, some patents

*Corresponding author: asimguven@kocaeli.edu.tr

Received: 30.10.2022, Accepted: 09.03.2023

have been released related to this method. One of them is construction named Acid-Free Scale Removal (AFSR) line and belongs to Danieli Wean United [8].

AFSR line consists of three main components. The first section of this line is heating section that heats sheet metal up to 400 °C. After that, sheet metal is moved by the table roller to the reduction section. In reduction section, reductive atmosphere is supplied by nozzles to the sheet metal surface. Thanks to turbulence effect of reduction atmosphere, most of the oxide is reduced in this area. Finally, sheet metal surface is cooled down in cooling section to prevent oxide layer emergence again [9].

The other method which is alternative to the pickling is slurry blast method. This method uses water-iron pellets mixture as a blasting media and this media is applied to the steel surface by the pressure which comes from rotational movement of dispersion head. Although, one of the challenging conditions of this method is non-homogenous scale distribution on steel surface, it is solved with mounting combination of dispersion head which is developed by The Material Works Company. After blasting process, sheet metal surface is cleaned from residual scale and blasting media with water and blasting mixture can be filtered to use again [7].

In a test report comparing the slurry blasted samples and the pickled samples, different tests are applied to the slurry blasted samples. According to the result, it was decided that the slurry blasting method can be applied instead of pickling process [10].

Although these methods seem to be environment-friendly, slurry blast method has high energy and operation costs [11]. The gas reduction method, on the other hand, has poor descaling properties and requires additional mechanical brushing [12].

In this research, dry ice blasting method, one of the eco-friendly and efficient cleaning methods was used for scale removing. Although there is only one study of the dry ice blasting method on hot rolled carbon steel slab, it is thought that this method can be used for scale removal due to its surface cleaning performance.

Dry ice blasting process is a simple, environment-friendly, low cost and abrasive-free surface cleaning method. Dry ice pellets transmit their kinetic energy to the surface when they blast with air. After pellets bump into surface, their solid phase changes to the gaseous and this is called as sublimation. In this way, dry ice blasting method reduces second waste ratio up to 95% [13]. The most important advantage of cleaning with dry ice blasting method is eco-friendly. After application, the CO₂ gas formation occurs besides contamination leaving of

the surface. The CO₂ is not harmful for the environment. However, after dry ice blasting it should not be exceeded the allowed concentration [14].

The temperature of dry ice is -78.5 °C under normal conditions. The temperature difference with dry ice pellets and surface creates a thermal shock effect. Due to this effect, contamination of the steel surface is more brittle and bonds between contamination and surface are weaker [15]. The difference between dry ice blasting and other blasting-based cleaning methods is that dry ice blasting method has thermal, mechanical and expansion effects [16].

The application of dry ice blasting on to the steel surface for removal of scale surface was patented in 1994 by Sumitomo Metal Industries Ltd. In this research, inventors applied five different blasting methods to the surface of slab which is 235 mm thickness and 1140 °C surface temperatures.

- Method A: Water spraying at 60 °C temperature and 150 bar pressure.
- Method B: Stainless steel brushing under 100 kg/m pressure
- Method C: Slurry blasting under 150 bar pressure with iron pellets, which constitute 20% of the total weight, and water at 60 °C.
- Method D: Water ice blasting under 20 bar pressure in which the ice dimension is 5 mm.
- Invention Method: Dry ice blasting under 20 bar pressure and 720 kg/h flow rate in which the diameter of ice pellets is 5 mm.

As a result, invention method has a definite solution for removing scale from slab surface. In addition, it presents better solution compared to Method A and Method D, especially Method D [17].

2. Material and Method

The samples were chosen from commercial products of Ereğli Iron-Steel Production Company, widely known as Erdemir. The pseudonym of the samples indicates which properties would have been gained after cold rolling operations. Each sample group has different quality that includes different chemical composition. All samples were taken from coil tail and/or head. The mechanical descaling such as tension leveling were not applied to these samples.

Dry ice blasting was applied to the samples which are shown in Table 1 with fixed pressure of 10 bar. Diameter of dry ice pellet was 3 mm. Dry ice blasting nozzle was approximately at the same distance to all samples and angle between nozzle and sample was about 90°. The experimental mechanism is shown in Figure 1.

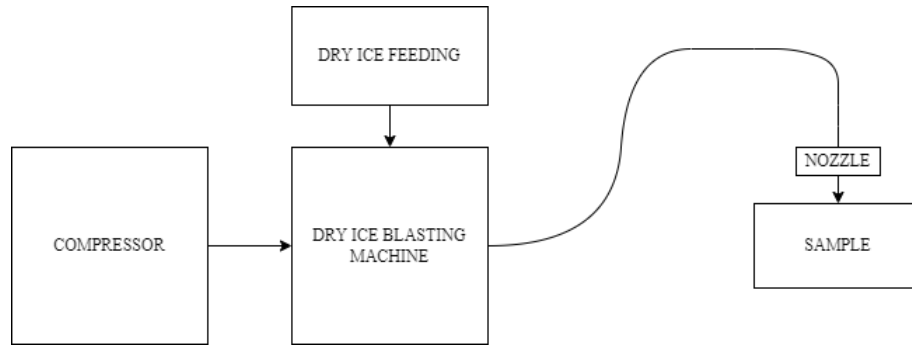


Figure 1. Schematic drawing of the dry ice blasting experiment

Table 1. Dry ice blasting parameters

Samples	Flow Rate (m ³ /h)	Time (min)
TNR1	0.5	1
TNR2	2.0	2
TNR3	3.5	3
ICCR1	0.5	1
ICCR2	2.0	2
ICCR3	3.5	3
RP1	0.5	1
RP2	2.0	2
RP3	3.5	3

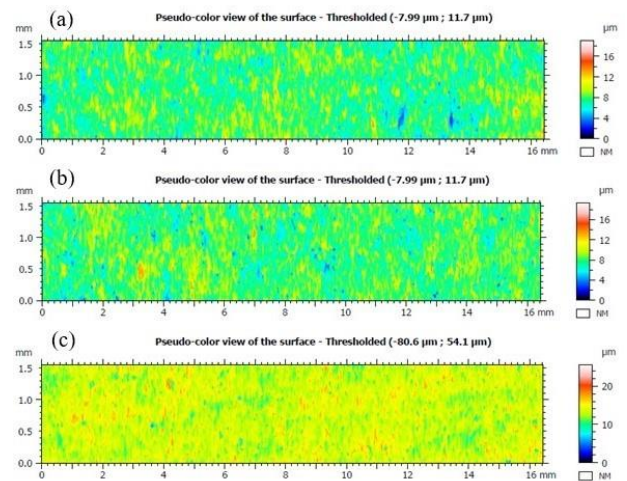


Figure 2. Topography of metal surface a) TNR1, b) TNR2, c) TNR3

3. Results and Discussion

After dry ice blasting process, surface roughness of samples was measured to observe blasting effect on scale layer by Nanofocus MarSurf CM Mobile. The surface topographies are shown in Figure 2, Figure 3 and Figure 4. The surface roughness values with standard deviations after dry ice blasting are listed in Table 2. The same threshold values were chosen in each sample. The top and valley points of surface could be obtained by automatic topography measurement system. Similar morphological features such as depth profile and distribution of points were observed according to the colored scale next to the figures.

The roughness of the surface was decreased by decreasing flow rate value under 2.0 m³/h. It should here be noted that, the critical flow rate value could be higher than 0.5 m³/h. As shown in the Figure 2, Figure 3 and Figure 4, there are no crucial differences between 2.0 and 3.5 m³/h. According to the roughness values which are shown in Table 2, IC CR samples are more stable than TNR and RP samples with respect to the Ra values. Since some scale remains on the surface after the dry ice process, the roughness values may be affected.

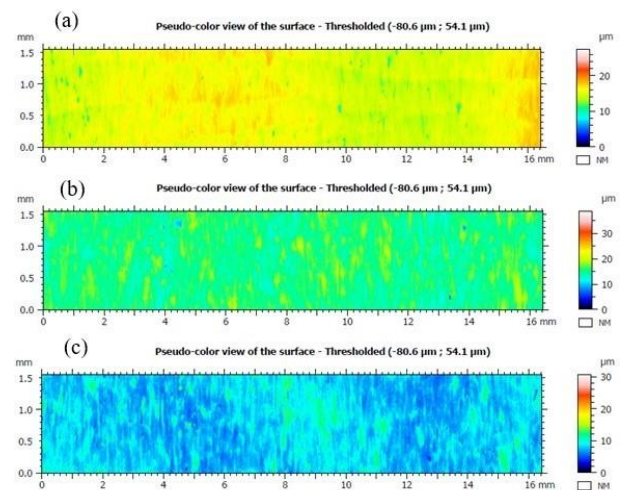


Figure 3. Topography of metal surface a) ICCR1, b) ICCR2, c) ICCR3

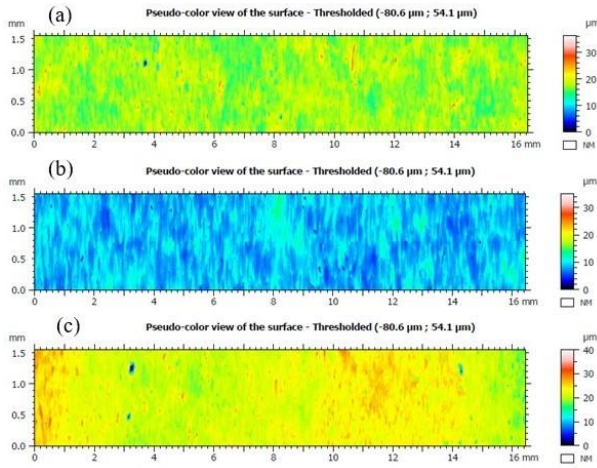


Figure 4. Topography of metal surface a) RP1, b) RP2, c) RP3

Table 2. Surface roughness values and standard deviations after dry ice blasting

Samples	Ra (μm)	Std Deviation
TNR1	0.931	0.055
TNR2	0.948	0.061
TNR3	0.902	0.051
ICCR1	0.454	0.027
ICCR2	0.921	0.071
ICCR3	0.836	0.057
RP1	0.971	0.083
RP2	1.030	0.061
RP3	0.922	0.068

After surface roughness measurement, samples were prepared according to the ASTM E3 [18]. The samples were hot mounted with Struers Citopres-20 machine. Struers Tegra Pol-21 and Struers Tegra Force-5 devices were used for grinding and polishing, respectively. Then, they were etched according to the ASTM E407 with 2% nitrile solution [19].

Prepared samples were examined with microscope of Nikon Epiphot 200 according to the ASTM E45 and ASTM E112 to observe deformation of scale layer [20-21]. The sectional view of scale layers is shown with x500 scale in Figure 5, Figure 6 and Figure 7. The scale on the surface is crushed by the effect of dry ice blasting deformation.

As there are some porosity and crack on the scale layer, especially in ICCR samples which are shown in Figure 6, it could be seen that dry ice blasting applications which are applied in all different parameters are effective.

In RP named samples whose cross-sectional view is shown in Figure 7, RP1 was more affected one compared to the others even though all three samples were taken from same sheet.

In TNR samples, it could be said that dry ice blasting application had limited effect. Especially small cracking on scale surface of TNR2 samples might have happened while preparing for hot mounting application.

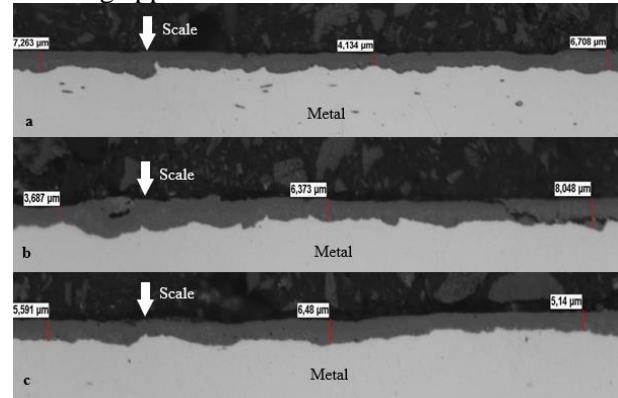


Figure 5. Sectional view of scale layer a) TNR1, b) TNR2, c) TNR3

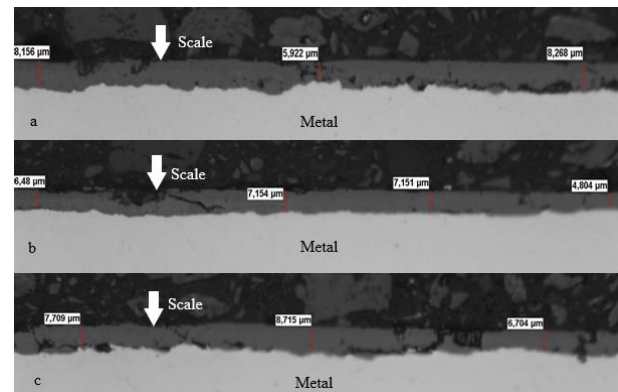


Figure 6. Sectional view of scale layer a) ICCR1, b) ICCR2, c) ICCR3

4. Conclusion and Suggestions

In some samples, dry ice blasting method achieves to break surface layer on carbon steel samples. However, this method is not enough for descaling by itself. According to the surface roughness value, it can be seen that, dry ice blasting method affected scale layer of some samples more than the other samples.

In blasting methods, there are many parameters on method achievement. Some of these parameters are pressure, flow rate, dry ice pellet diameter, nozzle type, angle of nozzle, distance from sample, etc. Therefore, dry ice blasting method should

be applied again with different parameters.

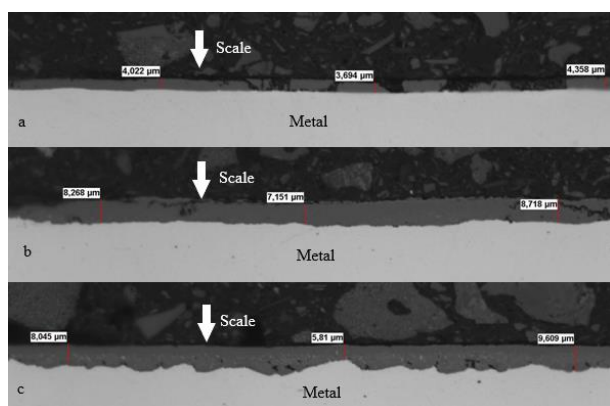


Figure 7. Sectional view of scale layer a) RP1, b) RP2, c) RP3

Acknowledgment

We would like to thank to Ereğli Iron-Steel Production Company, known as Erdemir, for their support and offering technical sources.

Contributions of the Authors

The contributions of each author to the article should be indicated.

Conflict of Interest Statement

There is no conflict of interest between the authors.

Statement of Research and Publication Ethics

The study is complied with research and publication ethics.

References

- [1] W. Sun, "A study on the characteristics of oxide scale in hot rolling of steel," Ph.D. dissertation, School of Mechanical, Materials and Mechatronic Engineering, University of Wollongong, Wollongong, Australia, 2005.
- [2] M. Maanonen, "Steel Pickling in Challenging Conditions," M.S. thesis, Materials Technology and Surface Engineering, Helsinki Metropolia University of Applied Sciences, Helsinki, Finland, 2014.
- [3] K. Esendağ, S. Bilgin, İ. Kayabaşı, V. Kılıç, and C. Yılmaz, "Sürekli Asitleme Hattının Mekanik Modellemesi," *Engineering and Machinery*, vol 58, no 689, p 63-80, 2017.
- [4] L. Garveric, "Corrosion in the Petrochemical Industry," *The Materials Information Society*, Ohio: ASM International, USA, 1994, pp. 78.
- [5] T. J. Fox, C. G. Randal, and D. H. Gross, "Steel Pickling: A Profile," *Research Triangle Institute*, EPA Contract Number 68-D1-0143, Section-2, 1993, pp. 4-10.
- [6] A. Devi, A. Singhal, R. Gupta, and P. Panzade, "A Study on Treatment Methods of Spent Pickling Liquor Generated by Pickling Process of Steel," *Clean Technologies and Environmental Policy*, pp. 1515-1527, 2014, DOI 10.1007/s10098-014-0726-7.
- [7] K. Voges, A. Mueth, B. Lehane, and S. Critchley, "Eco-Pickled Surface: An Environmentally Advantageous Alternative to Conventional Acid Pickling," *Iron&Steel Technology*, vol. 5, pp. 81-96, 2008.
- [8] C. Guan, J. Li, N. Tan, Q. Y. He, and S. G. Zhang, "Reduction of Oxide Scale on Hot-Rolled Steel by Hydrogen at Low Temperature," *International Journal of Hydrogen Energy*, pp. 15116-15124, 2014, DOI: 10.1016/j.ijhydene.2014.07.024.
- [9] S. L. Feldbauer, and B. H. Braho, "Apparatus and Method for Sequential Removal of Oxides from Steel," World Intellectual Property Organization. Patent No: WO0191929A1, 2001.
- [10] The Material Works, LTD. "EPS End Use and Application Test Results," Illinois, USA, Rev.9, 2014.
- [11] X. Wang, R. Ai, Q. Yang, S. Wang, Y. Zhang, Y. Meng, and X. Ma, "Effect of Oxide Scale Structure on Shot-Blasting of Hot-Rolled Strip Steel," *PeerJ Materials Science*, 2:e9, 2020, DOI 10.7717/peerj-matsci.9.
- [12] M. Duan, S. Li, S. Chen, X. Fang, X. Yang, and J. Xu, "Development and Application of Baosteel Mechanical Descaling Technology," *Baosteel Technical Research*, vol. 12, no 1, p 17-26, 2018.
- [13] R. Kohli, and K. L. Mittal, "Developments in Surface Contamination and Cleaning: Applications of Cleaning Techniques (Ch. 4)," vol. 11, p 117-169, 2019.
- [14] E. Uhlmann, R. Hollan, A. El Mernissi, "Dry Ice Blasting – Energy-Efficiency and New Fields of Application", *Engineering Against Fracture*, Dordrecht, p 399-409, 2009, DOI: 10.1007/978-1-4020-9402-6_32.
- [15] R. W. Foster, "Carbon Dioxide (Dry-Ice) Blasting," *Good Painting Practice: SSPC Painting Manual*, vol. 1, Chapter 2.9.5, pp. 161-167, Society for Protective Coatings, Pittsburgh, USA, 2011.
- [16] A. Dzido, P. Krawczyk, K. Badyda, and P. Chondrokostas, "Operational Parameters Impact on the Performance of Dry-Ice Blasting Nozzle," *Energy*, vol. 214, 2021, DOI: 10.1016/j.energy.2020.118847.
- [17] K. Ushio, "Descaling Method and Rolling Method for Slab," Japan Patent Office. Patent No: JPH06269839A, 1994.
- [18] "Standard Guide for Preparation of Metallographic Specimens". <https://www.astm.org/e0003-11r17.html> (access 04.02.2023).
- [19] "Standard Practice for Microetching Metals and Alloys". <https://www.astm.org/e0407-07r15e01.html> (access

04.02.2023).

[20] “Standard Test Methods for Determining the Inclusion Content of Steel”. <https://www.astm.org/e0045-18a.html> (access 04.02.2023).

[21] “Standard Test Methods for Determining Average Grain Size”. <https://www.astm.org/e0112-13r21.html> (access 04.02.2023).



A Study on Changes in Some Physicochemical Properties, Volatile Compounds, Sugar, and Organic Acid Contents of Grape Juice During Molasses Production

Aziz KORKMAZ^{1*}

¹Mardin Artuklu University, Faculty of Health Sciences, Department of Nutrition and Dietetics
Mardin/Türkiye
(ORCID: 0000-0002-5221-6722)



Keywords: *Verdani* Grape, Molasses, Volatile Compound, Organic Acid, HMF

Abstract

This study aimed to investigate both qualitative and quantitative changes in the taste and aroma components of grape juice during the production of traditional molasses (pekmez). For this purpose, the changes in some physicochemical properties, such as sugar, organic acid, and volatile compound contents, in fresh *Verdani* grape (*Vitis vinifera* L.) juice (FGJ) were evaluated in the production of its traditional molasses. After the production, the total soluble solid (TSS), titratable acidity (TA), glucose, fructose, malic, citric, and succinic acid concentrations were increased ($P<0.05$) with the rising concentration. However, the level of glucose and fructose in TSS decreased by 4.67% and 11.78%, respectively ($P<0.05$), based on their degradation. Similarly, as the major organic acids, the rates of tartaric and malic acids in the TSS were decreased by 73.91% and 67.25%, respectively. These reductions raised the pH value of molasses ($P<0.05$). In addition, the majority of volatile compounds in FGJ disappeared after the production of molasses, whereas some volatile furans were formed in significant amounts.

1. Introduction

Grape (*Vitis vinifera* L.) is one of the most consumed fruits worldwide. The annual amount of grapes produced in the world is approximately 78 million tons. Türkiye is the sixth largest country in the world, with an annual grape production of 4.2 million tons, depending on its suitability for growing conditions [1]. This fruit is mostly consumed fresh in the country, but it is also used in the production of its juice, wine, raisins, vinegar, and certain traditional foods, including molasses and orcik [2]. In 2021, 50.6% of grapes produced in Türkiye were table varieties, 39 percent were raisin varieties, and the rest were wine varieties [3]. In addition to these uses, it is estimated that 10-20% of the total amount of grapes harvested in Türkiye is used in the production of molasses, although the exact amount is unknown [4].

Molasses is a traditional Turkish food and has been produced in Anatolia for a long time, from certain fruits such as grape and mulberry [5]. It is a nutritious food in terms of its high sugar, mineral, and organic acid contents. Moreover, molasses is also used to prepare various desserts due to its typical taste, consistency, and caramel color [6]. The quality of molasses types generally depends on their physicochemical properties, and the composition of their sugars, organic acids, and volatile compounds, as well as their non-enzymatic browning levels. Also, there are some phenolic and flavonoid components in both grapes and molasses that can function as bioactive substances [5]. These properties are affected by the variety, ripening degree, and growing conditions of the grape used [7], but also depend on the production method used [4], [8].

In Turkey, molasses is produced in two ways: traditional and industrial (vacuum) methods. The

*Corresponding author: azizkorkmaz@atuklu.edu.tr

Received: 30.10.2022, Accepted: 09.03.2023

main difference between these two productions is the concentration method followed by the deacidification and clarification of fresh grape juice (must) during the production process. In the vacuum method, the must of grapes is concentrated under a vacuum at a lower temperature (60-70 °C), whereas in the traditional method, the concentration is done by cooking the must in a wide and shallow copper cauldron for a longer time. On the other hand, in some regions of Turkey, the deacidified and clarified must of grapes is concentrated by laying it thinly on the trays and keeping them under the sun, as an alternative traditional method. The molasses obtained in this way is called 'gün pekmezi' or 'gün balı' (like-honey) [2]. Mardin, a province located in the southeast of Turkey, is a region where traditional molasses is widely made. Mardin has the second-largest area of vineyards in the country [3]. In this region, around 30 different local varieties of grapes are grown [9].

There are several studies on the general physicochemical properties of grape molasses. Some of these studies were carried out on molasses whose varieties are known, while [2], [10], some of them were conducted on molasses whose grape variety is not known [11]. Studies have also been conducted to determine the imitation and the adulteration [12]; the rheological properties [13], [14]; changes in the amount of hydroxymethylfurfural [15], [16]; and bioactive properties [17], [8] of the kinds of molasses. As a result of the literature research, it has been seen that the studies comparing the main quality characteristics of some grape varieties with their traditional molasses are limited. Therefore, the purpose of this study is to evaluate the changes in some physicochemical properties, volatile compounds, sugars, and organic acids of *Verdani* (Werdani) grape during its production of traditional molasses.

2. Material and Method

2.1. Material

The mature grapes of a variety of Mardin (*Vitis vinifera* L. cv. *Verdani*) (red) used in this study were collected from a vineyard (37°24'12.4"N 41°16'35.2"E) in Gelinkaya village of Midyat district, Mardin, Türkiye. Approximately 100 kg of the bunches of this grape were harvested (28 October 2019) and transferred to the house where molasses is made by the traditional method, locally called 'mahsere'. The manufacturing of molasses started early the next day. Meanwhile, about one liter of squeezed FGJ obtained from the variety used was stored at -18 °C until analysis.

2.2. Production of Molasses

In this study, the sweet molasses type with a liquid consistency was produced, as specified in the Turkish Food Codex for grape molasses [18]. It was produced by the traditional method (Figure 1). First, the rotten or damaged berries were removed from the bunches, and then the bunches were washed with potable water. After that, the bunches were placed in porous bags and crushed with foot (by using clean plastic boots) on a specially designed sloped concrete floor to collect the squeezed juice into a cauldron. After that, the grape juice (must) obtained (~83 L) was mixed with molasses soil (1.7 kg) with high a CaCO₃ (80-90%) content, then boiled for 10 minutes and also rested for 2 hours to deacidify and clarify it. After this period, the must was taken into an open cauldron (85x25 cm) without removing the sediment and boiled using wood fire for 3.5 hours till it reached a Brix of 70. The foams that formed on the edge of the cauldron during boiling were taken continuously. In addition, the foams adhering to the wall of the cauldron were periodically cleaned with a clean cotton rag during this time. The temperature of the molasses during boiling ranged between 101-112 °C. At the end of production, the obtained molasses was cooled, and a sufficient amount of its samples, taken into plastic tubes, was stored at -18 °C until analysis.

2.3. Physicochemical Analyses

The dry matter (DM) content of samples was determined according to the AOAC (2000) method [19]. The amount of TSS (°Brix) in samples was determined using a digital refractometer (HI 96801, Hanna Instruments Inc., Woonsocket, RI, USA) at 22 °C. The amount of TA was determined potentiometrically by the titration method [20]. The pH value of the samples was measured with a digital pH meter (HI 2211, Hanna Instrument Inc., Limena, Italy).

2.4. Sugar Analyses

The sugar (glucose, fructose, and sucrose) contents of the samples were determined by an HPLC (Waters e2695, Waters, Milford, MA, USA) system by adapting the IHC (2002) method to molasses [21]. A 1 g of sample was dissolved in 10 ml of deionized water and centrifuged at 5000 rpm (2300 g) (Hettich Mikro 220 R; Tuttlingen, Germany) for 5 minutes at 4 °C. The supernatant liquid was passed through a 0.45 µm porous PVDF filter and injected into HPLC. The separations and detection were performed by a YMC-Pack Polyamine II (250x4.6 mm, 5µm) carbohydrate

column and a Refractive Index detector (Waters, USA), respectively. The acetonitrile-water (80:20) mixture was used as the mobile phase with an isocratic flow. The furnace temperature was set to 25 °C, the flow rate to 1.2 ml min.⁻¹ and the injection volume to 20 µl. The

quantitation of sugars was made with calibration curves obtained from commercial standard (Sigma-Merck) solutions prepared at different concentrations, and the results were expressed as g 100 g⁻¹.

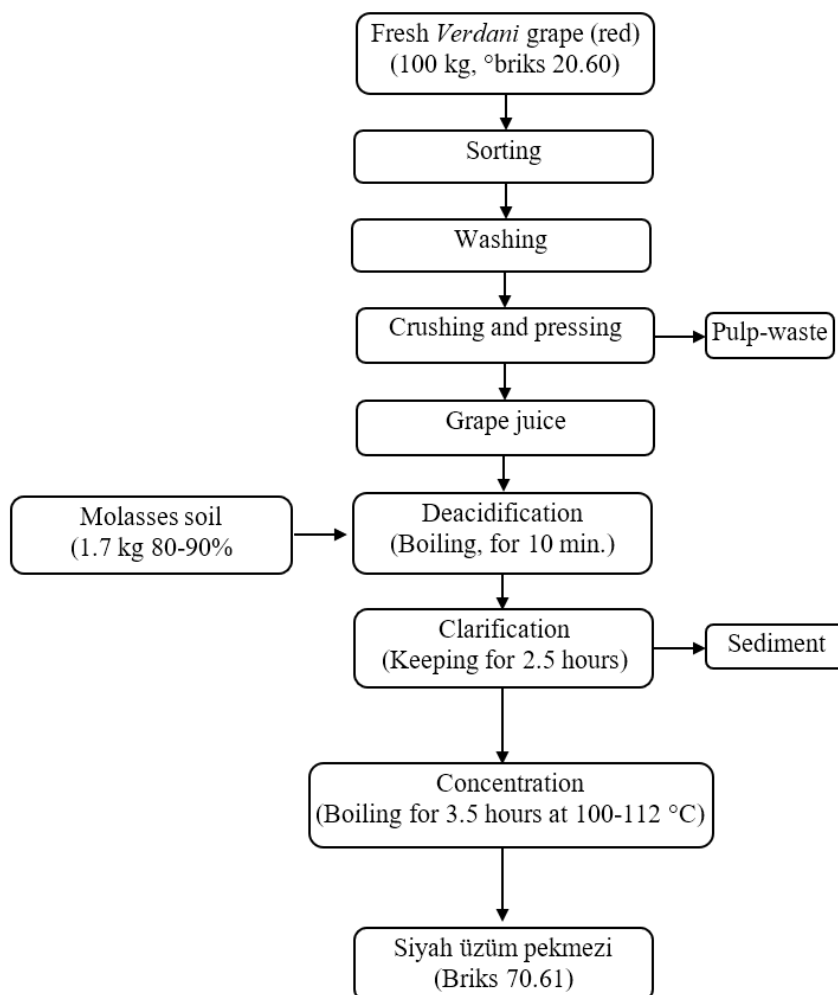


Figure 1. The flow chart of production of the traditional grape molasses

2.5. Organic Acid Analyses

Organic acid (tartaric, citric, malic, and succinic acids) contents were determined by an HPLC (Waters e2695) system [22]. A 2 g of molasses was weighed (10 g for FGJ) and the volume was adjusted to 50 ml with deionized water. Then, the mixture was homogenized, and centrifuged at 5000 rpm for 20 minutes. The supernatant was passed through a 0.45 µm porous PVDF filter and injected into HPLC. The HPLC system was equipped with an Atlantis dC18 (4.6x250 mm, 5 µm,) column at 25 °C and a PDA detector (photodiode array) (Waters) set at 210 nm. 20 mM NaH₂PO₄ solution acidified with H₃PO₄ until pH 2.7 was used as an isocratic elution. The flow rate of the mobile phase was 0.8 ml min.⁻¹, and the injection volume was 10 µl. The quantification of

organic acids was performed with calibration curves obtained from solutions prepared at different concentrations from the commercial standards (Sigma-Merck) of each compound, and the results were expressed as g kg⁻¹.

2.6. Volatile Compound Analysis

Volatile compounds were analyzed by gas chromatography-mass spectrometry (GC-MS) using the Solid Phase Micro-Extraction (SPME) according to Korkmaz et al. (2020) [23].

2.7. Statistical analyses

The statistical differences between the means of the data were determined by the independent sample test

(t-Test) ($P < 0.05$). This statistical analysis was carried out by SPSS (SPSS 16.0 for Windows, IBM, New York, USA) software package.

3. Results and Discussion

3.1. Changes in Physicochemical Properties

DM, TA, and TSS contents and pH values of the FGJ and molasses of the Verdani grape are given in Table 1. TSS ($20.60 \pm 0.15\%$) in the FGJ of the grape used was similar to that of 6 different Brazilian grape varieties [22], whereas it was higher than that of other grape varieties of the same country [24]. Additionally, Dölek (2017) found that TSS and TA in Verdani grape ranged from 17.0% to 19.8% and from 0.61% to 0.78% [25]. The main physicochemical properties such as TSS, DM, TA, and pH in grape varieties are primarily affected by their genetic variability, growing conditions, and ripening degree [26].

TSS and TA increased to $70.61 \pm 0.65\%$ and to $0.921 \pm 0.010\%$, respectively ($P < 0.05$), with the increase in the concentration of molasses during production. The increase in TA level in molasses compared to its level in FGJ was due to the increase in DM during molasses production. It was found that the amount of TA per dry matter decreased by 30.63% during molasses production ($P < 0.05$). This is mostly possible because the main organic acids in the grape are neutralized during the deacidification treatment. Also, it is reported that long-term cooking in molasses production can cause some losses in organic acid [27].

Table 1. Values of quality parameters of the fresh grape juice and the molasses sample

Quality parameters	Fresg grape juice	Molasses
Dry matter (DM) (%)	21.13 ± 0.65^b	74.81 ± 0.37^a
pH	4.23 ± 0.01^b	5.09 ± 0.02^a
Titrateable acidity (TA) (%) [*]	0.375 ± 0.014^b	0.921 ± 0.010^a
Total soluble solid (TSS) (°Brix, %)	20.60 ± 0.15^b	70.61 ± 0.65^a

^{*}g Tartaric acid 100 g^{-1} , TA: Titrateable acidity, ^{a-b} Means with different lowercase in some rows were significantly different between samples ($P < 0.05$).

The increase (by 20.33%) ($P < 0.05$) in pH value at the end of production was the result of this decrease in TA. Türkben et al. (2016) found that the TSS, TA, and pH values of molasses samples made by the traditional method from 14 different grape cultivars ranged between 66.30%-80.27%, 0.27%-1.81% and 3.59-5.23, respectively [28]. These characteristics of molasses types produced from grapes can vary

depending on the concentration method or the production conditions as well as the grape variety used. On the other hand, the molasses obtained in this study was classified as sweet and liquid molasses in terms of pH and TSS [18].

3.2. Changes in Sugar Content

The composition of the sugar and organic acid in fruits has critical effects on their taste and flavor properties and therefore on consumer perception [29]. The sugar and organic acid contents of the samples are presented in Table 2. As the main sugars in grapes, glucose ($9.57 \pm 0.50 \text{ g } 100^{-1}$) and fructose ($9.97 \pm 0.41 \text{ g } 100 \text{ g}^{-1}$) contents in FGJ were found to be close to each other. Their sum ($19.55 \pm 0.12 \text{ g } 100 \text{ g}^{-1}$) accounted for 92.47% of the DM in the FGJ. The amount of sucrose was negligible in both GFJ and molasses. Aubert and Chalot (2018) reported that the glucose and fructose contents in six different mature grape varieties varied between 7.58-9.37 $\text{g } 100 \text{ g}^{-1}$ and 7.91-10.21 $\text{g } 100 \text{ g}^{-1}$, respectively [30].

Table 2. Sugar and organic acid contents of the fresh grape juice and the molasses

Component	Fresh grape juice	Molasses
<i>Sugar (g 100 g⁻¹)</i>		
Glucose	9.57 ± 0.50^d	32.30 ± 0.29^a
Fructose	9.97 ± 0.41^d	31.14 ± 0.32^a
Total sugar	19.55 ± 0.12^d	63.44 ± 0.17^a
Fructose/glucose	1.04 ± 0.01^a	0.96 ± 0.02^a
<i>Organic acid (g kg⁻¹)</i>		
Tartaric	4.06 ± 0.05^a	3.75 ± 0.06^a
Malic	1.38 ± 0.03^a	1.60 ± 0.10^a
Citric	0.09 ± 0.00^b	0.45 ± 0.03^a
Succinic	0.20 ± 0.00^a	0.35 ± 0.02^a
Total organic acid	5.72 ± 0.07^b	6.15 ± 0.05^a

^{a-b} Means with different lowercase in some rows were significantly different between samples ($P < 0.05$).

In the molasses sample, glucose and fructose contents increased to $32.30 \pm 0.29 \text{ g } 100 \text{ g}^{-1}$ and $31.14 \pm 0.32 \text{ g } 100 \text{ g}^{-1}$, respectively, due to the concentration process during production. However, as a point to be noted, it was found that during the conversion of FGJ into molasses, there were decreases in the amounts of both glucose (4.67%) and fructose (11.78%) based on their percent in DM ($P < 0.05$). The fructose/glucose ratio decreased partially ($P > 0.05$) as a result of the decrease in the amount of fructose being higher than that of glucose. The higher decrease in fructose during the molasses production could be explained by the greater participation of this sugar in Maillard and/or caramelization reactions compared to glucose [31].

Türkben et al. (2016) reported that the amounts of glucose and fructose in 14 different traditional molasses from different varieties of grapes ranged from 27.57 g 100⁻¹ to 41.11 g 100⁻¹ and from 22.34 g 100⁻¹ to 34.69 g 100 g⁻¹, respectively [28]. The sugar content of different molasses types is mostly affected by the duration of the concentration process.

3.3. Changes in Organic Acid Content

Tartaric and malic acids are the main organic acids in grape varieties and the total amount of the two accounts for more 80% of the total organic acid contents in many grapes [24]. It was found that the sum of (5.44±0.08 g kg⁻¹) of tartaric (4.06±0.05 g kg⁻¹) and malic (1.38±0.03 g kg⁻¹) acids in the FGJ corresponded to 94.93% of the total organic acid content (Table 2). In a previous study, it was reported that the tartaric, malic, and citric acid contents in 11 different cultivars of grapes were between 4.98-7.48, g l⁻¹, 1.43-3.40 g l⁻¹ and 0.03-0.164 g l⁻¹, respectively [7]. In another study, it was found that tartaric and malic concentrations in 6 different varieties of grapes ranged between 4.3-6.2 g l⁻¹ and 1.5-2.9 g l⁻¹, respectively [30]. The organic acid content in grapes depends on genetic characteristics, growing conditions, and maturity level [24].

Tartaric, malic, citric, and succinic acid contents in the molasses sample were found to be 3.75±0.06 g l⁻¹, 1.60 ± 0.10 g l⁻¹, 0.45 ± 0.03 g l⁻¹ and 0.35±0.02 g l⁻¹, respectively. The amount of major organic acids in FGJ decreased during the production of molasses, probably due to the deacidification process, which precipitated tartaric and malic acids as salts of calcium tartrate and calcium maleate, respectively. Based on the ratios of tartaric and malic acids in the DM, it was also found that the initial contents of tartaric and malic acid were decreased by 73.91% and 67.25%, respectively (P<0.05). In addition, some of the reductions in organic acid amounts could be due to the boiling treatment during production [27]. It was reported that the reductions in malic, citric, and tartaric acid of a grape molasses type produced by the traditional method were 9.19%, 24.61%, and 3.89%, respectively [32].

3.4. Changes in volatile compounds

The profile of volatile compounds in fruits and vegetables has a wide diversity and affects their aroma characteristics [33]. The volatile compounds identified in FGJ and molasses are given in Table 3. In the FGJ sample, a total of 28 different volatile compounds were identified in different groups:

terpenoid (6), aldehydes (7), alcohols (10), ketones (2), ester (1), acid (1) and other (1).

Terpenoids and various aldehydes, alcohols, and ketones formed by lipoxygenase (LOX) enzyme activity were the most common volatile compounds in FGJ, both quantitatively and qualitatively. Terpenoids in grapes are generally responsible for their characteristic floral odor [30]. D-Limonene (152.91 ±5.07 mg kg⁻¹), β-linalool (11.40±0.58 mg kg⁻¹), carvone (43.02 ±4.62 mg kg⁻¹) and o-cymene (10.65±0.49 mg kg⁻¹) compounds were found as the most common terpenoids in FGJ. Hexanal (14.05±2.27 mg kg⁻¹), (E)-2-hexenal (27.81±8.94 mg kg⁻¹), 1-hexanol (178.92±9.21 mg kg⁻¹), (Z)-3-hexenol (11.68±0.43 mg kg⁻¹) and (E)-2-hexenol (50.04±2.69 mg kg⁻¹), which have fresh leaf grassy aroma, were found to be other compounds with higher amounts in the FGJ sample. Most of these volatile compounds, known also as C6-compounds, are formed by the LOX activity of certain unsaturated fatty acids. These compounds have also been found as predominant volatile compounds in different grape varieties in previous studies [34, 35]. Apart from these, hexyl phenylacetate (23.11±2.05 mg kg⁻¹), nonanal (15.13±1.48 mg kg⁻¹), ethanol (11.35±2.06 mg kg⁻¹), 6-methyl-5-hepten-2-one (13.36±0.26 mg kg⁻¹) and nonanoic acid (36.59±4.11 mg kg⁻¹) were found to be other important volatile compounds in FGJ.

The composition of volatiles in FGJ changed markedly during its conversion into molasses. The majority of the number (20) of compounds responsible for freshness and fruity odors in FGJ disappeared during the production of molasses, probably because of their degradation and/or volatilization during the production processes [36]. Conversely, 11 new compounds responsible for typical grape molasse were formed in the molasses. In particular, some volatile furans were formed abundantly during molasses production. As the newly formed furans, the concentration of furfural, 2-acetylfuran, 5-methylfurfural, dihydro 2 (3H)-furanone, 2-furanmethanol and methyl 2-furoate in molasses were 319.16±36.61 mg kg⁻¹, 24.53±2.92 mg kg⁻¹, 21.93±3.95 mg kg⁻¹, 7.28±2.24 mg kg⁻¹, 16.12±0.53 mg kg⁻¹, 6.11±1.53 mg kg⁻¹, respectively. Among these, only the amount of furfural corresponded to 57.37% of the total amount of volatile compounds in the molasses sample. These furans are responsible for the characteristic caramel, roasted-cooked and coffeelike aromas of grape molasses. They can be formed by Maillard reactions [32], Strecker degradation [23] and caramelization reactions [37] during the cooking process in production. Various volatile furan compounds have

also been found in other molasses types made from various grapes [38], [32].

Table 3. Volatile compound contents in the fresh grape juice and the molasses (mg kg⁻¹)

No	Compound	RI*	Fresgh grape juice	Molasses
	Total terpenoid		231.65±5.66^a	4.39±1.38^b
1	D-Limonene	1231	152.91±5.07 ^a	nd
2	1,8-Cineole	1233	7.33±2.01 ^a	nd
3	γ-Terpinene	1268	6.35±0.98 ^a	nd
4	o-Cymene	1287	10.65±0.49 ^a	nd
5	β-Linalool	1553	11.40±0.58 ^a	4.39±1.38 ^b
6	Carvone	1760	43.02±4.62 ^a	nd
	Total aldehyde		84.60±9.77^a	31.71±7.38^b
7	2-Methylbutanal	979	5.57±0.19 ^a	6.16±1.91 ^a
8	3-Methylbutanal	983	4.71±0.55 ^a	7.71±1.23 ^a
9	Hexanal	1121	14.05±2.27 ^a	nd
10	(E)-2-Hexenal	1245	27.81±8.94 ^a	nd
11	(Z)-2-Heptenal	1344	8.69±1.47 ^a	nd
12	Nonanal	1410	15.13±1.48 ^a	nd
13	Phenylmethanal	1546	8.62±0.24 ^a	nd
14	Phenylethanal	1666	nd	10.52±1.95 ^a
15	2,4-Dimethylbenzaldehyde	1840	nd	7.31±2.28 ^a
	Total alcohol		329.31±8.78^a	17.07±5.34^a
16	Ethanol	997	11.35±2.06 ^a	2.31±0.28 ^b
17	3-Methylbutanol	1230	28.17±2.53 ^a	nd
18	1-Hexanol	1366	178.92±9.21 ^a	nd
19	(Z)-3-Hexenol	1396	11.68±0.43 ^a	nd
20	(E)-2-Hexenol	1418	50.04±2.69 ^a	nd
21	1-Heptanol	1464	3.91±0.37 ^a	nd
22	2-Ethylhexanol	1497	16.98±2.47 ^a	5.81±0.61 ^a
23	2-Heptenol	1520	8.17±1.29 ^a	nd
24	1-Octanol	1565	10.69±0.56 ^a	nd
25	2-Tridecanol	1723	nd	1.47±0.10 ^a
26	β-Phenylethanol	1928	8.76±0.44 ^a	8.94±2.58 ^a
	Total cetone		19.87±1.49^a	9.87±2.85^a
27	3-Octanone	1277	6.51±0.88 ^a	nd
28	Hydroxyacetone	1323	nd	9.87±2.85 ^a
29	6-Methyl-5-hepten-2-one	1357	13.36±0.26 ^a	nd
	Total ester		23.11±2.05^a	nd
30	Hexyl phenylacetate	1666	23.11±2.05 ^a	nd
	Total acid		36.59±4.11^b	109.77±16.96^a
31	Acetic acid	1475	nd	51.92±5.61 ^a
32	Nonanoic acid	2184	36.59±4.11 ^a	49.51±1.08 ^a
33	Decanoic acid	2271	nd	8.34±2.27 ^a
	Total furan		nd	395.15±46.66^a
34	Furfural	1484	nd	319.16±36.61 ^a
35	2-Acetylfuran	1524	nd	24.53±2.92 ^a
36	5-Methylfurfural	1592	nd	21.93±3.95 ^a
37	Dihydro 2(3H)-furanone	1653	nd	7.28±2.24 ^a
38	2-Furanmethanol	1671	nd	16.12±0.53 ^a
39	Methyl 2-furoate	2040	nd	6.11±1.53 ^a
	Miscellaneous		3.31±0.63^a	3.56±0.34^a
40	2,3-Bütandiol	1557	3.31±0.63 ^a	3.56±0.34 ^a
	Total		728.17±18.44^a	556.27±61.30^a

*RI: Retention index calculated on DB-HeavyWax column, nd: not detected, ^{a-b} Means with different lowercase in some rows were significantly different between samples (P<0.05)

4. Conclusion and Suggestions

In this study, the changes in physicochemical properties, sugar, organic acid, and volatile compound content of the *Verdani* grape variety were evaluated for the first time during the production of its molasses by the traditional method. The initial TSS, TA, sugar, and organic acid contents increased depending on the rising concentration during the processing of FGJ into the molasses. However, the results showed that the method of traditional molasses production caused significant losses in the amounts of glucose, fructose, tartaric acid, and malic acid, indicating that this method can reduce their portion in the total dry matter after the molasses production. On the other hand, the data showed that the most of volatile compounds in FGJ disappeared during the conversion into its molasses, and also indicated that the traditional manufacturing method of grape molasses can lead to the generation of volatile furans in large amounts. Based on the results of this study, an evaporation under vacuum or open natural

conditions instead of the long-term and high-temperature cooking process in the traditional method can be more suitable for the concentration process in molasses production. In future studies, the effects of this production method on hydroxymethylfurfural (HMF) and bioactive properties in grapes should be investigated.

Acknowledgment

This research was funded by Mardin Artuklu University Scientific Research Institution (Project No: MAÜ.BAP.18.SYO.038). The author would like thanks to Assoc. Prof. Dr. Velid Unsal for providing the grape variety used.

Statement of Research and Publication Ethics

The study is complied with research and publication ethics

References

- [1] Food and Agriculture Organization (FAO), "Statistical data, 2020". [Online]. Available: <https://www.fao.org/faostat/en/#data/QCL>, [Accessed: Aug. 25, 2022].
- [2] A. Toker, ve İ. Hayoğlu, "Şanlıurfa Yöresi Gün Pekmezlerinin Üretim Tekniği ve Bazı Fiziksel-Kimyasal Özellikleri," *Harran Üniversitesi Ziraat Fakültesi Dergisi*, vol. 8, no. 2, pp. 67-73, 2004
- [3] Türkiye İstatistik Kurumu (TÜİK), "Bitkisel Üretim İstatistikleri, 2021". [Online]. Available: <https://biruni.tuik.gov.tr/medas/?kn=92&locale=tr>, [Accessed: Sept. 20, 2022].
- [4] A. Batu, "Klasik ve Modern Yönteme Göre Sıvı ve Beyaz Katı Üzüm Pekmezi (Zile Pekmezi) Üretimi," *Gıda Teknolojileri Elektronik Dergisi*, Vol. 2, pp. 9-26, 2006
- [5] E. Karababa and N. Develi Isikli, "Pekmez: A Traditional Concentrated Fruit Product," *Food Rev. Int.*, vol. 21, no. 4, pp. 357-366, 2005
- [6] M. M. Özcan, Ş. Alpar, and F. AL Juhaimi, "The effect of boiling on qualitative properties of grape juice produced by the traditional method," *J. Food Sci. Technol.*, vol. 52, no. 9, pp. 5546-5556, 2015
- [7] Y. Soyer, N. Koca, and F. Karadeniz, "Organic acid profile of Turkish white grapes and grape juices," *J. Food Compos. Anal.*, vol. 16, no. 5, pp. 629-636, 2003
- [8] S. Helvacıoğlu, M. Charehsaz, E. Güzelmeriç, E. Türköz Acar, E. Yeşilada and A. Aydın, "Comparatively Investigation of Grape Molasses Produced by Conventional and Industrial Techniques," *Marmara Pharm. J.*, vol. 22, no. 1, pp. 44-51, 2018
- [9] N. Kaplan, "Diyarbakır ve Mardin İllerinde Yetiştirilen Üzüm Çeşitlerinin Ampelografik Özelliklerinin Saptanması Üzerine Bir Araştırma," Doktora tezi, Fen Bil. Ens., Ankara Üniv., Ankara, TR, 1994
- [10] T. Cihat; SUNA, "Physical and chemical properties of pekmez (molasses) produced with different grape cultivars," *Tarım Bilim. Derg.*, vol. 22, no. 3, pp. 339-348, 2016
- [11] C. Türkben ve V. Uylaşer, "Türkiye'de Farklı Lokasyonlarda Üretilen Pekmezin (Üzüm Pekmezi) Fiziksel ve Kimyasal Özellikleri," *Türkiye 9. Bağcılık ve Teknolojileri Sempozyumu Bahçe*, Vol 47, no 1 (Özel Sayı), pp. 131-139, 2018
- [12] A. Şimşek, N. Artık, and E. Baspınar, "Detection of raisin concentrate (Pekmez) adulteration by regression analysis method," *J. Food Compos. Anal.*, vol. 17, no. 2, pp. 155-163, 2004
- [13] H. Yoğurtçu and F. Kamışlı, "Determination of rheological properties of some pekmez samples in Turkey," *J. Food Eng.*, vol. 77, no. 4, pp. 1064-1068, 2006

- [14] S. Karaman and A. Kayacier, "Effect of temperature on rheological characteristics of molasses: Modeling of apparent viscosity using Adaptive Neuro – Fuzzy Inference System (ANFIS)," *LWT.*, vol. 44, no. 8, pp. 1717–1725, 2011
- [15] I. Tosun and N. S. Ustun, "Nonenzymic browning during storage of white hard grape pekmez (Zile pekmezi)," *Food Chem.*, vol. 80, no. 4, pp. 441-443, 2003, doi: 10.1016/S0308-8146(02)00196-6.
- [16] O. S. Toker, M. Dogan, N. B. Ersöz, and M. T. Yilmaz, "Optimization of the content of 5-hydroxymethylfurfural (HMF) formed in some molasses types: HPLC-DAD analysis to determine effect of different storage time and temperature levels," *Ind. Crops Prod.*, vol. 50, pp. 137–144, 2013
- [17] S. Kamiloglu and E. Capanoglu, "In vitro gastrointestinal digestion of polyphenols from different molasses (pekmez) and leather (pestil) varieties," *Int. J. Food Sci. Technol.*, vol. 49, no. 4, pp. 1027–1039, 2014
- [18] Türkiye Cumhuriyeti Resmi Gazete, Türk Gıda Kodeksi Üzüm Pekmezi Tebliği, Tebliğ No: 2017/8, Available: <https://www.resmigazete.gov.tr/eskiler/2017/06/20170930-24.htm>
- [19] AOAC Int. (2000). Official methods of analysis. 17th ed. AOAC Int., Arlington, VA. In Association of Official Analytical Chemists, Rockville, MD, USA.
- [20] E. Nicolosi, F. Ferlito, M. Amenta, T. Russo, and P. Rapisarda, "Changes in the quality and antioxidant components of minimally processed table grapes during storage," *Sci. Hortic. (Amsterdam)*, vol. 232, pp. 175-183, 2018.
- [21] Harmonised Methods of the International Honey Commission (IHC). "Bee Product Science, 2002", Available: <https://www.ihc-platform.net/ihcmethods2009.pdf>, [Accessed: Oct. 11, 2022]
- [22] M. D. S. Lima et al., "Phenolic compounds, organic acids and antioxidant activity of grape juices produced from new Brazilian varieties planted in the Northeast Region of Brazil," *Food Chem.*, vol. 161, pp. 94-103, 2014
- [23] A. Korkmaz, A. F. Atasoy, and A. A. Hayaloglu, "Changes in volatile compounds, sugars and organic acids of different spices of peppers (*Capsicum annuum* L.) during storage," *Food Chem.*, vol. 311, p. 125910, 2020
- [24] M. J. R. da Silva et al., "Grape juices produced from new hybrid varieties grown on Brazilian rootstocks – Bioactive compounds, organic acids and antioxidant capacity," *Food Chem.*, vol. 289, pp. 714-722, 2019
- [25] Dölek, T., "Siirt Yöresinde Yetiştirilen Bazı Üzüm Çeşitlerinin Göz Verimliliklerinin Belirlenmesi Ve Farklı Göz Şarjı Uygulamalarının Verim Ve Kaliteye Etkisi", Yüksek Lisans Tezi, Fen Bil. Enst. Siirt Üniv., Siirt, Türkiye, 2017
- [26] D. Granato, M. de Magalhães Carrapeiro, V. Fogliano, and S. M. van Ruth, "Effects of geographical origin, varietal and farming system on the chemical composition and functional properties of purple grape juices: A review," *Trends Food Sci. Technol.*, vol. 52, pp. 31-48, 2016
- [27] H. Darvishi, M. Koushesh Saba, N. Behrooz-Khazaei, and H. Nourbakhsh, "Improving quality and quantity attributes of grape juice concentrate (molasses) using ohmic heating," *J. Food Sci. Technol.*, vol. 57, no. 4, pp. 1362–1370, Apr. 2020, doi: 10.1007/s13197-019-04170-1.
- [28] C. Türkben, S. Suna, G. İzli, V. Uylaşer, and C. Demir, "Physical and chemical properties of Pekmez (Molasses) produced with different grape cultivars," *Tarım Bilim. Derg.*, vol. 22, no. 3, pp. 339-348, 2016
- [29] P. Muñoz-Robredo, P. Robledo, D. Manríquez, R. Molina, and B. G. Defilippi, "Characterization of sugars and organic acids in commercial varieties of table grapes," *Chil. J. Agric. Res.*, vol. 71, no. 3, pp. 452-458, 2011
- [30] C. Aubert and G. Chalot, "Chemical composition, bioactive compounds, and volatiles of six table grape varieties (*Vitis vinifera* L.)," *Food Chem.*, vol. 240, pp. 524-533, 2018
- [31] E. H. Ajandouz, L. S. Tchiakpe, F. D. Ore, A. Benajiba, and A. Puigserver, "Effects of pH on Caramelization and Maillard Reaction Kinetics in Fructose-Lysine Model Systems," *J. Food Sci.*, vol. 66, no. 7, pp. 926-931, 2001
- [32] A. Kuşçu and Ö. Bulantekin, "The effects of production methods and storage on the chemical constituents of apple pekmez," *J. Food Sci. Technol.*, vol. 53, no. 7, pp. 3083-3092, 2016
- [33] S. Marín-San Román, P. Rubio-Bretón, E. P. Pérez-Álvarez, and T. Garde-Cerdán, "Advancement in analytical techniques for the extraction of grape and wine volatile compounds," *Food Res. Int.*, vol. 137, p. 109712, 2020

- [34] E. Sánchez-Palomo, M. C. Díaz-Maroto, and M. S. Pérez-Coello, "Rapid determination of volatile compounds in grapes by HS-SPME coupled with GC-MS," *Talanta*, vol. 66, no. 5, pp. 1152-1157, 2005
- [35] Y. Wu et al., "Evolution of volatile compounds during the development of Muscat grape 'Shine Muscat' (*Vitis labrusca* × *V. vinifera*)," *Food Chem.*, vol. 309, p. 125778, 2020
- [36] M. Cissé et al., "Athermal concentration by osmotic evaporation of roselle extract, apple and grape juices and impact on quality," *Innov. Food Sci. Emerg. Technol.*, vol. 12, no. 3, pp. 352–360, 2011
- [37] K. Samborska, R. Bonikowski, D. Kalemba, A. Barańska, A. Jedlińska, and A. Edris, "Volatile aroma compounds of sugarcane molasses as affected by spray drying at low and high temperature," *LWT*, vol., 145, p 111288, 2021
- [38] A. C. T. Biasoto, K. de L. Sampaio, E. J. N. Marques, and M. A. A. P. da Silva, "Dynamics of the loss and emergence of volatile compounds during the concentration of cashew apple juice (*Anacardium occidentale* L.) and the impact on juice sensory quality," *Food Res. Int.*, vol. 69, pp. 224-234, 2015



Astrophysical Parameters of the Open Cluster Berkeley 6

Seliz KOÇ^{1*}, Talar YONTAN²

¹Istanbul University, Institute of Graduate Studies in Science, Programme of Astronomy and Space Sciences, 34116, Beyazıt, Istanbul, Turkey

²Istanbul University, Faculty of Science, Department of Astronomy and Space Sciences, 34119, Beyazıt, Istanbul, Turkey
(ORCID: [0000-0001-7420-0994](https://orcid.org/0000-0001-7420-0994)) (ORCID: [0000-0002-5657-6194](https://orcid.org/0000-0002-5657-6194))



Keywords: Open cluster and associations, individual, Berkeley 6, Stars, Hertzsprung Russell (HR) diagram, Galaxy.

Abstract

In this study, the structural and basic astrophysical parameters of the poorly studied open cluster Berkeley 6 are calculated. Analyses of the cluster are carried out using the third photometric, spectroscopic, and astrometric data release of *Gaia* (*Gaia* DR3). The membership probabilities of stars located in the direction of the cluster region are calculated by considering their astrometric data. Thus, we identified 119 physical members for Berkeley 6. The colour excess, distance, and age of the cluster are determined simultaneously on the colour-magnitude diagram. We fitted solar metallicity PARSEC isochrones to the colour-magnitude diagram by considering the most probable member stars and obtained $E(G_{BP}-G_{RP})$ colour excess as 0.918 ± 0.145 mag. The distance and age of the cluster are determined as $d=2625 \pm 337$ pc and $t=350 \pm 50$ Myr, respectively.

1. Introduction

Open star clusters (OCs) are groups of stars that are bound under weak gravitational forces and formed from the same molecular cloud that collapses under the same physical conditions. Therefore, the distance, metallicity, and age of the stars are similar, whereas their masses are different. So as the ages of OCs range from a few million to billions of years, they are essential objects to understand the star formation process and stellar evolution theories ([1]; [2]). OCs are located on the Galaxy disc. These characteristics make OCs important tools to understand the structure and dynamical evolution of the Galaxy disc (e.g., [3]; [4]; [5]).

The available information in the literature for the Berkeley 6 ($\alpha_{2000.0} = 01^{\text{h}}51^{\text{m}}12.7^{\text{s}}$, $\delta_{2000.0} = 61^{\circ}03'40''$; $l = 130^{\circ}.1008$, $b = -00^{\circ}.9760$; [6]) is as follows: [7] analysed the CCD *UBVRI* observations of Be 6 and determined its structural and fundamental astrophysical parameters.

They considered the radial density profile model of [8] and determined the core radius of the cluster as $r_c = 0.54 \pm 0.29$ arcmin. By fitting theoretical isochrones of [9] to the observed $(B-V) \times (V-I)$ colour-colour diagram, [7] obtained the reddening of the Be 6 as $E(B-V) = 0.90 \pm 0.05$ mag. Also, they shifted theoretical isochrones to the observed $(B-V) \times V$, $(V-R) \times V$, and $(V-I) \times V$ colour-magnitude diagrams and found the distance modulus, distance and age of Be 6 as $\mu_V = 14.80$ mag, $d = 2.52 \pm 0.12$ kpc and $\log t = 7.5 \pm 0.1$ yr, respectively. [10] improved an algorithm to obtain simultaneously reddening, distance, and age of clusters, and obtained parameters of Be 6 as $E(B-V) = 0.781$ mag, $d = 2.5$ kpc, and $\log t = 8.6$ yr, respectively. [6] estimated the distance and age of the Be 6 as $d = 3.05$ kpc and $\log t = 8.35$ yr using *Gaia* DR2 astrometric and photometric data. The mean proper-motion components of the cluster were calculated as $(\mu_{\alpha} \cos \delta, \mu_{\delta}) = (-0.857 \pm 0.076, -0.485 \pm 0.094)$ mas/yr by [6] (Table 1).

*Corresponding author: seliskoc@gmail.com

Received: 01.12.2022, Accepted: 08.06.2023

Table 1: Fundamental parameters for Berkeley 6 gathered from the literature. Columns denote the colour excess ($E(B-V)$), metallicity ($[Fe/H]$), distance moduli and distance (μ , d), age (t), proper-motion components ($\mu_{\alpha\cos\delta}$, μ_{δ}), trigonometric parallaxes (ϖ) and reference. Errors of the parameters are shown in parenthesis.

$E(B-V)$ (mag)	$[Fe/H]$ (dex)	μ (mag)	d (pc)	t (Myr)	$\mu_{\alpha\cos\delta}$ (mas/yr)	μ_{δ} (mas/yr)	ϖ (mas)	Reference
0.90 (0.05)	---	14.80	2520 (120)	32 (8)	---	---	---	[7]
0.781	---	---	2500	400	-1.29	-3.22	---	[10], [11]
---	---	---	2950 (932)	---	-0.857 (0.076)	-0.485 (0.094)	0.31 (0.05)	[12], [13]
0.581	---	12.42	3051	224	-0.857 (0.076)	-0.485 (0.094)	0.31 (0.05)	[6]
0.758 (0.032)	-0.182 (0.095)	---	2417 (212)	110 (150)	-0.858 (0.090)	-0.495 (0.105)	0.310 (0.048)	[14]

2. Material and Method

2.1 Astrometric and Photometric Data

The third data release of *Gaia* (hereafter *Gaia* DR3, [17]) provides high quality astrometric and photometric data on more than 1.5 billion celestial objects. By using the equatorial coordinates of Be 6 given by [6] as the center of the cluster, we obtained 23,139 stars within a 20 arcmin radius with a magnitude range of $7 < G \leq 22$ mag. The obtained data from the catalogue are radius distance (r) from the centre, equatorial coordinates (α , δ), photometric magnitude and colours (G , $G_{BP}-G_{RP}$). The third data release of *Gaia* (hereafter *Gaia* DR3, [17]) provides high quality astrometric and photometric data on more than 1.5 billion celestial objects. By using the equatorial coordinates of Be 6 given by [6] as the center of the cluster, we obtained 23,139 stars within a 20 arcmin radius with a magnitude range of $7 < G \leq 22$ mag. The obtained data from the catalogue are radius distance (r) from the centre, equatorial coordinates (α , δ), photometric magnitude and colours (G , $G_{BP}-G_{RP}$), proper-motion components ($\mu_{\alpha\cos\delta}$, μ_{δ}) and trigonometric parallaxes (ϖ). The identification map of the open cluster Be 6 is shown in Figure 1.

2.2 Photometric Completeness Limits and Photometric Errors

To derive precise parameters, we identified the photometric completeness limit according to the G magnitude of the stars. For this, we constructed star count versus G magnitude histograms, as shown in

Figure 2. In the figure, it can be seen that the star counts increase up to $G=21$ mag and start to decrease after this limit, which indicates that stellar incompleteness has set in. Thus, we adopted this value as the cluster photometric completeness limit and took into account

the stars brighter than this limit for further analyses. The uncertainties of the *Gaia* DR3 photometric data were adopted as their interval errors. We calculated the mean errors of the G magnitudes and $G_{BP}-G_{RP}$ colours of detected stars as a function of G interval magnitudes and listed them in Table 2. Considering the adopted photometric completeness limit $G=21$ mag for Be 6, it can be seen from Table 2 that the mean internal errors for G magnitudes and $G_{BP}-G_{RP}$ colours of the stars reach up to 0.007 and 0.146 mag, respectively.

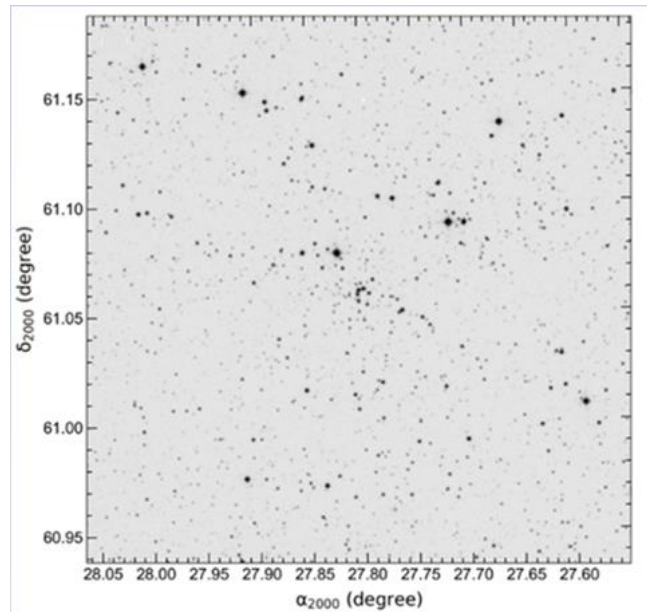


Figure 1: Identification chart of stars located in the region of Berkeley 6. Field of view of the optical chart is $20' \times 20'$. North and East correspond to the up and left directions, respectively.

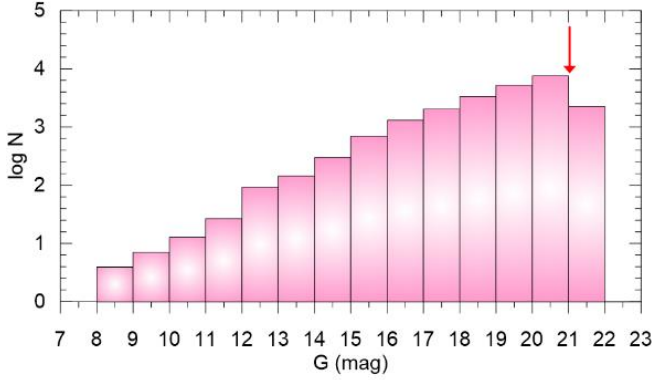


Figure 2: Histogram of number of stars according to G apparent magnitude intervals. The red arrow represents the faint limiting magnitude of the Berkeley 6.

Table 2: Mean photometric errors calculated for apparent G magnitude for Berkeley 6. N indicates the number of stars within the selected G magnitude intervals.

G (mag)	N	σ_G (mag)	$\sigma_{\text{GBP-GRP}}$ (mag)
(6, 12]	51	0.003	0.005
(12, 14]	238	0.003	0.005
(14, 15]	301	0.003	0.005
(15, 16]	703	0.003	0.006
(16, 17]	1319	0.003	0.008
(17, 18]	2050	0.003	0.014
(18, 19]	3393	0.003	0.031
(19, 20]	5232	0.004	0.063
(20, 21]	7556	0.007	0.146
(21, 22]	2296	0.025	0.397

3. Results and Discussion

3.1 Structural Parameters of the Berkeley 6

To determine structural parameters such as the limiting and effective radii of the core region of Be 6, we carried out the Radial Density Profile (RDP) model given by [15]. For this, we first divided the cluster area into the series of concentric rings, which were adjusted to the central coordinates taken from [6]. Then we calculated the stellar densities (ρ) for each ring by dividing the number of stars by the ring area. We plotted stellar densities versus radius from the cluster centre (Figure 3) and fitted the RDP model of [15] to this distribution by following χ^2 minimization. [15] described the model as $\rho(r) = f_{\text{bg}} + (f_0 / (1 + (r/r_c)^2))$, where r is the radius from the cluster centre, f_{bg} , f_0 and r_c are the background stellar density, the central density and the core radius, respectively. Figure 3 shows the RDP of the cluster together with the best fitting [15] model for it. The best fit resulted in the core radius, background stellar density and central density, being $r_c = 0.501 \pm 0.029$ arcmin, $f_{\text{bg}} = 10.705 \pm 0.269$ stars/arcmin² and $f_0 = 38.844 \pm 1.226$ stars/arcmin², respectively. Also, we took into account the radius value at which stellar density is about to meet the background density (Figure 3 a grey horizontal line) as the cluster limiting radius (r_{lim}). This limit was adopted as $r = 5'$ (3.82 pc) for Be 6, and we used only the stars inside this limiting radius in further analyses.

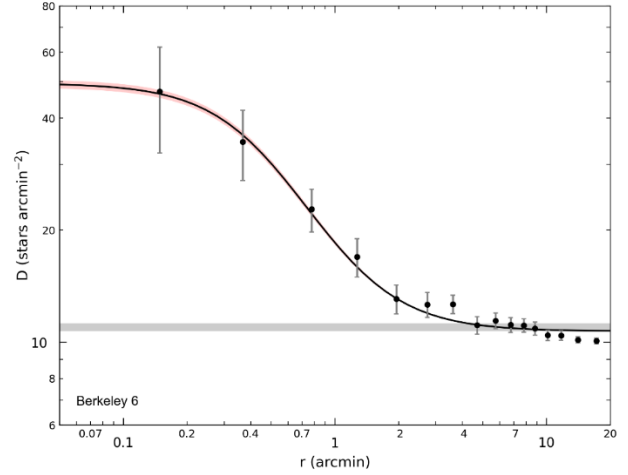


Figure 3: Radial density profile of Berkeley 6. Errors were derived using the expression of $1/\sqrt{N}$, where N represents the number of stars used in the density estimation. The solid line represents the optimal [15] profiles. The background density level and its errors are the horizontal grey bands. The King fit uncertainty (1σ) is shown with the red shaded region.

3.2 Membership Probabilities of Stars

Because the OCs are located near the Galactic plane, their members are highly affected by background star contamination. This makes it difficult to identify cluster members using only photometric data. Instead of this, the radial velocity and proper-motion values of stars are more useful in determining the membership. Astrometric and spectroscopic observations provide information on the radial velocity and proper-motion components of stars. However, spectroscopic observations of a great number of objects require much observing time, including larger telescopes. For this reason, the radial velocities of stars remain incapable of determining their membership. Because the components of OCs share a common origin, their movement vectors in the sky commonly point in the same direction. These properties make proper-motion components useful tools to separate cluster stars from field stars. Thanks to the astrometric data with high accuracy of *Gaia* DR3, the cluster members can be separated more precisely. In the study, we took into account *Gaia* DR3 proper-motion components as well as the trigonometric parallaxes of stars in the direction of Be 6 to calculate the membership probabilities of each. Membership analyses were utilized by using the UPMASK (Unsupervised Photometric Membership Assignment in Stellar Clusters; [16]) method. UPMASK is based on the clustering method, which is represented by k -means clustering, by detecting spatially concentrated groups and identifying the most likely cluster members. k -means is an integer number that varies from 5 to 25 and is not set directly by the user ([16]; [13]). [13] used *Gaia* DR2 astrometric data on 1,481 open clusters with the UPMASK methodology, and [6] successfully calculated the membership probabilities of stars in these clusters as a continuation of his work. We applied UPMASK by considering five-dimensional astrometric parameters of stars that contain positions (α , δ), proper-motion components ($\mu_\alpha \cos \delta$, μ_δ), trigonometric

parallaxes (ϖ), and their uncertainties. During the application, we run 1000 iterations for Be 6. Membership probability is defined as the frequency with which a star is defined as a part of a clustered group. We reached the best result when the *k-means* value was set to 11 for Be 6. The possible cluster members were selected among the stars that were brighter than $G=21$ mag with membership probabilities $P \geq 0.5$ and located on the inside of the cluster limiting radius ($r = 5'$). These stars were adopted as physical members of Be 6. Thus, the number of member stars we reached for Be 6 is 119. These stars were used in the determination for the astrometric and astrophysical parameters of Be 6. In order to visualize the positions of the most probable member stars in Be 6, we constructed a vector-point diagram (VPD), as shown in Figure 4. It can be seen in the figure that Be 6 is embedded in the field stars. In Figure 4, the intersection of blue dashed lines represents the values of mean proper motion components calculated from the most probable cluster members (119 stars with $P \geq 0.5$). These values were estimated as $(\mu_{\alpha \cos \delta}, \mu_{\delta}) = (-0.894 \pm 0.004, -0.533 \pm 0.004)$ mas/yr, which are compatible with the results of all studies performed with *Gaia* observations for the Be 6 (see Table 1). To calculate the mean trigonometric parallax (ϖ) of Be 6 we plotted the parallax histogram considering the most probable cluster members and applied the Gaussian fit to the histogram of the selected stars (Figure 5). During the calculation of ϖ , we considered the stars with a relative parallax error (σ_{ϖ}/ϖ) of less than 0.2 to minimize uncertainties. We obtained the mean ϖ of Be 6 as 0.32 ± 0.03 mas. By applying the linear equation of d (pc) = $1000/\varpi$ (mas) to the mean trigonometric parallaxes, we reached the parallax distance as $d_{\varpi} = 3125 \pm 332$ pc. Also, to compare results, we calculated the arithmetic mean (ϖ_{mean}) of trigonometric parallaxes from the most probable cluster members ($P \geq 0.5$) as $\varpi_{\text{mean}} = 0.325 \pm 0.034$ mas, which is the same result as Gaussian fit. A histogram of the most probable stars, as well as the Gaussian fit (dashed black line) to the distribution are given in Figure 5.

3.3 Astrophysical Parameters of Berkeley 6

As the cluster members stars share similar physical properties and they contain a wide range of stellar masses, observational colour-magnitude diagrams (CMDs) are essential tools to visualize the morphology of open clusters, as well as determine their reddening, distances, and age.

To determine the metallicity, colour excesses, distance, and age of the Be 6, we fitted PARSEC isochrones of [18] to the observed CMD, considering the most probable cluster member stars. In the analyses, we fitted theoretical isochrones by eye, taking into account the most probable main-sequence and turn-off point members of the cluster. The CMD with the best fit isochrone is shown in Figure 6. We used the isochrones of $\log t = 8.48, 8.54$ and 8.60 yr. We considered solar metallicity value ($[\text{Fe}/\text{H}] = 0$ dex or $z = 0.0152$) for relevant isochrones. The best fit isochrone provides colour excess of $E(G_{\text{BP}}-G_{\text{RP}}) = 0.918 \pm 0.145$ mag. Also, to compare this value with the literature, we used the equation of $E(G_{\text{BP}}-G_{\text{RP}}) = 1.41 \times E(B-V)$ given by [19] and

calculated the *UBV* based colour excess as $E(B-V) = 0.651 \pm 0.103$ mag. The errors for colour excesses were estimated by considering the mean photometric error of *Gaia* ($G_{\text{BP}}-G_{\text{RP}}$) colour in the *G* completeness limit (see Table 2). The estimated $E(B-V)$ colour excess is compatible with the studies of [6], [10] and [14] within the errors. Moreover, the fitting procedure gives the age and distance moduli of Be 6 to be $t = 350 \pm 50$ Myr and $(m-M_G) = 13.806 \pm 0.263$ mag, respectively, which corresponds to the isochrone distance to be $d_{\text{iso}} = 2625 \pm 337$ pc (see Table 3). In addition to this, we calculated errors in distance moduli and distances using the relations presented in [22], [24], [25], [26].

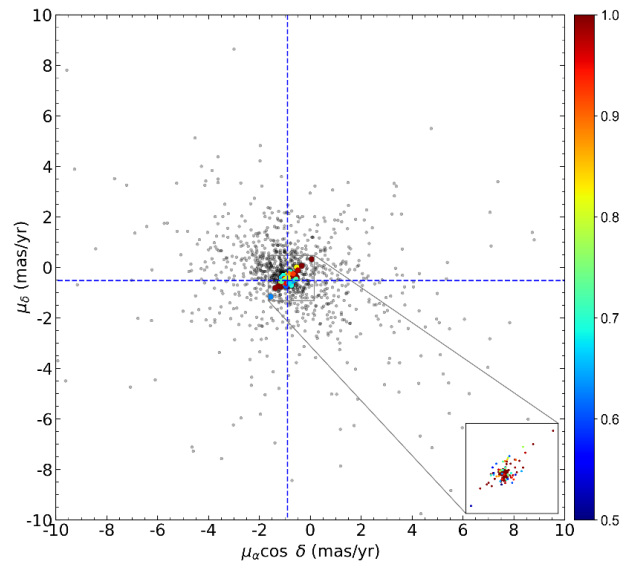


Figure 4: VPD of Berkeley 6 based on *Gaia* DR3 astrometry. The membership probabilities of the stars are showed with the colour scale shown on the right. In the zoomed frame represents the region of condensation for Berkeley 6 in the VPD. The intersection of the dashed blue lines is the point of mean proper motion of Berkeley 6.

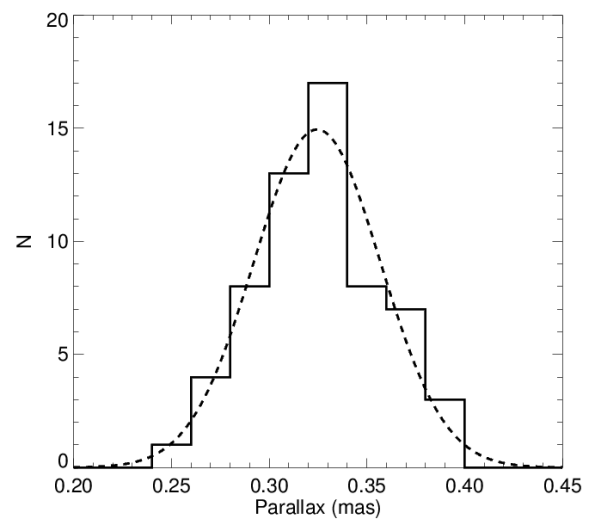


Figure 5: *Gaia* DR3 based trigonometric parallax histogram for Berkeley 6. The distribution of member stars with relative parallax error is less than 0.2 and the calculated Gaussian fit which shown with the dashed line.

These relations take into account the uncertainty in colour excess. The age obtained for Be 6 in this study ($t = 350 \pm 50$ Myr) is in good agreement with the results given by [10] and [11], whereas the isochrone distance value ($d_{\text{iso}} = 2625 \pm 337$ pc) is compatible with almost all the studies (except for the value of [6]) given by different researchers (see Table 1). The Galactocentric distance and Galactocentric coordinates were obtained as $R_{\text{gc}} = 9.90$ kpc and $(X, Y, Z)_{\odot} = (-1691, 2008, -45)$ pc. These are compatible with the corresponding estimates in [12]. The basic parameters of Be 6 are listed in Table 3.

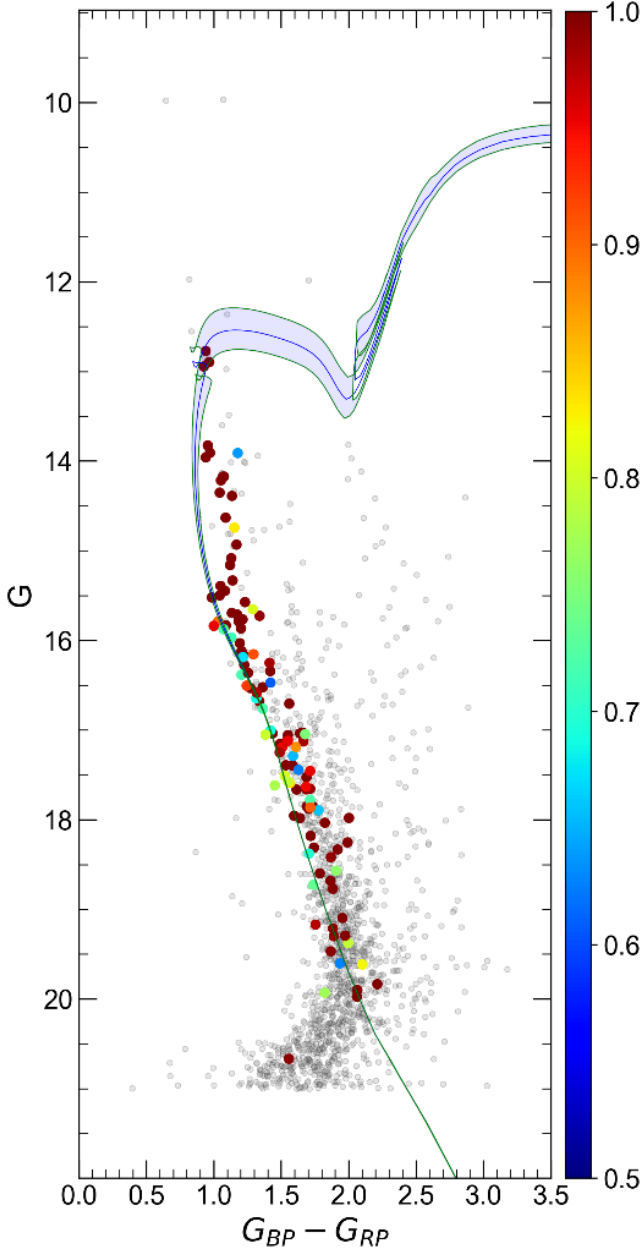


Figure 6: Colour-magnitude diagram of Berkeley 6. Different coloured circles show the membership probabilities according to the colour scales shown on the right side of the diagrams. Gray dots represent field stars. The blue lines show the PARSEC isochrones, while the shaded areas surrounding these lines are their associated errors.

Table 3: Basic parameters of Berkeley 6 derived in this study.

Parameter	Value
α (hh:mm:ss.s)	01:51:12.7
δ (dd:mm:ss.s)	61:03:40.0
l ($^{\circ}$)	130.1008
b ($^{\circ}$)	-0.9760
f_0 (star/arcmin 2)	38.844 ± 1.226
r_c (arcmin)	0.501 ± 0.029
f_{bg} (star/arcmin 2)	10.705 ± 0.269
r_{lim} (arcmin)	5
r (pc)	3.82
$\mu_{\alpha} \cos \delta$ (mas/yr)	-0.894 ± 0.004
μ_{δ} (mas/yr)	-0.533 ± 0.004
Cluster members ($P \geq 0.5$)	119
ϖ (mas)	0.325 ± 0.034
d_{ϖ} (pc)	3077 ± 322
$E(G_{\text{BP}} - G_{\text{RP}})$ (mag)	0.918 ± 0.145
$E(B-V)$ (mag)	0.651 ± 0.103
[Fe/H] (dex)	0 (assumed)
Age (Myr)	350 ± 50
Distance module (mag)	13.806 ± 0.263
Isochrone distance (pc)	2625 ± 337
X (pc)	-1691
Y (pc)	2008
Z (pc)	-45
R_{gc} (kpc)	9.90

4. Conclusion and Suggestions

In this study, we presented structural and astrophysical parameters of the Be 6 open cluster by using *Gaia* DR3 photometric and astrometric data. The astrometric parameters of *Gaia* DR3 were used to calculate the membership probabilities of stars located in the cluster region. The main results are given below:

- RDP analyses show that the limiting radius of the cluster is $r_{\text{lim}} = 5'$ (3.82 pc).
- We classified 119 most likely cluster member stars with a membership probability $P \geq 0.5$ which are also lying within the limiting radius. The mean proper motion of Be 6 is estimated as $(\mu_{\alpha} \cos \delta, \mu_{\delta}) = (-0.894 \pm 0.004, -0.533 \pm 0.004)$ mas/yr.
- We considered the most likely member stars with a relative parallax error (σ_{ϖ}/ϖ) of less than 0.2 and determined the trigonometric parallax of the cluster as $\varpi = 0.325 \pm 0.034$ mas. This value corresponds to the parallax distance of Be 6 to be $d_{\varpi} = 3077 \pm 322$ pc.
- Astrophysical parameters were derived simultaneously by considering *Gaia* based CMD. PARSEC isochrones of solar metallicity [Fe/H] = 0 dex or $z = 0.0152$ were fitted through the most likely cluster members ($P \geq 0.5$). We took into account the morphology, such as the main-sequence, and turn-off point of the cluster, that is viewable on CMD during the fitting procedure. Hence, we determined the colour excess, age, and isochrone

distance of Be 6 as $E(G_{BP}-G_{RP}) = 0.918 \pm 0.145$ mag, $t = 350 \pm 50$ Myr, and $d_{iso} = 2625 \pm 337$ pc, respectively.

- Although there is a difference of about 450 pc between the calculated parallax distance ($d_{\pi} = 3077 \pm 322$ pc) and isochrone distance ($d_{iso} = 2625 \pm 337$ pc) results, the two distance values are compatible within the errors. For objects far from the 2 kpc, the zero-point problem and observational biasness cause the measured *Gaia* trigonometric parallaxes to be smaller ([20];[21];[23]).

Acknowledgment

We thank the anonymous referees for the insightful and constructive suggestions, which significantly improved the paper. This study is a part of the doctoral thesis of Seliz Koç. This study has been supported in part by the Scientific and Technological Research Council (TÜBİTAK) 122F109. We also made use of Vizier and Simbad databases at CDS,

Strasbourg, France. We made use of data from the European Space Agency (ESA) mission *Gaia*², processed by the *Gaia* Data Processing and Analysis Consortium (DPAC)³. Funding for DPAC has been provided by national institutions, in particular the institutions participating in the *Gaia* Multilateral Agreement.

Contributions of the Authors

Seliz Koç: Article writing, analysis.

Talar Yontan: Article writing, analysis.

Conflict of Interest Statement

There is no conflict of interest between the authors.

Statement of Research and Publication Ethics

The study is complied with research and publication ethics

References

- [1] S. F. Portegies Zwart, S. L. W. McMillan, and M. Gieles, “Young massive star clusters,” *Annu. Rev. Astron. Astrophys.*, vol. 48, no. 1, pp. 431–493, 2010.
- [2] S. C. Kim et al., “Bvi photometric study of the old open cluster Ruprecht 6,” *J. Korean Astron. Soc.*, vol. 50, no. 3, pp. 79–92, 2017.
- [3] E. D. Friel, “The old open clusters of the milky way,” *Annu. Rev. Astron. Astrophys.*, vol. 33, no. 1, pp. 381–414, 1995.
- [4] Y. Xu, L.-G. Hou, and Y.-W. Wu, “The spiral structure of the Milky Way,” *Res. Astron. Astrophys.*, vol. 18, no. 12, p. 146, 2018.
- [5] Z.-H. He, Y. Xu, C.-J. Hao, Z.-Y. Wu, and J.-J. Li, “A catalogue of 74 new open clusters found in *Gaia* Data-Release 2,” *Res. Astron. Astrophys.*, vol. 21, no. 4, p. 093, 2021.
- [6] T. Cantat-Gaudin et al., “Painting a portrait of the Galactic disc with its stellar clusters,” *Astron. Astrophys.*, vol. 640, p. A1, 2020.
- [7] S. Lata, A. K. Pandey, B. Kumar, H. Bhatt, G. Pace, and S. Sharma, “A deepubvriccd photometry of six open star clusters in the galactic anticenter region,” *Astron. J.*, vol. 139, no. 2, pp. 378–389, 2010.
- [8] J. Kaluzny, and A. Udalski . “Photometric Study of the Old Open Cluster NGC 6791”, *Acta Astronomica*, vol. 42, no. 1, pp. 29-47, 1992
- [9] L. Girardi et al., “Theoretical isochrones in several photometric systems: I. Johnson-Cousins-Glass, HST/WFPC2, HST/NICMOS, Washington, and ESO Imaging Survey filter sets,” *Astron. Astrophys.*, vol. 391, no. 1, pp. 195–212, 2002.
- [10] N. V. Kharchenko, A. E. Piskunov, E. Schilbach, S. Röser, and R.-D. Scholz, “Global survey of star clusters in the Milky Way: I. The pipeline and fundamental parameters in the second quadrant***,” *Astron. Astrophys.*, vol. 543, p. A156, 2012.
- [11] N. V. Kharchenko, A. E. Piskunov, E. Schilbach, S. Röser, and R.-D. Scholz, “Global survey of star clusters in the Milky Way: II. The catalogue of basic parameters *,” *Astron. Astrophys.*, vol. 558, p. A53, 2013.
- [12] T. Cantat-Gaudin et al., “A *Gaia* DR2 view of the open cluster population in the Milky Way,” *Astron. Astrophys.*, vol. 618, p. A93, 2018.
- [13] T. Cantat-Gaudin and F. Anders, “Clusters and mirages: cataloguing stellar aggregates in the Milky Way,” *Astron. Astrophys.*, vol. 633, p. A99, 2020.
- [14] W. S. Dias et al., “Updated parameters of 1743 open clusters based on *Gaia* DR2,” *Mon. Not. R. Astron. Soc.*, vol. 504, no. 1, pp. 356–371, 2021.

- [15] I. King, "The structure of star clusters. I. an empirical density law," *Astron. J.*, vol. 67, p. 471, 1962.
- [16] A. Krone-Martins and A. Moitinho, "UPMASK: unsupervised photometric membership assignment in stellar clusters," *Astron. Astrophys.*, vol. 561, p. A57, 2014.
- [17] Gaia Collaboration et al., "Gaia Data Release 3: Summary of the content and survey properties," arXiv [astro-ph.GA], 2022.
- [18] A. Bressan et al., "parsec: stellar tracks and isochrones with the PAdova and TRieste Stellar Evolution Code: Parsec:tracks and isochrones," *Mon. Not. R. Astron. Soc.*, vol. 427, no. 1, pp. 127–145, 2012.
- [19] M. Sun, B. Jiang, H. Yuan, and J. Li, "The ultraviolet extinction map and dust properties at high Galactic latitude," *Astrophys. J. Suppl. Ser.*, vol. 254, no. 2, p. 38, 2021.
- [20] L. Lindgren et al., "Gaia Data Release 2: The astrometric solution," *Astron. Astrophys.*, vol. 616, p. A2, 2018.
- [21] B. Akbulut et al., "A study of the Czernik 2 and NGC 7654 open clusters using CCD UBV photometric and Gaia EDR3 data," *Astrophys. Space Sci.*, vol. 366, no. 7, 2021.
- [22] G. Carraro, G. Baume, A. F. Seleznev, and E. Costa, "On the assessment of the nature of open star clusters and the determination of their basic parameters with limited data," *Astrophys. Space Sci.*, vol. 362, no. 7, 2017.
- [23] S. Koç et al., "A Photometric and Astrometric Study of the Open Clusters NGC 1664 and NGC 6939," *Astron. J.*, vol. 163, no. 4, p. 191, 2022.
- [24] T. Yontan et al., "A Study of the NGC 1193 and NGC 1798 Open Clusters Using CCD UBV Photometric and Gaia EDR3 Data," *Rev. Mex. Astron. Astrofis.*, vol. 58, no. 2, pp. 333–353, 2022.
- [25] T. Yontan, "An investigation of open clusters Berkeley 68 and Stock 20 using CCD UBV and Gaia DR3 data," *Astron. J.*, vol. 165, no. 3, p. 79, 2023.
- [26] S. Taşdemir, S., and Yontan, T., "Analysis of the Young Open Cluster Trumpler 2 Using Gaia DR3 Data", *Physics and Astronomy Reports*, vol. 1, pp.1-10, 2023

The Effect of The Bearing Capacity of Sub-Grade Soil on The Thickness and Cost of The Superstructure of Chip Seals

Muhammed TANYILDIZI^{1*}, Muhammet ÇINAR²

1 Bitlis Eren University, Department of Civil Engineering, Bitlis, Türkiye

*2 Kahramanmaraş Sütçü İmam University, Department of Civil Engineering, Kahramanmaraş, Türkiye
(ORCID: 0000-0002-8507-2825) (ORCID: 0000-0001-5475-7787)*



Keywords: Sub-grade, Chip Seal, Pavement, Resilient Modulus, Plaxis

Abstract

Chip seal is an economical flexible pavement type consisting of layers of aggregate and bituminous binders. Chip seal is generally applied for preventative treatment of an existing road or to overlay low-trafficked roads. The thickness of the superstructure of a chip seal is directly related to the bearing capacity of sub-grade soil. The bearing capacity of soil is represented by Resilient Modulus (M_R) during the design of the thickness of pavement layers. This study has focused on the effect of the bearing capacity of sub-grade soil on the thickness and cost of the superstructure of chip seals. In addition, two-dimensional numerical modeling was also performed with the thicknesses of the layers found according to the M_R . It was indicated that there was a strong correlation between the bearing capacity of sub-grade soil and the thickness of the superstructure of chip seals with high R-square values. An increase in the bearing capacity of the sub-grade soil resulted in a decrease in the thickness of the superstructure of the chip seals. Additionally, Plaxis 2D modeling showed that a double-chip seal had less deformation and better bearing capacity compared to a single-chip seal. For this reason, it is economically important to choose the sub-grade soil to be used in the chip seals most properly by also considering the environmental conditions

1. Introduction

The roads are designed to meet the needs and demands depending on the socio-economic situation of the region. As road users, drivers demand smooth, comfortable, high slip resistance, fast access, low transportation costs, and low noise levels, while road authorities aim for durable, minimum maintenance, resistance to permanent deformations, high traffic safety, and long-lasting roads [1]. A road pavement consists of different elements such as sub-grade, base, and surface course [2]. These elements must be able to fulfill the conditions that will ensure that the superstructure can serve safely in all climatic conditions throughout the project life and that a large number of vehicles can pass over it [3-5]. Road pavements are generally divided into two groups as

flexible and rigid pavements [6, 7]. Flexible pavements are those that are covered with bituminous or asphaltic materials, while rigid pavements consist of a surface layer of Portland cement concrete [8-11]. Chip seal is an economical flexible pavement surfacing type that consists of layers of aggregate and bituminous binder to protect and prolong the life of an existing road or to overlay low-volume roads. In other words, a chip seal is the spreading out of bitumen and aggregate one after another and is formed by compaction [12-14]. Additionally, chip seal, which can be successfully applied on both high and low-traffic volume roads, is generally used on low-traffic roads.

Chip seal is one of the most preferred flexible pavement types because it has some advantages, such as being low-cost, easy, and rapid to construct and

* Corresponding author: : mtanyildizi@beu.edu.tr

Received: 02.12.2022, Accepted: 23.05.2023

improving skid resistance and smooth surface properties. This type of pavement is widely used in Turkey, South Africa, Australia, New Zealand, and England [15-22]. Chip seals could consist of one or more layers, as shown in Figure 1. Single chips are formed by spreading bituminous binder on an existing road or granular base and then laying and compacting aggregate. A single chip with double aggregate surfacing pavement type is formed by successively laying uniformly graded coarse and relatively fine aggregate over the bituminous binder. The double chip seal is formed with relatively fine aggregate and bituminous material on the top of the single-layer surface coating, which was previously formed with a coarse aggregate laid on the bituminous material. A sandwich chip seal is formed by first laying coarse aggregate on an existing road or granular base and bituminous binder on it. Then, over the bituminous binder, a relatively fine aggregate is laid and followed by compaction [12, 16, 19, 23, 24]. In Turkey, single and double chip seals are mostly preferred types. Generally, chip seal is applied on roads that have a total traffic volume of 8.2 tons equivalent standard axle load of less than 2×10^6 in one way during the service period. It should be designed as a single chip if the traffic volume is less than 500000, and for the traffic volume over that value, it should be designed as a double chip. However, it is required to apply hot mix asphalt for the roads that have traffic volume between $2-3 \times 10^6$ as the total equivalent standard axle load, it can be implemented double chip by thinking about economic conditions and shortening the project life [25].

A road body consists of two parts: the substructure and the superstructure. The substructure is composed of cut and fill processes. Then, the superstructure consists of layered structures, such as sub-base, base, and pavement that transfer the traffic loads to the sub-grade soil. Before the construction of a superstructure, a sub-grade should be prepared, following the specifications, in a way supports the superstructure. The superstructure is affected by traffic loads and the environment. The traffic loads create radial shrinkage and compressive stresses with the movement of vehicles. The intensity and degree of stresses are directly proportional to the repetition of axle loads. It is required from sub-grade soil to resist these loads transferred from superstructures. The bearing capacity of soil is represented by Resilient Modulus (M_R) which provides insight into the elastic properties of materials used under roads and railways [26-29].

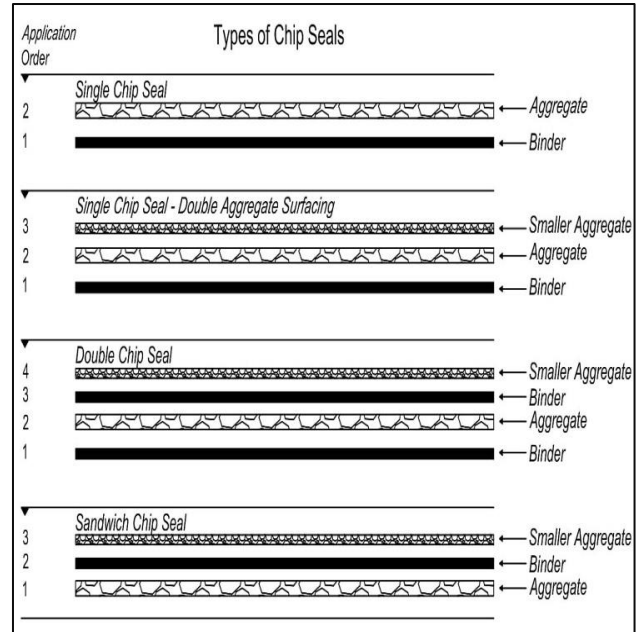


Figure 1. Types of chip seals.

This study has focused on the investigation of the effect of sub-grade soil bearing capacity on the thickness of the superstructure (sub-base and base) and the cost of chip seals. A design chart for chip seals presented in "Project Guide for Flexible Superstructure" was utilized to determine the thickness of the sub-base and base layers depending on the M_R of the sub-grade soil. This guide was prepared by the General Directorate of Highways in Turkey in 2008 [25]. A regression analysis was made to reveal the relationship between M_R and the thickness of the superstructure. Moreover, the displacements and stresses of the sub-base and base created by using the finite element method were shown. It has been indicated in this study that there is a strong relationship between the bearing capacity of the soil and the thickness of the sub-base layers. Thinner upper layers were obtained with the sub-grade soil with a higher M_R , and it was determined that the superstructure thicknesses increased as the bearing capacity of the sub-grade soil decreased. More realistic results were obtained by modeling the sub-base and base in Plaxis 2D. The general results indicate that it is economically important to choose the sub-grade soil to be used in the chip seals in the most appropriate way by paying attention to the environment and conditions.

2. Material and Method

In this study, the design chart of chip seals given in the "Project Guide for Flexible Superstructure" in Turkey was followed to determine the sub-base and base thickness in response to M_R

values. The relationship between the M_R of sub-grade soil and the thickness of the sub-base and base layers of chip seal pavement was determined. A regression analysis was performed to indicate the degree of relationship between these two parameters.

2.1. Resilient Modulus (M_R)

Pavements are designed based on the elastic theory. In this method, it is preferred to destinate M_R under repeated loads instead of the direct bearing capacity of materials. M_R is the elasticity modulus of material under cyclic loads and is the measure of the distribution of loads through pavement layers. In other words, it is the measure of the stiffness of pavement materials. The M_R is one of the main input parameters that affects the thickness of the superstructure of chip seals. The modulus of elasticity is an application of elastic theory. An approach was developed to determine the modulus of elasticity of pavement materials under repetitive traffic loads rather than static loads. Pavement materials are normally inelastic and showed some permanent deformation (plastic) after each load repetition. However, if the traffic load is small compared to the strength of the material, the material starts to show elastic behavior after a certain amount of load repetition. Figure 2 shows the deformation curve of a pavement material under the effect of repeated loads. As can be seen in the figure, in the elastic modulus test, while plastic deformations develop at a high rate under repetitive loads, as the number of repetitive loads increases, the increase in plastic deformation gradually decreases, and practically elastic behavior is observed after approximately 100-200 load repetitions [25, 30-32].

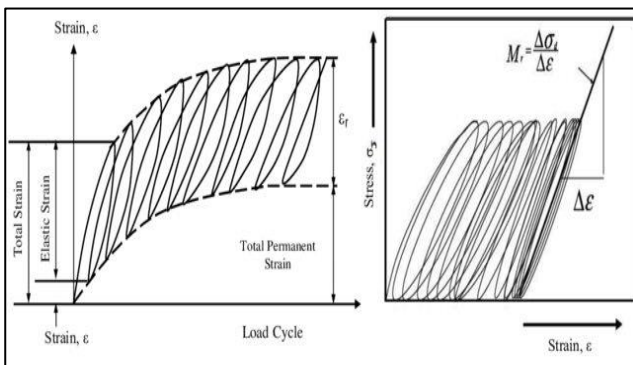


Figure 2. The behavior of the pavement materials under repetitive loads, and M_R [25].

The modulus of elasticity is the division of stress occurred by a slowly applied load divided by

$$M_R = 1750 \cdot (D_{BSK} + k)^{0.436} \cdot CBR^{0.4} \cdot \left[\frac{1}{1 + \log(N_{O200})} \right]^{0.35(LL.PI+1)^{0.06}} \cdot \left[\frac{Y_{max}^2}{No_4} \right]^{0.09 \log(w_{opt})} \quad (2)$$

the recoverable strain. When the stress that occurred with rapidly applied loads is divided into recoverable strains, M_R is obtained. The M_R is measured from the cyclic load triaxial test where given a constant confining pressure and it is calculated from the relationship between the axial deviator stress and the recoverable axial strain. The schematic diagram of the triaxial test is given in Figure 3.

In the triaxial test, the ratio of deviator stress ($\sigma_d = \sigma_1 - \sigma_3$) to recoverable strain (ϵ_r) is called the M_R and it is calculated with the formula given below:

$$M_R = \frac{\sigma_d}{\epsilon_r} \quad (1)$$

The M_R for granular layers could be determined by laboratory or in-situ tests. However, these tests are very complex, sensitive, and expensive, and they require information and experience to apply. Therefore, the M_R could be determined by creating some empirical correlations with some easily found properties of the material sample. Since the M_R in granular materials depends on the soil structure, moisture content, and stress conditions, it differs in each pavement layer. The M_R tests were carried out on base, sub-base, and sub-grade samples were taken from different regions of Turkey in a way to represent all kinds of materials at the General Directorate of Highways, Superstructure Branch Directorate. The following general formula was obtained for the M_R of granular materials by analyzing the obtained test results with statistical methods.

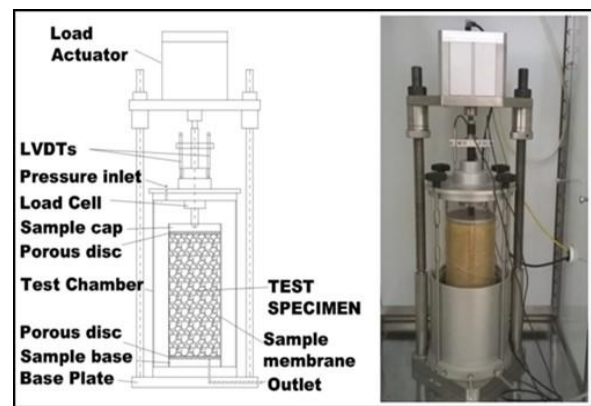


Figure 3. Testing apparatus of M_R [27].

- Here;
- M_R : Resilient modulus, psi
 - D_{BSK} : Total thickness of bituminous hot mix, cm
 - CBR : California bearing ratio, %
 - ω_{opt} : Optimum moisture content, %
 - γ_{max} : Maximum dry unit weight, g/cm³
 - LL : Liquid limit, %
 - PI : Plasticity index, %
 - No₂₀₀ : Percentage passing through No₂₀₀ sieve
 - No₄ : Percentage passing through No₄ sieve
 - k : Depth correction factor, cm

The ($D_{BSK}+k$) represents the variation of stress levels depending on the depth of the superstructure layer. D_{BSK} is the total thickness of a bituminous hot mixture and is taken as 2 cm for single chips and 4 cm for double chip pavements. The depth correction factor k is selected from Figure 4 according to the layer and pavement section type.

Layer	k (cm)	Layer	k (cm)	Layer	k (cm)	Layer	k (cm)
Chip seal	-	Chip seal	-	Chip seal	-	Chip seal	-
Base	15 cm	Base	15 cm	Base	15 cm	Base	15 cm
Sub-base	15 cm	Sub-grade	15 cm	Sub-base	15 cm	Selected-material	15 cm
Sub-grade	32 cm			Sub-grade	45 cm	Sub-grade	32 cm
(1)		(2)		(3)		(4)	

Figure 4. Depth correction coefficient (k) according to the superstructure section type [25].

In addition, various other correlations are used throughout the world. The AASHTO design guide suggests that the M_R of fine-grained soils can be estimated as [33]:

$$M_R(\text{psi}) = 1,500 \cdot \text{CBR} \quad (3)$$

U.S. Army Corps of Engineers [34]:

$$M_R(\text{psi}) = 5,409 \cdot \text{CBR}^{0.71} \quad (4)$$

South African Council on Scientific and Industrial Research (CSIR):

$$M_R(\text{psi}) = 3,000 \cdot \text{CBR}^{0.65} \quad (5)$$

Transportation and Road Research Laboratory (TRRL):

$$M_R(\text{psi}) = 2555 \cdot \text{CBR}^{0.64} \quad (6)$$

2.2. Design of Chip seals

It is the main aim to keep or restrain the distress resulting from traffic and environmental conditions within a limit in pavement design methods. There are two basic approaches created within the scope of the design of pavements: Mechanistic-Empirical (ME) and Empirical. The ME design method analyzes the stress and deformations caused by traffic and environmental factors on the road according to mechanical theories. Empirical design is based on experimental and observational results. Empirical design methods are widely used in road design today. In this method, the performance of the road is estimated according to the damages that will occur for a certain stress and deformation value of the road, taking into account a certain traffic load, physical properties of materials, and climatic conditions. It is important in the empirical design method to benefit from field experiences and observational results [35, 36]. In Turkey, the chip seal design guide is more empirical and based on AASHTO-1993. The thickness of chip seals is determined following the design chart given in Figure 5.

The bearing capacity of sub-grade soil and the traffic are the main parameters in the design phase of chip seals. Chip seals should be designed according to the M_R of the sub-grade soil and the total number of equivalent standard axle loads that will pass during the project life. Although the project period taken into account in the design chart is 10 years, the designer may accept the project duration as less or more, taking into account the importance and characteristics of the road [25, 37, 38]. The determination of the pavement thickness of the road, for which the M_R of the sub-grade soil and the equivalent standard axle traffic loads ($T_{8.2}$) is determined, will be as follows: By finding the number $T_{8.2}$ on the horizontal axis, a vertical line will be drawn to the axis and the point where this line intersects the curved line showing the sub-grade soil M_R value will be found. The required sub-base thickness will be found from the point where the parallel line drawn from this point to the horizontal axis intersects the vertical axis. From the upper part of the chart, the foundation thickness and chip seal type corresponding to $T_{8.2}$ will be selected.

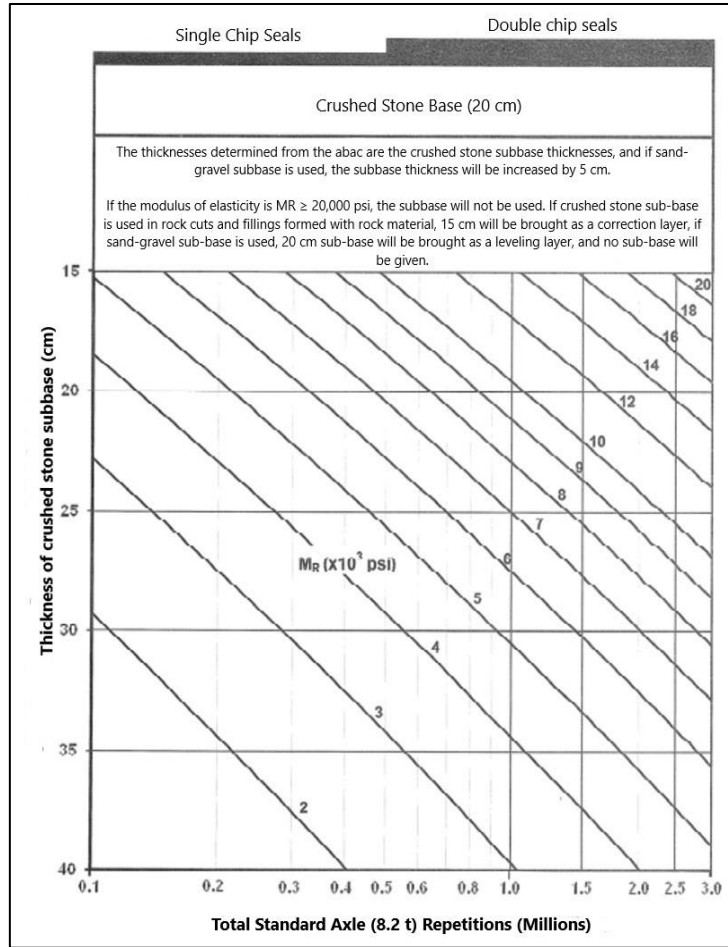


Figure 5. Design chart of Chip seals in Turkey [25].

2.3. Modeling of chip seals and substrates in Plaxis 2D

The behavior of many soil structures is analyzed using the finite element method [39]. Two- and three-dimensional analyses are made with the Plaxis finite element program, which is widely used in geotechnical engineering problems. Generally, it provides a faster and simplified solution with Plaxis 2D modeling. Therefore, the plaxis 2D finite element program was used in this study. The geometric model created in the Plaxis 2D program is shown in Figure 6. While creating the geometry of this model, it was prepared based on the technical specifications of the highways and the measurements in similar modeling studies [39-41].

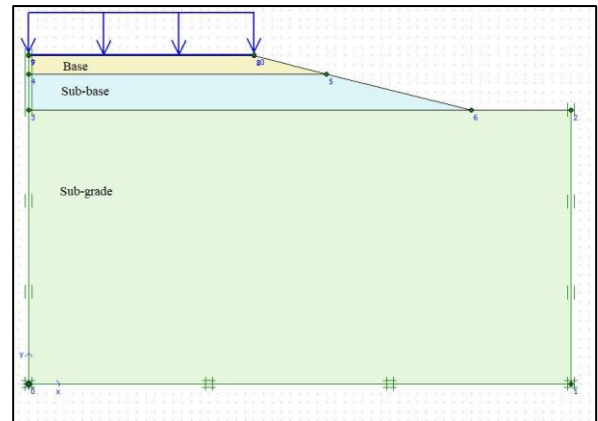


Figure 6. Layer representation used in modeling

The numerical model was created according to the plane unit deformation conditions and there is no groundwater table. In addition, a medium-density finite element mesh is used. It has been seen in the analysis that the geometric dimensions of the sub-grade are sufficient in terms of boundary conditions. In the Plaxis 2D program, they are defined as sub-grade, sub-base, base, and

chip seal, respectively. The soil layer properties are given in Table 1. Layer thicknesses were solved separately for the cases indicated in Tables 2 and 3. The slope was chosen as 1 (vertical): 4 (horizontal) from the applied in highway road embankments. In addition, in the modeling, a load of 15 kPa, which corresponds to the heavy traffic load, is loaded evenly on the road surface [39]. Analyzes were made using the Mohr coulomb model in the Plaxis 2D program. The parameters specified in Table 1 are, respectively, the modulus of elasticity (E), unit weight (γ), Poisson's ratio (ν), cohesion (c), internal friction angle (ϕ), and dilatation angle (Ψ).

Table 1. Properties of materials defined in Plaxis 2D

Parameters	Sub-grade	Sub-base	Base	Chip seal
E(kPa)	12500	50000	40000	120000
γ (kN/m ³)	16	16	17	27
ν	0.4	0.3	0.3	0.3
c (kPa)	15	1	1	1
ϕ (°)	12	30	32	35
Ψ (°)	0	0	0	0

3. Result and Discussion

This study focused on the effect of the bearing capacity of sub-grade soil on the thickness and cost of the superstructure of chip seals. In addition, a linear regression analysis was performed to investigate the relationship between the bearing capacity of the subgrade soil and the thickness of the superstructure. Two-dimensional numerical modeling (Plaxis 2D) was also performed with the layer thicknesses found according to the M_R .

3. 1 Thickness of superstructures of chip seals

In this study, the relationship between the M_R of sub-grade soil and the thickness of the superstructure of chip seals was studied. In this manner, two traffic loads ($T_{8.2}$) were selected as 400.000 and 1.000.000. For these two values and some M_R values, the thickness of the sub-base and base layer of chip seals were determined as given in Tables 2 and 3. It is noticed that decreasing of M_R results in increasing sub-base thickness when Tables 2 and 3 are examined. The maximum and minimum values of the sub-base are 40 and 15 cm, respectively, for all conditions. And, the base thickness is 20 cm and constant for all M_R and $T_{8.2}$ values. Also, increasing $T_{8.2}$ values causes a thicker

sub-base and results in changing of chip seal type from single to double.

Table 2. The thickness of the superstructure of Chip Seals for $T_{8.2}$ of 400.000

Traffic ($T_{8.2}$) ($\times 1000$)	Resilient Modulus (M_R)	Thickness of Sub-base (cm)	Thickness of Base (cm)	Chip Seal Type
400	2	40	20	Single
	3	33		
	4	28		
	5	25		
	6	22		
	7	20		
	8	18		
	9	16		
	10	15		

Table 3. The thickness of superstructure of Chip seals for $T_{8.2}$ of 1.000.000

Traffic ($T_{8.2}$) ($\times 1000$)	Resilient Modulus (M_R)	Thickness of Sub-base (cm)	Thickness of Base (cm)	Chip Seal Type
1.000	2	40	20	Double
	3	39		
	4	34		
	5	31		
	6	28		
	7	25		
	8	23		
	9	21		
	10	20		
	12	17		
	14	15		

A regression analysis was made to reveal the relationship between M_R and sub-base thickness for the value of $T_{8.2}$ 400.000. The analysis results are given in Figure 7. The R-square value and power function equation are also illustrated in the figure. The coefficient of determination (R^2) is 0.9304 and indicates a strong relationship and a confidence level between M_R and sub-base thickness.

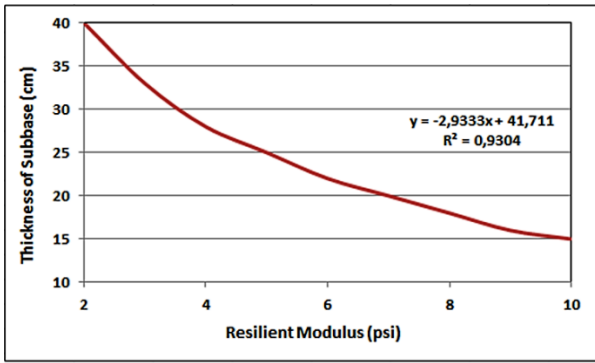


Figure 7. The relationship between Resilient Modulus (M_R) and sub-base thickness of chip seal for $T_{(8.2)}$ of 400.000.

Figure 8 shows the relationship between M_R and sub-base thickness for a traffic value of 1.000.000. The R-square value and power function equation are also presented in the figure. The correlation between M_R and sub-base thickness provided a higher R^2 value of 0.9478, thereby indicating a confidence level for the correlations.

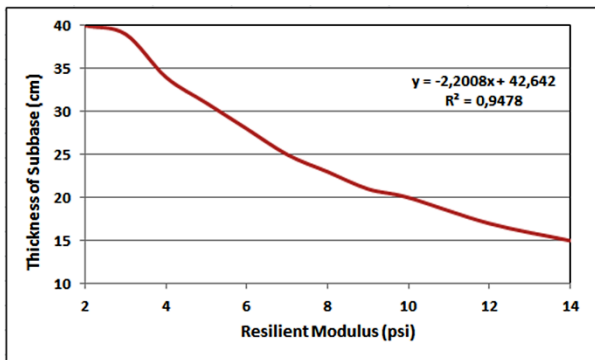


Figure 8. The relationship between Resilient Modulus (M_R) and sub-base thickness of chip seal for $T_{(8.2)}$ of 1.000.000

3.2. Modeling of Chip seals in Plaxis 2D program according to sub-base and base thickness

Single and double chip seals are modeled with the Plaxis 2D program. Soil parameters are given in Table 1, and layer thicknesses are given in Tables 2 and 3, which were used in the modeling. As a result, the total displacement, horizontal displacement, and total stresses of the single and double-chip seals in Tables 4 and 5 were found.

In Table 4, the total displacement increases as the single-chip seal thickness of the sub-base decreases, and accordingly, the stresses increase as the layer thickness decreases. In addition, as the sub-base layer thickness decreases, the horizontal displacement decreases.

In Table 5, as the double chip seal sub-base layer thickness decreases, the total displacement increases, and the total stresses increase. Moreover, horizontal displacement decreases as the layer thickness decreases in the double-chip seal.

Comparing the results of the Plaxis 2D program for single and double chip seals, the double chip seal produced 50% less total displacement and 20% less total stress on the substrates. As can be seen from the results, it is understood that the double-chip seal provides more bearing capacity and is less deformed. According to the results; since the double chip seal is less deformed, it provides a longer service life and requires less maintenance cost. In the literature, it has been observed that there are close results in experimental studies conducted in the field [40].

Table 4. Modeling results of the total displacement, horizontal displacement, and total stresses of the single-chip seal for $T_{8.2}$ of 400.000

Traffic ($T_{8.2}$) ($\times 1000$)	Resilient Modulus (M_R)	Thickness of Sub-base (cm)	Thickness of Base (cm)	Chip Seal Type	Total Displacement (mm)	Horizontal displacement (mm)	Total Stress (kN/m^2)
400	2	40		Single	0.186	0.127	65.64
	3	33			0.189	0.119	65.78
	4	28			0.191	0.114	66.05
	5	25			0.193	0.110	66.31
	6	22	20		0.194	0.108	66.59
	7	20			0.195	0.106	66.99
	8	18			0.196	0.104	67.41
	9	16			0.197	0.102	68.10
	10	15			0.197	0.101	69.11

Table 5. Modeling results of the total displacement, horizontal displacement, and total stresses of the double-chip seal for $T_{8.2}$ of 1.000.000

Traffic ($T_{8.2}$) ($\times 1000$)	Resilient Modulus (M_R)	Thickness of Sub-base (cm)	Thickness of Base (cm)	Chip Seal Type	Total Displacement (mm)	Horizontal displacement (mm)	Total Stress (kN/m^2)
	2	40			0.0647	0.0837	54.15
	3	39			0.0686	0.0827	54.43
	4	34			0.0726	0.0777	54.89
	5	31			0.0739	0.0743	54.94
	6	28			0.0767	0.0713	55.33
1000	7	25	20	Double	0.0807	0.0685	55.58
	8	23			0.0847	0.0652	56.06
	9	21			0.0889	0.0630	56.49
	10	20			0.0937	0.0625	56.97
	12	17			0.1010	0.0590	57.77
	14	15			0.1020	0.0557	57.95

3.3. Cost Analysis of Chip Seals

The layers that constitute the superstructure of chip seals have top and bottom limits. The sub-base of chip seals has a bottom limit of 15 cm. The thickness of the base is generally taken as 20 cm for crushed stone and the thickness of the crushed stone base is also taken as 20 cm for this study [25]. In this study, the effect of sub-grade soil bearing capacity on the cost of chip seals for the aforementioned traffic loads of $T_{8.2}$ was investigated. In the Highways General Directorate unit price lists, the cost of the bituminous layer is given in decare (1000 m²) units. The unit of plant-mix base and sub-base layer is given in tons and m³ respectively. The cost and unit price of layers of chip seals according to the year 2022 are clearly given in Table 6 [42].

The total costs of a 1 decare (1000 m²) of a single chip with M_R 10 (psi) and 5 (psi) and traffic loads of 400.000 $T_{8.2}$ are 84992,23 TL and 96652,23 TL, respectively.

The total costs of 1 decare (1000 m²) of a double chip with resilient modulus 10 (psi) and 5 (psi) and traffic loads 1.000.000 $T_{8.2}$ are 94003,03 TL and 106829,03 TL respectively. If the bearing capacity is taken as approximately 50% less than the actual value, the total cost of both single and double chip seals increases by approximately 14% for 1000 m² chip seals type pavement. When Tables 2 and 3 are examined, it is seen that with the doubling of the M_R , significant reductions in layer thickness occur.

4. Conclusions

Chip Seal is an economical, flexible type of pavement consisting of layers of aggregates and bituminous binders and is applied as a preventative improvement to an existing road or for paving low-traffic roads. The main parameters for the design of chip seals are the bearing capacity of sub-grade soil and traffic values. The bearing capacity of sub-grade soil is represented by the Resilient Modulus (M_R) of pavement material. This study presented hereby focused on the investigations of the relationship between the bearing capacity of sub-grade soil and the thickness of the superstructure of chip seals. In addition, the displacement and stresses of the sub-base and base created by using the finite element method are shown. The study has revealed that there is a strong relationship between these two parameters. Increasing M_R , in other words, the bearing capacity of sub-grade soil resulted in a decrease in the thickness of the superstructure of chip seals in all observed traffic values. The higher coefficients of the R-square of relationships between the bearing capacity of soil and the superstructure thickness of chip seals indicate a high confidence level for the correlation. It is important to take exact values of M_R of sub-grade soil in calculations of the thickness of pavements because of having a great impact on bearing capacity on the thickness of pavement layers considering economic. In addition, the importance of M_R in Plaxis 2D modeling has been

seen. No matter how much the thicknesses changed, it was observed that the settlements and stresses did not increase as the M_R increased. According to the conclusion reached together with the general evaluation, it is economically important

to choose the sub-grade soil to be used in the chip seals in the most correct way by paying attention to the environment and conditions.

Table 6. Unit costs according to layer types

No	Definition	Unit	Unit Price
KGM/6540	A bituminous surface coating with one layer lining (Type-1) (With crushed and sifted quarry stone)	daa	3719,83
KGM/6560	A bituminous surface coating with double layer lining (Type-1+Type-3) (With crushed and sifted quarry stone)	daa	6900,63
KGM/6100/3	A plant-mix base layer (with crushed and sifted quarry stone) (Note: The density of the layer is 2,4 gr/cm ³)	ton	132,88
KGM/6000	Sub-base construction (with 2" crushed and sifted quarry material)	m ³	116,60

Contributions of the authors

Muhammed TANYILDIZI: Conceptualization, Methodology and Writing- Original Draft Preparation, Visualization, Supervision, Reviewing and editing.

Muhammet ÇINAR: Data curation, Writing- Original draft preparation, Software, Validation, Reviewing and editing

Conflict of Interest Statement

There is no conflict of interest between the authors.

Statement of Research and Publication Ethics

The study is complied with research and publication ethics.

References

- [1] M. Plessis-Fraissard, "Planning roads for rural communities," *Transportation Research Record*, vol. 1989, no. 1, pp. 1-8, 2007.
- [2] A. Tuñç, *Kaplama mühendisliği ve uygulamaları*. Asil Yayın Dağıtım, 2004.
- [3] A. Tuñç, *Yol malzemeleri (agrega, asfalt, bitümlü karışımlar, beton, zemin) ve uygulamaları (kaplamalar ve zemin ıslahı-dizayn ve yapım metotları)*. Atlas-Nobel yayın dağıtım, 2001.
- [4] M. M. Tanyıldızı and T. Geçkil, "Zemin taşıma gücünün rijit ve esnek üstyapıların kalınlıklarına ve maliyetlerine etkisi," *Fırat Üniversitesi Mühendislik Bilimleri Dergisi*, vol. 31, no. 2, pp. 399-406, 2019. <https://doi.org/10.35234/fumbd.521364>.
- [5] M. A. Önal and Z. Temren, "Comparison of flexible pavement designs of Turkey and some European countries," presented at the National Asphalt Symposium, 2004.
- [6] D. Croney and P. Croney, *The design and performance of road pavements*. 1991.
- [7] M. Tanyıldızı, "Joints in rigid pavements," *Advanced Engineering Days (AED)*, vol. 4, pp. 67-70, 2022.
- [8] E. Ağar, İ. Süttaş, and G. Öztaş, *Beton yollar: rijit yol üstyapıları; malzeme-tasarım-üretim-yapım-bakım teknikleri*. İstanbul Teknik Üniversitesi, 1998.

- [9] M. Saltan and F. S. Fındık, "Stabilization of subbase layer materials with waste pumice in flexible pavement," *Building and Environment*, vol. 43, no. 4, pp. 415-421, 2008. <https://doi.org/10.1016/j.buildenv.2007.01.007>.
- [10] M. V. Mohod and K. Kadam, "A comparative study on rigid and flexible pavement: A review," *IOSR Journal of Mechanical and Civil Engineering (IOSR-JMCE)*, vol. 13, no. 3, pp. 84-88, 2016.
- [11] G. Taunk, "Rigid pavement vs. flexible pavement," *Indian Highways*, vol. 26, no. 2, 1998.
- [12] A. Buss, M. Guirguis, and D. Gransberg, "Chip seal aggregate evaluation and successful roads preservation," *Construction and Building Materials*, vol. 180, pp. 396-404, 2018/08/20/ 2018. <https://doi.org/10.1016/j.conbuildmat.2018.05.255>.
- [13] S. Shuler, "Chip seals for high traffic pavements," *Transportation Research Record*, vol. 1259, pp. 24-34, 1990.
- [14] V. Uz, "Sathi kaplamalardaki kalıcı deformasyona etki eden parametrelerin incelenmesi," Doktora Tezi, Fen Bilimleri Enstitüsü, Süleyman Demirel Üniversitesi, Isparta, 2012.
- [15] P. Cui, S. Wu, Y. Xiao, R. Hu, and T. Yang, "Environmental performance and functional analysis of chip seals with recycled basic oxygen furnace slag as aggregate," *Journal of Hazardous Materials*, vol. 405, p. 124441, 2021. <https://doi.org/10.1016/j.jhazmat.2020.124441>.
- [16] İ. Gökalp, "Laboratory investigation of the effects of aggregates type, size and polishing level to skid resistance of surface coatings," Master Thesis, Graduate School of Natural and Applied Sciences, Department of Civil Engineering, Adana Science and Technology University, Adana, 2016.
- [17] D. D. Gransberg and D. M. James, *Chip seal best practices*. Transportation Research Board, 2005.
- [18] C. Gürer, B. E. Korkmaz, Ş. Yarcı, and M. B. Rahmany, "Sıcak agrega ile sathi kaplama uygulamasının araştırılması," *Afyon Kocatepe Üniversitesi Fen ve Mühendislik Bilimleri Dergisi*, vol. 19, no. 2, pp. 401-409, 2019. <https://doi.org/10.35414/akufemubid.543410>.
- [19] M. Kardeşahin, C. Gürer, M. Saltan, M. V. Taciroğlu, and V. E. Uz, "Investigation of chip seal performance under cold climate conditions," *Science and Engineering of composite materials*, vol. 23, no. 6, pp. 649-658, 2016. <https://doi.org/10.1515/secm-2014-0041>.
- [20] J. Lee, J. Lee, Y. R. Kim, and S. Mun, "A comparison study of friction measurements for chip seal," *Journal of Testing and Evaluation*, vol. 40, no. 4, pp. 603-611, 2012.
- [21] I. Gökalp, V. E. Uz, and M. Saltan, "Comparative laboratory evaluation of macro texture depth of chip seal samples using sand patch and outflow meter test methods," in *Bearing Capacity of Roads, Railways and Airfields*: CRC Press, 2017, pp. 915-920.
- [22] V. E. Uz and İ. Gökalp, "The effect of aggregate type, size and polishing levels to skid resistance of chip seals," *Materials and Structures*, vol. 50, pp. 1-14, 2017. <https://doi.org/10.1617/s11527-017-0998-6>.
- [23] K. B. Akalın and M. Karacasu, "Çevresel atıklarla modifiye edilmiş sathi kaplamaların performansının agrega-bitüm ilişkisi bağlamında değerlendirilmesi," *Fırat Üniversitesi Mühendislik Bilimleri Dergisi*, vol. 32, no. 1, pp. 127-136, 2020. <https://doi.org/10.35234/fumbd.599096>.
- [24] Y. Abut, "Sathi kaplamalı üst yapı tasarımında mekanistik yaklaşım," 2022: 4th International Conference on Applied Engineering and Natural Sciences.
- [25] A. Güngör and A. Sağlık, "Karayolları esnek üst yapılar projelendirme rehberi," *Karayolları Genel Müdürlüğü, Teknik Araştırma Dairesi Başkanlığı, Ankara*, pp. 7-9, 2008.
- [26] P. Garnica Anguas, N. Pérez García, and J. Gómez López, "Módulos de resiliencia en suelos finos y materiales granulares," *Publicación Técnica*, no. 142, 2000.
- [27] C. Plati and B. Cliatt, "A sustainability perspective for unbound reclaimed asphalt pavement (RAP) as a pavement base material," *Sustainability*, vol. 11, no. 1, p. 78, 2018. <https://doi.org/10.3390/su11010078>.
- [28] H. B. Seed, C. K. Chan, and C. L. Monismith, "Effects of repeated loading on the strength and deformation of compacted clay," in *Highway research board proceedings*, 1955, vol. 34.
- [29] C. H. Signes, P. M. Fernández, J. Garzón-Roca, M. E. G. de la Torre, and R. I. Franco, "An evaluation of the resilient modulus and permanent deformation of unbound mixtures of granular materials and rubber particles from scrap tyres to be used in subballast layers," *Transportation Research Procedia*, vol. 18, pp. 384-391, 2016. <https://doi.org/10.1016/j.trpro.2016.12.050>.
- [30] R. Carmichael and E. Stuart, "Predicting resilient modulus: A study to determine the mechanical properties of subgrade soils (abridgment)," *Transportation Research Record*, no. 1043, 1985.
- [31] E. Sadrossadat, B. Ghorbani, P. R. Oskoei, and M. H. M. Sheikhanloo, "A new model for estimating the resilient modulus of silt-clay subgrade soils," presented at the International Conference on Modern Research in Civil Engineering, Architecture Urban Management and Environment, 2018.

- [32] A. Sağlık and A. G. Gungor, "Resilient modulus of unbound and bituminous bound road materials," in *5th Eurasphalt & Eurobitume congress*, 2012, pp. 455-463.
- [33] W. Heukelom and A. Klomp, "Dynamic testing as a means of controlling pavements during and after construction," in *International Conference on the Structural Design of Asphalt Pavements University of Michigan, Ann Arbor*, vol. 203, no. 1, 1962
- [34] J. L. Green and J. W. Hall, *Nondestructive vibratory testing of airport pavements: Experimental test results and development of evaluation methodology and procedure*. US Army Engineer Waterways Experiment Station, Soils and Pavements Laboratory, 1975.
- [35] F. Ahmed, J. Thompson, D. Kim, N. Huynh, and E. Carroll, "Evaluation of pavement service life using AASHTO 1972 and mechanistic-empirical pavement design guides," *International Journal of Transportation Science and Technology*, 2021. <https://doi.org/10.1016/j.ijtst.2021.11.004>.
- [36] R. L. E. de Carvalho, *Mechanistic-empirical design of flexible pavements: a sensitivity study*. University of Maryland, College Park, 2006.
- [37] S. Ozcanan and M. Akpınar, "Determining the critical tire and axle configuration for flexible pavements based on mechanistic analysis," *Teknik Dergi*, vol. 25, no. 1, 2014.
- [38] V. E. Uz, M. Saltan, and İ. Gökalp, "Feasibility of using 4th power law in design of plastic deformation resistant low volume roads," *Procedia Engineering*, vol. 143, pp. 961-970, 2016. <https://doi.org/10.1016/j.proeng.2016.06.084>.
- [39] Ü. Karadoğan, G. Çevikbilen, and B. Teymur, "Deniz dibi tarama malzemelerinin yol dolgusu olarak kullanımı," *Uludağ Üniversitesi Mühendislik Fakültesi Dergisi*, vol. 25, no. 2, pp. 1059-1070, 2020. <https://doi.org/10.17482/uumfd.679700>.
- [40] O. Sarıoğlu and M. Saltan, "Sathi kaplamalı yolların yapısal performansının değerlendirilmesi," *Mühendislik Bilimleri ve Tasarım Dergisi*, vol. 9, no. 2, pp. 463-475, 2021. <https://doi.org/10.21923/jesd.884480>.
- [41] H. İ. Fedakar, "Poliüretan ile güçlendirilmiş balastın hareket eden tekerlek yükü altındaki deformasyon davranışının nümerik olarak İncelenmesi," *Çukurova Üniversitesi Mühendislik Fakültesi Dergisi*, vol. 37, no. 1, pp. 79-91, 2022. <https://doi.org/10.21605/cukurovaumfd.1094976>.
- [42] "2022 Yılı Yol, Köprü, Tünel, Bitümlü Kaplamalar, Bakım Ve Trafik İşlerine Ait Birim Fiyat Listesi." Karayolları Genel Müdürlüğü. <https://www.kgm.gov.tr/SiteCollectionDocuments/KGMdocuments/MerkezBirimler/ProgramIzlemeDairesiBaskanligi/2022BirimFiyatListesi.pdf> [Accessed: Oct.10, 2022].



Investigation of The Effect of Cr₂O₃ Particles on Al-Si Matrix Composites Produced by Powder Metallurgy

Serkan ÖZEL^{1*}, Kübra ASLAN¹

¹Bitlis Eren Üniversitesi, Mühendislik Mimarlık Fakültesi, Makine Müh. Böl., 13000, Bitlis
(ORCID: 0000-0003-0700-1295) (ORCID: 0000-0002-9934-1221)



Keywords: Powder Metallurgy, Metal matrix composite materials, Al, Cr₂O₃, Microstructure.

Abstract

In this study, composite material with Al-12Si (wt%) matrix was produced by powder metallurgy (PM) method. Al-12Si powder was mixed by adding 5, 10 and 15wt% Cr₂O₃ powder. Al-12Si+ Cr₂O₃ powder mixture were pressed unidirectional with 500MPa pressure in a cylindrical mold and sintered at 500 °C. After sintering, optical microstructure (OM), Scanning Electron Microscope (SEM), Energy Dispersive Spectrometer (EDS) and microhardness analyzes of the samples were made. When the results were examined, it was observed that a porous structure was formed in all of the samples. Moreover, the lowest hardness was measured in the sample added %15wt Cr₂O₃ powder sintered at 500 °C.

1. Introduction

Metal matrix composites (MMCs) can be formed by the reinforcement added of one or more ceramic particles (for instance: oxide, carbide, boride or others compounds) in a metallic matrix phase. This types composites possess good value of strength and hardness, improved corrosion and wear resistance. Aluminum matrix composites (AMCs), which are generally used for light materials, have high rigidity, enhanced wear and corrosion resistance. AMCs are used in aircraft, automotive and various engineering fields [1-5].

Different primary reinforcements such as SiC, Al₂O₃, B₄C, TiC, MgO are used in the aluminum matrix to produce AMCs. Discontinuously reinforced AMCs are key candidates at light applications as they exhibit high strength, high wear resistance, high hardness and excellent mechanical, physical and thermal properties [2].

Powder metallurgy (PM) is a technology used in the production of high-

strength materials to be used in aerospace, automotive and engineering fields. With this method, composite materials can be produced with the addition of reinforcing particles into the metal matrix that can be heat treated with high strength [6, 7]. Powder metallurgy technique requires a series of processes such as mixing, pressing and sintering of pre-alloyed or pre-mixed powders [8, 9, 10].

The PM method offers several advantages over other MMC manufacturing techniques, such as low processing temperature, low energy consumption and high material usage. In the powder metallurgy process, the reinforcing materials are mixed with the matrix material and compressed at sufficient pressure (depending on the required porosity in the final material). Thereafter, a heating process called sintering is carried out at high temperature (below the melting point of the matrix material) for a sufficient time for diffusion bonding to occur. Compression pressure, sintering temperature and holding time are the parameters that most affect the powder metallurgy process [10, 11, 12].

*Corresponding author: sozel@beu.edu.tr

Received: 23.12.2022, Accepted: 19.03.2023

Chromium oxide (Cr_2O_3) is a hexagonal crystal with a melting point of 2435°C and it has a Vickers hardness of 1825 HV. Cr_2O_3 is commonly known as a catalyst, but it also exhibits high abrasive properties and is therefore widely used in the form of polishing pastes. It is an important refractory material with its high melting temperature and oxidation resistance at high temperatures [13, 14].

In this study, %5, %10 and %15wt Cr_2O_3 powders were added to Al-12Si powder as reinforcement. Then, the samples were pressed and sintered at 500 MPa and 500°C , respectively. After these processes, the effect of reinforcement particle was investigated.

2. Material and Method

In this study, Al-12Si powder was used as matrix material. Al-12Si powder is a standard powder produced by gas atomization in the size of $-90 +45 \mu\text{m}$ by Metco-Oerlikon company. 5, 10 and 15wt% Cr_2O_3 powder ($-35 +15 \mu\text{m}$ by Metco-Oerlikon company, 99.8% purity) was added to the Al-12Si powder mixture as reinforcement material. For the homogeneous distribution of the powders, the mixing process was carried out at a speed of 45 rpm for 45 minutes. The prepared mixtures are given in Table 1.

Table 1. Powder mixing ratios of the samples.

Sample No.	Powder (wt%)	Cr_2O_3 Powder (wt%)
1	100	0
2	95	5
3	90	10
4	85	15

The mixed powder were cold pressed unidirectional at 500 MPa pressure. The pressed samples were sintered for 60 minutes at 500°C in the Protherm brand heat treatment furnace



Figure 1. Heat treatment furnace.

After sintering, the samples were grinded with abrasives with different surface roughness, polished and then etched, for metallographic characterization. A mixture of 95 ml H_2O , 1 ml of HF, 2.5 ml of HNO_3 and 1.5 ml of HCl was used as etchant. Etching was carried out for 30-35 seconds. Afterward, the microstructural examination were carried out with Nikon brand optical microscope (Figure 2) in Yahya Eren Advanced Research Laboratory of Bitlis Eren University.



Figure 2. Optical microscope

Scanning electron microscope (SEM) and EDS analyzes were performed for microstructure characterization of samples. Hardness measurements were taken with Qness Q10M brand microhardness device (Figure 3). Phase analyzes of the samples were performed on the Rigaku brand RadB model XRD device.

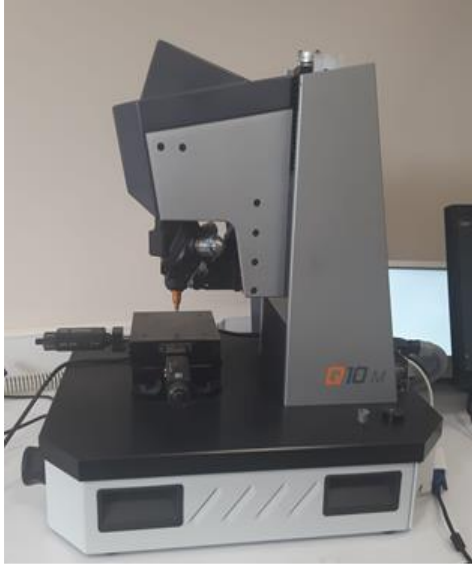
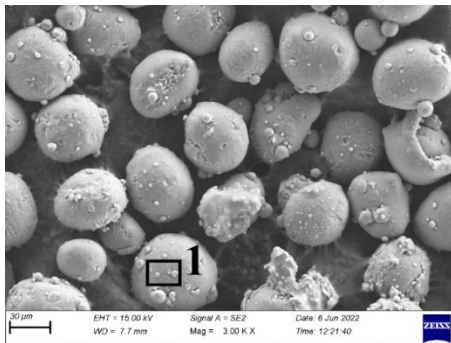


Figure 3. Microhardness tester.

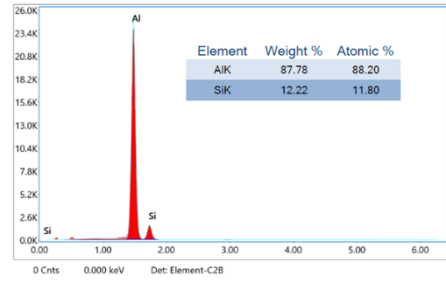
3. Results and Discussion

3.1. Microstructure Analysis of the Samples

Figure 4 shows the SEM pictures and EDS analysis of the pre-alloyed Al-12Si powder.



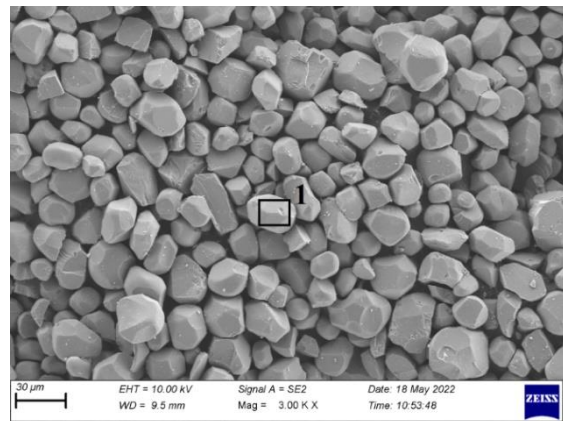
(a)



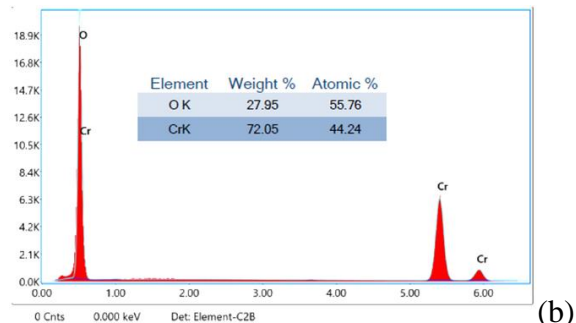
(b)

Figure 4. a) SEM photograph taken from Al-12Si powder, b) EDS analysis taken from area 1 in Figure 3 a.

In the EDS analysis taken from area 1 in Figure 4a, the presence of Al element and Si element can be seen (see Figure 4b). Al-12Si powder is a pre-alloyed powder containing 12% Si. According to the EDS analysis, 12.22% Si element was detected in the Al element.



(a)

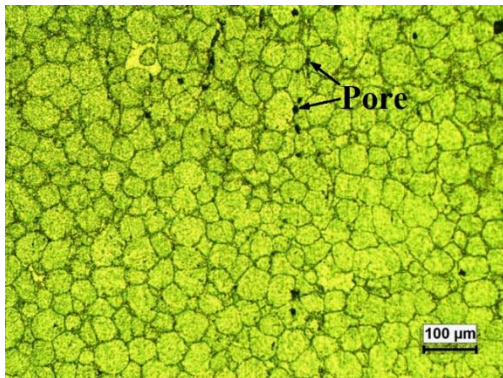


(b)

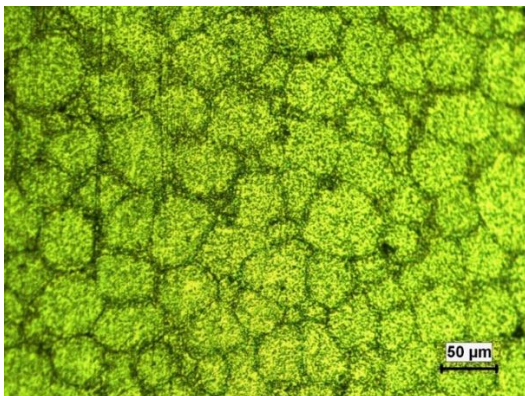
Figure 5. a) SEM photograph taken from Cr₂O₃ powder, b) EDS analysis of Cr₂O₃ powder taken from area 1 in Figure 4 a.

Figure 5 shows the SEM pictures and EDS analysis of the Cr₂O₃ powder. The presence of Cr and O elements can be seen from the results of the EDS analysis of Cr₂O₃ powder shown in Figure 5b. In the EDS analysis, a percentage of 72.05% Cr and 27.95% O element were determined. Therefore, it can be said that the Cr and O elements and the oxide compound (such as Cr_xO_y) are present.

In Figure 6, optical microstructure pictures of sample 1 are shown. Grain boundaries are clearly visible in the microstructure. It is seen that there are pores in the structure consisting of equiaxed grains. Porosity is inevitable in samples produced with powder metallurgy for reasons such as purity of powders used, mixing ratio of powders, compression pressure and speed [15]. Figure 6 shows the pores located at the grain boundaries.



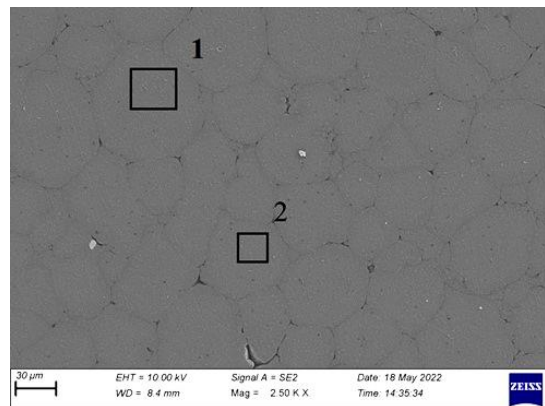
(a)



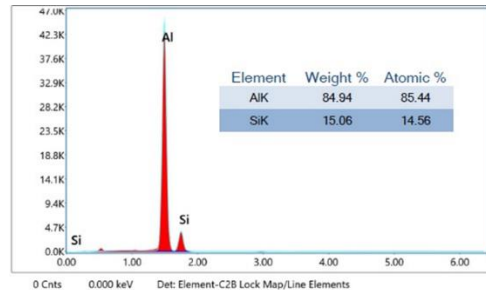
(b)

Figure 6. Optical microstructure pictures of the sintered sample 1.

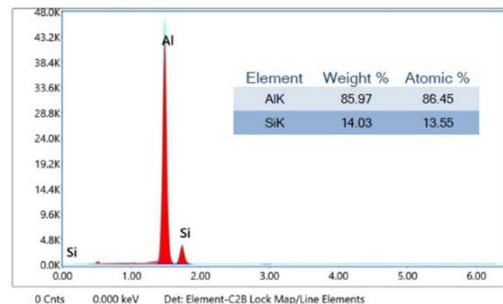
SEM photograph and EDS analysis results taken from sample 1 are shown in Figure 7. Al-Si eutectic structures are thought to be present in the grain and grain boundaries. It is seen that 84.94% Al and 15.06% Si elements are present in area 1 according to EDS analysis (Figure 7a and b). As a result of this EDS, area 1 is thought to be composed of intermetallic compounds with Al-Si eutectic structure. In addition, it is also assumed that the Al-Si eutectic structure is present at a certain percentage in area 2 as a result of the EDS analysis (Figure 7a and c).



(a)



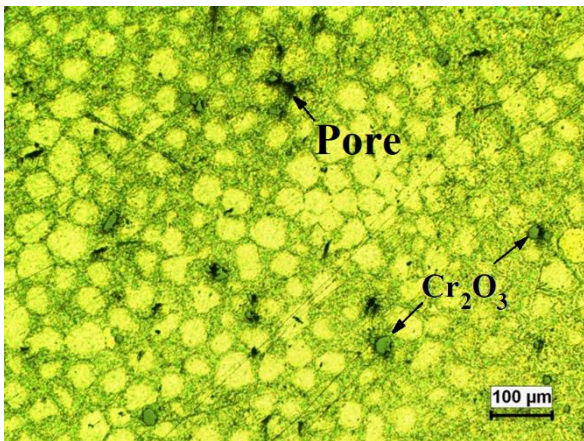
(b)



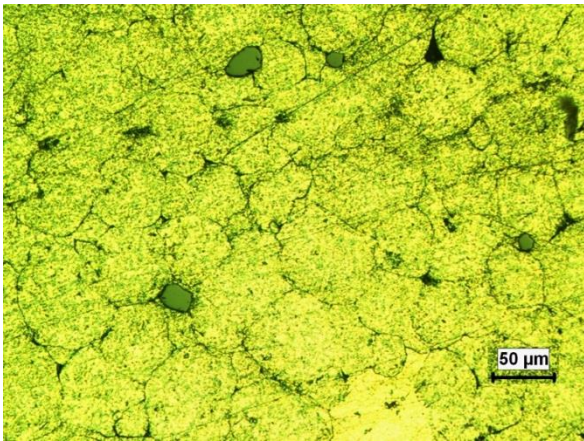
(c)

Figure 7. a) SEM photograph, b) EDS analysis area 1 c) EDS analysis area 2 taken from the sintered sample 1

In Figure 8, optical microstructure pictures of the sample 2 are shown. Grain boundaries are seen in the microstructure of the sample. It is thought that there are intermetallic compounds with Al-Si eutectic structure at the grain and grain boundaries of the microstructure consisting of equiaxed grains. It can also be seen that there are pores in black color at the grain boundaries. The sample 2 which possess 5wt% Cr_2O_3 compound + 95wt% Al-Si possesses more pores in comparison to the sample 1.



(a)

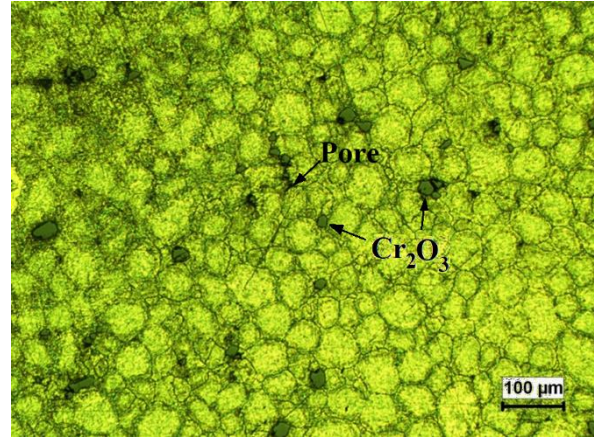


(b)

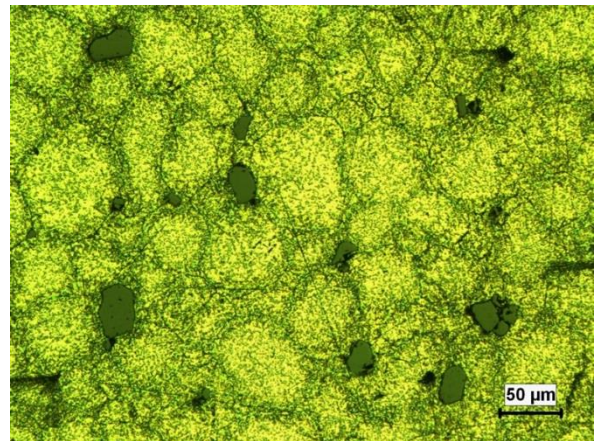
Figure 8. Optical microstructure pictures of the sintered sample 2.

Optical microstructure pictures of sintered sample 3 are shown in Figure 9. Grain boundaries can also be seen in the microstructure of this sample. There is similar structure compared to the sample 2 such as the Al-Si eutectic structure is

present in the grain and grain boundaries. 10wt% Cr_2O_3 powder added into the Al-Si matrix structure exhibits a homogeneous distribution in the sample 3 (see Figure 9). Partial porosity can also be seen in the microstructure.



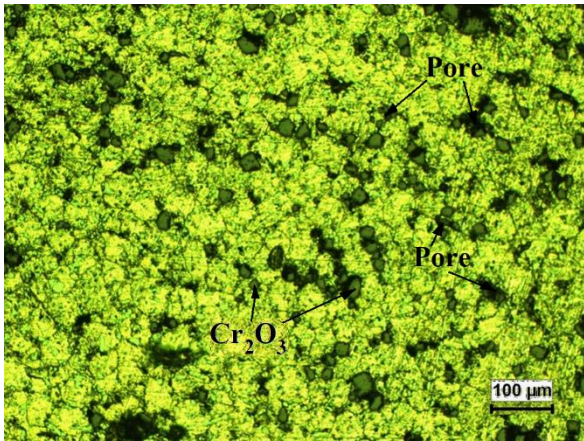
(a)



(b)

Figure 9. Optical microstructure pictures of the sintered sample 3.

In Figure 10 shows the optical microstructure pictures of the sample 4. In this sample, grain boundaries are seen in the microstructure. The porosity increased considerably with the addition of 15wt% Cr_2O_3 into the Al-Si matrix structure. Al-Si eutectic structure intermetallic compounds are observed in grain boundaries and grain interiors. It can also be seen that the amount of pores around the added Cr_2O_3 is more concentrated (see Figure 10).



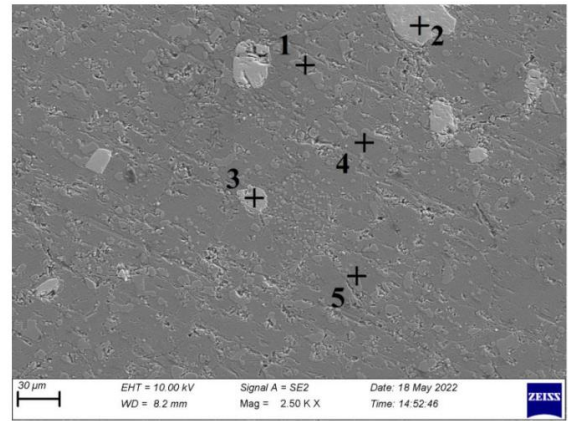
(a)

(b)

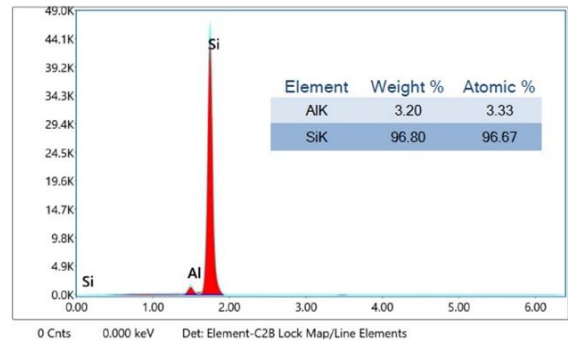
Figure 10. Optical microstructure pictures of the sintered sample 4.

SEM photograph and EDS analysis results taken from sample 4 are shown in Figure 11. EDS analyzes were taken from matrix structure, grain boundaries and powder particles. The presence of Al and Si elements is seen in the EDS analysis given in Figure 11-b, taken from the light gray area 1. It is seen that area 1 is rich in Si element with 96.80% Si value and Al matrix element is present with a value of 3.20%. It is understood that there is no oxidation in this area.

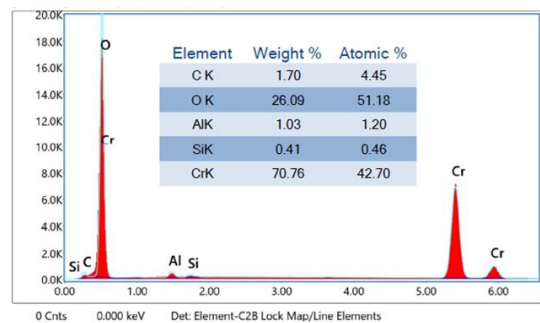
According to EDS analyses taken from point 2 and 3, Cr, Si, Al and O elements are present in these locations (see Figure 11-c and d). It is assumed that both places are composed of Cr₂O₃ compound. There is a small amount of Al and Si elements, which are matrix structures. It is believed that the element C detected in point 2 comes from the carbon tape used while sticking the samples and powders during the SEM analysis. In the EDS analysis taken from point 4 (see Figure 11-e), it is seen that the Al element has a high value of 99.43%. In addition, a small amount of Si element (0.57%) was detected at this location. 67.4% Si, 24.13% Al and 8.47% O elements were detected in the EDS analysis taken from point 5 (see Figure 11-f). At this point, it is thought that the powders in the matrix structure are oxidized.

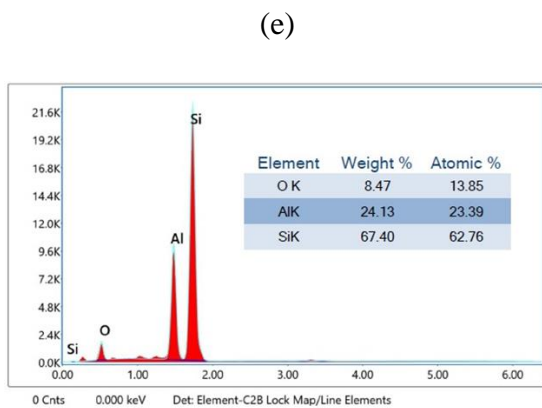
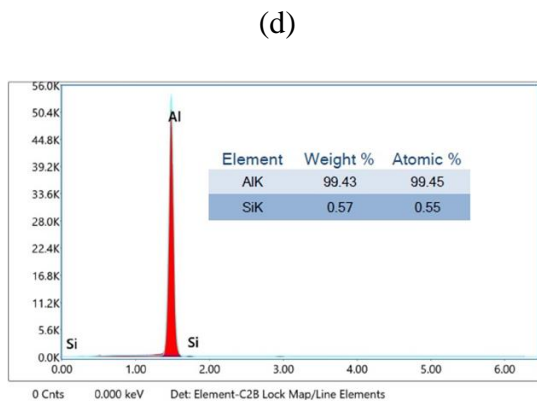
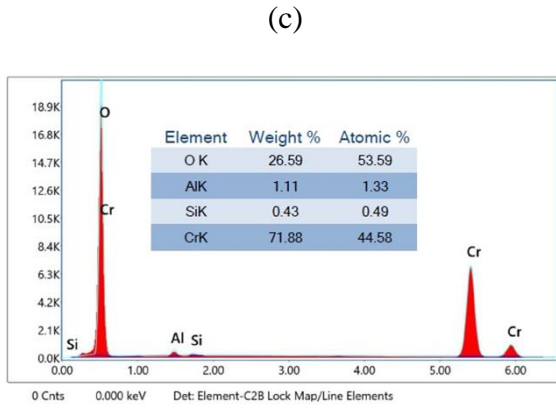


(a)



(b)





(f)

Figure 11. a) SEM photograph taken from the sample 4. EDS analysis of the sample 4 taken from b) point 1, c) point 2, d) point 3, e) point 4, and f) point 5 shown in Figure 11a.

XRD analysis of the sample 4 is shown in Figure 12. As a result of XRD analysis, it was determined that different types of compounds were formed.

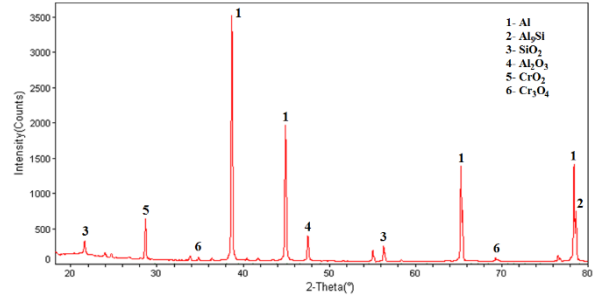


Figure 12. XRD analysis of sample 4.

The main phase was determined as Al matrix. In addition, Al_9Si , Al_2O_3 , CrO_2 and Cr_3O_4 compounds were formed depending on the Cr_2O_3 addition. Moreover, it was observed that the elements detected in the EDS analyzes (Figure 11) taken from the sample 4 and the compounds detected in the XRD analysis (Figure 12) taken from the same sample matched.

3.2. Microhardness Test Results

The microhardness values of the samples with and without the addition of Cr_2O_3 powder after sintering are given in Figure 13.

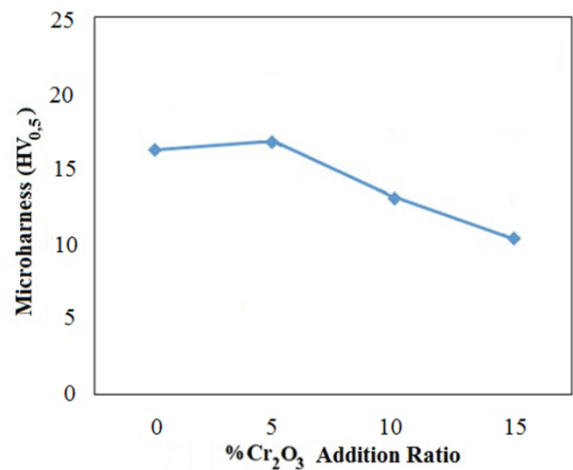


Figure 13. Microhardness values of the samples after sintering.

The microhardness value of the sample 1, which has no addition of Cr_2O_3 , was measured as 16,9 HV. Adding %5wt Cr_2O_3 compound into the Al-Si matrix resulted in 16,8 HV. However, increasing the amount of

Cr₂O₃ from %5wt to %10wt caused the micro hardness to decrease from 16,19 HV to 13,15 HV, respectively. In the sample 4 with 15% Cr added, the hardness was measured as 10,33 HV. With the addition of Cr₂O₃ powder, the pore partly increased in the microstructure as seen in the microstructure photographs (Figures 8, 9, 10). The highest number of pores was detected in the sample 4 to which %15wt Cr₂O₃ was added. In powder metallurgy manufacturing, the formation and growth of sintering necks is mainly driven by surface diffusion. The high amount of oxide makes it difficult to neck [17]. It can be said that the amount of pores increases with decreasing necking. Due to this increase in the amount of pores, a small decrease in the amount of microhardness was detected.

4. Conclusion and Suggestions

1. A porous structure was detected in the samples. The pores become more prominent at the grain boundaries. Cr₂O₃ powders are also located in the grain boundaries.
2. After sintering, the microhardness value of the samples decreased partially due to the

increase in the amount of pores with the addition of Cr₂O₃ powder.

3. The lowest microhardness value after sintering was found in the %15wt Cr₂O₃ added sample 4 with an HV value of 10,33.

Acknowledgment

Part of this article was presented as a summary paper at the "2st International Rahva Technical And Social Researches Congress" congre.

Contributions of the authors

This study is a part of Kübra ASLAN's master thesis.

Conflict of Interest Statement

There is no conflict of interest between the authors.

Statement of Research and Publication Ethics

The study is complied with research and publication ethics.

References

- [1] M. Yadav, L. A. Kumaraswamidhas, and S. K. Singh, "Investigation of solid particle erosion behavior of Al-Al₂O₃ and Al-ZrO₂ metal matrix composites fabricated through powder metallurgy technique," *Tribol. Int.*, vol. 172, no. 107636, p. 107636, 2022.
- [2] K. C. Nayak, P. R. Deshmukh, A. K. Pandey, P. Vemula, and P. P. Date, "Microstructural, physical and mechanical characterization of grinding sludge based aluminium metal matrix composite," *Mater. Sci. Eng. A Struct. Mater.*, vol. 773, no. 138895, p. 138895, 2020.
- [3] I. Bahaj, M. Kaddami, A. Dahrouch, N. Labjar, and M. Essahli, "The effect of particle content and sintering time on the properties of Al-Al₉Co₂-Al₁₃Co₄ composites, made by powder metallurgy," *Mater. Today*, vol. 62, pp. A1-A7, 2022.
- [4] M. Ardestani and F. Karpasand, "Chemical synthesis and densification of a novel Ag/Cr₂O₃-AgCrO₂ nanocomposite powder," *Sci. Eng. Compos. Mater.*, vol. 25, no. 4, pp. 739-743, 2018.
- [5] O. Adıyaman, "Investigation of Mechanical Properties of Composite Al6061/Ni-Al₂O₃ Produced by Stir Casting Process", *European Journal of Technique (EJT)*, vol. 12, no. 1, pp. 30-35, 2022.
- [6] H. Su et al., "Research on high-temperature mechanical properties and microstructure of powder metallurgical rhenium," *Int. J. Refract. Hard Met.*, vol. 106, no. 105861, p. 105861, 2022.
- [7] M. Boz ve A. Kurt, "Toz metal fren balata malzemelerinin sürtünme-aşınma performansı üzerine çinkonun etkisi," *Mühendislik Mimarlık Fakültesi Dergisi*, vol. 21, no 1, p. 115-121, 2006.
- [8] K. Köprülü, N. Mutlu, A. Kurt, B. Gülenç, Y. Özçatalbaş, "Al+%4,5 Cu ön karışimli tozların alaşımlanmasına ısıl işlemlerin etkisi," *Gazi Uni. J. of Sci. Part C: Des. and Tech.*, vol. 6, no 2, p. 283-293, 2018.

- [9] Y. Sayan, J.-S. Kim, and H. Wu, “Residual stress measurement of a single-step sintered planar anode supported SC-SOFC using fluorescence spectroscopy,” *Bitlis Eren Üniversitesi Fen Bilimleri Dergisi*, vol. 11, no. 3, pp. 902–910, 2022.
- [10] M. Kılıç, I. Kırık, M. Okumus, “Microstructure examination of functionally graded NiTi/NiAl/Ni₃Al intermetallic compound produced by self-propagating high-temperature synthesis,” *Kovove Mater.*, vol. 55, no 2, pp. 97–106, 2017.
- [11] N. Kumar, A. Bharti, and K. K. Saxena, “A re-investigation: Effect of powder metallurgy parameters on the physical and mechanical properties of aluminium matrix composites,” *Mater. Today*, vol. 44, pp. 2188–2193, 2021.
- [12] Ş. Çetinkaya, “Karbon katkılı alaşımlı demir tozu peletlerinin sinterleme sonrası özellikleri,” M.S. thesis, İstanbul Univ. Graduate Sch. of Nat. and App. Sci., İstanbul, Türkiye, 2005.
- [13] Y. Sayan, V. Venkatesan, E. Guk, H. Wu, and J.-S. Kim, “Single-step fabrication of an anode supported planar single-chamber solid oxide fuel cell,” *Int. J. Appl. Ceram. Technol.*, vol. 15, no. 6, pp. 1375–1387, 2018.
- [14] E. Gevorkyan, L. Cepova, M. Rucki, V. Nerubatskyi, D. Morozow, W. Zurowski, V. Barsamyan and K. Kouril, “Activated sintering of Cr₂O₃-based composites by hot pressing”, *Mater.* , vol. 15, pp. 5960, 2022.
- [15] K. Aslan, “Toz metalurjisi yöntemiyle Al+Si matrisli kompozitlerin aşınma dayanımlarının incelenmesi,” M.S. thesis, Bitlis Eren Univ. Inst. of Graduate Edu., Bitlis, Türkiye, 2022.
- [16] M. Kılıç, “Toz metalurjisi ile Üretilen NiTi Alaşımına Al’un Etkisi,” *Bitlis Eren Üniversitesi Fen Bilimleri Dergisi*, vol. 10, no. 1, pp. 256-267, 2021.
- [17] H. He, J. Lou, Y. Li, H. Zhang, S. Yuan, Y. Zhang, X. Wei, “Effects of oxygen contents on sintering mechanism and sintering-neck growth behaviour of FeCr powder,” *Powder Techn.*, vol. 329, pp. 12-18, 2018.

Comparison Of Anomalous Higgs Couplings at the Large Hadron Collider and at Proton-Proton Collider with 100 TeV Energy

Gülistan AKKAYA SELÇİN^{1*}

Bitlis Eren Üniversitesi, Tatvan Meslek Yüksekokulu, Elektrik ve Enerji Bölümü,
Bitlis
(ORCID: 0000-0003-4720-6631)



Keywords: Photon Induced Process, Anomalous Higgs Couplings, Large Hadron Collider Proton-Proton Collider with 100 TeV Energy.

Abstract γp and $\gamma\gamma$, called photon induced processes, have been examined in various colliders like Large Hadron Collider (LHC) and proton-proton collider with 100 TeV energy. One of the importance of these processes is that they allow for probing the anomalous Higgs couplings. The anomalous Higgs couplings constitute a testing ground for electroweak symmetry breaking (EWSB) mechanism and mass production system. For measuring anomalous $H\gamma\gamma$ and $HZ\gamma$ couplings at the LHC and at the proton-proton collider with 100 TeV energy, the potential of the $pp \rightarrow p\gamma p \rightarrow pHqX$ has been examined. Sensitivity bounds on anomalous Higgs couplings have been obtained at %95 confidence level. The analyses have been done for various integrated luminosities and different scenarios. Then the results of them have been compared. Model-independent effective Lagrangian technique has been used, and the Higgs boson couplings to gauge bosons have been examined by dimension-six operators.

1. Introduction

The Large Hadron Collider (LHC) which has a center of mass energy with 14 TeV and luminosity of $10^{34} \text{ cm}^{-2} \text{ s}^{-1}$ is one of the the most important accelerator of the world.

ATLAS and CMS Collaborations discovered the Higgs boson estimated by Standard Model (SM) of particle physics at the LHC [1,2]. The next stage is to examine the features of this significant particle and its couplings to other SM particles. These studies have a great importance for supporting SM and investigating new physics. On the other hand the future 100 TeV proton-proton collider ensures an ideal venue to examine new physics. [3-5]. Such studies on anomalous Higgs couplings at LHC and at future 100 TeV proton-proton collider have been speedily increasing in the literature. (6-18) In this paper Higgs boson production via the main process $pp \rightarrow p\gamma p \rightarrow pHqX$ haven been examined at the LHC

and at future 100 TeV collider. This process can be shown as follow diagram(40):

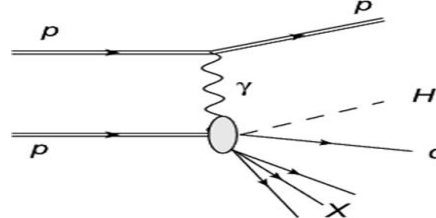


Figure 1. Representation of the process $pp \rightarrow p\gamma p \rightarrow pHqX$.

Here, q and X constitute quarks and proton remnants respectively.

The top quark distribution has been ignored and 10 independent subprocess for $q = u, d, s, c, b, \bar{u}, \bar{d}, \bar{s}, \bar{c}, \bar{b}$ have been considered. In the existence of anomalous $H\gamma\gamma$ and $HZ\gamma$ couplings the Feynmann diagrams of subprocess $\gamma q \rightarrow Hq$ is drawn as follows(40):

* Corresponding author: gakkaya@beu.edu.tr

Received: 29.12.2022, Accepted: 18.03.2023

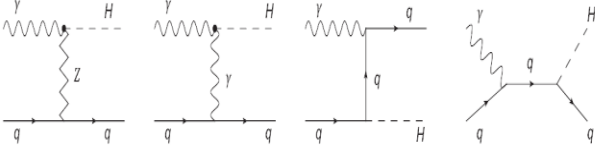


Figure 2. Feynman diagrams of $\gamma q \rightarrow Hq$ at the tree-level.

At last studies, the presence of these photon-induced processes have been confirmed by CMS ATLAS Collaborations [19-23]. And also it is verified that these reactions have an important potential to examine new physics [21-23]. In such a process, photon-proton collision takes place when a quasi-real photon has been emitted from one of the incoming protons. So that it can be thought that proton-photon collision is a subprocess of the proton-proton collision. In that paper equivalent photon approximation (EPA) [24-26] has been taken into account. According to this approximation, emitted photons are accepted to be real because of having a very low virtuality. The protons which emit quasi-real photons do not divide into partons and they keep to be intact [27-28].

2. Material and Method

2.1. Anomalous $H\gamma\gamma$ and $HZ\gamma$ Couplings And The Cross Section

For examining anomalous $HZ\gamma$ and $H\gamma\gamma$ couplings one of the ways is to employ effective Lagrangian formalism. [7-9,29-33]

In this formalism total effective Lagrangian can be expressed as follows:

$$L_{eff} = \sum_n \frac{f_n}{\Lambda^2} O_n \quad (1)$$

Here f_n indicates the anomalous couplings and the scale of new physics is described by Λ . Also O_n indicates five dimension- six operators which alter the Higgs boson couplings to Z and γ bosons [7-9,29-33] They can be explicitly expressed as follows:

$$\begin{aligned} O_{ww} &= \phi^\dagger W_{\mu\nu} W^{\mu\nu} \phi \\ O_W &= (D_\mu \phi)^\dagger W^{\mu\nu} (D_\nu \phi) \\ O_{BB} &= \phi^\dagger B_{\mu\nu} B^{\mu\nu} \phi \\ O_B &= (D_\mu \phi)^\dagger B^{\mu\nu} (D_\nu \phi) \\ O_{BW} &= \phi^\dagger B_{\mu\nu} W^{\mu\nu} \phi \end{aligned} \quad (2)$$

Here, Φ indicates the scalar doublet and D_μ indicates the covariant derivative. Also the other fields can be expressed as follows:

$$\begin{aligned} W_{\mu\nu} &= i \frac{g}{2} (\vec{\sigma} \cdot \vec{W}_{\mu\nu}) \\ B_{\mu\nu} &= i \frac{g'}{2} \vec{B}_{\mu\nu} \end{aligned} \quad (3)$$

where g is the $SU(2)_L$ gauge coupling and g' is the $U(1)_Y$ gauge coupling. Also σ is the Pauli matrices. The effective Lagrangian in Eq-1 can be described as follows after the symmetry breaking. :

$$L_{eff} = g_{H\gamma\gamma} H A_{\mu\nu} A^{\mu\nu} + g_{HZ\gamma}^1 A_{\mu\nu} Z^\mu \partial^\nu H + g_{HZ\gamma}^2 H A_{\mu\nu} Z^{\mu\nu} \quad (4)$$

Here, $V_{\mu\nu} = \partial_\mu V_\nu - \partial_\nu V_\mu$ with $V=A(\text{photon})$ and Z field. Also $g_{H\gamma\gamma}$, $g_{HZ\gamma}^1$ ve $g_{HZ\gamma}^2$ are anomalous couplings which involve the couplings f_n as follows:

$$g_{H\gamma\gamma} = - \left(\frac{g m_w}{\Lambda^2} \right) \sin^2 \theta_w \left(\frac{f_{BB} + f_{ww} - f_{BW}}{2} \right) \quad (5.1)$$

$$g_{HZ\gamma}^1 = \left(\frac{g m_w}{\Lambda^2} \right) \sin \theta_w \left(\frac{f_w - f_B}{2 \cos \theta_w} \right) \quad (5.2)$$

$$g_{HZ\gamma}^2 = \left(\frac{g m_w}{\Lambda^2} \right) \frac{\sin \theta_w}{2 \cos \theta_w} [2 \sin^2 \theta_w f_{BB} - 2 \cos^2 \theta_w f_{ww} + (\cos^2 \theta_w - \sin^2 \theta_w) f_{BW}] \quad (5.3)$$

Here, θ_w and m_w indicates Weinberg angle and W boson's mass respectively. Also in the calculations taken into account the energy scale of new physics as $\Lambda=1$ TeV. For the aim of the easiness six scenarios of new physics have been considered as follows:

- Senaryo I ; $f_B = f_w = 0$, $f_{ww} = f_{BB}$
- Senaryo II ; $f_{ww} = f_{BB} = 0$, $f_B = -f_w$
- Senaryo III ; $f_B = f_w = 0$, $f_{ww} = -f_{BB}$
- Senaryo IV ; $f_B = f_w = 0$, $f_{ww} = \tan^2 \theta_w f_{BB}$
- Senaryo V ; $f_{ww} = f_w = 0$
- Senaryo VI ; $f_{BB} = f_B = 0$

For ignoring the contributions of HZZ and HWW couplings in the calculations f_{BW} is taken to be zero ($f_{BW} = 0$). Taking into account one-loop level contribution of SM for the anomalous $H\gamma\gamma$ ve $HZ\gamma$ couplings, the effective Lagrangian can be written as follows [34,35] ;

$$\mathcal{L}_{eff}^{(SM)} = g_{H\gamma\gamma}^{(SM)} HA_{\mu\nu} A^{\mu\nu} + g_{HZ\gamma}^{(SM)} HA_{\mu\nu} Z^{\mu\nu} \quad (6)$$

Here, $g_{HZ\gamma}^{(SM)} = \frac{\alpha}{4\pi v \sin\theta_W} (5.508 - 0.004i)$ and

$$g_{H\gamma\gamma}^{SM} = \frac{2\alpha}{9\pi v}.$$

The cross section of the main process is given as;

$$\frac{\sigma(pp \rightarrow p\gamma p \rightarrow pHqX)}{\sigma(\gamma q \rightarrow Hq)} = \int_{x_{1min}}^{x_{1max}} dx_1 \int_0^1 dx_2 \int_{Q_{min}^2}^{Q_{max}^2} dQ^2 \left(\frac{dN_\gamma}{dx_1 dQ^2} \right) \left(\frac{dN_q}{dx_2} \right) \times \quad (7)$$

where $\left(\frac{dN_q}{dx_2} \right)$ and $\left(\frac{dN_\gamma}{dx_1 dQ^2} \right)$ are quark distribution and equivalent photon functions, respectively.

Detailed information and the integral bounds for equivalent photon distribution function can be found in the literature [36,37]. Also, using the MSTW2008 programme (38), the quark distribution functions can be calculated numerically. At the high energies ($E \gg m_p$), x_1 can be taken as $x_1 = \frac{E-E'}{E} = \frac{E_\gamma}{E} \approx \xi$. ξ is called forward detector acceptance. Here, E is energy of the initial proton and E' is energy of final (scattered) proton. Also E_γ indicates the equivalent photon energy. ξ is called forward detector acceptance. Therefore during the calculations x_{1min} and x_{1max} are taken as $x_{1min} = \xi_{min} = 0.015$ ve $x_{1max} = \xi_{max} = 0.15$.

In the analysis χ^2 criterion has been used and bounds on anomalous Higgs couplings have been determined at 95% (C.L.). χ^2 criterion is taken as follows:

$$\chi^2 = \left(\frac{N_{AN} - N_{SM}}{N_{SM} \delta_{err}} \right)^2 \quad (8)$$

Here, N_{AN} is number of events which contains SM and new physics contributions, N_{SM} is number of events in the SM and δ_{err} is the statistical error. $N_{AN(SM)}$ is calculated from the formula:

$N_{(AN)SM} = E \times S \times L_{int} \times Br \times \sigma_{(AN)SM}$, where S represents the survival probability factor ($S=0.7$), E represents the b-tagging efficiency ($E = 0.6$), L_{int} represents the integrated luminosity and BR is the branching ratio for $H \rightarrow b\bar{b}$ ($Br = 0.6$). Also, σ_{SM} and σ_{AN} are SM and anomalous cross sections respectively.

The background subprocesses $\gamma q \rightarrow k, b, b$ ($q = u, d, s, c, b, u, d, s, c, b$; $k = u, d, s, c, b, t, u, d, s, c, b, t$) which contribute to main process $pp \rightarrow p\gamma p \rightarrow pbbqX$, are calculated by using CalcHEP 3.6.20. [39]

At the background calculations, $H \rightarrow b\bar{b}$ decay channel of Higgs boson has been considered and $b\bar{b}$ final state with invariant mass in the interval $120 \text{ GeV} < M(b, \bar{b}) < 130 \text{ GeV}$ is identified as the signal. When these cuts are applied to the signal, the cross section of the background decline dramatically.

For LHC, taking into account scenarios I-IV, the bounds on anomalous f_w, f_{wW} and f_{BB} couplings are obtained in the Table -I at 95% C.L.

Table I. For various scenarios and luminosities the anomalous bounds are given at 95% C.L for LHC ($\sqrt{s}=14 \text{ TeV}$)

Luminosite	(Senaryo-I) f_{ww}	(Senaryo-II) f_w	(Senaryo-III) f_{bb}	(Senaryo-IV) f_{bb}
10 fb^{-1}	(-6.3,7.9)	(-19.8,15.4)	(-9.9,7.7)	(-13.2,15.6)
30 fb^{-1}	(-4.6,6.2)	(-15.6,11.3)	(-7.8,5.6)	(-9.8,12.2)
50 fb^{-1}	(-3.9,5.6)	(-14.1,9.7)	(-7.0,4.9)	(-8.5,10.8)
100 fb^{-1}	(-3.2,4.8)	(-12.2,7.9)	(-6.1,3.9)	(-7.0,9.3)
200 fb^{-1}	(-2.6,4.2)	(-10.7,6.4)	(-5.3,3.2)	(-5.7,8.1)
500 fb^{-1}	(-1.9,3.6)	(-9.0,4.7)	(-4.5,2.4)	(-4.3,6.7)

For scenarios V and VI, at LHC, with 95% C.L. restricted regions in two-dimensional $f_B - f_{BB}$ and $f_w - f_{wW}$ parameter spaces are given in Figure 3-4.

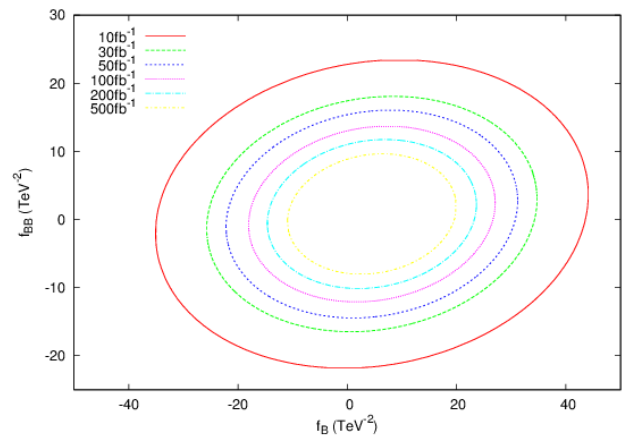


Figure 3. At 95% C.L. the restricted areas on $f_B - f_{BB}$ parameter spaces are shown for LHC. ($\sqrt{s}=14 \text{ TeV}$)

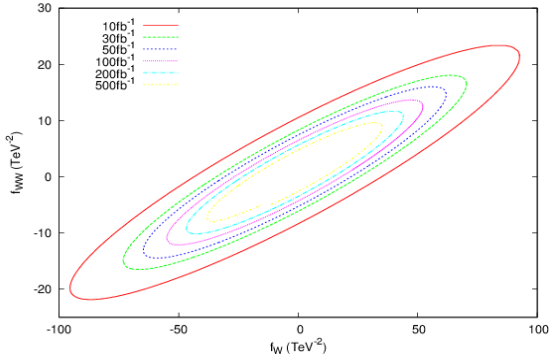


Figure 4. At 95% C.L. the restricted areas on $f_W - f_{WW}$ parameter spaces are shown for LHC. ($\sqrt{s}=14$ TeV) Similarly, for 100 TeV proton-proton collider, taking into account scenarios I-IV, the bounds on anomalous f_W , f_{WW} and f_{BB} couplings are obtained in the Table -II at 95% C.L.

Table II. For various scenarios and luminosities the anomalous bounds are given at 95% C.L. for future 100 TeV proton-proton collider .

Luminosity	(Scenario-I) f_{WW}	(Scenario-II) f_W	(Scenario-III) f_{bb}	(Scenario-IV) f_{bb}
$100fb^{-1}$	(-1.9,4.2)	(-8.2,4.0)	(-4.1,2.0)	(-4.9,9.0)
$500fb^{-1}$	(-1.1,3.3)	(-6.4,2.2)	(-3.2,1.1)	(-2.8,6.9)
$3000fb^{-1}$	(-0.5,2.8)	(-5.3,1.1)	(-2.7,0.6)	(-1.4,5.6)

For scenarios V and VI, at 100 TeV proton-proton collider, with 95% C.L. restricted regions in two-dimensional $f_B - f_{BB}$ and $f_W - f_{WW}$ parameter spaces are given in Figure 5-6.

References

[1] G. Aad et al., “Observation of a new particle in the search for the Standard Model Higgs boson with the ATLAS detector at the LHC,” *Phys. Lett. B*, vol. 716, no. 1, pp. 1–29, 2012.
 [2] S. Chatrchyan et al., “Observation of a new boson at a mass of 125 GeV with the CMS experiment at the LHC,” *Phys. Lett. B*, vol. 716, no. 1, pp. 30–61, 2012.
 [3] N. Arkani-Hamed, T. Han, M. Mangano, and L.-T. Wang, “Physics opportunities of a 100 TeV proton-proton collider,” *Phys. Rep.*, vol. 652, pp. 1–49, 2016.

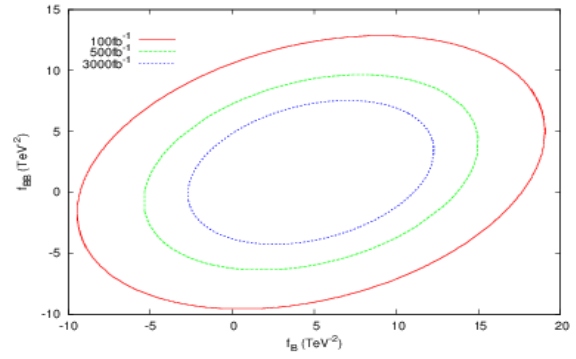


Figure 5. At 95% C.L. the restricted areas on $f_B - f_{BB}$ parameter spaces are shown for 100 TeV proton-proton collider.

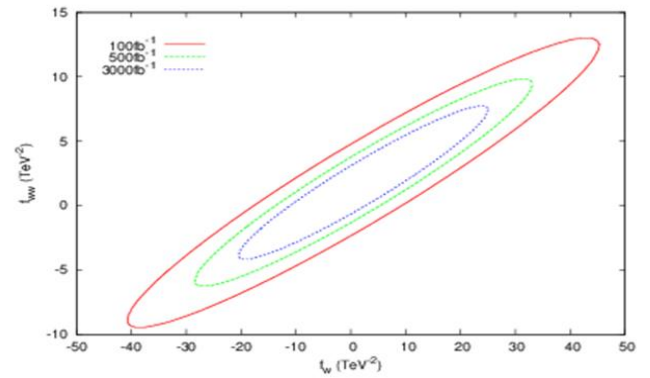


Figure 6. At 95% C.L. the restricted areas on $f_W - f_{WW}$ parameter spaces are shown for 100 TeV proton-proton collider.

3. Conclusion and Suggestions

As expected, γp collision at 100 TeV proton-proton collider with a higher energy and a higher luminosity relatively, probes the anomalous $H\gamma\gamma$ and $HZ\gamma$ couplings with better sensitivity than γp collision at the LHC. Consequently, we can say that, the sensitivity bounds on anomalous Higgs couplings are refined by an improvement factor of 2.

- [4] M.L. Mangano, G. Zanderighi, J.A Aguilar Saavedra, S. Alekhin, S. Badger, C.W. Bauer, T. Becher, V. Bertone, S. Bonvini Boselli, E. Bothmann, et al. "Physics at the FCC-hh, a 100 TeV pp collider," *Cern Yellow Report.*, vol. 3, pp.1-254, Oct 2017.
- [5] R. Contino, D. Curtin, A. Katz, M.L. Mangano, G. Panico, M.J Ramsey-Musolf, G. Zanderighi, C. Anastasiou, W. Astill, G. Bambhaniya, et al. "Physics at a 100 TeV pp collider: Higgs and EW symmetry breaking studies," *Cern Yellow Report.*, vol. 3, pp. 255-440, Jun 2016.
- [6] V. Khachatryan et al., "Constraints on the spin-parity and anomalous HVV couplings of the Higgs boson in proton collisions at 7 and 8 TeV," *Phys. Rev.*, vol. 92, no. 1, 2015.
- [7] T. Corbett, O. J. P. Éboli, J. Gonzalez-Fraile, and M. C. Gonzalez-Garcia, "Constraining anomalous Higgs boson interactions," *Phys. Rev.*, vol. 86, no. 7, 2012.
- [8] T. Corbett, O. J. P. Éboli, J. Gonzalez-Fraile, and M. C. Gonzalez-Garcia, "Robust determination of the Higgs couplings: Power to the data," *Phys. Rev.*, vol. 87, no. 1, 2013.
- [9] E. Massó and V. Sanz, "Limits on anomalous couplings of the Higgs boson to electroweak gauge bosons from LEP and the LHC," *Phys. Rev.*, vol. 87, no. 3, 2013.
- [10] S. Banerjee, S. Mukhopadhyay, B. Mukhopadhyaya, "Higher dimensional operators and LHC Higgs data : the role of modified kinematics" *Phys. Rev. D.*, vol.89, pp.1-5, March 2014.
- [11] S. Taheri Monfared, S. Fayazbakhsh, and M. Mohammadi Najafabadi, "Exploring anomalous HZ γ couplings in γ -proton collisions at the LHC," *Phys. Lett. B*, vol. 762, pp. 301–308, 2016.
- [12] F. P. An et al., "New measurement of antineutrino oscillation with the full detector configuration at Daya Bay," *Phys. Rev. Lett.*, vol. 115, no. 11, p. 111802, 2015.
- [13] A. J. Barr, M. J. Dolan, C. Englert, D. E. F. de Lima, and M. Spannowsky, "Higgs self-coupling measurements at a 100 TeV hadron collider," *J. High Energy Phys.*, vol. 2015, no. 2, 2015.
- [14] C. Degrande, V. V. Khoze, and O. Mattelaer, "Multi-Higgs-boson production in gluon fusion at 100 TeV," *Phys. Rev. D.*, vol. 94, no. 8, 2016.
- [15] B. Fuks, J. H. Kim, and S. J. Lee, "Probing Higgs boson self-interactions in proton-proton collisions at a center-of-mass energy of 100 TeV," *Phys. Rev. D.*, vol. 93, no. 3, 2016.
- [16] J. Baglio, A. Djouadi, and J. Quevillon, "Prospects for Higgs physics at energies up to 100 TeV," *Rep. Prog. Phys.*, vol. 79, no. 11, p. 116201, 2016.
- [17] A. Papaefstathiou and K. Sakurai, "Triple Higgs boson production at a 100 TeV proton-proton collider," *J. High Energy Phys.*, vol. 2016, no. 2, 2016.
- [18] A. Abada et al., "FCC-hh: The hadron collider: Future circular collider conceptual design report volume 3," *Eur. Phys. J. Spec. Top.*, vol. 228, no. 4, pp. 755–1107, 2019.
- [19] The CMS collaboration et al., "Exclusive $\gamma\gamma \rightarrow \mu^+ \mu^-$ production in proton-proton collisions at $\sqrt{s} = 7$ TeV," *J. High Energy Phys.*, vol. 2012, no. 1, 2012.
- [20] The CMS collaboration et al., "Search for exclusive or semi-exclusive $\gamma\gamma$ production and observation of exclusive and semi-exclusive e^+e^- production in pp collisions at $\sqrt{s}=7$ TeV," *J. High Energy Phys.*, vol. 2012, no. 11, 2012.
- [21] The CMS collaboration et al., "Study of exclusive two-photon production of W^+W^- in pp collisions at $\sqrt{s}=7$ TeV and constraints on anomalous quartic gauge couplings," *J. High Energy Phys.*, vol. 2013, no. 7, 2013.
- [22] V. Khachatryan et al., "Evidence for exclusive $\gamma\gamma \rightarrow W^+ W^-$ production and constraints on anomalous quartic gauge couplings in pp collisions at $s = 7$ TeV and 8 TeV," *J. High Energy Phys.*, vol. 2016, no. 8, 2016.
- [23] M. Aaboud et al., "Measurement of exclusive $\gamma\gamma \rightarrow W^+W^-$ production and search for exclusive Higgs boson production in pp collisions at $s=8$ TeV using the ATLAS detector," *Phys. Rev. D.*, vol. 94, no. 3, 2016.
- [24] V. M. Budnev, I. F. Ginzburg, G. V. Meledin, and V. G. Serbo, "The two-photon particle production mechanism. Physical problems. Applications. Equivalent photon approximation," *Phys. Rep.*, vol. 15, no. 4, pp. 181–282, 1975.
- [25] G. Baur, "Coherent $\gamma\gamma$ and γA interactions in very peripheral collisions at relativistic ion colliders," *Phys. Rep.*, vol. 364, no. 5, pp. 359–450, 2002.
- [26] K. Piotrkowski, "Tagging two-photon production at the CERN Large Hadron Collider," *Phys. Rev. D Part. Fields*, vol. 63, no. 7, 2001.

- [27] X. Rouby, “Measurements of photon induced processes in CMS and forward proton detection at the LHC,” Universite Catholique de Louvain, Ph.D. thesis, Dept. Phys. Universite Catholique de Louvain, Belgique, Sept.2008. [Online] Available: http://cp3.irmp.ucl.ac.be/~rouby/files/xavier_rouby_final.pdf.
- [28] N. Schul, “Measurements of two-photon interactions at the LHC”, Universite Catholique de Louvain, Ph.D. thesis, Dept. Phys. Universite Catholique de Louvain, Belgique, July 2011 [Online] Available: http://cds.cern.ch/record/1423327/files/TS2011_030_2.pdf.
- [29] W. Buchmüller and D. Wyler, “Effective lagrangian analysis of new interactions and flavour conservation,” *Nucl. Phys. B.*, vol. 268, no. 3–4, pp. 621–653, 1986.
- [30] C. N. Leung, S. T. Love, and S. Rao, “Low-energy manifestations of a new interactions scale: Operator analysis,” *Z. Phys. C - Particles and Fields*, vol. 31, no. 3, pp. 433–437, 1986.
- [31] A. De Rújula, M. B. Gavela, P. Hernandez, and E. Massó, “The self-couplings of vector bosons: does LEP-1 obviate LEP-2?,” *Nucl. Phys. B.*, vol. 384, no. 1–2, pp. 3–58, 1992.
- [32] K. Hagiwara, S. Ishihara, R. Szalapski, and D. Zeppenfeld, “Low energy effects of new interactions in the electroweak boson sector,” *Phys. Rev. D Part. Fields*, vol. 48, no. 5, pp. 2182–2203, 1993.
- [33] M. C. Gonzalez-Garcia, “Anomalous Higgs couplings,” *Int. J. Mod. Phys. A*, vol. 14, no. 20, pp. 3121–3156, 1999.
- [34] J. F. Donoghue, E. Golowich, and B. R. Holstein, *Dynamics of the standard model*. Cambridge, England: Cambridge University Press, 2014.
- [35] M. Farina, Y. Grossman, and D. J. Robinson, “Probing CP violation $inh \rightarrow Z\gamma$ with background interference,” *Phys. Rev.*, vol. 92, no. 7, 2015.
- [36] V.M. Budnev, I.F. Ginzburg, G.V. Meledin, V.G. Serbo, “The two-photon particle production mechanism. Physical problems. Applications. Equivalent photon approximation,” *Phys. Rep*, vol.15, pp.181-282, Jan.1975.
- [37] O. Kepka and C. Royon, “Anomalous $WW\gamma$ coupling in photon-induced processes using forward detectors at the CERN LHC,” *Phys. Rev.*, vol. 78, no. 7, 2008.
- [38] A. D. Martin, W. J. Stirling, R. S. Thorne, and G. Watt, “Parton distributions for the LHC,” *Eur. Phys. J. C Part. Fields*, vol. 63, no. 2, pp. 189–285, 2009.
- [39] A. Belyaev, N. D. Christensen, and A. Pukhov, “CalcHEP 3.4 for collider physics within and beyond the Standard Model,” *Comput. Phys. Commun.*, vol. 184, no. 7, pp. 1729–1769, 2013.
- [40] G. Akkaya Selçin and İ. Şahin, “Non-standard Higgs couplings in single Higgs boson production at the LHC and future linear collider,” *Chin. J. Phys.*, vol. 55, no. 6, pp. 2305–2317, 2017.

An Optimization Approach for a Biogas Supply Chain using Goal Programming and Mixed Integer Linear Programming

Onur DERSE^{1*}, Elifcan GÖÇMEN POLAT²

¹Tarsus University, Faculty of Engineering, Department of Industrial Engineering

²Munzur University, Faculty of Engineering, Department of Industrial Engineering
(ORCID: 0000-0002-4528-1999) (ORCID: 0000-0002-0316-281X)



Keywords: Biogas Supply Chain Optimization, Biogas Vehicle Charging Stations, Location Problem, Mixed Integer Linear Programming, Goal Programming

Abstract

Environmental concerns prompt the world for a transition to renewable energy sources from fossil energy. Reducing the dependency on non-renewable energy sources is needed for the sustainable world and less environmental pollution. Biogas energy, which is one of the most important renewable energy sources, is produced by burning organic wastes and can be used in many different fields. In this study, a two-stage approach was presented to optimize a biogas supply chain problem by incorporating of 30 districts in Izmir. In the first stage, the selection of the most suitable biogas plants was considered by the goal programming approach, which is of great importance to decide the optimal location with high energy potential. The most suitable sites for the biogas plants were obtained as Konak and Narlıdere districts. In the second stage, the location problem of the biogas vehicle charging stations (BVS) for biogas vehicles was handled considering the results of the first stage using mixed integer linear programming (MILP) approach. Computational results demonstrate that it would be more appropriate to establish BVS in 12 districts of İzmir. The model and solution approach are pioneering for supply chain problems and an efficient tool for renewable energy plans.

1. Introduction

In response to global warming, the optimal option for the green challenge is to reduce the dependency on fossil fuels and transition to renewable energy sources. Alternative energy sources have been gained attraction since the utilization of fossil fuels threatens human health and the environment. There has been a considerable impact on the alternative energy systems and most countries have attempted new energy policies such as bio-sources [1]. Biogas is one of the cleanest energy sources for human living and energy production is carried out using manure. Animal manure, which is the source of biogas production, ensures an environmentally friendly way to produce clean energy [2]. This energy can reduce the harmful effects of fossil fuels in various sectors including the transportation sector [3]. However, biogas is an alternative source of energy, which can be used

instead of diesel, LPG, and natural gas. The integration of the biogas energy and transportation sector is important in the context of economic and environmental aspects. The optimal planning of the BVS should be conducted by incorporating these aspects. The usage of biogas for the transport sector increases in EU countries [4]. Considering the environmental view, the location problem of the BVS should be handled with the city traffic situations. Candidate locations of BVS should be decided with the environmental factors. Considering the economic aspect, the candidate BVS should meet the requirements including minimum investment, operation, and maintenance costs.

Although biogas is getting attractive in recent years, biogas technology requires financial support due to the expensive feedstock, feedstock availability, and limited innovations [5]. This innovation is associated with the improvement of products,

*Corresponding author: onurderse@tarsus.edu.tr

Received: 03.01.2023, Accepted: 21.04.2023

processes, and marketing and organization systems. This study includes innovations in the context of location and distribution systems. The main challenge is to demonstrate the effectiveness of a potential biogas supply chain system for a real case study.

The present paper provides the interactions between location of biogas production sites and the location of the BVS for a biogas supply chain. A BVS is a structure that supplies biogas energy for the recharging of vehicles. In the first step, optimal biogas production locations were decided by incorporating the minimization of the costs and maximizing of the biogas energy of cities using the set-covering model. During the second step, BVS location problem, in which population density is included to reduce the total costs, is conducted.

The main contributions of the paper, to the best of our knowledge, it is the first paper to provide a biogas network system including biogas production, distribution, charging of the vehicles with a two-stage approach. New modelling optimization approaches are provided using real-world data. Furthermore, this paper contributes to the literature by regarding maximizing the animal manure amount in addition to the economic benefit for biogas plant production problems. Impacts of vehicle congestion on the optimal BVS location were also investigated.

The rest of the study is organized as follows. Biogas potential for the study area is mentioned. Then, the literature review is examined in detail. Material and method section provide the data used in the case study and methods carried out to solve the problems. The obtained results are presented in the Results and Discussion, Conclusion sections.

2. Literature Review

One of the critical aims in the context of the biogas subject is where to establish the biogas production sites and charging stations. A location problem of biogas reactors was studied in a work [6]. They proposed a mixed-integer nonlinear problem for a biogas supply chain system. They developed a heuristic to obtain the locations of the reactors. A four-stage biogas network was also presented in another work [7]. They developed a mixed-integer mathematical model to decide the locations of hubs and reactors. The paper comprised from collection of the feedstock to delivery of biogas. A linear programming model was provided for the supply chain of bio-fuel production. They also decided feedstock amounts in the model [8]. A biogas network was presented by incorporating energy and mass losses. They proposed a mixed-integer programming to optimize production and investment decisions [9].

The bioenergy supply chain problem was addressed. A mixed-integer linear programming was used to optimize the biogas network considering seasonal and available resource, product recycling [10]. A nonlinear mixed integer model was proposed to locate biogas plants. The model aimed to minimize construction, transportation, labor costs. The model consisted of the collection and storing feedstock and production of the biogas from the feedstock [11]. A facility location selection for biogas energy was provided [12]. Yuruk and Erdogmus [13] addressed optimum location for biogas plant in Düzce, Turkey. The problem including various parameters such as animal species, biogas amounts, agricultural lands, etc. was solved using a goal programming approach.

In recent years, many studies have been conducted to locate the charging stations of alternative energy sources. Many researchers provided location problems of electric vehicle charging stations. A Bayesian model has been developed for the optimal electric vehicle charging station by incorporating sustainability and technical aspects [14]. The problem of the electric vehicle charging stations was addressed by using a genetic algorithm. They also considered the demands and generation of electric vehicles by using the Monte Carlo method [15]. A mathematical model was developed for the optimal location of electric vehicle charging stations and the problem is solved with a modified algorithm. They used k-means clustering to show the relation between charging distance and satisfaction. The results showed that satisfaction increases with the increasing number of electric vehicle stations [16]. A mathematical model was developed to find the optimum location of an electric vehicle charging station. They aimed to provide minimum waiting time, cost, and travel time [17]. P-median model, set covering model, and maximal covering location model are used to compare for the optimal location of electric vehicle stations considering driver behaviors. The P-median model gave better results than other models [18]. An optimization problem was studied for the optimal electric vehicle charging station. They firstly considered the station accessibility and electric vehicle capacity. Four methods including iterative mixed-integer linear programming (MILP), greedy approach, effective MILP, and chemical reaction optimization were used in the study [19]. A mixed-integer nonlinear problem was proposed for optimal electric vehicle charging stations. They aimed to minimize the total costs comprising location costs and electric costs. The problem was solved by a genetic algorithm [20]. A multiple criteria decision-making method was presented to choose the optimal electric

vehicle charging station. Environmental, economic, and social criteria were examined with the Fuzzy TOPSIS (Technique for Order Preference by Similarity to Ideal Solutions) method [21]. Hydrogen energy was also a clean energy source considered as an alternative to other fossil fuels in automotive applications. Therefore, hydrogen-fuelling stations are examined in the context of setup and energy costs [22]. A hydrogen production facility location problem integrating various decisions such as production, storage and transportation, safety, location, and staff assignment was provided in a hydrogen network study [23].

The main novelty of this paper is to present a biogas network system using a developed two-stage mathematical modelling approach for the location of biogas production plant and charging stations of the biogas vehicles. The paper is first dealing with the biogas network in Turkey and a guide for the decision-makers in the energy sector.

The present work contributes to the literature by presenting both maximizing the animal mature term and minimizing the cost for a location decision. Vehicle congestion has not been addressed in the BVS literature. Considering the integration of both biogas production facility and BVS location decisions overcomes the gap.

3. Material and Method

In this section, the first stage considers the location of biogas production facilities using a goal programming approach to handle the two objectives which are

minimization of the costs and maximizing of the biogas energy obtained from the sources. During the second stage, BVS location selection is handled considering population, capacity, cost, density. A simple illustration is given in Figure 1.

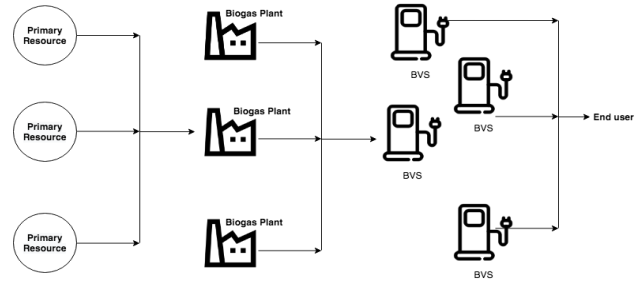


Figure 1. Biogas network proposed in the presented work

Izmir has a high potential with the climate and vegetation geography in terms of agriculture and livestock in Turkey. In addition, İzmir has the potential of biogas with poultry farming [24]. Table 1 demonstrates the total agricultural area, total number of animals (cattle and sheep) of İzmir’s districts in 2018.

Table 2 depicts the total cost to install a biogas facility. The data was obtained from the work of [25].

The goal programming approach was used to achieve more than one goal. Since it is a problem involving binary and integer decision variables, MILP approach was used. During the first stage, a location problem was provided for a biogas production facility. In the second stage, a location problem was provided for a BVS. Nomenclature for the models is demonstrated in Table 3

Table 1. Total agricultural area, total number of animals of İzmir’s districts

Districts	Total Agricultural Area (decare)	Total Number of Animals (Cattle)	Total Number of Animals (Sheep)
Balçova	4.642,6	249	319
Bornova	27.728,4	3.051	5.059
Buca	29.634,0	4.907	5.000
Çiğli	13.504,0	2.615	1.225
Gaziemir	2.704,5	351	399
Güzelbahçe	14.569,3	1.840	5.273
Karşıyaka	3.765,0	189	1.250
Konak	100,0	0	0
Narlıdere	1.787,5	68	306

Aliğa	121.388,0	7.510	5.770
Bayındır	305.593,0	95.264	6.408
Bergama	424.361,0	231	50
Beydağ	49.366,0	67.880	12.565
Çeşme	18.667,0	24.321	489
Dikili	120.967,0	1.824	3.556
Foça	48.222,0	10.507	20.346
Karaburun	38.473,0	18.921	5.412
Kemalpaşa	226.831,0	28	4.517
Kinik	90.791,0	191	30.277
Kiraz	184.152,6	35.099	18.538
Menderes	236.083,0	10.280	14.750
Menemen	232.236,0	99.893	2.747
Ödemiş	336.214,0	25.016	13.326
Seferihisar	87.430,0	16.481	19.521
Selçuk	153.108,0	172.550	13.145
Tire	276.975,0	4.750	22.766
Torbali	309.933,0	3.766	5.559
Urla	86.011,0	127.662	9.530
Bayrakli	215,7	22.280	9.735
Karabağlar	4.771,0	4.850	12.107
Total	3.450.223,6	762.574	249.945

Table 2. Installation cost of biogas facility

Biogas Capacity	250 m ³ /h	500 m ³ /h	750 m ³ /h	1000 m ³ /h	2000 m ³ /h
Installation (Euro)	72.500	97.000	120.000	145.000	195.000
Maintenance	25.000	40.000	60.000	75.000	100.000
Management	10.000	12.000	15.000	17.500	20.000
Electricity	30.000	55.000	86.000	107.500	193.500
Water	8.050	16.125	24.188	32.250	64.500
Chemicals	1.250	2.500	3.750	5.000	10.000
Feedstock	350	625	950	1.205	2.500

Table 3. Nomenclature of the first stage's model

Nomenclature	Description
--------------	-------------

I, J, R	set of biogas facilities, potential districts, primary resources
demand _j	demand for biogas of district j
c _i	installation cost (TL)
d _{ij}	distance between cities
b _i	maintenance cost (TL)
s _i	operating cost (TL)
e _i	electricity cost (TL)
f _i	chemical cost (TL)
h _i	water cost (TL)
a _i	substance cost (TL)
anb _{j,r}	source number
ax _r	animal manure amount obtained from the sources
ay _r	biogas energy obtained from the sources
az _r	processing cost of the animal manure obtained from the source (TL)
sbt	waste transportation cost (TL)
pw _{ri}	the amount of power potential of the station to be installed
w _j	district population
v _{hc}	gasoline vehicles per person
eu	daily euro rate
prc	percentage of all demand to be met
pt	BVS numbers (unit)
km	BVS installation cost
Md	Maximum distance
c _{pti}	biogas facility capacity
v _j	vehicle density
cap	BVS capacity
fp	unit price of fuel divided by euro's fixed rate
goal1	goal 1 value
goal2	goal 2 value
d1, d2	positive and negative deviation values from goal 1, respectively
d3, d4	positive and negative deviation values from goal 2, respectively
x _{ij}	binary decision variable indicating whether the facility i has been decided to be established in district j
y _{ji}	binary decision variable indicating whether the facility i has been decided to be assigned in district j

3.1. First Stage Model

In the first objective function, Equation 1 shows the goal equation. Animal manure amount obtained is maximized (Equation 2), while total costs in which main costs regarding installation costs, animal manure processing cost, and waste transportation cost are available, are minimized Equation (3). Equation (4) shows that all demands must be met. Equation (5) provides a maximum of one plant for the region. Equation (6) calculates the demand parameter. Equation (7) is the non-negativity constraint for decision variables and binary variable constraint.

$$Z = d_1 + d_4 \tag{1}$$

$$\sum_{j=1}^J \sum_{r=1}^R \text{anb}_{jr} * \text{ax}_r * \text{ay}_r * x_{ij} + d_1 - d_2 = \text{goal1} \tag{2}$$

$$\sum_{i=1}^I \sum_{j=1}^J (c_i + b_i + s_i + e_i + h_i + f_i + a_i) * x_{ij} + \sum_{j=1}^J \sum_{r=1}^R \text{anb}_{jr} * \text{ax}_r * \text{ay}_r * x_{ij} * \left(\frac{\text{az}_r}{\text{eu}}\right) \tag{3}$$

$$+ \sum_{i=1}^I \sum_{j=1}^J \sum_{k=1}^K d_{ij} * x_{ij} * \text{sbt} + d_3 - d_4 = \text{goal2}$$

$$\sum_{j=1}^J \sum_{i=1}^I \text{pwr}_i * x_{ij} \geq \sum_{j=1}^J \text{demand}_j * \text{prc} \tag{4}$$

$$\sum_{i=1}^I x_{ij} \leq 1, \forall j \tag{5}$$

$$\text{demand}_j = \text{vhc} * w_j, \quad j = 1, \dots, J \tag{6}$$

$$x_{ij} \in (0, 1) \tag{7}$$

3.2. Second Stage Model

In the objective function, the total transport cost, the total BVS installation cost are minimized and the profit to be gained from the vehicle density is maximized in Equation (8). Equation (9) ensures that minimum one BVS is installed for each region in which a biogas plant is available. Equation (10) defines the vehicle density in the region. Equation (11) ensures that the distance between biogas plant and BVS should be under the given maximum distance constraint. Equation (12) ensures that each BVS is assigned to a biogas plant. Equation (13) is a capacity constraint between the biogas plant and

BVS. Equation (14) addresses the total BVS numbers. Equation (15) is the non-negativity constraint for decision variables and binary variable constraint.

$$\min z = \sum_{i=1}^I \sum_{j=1}^J d_{ij} * \text{sbt} * y_{ji} + \sum_{i=1}^I \sum_{j=1}^J y_{ji} * (\text{km})/\text{eu} - \sum_{i=1}^I \sum_{j=1}^J v_j * y_{ji} * \text{fp} \tag{8}$$

$$\sum_{j=1}^J y_{ji} \geq 1, \forall i \tag{9}$$

$$v_j = \text{vhc} * w_j, \forall j \tag{10}$$

$$d_{ij} * y_{ji} \leq \text{Md}, \forall j, \forall i \tag{11}$$

$$\sum_{i=1}^I y_{ji} \leq 1, \forall j \tag{12}$$

$$\sum_{j=1}^J y_{ji} * \text{cap} \geq \text{cpt}_i, \forall i \tag{13}$$

$$\sum_{i=1}^I \sum_{j=1}^J y_{ji} = \text{pt} \tag{14}$$

$$y_{ji} \in (0, 1), \text{pt} \geq 0 \tag{15}$$

4. Results and Discussion

During the first stage, a location problem of biogas production plants was solved. Goal 1 value as 2*106 and Goal 2 value as 5*107 were incorporated into the system at first. Obtained results demonstrated that defined goals were achieved. d2 and d3 deviations were obtained as 18.510 and 260.399, respectively. Decision variable p, which is the number of the facilities to be opened, was obtained as 2. xij, which is the binary decision variable that gives the status of the plants, implies that 5th type plant which represents 2000 m³ capacity in the Konak region should be installed, 5th type plant which represents 2000 m³ capacity in the Narlidere region should be installed. Table 4 depicts the demands of the districts. demandj was obtained as a need for gasoline per vehicle as a result of multiplying the number of populations in the region (wj), the average number of vehicles per head and the number of gasoline vehicles.

Table 4. Demand results of the districts

Districts	Biomass demand of the region	Districts	Biomass demand of the region
Balçova	3.539,64	Foça	1.477,775
Bornova	19.859,128	Karaburun	472,936
Buca	22.271,892	Kemalpaşa	4.741,316
Çiğli	8.676,593	Kinik	1.329,333
Gaziemir	6.135,414	Kiraz	1.962,085
Güzelbahçe	1.587,546	Menderes	4.183,677
Karşıyaka	15.350,021	Menemen	7.786,253
Konak	15.904,136	Ödemiş	5.910,521
Narlıdere	2.952,919	Seferihisar	1.942,326
Aliağa	4.254,865	Selçuk	1.621,801
Bayındır	1.810,209	Tire	3.767,12
Bergama	4.602,464	Torbali	7.973,946
Beydağ	557,862	Urla	2.959,921
Çeşme	1.939,783	Bayrakli	13.895,216
Dikili	1.970,248	Karabağlar	21.409,296

The number of stations was obtained as 12. The z function, which is the objective function, shows that at the end of one year, the station installation by the value 9952.154 TL will provide the profit rate. Güzelbahçe, Çeşme, Dikili, Seferhisar and Urla districts should obtain biomass resources from the Konak region, while Narlıdere, Balçova, Bayındır, Foça, Karaburun, Kınık and Selçuk should take these resources from the Narlıdere. As a result of the pt decision variable, a total of 12 BVS has been installed.

4.1. Sensitivity Analysis

At the beginning of the model, it is planned to meet 2% of all demand with biofuels. The effects of the coverage rate on the chosen regions are presented in Table 5. When the planning is decided to meet

2,5% of all demand, x_{ij} results as 5th type plant which represents 2000 m³ capacity in the Narlıdere and Bergama regions, as 4th type plant which represents 1000 m³ capacity in the Konak region. When the planning is decided to meet 3% of all demand, x_{ij} results as 5th type plant which represents 2000 m³ capacity in the Konak, Narlıdere and Bergama regions. When the planning is decided to meet 3,5% of all demand, x_{ij} results as 5th type plant which represents 2000 m³ capacity in the Balçova, Narlıdere and Bergama regions and as 3th type plant which represents 750 m³ capacity in the Konak region. When the planning is decided to meet 4% of all demand, x_{ij} results as 5th type plant which represents 2000 m³ capacity in the Balçova, Konak, Narlıdere and Bergama.

Table 5. The effect of demand coverage rate change on the selected region and its structure

prc value	Districts	pwr _i
%2	Konak	5
	Narlıdere	5
%2,5	Konak	4
	Narlıdere	5

	Bergama	5
	Konak	5
	Narlıdere	5
%3	Bergama	5
	Balçova	5
	Konak	3
	Narlıdere	5
%3,5	Bergama	5
	Balçova	5
	Konak	5
	Narlıdere	5
%4	Bergama	5

4.2. Discussion

The usage of biofuels provides both the elimination of wastes and the emergence of clean energy by burning organic wastes. In this study, the location of biogas plant sites and BVS were considered in the province of İzmir in Turkey. In the study, installation decisions were decided for Konak and Narlıdere with a capacity of 2000 m³ and a total capacity of 4000 m³. In the Durmaz and Bilgen [26] study, in which the province of Izmir was discussed and the MILP model was developed, for a 60 km coverage area, Aliğa (150 capacity (1), 1000 capacity (1)), Bayındır (1000 capacity (1)), Foça (1000 capacity (2)), Kemalpaşa (1000 capacity (3)), Seferihisar (150 capacity (1)), Tire (500 capacity (1)), Urla (500 capacity (1)) were obtained. Installing a total capacity of 8300 m³ was decided in this study. Since the share of 2% in total usage was considered in our study, installation of 4000 m³ capacity was decided. However, using the sensitivity analysis, the share of 4% in total usage resulted as the installation in the Balçova, Bergama, Konak, Narlıdere and total 8000 m³ capacity.

5. Conclusion

In this paper, the presenting problem provided a biogas supply chain network problem integrating

biogas plant production problems to minimize the installation costs and to maximize the animal manure amount and BVS installation problem. It is worthy to note that various studies related to the optimization of biogas networks are available in the literature. However, the novelty of this paper lies in maximizing the animal manure amount and impacts of vehicle congestion on the optimal BVS location. The limitation of the study is to consider only İzmir district in Turkey. Since Turkey has a goal to reduce emissions, other cities can be included to generalize the problem. Also, the stochastic optimization approach [27] and fuzzy logic [28] can be considered for the uncertain criteria to decide the biogas plant locations. Considering designing a novel biogas network with low installation, maintenance, process costs and carbon prices [29] is a need for future research.

Data availability

All data and materials are available in manuscript.

Conflict of Interest Statement

All authors declare that they have no conflicts of interest.

Statement of Research and Publication Ethics

The study is complied with research and publication ethics

References

- [1] A. Nikkhah, B. Emadi, H. Soltanali, S. Firouzi, K. A. Rosentrater, and M. S. Allahyari, "Integration of life cycle assessment and Cobb-Douglas modeling for the environmental assessment of kiwifruit in Iran," *Journal of Cleaner Production*, vol. 137, pp. 843-849, 2016.

- [2] E. M. M. Esteves, A. M. N. Herrera, V. P. P. Esteves, and C. D. R. V. Morgado, "Life cycle assessment of manure biogas production: A review," *Journal of Cleaner Production*, vol. 219, pp. 411-423, 2019.
- [3] K. A. Lyng, A. E. Stensgård, O. J. Hanssen, and I. S. Modahl, "Relation between greenhouse gas emissions and economic profit for different configurations of biogas value chains: A case study on different levels of sector integration," *Journal of Cleaner Production*, vol. 182, pp. 737-745, 2018.
- [4] N. Scarlat, J. F. Dallemand, and F. Fahl, "Biogas: Developments and perspectives in Europe," *Renewable Energy*, vol. 129, pp. 457-472, 2018.
- [5] W. M. Budzianowski, "A review of potential innovations for production, conditioning and utilization of biogas with multiple-criteria assessment," *Renewable and Sustainable Energy Reviews*, vol. 54, pp. 1148-1171, 2016.
- [6] B. R. Sarker, B. Wu, and K. P. Paudel, "Optimal number and location of storage hubs and biogas production reactors in farmlands with allocation of multiple feedstocks," *Applied Mathematical Modelling*, vol. 55, pp. 447-465, 2018.
- [7] O. Yaldız, "Biogas technology and investigation for Turkey," *Biyoyakıt Dünyası*, vol. 9, pp. 8-14, 2007.
- [8] P. Illukpitiya, J. F. Yanagida, R. Ogoshi, and G. Uehara, "Sugar-ethanol-electricity co-generation in Hawai'i: An application of linear programming (LP) for optimizing strategies," *Biomass and Bioenergy*, vol. 48, pp. 203-212, 2013.
- [9] I. G. Jensen, M. Münster, and D. Pisinger, "Optimizing the supply chain of biomass and biogas for a single plant considering mass and energy losses," *European Journal of Operational Research*, vol. 262, no. 2, pp. 744-758, 2017.
- [10] L. Čuček, J. J. Klemeš, and Z. Kravanja, "Nitrogen-and climate impact-based metrics in biomass supply chains," *Computer Aided Chemical Engineering*, vol. 34, pp. 483-488, 2014.
- [11] B. Wu, B. R. Sarker, and K. P. Paudel, "Sustainable energy from biomass: Biomethane manufacturing plant location and distribution problem," *Applied Energy*, vol. 158, pp. 597-608, 2015.
- [12] O. Derse, "Biyogaz enerji tesisi için hedef programlama ile yer seçimi problem [Facility location selection problem for biogas energy plant by goal programming]," *Süleyman Demirel Üniversitesi Fen Bilimleri Enstitüsü Dergisi*, vol. 22, pp. 121-126, 2018.
- [13] F. Yuruk, and P. Erdogmus, "Finding an optimum location for biogas plant: a case study for Duzce, Turkey," *Neural Computing and Applications*, vol. 29, no. 1, pp. 157-165, 2018.
- [14] S. Hosseini, and M. D. Sarder, "Development of a bayesian network model for optimal site selection of electric vehicle charging station," *International Journal of Electrical Power & Energy Systems*, vol. 105, pp. 110-122, 2019.
- [15] J. A. Domínguez-Navarro, R. Dufo-López, J. M. Yusta-Loyo, J. S. Artal-Sevil, and J. L. Bernal-Agustín, "Design of an electric vehicle fast-charging station with integration of renewable energy and storage systems," *International Journal of Electrical Power & Energy Systems*, vol. 105, pp. 46-58, 2019.
- [16] Z. Liu, F. Wen, and G. Ledwich, "Optimal planning of electric-vehicle charging stations in distribution systems," *IEEE Transactions on Power Delivery*, vol. 28, no. 1, pp. 102-110, 2013.
- [17] Z. Moghaddam, I. Ahmad, D. Habibi, and Q. V. Phung, "Smart charging strategy for electric vehicle charging stations," *IEEE Transactions on Transportation Electrification*, vol. 4, no. 1, pp. 76-88, 2018.
- [18] Z. Tian, W. Hou, X. Gu, F. Gu, and B. Yao, "The location optimization of electric vehicle charging stations considering charging behavior," *Simulation*, vol. 94, no. 7, pp. 625-636, 2018.

- [19] A. Y. Lam, Y. W. Leung, and X. Chu, "Electric vehicle charging station placement: Formulation, complexity, and solutions," *IEEE Transactions on Smart Grid*, vol. 5, no. 6, pp. 2846-2856, 2014.
- [20] P. Sadeghi-Barzani, A. Rajabi-Ghahnavieh, and H. Kazemi-Karegar, "Optimal fast charging station placing and sizing," *Applied Energy*, vol. 125, pp. 289-299, 2014.
- [21] S. Guo, and H. Zhao, "Optimal site selection of electric vehicle charging station by using fuzzy TOPSIS based on sustainability perspective," *Applied Energy*, vol. 158, pp. 390-402, 2015.
- [22] C. Blazquez-Diaz, "Techno-economic modelling and analysis of hydrogen fuelling stations," *International Journal of Hydrogen Energy*, vol. 44, no. 2, pp. 495-510, 2019.
- [23] O. Derse, E. Göçmen, E. Yılmaz, and R. Erol, "A mathematical programming model for facility location optimization of hydrogen production from renewable energy sources," *Energy Sources, Part A: Recovery, Utilization, and Environmental Effects*, vol. 44, no. 3, pp. 6648-6659, 2022.
- [24] A. O. Avcioğlu, and U. Türker, "Status and potential of biogas energy from animal wastes in Turkey," *Renewable and Sustainable Energy Reviews*, vol. 16, no. 3, pp. 1557-1561, 2012.
- [25] M. Eyidoğan, "Biyogazın saflaştırılması ve motorlu taşıtlarda yakıt olarak kullanılması," *Makine ve Mühendis*, vol. 584, no. 49, pp. 18-24, 2008.
- [26] Y. G. Durmaz, and B. Bilgen, "Multi-objective optimization of sustainable biomass supply chain network design," *Applied Energy*, vol. 272, page 115259, 2020.
- [27] A. B. Ceylan, L. Aydın, M. Nil, H. Mamur, İ. Polatoğlu, and H. Sözen, "A new hybrid approach in selection of optimum establishment location of the biogas energy production plant," *Biomass Conversion and Biorefinery*, pp. 1-16, 2021.
- [28] M. Nosratinia, A. A. Tofigh, and M. Adl, "Determining optimal locations for biogas plants: Case study of Tehran province for utilization of bovine and aviculture wastes," *Journal of Renewable Energy and Environment*, vol. 8, no. 3, pp. 36-44, 2021.
- [29] Y. S. Park, J. Szmerekovsky, and A. Dybing, "Optimal location of biogas plants in supply chains under carbon effects: Insight from a case study on animal manure in North Dakota," *Journal of Advanced Transportation*, vol. 2019, pp. 1-13, 2019.



Sentiment Analyzing from Tweet Data's Using Bag of Words and Word2Vec

Yıldız AYDIN^{1*}

¹Department of Computer Engineering, Erzincan Binali Yildirim University,
Erzincan 24000, Turkey
(ORCID: 0000-0002-3877-6782)



Keywords Natural language processing, Bag of Words, Word2Vec, sentiment analysis

Abstract

Twitter sentiment classification is an artificial approach for examining textual information and figuring out what people's public tweets from a variety of industries are experiencing or thinking. For instance, a large number of tweets containing hashtags are posted online every minute from one user to some other user in the commercial and political fields. It can be challenging for scientists to correctly comprehend the context in which specific tweet terms are used, necessitating a challenge in determining what is actually a positive or negative comment from the vast database of twitter data. The system's authenticity is violated by this issue and user dependability may be significantly diminished. In this study, twitter data sent to interpret movies were classified using various classifiers and feature methods. In this context, the IMDB database consisting of 50000 movie reviews was used. For the purpose of anticipating the sentimental tweets for categorization, a huge proportion of twitter data is analyzed. In the proposed method, bag of words and word2vec methods are given by combining them instead of giving them separately to the classifier. With both the suggested technique, the system's effectiveness is increased and the data that are empirically obtained from the real world situation may be distinguished well. With experimental efficiency of 90%, the suggested approach algorithms' output attempts to assess the reviews' tweets as well as be able to recognize movie reviews..

1. Introduction

The artificially intelligent technique of using natural language to communicate with an information system is known as natural language processing (NLP). Sentiment classification on social media platforms like Facebook and Twitter is one of the most popular uses of NLP. Chatbot, voice recognition, translation software, grammar verification, phrase scanning, information retrieval, and advertising pairing are the possibilities at the following level. This one will make it possible to create a twitter program that can comprehend linguistic forms. It is a component of data analytics that holds the effective algorithm of comprehending, extrapolating, and analyzing text

data in the appropriate manner. Which enables one to process

enormous amounts of textual information, carry out several common operations, and provide answers to a specific set of issues for the previously mentioned future step NLP applications.

NLP and Twitter research are used while performing sentiment analysis and determining the individual emotions of tweets' necessary data. Sentiment classification is now being used to manage tweets' good, unfavorable, and neutral opinions. Sentiment analysis is commonly used in the spirit of community evaluations and poll answers, as well as medical billing and coding information that ranges from a marketing agency to civil administration. It may be

*Corresponding author: yciltas@erzincan.edu.tr

Received: 05.01.2023, Accepted: 09.05.2023

used to write textual information, photos, videos, voice recognition, and other types of information. Sentiment Classification uses comparable types of tweet data; after obtaining this information, it separates the input into individual words or phrases. This process is known as tokenization.

A movie review is similar to a language that expresses a view of the film and forecasts whether the general audience will have a favorable or unfavorable judgment. From all this, we may determine whether to see a certain film or not. A group of producers, actors, and others who participate in making films will be there. The community opinions made on specific cinematic sites determine a film's either success or failure. Website is essential tool for people since they allow them to express their thoughts on a film and submit customer reviews. Community evaluations are therefore gathered as a twitter data set, and after that, specific operations are carried out with this method to find the purchasing habits of customers and to foresee any upcoming releases in the film industry. For this purpose, sentiment analysis studies were conducted with the use of tweets expressing opinions about films in the literature. After receiving the twitter data and information from WordNet, Sahu and Ahuja [1] utilized SentiWordNet to determine the overall polarization of the film critic tweets. The mood of the phrases is included, and the ratings are divided into and positive. Also, there are objective scores in this method. The relative strength of it is determined by the measurement of each of those ratings. An artificial neural model called ConvLstm, built on the CNN and LSTM algorithms, was suggested by Hassan and Mahmood [2]. To lessen the waste of particular local knowledge and catch long-term interdependence in the series of words, they use LSTM as a replacement for CNN's pooling layers. The IMDB and Stanford Sentiment Treebank (SSTb) sentiment databases were used to test this concept. In order to compare their model to SVM and NB, Liao et al. [3] built a straightforward CNN method using word2vec using the data from twitter they acquired. CNN has therefore demonstrated to have an uses better accuracy when it comes to accuracy in comparison to other methods.

Sentiment analysis is now mostly concentrated on social networking, which includes sites like Facebook, Twitter, and IMDB [3], which is driving up demand for general opinions data and gathering it in textual form. Additionally, it is a difficult effort to anticipate the twitter data with an adequate understanding of the language for a movie critic. This study uses the IMDB database for sentiment analysis on English film reviews and identifies the reviews as either positive or negative applying classical machine classifiers. The primary objective of this research is to obtain more successful results by obtaining stronger features with the combination of bag of words and word2vec techniques. Also, NLP feature called stop keywords, which is used to filter frequently occurring tweet terms in the IMDB dataset, is also preprocessed in the proposed method. Due to the fact that these keywords will take up more room in our movie review information or they will fail to provide a coherent phrase for that information. This text content was used to eliminate certain terms for this cause. Word2vec and the bag of words (BoW) method were used in the feature extraction step, while support vector machine (SVM) and logistic regression methods were used in the classification step.

2. Material and Method

A paradigm for sentiment classification is suggested within that chapter. We must analyze the content to extract customer sentiment in an orderly fashion, despite the fact that we are aware that data from social media is not always clear, not always arranged appropriately, and sometimes even contains grammatical mistakes. As a result, we must pre-process the text in order to discern the text's mood. In order to determine whether a particular event is positive or negative, after the preprocessing step, the word is vectorized into numerical form and feature vectors are obtained. In the last step, classification is made using the obtained feature vectors. The methods used in the proposed approach are detailed in the following sub-sections. Figure 1 (the proposed framework for sentiment analysis) depicts all the processes.

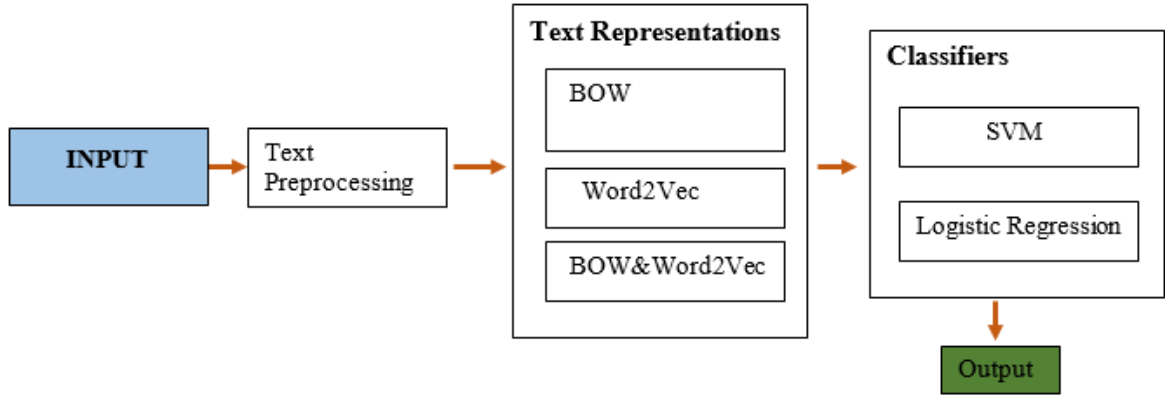


Figure 1. The proposed framework for sentiment analysis

1.1. Pre-processing

To provide a more distinctive representation of tweets data, the following actions have been taken

Cleaning: The goal of cleanliness is to eliminate unnecessary grammar and characters within textual data.

Stop Words Removal: Eliminating words such "the," "a," "an," "they," "she," and others that have no significance and do not sound right inside the content.

1.2. Text Representations

Bag of Words

Bag-of-Words (BoW) [4] presentations is widely used techniques in the field [5]. The i^{th} component of the matrix in the context of the BoW approach denotes the frequency with which the i^{th} vocabulary phrase appeared in the provided content. In other words, rather of utilizing a binary 1 or 0, frequency analysis is utilized to indicate the frequency of a certain word. Although these techniques are straightforward, the presentation does not keep the word's meaning. The linear combination is dense and have the same size as the vocabulary.

Word2Vec

Two linguistic methods are used by Word2vec [6]: the continuous bag-of-words (CBOW) method and the skip-gram method. These techniques use shallow neural network models to map the original word(s) to the targeted word(s).

Processing elements are then used to symbolize the phrases after the system has learned their weights throughout learning. In the CBOW approach, a given target word is produced from a

collection of nearby terms. However, the skip-gram method operates precisely the opposite of the CBOW method. The Skip-gram method uses a single origin word as its input and seeks to identify a cluster of nearby words as its result.

Bag of Words & Word2Vec

The columns of the feature vectors obtained using the bag of words and Word2vec methods were combined and used in the Classifier. The same procedure was applied for each sample.

1.3. Classifiers

Support Vector Machines

Finding a hyper-plane that divided the training data set into two distinct groups is the basic idea behind this classification method [7]. The equations following may be used to make the following claim:

$$w^t x + b = 0 \quad (1)$$

wherein w : denotes the hyper-direction plane's. b depicts the location of the hyper-plane with regard to the origin.

Logistic Regression:

As a technique for classification model, we have employed logistic regression. The logistic regression method, which is one of the supervised classification methods, classifies the test sample using the logistic function [8].

3. Results And Discussion

During the testing stage, an Intel Core i7 CPU, 64-bit operating software, and 8GB RAM were used to run the system design in Python. The IMDB film critic database was used in the suggested approach. The IMDB database includes 50000 reviews in total, of which 25000 are labeled positive and 25000 are labeled negative.

The validity criteria are taken into account as the measuring performance of certain tests on databases for recall, precision, and F score in order to more clearly illustrate the method's analysis. Recall shows the ratio of positive samples correctly detected by the classifier to samples that are actually positively labeled (Equation 2).

$$\text{recall}(r_c) = \frac{TP}{TP+FN} \quad (2)$$

Precision, on the other hand, shows the ratio of samples labeled positively by the classifier and samples correctly detected by the classifier (Equation 3).

$$\text{Precision}(p_r) = \frac{TP}{TP+FP} \quad (3)$$

F score is a metric obtained from precision and recall values, and the size of the F score shows the success of the application (Equation 4).

$$\text{F1 Score} = 2 * \frac{\text{Recall} * \text{Precision}}{\text{Recall} + \text{Precision}} \quad (4)$$

In the experiments carried out within the scope of this manuscript, the feature vectors obtained from the word2vec, bag of words methods and the hybrid feature obtained from the combination of these two features were given to the SVM, logistic regression classifiers and their classifier performances were evaluated. The recall, precision and F1 values of the experiments are given in Table 1, and the confusion matrix graphics are given in Figure 2.

Table 1. Results of experiments

Features	Classifier	Precision	Recall	F-score	Accuracy
Bag of Words	SVM	0.89	0.87	0.88	0.88
	Logistic regression	0.88	0.87	0.87	0.87
Word2Vec	SVM	0.88	0.86	0.87	0.87
	Logistic regression	0.86	0.86	0.86	0.86
Proposed-Method	SVM	0.90	0.89	0.89	0.89
	Logistic regression	0.89	0.88	0.89	0.89

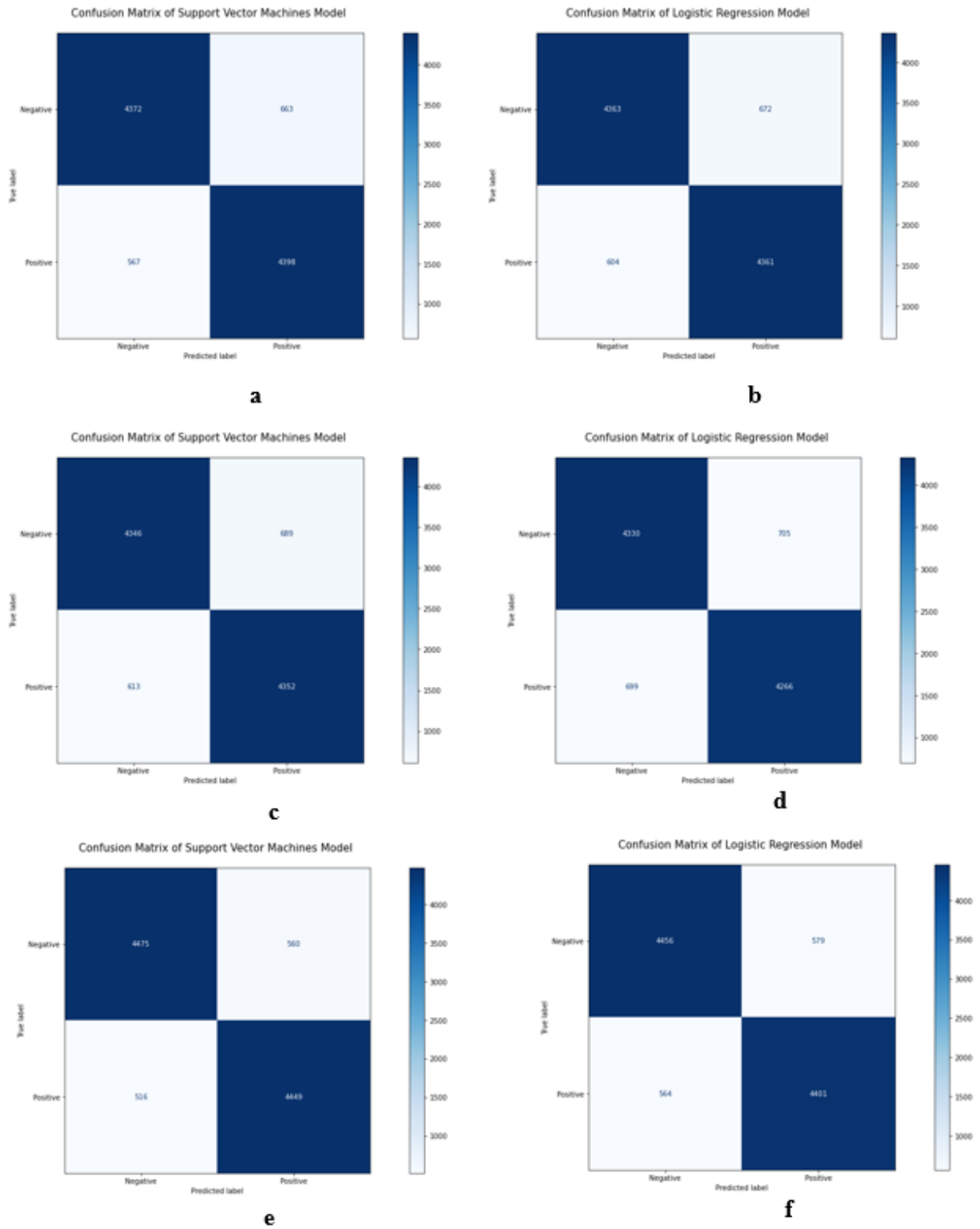


Figure 1. Confusion matrix of applications. a) BoW+SVM, b)BoW+Logistic Regression, c) Word2Vec+SVM, d) Word2Vec+Logistic Regression, e) BoW&Word2vec+SVM, f) BoW&Word2vec +Logistic Regression

As can be seen from Table 1 and Figure 2, using the features together instead of using them separately gave more successful results.

4. Conclusion and Suggestions

In this manuscript, it is proposed to use hybrid features to perform sentiment analysis from tweet data. Word2vec, bag of words and the vector obtained by combining these two methods were used as word representation techniques. As a classifier, the performance of the test results was evaluated by using SVM and logistic regression. In the experiments carried out using the IMDB dataset, 0.88 accuracy value was obtained with bag of words and SVM, 87 percent accuracy rate was obtained with Word2Vec and SVM, while the success rate in the proposed method was 0.89, which was the most successful method.

In addition, more successful results were obtained by combining these two methods rather than using a single bag of words or Word2Vec in other classifiers. In future studies, it is planned to perform sentiment analysis with the hybrid use of these word representation methods and deep learning methods.

Acknowledgment

This project did not receive any funding source

Conflict of Interest Statement

There is no conflict of interest between the authors.

Statement of Research and Publication Ethics

The study is complied with research and publication ethics

References

- [1] T. P. Sahu and S. Ahuja, "Sentiment analysis of movie reviews: A study on feature selection and classification algorithms," *Int. Conf. Microelectron. Comput. Commun. MicroCom 2016*, 2016, doi: 10.1109/MicroCom.2016.7522583.
- [2] A. Hassan and A. Mahmood, "Deep Learning approach for sentiment analysis of short texts," *2017 3rd Int. Conf. Control. Autom. Robot. ICCAR 2017*, pp. 705–710, 2017, doi: 10.1109/ICCAR.2017.7942788.
- [3] S. Liao, J. Wang, R. Yu, K. Sato, and Z. Cheng, "CNN for situations understanding based on sentiment analysis of twitter data," *Procedia Comput. Sci.*, vol. 111, no. 2015, pp. 376–381, 2017, doi: 10.1016/j.procs.2017.06.037.
- [4] J. R. Quinlan, "Programs for machine learning. Part II," in *Machine Learning*, vol. 7, pp. 135–240, 1994.
- [5] J. D. Bodapati, N. Veeranjanyulu, and S. Shaik, "Ingenierie des Systemes d' Information Sentiment Analysis from Movie Reviews Using LSTMs," vol. 24, no. 1, pp. 125–129, 2019.
- [6] T. Mikolov, K. Chen, G. S. Corrado, and J. A. Dean, "Computing numeric representations of words in a high-dimensional space," 2015.
- [7] C. CORTES and V. VAPNIK, "Support-Vector Networks," *Mach. Learning*, vol. 20, no. 3, pp. 273–297, 1995, doi: 10.1109/64.163674.
- [8] Y. Y. Liu, M. Yang, M. Ramsay, X. S. Li, and J. W. Coid, "A Comparison of Logistic Regression, Classification and Regression Tree, and Neural Networks Models in Predicting Violent Re-Offending," *J. Quant. Criminol.*, vol. 27, no. 4, pp. 547–573, 2011, doi: 10.1007/s10940-011-9137-7.



Carbon Dioxide Absorption Using Different Solvents (MEA, NaOH, KOH and Mg(OH)₂) in Bubble Column Reactor

Ayşe GÜL^{1*}, Umran TEZCAN UN²

¹Department of Civil Engineering, Abdullah Gul University, Kayseri, TURKEY

²Department of Environmental Engineering, Eskisehir Technical University, Eskisehir, TURKEY
(ORCID: 0000-0002-2305-6408) (ORCID: 0000-0003-3882-9175)



Keywords: Absorption, Alkaline solvent, Bubble column reactor, MEA (Monoethanolamin)

Abstract

Carbon dioxide is considered to be one of the greenhouse gases potentially responsible for climate change. The aim of this research is to reduce emissions by capturing carbon dioxide in a solution using an absorption method. The absorption capacity, absorption rate, carbon dioxide removal efficiency, and overall mass transfer coefficient of MEA (Monoethanolamin) and alkaline solvents (NaOH, KOH, Mg (OH)₂) were investigated using a bubble column gas absorption reactor with counter current flow. The effects of operational parameters such as solvent concentration (0.01, 0.05, and 0.25M) and solvent type were studied. The research showed that KOH, NaOH, and MEA were more efficient in capturing CO₂ than Mg (OH)₂ was. For all solvent types, the total mass transfer coefficient, absorption rate, and CO₂ removal efficiency were increased with the increase in the concentration of solvent. The solvent concentration is increased from 0.01 M to 0.25 M to obtain the highest KGa values for MEA, NaOH, and KOH, 3.75 1/min for MEA, 3.70 1/min for NaOH, and 3.93 1/min for KOH. The MEA, NaOH, and KOH absorption rates were maximum at 0.25 M solvent concentrations as 0.19x10³ mol/Ls. The maximum CO₂ removal efficiencies for MEA, NaOH, and KOH at 0.25 M solvent concentration are greater than 60%. Absorption capacity of NaOH and KOH is 0.313 mol CO₂/mol NaOH and 0.316 (mol CO₂/mol KOH). The highest absorption capacity, 0.576 mol CO₂/mol MEA, was obtained at a solvent concentration of 0.01M MEA.

1. Introduction

The temperature of the Earth has risen especially quickly since the middle of the 20th century. Global warming emerges as one of the concerns facing the planet during the industrial revolution. Natural and human systems have undergone significant changes in response to long-term changes in the climate system caused by global warming. These changes include an increase in the frequency of catastrophic events like floods and droughts, a rise in sea level caused by glacier and polar ice cap melting, and severe ecological destruction that threatens the sustainability of the economy [1, 2].

Fossil fuels are used to generate the majority of the energy needed to meet the growing demand, which raises the atmospheric carbon concentration. Fossil fuel consumption contributes to the release of greenhouse gases such carbon dioxide (76%), methane (16%), nitrous oxide (6%), and fluorinated gases (2%) on a worldwide scale. Carbon dioxide (CO₂) is therefore frequently viewed as the main contributor to rising world average temperatures [3, 4].

The majority of today's energy needs are met by the generation of electricity from fossil fuels, carbon capture and storage (CCS) is the best option for decreasing CO₂ emissions. Pre-combustion capture, post-combustion capture, and oxy-fuel

*Corresponding author: ayse.gul@agu.edu.tr

Received: 06.01.2023, Accepted: 09.05.2023

combustion are three groups of CO₂ capturing technologies. Among these, post-combustion capture using alkanolamines is considered as one of the most practical and widely used for the removal of CO₂ successfully [5]. There are various methods to reduce emissions of CO₂ post combustion such as chemical absorption [6], physical absorption [7], membrane separation [8], adsorption [9], cryogenic separation [10] and algal system [11]. In these processes, chemical absorption with NaOH and amine solutions are extensively used for the capture of CO₂ [12].

Aqueous MEA solution has been widely used to capture CO₂ in industrial processes due to its strong CO₂ reaction kinetics, high solubility in water, low viscosity, lower energy use, and low cost. [13]. Alkaline solvents that widely used in CO₂ removal are NaOH which has high absorption efficiency and potassium hydroxide (KOH) [14]. It is possible to enhance CO₂ absorption by utilizing different scrubber and solvent kinds. Numerous scrubbers, such as packed bed columns, sieve tray columns, and bubble columns, are used to capture CO₂.

Bubble column reactors offer a variety industrial application due to its simple design and operation, lack of moving parts, highly complicated hydrodynamic behavior, and high rates of mass and heat transfer [15]. Specifically, the packed tower and bubble column have been effectively used on pilot and industrial scales for post-combustion CO₂ capture [16].

The aim of this research is to improve the CO₂ absorption using different solvents. For this aim, the capture of CO₂ was performed using MEA and alkaline solvents (NaOH, KOH and Mg (OH)₂) in a bubble column. The effect of solvent types on the CO₂ removal capacity, absorption rate and overall mass transfer coefficient was determined.

2. Calculations

CO₂ Removal Efficiency

CO₂ removal efficiency is a critical consideration when assessing the performance of an absorption and calculated using Eq.1.

$$E = \left(\frac{y_1 - y_2}{y_1} \right) * 100\% \quad (1)$$

y₁ = CO₂ input concentration; y₂ = CO₂ output concentration

Absorption Rate

The most crucial factor in determining solvent costs, which account for around 30% of overall capital costs, is CO₂ absorption rate (RA) [17]. Liquid holdup (and gas holdup) is considered constant throughout the column to determine the absorption rate. As a result, under steady-state operation, the rate of carbon dioxide absorption can be determined. Absorption rate is determined using Eq.2 by measuring the effluent concentration of carbon dioxide and the gas-flow rate:

$$R_A = \frac{FA_1}{V_L} \left[1 - \left(1 - \frac{y_1}{y_2} \right) \left(\frac{y_2}{1 - y_2} \right) \right] \quad (2)$$

FA₁ = molar flow rate of CO₂ inlet

V_L = Solvent solution volume (final volume)

y₁ and y₂ = CO₂ concentration of inlet and outlet

R_A = Absorption rate

Overall Mass Transfer Coefficient

In separation processes, the diffusion of mass from one phase to the other is occurred, and the diffusion rate is a crucial factor that effect the overall mass transfer coefficient. The two-film model, a helpful model for mass transfer between phases, is used to calculate the mass transfer coefficient and the mass transfer of CO₂. CO₂ is transferred from the bulk of the gas phase to the interface and then moved from the interface into the bulk of the liquid phase during mass transfer. The two film model assumes equilibrium at the interface (Fig. 1).

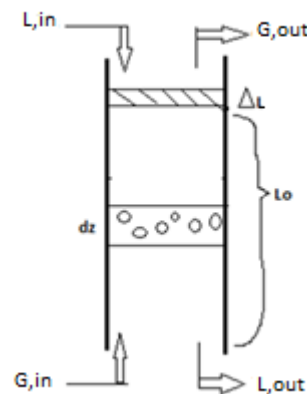


Figure 1. Schematic representation of two film theories

According to two film model, the absorption rate at a local point on both the gas and liquid side is expressed as total mass transfer coefficients and can be written as follows;

$$r_A = (K_G a)(C_g - HC_L) \quad (3)$$

With the assumption of plug flow condition at the gas phase and well mixed flow condition at the liquid phase and steady state condition, the mass equilibrium at z will be;

$$(U_g C_g)_z^S - (U_g C_g)_{z+\Delta z}^S = r_A \Delta V \quad (4)$$

$$\Delta V = \Delta z * S \quad (5)$$

Readjust the equation;

$$(U_g C_g)_z \cdot S - (U_g C_g)_{z+\Delta z} \cdot S = K_G a \cdot (C_g - HC_L) (\Delta z \cdot S); \quad (6)$$

$$\frac{S \cdot U (C_{gz} - C_{gz+\Delta z})}{\Delta z} = K_G a \cdot (C_g - HC_L) \cdot S \quad (7)$$

$$HC_L \approx 0$$

$$S \cdot U \frac{dC}{dz} = S \cdot K_G a \cdot (C_g) \quad (8)$$

$$Q \frac{dC}{c} = S \cdot K_G a \cdot dz \quad (9)$$

$$Q \int_{C_{in}}^{C_{out}} \frac{dC}{c} = \int_0^{L+\Delta L} S \cdot K_G a \cdot dz \quad (10)$$

$$K_G a = \frac{Q_g \ln \frac{C_0}{C}}{(\Delta L + L) \cdot S} \quad (11)$$

Where; C_g , CO_2 gas concentration in gas phase (mol/L); CL , CO_2 gas concentration in liquid phase (mol/L); r_A , absorption rate (mol/Ls) ; $K_G a$, mass-transfer coefficient (1/min), S : column cross sectional area (cm^2), U : surface velocity (m/s) , Q , velocity of gas flow (l/min)

Absorption capacity

The area over the CO_2 -time profile graph (Fig. 2) corresponds to the total absorbed CO_2 . The input flow rate of CO_2 was calculated from total flow rate and the inlet concentration. The outlet flow rate of CO_2 was calculated based on the fixed flow rate of N_2 which was an inert compound and the read CO_2 concentration. The following relation was used to calculate the CO_2 outlet flow;

$$Q_{CO_2out} = Q_{totalin} \times y_{N_2in} \left(\frac{y_{CO_2out}}{y_{N_2out}} \right) \quad (12)$$

The volumetric flow rates were converted to molar mass flow rate using conversion factors with the assumption of ideal gas of state where each mole at standard temperature (273 K) and pressure (1 atm) occupies 22.4 L. Then it calculated again for the adjusted temperature of gas. Then the concentration (ppm)-time graph was replotted for mass flow rate-time.

The rate of absorbed CO_2 at certain time intervals was then calculated using following equation;

$$R_{CO_2} = \dot{M}_{CO_2in} - \dot{M}_{CO_2out} \quad (13)$$

The amount of absorbed CO_2 at each time interval was calculated using following equation;

$$M_{CO_2ab} = R_{CO_2} \times (t_2 - t_1) \quad (14)$$

The absorption capacity of the absorbent was calculated using below equation;

$$Ab. Cap = \frac{\sum_1^n M_{CO_2ab}}{M_{MEA}} \quad (15)$$

Where n is the number of time intervals, M_{CO_2} is the mass of absorbed CO_2 and M_{MEA} is the mass of MEA in the solution. Spreadsheets in MS Excel was used for calculation procedures.

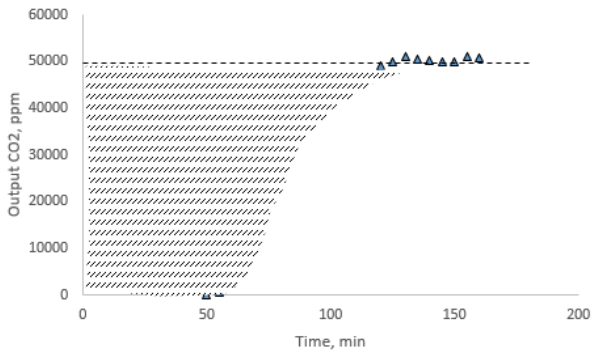


Figure 2. A sample of the CO₂ concentration profile at the output

2.1. Chemical Reaction Mechanism

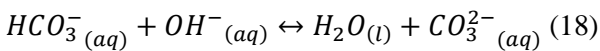
NaOH

NaOH is the widely used solvent for the CO₂ capture even though, solvent is not recoverable from the reaction between CO₂ and NaOH, because it is more abundant, cheaper than MEA, and has higher CO₂ absorption capacity than MEA. Theoretically, 1.39 tons MEA and 0.9 tons NAOH required to capture one ton of CO₂, respectively. As shown below, the process by which CO₂ is absorbed by NaOH in aqueous solution [15];

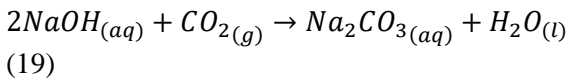
Firstly, NaOH is completely ionized in water. Secondly, when gas fed into the NaOH solution, carbon dioxide is physically absorbed as aqueous carbon dioxide because NaOH is strongly alkaline.



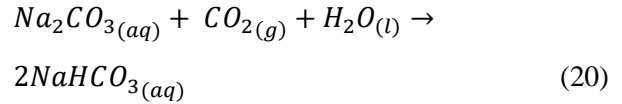
Subsequently, aqueous CO₂ reacts with OH⁻ as expressed in Eqs. 17 and 18 to form HCO₃⁻ and CO₃²⁻



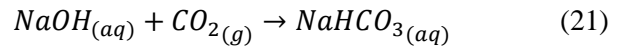
The reaction that occurring during CO₂ absorption is shown below;



The Na₂CO₃ produced in this reaction exists in solvent as ionized Na⁺ and CO₃²⁻. The NaOH solution is continuously fed CO₂, which causes CO₂ to be absorbed and deplete the OH⁻ level. The general absorption reaction is shown in equation 20.

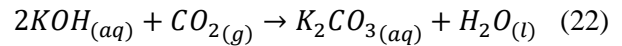


The net reaction of equations 2.19 and 2.20 can be summarized as equation 21 [12].



KOH

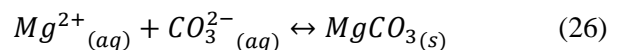
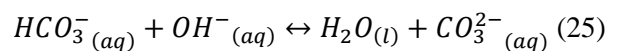
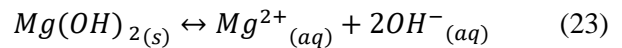
In the process of removing CO₂, potassium hydroxide (KOH) is the second-most-used solvent. The reaction with carbon dioxide can be seen in Eq. 22.



KOH and NaOH are both used in the same chemical reaction for the absorption of CO₂. However, KOH is more expensive than NaOH, but the cost of KOH can be reduced by selling the side product of K₂CO₃ [18].

Mg (OH)₂

Absorption with magnesium hydroxide Mg (OH)₂ occur in several stages and the main reactions involved in the absorption process are as follows:



Dissolution of solid particles in the liquid film increases the absorption rate [19].

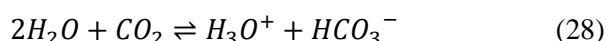
MEA

A key solvent in the CO₂ removal process is monoethanolamine (MEA) solution due to how rapidly it reacts with carbon dioxide [20]. The reaction mechanism among H₂O-CO₂-amine differs based on the number of amine functionality. The reaction mechanism for single amine functionality like MEA has been suggested as follow [21]:

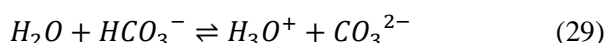
Water dissociation:



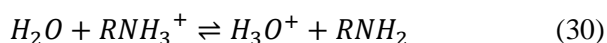
Carbon dioxide dissociation:



Bicarbonate dissociation:



Dissociation of protonated MEA:



Carbamate reversion to bicarbonate:



3. MATERIALS AND METHOD

3.1. Chemicals

The chemicals of NaOH, KOH, Mg(OH)₂, MEA were purchased from Merck, Germany. All of the chemical was of the reagent grade. Double-distilled water which was obtained in the lab using a water purification equipment (Thermo Scientific, Germany) was used to prepare the aqueous solutions. The gas phase consisted of CO₂ and N₂ was prepared using CO₂ and N₂ gas cylinders (99.99% purity) obtained from Oksan LTD, Turkey.

3.2. Experimental setup

The absorption bubble column used in this study can be seen in Fig.3. It is made from plexiglass with the height of 1m and internal diameter (ID) of 5 cm. It was operated counter current flow in which downflow of the liquid and upflow of the gas were applied. All the absorption experiment were carried out at room temperature, For each experiment, the temperature of the water circulation bath was adjusted on the desired temperature and run for almost 25 min to ensure stable temperature on the vessel wall. The solutions was prepared in parallel and put over hot plate to obtain the desired temperature and quickly empty into solvent tank and left for 10 minutes to stabilize the temperature. The desired solvent concentration was prepared and poured into the feed tank. The pump is used to control the required liquid flow rate. The gas mixture was supplied using two separate mass flow controllers (ALICAT Scientific Mass Flow Controller, Range:0-10L/min, accuracy; %0,2 of full-scale) for nitrogen and carbon dioxide. The gas mixture was sent directly to the CO₂ analyzer to confirm the initial CO₂ concentration, and then the main line valves were opened to transfer the gas mixture to the column containing MEA solution. The carbon dioxide concentration in the gas phase in the output was monitored using a Vernier CO₂ gas sensor (USA). The process continued until there was no further absorption. This was confirmed by the concentration/time profile as shown in Fig. 2.

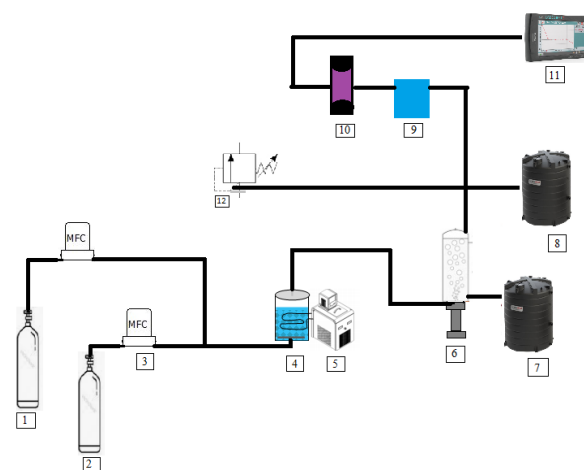


Figure 3. Experimental setup of CO₂ absorption.

(1: CO₂ cylinder, 2: N₂ cylinder, 3: Mass flow controller, 4: Humidifier, 5: Heat exchanger, 6: Column, 7: Waste tank, 8: Solvent tank, 9: Dehumidifier gas regulator, 10: Dehumidifier, 11:

CO₂ Analyzer (10.000-100.000ppm), 12: Relief valve.)

4. Results and Discussion

In this study various solvent type and concentrations were used to determine its effects on CO₂ absorption. MEA, NaOH, KOH, and Mg(OH)₂ solvents were used for this purpose at concentrations of 0.01 M, 0.05 M, and 0.25 M. Results are presented for a gas flow rate of 4 L/min and a liquid flow rate of 500 mL/min.

4.1. Effect of Solvent Concentration on CO₂ Removal Efficiency

The effects of MEA, NaOH, KOH and Mg(OH)₂ solvents concentrations (0.01-0.05-0.25M) on carbon dioxide removal efficiency were investigated at 4.0 L/min gas flow rate, 500 mL/min liquid flow rate and 5% CO₂ initial concentration (50 000 ppm) and results can be seen from Fig. 4. For all solvent types, it has been observed that the CO₂ removal efficiency increases when the solvent concentration increases. However, the difference in CO₂ removal efficiency is not very noticeable at high concentrations of NaOH and KOH. High CO₂ removal efficiencies were also obtained at low solvent concentrations. The regeneration of NaOH, KOH, and Mg(OH)₂ is quite difficult, in contrast to MEA regeneration. The regeneration of NaOH and KOH solvents is difficult because the final products Na₂CO₃ and K₂CO₃ are formed as a result of absorption and their regeneration is costly due to their high energy requirements [18]. The increase in solvent concentration also means the increase in the reactant amount which leads to higher CO₂ removal [15]. High active MEA concentration in the liquid solution encourages its diffusion to the gas-liquid interface [22]. Similarly, Yincheng et al. found that a higher NaOH concentration increases CO₂ removal efficiency [23].

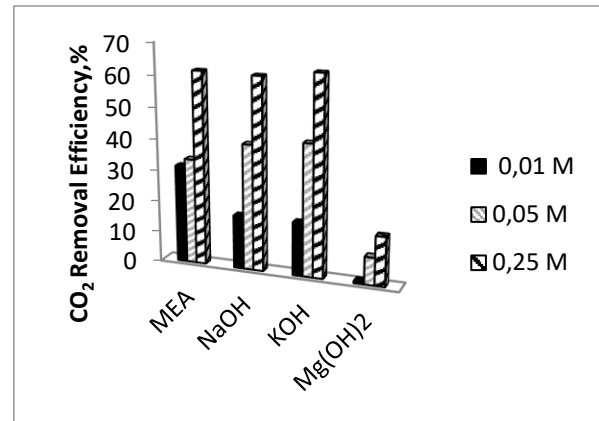


Figure 4. Effects of solvent concentrations on CO₂ removal efficiency.

4.2. Effect of Solvent Concentration on Absorption Capacity

The solvent concentration has a significant effect on absorption capacity. The impact of various solvent concentrations on absorption capacity in the bubble column is shown in Fig. 5. The gas flow rate of 4.0 L/min, solvent flow rate of 500 mL/min and the CO₂ concentration of 50000 ppm are used. As seen from Fig.5, low concentration of solvents has a better absorption capacity, which means that higher amount of CO₂ was absorbed by a mol of solvent. The highest absorption capacity was obtained at solvent concentration of 0.01M MEA as 0.576 mol CO₂/mol MEA. Absorption capacity of NaOH and KOH is 0.313 mol CO₂/mol NaOH and 0.316 (mol CO₂/mol KOH), respectively.

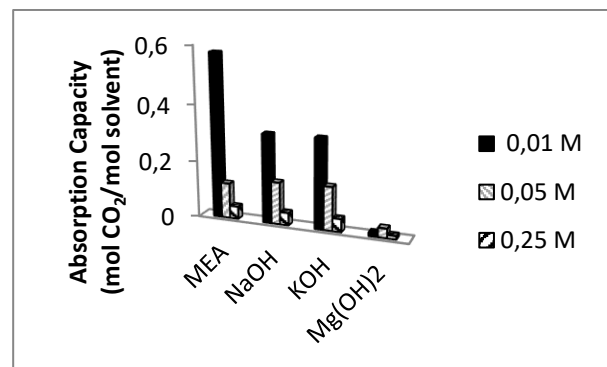


Figure 5. Effects of solvent concentrations on absorption capacity.

The increase in the solvent concentrations from 0.01 to 0.25 mol/L, decreases the absorption

capacity in the bubble column. Similar trends were found in the literature [15].

4.3. Effect of Solvent Concentration on Absorption Rate

The effect of different solvent concentrations on absorption rate in the bubble column is shown in Fig. 6. The absorption rates were increased with the increase of solvent concentration and absorption rates of MEA, NaOH and KOH are almost same at 0.25M.

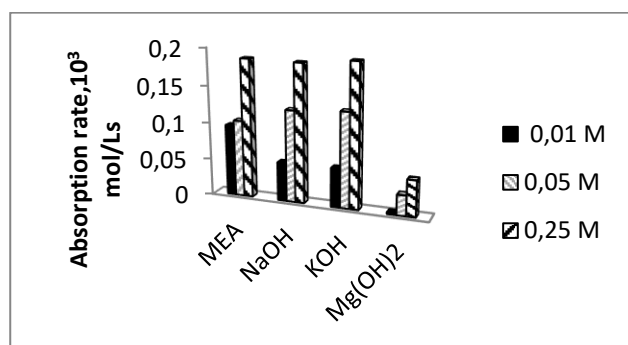


Figure 6. Effects of solvent concentrations on absorption rate.

Chen Chi obtained absorption rate of 0.0135 - 0.622 (103 mol / Ls) at 4 M MEA in bubble column [25]. Yoo et al. investigated the capacity, rate, and efficiency of CO₂ absorption by NaOH aqueous solution in a batch-style Pyrex cylindrical reactor. They found that the absorption rate increased with the concentration of NaOH [14].

4.4. Effect of Solvent Concentration on Overall Mass Transfer Coefficient

The effect of various solvent concentrations on the total mass transfer coefficient in the bubble column is shown in Fig. 7. Except for Mg (OH)₂, the mass transfer coefficients of the solvents were similar at 0.25 M solvent concentration, however it sharply declined at lower concentrations. As shown in Fig. 7, an increase in the solvent concentration results a higher KGa value. When the solvent concentration is increased from 0.01 M to 0.25 M, the KGa value increases from 1.47 1/min to 3.75 1/min for MEA, from 0.72 1/min to 3.70 1/min for NaOH, from 0.74 1/min to 3.93 1/min for KOH, and from 0.027 1/min to 0.67 1/min for Mg (OH)₂.

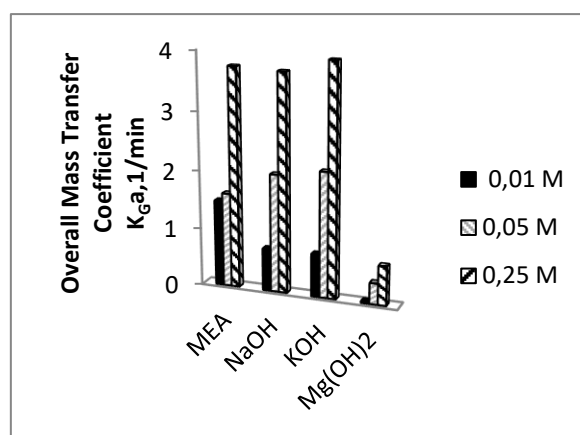


Figure 7. Effects of solvent concentrations on overall mass transfer coefficient.

Wu et al. found that when the MEA concentrations increase from 10 wt.% to 40 wt.% at a fixed 12 vol% CO₂ inlet concentration, the overall mass transfer coefficient increases from 0.2943 to 0.4044 kmol/m³. h. kPa. This is caused by the fact that an increase in MEA concentration produces more active MEA molecules that are available to diffuse toward the gas-liquid surface and subsequently react with CO₂ molecules, which increases the reaction enhancement factor and results in better mass transfer performance [26]. According to Cheng et al., a higher Mg (OH)₂ concentration results in a higher mass transfer coefficient [27].

5. Conclusion

In this study, the effects of solvent type and concentration on absorption capacity (mol CO₂/mol solvent), absorption rate (mol/Ls), carbon dioxide removal efficiency (%), and total mass transfer coefficient (1/min) was investigated using a bubble column reactor with a countercurrent flow. Experiments were performed at gas flow rate of 4.0 L/min, liquid flow rate of 500 mL/min and 5% CO₂ initial concentration. Experimental results show that the aqueous solvent concentrations have a great effect on the absorption capacity, absorption rate, carbon dioxide removal efficiency and total mass transfer coefficient. With the increasing solvent concentration, the overall mass transfer coefficient, absorption rate, and CO₂ removal efficiency increased while the absorption capacity decreased. The CO₂ concentration of 50000 ppm

was reduced to the 20000 ppm with the approximately removal efficiency of %60 using bubble column. When the solvent concentration is increased from 0.01 M to 0.25 M, the KGa value increases from 1.47 1/min to 3.75 1/min for MEA, from 0.72 1/min to 3.70 1/min for NaOH, from 0.74 1/min to 3.93 1/min for KOH, and from 0.027 1/min to 0.67 1/min for Mg (OH)₂. The highest absorption rates for MEA, NaOH, and KOH were obtained at 0.25 M solvent concentrations as 0.19x10³ mol/Ls. The highest absorption capacity was obtained at solvent concentration of 0.01M MEA as 0.576 mol CO₂/mol MEA. Absorption capacity of NaOH and KOH is 0.313 mol CO₂/mol NaOH and 0.316 (mol CO₂/mol KOH), respectively. As a result of the study, it can be said that the removal of CO₂ from flue gases using bubble column can be achieved successfully.

Acknowledgment

This project was funded by Anadolu University under project no. 1706F386.

Contributions of the Authors

All authors contributed to the study conception and design. Material preparation, data collection and analysis were performed by Ayse Gul and Umran Tezcan Un.

Conflict of Interest Statement

There is no conflict of interest between the authors.

Statement of Research and Publication Ethics

The study is complied with research and publication ethics

References

- [1] H. B. Ameer, X. Han, Z. Liu, and J. Peillex, "When did global warming start? A new baseline for carbon budgeting," *Econ. Model.*, vol. 116, no. 106005, p. 106005, 2022.
- [2] H.-I. Eum, B. Fajard, T. Tang, and A. Gupta, "Potential changes in climate indices in Alberta under projected global warming of 1.5–5 °C," *J. Hydrol. Reg. Stud.*, vol. 47, no. 101390, p. 101390, 2023.
- [3] A. Elhambakhsh, M. R. Zaeri, M. Mehdipour, and P. Keshavarz, "Synthesis of different modified magnetic nanoparticles for selective physical/chemical absorption of CO₂ in a bubble column reactor," *J. Environ. Chem. Eng.*, vol. 8, no. 5, p. 104195, 2020.
- [4] A. Balraj, A. P. C. Sekaran, N. Ramamurthy, R. Babarao, K. K. Nagarajan, and S. A. Mayilvahanan, "Systematic review on sono-assisted CO₂ stripping, solvent recovery and energy demand aspects in solvent-based post-combustion carbon dioxide capture process," *Chem. Eng. Process.*, vol. 170, no. 108723, p. 108723, 2022.
- [5] H. Ling, S. Liu, H. Gao, and Z. Liang, "Effect of heat-stable salts on absorption/desorption performance of aqueous monoethanolamine (MEA) solution during carbon dioxide capture process," *Sep. Purif. Technol.*, vol. 212, pp. 822–833, 2019.
- [6] W. He, S. Zhang, C. Zhu, T. Fu, and Y. Ma, "CO₂ chemical absorption into AMP aqueous solution and mass transfer intensification in cascade sudden expansion microchannels," *Chem. Eng. Process.*, no. 109142, p. 109142, 2022.

- [7] Y. Li et al., "Synergetic effect and mechanism between propylene carbonate and polymer rich in ester and ether groups for CO₂ physical absorption," *J. Clean. Prod.*, vol. 336, no. 130389, p. 130389, 2022.
- [8] W.-H. Lai, D. K. Wang, M.-Y. Wey, and H.-H. Tseng, "ZIF-8/styrene-IL polymerization hollow fiber membrane for improved CO₂/N₂ separation," *J. Clean. Prod.*, vol. 372, no. 133785, p. 133785, 2022.
- [9] K. Kielbasa, Ş. Bayar, E. A. Varol, J. Sreńscek-Nazzal, M. Bosacka, and B. Michalkiewicz, "Thermochemical conversion of lignocellulosic biomass - olive pomace - into activated biocarbon for CO₂ adsorption," *Ind. Crops Prod.*, vol. 187, no. 115416, p. 115416, 2022.
- [10] Y. Bi and Y. Ju, "Design and analysis of CO₂ cryogenic separation process for the new LNG purification cold box," *Int. J. Refrig.*, vol. 130, pp. 67–75, 2021.
- [11] H. Leflay, J. Pandhal, and S. Brown, "Direct measurements of CO₂ capture are essential to assess the technical and economic potential of algal-CCUS," *J. CO₂ util.*, vol. 52, no. 101657, p. 101657, 2021.
- [12] P.-C. Chen, W. Shi, R. Du, and V. Chen, "Scrubbing of CO₂ greenhouse gases, accompanied by precipitation in a continuous bubble-column scrubber," *Ind. Eng. Chem. Res.*, vol. 47, no. 16, pp. 6336–6343, 2008.
- [13] Z. Ziobrowski, R. Krupiczka, and A. Rotkegel, "Carbon dioxide absorption in a packed column using imidazolium based ionic liquids and MEA solution," *Int. J. Greenhouse Gas Control*, vol. 47, pp. 8–16, 2016.
- [14] M. Yoo, S.-J. Han, and J.-H. Wee, "Carbon dioxide capture capacity of sodium hydroxide aqueous solution," *J. Environ. Manage.*, vol. 114, pp. 512–519, 2013.
- [15] H. Pashaei, M. N. Zarandi, and A. Ghaemi, "Experimental study and modeling of CO₂ absorption into diethanolamine solutions using stirrer bubble column," *Chem. Eng. Res. Des.*, vol. 121, pp. 32–43, 2017.
- [16] F. Chu, L. Yang, X. Du, and Y. Yang, "Mass transfer and energy consumption for CO₂ absorption by ammonia solution in bubble column," *Appl. Energy*, vol. 190, pp. 1068–1080, 2017.
- [17] Y. Yuan and G. T. Rochelle, "CO₂ absorption rate in semi-aqueous monoethanolamine," *Chem. Eng. Sci.*, vol. 182, pp. 56–66, 2018.
- [18] F. R. H. Abdeen, M. Mel, M. S. Jami, S. I. Ihsan, and A. F. Ismail, "A review of chemical absorption of carbon dioxide for biogas upgrading," *Chin. J. Chem. Eng.*, vol. 24, no. 6, pp. 693–702, 2016.
- [19] T. Li, T. C. Keener, and L. Cheng, "Carbon dioxide removal by using Mg(OH)₂ in a bubble column: Effects of various operating parameters," *Int. J. Greenhouse Gas Control*, vol. 31, pp. 67–76, 2014.
- [20] R. Maceiras, E. Álvarez, and M. Á. Cancela, "Effect of temperature on carbon dioxide absorption in monoethanolamine solutions," *Chem. Eng. J.*, vol. 138, no. 1–3, pp. 295–300, 2008.
- [21] U. E. Aronu et al., "Solubility of CO₂ in 15, 30, 45 and 60 mass% MEA from 40 to 120°C and model representation using the extended UNIQUAC framework," *Chem. Eng. Sci.*, vol. 66, no. 24, pp. 6393–6406, 2011.

- [22] H. N. Abdul Halim, A. M. Shariff, L. S. Tan, and M. A. Bustam, "Mass transfer performance of CO₂ absorption from natural gas using monoethanolamine (MEA) in high pressure operations," *Ind. Eng. Chem. Res.*, vol. 54, no. 5, pp. 1675–1680, 2015.
- [23] G. Yincheng, N. Zhenqi, and L. Wenyi, "Comparison of removal efficiencies of carbon dioxide between aqueous ammonia and NaOH solution in a fine spray column," *Energy Procedia*, vol. 4, pp. 512–518, 2011.
- [24] J. I. Huertas, M. D. Gomez, N. Giraldo, and J. Garzón, "CO₂ Absorbing Capacity of MEA," *J. Chem.*, vol. 2015, pp. 1–7, 2015.
- [25] P.-C. Chen, "Absorption of carbon dioxide in a bubble-column scrubber," in *Greenhouse Gases - Capturing, Utilization and Reduction*, InTech, 2012.
- [26] X. Wu, M. He, Y. Yu, Z. Qin, and Z. Zhang, "Overall mass transfer coefficient of CO₂ absorption in a diameter-varying spray tower," *Energy Procedia*, vol. 114, pp. 1665–1670, 2017.
- [27] L. Cheng, T. Li, T. C. Keener, and J. Y. Lee, "A mass transfer model of absorption of carbon dioxide in a bubble column reactor by using magnesium hydroxide slurry," *Int. J. Greenhouse Gas Control*, vol. 17, pp. 240–249, 2013.

NMR Spectroscopy in the Earth's Magnetic Field

Cengiz AKAY¹, Handan ENGİN KIRIMLI^{1*}

¹ Bursa Uludağ University, Sciences and Arts Faculty, Physics Departments, Bursa, Turkey
(ORCID: 0000-0002-8037-0364) (ORCID: 0000-0003-0300-3381)



Keywords: Spin concept, NMR signals, MR imaging, NMR parameters, Magnetic field of the earth (EFNMR).

Abstract

Today, magnetic imaging systems used are quite expensive and are generally used for medical purposes. Apart from this purpose, there are many scientific fields of study whose internal structure is desired to be displayed. Especially in science, different from the techniques used to understand the internal structure of matter, magnetic imaging techniques are also needed. Therefore, the interest in more useful and smaller magnetic imaging systems is increasing. For this purpose, studies on magnetic particle imaging and magnetic resonance imaging techniques have gained momentum. The magnetic resonance imaging technique, which is one of the magnetic imaging systems based on the NMR phenomenon, has passed through numerous stages and has become smaller and more useful. This study examines the basic components of the NMR images made in the earth's magnetic field for different liquids, the T_1 and T_2 proton relaxation parameters, and the technique of the obtained two-dimensional images with the EFNMR system.

1. Introduction

There are various imaging techniques in the field of biomedical and medical physics. Among the imaging techniques, magnetic resonance imaging (MRI) is an effective, powerful, and reliable method. Medical physicists are finding better opportunities by working towards the design of this imaging technique every day [1,2]. MRI is widely used to visualize the structures and functions of living systems and protozoa. However, MRI is an imaging technique that is also used in medical radiology and has no harmful effects. It is best today, especially for anatomical images of organ tissues [3,4]. Nuclear magnetic resonance (NMR) spectroscopy is a complementary method in determining the structure and behavior of solid-state materials [5-7]. This technique is often used in many fields of materials research, as it can provide comprehensive information at the atomic scale [8,9].

The magnetic resonance imaging technique is based on the resonance phenomenon, which is the nuclear magnetic resonance phenomenon, which is realized by stimulating the protons in a uniform magnetic field with a radio frequency field of

appropriate frequency. In order to obtain an image of the molecular structure and dynamics that are desired to be visualized, a magnetic field environment as homogeneous as possible is required. Thanks to the perfection of the magnetic medium, the signal intensities obtained are large and this affects the quality of the images. The source of the signals is due to the spin property inherent in NMR-sensitive nuclei. Atoms with an odd number of protons or neutrons such as hydrogen (^1H), oxygen (^{17}O), fluorine (^{19}F), sodium (^{23}Na), phosphorus (^{31}P), and potassium (^{39}K) have a spin property and these atoms are used as signal sources in MRI [10]

In magnetic resonance imaging, hydrogen, also known as the proton, which has a spin feature is used. Especially in organic chemistry, NMR signals of protons give essential information about the internal structure of compounds. Chemical shift, spin-spin interactions, diffusion coefficients, and spin relaxation times are the most important NMR parameters used to determine the characteristic structure of liquids. The NMR signal intensity also presents information about the proton density of the sample. The spin relaxation times of the nuclei and the intensity of the signals they generate form the

*Corresponding author: hengin@uludag.edu.tr

Received: 11.01.2023, Accepted: 22.05.2023

basis of NMR imaging. These images obtained depending on the parameter they are used, are T_1 , T_2 , and proton density (PD) images, respectively [11]. How NMR signals are formed has been reported in detail in the literature [12,13].

The spins of the protons that make up water in tissues have a magnetic moment because they are also charged particles. These magnetic moments, which are one of the basic components of magnetic resonance imaging systems and under the influence of the external magnetic field, are aligned in the same direction with the field and have an average magnetic moment. It is the average magnetic momentum of this spin ensemble that will give the MR signal. This mean is called the magnetization of the spin ensemble. It is not the hydrogen nuclei themselves that align with the outer field, but the individual magnetic moments of the hydrogen nuclei. Since it represents only two possible energy states of the proton, spins can only align in one of two directions, parallel to the field or in the opposite direction. The hydrogen nucleus itself does not change direction, it just rotates on its axis. The NMR signal is the sum of the individual spins. If it is found from which parts of the tissue these NMR signals come, we obtain a magnetic resonance image of the tissue. Field gradients are used to accomplish this. Field gradients, which are part of the magnetic imaging system, determine the spatial position of the tissue. If the direction of the external magnetic field is accepted as the z-axis, a linearly increasing magnetic field change along the z-axis and gradient $G_z = dB_z/dz$ is applied to measure the NMR signals of the image on this axis. The spectrum obtained with the magnetic field gradient applied along one of the axes and along the axis of the NMR measurement should accurately reflect the geometry of the sample.

$$\omega(z) = \gamma(B_0 + zG_z) \quad (1)$$

Here, ω is the frequency of the radio signal applied perpendicular to the external magnetic field and γ is the gyromagnetic ratio constant of the spin system. This constant also determines the resonance frequency of the spin system. These NMR signals, which are formed in the time dimension, are subjected to two consecutive Fourier transform. The first transform provides a transformation to the position space corresponding to the time signals, the data in this position space called k-space is subjected to a Fourier transform again to display the internal structure of the tissue or the examined sample. NMR signals are pure data [14,15]. The known original magnetic resonance image is created by twice Fourier transform of pure NMR signals.

This study is about the use of spectroscopy, relaxivity, and magnetic resonance imaging method, whose theory is too broad to fit in this article, in the laboratory environment. In recent years there has been an increasing interest in nuclear magnetic resonance spectroscopy (EFNMR) in the Earth's magnetic field [9, 16, 17]. The purposes of this paper are to measure the parameters T_1 and T_2 relaxation times for ^1H nuclei in different chemical environments; to study two-dimensional (2D) imaging in the earth's magnetic field; and to demonstrate the benefit of the EFNMR method to characterize relaxation parameters consisting of five different chemical solvents in the earth's magnetic field (the typical earth magnetic field in Bursa, Turkey, is 0.047 mT) at room temperature. The described EFNMR system does not have a permanent magnetic field generator. It uses the very smooth but very weak (about 0.047 mT) magnetic field of the Earth. Such a method is very advantageous due to the minimum cost of purchase, installation, and maintenance.

2. Material and Method

In this study, T_1 and T_2 relaxation times of five different chemical compounds, namely Bromobenzene, Chlorobenzene, Iodobenzene, Ethanol, and distilled water, were measured using Terranova-MRI imaging device produced by Magritek company in New Zealand. In addition, two-dimensional images of the ethanol from the top (transverse), front (sagittal), and side (coronal) were recorded.

2.1. Polarization Coil

This system consists of three base units with a nested three-component probe, an ultra-low frequency spectrometer, and a computer-operated Prospa software package. Figure 1 shows the internal structure of this coil set [18].

2.2. B_1 Transmit/Receive Coil

This most inwardly positioned coil generates radio frequency, first stimulating the spin system in the sample and then detecting the NMR signals coming from the spin ensemble. This coil is connected to a series of capacitors. By changing the capacitance values, the B_1 coil is adjusted to the Larmor frequency of the spin ensemble. The value of the Larmor resonance frequency varies according to the value of the local magnetic field. This frequency, which is

usually in the range of 1-3 kHz, should be found experimentally.

2.3. B_1 Gradient Coil

It is necessary to deregulate the Earth's magnetic field in a very controlled manner to encode spatial information into the NMR signal so that the magnitude of the field changes in the direction of the desired spatial coding. This is succeeded using a three-axis gradient coil set.

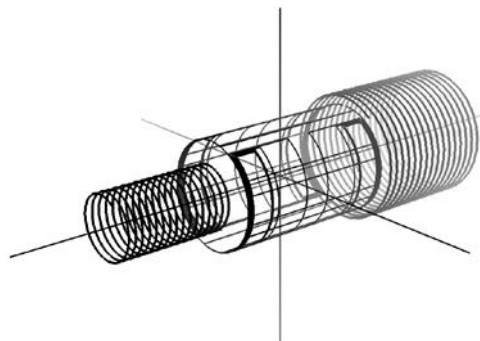


Figure 1. A schematic of the three-coil probe

2.4. Ultra-Low Frequency Spectrometer

In a sense, the Terranova-MRI device is the essence of EFNMR spectroscopy. It is controlled by a digital signal processor (Digital Signal Processing) driven by a personal computer running its software, Prospa. In a typical earth field NMR (EFNMR) experiment, Prospa sends a precompiled DSP pulse packet and all necessary parameters to the DSP unit via the computer's USB port. It then starts running this program. This program controls the entire NMR experiment by sending pulses to the B_p , gradient and B_1 coils and then receiving the NMR data at appropriate time intervals. After this data is collected, it is displayed, all necessary analyzes are made, and then the experiment is terminated or, if desired, the experiment is repeated by sending new parameters to the DSP.

2.5. Ethanol Tube

To obtain two-dimensional images of ethanol in the EFNMR experiment, the nested tube system shown in Figure 2 was made. The inner tube is filled with ethanol and placed in a large tube filled with distilled water. These two tube systems, insulated from each other, represent two separate tissue samples.

2.6. Determination of the Relaxation Parameters

The first of the NMR parameters expected to be measured in an NMR spectrometer is the measurement of the relaxation times. All chemicals used are technical and at least 99% pure. In the measurement of T_1 relaxation times, also known as spin-lattice or longitudinal relaxation time, the time intervals between the applied B_p polarization pulse and 90° pulses are changed and measured by repeating the desired number of steps (measurements) one after the other. The obtained T_1 relaxation time graphs are presented in Figure 3 and the numerical data are summarized in Table 1.

In the measurement of T_2 relaxation times, also known as spin-spin or transverse relaxation times, T_2^* values are measured in conjunction with T_1 spin-lattice relaxation. T_2^* is shorter than T_2 because of the unevenness of the field. For this reason, spin-echo pulse sequences are used.



Figure 2. Nested tube system used for imaging

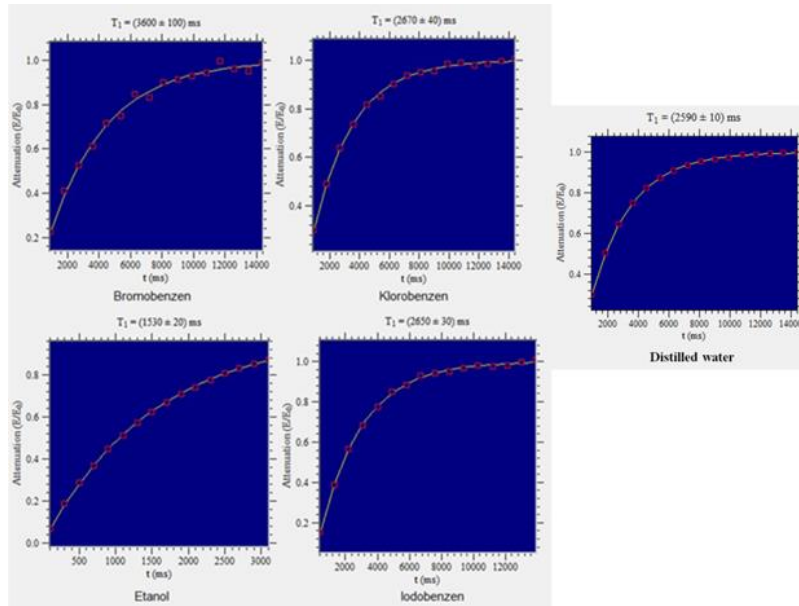


Figure 3. The obtained T_1 relaxation times

The application of a spin-echo pulse array refocuses the phase dissolution of the spin ensemble caused by the non-uniform field, allowing accurate measurement of T_2 . Disruption of phase harmony between spins is known as phase dissolution. The EFNMR system uses shimming coils, to minimize the effect of this phase dissolution. For samples with weak signal strength, the system must first be calibrated for the homogeneity of the field.

T_2 relaxation time graphs obtained using spin-echo pulse sequences are presented in Figure 4 and numerical data are summarized in Table 1.

3. Results and Discussion

When the T_1 relaxation times in Table 1 are examined, it is seen that the relaxation times of the benzene

group are close to each other. The T_1 -weighted image obtained using an ethanol tube in distilled water is given in Figure 5. T_1 -weighted images will be clear as there is a difference between the relaxation times of distilled water and ethanol. When Figure 5 is examined, it is seen that the images of distilled water and ethanol are clearly separated. The presence of the tube is noticeable in the top and side views. In both of these images, it is seen that the redness does not continue between the two bright red spots. The reason is that there is an air gap there. In the front (sagittal) view, the presence of ethanol is clearly visible.

In the table, it is noticed that the T_1 and T_2 relaxation values of the benzene group are actually close to each other. This is due to the closeness of T_1 and T_2 relaxation times in liquids. However, it seems that distilled water does not comply with this rule.

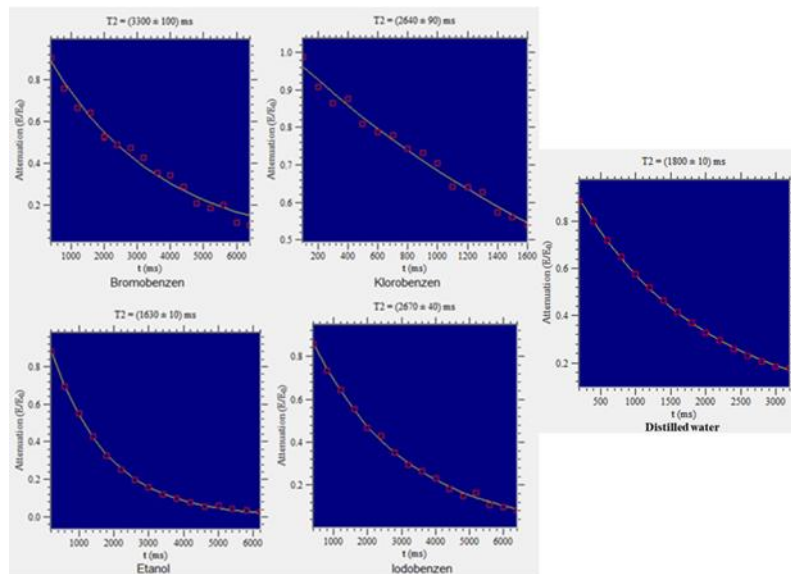
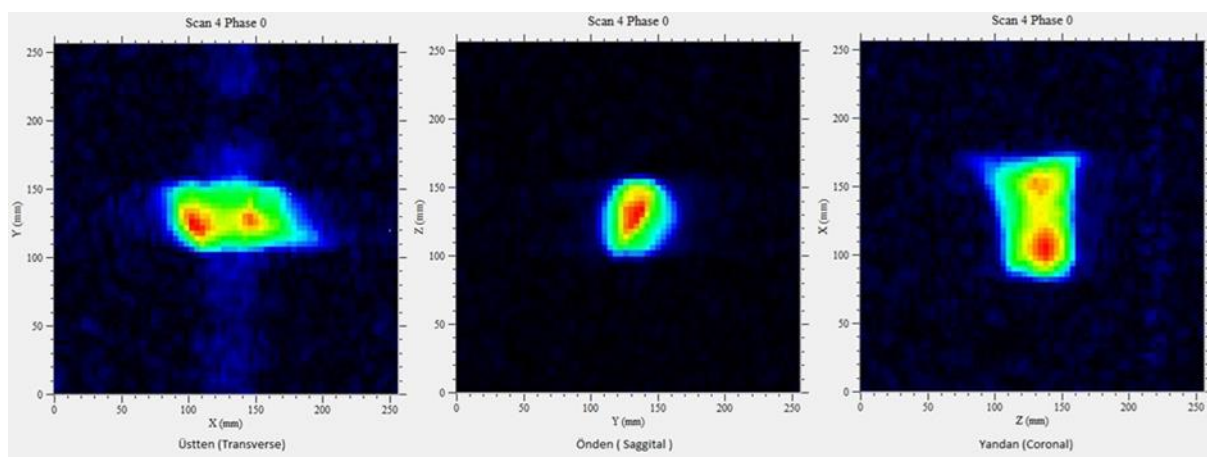


Figure 4. The obtained T_2 relaxation times**Table 1.** T_1 and T_2 relaxation times of the compounds used

Solvent	T_1 (ms)	T_2 (ms)
Bromobenzene	3600 ± 100	3300 ± 60
Chlorobenzene	2670 ± 40	2450 ± 50
Iodobenzene	2650 ± 30	2670 ± 40
Ethanol	1530 ± 20	1630 ± 10
Distilled Water	2590 ± 10	1800 ± 10

**Figure 5.** The T_1 -weighted image of ethanol obtained using an ethanol tube in distilled water.

In addition, the homogeneity of the magnetic field of the EFNMR system must be calibrated before the T_1 or T_2 weighted images of this group are taken. In addition, the homogeneity of the magnetic field of the EFNMR system must be calibrated before the T_1 or T_2 weighted images

of the studied solvents are obtained. For this, the NMR signal of pure water can be used. The free induction decay (FID) and NMR signal of pure water obtained in its calibrated form are shown in Figure 6. In Figure 6, it can be seen that the magnetic field is perfect in a wide band gap.

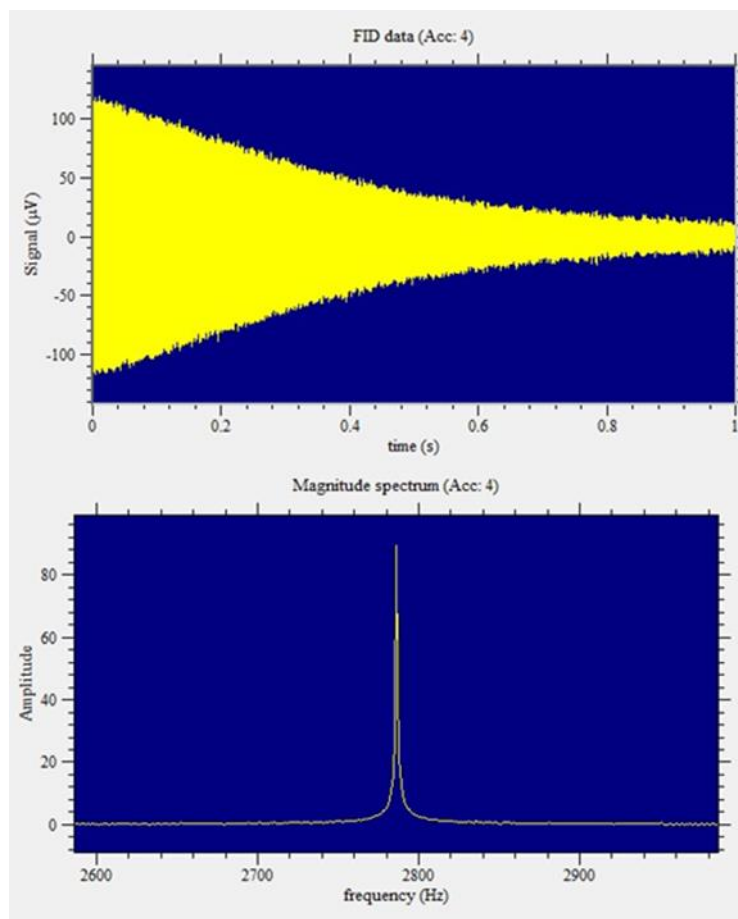


Figure 6. FID and NMR signal of pure water

4. Conclusion and Suggestions

Newly developed mobile NMR devices using weak magnetic fields, namely EFNMR desktop magnetic resonance imaging systems, have now turned into a functional examination method in the laboratory environment due to their small size, low weight, and mobility.

T_1 and T_2 relaxation times of five different solvents and two-dimensional ethanol-water image studies were performed in the world's magnetic field, which is a less costly option. Using NMR with a small and affordable permanent magnet, it was investigated whether it was possible to distinguish between different liquids. It was demonstrated that basic FID envelopes may be utilized in the laboratory to study the relaxation of hydrogen-atom-containing materials using EFNMR. NMR measurements at a high magnetic field can be replaced by magnetic field measurements of the earth, which is a less costly option and has a lower magnetic field.

Using T_1 and T_2 parameters or including information about signal strength can help improve identification accuracy. Thus, additional information

can be provided on samples and structures of new solvents in the future. From the measurements of the T_1 and T_2 parameters and 2D image studies, it was finally concluded that the EFNMR method is useful for characterizing relaxation parameters in various solvents in Earth's magnetic field. Experimental applications of the technique demonstrated that EFNMR data with spatial resolution output may be obtained in a matter of minutes. The use of a low magnetic field (the earth's magnetic field is roughly 0.0047 mT) contributes to this field since there is little work in this field.

This paper is the study of NMR studies, which were previously done in a high magnetic field, in a very low magnetic field. With researchers working with EFNMR, these devices can be programmed at peak performance and used to understand the spin behavior of liquids.

Contributions of the authors

All authors contributed equally to the study.

Conflict of Interest Statement

There is no conflict of interest between the authors.

The authors declare that this study complies with Research and Publication Ethics

Statement of Research and Publication Ethics

References

- [1] C. Kurz, G. Buizza, G. Landry, F. Kamp, M. Rabe, C. Paganelli, G. Baroni, M. Reiner, P. Keall, C.A.T. Berg, and M. Riboldi, "Medical physics challenges in clinical MR guided radiotherapy," *Radiat. Oncol.*, vol. 15, no. 93, pp. 93-109, 2020, doi: 10.1186/s13014-020-01524-4.
- [2] D. Qiu, Y. Cheng, and X. Wang, "Gradual back-projection residual attention network for magnetic resonance image super-resolution," *Comput. Methods Programs Biomed.*, vol. 208, pp. 106252, Sept. 2021, doi: 10.1016/j.cmpb.2021.106252.
- [3] H. L. Ring, Z. Gao, A. Sharma, A., Z. H. Han, C. Lee, K. G. M. Brockbank, E. D. Greene, K. L. Helke, Z. Chen, and L. H. Campbell, "Imaging the distribution of iron oxide nanoparticles in hypothermic perfused tissues," *Magn. Reson. Med.*, vol. 83, no. 5, pp. 1750-1759, Dec. 2020, doi: 10.1002/mrm.28123.
- [4] T. Abe, R. S. Thiebaud, and J. P. Loenneke, "The mysterious values of adipose tissue density and fat content in infants: MRI-measured body composition studies," *Pediatric Res.*, vol. 90, no. 5, pp. 963-965, Jan. 2021, doi: 10.1038/s41390-021-01376-y.
- [5] A. Abraham, E. Salager, D. Krishnan, and Y.C. Su, "Advances of solid-state NMR spectroscopy in material sciences," *Magn. Reson. Chem.*, vol. 58, no. 11, pp. 987, Oct. 2020, doi: 10.1002/mrc.5086.
- [6] P. Chien, K. J. Griffith, H. Liu, Z. Gan, and Y. Hu, "Recent Advances in Solid-State Nuclear Magnetic Resonance Techniques for Materials Research," *Annu. Rev. Mater. Res.*, vol. 50, no. 1, pp. 493-520, May. 2020, doi: 10.1146/annurev-matsci-091019-011049.
- [7] S. Bjorgvinsdottir, and L. Emsley, "Bulk hyperpolarization of inorganic materials," *Chimia*, vol. 75, no. 4, pp. 333-337, Feb. 2021, doi: 10.2533/chimia.2021.333.
- [8] G. Foran, N. Verdier, D. Lepage, C. Malveau, N. Dupre, and M. Dolle, "Use of solid-state NMR spectroscopy for the characterization of molecular structure and dynamics in solid polymer and hybrid electrolytes," *Polymers*, vol. 13, no. 8, pp. 1207-1241, Apr. 2021, doi: 10.3390/polym13081207.
- [9] H. Ovaloğlu, "Application of nuclear magnetic resonance/magnetic resonance imaging techniques to estimate proton relaxation parameters at earth field," *Emerg. Mater. Res.*, vol. 11, no. 3, pp. 303-312, Sept. 2020, doi: 10.1680/jemmr.21.00180.
- [10] Z. Yüksel, "Manyetik Rezonans Görüntüleme, Fizik Temelleri ve Sistem Bileşenleri," *BSJ Eng. Sci.*, vol. 2, no. 2, pp. 57-65, Apr. 2019.
- [11] W. Catherine, C. K. Roth, and J. Talbot, *MRI in Practice*, 4th ed. USA, Wiley-Blackwell Publishing Ltd., 2011, pp: 21-58.
- [12] M. Balci, *Basic ^{1H}- and ^{13C}-NMR Spectroscopy*. Ankara-Turkey, Elsevier, 2005. pp. 9-23.
- [13] G. Harald, *NMR Spectroscopy*, Weinheim-Germany, Wiley-VCH Verlag GmbH&Co, 2013, pp: 13-27.
- [14] M. S. Hansen, and P. Kellman, P., "Image reconstruction: An overview for clinicians," *Magn. Reson. Imaging*, vol. 41, no. 3, pp. 573-585, Jun. 2015, doi: 10.1002/jmri.24687.
- [15] G. A. Wright, "Signal acquisition and processing for magnetic resonance imaging," in *Proc. ICIP-94, IEEE Comput. Soc. Press 1st Int. Conf. on Image Proc.*, Aug. 2002, pp. 523-527, doi: 10.1109/ICIP.1994.413751.
- [16] E. Balci, B. Rameev, H. Acar, G.V. Mozzhukhin, B. Aktas, B. Colak, P.A. Kupriyanov, A.V. Levlev, Y.S. Chernyshev, and V.L. Chizhik, "Development of Earth's Field Nuclear Magnetic Resonance (EFNMR) technique for applications in security scanning devices," *Appl. Magn. Reson.*, vol. 47, no. 1, pp. 87-99, Oct. 2015, doi: 10.1007/s00723-015-0730-z.
- [17] M. Trybus, "Measurements of Longitudinal and Transverse Relaxation Times of Selected Liquids Using the EFNMR Scanner," *Przegląd Elektrotechniczny*, vol. 963, pp. 115-118, Oct. 2020, doi: 10.15199/48.2020.10.21.
- [18] M. E. Halse, "Multi-acquisition and multi-dimensional earth's field nuclear magnetic resonance spectroscopy," Ph.D. dissertation, Dept. Phys., Victoria Univ. of Wellington, Wellington, New Zealand, 2009.



Investigation of Pyrolysis of Walnut Shells and Pyrolysis Oil Quality

Faruk ORAL¹, Rasim BEHÇET², Emre GONEL^{1*}

¹Bitlis Eren University, 13000, Bitlis, Turkey

²İnönü University, 44000, Malatya, Turkey

(ORCID: 0000-0002-4114-0785) (ORCID: 0000-0002-6897-3066) (ORCID: 0000-0003-0604-1439)



Keywords: Pyrolysis, Walnut Shells, Bio Oil, Wastes

Abstract

The energy demand is increasing in parallel with the technological developments and population in the world. Fossil fuels are the main source for this demand. As a result of energy production from fossil fuels, natural environment is adversely affected. Furthermore, many countries depend on the fossil fuels for their energy need. Researchers have been interested in alternative energy sources such as solar, biomass, and wind. There are many studies for investigating pyrolysis of lignocellulosic biomass. Studies mainly focused on the chemical structure of pyrolysis oil from different feedstocks. In this study, pyrolysis oil was produced from walnut shells in a pyrolysis reactor. Pyrolysis oil properties were investigated and compared with fossil fuels. The effect of pyrolysis reaction temperature on pyrolysis oil yield is studied. The results indicate that pyrolysis oil can be produced from walnut shells, the reaction temperature is an important factor on pyrolysis oil yield and pyrolysis oil has complex nature compared to fossil fuels.

1. Introduction

The amount of fossil fuels has been consumed dramatically over the decades. This consumption has had a detrimental impact on our environment because of releasing harmful exhaust gases. The demand on the fossil fuels is very high while the sources for these fuels are limited. Having environmental considerations and limited sources for fossil fuels has caused a need for researchers to find alternative energy sources [1].

There have been many studies about producing fuels from different alternative energy sources. In one of the studies, researchers focused on producing biodiesel from fish fat and vegetable oils with the transesterification method. After emission tests, it was concluded that there was reduction in HC and CO emissions while using the new biodiesel compared the diesel fuel [2]. Similar results were obtained by [3]. In their study, an alternative biodiesel was produced from micro algae, yeast and bacteria, and this type of biodiesel was tested in an internal combustion engine.

According to the Environmental Protection Agency, lignocellulosic biomass is considered one of the alternative energy sources. Because plants convert the energy taken from the sun into chemical energy by photosynthesis and store it in their body. When vegetable wastes are burned, the chemical energy in their body is thrown out in the form of heat [4]. It is very crucial to utilize lignocellulosic biomass as an alternative energy production.

Understanding the chemistry of lignocellulosic biomass and oil produced from this source has a great importance to be able to use it as an alternative fuel. Some researchers have used different methods to produce valuable oils from different feedstocks. For instance, pyrolysis oil was obtained from rice husk with using fast pyrolysis method. The relationship between reaction temperature and oil yield was studied and some properties oil was presented [5].

Akubo et al studied the pyrolysis of coconut shell, cotton stalk, palm kernel shell, rice husk, sugarcane, and wheat straw. Elemental analysis and the effect of temperature on product yield were

*Corresponding author: egonel@beu.edu.tr

Received: 16.01.2023, Accepted: 24.04.2023

studied. According to elemental analysis of raw material, the raw materials mainly consisted of carbon and oxygen elements. Main weight loss was observed at temperature range between 200 °C and 400 °C [6].

In another study, the pyrolysis of demineralized softwood sawdust was investigated. Ultimate and proximate analysis of raw material were conducted. GC-MS analysis of pyrolysis oil shows that the oil has complex nature [7].

Moreover, R. Maggi and B. Delmon indicated that pyrolysis oils were produced from the wastes of acacia tree, eucalyptus tree, red pine bark in pyrolysis reaction and the oil quality was studied using GC-MS and FTIR analysis [8]. According to results, pyrolysis oil had good amount of oxygen content and contained different groups and functions. In another study, pistachio soft shells used as a feed stock in a fixed bed reactor. The pyrolysis oil was investigated with elemental analyzer, FT-IR, and ¹H NMR. It was determined that the pyrolysis liquid is a mixture of aliphatic, aromatic and polar hydrocarbons [9].

Yücedağ and Durak presented their study on pyrolysis of lactuca scariola. According to GC-MS analysis results, 98 different compounds identified within pyrolysis oil [10].

Walnut shells are one of the lignocellulosic biomass sources. There are a few studies on using walnut shell as an alternative energy. In one study, proximate and ultimate analysis of walnut shell were studied according to American standard testing methods. High heating value was found as 21.6 MJ / kg [11]. This study shows that walnut shells have calorific value. Onay et al studied pyrolysis of walnut shell to determine the effect of pyrolysis conditions on oil yield such as reaction temperature, heating rate, and particle size and conducted elemental analysis on pyrolysis oil. They concluded that oil yield increased with temperature up to 500 °C and it decreased beyond this temperature. Pyrolysis oil contains high amount carbon and oxygen [12]. It is crucial to investigate the chemistry of pyrolysis oil obtained from walnut shells. In this study, walnut shells from Bitlis region are chosen as a feed stock to produce pyrolysis oil in a fixed bed reactor. The chemistry of walnut shells is investigated. The effect of different reaction temperatures on pyrolysis oil yield was studied while determining the optimum temperature for maximum oil yield. The chemical analysis of this oil was conducted by using different methods to understand chemical structure and quality of pyrolysis oil to be able utilize as an alternative energy source.

2. Material and Method

2.1. Material

Walnut trees are planted commonly in higher elevations in Turkey. According to the data obtained from TÜİK [13], there were 26,618 pieces walnut trees in Turkey and 325,000 tones walnut fruits produced in 2021. Walnut is considered as a hard-shelled fruit. Due to its different fatty acid composition, it is a type of fruit that has an important health benefit, and the consumption of this fruit has been increasing [14]. The shells are wastes of walnut fruit and burned directly in ovens for baking or thrown away. Walnuts are grown in Bitlis region, Turkey. Bitlis is located in Eastern Turkey and at the elevation of 1,545 meters. They were procured from local producers in the city of Bitlis. Walnut shells were separated from walnuts and let air dried for experimental studies.

2.2. Method

Air dried walnut shells were grounded as maximum 0,5 cm sample size in a grinder. Then raw material was dried in the oven at 105 °C. Ash, volatile, moisture, and fixed carbon content of the material were determined according to ASTM E1755, ASTM E871 & E872 specifications. Fixed carbon content was calculated by difference between 100 and sum of ash, volatile and moisture content. Moreover, the samples were tested for Ultimate analysis in an elemental analyzer named LECO-CHNS-932.

The pyrolysis experiments were conducted in mechanical engineering department laboratory, Bitlis Eren University. The experimental set up is shown in Figure 1. It is fixed bed reactor. Reactor was made of stainless steel and has the diameter of 10 cm and the height of 20 cm. Further information can be found in this study [15].



Figure 1. Pyrolysis experimental set up.

Table 1. Technical Properties of Fixed Bed Pyrolysis Reactor.

Capacity	Material	Temperature Range	Temperature Display	Heater	Temperature Control	Data Saver	Gas Nozzle	Power
1 lt	316 Stainless Steel	50°C /800°C	Digital	Heating Mantle	PID Control , 10 steps 80 programs	Transferring data to computer	¼ npt threaded gas inlet, needle valve (2)	220 V, 50 Hz

Technical properties of the reactor are given in Table 1. Nitrogen gas was used as a sweep gas to provide vacuum environment in the reactor. Traps were placed to condense the gasses leaving the reactor. Salt-alcohol-ice mixture was used to keep the temperature of the traps below 0 °C. The reactor temperature change with time was recorded in the computer. Experiments were performed at 5 different reaction temperatures (400, 450, 500, 550, 600 °C), 40 °C/min constant heating rate, in vacuum environment by providing nitrogen gas at 100 ml/min gas flow rate. 100-gram raw material was used in experiments.

Oil yield was calculated by equation (1), ash content was calculated by equation (2), and non-condensable gas content was calculated by equation (3). At the end of the experiment, the liquid product was taken from the traps and stored in glass bottles. The liquid product is called pyrolysis oil. The amount of solid product called ash is the amount remaining in the reactor at the end of the experiment. The weight difference between total amount in the beginning of experiments and the sum of liquid product and ash is non-condensable gases.

$$n_{oil\ yield}(\%) = \frac{Oil\ product\ (gram)}{initial\ weight} \times 100 \quad (1)$$

$$n_{ash\ yield}(\%) = \frac{Solid\ product\ (gram)}{initial\ weight} \times 100 \quad (2)$$

$$n_{non-condensable}(\%) = 100 - n_{oil\ yield}(\%) - n_{ash\ yield}(\%) \quad (3)$$

Further, pyrolysis oil obtained at 500 °C was analyzed to determine its chemical structure. Ultimate analysis was performed with same method used for walnut shells. In addition, different devices were used for further chemical analysis. Table 2 shows the additional devices were used in experimental studies.

2.3 Cost Analysis

In cost analysis calculations, the cost of a liter pyrolysis oil is calculated with below equations. Main inputs for production of pyrolysis oil are electricity and nitrogen gas. Equation (4) is the correlation between raw material and pyrolysis oil. ‘m’ is the required raw material (kg) to produce required ‘v’ amount (liter) pyrolysis oil. ‘d’ is the density of pyrolysis oil (kg/liter), $n_{oil\ yield}$ is the pyrolysis oil yield.

$$m = v \times d / n_{oil\ yield} \quad (4)$$

Capacity of reactor (f) is 500 gr. Required experiments (t) can be found below equation:

$$t = m / f \quad (5)$$

Table 2. Experimental devices for oil analysis.

The Type Analysis	Density	Calorific Value	FTIR Analysis	GC-MS	pH
Name of The device	Density meter DS7000	IKA C 2000 Basic Version 1 Calorimeter	Perkin Elmer	Agilent 7890A and 5975C	Merck - pH indicator strips

Table 3. The main properties of walnut shell (Weight %).

Moisture Content	Volatile Content	Fixed Carbon	Ash	Carbon	Hydrogen	Nitrogen	Oxygen	Sulfur
4,33	74,21	20,95	0,51	46,91	5,82	5,82	46,56	0,06

The heater is on total 0,72 hours (43 minutes) in each experiment. E (Turkish Lira), the total cost of electricity for t amount experiments can be found in equation (6). The constant, 2,23 is found by multiplying 0,72 hours with power of furnace, 4 KW and unit electricity cost, 3,1 Turkish Lira / kwh

$$E = 8,93 \times t \quad (6)$$

Nitrogen gas is on total 0,72 hour (43 minutes) in each experiment at 100 ml/min (0,006 m³ / hour) gas flow rate. N, the total nitrogen gas cost can be found in equation (7). The constant 0,384 is found by multiplying 0,72 hour with 0,006 m³/hour and unit gas cost 89 Turkish Lira / m³.

$$N = 0,384 \times t \quad (7)$$

Total unit cost for producing a liter pyrolysis oil (T) is the sum of E - the total cost of electricity and N - the total nitrogen gas cost.

3. Results and Discussion

3.1. The Analysis of Feedstock

The chemical properties of walnut shells were studied before pyrolysis experiments. Proximate and ultimate analysis results were given in Table 3. According to proximate analysis results, volatile content is the highest component. It means that we could obtain up to %74,21 gas or liquid products with pyrolysis regarding to pyrolysis reaction conditions.

Moreover, elemental analysis results indicate that Carbon and Oxygen elements constitute a great proportion the walnut shell while small amounts of Hydrogen, Nitrogen and Sulfur. Walnut shell shows similar properties compare to other lignocellulosic biomass feedstocks, such as pistachio soft shell [9] and corn and cotton stalks [16]. Higher Oxygen content is one of the disadvantages of lignocellulosic biomass feedstocks.

3.2. Pyrolysis Experiments

The main products of pyrolysis reaction are pyrolysis oil, non-condensable gases, and solid products. Figure 2 shows pyrolysis oil and solid product that are produced from walnut shells at 500 °C. The oil has a strong smell that is similar to vinegar. Solid product is black and alike a char coal. Same products are obtained at different temperatures ranging from 400 °C to 600 °C.



Figure 2. The products of pyrolysis reaction: pyrolysis oil (a), solid product (b).

Temperature is a main variable on pyrolysis oil yield. Figure 3. shows the relationship between reactor temperature and yield of pyrolysis oil, non-condensable gas and solid products. There is slight change on yield when temperature changed from 400 °C to 450 °C. When reaction temperature was increased from 450 °C to 500 °C, pyrolysis oil yield increased to maximum level of 31,6 % and solid production yield was decreased with slight increase on non-condensable gases. When temperature was increased from 500 °C to 550 °C, pyrolysis oil and solid production yield were decreased whereas non-condensable gas yield was increased. Same pattern was seen when temperature changed from 550 °C to 600 °C. This shows that higher temperature caused formation of strongly bonded molecules and it made harder to condense those molecules [17]. 500 °C is the optimum temperature for production of pyrolysis oil for walnut shells. The correlation between temperature and yield is similar with pyrolysis studies of furniture saw dust [18], palm kernel shells [19], and [20].

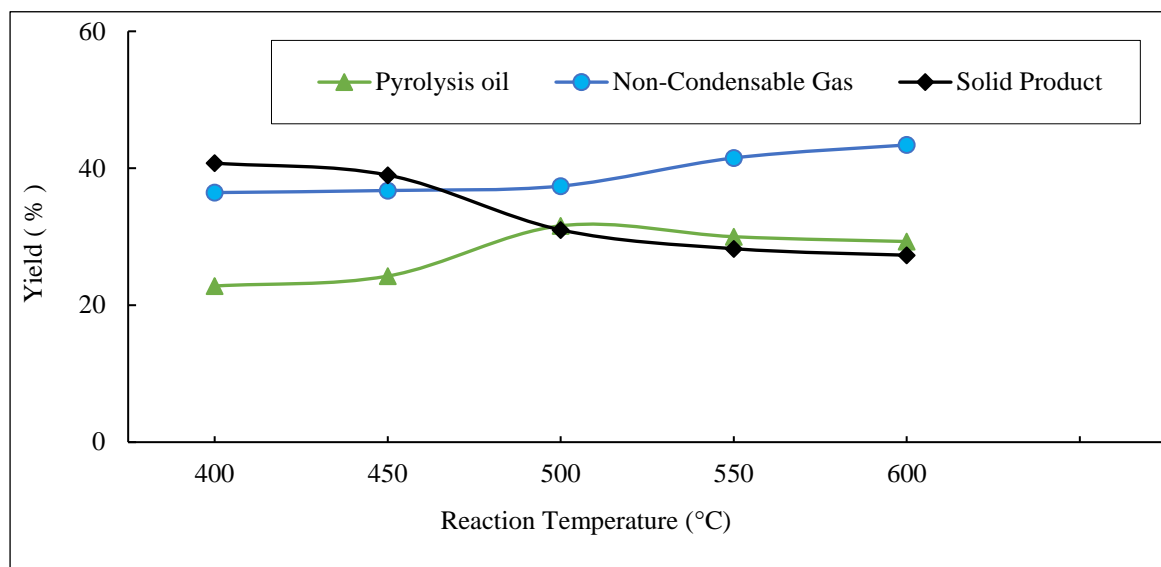


Figure 3. The effect of temperature on product yield.

3.3. Characterization of Pyrolysis Oil

The chemical properties of the pyrolysis oil obtained at 500 °C were investigated. The analysis results are shown in Table 4. Elemental analysis results are given by weight.

These results show that pyrolysis oil has high oxygen content and is denser than fossil fuels and a highly acidic product. Diesel fuel has %86,13 carbon, % 13,87 hydrogen by weight. The pyrolysis oil containing %43,04 oxygen is one of the drawbacks. Similar results were obtained from rice straw [21], wheat shell [22], and switch grass [23].

Higher oxygen content, density and being acidic for the oils is a big disadvantage to be utilized in combustion engines, or boiler as an alternative energy. Acidic oil would cause corrosion on metals. Moreover, the density of the oil is 1,0493 g/cm³. It is quite higher than diesel fuel of 0,85 g/cm³. Since there is difference in density, the oil and diesel do not mix homogeneously. Figure 4. shows the mixture of %95 diesel + %5 pyrolysis oil. It can be seen that the oil stayed in the bottom since it is denser than diesel fuel. The ethanol addition to mixture didn't change the

result. It can be concluded that pyrolysis oil has different chemical structure than fossil fuels. In one study, waste engine oil that has 870 kg/m³ density was able to mix with diesel fuel since waste oil has a close density with diesel and has similar chemical properties. The waste oil was successfully utilized in a diesel generator [24].



Figure 4. The mixture of diesel and pyrolysis oil.

Table 4. The chemical properties of pyrolysis oil.

Carbon	Hydrogen	Nitrogen	Oxygen	Sulfur	Calorific Value (cal/g)	Density (g/cm ³)	pH Value
48,10	8,64	0,18	43,04	0,04	7059	1,0493	2,5

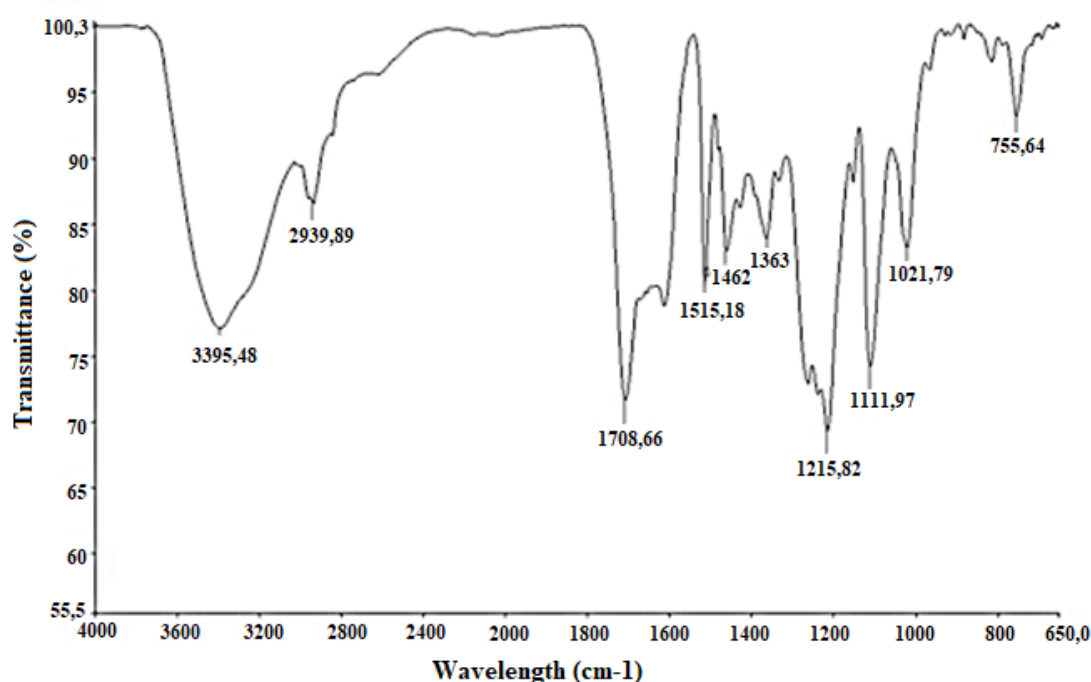


Figure 5. FTIR spectra of pyrolysis oil.

FTIR spectra of pyrolysis oil obtained at 500 °C reaction temperature is given on figure 5. According to figure 5 and the IR frequency table obtained from [25], the peak at 3395 cm⁻¹ is indicative of O-H stretching, the presence alcohols. The peak at 2939 cm⁻¹ indicates C-H stretching, the presence of alkenes [26]. The peak at 1708 cm⁻¹ indicates the C=O stretching, the presence of ketones or aldehydes. The peak at 1515 cm⁻¹ indicates skeletal stretching. The peaks at 1363 and 1462 cm⁻¹ indicate C-H bending and O-H bending, the presence of alkane groups and phenols. The peaks between at 1021 and 1215 cm⁻¹ indicate C-O stretching, the presence of ethers, esters, and alcohols. The peak at 755 cm⁻¹ indicates the presence of aromatics.

In addition to FTIR spectra analysis, GC-MS analysis was also performed. Table 5. shows GC-MS analysis results. Pyrolysis oil obtained from walnut shells is consisted of many different chemical groups. These groups are furans, esters, ketones, aldehydes, phenols, alkenes, alcohols, sugars, guaiacols, amides, and carboxylic acids. These groups were confirmed in FTIR spectra analysis. Total 17 compounds were identified. The highest amount of component in oil is C₇H₈O₂ (Guaiacol – monomethoxybenzene) at

%15,1. Guaiacol consists of phenol with a methoxy substituent at the ortho position. The lowest amount component is C₁₆H₃₄ (Hexadecane) at %0,5. Hexadecane is a straight-chain alkane with 16 carbon atoms [27]. Carbon distribution oil is in the range of C₄ – C₁₆. Molecular weights of these compounds are between 88 and 270. The similar results were obtained from [28]. They studied pyrolysis of mongolian type pine tree. Further, they applied distillation of the oil by molecular distillation method. However, the fractions of the oil have more complex nature than the bio oil because the oil doesn't have a stable nature. The chemical composition of the oil changes with temperature. In another study, the pyrolysis oils obtained from the wastes of the beech tree and the flax plant have the similar characteristics [29]. In the same study, pyrolysis of cellulose, hemicellulose and lignin was also investigated by GC-MS method. It was determined that many components were found in the pyrolysis oils obtained from the wastes of the beech tree and the flax plant, also found in pyrolysis of cellulose, hemicellulose and lignin.

Table 5. GC-MS analysis results.

Pick No	RT	Tentative Assignment	Empirical Formula	CAS#	Molecular Weight	Amount
1	6,284	Methyl propionate	C ₄ H ₈ O ₂	000554-12-1	88	0,8
4	8,007	2-Hexanone	C ₆ H ₁₂ O	000591-78-6	100	0,7
11	11,748	2-Cyclopenten-1-one	C ₅ H ₆ O	000930-30-3	82	1,8
13	12,708	Hexadecane	C ₁₆ H ₃₄	000544-76-3	226	0,5
15	12,972	Furfural	C ₅ H ₄ O ₂	000098-01-1	96	5,3
19	13,896	2-Cyclopenten-1-one, 3-methyl-	C ₆ H ₈ O	002758-18-1	96	1,2
28	17,346	2-Cyclopenten-1-one, 2-hydroxy-3-methyl-	C ₆ H ₈ O ₂	000080-71-7	112	4,3
29	17,668	Phenol, 2-methoxy-	C ₇ H ₈ O ₂	000090-05-1	124	15,1
31	18,120	2-Cyclopenten-1-one, 3-ethyl-2-hydroxy-	C ₇ H ₁₀ O ₂	021835-01-8	126	1,6
33	18,804	Creosol	C ₈ H ₁₀ O ₂	000093-51-6 93	138	7,3
36	19,313	Phenol	C ₆ H ₆ O	000108-95-2	94	3,4
37	19,707	Benzeneethanol, 2-methoxy-	C ₉ H ₁₂ O ₂	007417-18-7	152	4,5
40	20,278	p-Cresol	C ₇ H ₈ O	000106-44-5	108	1,9
45	22,924	Phenol, 2,6-dimethoxy-	C ₈ H ₁₀ O ₃	91-10-1	154	27
48	24,242	3,5-Dimethoxy-4-hydroxytoluene	C ₉ H ₁₂ O ₃	6638-05-07	168	13,6
51	25,171	Benzocyclooctene-7,8-dicarboxylic acid dimethyl ester	C ₁₆ H ₁₄ O ₄	099027-76-6	270	10,3
68	32,113	2-(Propynylthio)-5-methylthiophene-3-carbaldehyde - oxime	C ₉ H ₉ NOS ₂	2000236-59-0	211,3	0,7
Total						100,0

On the other hand, crude oil consists of paraffin, cycloparaffinic (naphthenic) aromatic hydrocarbons, and a trace amount sulfur, nitrogen, and oxygen compounds [30]. GC-MS analysis of pyrolysis oil obtained from walnut shells shows that the pyrolysis oil has a different chemical structure than crude oil.

3.4. Cost Analysis

Unit cost of pyrolysis oil was found after solving required equations in section 2.3. Table 6. shows the results of cost analysis.

Required raw material was found as 3,32 kg. 6,64 times required experiments to produce 1-liter pyrolysis oil. Total electricity cost was 59,30 Lira and nitrogen gas cost was 2,54 Lira. The cost of 1-liter pyrolysis oil was found as 62 Lira. The electricity cost is the main variable for oil production. The result indicates that the small size reactor is not cost

effective to produce pyrolysis oil since it was designed solely for research purposes. It is advised to have larger scale reactors for pyrolysis oil production.

Table 6. Cost analysis results

Variables	Results
v (liter)	1
d (kg/m ³)	1.05
n _{oil} yield (%)	31.6
m (kg)	3,32
t (times)	6,64
E (Lira)	59,30
N (Lira)	2,54
T (Lira)	62

4. Conclusion and Suggestions

The aim of this study is to produce bio oil from walnut shells in a pyrolysis reactor. Walnuts were procured from Bitlis, Turkey region. Pyrolysis oil, non-condensable gases, and solid products were obtained from the pyrolysis of walnut shells. The temperature effects the product yields greatly. Optimum temperature for pyrolysis oil yield is found at 500 °C reaction temperature.

To be able to understand if pyrolysis oil is similar to fossil fuels, a variety of chemical tests such as elemental analysis, calorific value, density, pH value, FTIR spectra and GC-MS analysis conducted. According to results, pyrolysis oil is highly acidic, denser than diesel fuel, and has high oxygen content and low calorific value. The pyrolysis oil also has a complex chemical groups in its nature. They are furans, esters, ketones, aldehydes, phenols, alkenes, alcohols, sugars, guaiacols, amides, and carboxylic acids. Since the oil has a complex nature, and high density, it doesn't mix with diesel fuel. The chemical nature changes with temperature and it makes the pyrolysis oil unstable.

It can be concluded that pyrolysis oil obtained from walnut shells is different than fossil fuels. The oil has similar characteristics with the oils obtained from different lignocellulosic biomass sources. The pyrolysis oil may be utilized in producing different chemical raw materials using appropriate chemical methods.

Acknowledgment

This study is supported by Bitlis Eren University Scientific Research Projects Coordinatorship (BEBAP) with BEBAP 2018.11 project code. We would like to thank for their support.

Contributions of the Authors

Authors did the work together and co-authored the publication

References

- [1] R. C. Saxena, D. K. Adhikari, and H. B. Goyal, "Biomass-based energy fuel through biochemical routes: a review". *Renewable and Sustainable Energy Reviews*, vol. 13, no. 1, pp. 167-178, 2009.
- [2] R. Behçet, R. Yumrutaş, and H. Oktay, "Effects of fuels produced from fish and cooking oils on performance and emissions of a diesel engine". *Energy*, vol. 71, pp. 645-655, 2014.
- [3] B. D. Wahlen et al., "Biodiesel from microalgae, yeast, and bacteria: Engine performance and exhaust emissions," *Energy Fuels*, vol. 27, no. 1, pp. 220–228, 2013.

Conflict of Interest Statement

There is no conflict of interest between the authors.

Statement of Research and Publication Ethics

The study is complied with research and publication ethics

- [4] U.S. Environmental Protection Agency (EPA) <https://www.epa.gov/rhc/biomass-heating-and-cooling-technologies>. [Accessed: September 5, 2022].
- [5] Z. Ji-Lu. "Bio-oil from fast pyrolysis of rice husk: Yields and related properties and improvement of the pyrolysis system". *Journal of Analytical and Applied Pyrolysis*, vol. 80, no.), pp. 30-35, 2007.
- [6] K. Akubo, M. A. Nahil, and P.T Williams, "Pyrolysis-catalytic steam reforming of agricultural biomass wastes and biomass components for production of hydrogen/syngas". *Journal of the Energy Institute*, vol. 92, no. 6, pp. 1987-1996, 2018.
- [7] H. Persson, and W. Yang, "Catalytic pyrolysis of demineralized lignocellulosic biomass". *Fuel*, vol. 252, pp. 200-209, 2019
- [8] R. Maggi and B. Delmon, "A review of catalytic hydrotreating processes for the upgrading of liquids produced by flash pyrolysis," in *Hydrotreatment and Hydrocracking of Oil Fractions, Proceedings of the 1st International Symposium/6th European Workshop*, Elsevier, 1997, pp. 99–113
- [9] I. Demiral, N. G. Atilgan, and S. Şensöz, "Production of biofuel from soft shell of pistachio (*Pistacia vera* L.)" *Chemical Engineering Communications*, vol. 196, no. (1-2), pp. 104-115, 2008.
- [10] H. Yücedağ, & H. Durak, "Bio-oil and bio-char from lactuca scariola: significance of catalyst and temperature for assessing yield and quality of pyrolysis". *Energy Sources, Part A: Recovery, Utilization, and Environmental Effects*, vol. 44, no. 1, pp. 1774-1787, 2022.
- [11] A. Demirbaş, "Fuel Characteristics of Olive Husk and Walnut, Hazelnut, Sunflower, and Almond Shells," *Energy Sources*, vol. 24, no. 3, pp. 215-221, 2002
- [12] O. Onay, S. BEIS and O. M. Kockar, "Pyrolysis of Walnut Shell in a Well-Swept Fixed-Bed Reactor," *Energy Sources*, vol. 26, no. 8, pp. 771-782, 2004.
- [13] Turkish Statistical Institute (TUİK) <https://www.tuik.gov.tr/> [Accessed: September 10, 2022].
- [14] S.M. Şen, "Cevizin Besin Değeri ve Sağlıklı Beslenmedeki Önemi". *Bahçe* vol. 46 (Special Edition 2): pp. 1–9, 2017.
- [15] E. Gonel, R. Behçet, and F. ORAL, Energy production from lignocellulosic biomass wastes, *22nd Congress on Thermal Science and Technology, Kocaeli*, 2019
- [16] X. Guo, Z. Xu, X. Zheng, X. Jin, and J. Cai, "Understanding pyrolysis mechanisms of corn and cotton stalks via kinetics and thermodynamics," *Journal of Analytical and Applied Pyrolysis*, 105521, 2022.
- [17] T. Aysu, "Catalytic pyrolysis of *Alcea pallida* stems in a fixed-bed reactor for production of liquid bio-fuels". *Bioresource Technology*, vol. 191, pp. 253-262, 2015
- [18] B. B. Uzun, and G. Kanmaz, "Effect of operating parameters on bio-fuel production from waste furniture sawdust," *Waste Management & Research*, vol. 31, no. 4, pp. 361-367, 2013
- [19] S. J. Kim, S. H. Jung, and J. S. Kim, "Fast pyrolysis of palm kernel shells: influence of operation parameters on the bio-oil yield and the yield of phenol and phenolic compounds," *Bioresource technology*, vol. 101, no. 23, pp. 9294-9300, 2010
- [20] W. T. Tsai, M. K. Lee, and Y. M. Chang, "Fast pyrolysis of rice husk: Product yields and compositions," *Bioresource technology*, vol. 98, no. 1, pp. 22-28, 2007.
- [21] B. M. Phan, L. T. Duong, V. D. Nguyen, T. B. Tran, M. H. Nguyen, L. H. Nguyen, and L. C. Luu, "Evaluation of the production potential of bio-oil from Vietnamese biomass resources by fast pyrolysis". *Biomass and Bioenergy*, vol. 62, pp. 74-81, 2014.
- [22] M. Bertero, G. de la Puente, and U. Sedran, "Fuels from bio-oils: Bio-oil production from different residual sources, characterization, and thermal conditioning," *Fuel*, vol. 95, pp. 263-271, 2012
- [23] T. Imam, and S. Capareda, "Characterization of bio-oil, syn-gas and bio-char from switchgrass pyrolysis at various temperatures,". *Journal of Analytical and Applied Pyrolysis*, vol. 93, pp. 170-177, 2012.
- [24] F. Oral, N. Y. Çolak and D. Şimşek , "Küçük çaplı enerji üretiminde kullanılan bir dizel jeneratörde ek yakıt olarak atık motor yağı ve alkol kullanımının emisyon etkileri", *Gazi Üniversitesi Mühendislik Mimarlık Fakültesi Dergisi*, vol. 38, no. 2, pp. 865-874, Oct. 2022, doi:10.17341/gazimmfd.811625
- [25] Sigma Aldrich <https://www.sigmaaldrich.com/> [Accessed: November 13, 2022].
- [26] E. Apaydin-Varol, B. B. Uzun, E. Önal, and A. E. Pütün, "Synthetic fuel production from cottonseed: fast pyrolysis and a TGA/FT-IR/MS study," *Journal of analytical and applied pyrolysis*, vol. 105, pp. 83-90, 2014
- [27] National Library of Medicine <https://pubchem.ncbi.nlm.nih.gov/> [Accessed: December 13, 2022].
- [28] X. Guo, S. Wang, Z. Guo, Q. Liu, Z. Luo, and K. Cen, "Pyrolysis characteristics of bio- oil fractions separated by molecular distillation," *Applied Energy*, vol. 87, no. 9, pp. 2892-2898, 2010.

- [29] C. Mohabeer, L. Abdelouahed, S. Marcotte, and B. Taouk, “Comparative analysis of pyrolytic liquid products of beech wood, flax shives and woody biomass components”. *Journal of Analytical and Applied Pyrolysis*, vol. 127, pp. 269-277, 2017.
- [30] S. C. Gad, “Petroleum Hydrocarbons,” in: Wexler, P.B.T.-E. of T. (Third E. (Ed.), *Academic Press, Oxford*, pp. 838–840. <https://doi.org/10.1016/B978-0-12-386454-3.00899-X>, 2014



Performance Optimization of Auxetic Structures on Energy Absorption of Cylindrical Sandwich Using Taguchi and ANOVA Methods

Onur KAYA^{1*}, Ali Husnu BADEMLIOGLU², Cihan KABOGLU³

¹ERMETAL Automotive, R&D Center, Bursa/Turkey

²Bursa Technical University, Faculty of Engineering and Natural Sciences, Department of Mechanical Engineering, Bursa/Turkey

³Bursa Technical University, Faculty of Engineering and Natural Sciences, Department of Metallurgical and Materials Engineering, Bursa/Turkey



(ORCID: 0000-0002-8010-6707) (ORCID: 0000-0001-6944-4900) (ORCID: 0000-0002-6249-0565)

Keywords: Auxetic, Energy Absorption, Taguchi, ANOVA

Abstract

High engineering requirements for shock absorbers have increased interest in auxetic materials, which have higher specific energy absorption performance compared to conventional solid absorbers. In the last decade, many optimization studies have been conducted to improve the energy absorption performance of auxetic tubular structures. Most studies focused on adding inner and outer shells to thin-walled auxetic tubular absorbers with different types of lattice structures to enhance the energy absorption of the cylindrical sandwiches. There are limited studies on thicker-walled auxetic tubes and their related shell thicknesses to optimize performance. In this study, the thickness of the thicker-walled auxetic core thickness (1.2 mm, 1.6 mm, and 2 mm), shell thickness (16 mm, 20 mm, and 24 mm), and auxetic lattice structure (Re-Entrant Circular, SiliComb, and ArrowHead) were optimized to improve the specific energy absorption of cylindrical sandwiches. The Taguchi method was used to determine the optimum parameters for cylindrical sandwiches. In addition, the effect ratio of the parameters on the specific energy absorption was investigated using the ANOVA method. The energy absorption properties of the cylindrical sandwiches were determined using the drop-weight test. The highest specific energy absorption was obtained using a shell thickness of 1.2 mm and a core thickness of 16 mm using a SiliComb lattice. It was determined that the lattice geometry was the most effective parameter for the specific energy absorption of cylindrical sandwiches, with an effect rate of 61.62%.

1. Introduction

In recent years, developments in the fields of design and technology have led to high engineering requirements. A challenge over a new lighter material without any strength or stiffness loss has been started to meet this demand. Alternatively, new structural materials that have a negative Poisson's ratio may be of interest. "Auxetic" refers to the behaviour of materials that have a negative Poisson's ratio. When auxetic materials are stretched in the longitudinal

direction, they elongate transversely, in contrast to conventional materials [1]. Along with superior indentation resistance, shearing resistance, and fracture toughness, auxetic materials also exhibit unique energy absorption compared to conventional materials [2].

The absorption behaviour of materials reduces the amount of energy transferred to the passengers of the vehicle in the event of a collision. Consequently, energy absorption performance is desired to be higher [3]. The energy absorption

*Corresponding author: o.kaya@ermetal.com

Received: 03.02.2023, Accepted: 16.06.2023

capacity of a material is directly related to its mass. Massive materials naturally absorb more energy. Specific Energy Absorption (SEA) enables the comparison of materials independent of mass. SEA refers to the energy absorption capacity of a material per mass. Auxetic materials have improved SEA compared to conventional materials [4].

Energy absorbers can basically be classified as solid or tubular. Research shows that tubular materials exhibit excellent energy absorption performance compared to solid materials under equal mass conditions [5]. Furthermore, when compared to straight tubular materials, auxetic tubular materials offer superior crashing performance [6], [7]. When the cylindrical inner and outer surfaces of the auxetic tubular material are covered with a shell, SEA increases dramatically. Guo et al. increased the SEA four times by covering the 4 mm thick auxetic tubes with 0.1 mm thick shells [8]. On the other hand, reinforcing a tubular absorber with a solid auxetic filler reduces the SEA value by about half [9]. A cylindrical sandwich consists of a tubular auxetic core with interior and exterior shells. The lattice geometry of the auxetic core, the thickness of the auxetic core, and the thickness of the shell are the essential factors influencing the SEA [10]. The lattice geometry is obtained by designing different patterns. Zhang et al., used the lattice design of tubular structures as a rotation and offset method [11]. It is possible to design a cylindrical sandwich from all auxetic lattices by the offset method. However, there is limited research on the energy absorption performance of different lattice geometries of the auxetic core, such as honeycomb, re-entrant, and Arrow-Head (AH) [8], [10], [12].

Applied compression to the energy absorbers under dynamic loading conditions indicates their crash performance. Test materials absorb the crashing energy of a free-falling load in the vertical direction or an accelerated load in the horizontal direction [7], [13]. A diagram is obtained by recording the contact force and displacement during the crash test. The absorbed energy is characterised by the area under the force-displacement plot. Experimental studies are used to determine the absorbed energy in order to enhance the material's crash performance.

Numerical methods such as FEA or experimental design methods such as Taguchi and ANOVA help to enhance the energy absorption behaviours of auxetic materials without additional experiments [14], [15]. The Taguchi design is provided to optimize the variables of the cylindrical sandwich in order to achieve SEA as a design objective. Taguchi is used to compare different

factors and their effects on the absorption energy of the auxetic structures [16]. It is also used to identify the main factors that influence the compression properties and failure behaviour of the structures. Additionally, Taguchi and ANOVA allow for the optimization of the parameters to obtain the optimal combination of the variables involved in the process, as well as the calculation of the signal-to-noise (S/N) ratio. This helps to improve the accuracy and reliability of the results and the efficiency of the process. [15]

In this study, the effect of lattice geometry (Re-Entrant Circular (REC), SiliComb (SC), and Arrow-Head (AH)), core thickness (1.2 mm, 1.6 mm, and 2 mm), and shell thickness (16 mm, 20 mm, and 24 mm) on the energy absorption performance of cylindrical sandwich composites were investigated. However, the impact of these parameters on the energy absorption performance of cylindrical sandwich composites with a statistical approach has not been encountered in the literature. For this reason, the purpose of this study is to examine the parameters that present the most significant effect on the energy absorption performance of cylindrical sandwiches and determine the importance order of these parameters by utilizing Taguchi and ANOVA methods. The results obtained from the statistical analyses can be used as a guide to determine the optimum working conditions.

2. Material and Method

2.1. Tensile Test

Dog-bone shaped specimens were 3D printed using the fused deposition modelling (FDM) method to obtain the tensile properties of the ABS. The 3D printing parameters of the test specimens are shown in Table 1. The overall dimensions of the test specimen are shown in Figure 1a. The changing of the raster angle according to the position of the 3D printed material on the print bed causes anisotropy in the material. To consider the variation of tensile properties, the test specimens shown in Figure 1b were positioned in the X and Y directions separately on the print bed.

The tensile test is adequate to validate the mechanical properties of the constitutive material of the auxetic lattice [17]. Tensile tests were conducted with the Zwick/Roell Z020 universal testing machine, whose maximum load capacity is 20 kN. Three tensile tests were performed for each direction (X and Y) according to EN ISO 527-1 at a rate of 2 mm/min. A

digital extensometer measured the deformation of the specimens to obtain the strain accurately.

dimensions of the lattices and sandwiches are given in Figure 2d.

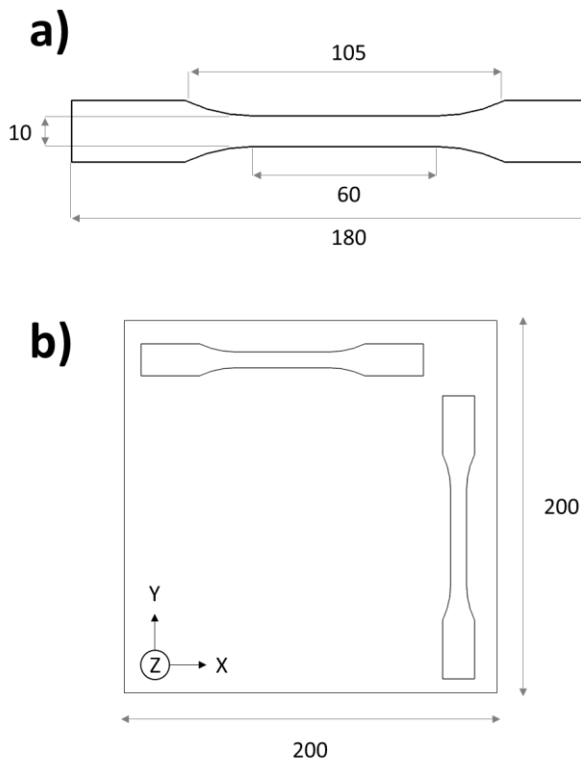


Figure 1. Dog-bone shaped strain test specimen a) Dimensions in 4mm thickness b) 3D Printing position on Print bed. (Dimensions given in mm unit)

2.2. 3D Printing of Cylindrical Sandwiches

Cylindrical sandwiches were designed using SolidWorks CAD software. Auxetic lattices shown in Figure 2 (upper) were expanded in the radial direction. The auxetic core consists of aligned multi-layered lattices around a cylinder. The 3D printed cylindrical sandwich consisted of an auxetic core covered by inner and outer shells. There is limited research on the lattice geometry of the auxetic core. In the literature, the effect of geometry on the energy absorption has been investigated. Based on this research, re-entrant, honeycomb, and AH geometry were used in the study. REC is a lattice geometry that has a higher SEA in panel form than Re-entrant lattice [18]. SILICOMB (SC) is a combination of the hexagonal and re-entrant lattices which has a higher SEA than both [8]. Figure 2a, b, and c (lower) show AH, REC, and SC structured cylindrical sandwiches, respectively. Core thickness, which describes the amount of expansion in the radial direction, was 16, 20, and 24 mm. Inner and outer shells had equal thicknesses of 1.2 mm, 1.6 mm, and 2 mm. The

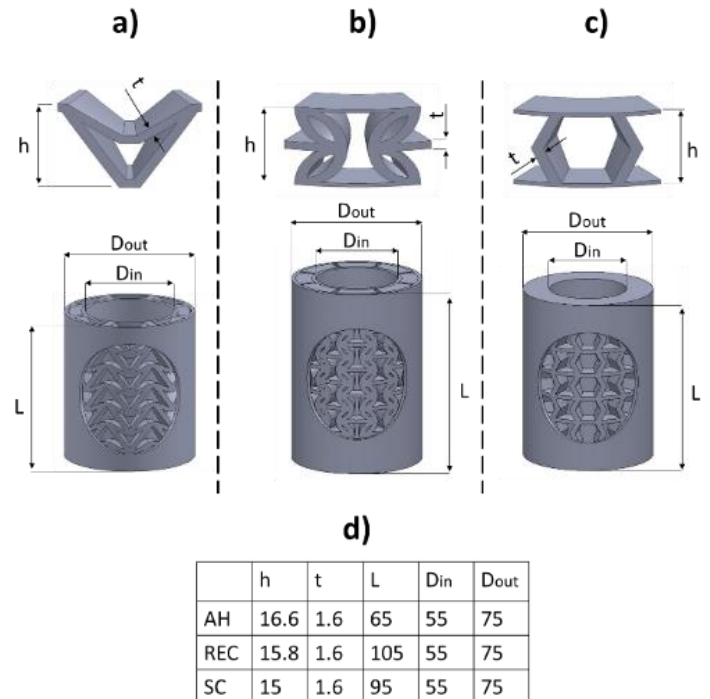


Figure 2. Structure of sandwiches a) AH lattice b) REC lattice c) SC lattice d) Dimensions. (Dimensions given by mm unit)

Cylindrical sandwiches were 3D printed using an Ekser 3B Plus 3D printer. ESUN commercial ABS filament was used for 3D printing. The effect of 3D printing parameters on surface, dimensional, and mechanical properties is researched in detail. Compressive strength is directly related to porosity. The lower porosity causes higher compressive strength [19], [20]. Also, surface quality, dimensional accuracy, tensile strength, and residual stresses are related to layer height, built orientation, raster angle, and speed of deposition, respectively [21]. The 3D printing parameters determined by considering physical properties, especially compressive strength, are the same as the tensile test specimens shown in Table 1. The 3D printing temperature, which slightly affects the physical properties, was adjusted to 270°C in accordance with the manufacturer's recommendation. There is no post-process such as grinding, polishing, thermal, or chemical treatment. The weights of the materials were determined by a precision scale.

Table 1. 3D Printing parameters of the tensile test specimens.

Parameter	Value
Raster Angle	30/-60°
Layer Height	0.3 mm
Extrusion Diameter	0.4 mm
Extrusion Temperature	272°C
Speed of deposition	32 mm/s

2.3. Drop Weight Tests

Analyzing an impacted weight from a drop hammer, a pendulum, or an inclined sled can identify a material's ability to absorb energy [22]. The characteristics of the impact weight influence material response. An impact weight that is liable to penetrate the material with a tip such as a hemispherical or square tip is preferred when blocking of the weight is desired. Besides, the holistic impact of the weight on the material is related to its energy transferring capacity. A flat drop hammer provides holistic impact, which distributes the energy across the lattice, whereas a hemispherical hammer provides penetration, which concentrates the energy in the centre of the lattice [23]. The holistic impact can be applied in horizontal, vertical, or inclined directions.

The drop-weight impact test is one of the common methods for the calculation of SEA [13], [14]. The transferred energy is absorbed by the deformed test material. The absorbed energy E_a given in Eq. (1) is equal to the product of reaction force F_r and amount of deformation Δ_S^f :

$$E_a = F_r \Delta_S^f \quad (1)$$

The drop-weight impact test reveals a series of F_r and Δ_S^f during the impact. Force-displacement curves are obtained by F_r and Δ_i^s , respectively. The area under the shadow of the force-displacement curve gives the total amount of absorbed energy E_t . The SEA given in Eq. (2) is the ratio of the total amount of E_t to the mass of the specimen m that was tested.

$$SEA = \frac{E_t}{m} \quad (2)$$

SEA is an indicator of the effect of parameter variations on the amount of absorbed energy for cylindrical sandwiches [8], [10], [12].

Set-up of the drop weight impact test shown in **Hata! Başvuru kaynağı bulunamadı.** was used in this study. The set-up of the drop weight, which is shown in **Hata! Başvuru kaynağı bulunamadı.**, impacted the cylindrical sandwich. The hammerhead, which has a weight of 580 kg, indicated by number 1, was released at a height of 350 mm from the test specimen placed on the support plate indicated by number 4. Contact forces and displacement of the hammerhead were recorded by the load cell and displacement sensor, indicated by numbers 2 and 3, respectively, during the impact. **Hata! Başvuru kaynağı bulunamadı.** b and c show test specimen #1 placed in the test machine before and after the impact is applied, respectively.

Force-displacement curves are obtained from the data of the load cell and displacement sensor. The area of each slice is formed by F_r and Δ_S^f is equal to E_a given in equation 1. E_t or the area under the shadow of the force-displacement curve is calculated by the total amount of slices. SEA is obtained by the ratio of each E_t to mass of the related sample.

2.4. Taguchi Method

The Taguchi method is one of the most reliable design and optimization techniques to determine the optimal combination of different parameters for the target function. The Taguchi method provides an effective and systematic way to achieve results with far less experimentation.

In this study, it was determined that lattice geometry, shell thickness, and core thickness were target factors for the optimization of the cylindrical sandwich. Several levels of the target factors were evaluated to optimize the energy absorption performance. SEA, which was obtained by drop weight tests, was the indicator of the target factors. The design of the experiment was utilized to compare the levels of each factor to find the optimum level. A full factorial design of experiments required 27 experiments for three factors at three levels. The Taguchi method was used to optimize the target factors with fewer experiments. The orthogonal array table (L9), which requires 9 experiments, is shown in In data analysis, the results of the target functions are converted into the S/N ratio. Depending on the objective function type, three different S/N ratios are used for the calculations, i.e., the lower is the better, the higher is the better, and the nominal is the best. In this study, since the highest specific energy

absorption is the target function, the higher the better characteristic has been selected. The S/N ratios for the higher is better situation are calculated using Eq. (3):

$$S/N = -10 \log \left(\frac{1}{n} \sum_{i=1}^n y_i^2 \right) \quad (3)$$

In this equation, n indicates the number of tests (i.e., number of case) and y_i defines the resulting value for the i th performance characteristics.

In data analysis, the results of the target functions are converted into the S/N ratio. Depending on the objective function type, three different S/N ratios are used for the calculations, i.e., the lower is the better, the higher is the better, and the nominal is the best. In this study, since the highest specific energy absorption is the target function, the higher the better characteristic has been selected. The S/N ratios for the higher is better situation are calculated using Eq. (3):

$$S/N = -10 \log \left(\frac{1}{n} \sum_{i=1}^n y_i^2 \right) \quad (3)$$

In this equation, n indicates the number of tests (i.e., number of case) and y_i defines the resulting value for the i th performance characteristics.

Table 2.

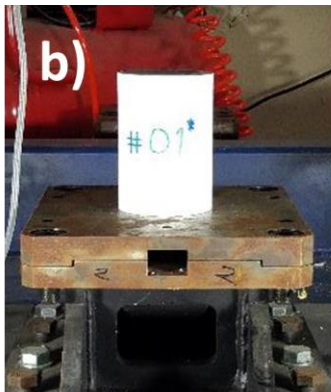
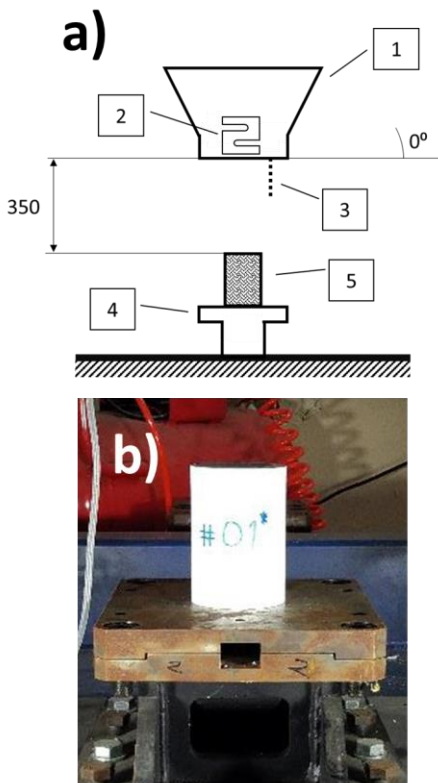


Figure 3. Drop weight test set-up a) schematic view (1: hammer head 2: load cell 3: displacement sensor 4: support plate 5: test specimen) b) detailed view of the test specimen #1 on the support plate c) overall view.

Table 2. Levels and factors in accordance with the Taguchi design.

Factor	Level 1	Level 2	Level 3
Lattice Geometry	REC	SC	AH
Shell Thickness	1.2	1.6	2.0
Core Thickness	16	20	24

2.5. ANOVA Method

ANOVA, which enables analysis with fewer experiments, compares the effect rates of factors, unlike the Taguchi method, which compares the levels of factors. The same 9 experiments from the Taguchi method were evaluated for ANOVA. SEA, which was obtained by drop weight tests, was the indicator of the target factors. Lattice geometry, shell thickness, and core thickness were the target factors to determine how much they affected the SEA. The power of each factor was represented by the contribution (P) ratio, which provides a numerical approach to compare factors. Data obtained from the drop weight test was analysed, and P values were calculated.

ANOVA is a statistical method that is utilized to determine the contribution ratios of each parameter to the response variable. By comparing the importance levels acquired from the Taguchi method, the ANOVA method can validate statistical analysis results. In the ANOVA method, contribution ratios of each parameter, degree-of-freedom (DOF), sum of

squares (SS), mean of squares (MS), and F values are calculated by the following equations:

$$F_{factor} = \frac{V_{factor}}{V_{error}} \quad (4)$$

$$V_{factor} = \frac{SS_{factor}}{DOF_{factor}} \quad (5)$$

$$DOF_{factor} = k - 1 \quad (6)$$

$$SS_{factor} = \frac{\sum \beta_{factor,i}^2}{N} - \frac{(\sum \beta_i)^2}{n} \quad (7)$$

where F_{factor} is the factor's test value and is used to determine whether the term is associated with the response. V_{factor} and V_{error} values are the variance of the factor and error, respectively. DOF_{factor} is the number of factor's degree of freedom, SS_{factor} is the sum of squares due to the factor, $\beta_{factor,i}$ is the sum of the S/N ratio at the i th level of the factor, β_i is the S/N ratio at the i th level of the factor, N is the repeating number of each level's factor, n is the number of tests. In these equations, "factor" represents the name of the individual factors. MS is equal to the ratio of the SS values of each parameter to the DOF of each parameter [24].

3. Results and Discussion

3.1. Tensile Tests

The ultimate tensile strength (UTS) of the 3D-printed ABS changes from 3.95 to 36.03 MPa depending on the part orientation, raster angle, and raster width [25]. Three tensile samples in each direction (X and Y) were tested. 3D printed ABS materials with 30° and -60° angled rasters had 30.1 and 32.27 MPa mean UTS, respectively. Table 3 shows the results of the tensile tests. A slight difference was found between the raster angles. The material used in this study with 30/-60° raster angle had a relatively high UTS compared to previous studies.

3.2. Drop Weight Tests

Nine drop weight tests were performed for each specimen. Force-displacement curves obtained from the drop weight tests are shown in Figure 4. Force-displacement curves had a characteristic slope depending on their lattice geometry. The force-displacement curve of the REC lattice shown in Figure 4a had a significant initial peak force at a large displacement area at the early stage of impact. A few peak forces, which do not contribute to enlarging the energy absorption area, followed the initial peak force. The force-displacement curves of the SC and AH lattices shown in Figure 4 b and c had a slightly separated initial peak force. Lots of balanced peak forces, which followed the initial peak force, kept the average force higher. SC lattice had sharper peak forces than AH lattice.

Table 3. Tensile properties of the ABS which constitutive material of the auxetic sandwiches.

Specimen	UTS (N/mm ²)	Strength at Break (N/mm ²)	Elongation at Break (%)
#X1	29.46	28.71	1.83
#X2	30.09	29.77	1.85
#X3	30.75	30.45	1.96
Std. Dev.	0.65	0.88	0.07
Mean X	30.10	29.64	1.88
#Y1	32.42	28.20	3.81
#Y2	32.22	27.48	3.29
#Y3	32.17	27.82	2.89
Std. Dev.	0.13	0.36	0.46
Mean Y	32.27	27.83	3.33

The amounts of absorbed energy were obtained from the area under the force-displacement curves for each experiment. SEA was calculated as the ratio of absorbed energy to mass. Absorbed energy and SEA values of experiments are shown in

Table 4. Considering the lattice geometry, REC had relatively high energy absorption, followed by SC and AH. SEA was too complexly distributed to explain the factors or levels related to mass. On the other hand, a clear relation wasn't found between values of absorbed energy, or SEA, without the Taguchi method or ANOVA.

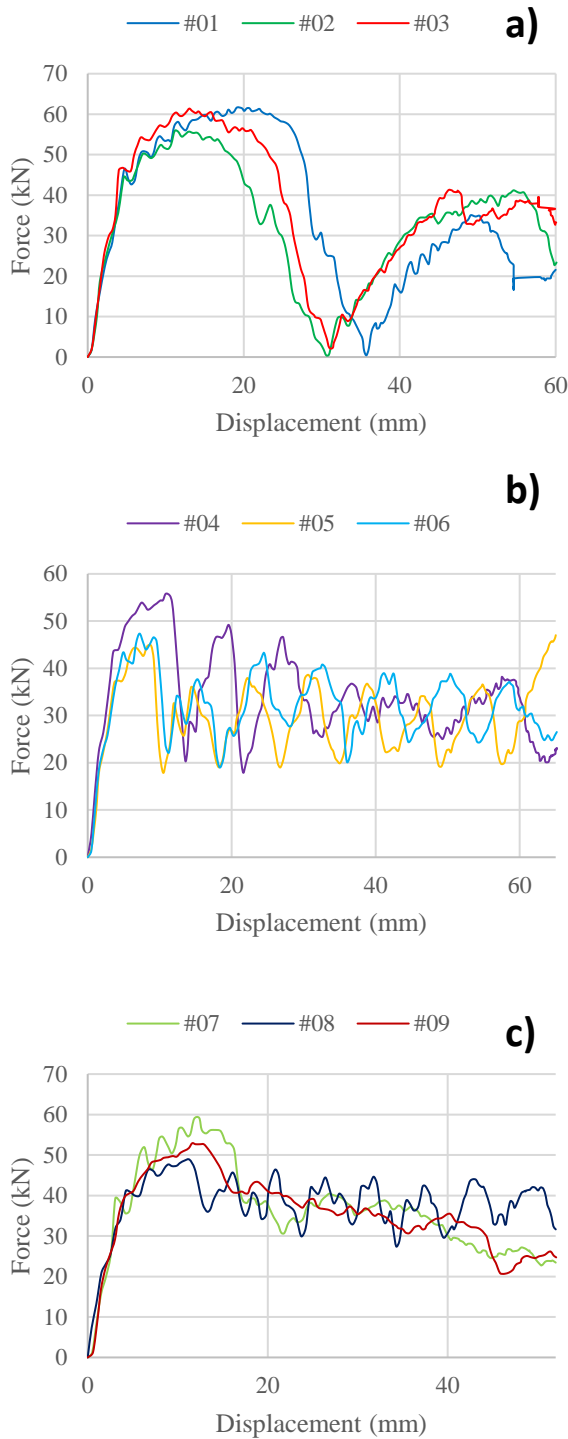


Figure 4. Force-displacement plots of; a) REC b) SC c) AH latticed sandwiches obtained by drop weight tests.

3.3. Optimization Study

Average S/N ratios and rankings of parameters are presented in Table 5. In this table, Delta states the

difference between the maximum and minimum of the S/N ratio for each parameter. Rank is the order of parameters according to the energy absorption performance of cylindrical sandwich composites. It is seen from Table 5 that the lattice geometry is the most effective parameter on the energy absorption performance, while the shell thickness is the least effective parameter.

The S/N ratio variation of each factor that can be used to determine the optimum combination is shown in Figure 5. The level with the largest S/N ratio gives the optimum level of design factors. Therefore, in this study, the optimum combination was determined to be SC for lattice geometry, 1.2 mm for shell thickness, and 16 mm for core thickness. In addition to the optimum combination, the worst combination for specific energy absorption was determined to be AH for lattice geometry, 2.0 mm for shell thickness, and 24 mm for core thickness.

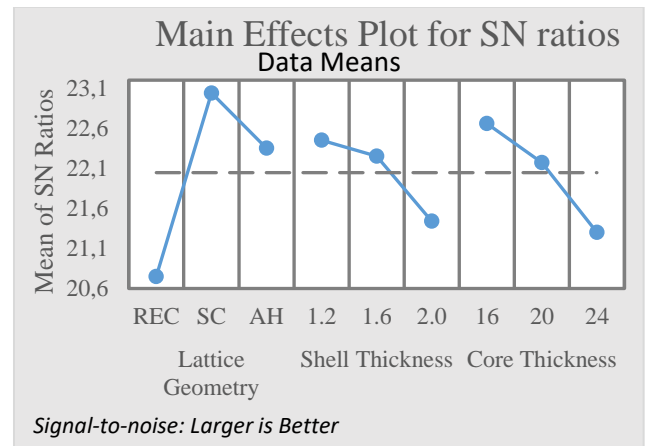


Figure 5. S/N ratios of the factors obtained by drop weight tests.

In addition to the Taguchi method, ANOVA has been used as a second method to support the reliability of the results. The level of each factor and specific energy absorption at these operating conditions are analysed by the ANOVA method, and the analysis results are given in Table 6. The calculated confidence level of the model was 93.44%. Lattice geometry was the most effective factor on specific energy absorption with a contribution ratio of 61.62%, and core thickness followed this parameter with a contribution ratio of 20.83%. Compared with these two factors, shell thickness had a slight effect on energy absorption, with a contribution ratio of 10.98%. These results show the same tendency as the results obtained from the Taguchi method.

Table 4. Results of the drop weight tests.

Experiment	Level of Lattice Geometry	Level of Shell Thickness	Level of Core Thickness	Absorbed Energy (kJ)	SEA (J/g)	S/N Ratio
#01	1	1	1	2.20	11.76	21.4070
#02	1	2	2	2.41	11.63	21.3084
#03	1	3	3	2.20	9.46	19.5200
#04	2	1	2	2.20	15.29	23.6872
#05	2	2	3	1.92	12.79	22.1384
#06	2	3	1	2.10	14.59	23.2832
#07	3	1	3	1.88	12.95	22.2438
#08	3	2	1	1.96	14.62	23.2965
#09	3	3	2	1.83	11.89	21.5042

Table 5. Average S/N ratios and ranking parameters

Level	Lattice Geometry	Shell Thickness	Core Thickness
1	20.75	22.45	22.66
2	23.04	22.25	22.17
3	22.35	21.44	21.3
Delta (max-min)	2.29	1.01	1.36
Rank	1	3	2

4. Conclusion and Suggestions

Applications of auxetic materials as energy absorbers are gaining increasing interest. To sum up, in this study, the energy absorption capability of the cylindrical sandwich consisting of an auxetic core and shells was examined. The auxetic parameters of materials were optimized to improve their energy

absorption performance. The following is a conclusion of the major findings drawn from experiments and analysis:

- Force-displacement plots of SC and AH lattices had a range of peak forces well-balanced around a line. On the other hand, the REC lattice had a single peak force following the initial peak force. Force-displacement plots of SC and AH lattices showed the characteristic behaviour of energy absorbers, unlike REC.
- The Taguchi method optimized the lattice geometry, shell thickness, and core thickness for the highest energy absorption performance. S/N responses indicated that cylindrical sandwiches had the highest SEA

Table 6. ANOVA test results of the factors obtained by drop weight tests.

Factor	DOF*	SS*	MS	F Value	P* (%)
Lattice Geometry	2	16.733	8.3664	9.39	61.62
Shell Thickness	2	2.982	1.4908	1.67	10.98
Core Thickness	2	5.657	2.8285	3.18	20.83
Error	2	1.781	0.89		6.56
Total	8	27.153			100

*DOF, Degree of Freedom; SS Sum of Square; P, Contribution

with a core thickness of 1.2 mm, a shell thickness of 16 mm, and a SC lattice.

- It was found that lattice geometry, which had a 61.62% rate of contribution, was the main factor affecting the energy absorption of the cylindrical sandwich by the ANOVA method.

As a result, this study can be a guide for researching new generation crash box design in the future. However, more studies are needed to evaluate crash performance beyond the energy absorption and correlate it with Poisson's ratios.

Acknowledgment

This work was supported by the Bursa Technical University Scientific Research Projects Coordination Unit (Project no: 220Y021) and TÜBİTAK 2210-D program. We would like to thank Ermetal Automotive for their support in the supply of the 3D Printed specimens.

Conflict of Interest Statement

There is no conflict of interest between the authors.

Statement of Research and Publication Ethics

The study is complied with research and publication ethics.

References

- [1] K. E. Evans and A. Alderson, "Auxetic materials: Functional materials and structures from lateral thinking!," *Advanced Materials*, vol. 12, no. 9, pp. 617–628, 2000, doi: 10.1002/(SICI)1521-4095(200005)12:9<617::AID-ADMA617>3.0.CO;2-3.
- [2] G. N. Greaves, A. L. Greer, R. S. Lakes, and T. Rouxel, "Poisson's ratio and modern materials," *Nat Mater*, vol. 10, no. 11, pp. 823–837, 2011, doi: 10.1038/nmat3134.
- [3] J. Zhang, G. Lu, and Z. You, "Large deformation and energy absorption of additively manufactured auxetic materials and structures: A review," *Compos B Eng*, vol. 201, no. 108340, pp. 1–36, 2020, doi: 10.1016/j.compositesb.2020.108340.
- [4] A. Alomarah, S. H. Masood, and D. Ruan, "Out-of-plane and in-plane compression of additively manufactured auxetic structures," *Aerosp Sci Technol*, vol. 106, pp. 106–107, 2020, doi: 10.1016/j.ast.2020.106107.
- [5] C. Luo, C. Z. Han, X. Y. Zhang, X. G. Zhang, X. Ren, and Y. M. Xie, "Design, manufacturing and applications of auxetic tubular structures: A review," *Thin-Walled Structures*, vol. 163, no. December 2020, 2021, doi: 10.1016/j.tws.2021.107682.
- [6] Q. Gao, L. Wang, Z. Zhou, Z. D. Ma, C. Wang, and Y. Wang, "Theoretical, numerical and experimental analysis of three-dimensional double-V honeycomb," *Mater Des*, vol. 139, pp. 380–391, 2018, doi: 10.1016/j.matdes.2017.11.024.
- [7] W. Lee *et al.*, "Effect of auxetic structures on crash behavior of cylindrical tube," *Compos Struct*, vol. 208, no. April 2018, pp. 836–846, 2019, doi: 10.1016/j.compstruct.2018.10.068.
- [8] Y. Guo *et al.*, "Deformation behaviors and energy absorption of auxetic lattice cylindrical structures under axial crushing load," *Aerosp Sci Technol*, vol. 98, p. 105662, 2020, doi: 10.1016/j.ast.2019.105662.
- [9] F. Usta, O. F. Ertaş, A. Atalp, H. S. Türkmen, Z. Kazancı, and F. Scarpa, "Impact behavior of triggered and non-triggered crash tubes with auxetic lattices," *Multiscale and Multidisciplinary Modeling, Experiments and Design*, vol. 2, no. 2, pp. 119–127, 2019, doi: 10.1007/s41939-018-00040-z.
- [10] H. Sun, C. Ge, Q. Gao, N. Qiu, and L. Wang, "Crashworthiness of sandwich cylinder filled with double-arrowed auxetic structures under axial impact loading," *International Journal of Crashworthiness*, pp. 1–10, 2021, doi: 10.1080/13588265.2021.1947071.

- [11] X. Y. Zhang *et al.*, “A novel type of tubular structure with auxeticity both in radial direction and wall thickness,” *Thin-Walled Structures*, vol. 163, no. March, p. 107758, 2021, doi: 10.1016/j.tws.2021.107758.
- [12] L. Chen *et al.*, “Dynamic crushing behavior and energy absorption of graded lattice cylindrical structure under axial impact load,” *Thin-Walled Structures*, vol. 127, no. October 2017, pp. 333–343, 2018, doi: 10.1016/j.tws.2017.10.048.
- [13] L. Jiang and H. Hu, “Finite element modeling of multilayer orthogonal auxetic composites under low-velocity impact,” *Materials*, vol. 10, no. 8, 2017, doi: 10.3390/ma10080908.
- [14] B. G. Çakan, C. Ensarioglu, V. M. Küçükakarsu, I. E. Tekin, and M. Cemal Çakir, “Experimental and numerical investigation of in-plane and out-of-plane impact behaviour of auxetic honeycomb boxes produced by material extrusion,” *Journal of the Faculty of Engineering and Architecture of Gazi University*, vol. 36, no. 3, pp. 1657–1667, 2021, doi: 10.17341/gazimmfd.829758.
- [15] M. Cherief, A. Belaadi, M. Bouakba, M. Bourchak, and I. Meddour, “Behaviour of lignocellulosic fibre-reinforced cellular core under low-velocity impact loading: Taguchi method,” *International Journal of Advanced Manufacturing Technology*, vol. 108, no. 1–2, pp. 223–233, 2020, doi: 10.1007/s00170-020-05393-9.
- [16] Q. Gao, X. Zhao, C. Wang, L. Wang, and Z. Ma, “Multi-objective crashworthiness optimization for an auxetic cylindrical structure under axial impact loading,” *Mater Des*, vol. 143, pp. 120–130, 2018, doi: 10.1016/j.matdes.2018.01.063.
- [17] C. Qi, F. Jiang, C. Yu, and S. Yang, “In-plane crushing response of tetra-chiral honeycombs,” *Int J Impact Eng*, vol. 130, no. April, pp. 247–265, 2019, doi: 10.1016/j.ijimpeng.2019.04.019.
- [18] C. Qi *et al.*, “Quasi-static crushing behavior of novel re-entrant circular auxetic honeycombs,” *Compos B Eng*, vol. 197, no. 108117, pp. 1–12, 2020, doi: 10.1016/j.compositesb.2020.108117.
- [19] S. H. Ahn, M. Montero, D. Odell, S. Roundy, and P. K. Wright, “Anisotropic material properties of fused deposition modeling ABS,” *Rapid Prototyp J*, vol. 8, no. 4, pp. 248–257, 2002, doi: 10.1108/13552540210441166.
- [20] K. C. Ang, K. F. Leong, and C. K. Chua, “Investigation of the mechanical properties and porosity relationships in fused deposition modelling-fabricated porous structures,” vol. 2, no. November 2005, pp. 100–105, 2006, doi: 10.1108/13552540610652447.
- [21] O. A. Mohamed, S. H. Masood, and J. L. Bhowmik, “Optimization of fused deposition modeling process parameters : a review of current research and future prospects,” pp. 42–53, 2015, doi: 10.1007/s40436-014-0097-7.
- [22] G. Lu and T. Yu, “Introduction,” *Energy Absorption of Structures and Materials*, pp. 68–87, 2003, doi: 10.1533/9781855738584.68.
- [23] T. Shepherd, K. Winwood, P. Venkatraman, A. Alderson, and T. Allen, “Validation of a Finite Element Modeling Process for Auxetic Structures under Impact,” *Phys Status Solidi B Basic Res*, vol. 257, no. 10, pp. 1–14, 2020, doi: 10.1002/pssb.201900197.
- [24] A. H. Bademlioglu, A. S. Canbolat, N. Yamankaradeniz, and O. Kaynakli, “Investigation of parameters affecting Organic Rankine Cycle efficiency by using Taguchi and ANOVA methods,” *Appl Therm Eng*, vol. 145, no. September, pp. 221–228, 2018, doi: 10.1016/j.applthermaleng.2018.09.032.
- [25] F. Rayegani and G. C. Onwubolu, “Fused deposition modelling (fdm) process parameter prediction and optimization using group method for data handling (gmdh) and differential evolution (de),” *International Journal of Advanced Manufacturing Technology*, vol. 73, no. 1–4, pp. 509–519, 2014, doi: 10.1007/s00170-014-5835-2.

An Approach to Determine of the Formation Stages of Volcanism Using Natural Gamma-Ray Spectrometer from Geophysical Methods (Example of Gölcük Volcanism)

Nurten Ayten UYANIK^{1*}

¹Isparta University of Applied Sciences, Vocational School of Technical Sciences, Isparta-Turkey.
(ORCID: 0000-00028912-0361)



Keywords: Geophysics, Natural radioactivity, Radioactive elements, Gölcük volcanism, Volcanic stage.

Abstract

Gölcük Caldera is in the Isparta Angle, which is an interesting tectonic structure in Southwest Anatolia. This caldera is formed as a result of back-arc volcanism associated with the northward subduction zone of the African plate under the Eurasian Plate during the Tertiary. It attracts the attention of many researchers with its tectonic and volcanic structure. In this article, the results of in situ natural gamma radiation measurements made in the caldera are evaluated. In the study, radioactive element (Potassium (%K), Uranium (eU), and Thorium (eTh)) contents of volcanic were measured in situ with the portable gamma-ray spectrometer, which is effectively used in Geophysical Engineering. The changes in natural gamma radiation of alkaline volcanic are presented with maps. When these maps are examined, it is understood that K%, U-ppm and Th-ppm concentrations of Gölcük volcanic are higher than the world average values. The high potassium concentration draws even more attention. The high potassium content indicates that the local volcanic are ultrapotassic and contain lithospheric materials. In addition, since the radioactive element concentration will reflect the magmatic development, the volcanic stages in the region have been tried to be determined. The number of these stages was determined from the curves of the radioactive data from a purely geophysical engineering (numerical) point of view, and the study area was interpreted as consisting of three different phases. This finding is supported by the results of the articles on the aging studies of the samples taken as a result of observations. In addition to these, the ranges of radioactive elements belonging to these stages were determined.

1. Introduction

Portable gamma-ray spectrometers are widely used in field studies for different purposes. As it is known, the most intense radioactive elements in nature are ⁴⁰K, ²³⁸U and ²³²Th. In situ gamma-ray spectrometry studies allow numerically in-situ and instant evaluation of these radioactive elements, which are more or less present in rocks. With these numerical values obtained, environmental radioactivity can be also determined quickly and accurately. The geological environment formed as a result of the ejection and precipitation of ash and rocks, especially during volcanic activities, consists of volcanic products. People living in these volcanic regions are exposed to radiation due to the geological environment. Therefore, it is important to determine the levels of natural radioactivity that will affect human health and to make comparisons according to [1]. For that purpose, many

researchers have identified areas with radiological risk in their studies [2]-[17]. Serious health problems may occur in people living in areas with this radiological risk, and it is stated in [18] that people living in environments where radioactive elements are concentrated have serious cancer disorders. Accordingly, many researchers have conducted studies on the effect of cancer (for example: Kırklareli-Türkiye [19]; Isparta-Türkiye [8]; Penang-Malaysia [20]; Afyon-Türkiye [21]). In addition to studies in terms of human health, gamma-ray spectrometry studies geological unit separation [8], [12], precious metal and radioactive element exploration [12], [22], [23], geothermal studies [11], agricultural areas [24], archaeological sites [25] and it are used for many such purposes. In addition, the radioactive element concentration in the field gives also additional information about the geodynamics and tectonics of that region. Generally, ⁴⁰K, ²³⁸U and ²³²Th are found in high concentrations in acidic intrusive rocks. As

*Corresponding author: aytenuyanik@isparta.edu.tr

Received: 20.01.2023, Accepted: 07.04.2023

the higher the silica contents of a rock, the higher the uranium content. Ultramafic rocks, on the other hand, have lower radioelement concentrations. Radioelement concentrations of sedimentary and igneous rocks vary depending on their composition and location [26]. The average concentrations of ^{40}K , ^{238}U and ^{232}Th elements in the continental crust are in the range of 2-2.5%, 2-3ppm and 8-12ppm, respectively [27]. Many studies show that the radioactive element concentrations in rocks formed as a result of volcanic activity are higher than the crustal averages [8], [11], [12], [28]-[31]. Similarly, it is stated that magmatic stages are also reflected by ^{40}K , ^{238}U and ^{232}Th radioelement concentrations [32]-[34].

The study area is mostly composed of volcanic units as a result of Gölcük volcanism. The volcanic products in the field are named as the Isparta volcanic series [35] and it is understood from the in situ gamma-ray spectrometer measurement results that they are quite rich in potassium. As a result of the dating studies carried out in Gölcük volcanism, it is stated that it consists of three different stages [36]-[38]. Gölcük volcanics have a medium-basic composition and are stated to be shoshonitic-ultrapotassic in character [38]. Field measurements include Plio-Quaternary trachytes, tefrifonolites, pyroclastics and Quaternary alluviums. In general, the concentration values of radioactive elements increase from the old to the young volcanic phase. This study presents the results of in situ gamma ray spectrometry on the Gölcük volcanic units and an approach for estimating the stages of volcanism based on these results.

2. Formation Stages of Tectonics and Volcanism

The existence of an extensional tectonic setting in Southwest Anatolia has been revealed as a result of analyzes based on earthquake waves [39], [40]. Similarly, tectonic structure can be determined using many Geophysical methods (Gravity [41]-[46], electric-electromagnetic [47], seismic reflection [46], [48] etc.). Gölcük volcanism is associated with dextral strike-slip faults that developed depending on the tension regime as a result of the clockwise rotation of the Pliocene tectonics. This tectonic regime in the Late Pliocene period created normal faulting and, accordingly, the depression areas such as the Kovada graben [49]. The volcanism that took place around Gönen in the north of Isparta, around Bucak in the south of Isparta and in Gölcük was emplaced on these faults approximately in the North-South direction [50]. [51] and [52] emphasize that this hyper-alkaline volcanism around Isparta may be associated with the intra-continental strike-slip regime. Gölcük volcanism is located in the volcanic sequence starting from Antalya and extending to Isparta-Afyon-Kırka within the tectonic structure defined as Isparta Bend [53 or Isparta Angle [54]-[56] by different researchers (Figure 1).

Located in the south of Kırka-Afyon-Isparta volcanic province and common in the southern region of Isparta, pyroclastics and volcanic rock components are the products of Gölcük volcanism. Gölcük volcanism is a maar-type (slightly swollen, wide, water-filled and shallow

crater lake formed by magma and lava as a result of eruption or eruption) volcanism [57], [58]. In many studies, the age determination of Gölcük volcanics has been made and the volcanics in question have been aged in the range of 4.7-4.0my [36], [37], [52], [59]. Gölcük volcano continued its explosion and eruption activity during the Pliocene [36], [60], [61]. [36] divided the volcanic activity in the region into two phases; (i) Lamprophyry, basaltic trachyandesitic, trachyandesitic and trachytic lava outcrops represented by Pliocene volcanic activity, and (ii) Pleistocene eruption that started with a big eruption forming the caldera. According to [62], the evolution and dating of the Isparta volcanism: (i) formation of lamprophyric dykes ($6.21 \pm 0.3\text{my}$), (ii) trachyandesitic-trachytic (4.6 ± 0.23 - $4.25 \pm 0.21\text{my}$), (iii) development of basaltic trachyandesitic-trachybasaltic volcanism (4.07 ± 0.2 - $3.68 \pm 0.5\text{my}$), formation of pyroclastics (1.5 ± 0.18 - $0.39 \pm 0.2\text{my}$) and phonolitic ring dykes ($0.35 \pm 0.1\text{my}$) due to volcanic eruption. In addition to these, [38] states that this volcanism developed in three different phases and these are (i) extrusive volcanism consisting of trachyte, trachyandesite, basaltic trachyandesite, phonolite, tefrite and lamprophyres; (ii) explosive volcanism consisting of ignimbrite, unconsolidated tuff, agglomerate and pumice; (iii) extrusive volcanism consisting of trachyte and trachyandesite.

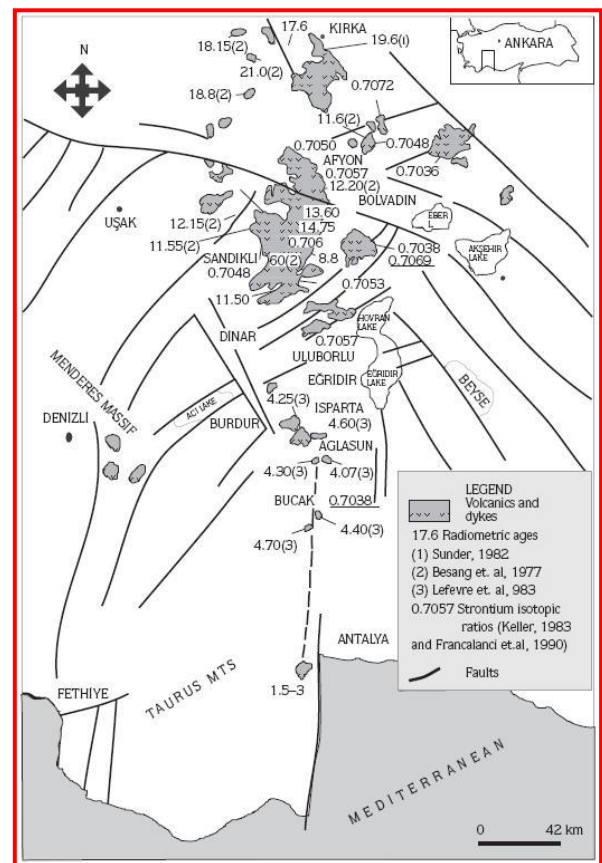


Figure 1. Distribution of Kırka-Afyon-Isparta alkaline volcanic rocks in relation to fault systems, Sr isotope and radiometric dating [52]

3. Applied Method and Study Area

3.1. Gamma-Ray Spectrometer Method

Although there are at least twenty elements known as natural and radioactive, Potassium (^{40}K), Uranium (^{238}U), and Thorium (^{232}Th) isotopes come to the fore in geophysical researches because they are more than other elements. In geophysical studies, gamma ray spectrometers are used to determine the amount of these three elements in soil and rock quickly and in situ. Gamma-ray spectrometers have the same working principle as scintillometers. However, the spectrometer is an electronically more advanced form of the scintillometer, which distinguishes characteristic gamma rays from ^{40}K , ^{238}U and ^{232}Th according to their energies (Figure 2).

Spectrometers with quad-window are standard, and a 512-channel gamma-ray spectrometer in which gamma rays are divided into 512 equal intervals in the 0-3MeV energy band was used in this study. Each channel of the spectrometer has an energy interval of about 6KeV. These types of spectrometers have been successfully used for the detection of artificial and natural radioactive elements [64]. The gamma-ray spectrometer device used in the study is suitable for point, profile and continuous measurements using external GPS. The spectrometer used is a 512-channel, 6.3-inch³-volume thallium-activated sodium iodide [NaI (TI)] crystal, Cs¹³⁷ external reference source, and an efficient and highly discrimination instrument with zero dead time. The purpose of gamma-ray spectrometry is to determine only the numbers of radioactive radiation emitted from the earth's crust. For this purpose, the potassium, uranium and thorium concentrations in the rock or soil are obtained using the equation below.

$$C_w = N_w * S_w \quad (1)$$

Here; C_w , w (K, U, Th) element concentration,
 N_w , The net radiation number in the channel belonging to the w (K, U, Th) elements,

S_w represents the sensitivity of the channels belonging to the w (K, U, Th) elements of the spectrometer.

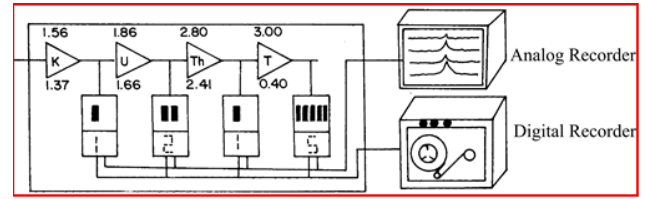


Figure 2. Schematic representation of a four-channel spectrometer and recorders [62]

3.2. Study Area and Simplified Geology

The units around Gölcük caldera are named as Gölcük volcanics by [35] and Pürenova formation by [65]. The lithological units of the Gölcük Caldera and its surroundings are trachyte, trachyandesite, andesite, volcanic tuff, and pumice series. Plio-Quaternary lithological units of Gölcük volcanism are limited by Middle Eocene aged flysch deposits in the north; Triassic-Cretaceous aged Akdağ limestones in the south, and Isparta plain alluviums in the west, including Gölcük volcanics. The Gölcük formation is intercalated with Plio-Quaternary lake sediments and its thickness is around 1000m [65]. The caldera and its surrounding rock assemblage are defined as an asymmetrical eruption structure with a diameter of 3-4km, located on the south-southwest edge of the Isparta graben at an altitude of 1378m above sea level [66]. In the study area, discontinuous circular tefrifonolitic lava flows on the caldera margins and dykes of the same composition cutting them and trachytic domes of different sizes are observed in the caldera (Figure 3).

In-situ measurements were made at 305 points with gamma-ray spectrometry in the Gölcük Caldera (Figure 3). Measurements include volcano-sediments consisting of alluvium, small and medium-sized trachytes (Trachytic domes in Pilav-Hill and its Southeast), pyroclastics and tefrifonolites within the caldera.

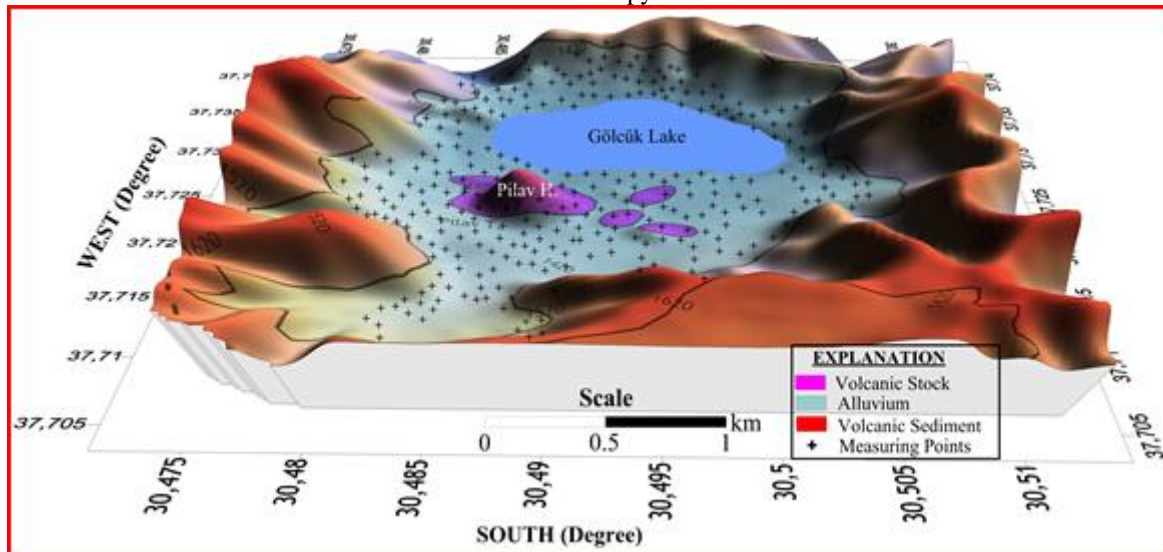


Figure 3. Simplified geology and measurement points of Gölcük Caldera and its surroundings (edited from [67])

4. Results and Discussion

4.1. Distribution of Radioactive Elements in Gölcük Volcanics

Looking at the maps created from gamma-ray spectrometry measurements (Figure 3) made at 305 different points on the Gölcük volcanics, the most striking feature is the high concentration of radioactive elements in all of the volcanics. Three different units are distinguished in the simplified geological map of the study area (Figure 3). These are volcanic stocks, Alluvial and Volcano sedimentary. It is observed that ^{40}K , ^{238}U and ^{232}Th concentration values in the study area vary between 2.80-6.1%, 9-28.2ppm and 41.3-70.7ppm for all units, respectively (Table 1). The ^{40}K , ^{238}U and ^{232}Th concentration values of trachyte in Pilavtepe and its southeast, which are specified as volcanic stock, vary between 3.9-5.3%, 15.8-23.2ppm and 49.1-66.6ppm, respectively. The average concentration values of these trachytic domes are 4.7%, 18.4ppm and 57.4ppm, respectively. The average values of the intra-caldera alluvial and volcanic sedimentary units are measured 4.4%, 17.2ppm and 51.9ppm, and 4.9%, 19.2ppm and 56.7ppm, respectively (Table 1). These values are considerably higher than the world average values. These changes in the concentration values of the radioactive elements reflect the geochemical differences of the Gölcük volcanics forming the Gölcük lake vicinity. In Figure 4, the distribution map of the study area and ^{40}K , ^{238}U , ^{232}Th concentration values

in the blue-red color range is presented. The blue color and the white areas indicate the area of the limestone block in the study area. Green, yellow and red colored areas show the products of Gölcük volcanic. The areas within the Gölcük volcanics with low (green colored areas) radioactive element concentration values can be interpreted as the fact that the older volcanic series are mafic (rock and silicate minerals rich in magnesium and iron). On the other hand, high (red colored areas) radioactive concentration values reflect the areas where the felsic (silicate minerals enriched with lighter elements such as silicon, oxygen, aluminum, sodium and potassium, and rocks rich in feldspar and quartz minerals) volcanics of the younger series outcrop. While rocks composed of mafic minerals (olivine, pyroxene, amphibole, biotite, etc.) are darker in color, felsic rocks are lighter in color and less dense. It is seen in Figure 4 that the ^{40}K and ^{232}Th concentration values are higher than the ^{238}U concentration values in the study area in general. While the color red is more common in the ^{40}K and ^{232}Th maps, the ^{238}U map has a red color (high concentration value) in a specific area in the northeastern and southern parts of the map. It is seen that high values of ^{40}K and ^{232}Th are also obtained in sections the high of the ^{238}U concentration value in Figure 4, and these values correspond to areas where volcanic sediments are located. However, in Pilavtepe and in the Southeast of this hill where volcanic stocks are located, ^{40}K and ^{232}Th values are measured high values while ^{238}U values are low. Areas with low ^{238}U values may be caused by ultramafic or ultrabasic rocks due to low silica content.

Table 1. Concentration values of radioactive elements measured in Gölcük caldera.

	^{40}K (%)			^{238}U (ppm)			^{232}Th (ppm)		
	Min.	Max.	Aver.	Min.	Max.	Aver.	Min.	Max.	Aver.
Volcanic Stock	3.9	5.3	4.7	15.8	23.2	18.4	49.1	66.6	57.4
Alluvium	2.8	5.9	4.4	9.1	20.9	17.2	41.3	55.8	51.9
Volcanic Sediment	3.6	6.1	4.9	15.0	28.2	19.2	46.5	70.7	56.7
World Average		1.6			4.05			12.32	

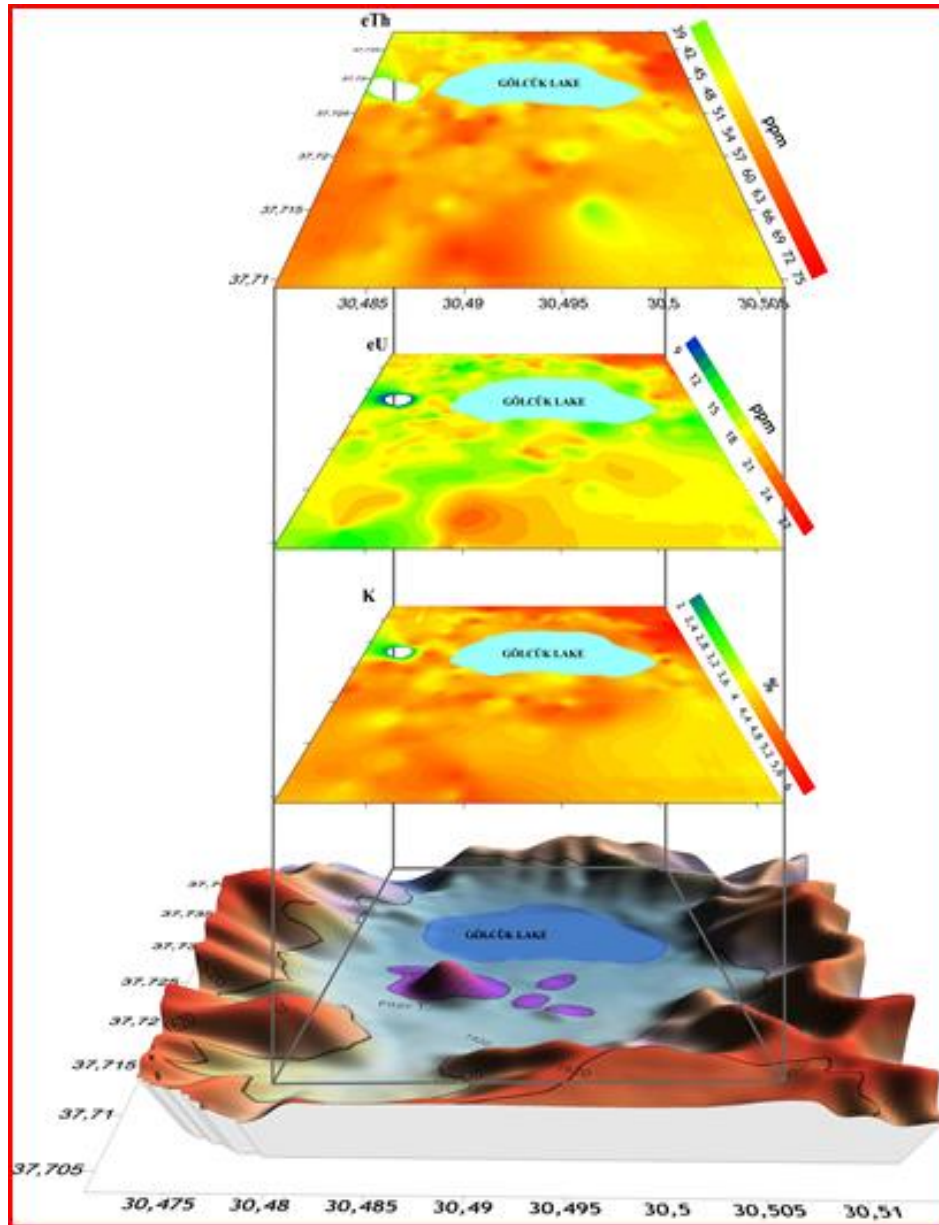


Figure 4. ^{40}K , ^{238}U and ^{232}Th concentration distribution maps of Gölcük volcanics

4.2. An Approach to Determining the Formation Stages of Gölcük Volcanism

Many researchers have stated that Gölcük volcanism occurred in three different geological stages [36]-[38], [62]. Researchers generally refer to these three stages as extrusive volcanism in the first stage, explosive volcanism in the second stage, and extrusive volcanism consisting of trachyte and trachyandesite in the third stage. As it is known, the concentration values of radioactive elements in the old volcanic phase are lower than the values of the young volcanic stage. In this meaning, Figure 5 is obtained when the concentration values of radioactive elements are arranged and plotted from smallest to largest. When the distribution of ^{40}K data is examined in Figure 5, these data are represented by three different lines (blue color) in three

different regions (red circles). Similarly, the distribution of ^{238}U and ^{232}Th data also shows that there are three different straight-line. The correlation coefficient of these lines ($R \geq 0.95$) is over 95% and the intersection points of the lines give the limit values of the lines. If we look at it in line with this logic, three different lines can be three different phases and the intersection points of the lines can be also the limit values of the stages. Accordingly, Table 2 can be created if Figure 5 is used. According to the data in Table 2, the average values of ^{40}K , ^{238}U and ^{232}Th concentrations of the volcanic products formed in the first stage of the Gölcük volcanism are obtained 3.5%, 13.4ppm and 44.0ppm, respectively. Similarly, the radioactive element values of the volcanic products of the second and third phases can be examined from Table 2. The variation in radioelement concentrations indicates the geochemical

variation in the volcanic products. In general, the difference in the average values of ^{40}K , ^{238}U and ^{232}Th in the first and second stages is 1.02%, 4.25ppm and 9.23ppm, respectively while the values in the second and third stages are 1.12%, 4.93ppm and 12.05ppm, respectively. As can be understood from these values, there is a concentration increase from the first and second volcanic phases to the third.

Figure 6 is created by using the limit values specified in Table 2 and the concentration values of radioactive elements measured on the Gölcük volcanics. The part seen as a white area on the maps in this figure is limestone and the data obtained in this area are not taken into account, so this area is white. Maps are created from the transitions of green, yellow and red colors. The inner areas of the sections indicated by the continuous lines on the maps show the first phase, the interior of the areas indicated by the dashed lines to the third phase, and the area between the continuous and dashed lines shows the second phase. In this case, the second phase volcanic units predominate in the study area. The areas where the high values of Uranium and Thorium overlap may be associated with shoshonitic composition rocks.

High Potassium values indicate that the volcanics of Isparta region are derived from the mantle containing lithospheric products due to stress tectonics, as indicated in [60]. It is stated that Gölcük volcanics are geochemically alkaline volcanic rocks and rich in silica, sodium, potassium and aluminum [38]. Figure 6 shows that the highest U value in the areas within the dashed line in the Southeast and South of the study area coincides with the high Th and K concentrations associated with the felsic (rich in silica, sodium, potassium) medium extruded volcanic rocks of the third phase.

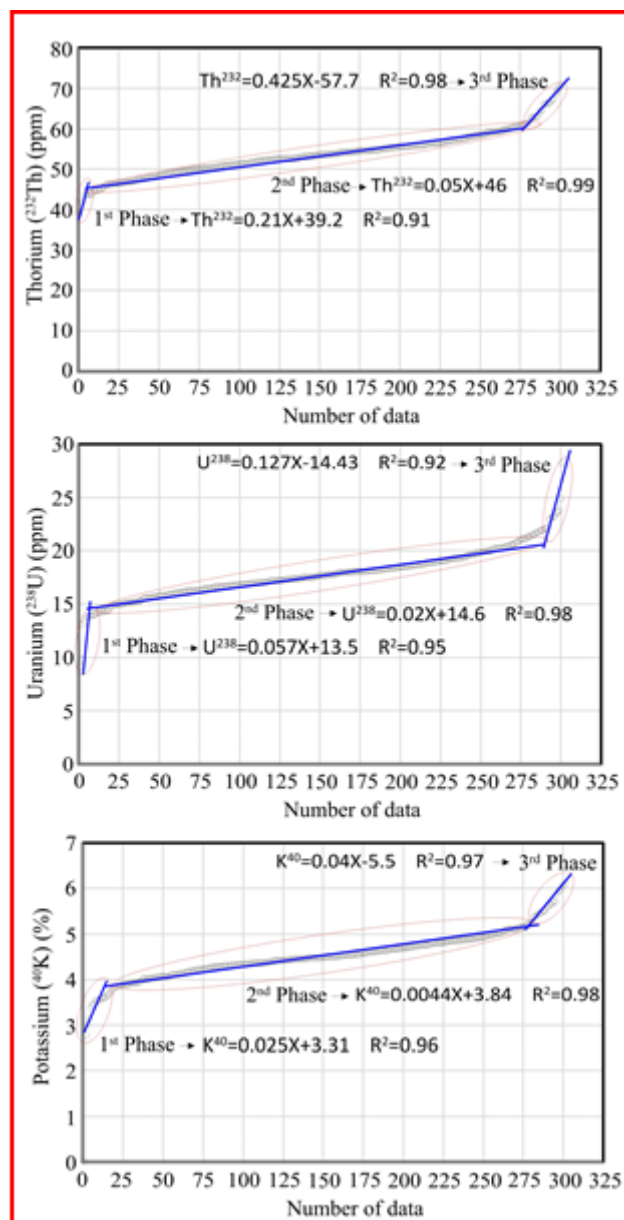


Figure 5. Separation of volcanism phases based on ^{40}K , ^{238}U and ^{232}Th values ordered from smallest to largest

Table 2. The limits of radioactive elements belonging to the phases of Gölcük volcanism from the radioactive data in Gölcük volcanics

Data Number		^{40}K	^{238}U	^{232}Th
		(%) Min.-Max. (Average)	(ppm) Min.-Max. (Average)	(ppm) Min.-Max. (Average)
1st PHASE	15	2.70 – 3.80 (3.48)	9.00 – 14.30 (13.37)	39.20 – 46.10 (43.98)
2nd PHASE	260	3.80 – 5.20 (4.50)	14.30 – 21.10 (17.62)	46.10 – 60.90 (53.21)
3rd PHASE	30	5.20 – 6.13 (5.62)	21.10 – 28.23 (22.55)	60.90 – 70.72 (65.26)

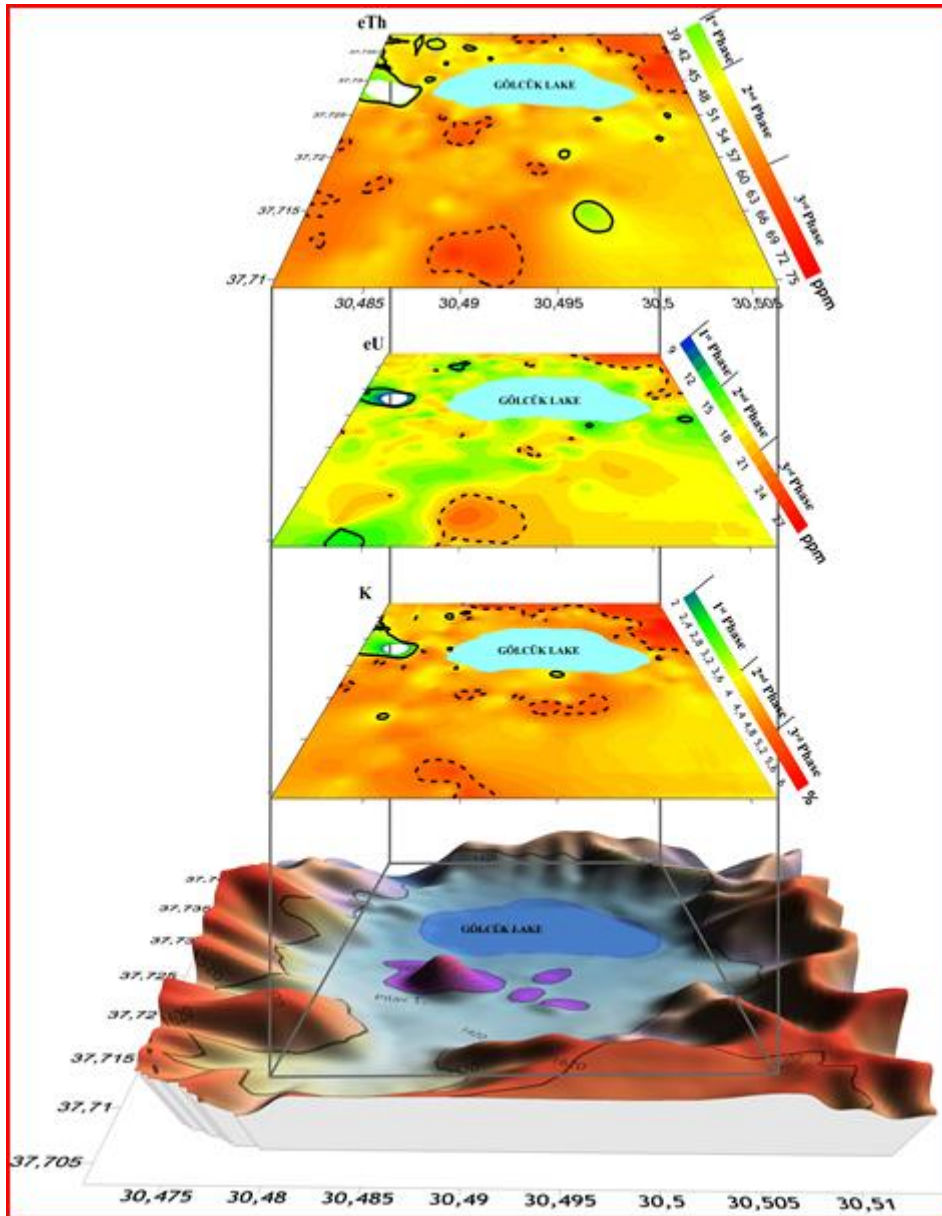


Figure 6. Maps showing the differentiation of volcanism phase products depending on the ^{40}K , ^{238}U and ^{232}Th concentration values of Gölcük volcanics

5. Conclusions

For the measurement of ^{40}K , ^{238}U and ^{232}Th in rocks or soils, in situ analysis, immediate and cost-effective good results are obtained with the gamma-ray spectrometer used in Geophysical engineering. Measuring, mapping and analyzing large areas in nature quickly and cheaply make gamma ray spectrometry a powerful tool.

As a result of natural gamma-ray spectrometry measurements on Gölcük volcanics, ^{40}K , ^{238}U and ^{232}Th concentration values were obtained between 2.80-6.1%, 9-28.2ppm and 41.3-70.7ppm, respectively. The volcanics in the study area have a maximum concentration of ^{40}K and a minimum of ^{238}U . The high ^{40}K indicates that it is a potassium-rich volcanism. It may be caused by ultramafic

or ultrabasic rocks due to the low silica content in areas with low ^{238}U values.

Difference in ^{40}K , ^{238}U and ^{232}Th concentration values reflect the geochemical differences of the rocks.

^{40}K , ^{238}U and ^{232}Th are related to each other and magmatic evolution is shown to be reflected by these three radioelements. Accordingly, the mean values of ^{40}K , ^{238}U and ^{232}Th concentrations of the volcanic units formed in the first, second and third stages of the volcanism are obtained 3.5%, 13.4ppm and 44.0ppm, 4.5%, 17.62ppm and 53.21ppm, and 5.62%, 22.55ppm and 65.26ppm, respectively.

The most suitable sample locations for age determination of rocks in the laboratory can be made quickly and accurately with the gamma-ray spectrometer method.

Acknowledgment

I would like to thank the editors and referees for their valuable contributions.

Statement of Research and Publication Ethics

The study is complied with research and publication ethics

References

- [1] UNSCEAR (United Nations Scientific Committee on the Effects of Atomic Radiation), "Sources and biological effects of ionizing radiation," New York, USA, 2000.
- [2] I. R. Ajayi, and O. O. Kuforiji, "Natural radioactivity measurements in rock samples of Ondo and Ekiti states in Nigeria," *Radiation Measurements*, vol. 33, pp. 13-16, 2001.
- [3] L. Xinwei, "Natural radioactivity in some building materials and by-products of Shaanxi, China," *Journal of Radioanalytical and Nuclear Chemistry*, vol. 262, pp. 775-777, 2004.
- [4] S. Singh, A. Rani, and R. K. Mahajan, "²²⁶Ra, ²³²Th and ⁴⁰K analysis in soil samples from some areas of Punjab and Himachal Pradesh, India using gamma ray spectrometry," *Radiation Measurements*, vol. 39, no. 4, pp. 431-439, 2005.
- [5] N. Sulekha Rao, D. Sengupta, R. Guin, and S. K. Saha, "Natural radioactivity measurements in beach sand along southern coast of Orissa, eastern India," *Environmental Earth Sciences*, vol. 59, pp. 593-601, 2009.
- [6] R. Mehra, S. Kumar, R. Sonkawade, N. P. Singh, and K. Badhan, "Analysis of terrestrial naturally occurring radionuclides in soil samples from some areas of Sirsa district of Haryana, India using gamma ray spectrometry," *Environmental Earth Sciences*, vol. 59, pp. 1159-1164, 2010.
- [7] N. A. Uyanık, I. Akkurt, and O. Uyanık, "A ground radiometric study of uranium, thorium and potassium in Isparta, Turkey," *Annals of Geophysics*, vol. 53, no. (5-6), pp. 25-30, 2010.
- [8] N. A. Uyanık, O. Uyanık, and İ. Akkurt, "Micro zoning of the natural radioactivity levels and seismic velocities of potential residential areas in volcanic fields The case of Isparta Turkey," *Journal of Applied Geophysics*, vol. 98, pp. 191-204, 2013a.
- [9] N. A. Uyanık, Z. Öncü, O. Uyanık, and İ. Akkurt, "Determination of Natural Radioactivity from ²³²Th with Gamma-Ray Spectrometer in Dereköy-Yazır (Southwestern Anatolia)," *Acta Physica Polonica A*, vol. 128, no. No 2-B, pp. B441-442, 2015a.
- [10] N. A. Uyanık, Z. Öncü, O. Uyanık, M. Bozcu, I. Akkurt, K. Günoglu, and F. Yagmurcu, "Distribution of Natural Radioactivity from ⁴⁰K Radioelement in Volcanics of Sandıklı-Suhut (Afyon) Area," *Acta Physica Polonica A*, vol. 128, no. No 2-B, pp. B438-440, 2015b.
- [11] N. A. Uyanık, B. Kurt, and O. Uyanık, "Determination of the hot dry rock from radiogenic heat production for potential geothermal sources and example of Isparta-Yakaören," *Pamukkale University Journal of Engineering Sciences*, vol. 26, no. 6, pp. 1170-1177, 2020.
- [12] N. A. Uyanık, Z. Öncü, O. Uyanık, and M. Bozcu, "Determination of alteration zones and geological unit limits using natural radioactivity properties of Sandıklı-Suhut areas". *Journal of Applied Geophysics*, vol. 196, art. no. 104525, 2022.
- [13] S. Fares, "Measurements of natural radioactivity level in black sand and sediment samples of the Tamsah Lake beach in Suez Canal region in Egypt," *Journal of Radiation Research and Applied Sciences*, vol. 10, no. 3, pp. 194-203, 2017.
- [14] A. Aziz, T. Attia, and M. Hanafi, "Radiological Impact and Environmental Monitoring of Gamma Radiations Along the Public Beach of Port Said, Egypt," *Pure and Applied Geophysics*, vol. 177, pp. 2871-2876, 2020.
- [15] G. Cinelli, E. Brattich, C. Coletti, V. De Ingeniis, C. Mazzoli, D. Mostacci, R. Sassi, and L. Tositti, "Terrestrial gamma dose rate mapping (Euganean Hills, Italy): comparison between field measurements and HPGe gamma spectrometric data," *Radiation Effects and Defects in Solids*, vol. 175, pp. 54-67, 2020.
- [16] A. S. Akingboye, A. C. Ogunyele, A. T. Jimoh, O. B. Adaramoye, A. O. Adeola, and T. Ajayi, "Radioactivity, radiogenic heat production and environmental radiation risk of the Basement Complex rocks of Akungba-Akoko, southwestern Nigeria: insights from in situ gamma-ray spectrometry," *Environmental Earth Sciences*, vol. 80, no. 6, 2021.
- [17] A. A. Abojassim, and L. H. Rasheed, "Natural radioactivity of soil in the Baghdad governorate," *Environmental Earth Sciences*, vol. 80, no. 1, 2021.
- [18] ATSDR (Agency for Toxic Substances and Disease Registry). "Toxicological Profile for Radon". Public Health Service, U.S. Department of Health and Human Services, Atlanta, USA, 1990.
- [19] H. Taskin, M. Karavus, P. Ay, A. Topuzoglu, S. Hindiroglu, and G. Karahan "Radionuclide concentrations in soil and lifetime cancer risk due to the gamma radioactivity in Kirklareli Turkey," *Journal of Environmental Radioactivity*, vol. 100, pp. 49-53, 2009.

- [20] B. A. Almayahi, A. A. Tajuddin, and M. S. Jaafar, "Effect of the natural radioactivity concentrations and $^{226}\text{Ra}/^{238}\text{U}$ disequilibrium on cancer diseases in Penang, Malaysia," *Radiation Physics and Chemistry*, vol. 81, no. 10, pp. 1547-1558, 2012.
- [21] N. A. Uyanık, "Determination of the Radiological Risk and the Cancer Effect Caused by Geological Units and Samples from Afyon, Turkey," *Pure and Applied Geophysics*, vol. 179, pp. 1295-1308, 2022.
- [22] S. Altundaş, and H. Çınar, "Uranium migration and radioactive characteristics of the Sariçiçek and Sarihan Granodiorites," *Turkish Journal of Engineering*, vol. 7, no. 3, pp. 208-226, 2023.
- [23] S. Altundas, "Investigation of natural radionuclide variations and the possible uranium migration by testing with gamma-ray spectrometer: An example from Tuğlu Tepe and Deliler Sites in Sefaati/Yozgat, Central Anatolia Region, Turkey," *Journal of Applied Geophysics* vol. 207, article no. 104866, 2022.
- [24] M. Bolca, M. M. Saç, B. Çokuysal, T. Karalı, and E. Ekdal, "Radioactivity in soils and various foodstuffs from the Gediz River Basin of Turkey," *Radiation Measurements*, vol. 42, pp. 263-270, 2007.
- [25] M. Martini, and E. Sibilila, "Radiation in archaeometry: archaeological dating," *Radiation Physics and Chemistry*, vol. 61, no. (3-6), pp. 241-246, 2001.
- [26] F. Birch, "Heat from radioactivity, in Nuclear Geology", ed. Henry Faul, New York, USA, John Wiley and Sons Inc., 1954.
- [27] IAEA (International Atomic Energy Agency), "Guidelines for Radioelement Mapping Using Gamma-Ray Spectrometry Data". Vienna, Austria, 1363p, 2003.
- [28] P. Chiozzi, P. De Felice, V. Pasquale, D. Russo, and M. Verdoya "Field γ -ray spectrometry on the Vulcano island (Aeolian Arc, Italy)," *Applied Radiation and Isotopes*, vol. 51, pp. 247-253, 1999.
- [29] İ. Aydın, "Jeofizikte Radyometrik Yöntem ve Gamma-Işın Spektrometrisi," SDU Publishing house, publication no.49, Isparta, Türkiye, 2004, p.150.
- [30] İ. Aydın, M. S. Aydoğan, E. Oksum, and A. Koçak, "An Attempt to Use Aerial Gamma-Ray Spectrometry Results in Petrochemical of the Volcanic and Plutonic Associations of Central Anatolia (Turkey)," *Geophysical Journal International*, vol. 167, pp. 1044-1052, 2006.
- [31] N. A. Uyanık, O. Uyanık, F. Gür, and İ. Aydın, "Natural radioactivity of bricks and brick material in the Salihli-Turgutlu area of Turkey," *Environmental Earth Sciences*, vol. 68, no. 2, pp. 499-506, 2013b.
- [32] R. Mazzuoli, L. Tortorici, and G. Ventura, "Oblique rifting in Salina, Lipari and Vulcano islands (Aeolian islands, southern Italy)," *Terra Nova*, vol. 7, pp. 444-452, 1995.
- [33] P. Chiozzi, V. Pasquale, and M. Verdoya, "Ground radiometric survey of U, Th and K on the Lipari Island, Italy," *Journal of Applied Geophysics*, vol. 38, pp. 209-217, 1998.
- [34] P. Chiozzi, V. Pasquale, M. Verdoya, and S. Minato, "Natural gamma-radiation in the Aeolian volcanic arc," *Applied Radiation and Isotopes*, vol. 55, pp. 737-744, 2001.
- [35] A. Poisson, "Recherches géologiques dans les Taurides occidentales (Turquies)," PhD thesis, University of Paris, 795p., Paris, France, 1977.
- [36] B. Platevoet, S. Scaillet, H. Guillou, D. Blamart, S. Nomade, M. Massault, A. Poisson, Ö. Elitok, N. Özgür, F. Yagmurlu, and K. Yılmaz, "Pleistocene eruptive chronology of the Gölcük volcano, Isparta Angle, Turkey," *Quaternaire*, vol. 19, no. 2, pp. 147-156, 2008.
- [37] B. Platevoet, Ö. Elitok, H. Guillou, J. M. Bardintzeff, F. Yagmurlu, S. Nomade, D. C. Poisson, and N. Özgür, "Petrology of quaternary volcanic rocks and related plutonic xenoliths from Gölcük volcano, Isparta Angle, Turkey: origin and evolution of the high-K alkaline series," *Journal of Asian Earth Science*, vol. 92, pp. 53-76, 2014.
- [38] K. Yılmaz, "Geochemistry of ultramafic, mafic, and felsic xenoliths from the Gölcük (Isparta, SW Turkey) alkali rocks: genetic relationship with arc magmas," *Arabian Journal of Geosciences*, vol. 12, art. no. 306, 2019.
- [39] D. Kalafat, "Güneybatı Anadolu ve Yakın Çevresinin Depremselliği, Aktif Tektoniği," *Deprem Araştırma Bülteni*, vol. 63, pp. 5-98, 1988.
- [40] S. A. Poyraz, "Isparta Büklümünü Oluşturan Tektonik Yapıların Sismolojik Yöntemlerle Araştırılması," PhD. Thesis, İstanbul Üniversitesi, İstanbul, Türkiye, 2009.
- [41] O. Pamukçu, T. Gönenç, O. Uyanık, H. Sözbilir, and O. Çakmak, "A microgravity model for the city of İzmir Western Anatolia and its tectonic implementations," *Acta Geophysica*, vol. 62, no. 4, pp. 849-871, 2014.
- [42] B. Oruç, "Structural interpretation of southern part of western Anatolian using analytic signal of the second order gravity gradients and discrete wavelet transform analysis," *Journal of Applied Geophysics*, vol. 103, pp. 82-98, 2014.
- [43] C. E. Toker, E. U. Ulugergerli, and A. R. Kılıç, "The Naşa intrusion (Western Anatolia) and its tectonic implication: A joint analyses of gravity and earthquake catalog data," *Bulletin of the Mineral Research and Exploration*, vol. 156, pp. 247-262, 2018.
- [44] Ç. Sarı, and E. Timur, "Interpretation of magnetic data using boundary analysis and inversion techniques: a case study from Gölcük/Isparta (Turkey) region," *Turkish Journal of Earth Sciences*, vol. 30, no. 5, pp 611-627, 2021.

- [45] E. Oksum, M. N. Dolmaz and L. T. Pham, "Inverting gravity anomalies over the Burdur sedimentary basin, SW Turkey," *Acta Geodaetica et Geophysica*, vol. 54, pp. 445-460, 2019.
- [46] E. Erbek Kiran, A. Ates and M. N. Dolmaz, "Upper Crustal Structure of Denizli Graben (Western Turkey) From Bouguer Gravity Data and Seismic Reflection Sections," *Surveys in Geophysics*, vol. 43, pp. 1947-1966, 2022.
- [47] E. Ulugergerli, G. Seyitoğlu, A. Başokur, C. Kaya, U. Dikmen, and M. Candansayar, "The geoelectrical structure of Northwestern Anatolia, Turkey," *Pure and Applied Geophysics*, vol. 164, no. 5, pp. 999-1026, 2007.
- [48] Y. Öz, "Engineering Seismology with Application to Geotechnical Engineering," ed. Richard D. Miller, *Investigation in Geophysics Series No. 17, Oklahoma, U.S.A.*, Society of Exploration Geophysicists, 2015.
- [49] C. Glover, and A. H. F. Robertson, "Neogen Intersection of the Aegean and Cyprus Arcs: Extensional and Strike-Slip Faulting in the Isparta Angle, SW Turkey," *Tectonophysics*, vol. 298, pp. 103-132, 1998.
- [50] M. E. Karaman, "Tectono-Stratigraphic Outline of the Burdur-Isparta Area (Western Taurides, Turkey)," *Geological Bulletin of Turkey*, vol. 43, no. 2, pp. 71-81, 2000.
- [51] F. Yağmurlu, Y. Savascin, and M. Ergun, "Relation of alkaline volcanism and active tectonism within the evolution of the Isparta angle, SW Turkey," *Journal of Geology*, vol. 105, no. 6, pp. 717-728, 1997.
- [52] M. Y. Savaşın, and T. Oyman "Tectono-Magmatic evolution of alkaline volcanics at the Kirka-Afyon-Isparta structural trend, SW Turkey," *Turkish Journal of Earth Sciences*, vol. 7, pp. 201-214, 1998.
- [53] M. M. Blumenthal, "Le Système Structural du Taurus Sud - Anatolien in Livre à la mémoire," *Prof. Paul Fellot, Mém., hs-sér., Société Géologique de France*, vol. II, pp. 611-662, 1963.
- [54] J. H. Brunn, "L'arc Concave Zagro-Taurique et les Arcs Convexes Taurique et Egeen. Collision et Arcs Induits," *Bulletin de la Society Geology*, vol. 2, pp. 553-567, 1976.
- [55] A. M. C. Şengör, "Türkiye'nin Neotektoniğinin Esasları," *Türkiye Jeoloji Kurultayı Konferanslar Dizisi*, vol. 2, 40p., 1980.
- [56] F. Yağmurlu, and M. Şentürk, "Güneybatı Anadolu'nun Güncel Tektonik Yapısı," *Türkiye Kuvaterner Sepozyumu*, İTÜ Avrasya Yer Bilimleri Enstitüsü, İstanbul, Türkiye, 02-03 Haziran 2005.
- [57] N. Kazancı, and M. E. Karaman, "Gölcük (Isparta) Pliyosen volkanoklastik istifinin sedimantolojik özellikleri ve depolanma mekanizmaları," *Akdeniz Üniversitesi Isparta Mühendislik Fakültesi Dergisi*, vol. 4, pp. 16-35, 1988.
- [58] W. Nemec, N. Kazancı, and J. G. Mitchell, "Pleistocene explosions and pyroclastic currents in west-Central Anatolia," *Boreas*, vol. 27, pp. 311-332, 1998.
- [59] C. Lefèvre, H. Bellon, and A. Poisson, "Présence de leucitites dans le volcanisme Pliocène de la région d'Isparta (Taurides occidentales, Turquie)," *CR Acad Sci Paris* vol. 297, no. II, pp. 367-372, 1983.
- [60] P. Alici, A. Temel, A. Gourgaud, G. Kieffer, and M. N. Gündoğdu, "Petrology and geochemistry of potassic rocks in the Gölcük area (Isparta, SW Turkey): genesis of enriched alkaline magmas," *Journal of Volcanology Geothermal Research*, vol. 85, no. 1, pp. 423-446, 1998.
- [61] A. K. Schmitt, M. Danişık, W. Siebel, Ö. Elitok, Y-W. Chang, and C. C. Shen, "Late Pleistocene zircon ages for intracaldera domes at Gölcük (Isparta, Turkey)," *Journal of Volcanology Geothermal Research*, vol. 286, pp. 24-29, 2014.
- [62] H. Coban, "New geochronologic, geochemical and isotopic constraints on the evolution of plio-quadernary alkaline volcanism from Isparta district, SW Turkey," *International symposium on the geodynamics of eastern Mediterranean: active tectonics of the Aegean region, Istanbul, Turkey, 15-18 June 2005*.
- [63] İ. Aydın, "Bir Jeofizik Yöntem: Gama-Işın Spektrometresi," *Jeofizik Dergisi*, vol. 7, pp. 109-122, 1993.
- [64] R. L. Grasty, J. E. Glynn, and J. A. Grant, "The Analysis of Multichannel Airborne Gamma-Ray Spectra," *Geophysics*, vol. 50, no. 12, pp. 2611-2620, 1985.
- [65] S. Yalçınkaya, "Isparta-Ağlasun (Burdur) Dolaylarının Jeolojisi," PhD. Tesis, İstanbul Üniversitesi Fen Bilimleri Ens., 176p., İstanbul, 1989.
- [66] A. Koçyiğit, "Ağlasun-Gölcük (Isparta) Bölgesinin Aktif Tektoniği: Neotektonik Rejimin Türü ve Sagalassos Tarihsel Depremlerinin Kaynağı," *Aktif Tektonik Araştırma Grubu 12. Çalıştayı*, 7-8, Ankara, 2008.
- [67] N. A. Uyanık, "Isparta Alkali Volkanitlerinin Radyometrik ve Manyetik Yöntemlerle İncelenmesi," PhD. Tesis, SDU Fen Bilimleri Enstitüsü, Isparta, 2011.



Analysis of Intrusion Detection Systems in UNSW-NB15 and NSL-KDD Datasets with Machine Learning Algorithms

Fuat TÜRK^{1*}

¹ Cankiri Karatekin University, Department of Computer Engineering, Cankiri/Turkey
(ORCID: 0000-0001-8159-360X)



Keywords:

Instruction
Detection Systems, Network
Attacks, NSL-KDD Dataset,
UNSW-NB15 Dataset.

Abstract

The use of intelligent devices in almost every sector, and the provision of services by private and public institutions through network servers, cloud technologies, and database systems are now mostly remotely controlled. Due to the increasing demands on network systems, unfortunately, both malicious software and users are showing more interest in these areas. Some organizations are facing almost hundreds or even thousands of network attacks daily. Therefore, it is not enough to solve the attacks with a virus program or a firewall. Detection and accurate analysis of network attacks are crucial for the operation of the entire system. With the use of deep learning and machine learning, attack detection, and classification can be successfully performed. This study conducted a comprehensive attack detection process on the UNSW-NB15 and NSL-KDD datasets using existing machine learning and deep learning algorithms. In the UNSW-NB15 dataset, an accuracy of 98.6% and 98.3% was achieved for two-class and multi-class classification, respectively, and 97.8% and 93.4% accuracy were obtained in the NSL-KDD dataset. The results prove that machine learning algorithms are an effective solution for intrusion detection systems.

1. Introduction

Today, the rapid development of big data, cloud technologies, and smart devices has significantly increased our dependence on internet systems. In addition, the use of the internet in economic, military, and institutional contexts has become extremely important. For this reason, data confidentiality, data integrity, and information security are fundamental tasks. While network authorities try to meet the increasing needs and security demands, malicious software and intruders, on the other hand, try to infiltrate systems, and destroy and change information. This situation has advanced so much that intrusion detection systems and intrusions now reach the level of interstate cyber wars. Therefore, network systems should be developed in terms of confidentiality, integrity, and usability, and information security should be prioritized. Intrusion detection systems (IDS) are one of the biggest

problems caused by malicious users in cybersecurity [1].

IDS is mainly used to detect suspicious logins. It can be in the form of software or hardware or a combination of both. Two methods are mostly preferred in IDS screening. The first is the HIDS and the second is the NIDS. HIDS follows the network interfaces and configurations of the target machine and requires certain settings compatible with the server [2], [3]. With the proliferation of attacks, databases are forced to constantly update. Also, specification-based types require expert experience to detect intrusions. Artificial intelligence can be used easily since the detection of such anomaly situations is a classification problem. For this reason, many data sets have been created to control intrusion detection systems [4].

The main ones are NSL-KDD, UNSW-NB15, KDDCUP99, and CICICS2017. Existing machine learning algorithms are used with these

*Corresponding author: turk_fuat@hotmail.com

Received: 22.01.2023, Accepted: 24.04.2023

datasets and offer extremely important ideas for intrusion detection systems.

It is possible to detect features and select appropriate features using machine learning algorithms, filter methods, or learning-based methods. Additionally, ensemble learning methods are also in demand for feature selection. Ensemble algorithms in machine learning are a technique that aims to achieve higher performance by combining multiple learning algorithms. These algorithms can combine the predictions of various learning algorithms to obtain more accurate results. Therefore, ensemble algorithms can be used to eliminate the weak points of individual algorithms and make more

general predictions. Using a combination of machine learning and deep learning algorithms sometimes outperforms classification problems [5]. At this stage, it is extremely important to determine which models will be used and the strengths and weaknesses of the models. For this reason, existing machine learning or deep learning algorithms should be applied to accepted data sets. This study involved an extensive detection analysis of the NSLKDD and UNSW-NB15 datasets. Consequently, it is crucial to offer new approaches to intrusion detection systems and to develop different solutions. The workflow of the proposed approach model is shown in Figure 1.

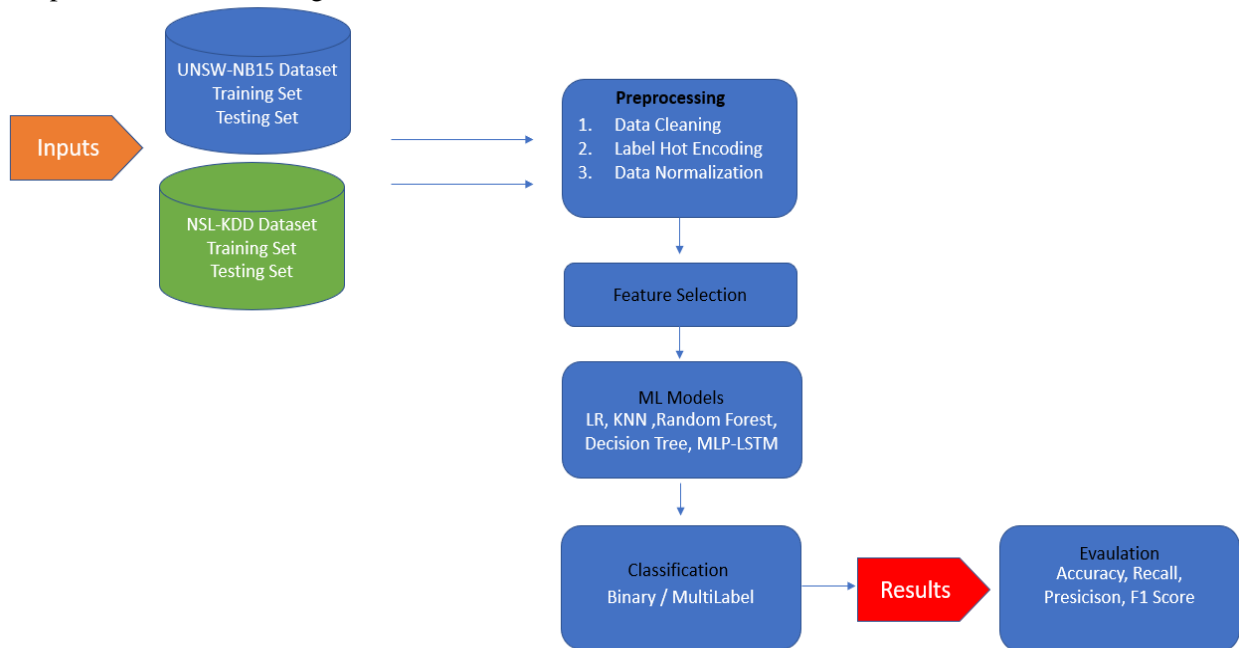


Figure 1. Workflow diagram of the proposed system.

According to the proposed workflow line, data cleaning is performed before all the algorithms are applied. To fix data cleaning dataset defects, follow the steps of concatenating the textual values, processing the empty columns according to their nature, and converting the values stored as text type to number type. One hot encoding stage is the step of converting nominal properties to numeric values before machine learning. The data normalization process is considered a process where the attribute values are scaled in the range of [0 and 1] and the computational load is reduced. Feature selection is an important step in artificial intelligence model building. First, it eliminates the dimensionality problem caused by having many features. Second, it saves the model from workload with many features and turns it into a simple and openable structure. Therefore, it is wise to simplify the model with the

effect of increasing complexity and training/testing time. After the feature selection process, machine learning algorithms, Multi-Layer Perception, and Long-Short Term Memory algorithms are used for classification. The classification was carried out as both binary and multiclass. Finally, experimental results were compared in terms of evaluation criteria.

2. Literature Review

Geurts et al. conducted research on the intrusion detection system with the Bi-Directional LSTM model. In this study, they explained that intrusion detection systems are a basic layer incorporated into the network system. They stated that due to the excessive amount of data traffic on the network, attackers could cause great harm to the network and its users. The Bidirectional LSTM model gave results

with 99% accuracy for both datasets. Paragraphs following the first paragraph should begin with the paragraph indentation [5]. Basati and Faghieh proposed an architecture PDAE for the security of IoT devices against network attacks. In this study, they stated that due to the limited resources of IoT devices, a high-fidelity neural network with a lightweight and efficient architecture is needed for intrusion detection. For this reason, they stated that the traditional architectural structures of neural networks were not feasible. The proposed PDAE greatly reduces the number of parameters, the amount of memory, and the need for processing power, while increasing the accuracy of the model. The results were calculated as superior to the existing algorithms in terms of both accuracy and performance [6]. Cil et al. conducted a study on the importance of early detection of network traffic in the fight against network attacks. The proposed model is a deep network that detects attacks on packet instances. As a result of the experiments, attack types were determined with an accuracy rate of 94.57% [7]. Amaizu et al. proposed a unified and efficient network attack detection framework for B5G networks. The proposed model includes multi-layered detectors combined with the feature extraction algorithm and was created to detect the r network attacks as well as revert the DDoS attack type. The results showed that the framework could detect network attacks with a high accuracy score of 99.66% [8]. Gowthul et al. proposed an SVM-based DEHO Classifier model to detect DDoS attacks. The main purpose of this article is to ensure that they are best detected as normal data samples and malicious/hacked data samples. The proposed approach was examined for four different databases. Experimental results reveal that the performance of detection system using this approach is higher than that of other approaches [9]. Mushtaq et al. proposed a two-stage auto-encoder-based LSTM architecture. Experimental results showed that the proposed AE-LSTM performance has fewer prediction errors compared to other deep and shallow machine learning techniques. The NSL-KDD dataset showed 89% classification accuracy [10]. Choudhary and Kesswani proposed a deep learning-based model for the detection of unauthorized attacks. They mentioned that the application of IoT technology is increasing rapidly, resulting in the need for the most efficient model to detect malicious activities as quickly and accurately as possible, and Deep Neural Networks are used to identify attacks. The performance of DNN to accurately identify the attack was evaluated on the most used datasets. Experimental results showed that the accuracy rate of the proposed method using DNN is over 90% [11].

Serinelli et al. proposed An Intrusion Detection System Architecture ANIDINR (an anomaly-based NIDS in R). In this study, they stated that the protection of computer networks is one of the most important and difficult problems in cyber security. The main purpose here is to try to provide step-by-step guidance on methodology selection and execution for training Machine and Deep Learning models. There is also a focus on developing ANIDINR to overcome the problems of detection of well-known attacks and the complex and up-to-date collection of rules. Based on this setup, the proposed system yielded over 90% accuracy results on the two datasets (NSL-KDD and KDDCup 1999) [3]. Moualla et al. proposed a machine learning-based system for the intrusion detection system. The proposed system is a dynamically scalable multi-class machine learning-based network IDS. The outputs of the extreme learning machine classifier are used as the inputs of a fully connected layer followed by a logistic regression layer to make smooth decisions for all classes. The results show that it outperforms the related studies in terms of accuracy [12]. Mohammadpour et al. proposed a convolutional neural network-based system for the intrusion detection system. In this paper, a deep learning method is proposed to implement an effective and flexible NIDS. The model was run with the NSL-KDD' dataset, which is a benchmark dataset for network intrusion. Experimental results of a 99.79% detection rate were obtained when compared with the test dataset. In line with the results, they stated that CNNs can be applied as a learning method for IDS. Paragraphs following the first paragraph should begin with the paragraph indentation [13].

Apart from these studies, machine learning and ensemble learning algorithms have been used in different fields. Ayşe et. al. proposed a new super Community learning model to enable early diagnosis of diabetes mellitus. The proposed super-learner model was created as a result of a case study with four basic learners (logistic regression, decision tree, random forest, and gradient boosting) and a meta-learner (support vector machines). This model found the early-stage diabetes risk estimation to be 99.6%, 92%, and 98%, respectively, in three different datasets [14]. In a study in the agricultural sector, Buyrukoğlu proposed a new hybrid model to predict the presence of Salmonella in agricultural surface waters based on a combination of heterogeneous ensemble approach for feature selection, clustering, regression, and classification algorithms. The ensemble ANN+RF model achieved the highest performance and performed well, with a prediction accuracy of 94.9% [15]. In his work on finance,

Buyrukoğlu aimed to analyze promising cryptocurrencies with deep learning methods. Five promising cryptocurrencies were analyzed using LSTM communities and single-base LSTM networks. The results of the study revealed that LSTM network ensembles do not always provide better accuracy performance than single-base LSTM network [16].

3. Materials and Method

3.1. Dataset

UNSW-NB15 Dataset: The UNSW-NB15 dataset was created in the Cyber Lab of the Australian Cyber

Security Center. The main objective of the dataset is to obtain a combination of real regular activities and synthetic modern attack behavior. The dataset consists of approximately 2 million records with 49 different features extracted using some special algorithms. The data set can be divided into normal and abnormal. However, it includes nine types of attacks [17],[18]. Figure 2 shows the distribution of the data set separately.

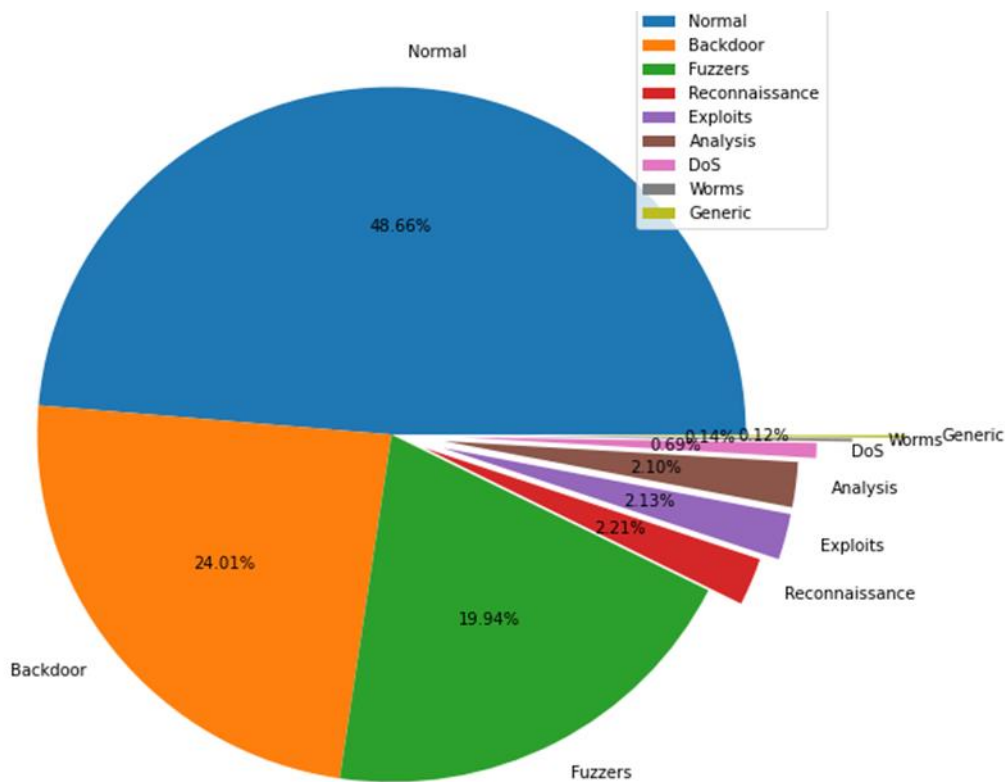


Figure 2. Pie chart distribution of multi-class labels for UNSW-NB15.

Fuzzer attack: These are the types of attacks obtained with randomly generated data trying to hack the program or network.

Analysis: Hosts different types of attacks, including web scripts for port scanning and spam-like email.

Backdoor: Backdoor is a technique where attackers use a legitimate system portal to gain illegal access.

Denial of service (DOS): These are the types of attacks in which the server or network is busy so that the users of the system cannot access it and cause

it to interfere with the services of the host on the Internet.

Exploits: Attacks that take advantage of a vulnerability caused by any bug and attempt to disrupt trusted behavior on the network.

Generic: This analysis can be applied to block verification code passwords, broadcast, and send messages.

Reconnaissance: These are the types of attacks that gather preliminary information about any public network or target host. Based on the collected

information, it is used to infiltrate target hosts or networks [19].

Shell Code: Shell code is an attack method that uses code to exploit a software vulnerability.

Worm: These are the types of attacks that regenerate and increase themselves to start on one computer and spread to another [20].

NSL-KDD Dataset: The NSL-KDD dataset is derived as a new dataset, consisting of records determined from the complete KDD dataset, which poses no problem in correcting the errors in the KDD-99 cup dataset [21]. However, the dataset is

subject to certain problems, such as not being representative of low-footprint attacks [22],[23]. The NSL-KDD dataset has better reduction rates and no duplicate records in the test set. Because NSL-KDD has fewer data points than KDD-99, it is inexpensive in terms of workload to use in training machine learning models. It can be classified as normal and abnormal, as in the UNSW-NB15 dataset. In addition, it is possible to multiclass as normal, DOS, R2L, U2R, and probe. Figure 3 shows the distribution of the data set separately.

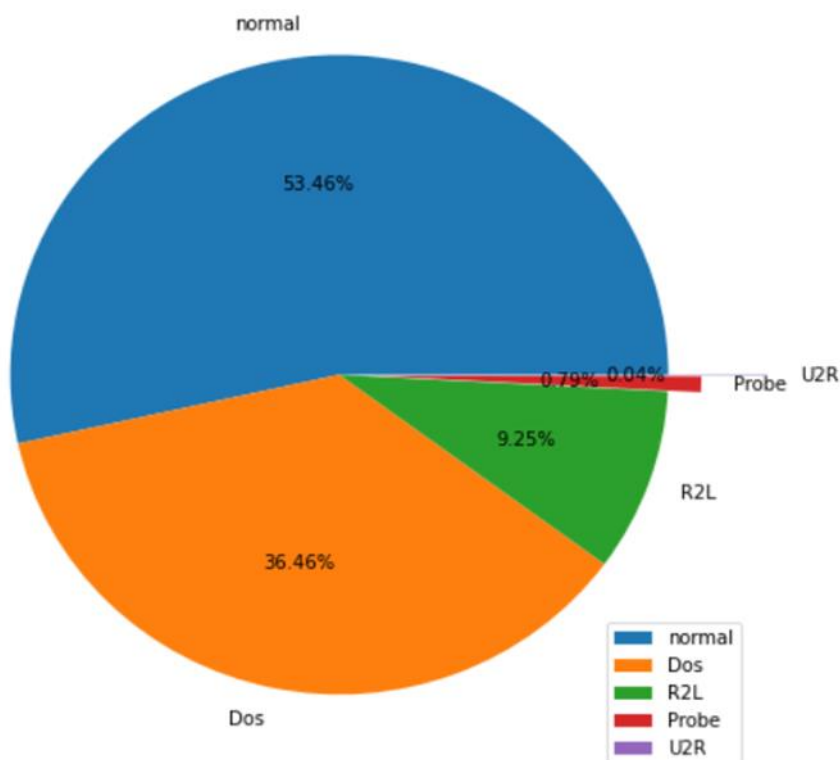


Figure 3. Pie chart distribution of multi-class labels for NSL-KDD.

Denial of Service (DOS): It is a type of attack that consumes the resources of the other party and thus renders it unable to meet requests.

Remote to Local (R2L): It is a type of attack that intrudes on another machine from a remote machine and gains local access to that machine.

User-to-Root (U2R): This is an unauthorized access method for root privileges. It is a form of attack that can enter a normal account into the system to be accessed, but tries to gain root / administrator privileges due to some security vulnerabilities in the system.

Probing: We can summarize it as the purpose of surveillance and other research attacks. The main purpose is to gather information about the remote machine.

3.2. Machine Learning Algorithms Used

Logistic Regression: Logistic Regression (LR) is a machine learning method for creating the most appropriate model to establish a relationship between class variables and features. Often, in binary class problems (with 0 and 1), the probability of being included in the class for an observation produces a value between (1) and non-existence (0). However, it can be adapted for multi-class problems with simple adjustments [24].

K-Nearest Neighbors: K-Nearest Neighbors (KNN) is a widely used classification algorithm. It is preferred in many classification problems due to its easy interpretation and low computation time. The

selection of the k parameter is extremely important in the KNN algorithm [25].

Random Forest (RF): Random Forest is an ensemble learning classification and regression algorithm suitable for grouping data into classes. During the training phase, a series of decision trees are created that are then used for class prediction. In the calculation process, the classes of all individual trees are considered, and the class with the highest votes is considered as the output [26].

Decision Tree: The Decision Tree has a root node, branches, and leaf nodes. Testing an attribute is in each internal node, and the result of the test is in the branch and class tags. The root node is the top node in the tree. A decision tree is a tree in which each node represents a feature, each link represents a decision, and each leaf represents a result [27].

3.3. Deep Learning Architecture Used

Multi-Layer Perception: Multi-Layer Perception (MLP) neural networks contain units arranged in layers in their internal structure. These units are the input layer, one or more hidden layers, and the output layer.

The input layer transfers the input to the next layers. Hidden volume nodes have non-linear enabled functionality, and outputs are linearly enabled. For true three-layer MLP, all inputs are also directly connected to all outputs [28]. Figure 4 shows the MLP neural network architecture.

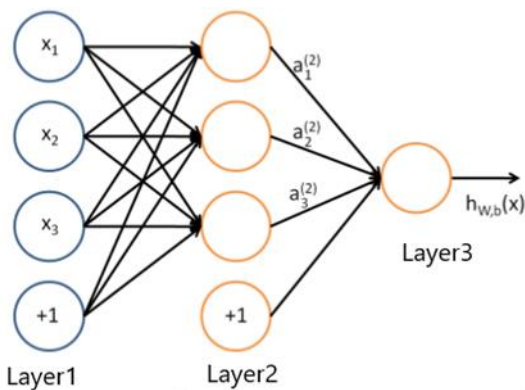


Figure 4. MLP neural network architecture.

Long-Short-Term Memory: LSTM was designed to overcome these error backflow problems. Although it is mentioned together with deep learning algorithms, it should be considered as a sub-unit of machine learning methods. In the noisy state, even with compact input arrays, it can learn to bridge time intervals over 1000 steps without losing its short time delay capabilities [29]. An efficient, gradient-based

algorithm achieves this for an architecture that enforces a constant stream of errors that does not explode or disappear through each unit's internal states. In principle, an LSTM could use memory cells to remember long-range information and monitor various attributes of the text it is currently processing. An LSTM unit consists of a cell, an entry gate, an exit gate, and a forgotten gate [30]. The cell gate can be expressed as the memory of the network that carries the information across the cells for prediction purposes. The input gate executes the function of updating the cell state. It decides whether to update the information according to the sigmoid function operation. The exit gate decides what the next cell's entrance will be. It is also used in forecasting. The forget gate is the gate that decides what information to forget or keep [31], [32]. The figure shows the LSTM architectural structure. Figure 5 shows the LSTM architectural structure.

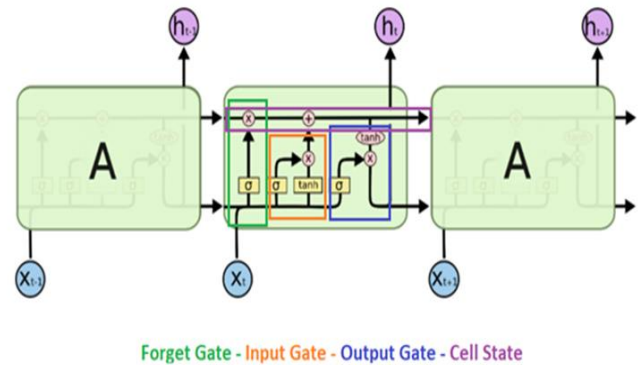


Figure 5. LSTM network architecture.

3.4. Performance Evaluation Metrics

Unless the images within the classes in the dataset are balanced, the measurement of classification accuracy is not sufficient on its own and may give deceptive results. Performance indicators for each class in the dataset are calculated based on the confusion matrix. These indicators are Accuracy, Recall, Precision, and F-1 Score values. The explanations of these parameters are given below in Table 1:

Table 1. Calculation criteria for evaluation metrics.

Total Instances	Predicted No	Predicted Yes
Actual No	TN (True Negative)	FP (False Positive)
Actual Yes	FN (False Negative)	TP (True Positive)

Recall

	Precision	Accuracy
Accuracy=TP/(Total Instances)	(1)	
Recall=TP/(Total Actual Yes)	(2)	
Precision=TP/(Total Predicted Yes)	(3)	
F1score=(2*Prec*Recall)/(Prec+ Recall)	(4)	

4. Results and Discussion

In both data sets, a random distribution phase was applied at 80% and 20% for the training and testing phases, respectively. In the UNSW-NB15 dataset selected as an input, 5 basic features were extracted, and for the NSL-KDD dataset, 9 basic features were extracted. In addition, the Pearson Correlation method was used for feature selection. The training process of the datasets was carried out using the GTX1050 TI graphics card and the TensorFlow-GPU 2.3 library.

Before the models were trained, certain hyperparameter settings were made for the

classification algorithms. The number of trees for the random forest algorithm is set to 120. The learning rate was taken as 0.01. The logistic regression iteration number was determined as 100 random states=0, decision tree max-leaf node=default, LSTM activation function was determined as tanh.

4.1 UNSW-NB15 Training Phase

Table 2 shows the evaluation results for UNSW-NB15. As can be seen from the results, the highest accuracy value for the binary class was calculated with the Random Forest and for the multi-class Logistic Regression algorithm. Their success in classification problems and their structures that provide good predictions show that Random Forest and Logistic Recession algorithms give good results. Since the Random Forest algorithm is based on Ensemble Learning, it is usually high in classification problems. In addition, it gives higher success rates on the definition of Logistic Regression in multi-class problems. In addition, we can say that the hyperparameters are chosen correctly.

Table 2. Evaluation results for UNSW-NB15.

	Binary Class					Multi Class				
	Accuracy	Recall	Precision	F1-Score	Total Time	Accuracy.	Recall	Precision	F1-Score	Total Time
LR	0.978	0.96	0.98	0.97	3.1	0.983	0.97	0.98	0.98	4.2
KNN	0.984	0.97	0.98	0.98	10.6	0.975	0.98	0.87	0.98	11.5
Random Forest	0.986	0.98	0.98	0.98	2.5	0.976	0.98	0.89	0.98	2.9
Decision Tree	0.980	0.98	0.97	0.97	2.3	0.973	0.98	0.87	0.90	2.7
MLP	0.983	0.97	0.98	0.98	12.4	0.975	0.97	0.88	0.91	14.4
LSTM	0.976	0.96	0.98	0.97	14.5	0.971	0.98	0.85	0.90	16.1

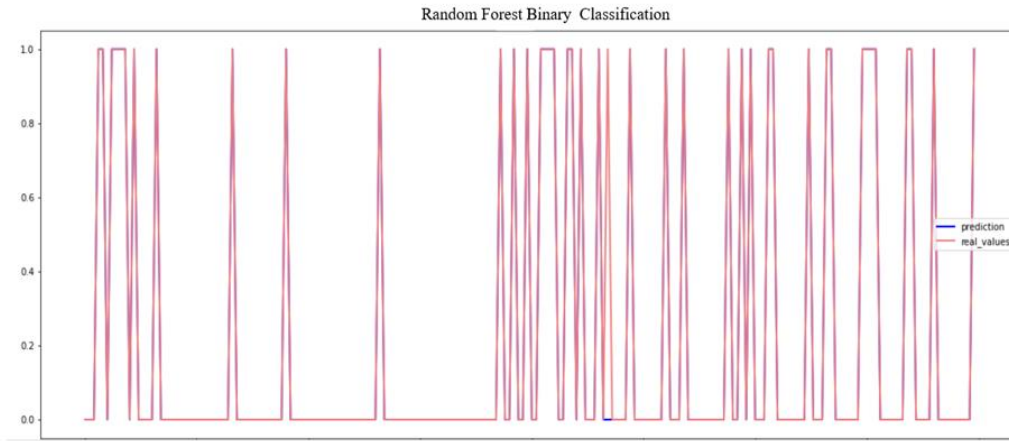


Figure 6. Random Forest binary classification prediction data signal.

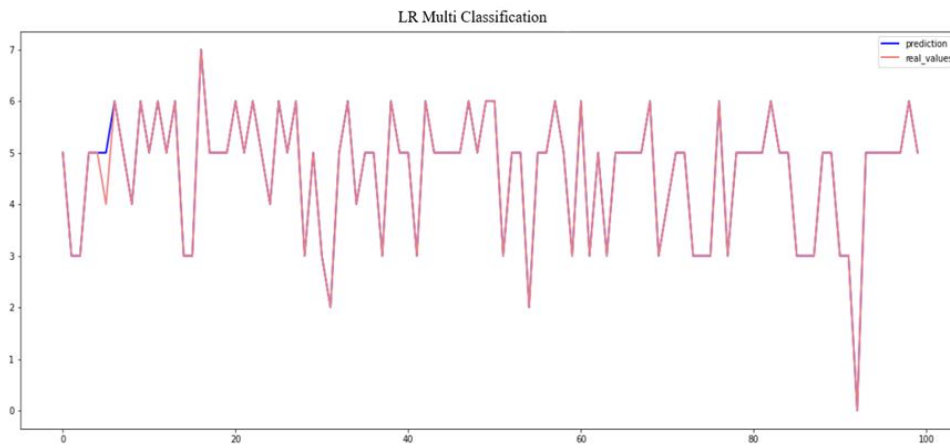


Figure 7. LR multi-label classification prediction data signal.

Figures 8 and 9 show the accuracy graphs of the RF and LR models. We can say that the results are close to each other and successful.

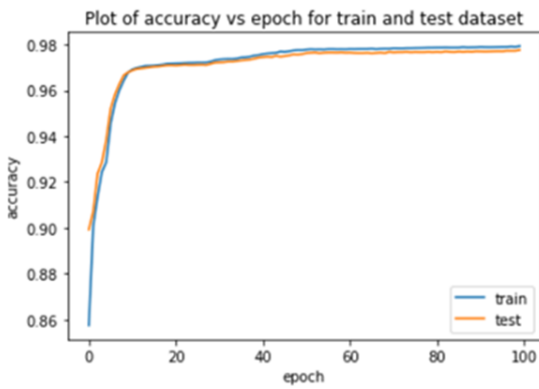


Figure 8. RF accuracy graph for binary class.

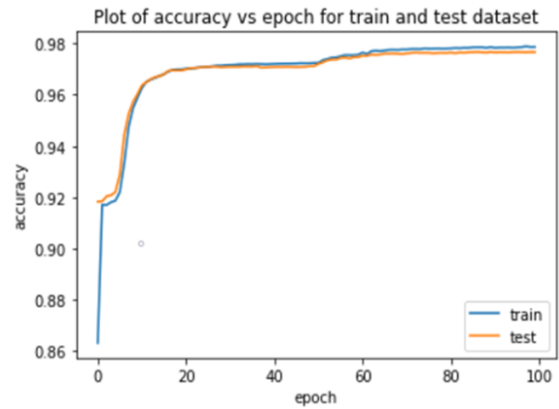


Figure 9. LR accuracy graph for multi-label class.

4.2 NSL-KDD Training Phase

Table 3 shows the evaluation results of NSL-KDD. As can be seen from the results, the highest accuracy

value for the binary class was calculated using the MLP algorithm and for the multi-class LSTM algorithm.

Table 3. Evaluation results for NSL-KDD.

	Binary Class					Multi Class				
	Accuracy	Recall	Precision	F1-Score	Total Time	Accuracy.	Recall	Precision	F1-Score	Total Time
LR	0.966	0.97	0.97	0.97	1.9	0.878	0.88	0.86	0.89	3.3
KNN	0.955	0.95	0.96	0.96	12.5	0.928	0.92	0.91	0.91	14.6
Random Forest	0.957	0.96	0.96	0.96	2.1	0.913	0.91	0.90	0.90	3.1
Decision Tree	0.967	0.97	0.97	0.97	2.3	0.905	0.89	0.90	0.90	3.7
MLP	0.978	0.98	0.97	0.98	11.7	0.892	0.88	0.89	0.89	15.1
LSTM	0.975	0.97	0.97	0.97	16.3	0.934	0.93	0.94	0.93	17.2

Analysis of data signals because of dual-class and multi-class testing is shown in Figures 10 and 11. Considering the estimated signal and actual signals,

there is some loss in the initial and intermediate stages. However, this loss is at an acceptable level.

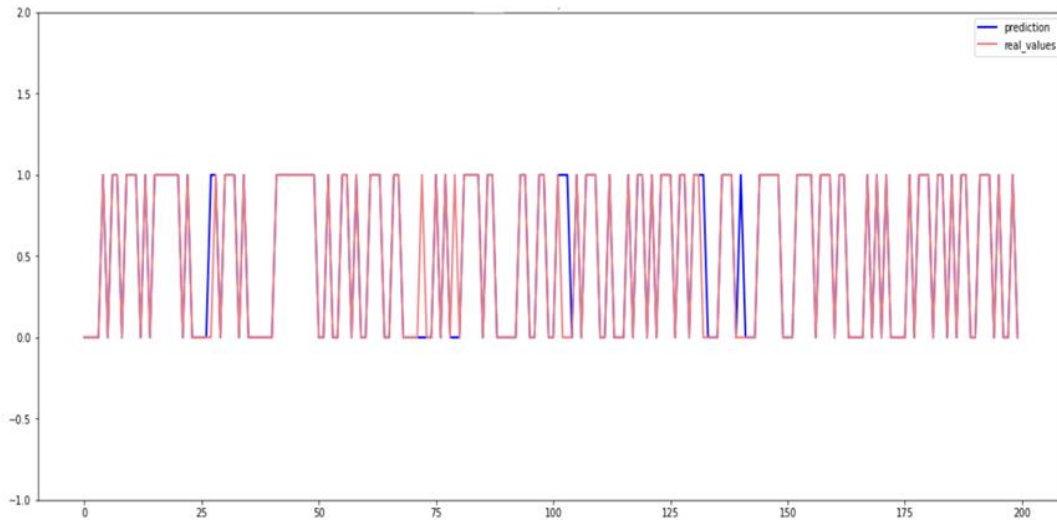


Figure 10. MLP binary classification prediction data signal.

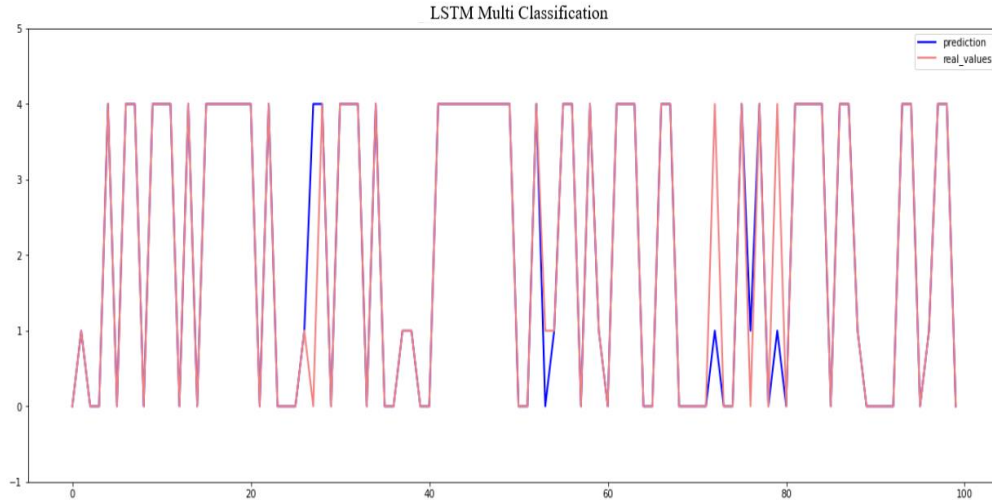


Figure 11. LSTM multi-label classification prediction data signal.

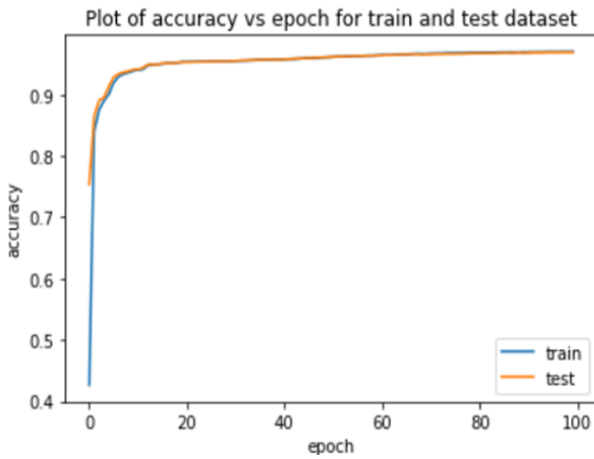


Figure 12. MLP accuracy graph for binary class.

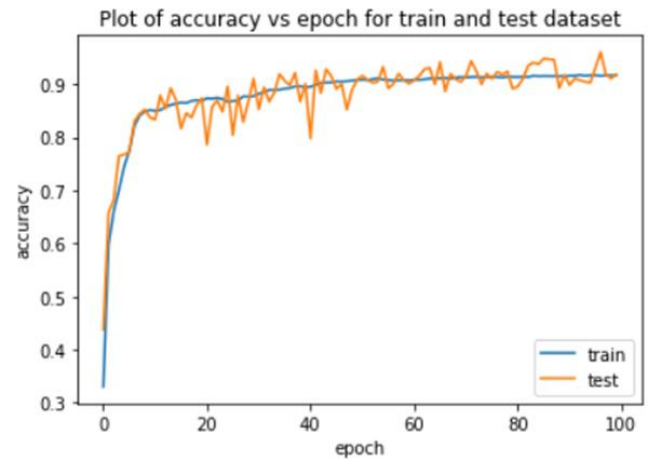


Figure 13. LSTM accuracy graph for binary class.

Table 4 shows a comparison of some studies in the literature and the methods we recommend. When the results are examined, the success of the Random Forest model in classifying the data for each study is remarkable. In addition, it is seen that the hyperparameters of the proposed model are well adjusted, and it gives successful results in both data sets. Classical machine learning algorithms have been

able to give more successful results compared to the LSTM learning model due to the uneven distributions on the data sets and some classes with small data samples. However, when these datasets are expanded and larger samples are created, the LSTM architecture will be able to give successful results, as in the current NSL-KDD dataset.

Table 4. Comparison with latest state-of-the artwork.

Author	Technique	Accuracy
Kazi Abu Taher et al. [33]	ANN	95.00%
Mohammad N. I. et al. [34]	Decision tree, RF	92.60%
Roberto M.-C. et [35]	Linear reg., random forest	94.00%
Razan A. et al. [36]	RF, Bayesian Network,	93.40%

Proposed approach	Binary Class (UNSW-NB15, NSL-KDD) RF, MLP	98.60%, 97.80%,
Proposed approach	Multi-Class (UNSW-NB15, NSL-KDD) LR, LSTM	93.40%, 98.30%

5. Conclusion

In this paper, machine learning algorithms for intrusion detection systems are run one by one. Applications are a guide for network attackers. The results obtained on two different data sets for binary and multi-class detection problems prove the success of machine learning algorithms in classification. In the UNSW-NB15 dataset, RF and LR algorithms gave the best results, respectively, and in the NSL-KDD dataset, the MLP and LSTM networks gave the best results. From this perspective, it can be said that almost all of the machine learning algorithms give good and close results. Deep learning and LSTM architectural structures were able to give successful results according to machine learning algorithms when large data sets and balanced class distributions were created. However, this study proves that classical machine learning algorithms are still a good alternative to deep learning models. Additionally, training and testing times were found to be close to each other. However, it is worth mentioning that attack classes are sometimes mislabeled.

Thanks to this and similar studies, it is possible to compare machine learning algorithms for network attacks. In addition, the option of detecting

the superior and deficient aspects of algorithms and developing new hybrid systems accordingly is offered.

In future studies, the datasets can be improved, and the missing classes can be made more balanced. Additionally, new models can be designed by considering the superior features of machine learning algorithms. Considering that attack detection systems are constantly exposed to attacks, I believe that it would be beneficial to conduct such studies at short intervals and with updated data sets. I recommend that real-time web interfaces and intrusion detection systems be supported, where the best results algorithms will be used as drafts.

Conflict of Interest Statement

The study is complied with research and publication Ethics

Statement of Research and Publication Ethics

The study is complied with research and publication ethics.

References

- [1] S. Moualla, K. Khorzom, and A. Jafar, "Improving the Performance of Machine Learning-Based Network Intrusion Detection Systems on the UNSW-NB15 Dataset," *Comput Intell Neurosci*, vol. 2021, pp. 5557577, 2021, doi: 10.1155/2021/5557577.
- [2] S. Choudhary and N. Kesswani, "Analysis of KDD-Cup'99, NSL-KDD and UNSW-NB15 Datasets using Deep Learning in IoT," *Procedia Comput Sci*, vol. 167, pp. 1561–1573, Jan. 2020, doi: 10.1016/J.PROCS.2020.03.367.
- [3] B. M. Serinelli, A. Collen, and N. A. Nijdam, "Training Guidance with KDD Cup 1999 and NSL-KDD Data Sets of ANIDINR: Anomaly-Based Network Intrusion Detection System," *Procedia Comput Sci*, vol. 175, pp. 560–565, Jan. 2020, doi: 10.1016/J.PROCS.2020.07.080.

- [4] N. v. Chawla, K. W. Bowyer, L. O. Hall, and W. P. Kegelmeyer, "SMOTE: Synthetic Minority Over-sampling Technique," *Journal of Artificial Intelligence Research*, vol. 16, pp. 321–357, Jun. 2002, doi: 10.1613/JAIR.953.
- [5] P. Geurts, D. Ernst, and L. Wehenkel, "Extremely randomized trees," *Machine Learning 2006 63:1*, vol. 63, no. 1, pp. 3–42, Mar. 2006, doi: 10.1007/S10994-006-6226-1.
- [6] A. Basati and M. M. Faghih, "PDAE: Efficient network intrusion detection in IoT using parallel deep auto-encoders," *Inf Sci (N Y)*, vol. 598, pp. 57–74, Jun. 2022, doi: 10.1016/J.INS.2022.03.065.
- [7] A. E. Cil, K. Yildiz, and A. Buldu, "Detection of DDoS attacks with feed forward based deep neural network model," *Expert Syst Appl*, vol. 169, p. 114520, May 2021, doi: 10.1016/J.ESWA.2020.114520.
- [8] G. C. Amaizu, C. I. Nwakanma, S. Bhardwaj, J. M. Lee, and D. S. Kim, "Composite and efficient DDoS attack detection framework for B5G networks," *Computer Networks*, vol. 188, p. 107871, Apr. 2021, doi: 10.1016/J.COMNET.2021.107871.
- [9] G. A. MM, J. N. K. S, U. M. R, and M. R. TF, "An efficient SVM based DEHO classifier to detect DDoS attack in cloud computing environment," *Computer Networks*, vol. 215, p. 109138, Oct. 2022, doi: 10.1016/J.COMNET.2022.109138.
- [10] E. Mushtaq, A. Zameer, M. Umer, and A. A. Abbasi, "A two-stage intrusion detection system with auto-encoder and LSTMs," *Appl Soft Comput*, vol. 121, p. 108768, May 2022, doi: 10.1016/J.ASOC.2022.108768.
- [11] S. Choudhary and N. Kesswani, "Analysis of KDD-Cup'99, NSL-KDD and UNSW-NB15 Datasets using Deep Learning in IoT," *Procedia Comput Sci*, vol. 167, pp. 1561–1573, 2020, doi: 10.1016/J.PROCS.2020.03.367.
- [12] S. Moualla, K. Khorzom, and A. Jafar, "Improving the Performance of Machine Learning-Based Network Intrusion Detection Systems on the UNSW-NB15 Dataset," *Computational Intelligence and Neuroscience*, vol. 2021, 2021, doi: 10.1155/2021/5557577.
- [13] L. Mohammadpour, T. C. Ling, C. S. Liew, and C. Y. Chong, "A convolutional neural network for network intrusion detection system," *Proceedings of the Asia-Pacific Advanced Network*, vol. 46, no. 0, pp. 50–55, 2018.
- [14] A. Dođru, S. Buyrukođlu, and M. Ari, "A hybrid super ensemble learning model for the early-stage prediction of diabetes risk," *Medical & Biological Engineering & Computing*, vol. 61, no. 3, pp. 785–797, 2023.
- [15] S. Buyrukođlu. "New hybrid data mining model for prediction of Salmonella presence in agricultural waters based on ensemble feature selection and machine learning algorithms," *Journal of Food Safety*, vol. 41, no. 4, 2021.
- [16] S. Buyrukođlu. "Promising cryptocurrency analysis using deep learning." In *2021 5th International symposium on multidisciplinary studies and innovative technologies (ISMSIT)*, pp. 372-376, 2021.
- [17] "The UNSW-NB15 Dataset | UNSW Research." <https://research.unsw.edu.au/projects/unsw-nb15-dataset> (accessed Sep. 08, 2022).
- [18] N. Moustafa and J. Slay, "UNSW-NB15: A comprehensive data set for network intrusion detection systems (UNSW-NB15 network data set)," *2015 Military Communications and Information Systems Conference, MilCIS 2015 - Proceedings*, Dec. 2015, doi: 10.1109/MILCIS.2015.7348942.
- [19] S. Bagui, E. Kalaimannan, S. Bagui, D. Nandi, and A. Pinto, "Using machine learning techniques to identify rare cyber-attacks on the UNSW-NB15 dataset," *Security and Privacy*, vol. 2, no. 6, p. e91, Nov. 2019, doi: 10.1002/SPY2.91.
- [20] P. TS and P. Shrinivasacharya, "Evaluating neural networks using Bi-Directional LSTM for network IDS (intrusion detection systems) in cyber security," *Global Transitions Proceedings*, vol. 2, no. 2, pp. 448–454, Nov. 2021, doi: 10.1016/J.GLTP.2021.08.017.
- [21] M. Tavallae, E. Bagheri, W. Lu, and A. A. Ghorbani, "A detailed analysis of the KDD CUP 99 data set," *IEEE Symposium on Computational Intelligence for Security and Defense Applications, CISDA 2009*, Dec. 2009, doi: 10.1109/CISDA.2009.5356528.

- [22] J. Mchugh, "Testing Intrusion detection systems," *ACM Transactions on Information and System Security (TISSEC)*, vol. 3, no. 4, pp. 262–294, Nov. 2000, doi: 10.1145/382912.382923.
- [23] R. D. Ravipati and M. Abualkibash, "Intrusion Detection System Classification Using Different Machine Learning Algorithms on KDD-99 and NSL-KDD Datasets - A Review Paper," *SSRN Electronic Journal*, Jun. 2019, doi: 10.2139/SSRN.3428211.
- [24] A. Karcioğlu and T. Aydin, "Sentiment Analysis of Turkish and English Twitter Feeds Using Word2Vec Model," *2019 27th Signal Processing and Communications Applications Conference (SIU)*, Sivas, Turkey, 2019, pp. 1-4, doi: 10.1109/SIU.2019.8806295.
- [25] A. Moldagulova and R. B. Sulaiman, "Using KNN algorithm for classification of textual documents," *ICIT 2017 - 8th International Conference on Information Technology, Proceedings*, pp. 665–671, Oct. 2017, doi: 10.1109/ICITECH.2017.8079924.
- [26] A. A. Akinyelu and A. O. Adewumi, "Classification of Phishing Email Using Random Forest Machine Learning Technique," *J. Appl. Math*, vol. 41, pp. 1-6, 2014, doi: 10.1155/2014/425731.
- [27] H. Patel, P. Prajapati, and H. H. Patel, "Study and Analysis of Decision Tree Based Classification Algorithms Extreme Multi-label Classification Problem View project Significance of the Transition to Outcome Based Education: Explore the Future View project Study and Analysis of Decision Tree Based Classification Algorithms," *International Journal of Computer Sciences and Engineering Open Access Research Paper*, no. 6, 2018, doi: 10.26438/ijcse/v6i10.7478.
- [28] W. H. Delashmit, "Recent Developments in Multilayer Perceptron Neural Networks".
- [29] S. Hochreiter and J. Schmidhuber, "Long Short-Term Memory," *Neural Comput*, vol. 9, no. 8, pp. 1735–1780, Nov. 1997, doi: 10.1162/NECO.1997.9.8.1735.
- [30] K. K. A. Ghany, H. M. Zawbaa, and H. M. Sabri, "COVID-19 prediction using LSTM algorithm: GCC case study," *Inform Med Unlocked*, vol. 23, Jan. 2021, doi: 10.1016/J.IMU.2021.100566.
- [31] S. Tanışman, A.A. Karcioğlu, U. Aybars and H. Bulut, "LSTM Sinir Ağı ve ARIMA Zaman Serisi Modelleri Kullanılarak Bitcoin Fiyatının Tahminlenmesi ve Yöntemlerin Karşılaştırılması," *Avrupa Bilim ve Teknoloji Dergisi*, vol. 32, pp. 514-520, 2021.
- [32] S. Tanışman, A.A. Karcioğlu, U. Aybars and H. Bulut, "Türkiye'de COVID-19 Bulaşısının ARIMA Modeli ve LSTM Ağı Kullanılarak Zaman Serisi Tahmini," *Avrupa Bilim ve Teknoloji Dergisi*, vol. 32, pp. 288-297, 2021.
- [33] K.A., Taher, B.M.Y., Jisan, and M.M. Rahman, "Network intrusion detection using supervised machine learning technique with feature selection," *In 2019 International conference on robotics, electrical and signal processing techniques*, pp. 643-646, 2019.
- [34] M. Injadat, A. Moubayed, A.B. Nassif, A. Shami, "Multi-stage optimized machine learning framework for network intrusion detection," *IEEE Trans. Netw. Serv. Manag*, 2020. Doi:10.1109/TNSM.2020.3014929
- [35] R., Magán-Carrión, D., Urda, I., Díaz-Cano, and B., Dorronsoro, "Towards a reliable comparison and evaluation of network intrusion detection systems based on machine learning approaches," *Applied Sciences*, vol. 10, no. 5, p. 1775, 2020.
- [36] R., Abdulhammed, H., Musafar, A., Alessa, M., Faezipour, and A., Abuzneid, "Features dimensionality reduction approaches for machine learning based network intrusion detection," *Electronics*, vol. 8, no. 3, p. 322, 2019.

Recycling Wastewater with Membrane Technology and The Case of Singapore

Mikail YENİÇERİ^{1*}, Kübra TORTUM YENİÇERİ²

¹Kırşehir Ahi Evran University Graduate School of Natural and Applied Sciences, Kırşehir, Turkey

²Anadolu University, Public Administration, Eskişehir, Turkey
(ORCID: 0000-0003-1698-6911) (ORCID: 0000-0002-0436-2119)



Keywords: Membrane Technology, Wastewater, Singapore, NEWater.

Abstract

As a result of the constantly increasing use of water in the world, countries have searched for alternatives to water resources and various studies have been carried out with the available opportunities. One of the studies carried out is the NEWater project on the treatment and reuse of wastewater in Singapore as drinking water. This project has been implemented in the country for 20 years and meets an average of 30% of the country's water needs. With this project, Singapore contributed to its transformation into a global hydroelectric power plant by pioneering innovative water treatment and technologies. However, in this model, the membranes used for wastewater treatment (forward, backward and pressure retarded osmosis and membrane bioreactors) are developed to use advanced oxidation processes, electrochemical methods to directly supply drinking water, especially in countries where water resources are insufficient, or to treat polluted water that causes disease and death. In this study, it is discussed through the NEWater application in Singapore that wastewater can be treated and reused with membrane technology.

1. Introduction

Membrane technologies play an important role in water and energy sustainability. Some are already implemented in large-scale industries. Examples include desalination with reverse osmosis (RO), wastewater treatment with membrane reactors (MBR), lithium-ion batteries, and membrane-based fuel cells. Membrane technologies meet sustainability criteria in terms of environmental impacts, land use, ease of use, flexibility and adaptability, as well as addressing water and energy scarcity. On the other hand, they need to be improved in terms of financial burden, affordability, energy consumption and expertise [12]. method should be given in detail and clearly in terms of reproducibility of the study. The methods used should be supported by previously published references. Changes that contribute to the method in the study should be described in detail [3], [4]. Membrane technology, which has grown greatly

in the last decade with the advantages it offers for treatment, offers various options in wastewater treatment [13]. Membrane technology has the potential to bridge the gap between affordability and sustainability, low or no chemical use, and eco-friendliness and easy accessibility. Membrane technology has proven to be a more advantageous option in wastewater treatment processes [14].

Membrane technology, which is not a new technology, has been available since the 18th century and many improvements have been made to make membranes more suitable for many different applications [15]. The changing nature and complexity of wastewater lead to further improvements in efficiency, space requirements, energy, filter quality and technique. Again, there is a continuous modification of membrane modules and elements to reduce membrane fouling, which is a major challenge in membrane processes. The possibility of combining two or more membrane

*Corresponding author: myeniceri@ahievran.edu.tr

Received: 26.01.2023, Accepted: 14.06.2023

processes with each other or with other forms of technology, such as coagulation or adsorption, in a hybrid fashion, is also being continuously explored, developed and implemented in many wastewater treatment plants [16].

Characteristically, these membranes are classified as isotropic and anisotropic (Figure 1) [12]. Isotropic membranes are identical in composition and physical structure. The permeation fluxes in the microporous case are relatively high compared to the non-porous (dense) case, and their applications are rather limited due to their low permeation fluxes. Isotropic microporous membranes are widely applied in microfiltration membranes. Anisotropic membranes, on the other hand, are not uniform over the membrane area and consist of different layers with different structures and compositions. These membranes have a thin selective layer supported by a thicker and highly permeable layer. It is especially applied in reverse osmosis (RO) processes. [17].

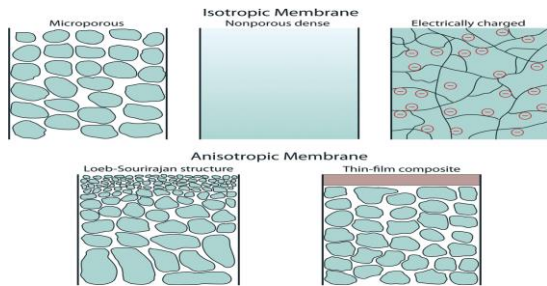


Figure 1. Schematic illustration of various classes of membranes.

In terms of membrane material structure, membranes are classified as organic or inorganic. Organic membranes are made from synthetic organic polymers. Often, membranes for pressure driven separation processes (microfiltration, ultrafiltration, nanofiltration and reverse osmosis) are made from synthetic organic polymers. These include polyethylene (PE), polytetrafluoroethylene (PTFE), polypropylene, and cellulose acetate, among others [18]. Inorganic membranes are made of materials such as ceramic, metal, zeolite or silica. They are chemically and thermally stable and are widely used in industrial applications such as hydrogen separation, ultrafiltration and microfiltration [17]. The structure of the membranes is shown below (Figure 2) [19].

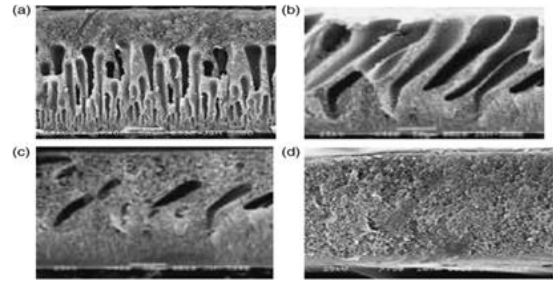


Figure 2. Structure of membrane.

The movement of the medium through the dice is based on different driving forces. There are equilibrium-based membrane processes, non-equilibrium membrane processes, pressure-driven and non-pressure-driven processes [20]. The schematic diagram below (Figure 3) shows a summary of some of these techniques according to their driving forces. These membrane techniques are discussed separately below.

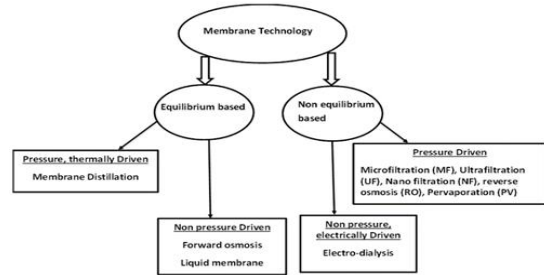


Figure 3. Schematic representation of some membrane processes

Membrane technologies have gained great importance in the advanced treatment and recycling of wastewater in recent years. The reason for this is that water recovery has prevailed in parallel with the increase in water demand and membrane technologies have come to the fore in this regard both in terms of quality and quantity. There are also high-efficiency systems for the removal of primary pollutants such as membrane technologies, endocrine disrupting compounds for the recovery of domestic wastewater and pharmaceutical actives. It is possible to reach the desired output quality by choosing the membrane type in wastewater treatment or recovery. Wastewater treatment systems integrated with membranes have advantages and disadvantages depending on output quality, energy consumption and system complexity factors. In general, membrane systems are used together with physical, chemical and biological processes to provide the most efficient form of regeneration/advanced purification [21].

Membrane technology has started to be used in some areas with significant effects. For example, during the Sydney Olympic Games held in 2000,

membrane technology was used in the stormwater recycling system, which used polypropylene hollow fiber microfiltration (MF) membrane as a pre-treatment to remove suspended pollutants and pathogens in rainwater, and then to desalinate with RO technique [22]. Later, the wastewater was chlorinated and used to flush toilets. With excellent processing efficiency, simple apparatus and easy integration with other processing facilities, membrane technology can be promising for emergency water supply. It has been proven that the quality of water treated with membrane technology, unlike conventional treatment methods, can reach or even exceed domestic or drinking water criteria [23]. Membrane bioreactor technology has become a promising technique for wastewater treatment using the use of activated sludge and membrane separation. The membrane bioreactor process has advantages over the traditional activated sludge process and provides stable and high effluent quality [24].

3. Examples of Membrane Technology in the World

Although the water obtained from the recycling of domestic wastewater is mainly used for agricultural irrigation, some technologies allow this water to be used directly or indirectly as a drinking water source. In much of the world, there are more than 450 water recycling facilities in Japan and the USA, and more than 3,300 water recycling facilities in Australia and the European Union [25].

3.1. Example of Sulaibiya, Kuwait

Sulaibiya is a wastewater recovery facility using the world's largest membrane technologies. The daily capacity of the facility is 375,000 m³/day. The water discharged from Sulaibiya is mixed with brackish water and used to improve existing brackish water distribution facilities. Following the biological wastewater treatment plant, the wastewater is treated at a secondary level and the effluent is treated in a recovery plant that includes UF (Ultrafiltration) and RO (Reverse Osmosis) processes. Thanks to the use of UF before RO, the life of RO membranes increases, operating pressures decrease, and chemical wash cycle time increases. The application of UF and RO together creates a quality water supply at drinking and utility water level, as well as the possibility of using water in agriculture and groundwater discharge. The effluent quality obtained from the facility is better than the drinking water standards set by WHO and is also used in agricultural irrigation as an alternative source [26].

3.2. Example of California, USA

Wastewater recovery practices have long been popular in non-water-rich California. In addition, for Orange Country, a wastewater recovery facility was established in this region due to the cost of water supply from Northern California. In this established facility, recovery includes MF (Membrane Filtration), TO and hydrogen peroxide as advanced oxidation and UV (Ultraviolet) treatment steps. The daily facility capacity is 270,000 m³/day and thanks to the membrane processes used, pharmaceuticals, pesticides and other harmful substances are removed before they are released into the receiving environment [27].

3.3. Example of Australian

At the facility where 18 million m³ of wastewater is recycled annually, tertiary treated wastewater from three different wastewater treatment plants is processed and recycled. The treated wastewater coming to the facility first comes to a balancing tank and passes through the mechanical filter. Then UF is passed through the membrane and suspended solids, bacteria, viruses, and some of the organic matter are removed. In the next stage, RO membranes are used, and advanced separation is carried out, and the purified water is passed through the decarbonator and then pH adjusted and given to Penrith tea [28].

4. Singapore and NEWater Project

One of the countries working in the field of water recycling is the NEWater project, which purifies the sewage water of Singapore and turns it back into clean drinking water. In this system, the waste water coming out of the sewage system is purified by microfiltration and reverse osmosis methods and brought to drinkable quality. This water is then transported by the municipalities to the cities of the city and to the industries that need clean water at a high rate [29].

Singapore has been using raw water imported from Johor (Malaysia) for many years as its primary water source, which meets around 40% of the country's water needs (250 Mm³ per year). The Singapore government's aim is to minimize the amount of water supplied from this source by 2061 [30].

The second water source of the country is the rain water, which is formed with approximately 2400 mm of precipitation per year. For this purpose, some major urban planning (reconstruction of parts of the city and relocation of houses and industries to improve water collection) has been taken, as well as

measures such as water tanks built to harvest rainwater in a large basin. With the addition of some settlements recently, it is aimed to increase the amount of water provided from rain water to 150 Mm³ per year and to collect 90% of the water collection area [31].

Third water source by desalination of sea water. In 2005 and 2013, two purification plants using microfiltration and reverse osmosis were built with a water production capacity of 50 Mm³ and 115 Mm³/year, respectively. These plants, which consume large amounts of energy in the desalination process, are mostly used as backup plants to meet the spikes in demand [32].

The fourth water source is water called NEWater, which consists of water produced by the combination of microfiltration, reverse osmosis and UV treatment of wastewater. Annual production of 110 Mm³ NEWater in 2012 met 18% of the total water needs, while meeting 32% of industrial and commercial needs. 2% of the recovered water is sent to rainwater tanks to be treated in drinking water standards. Urban wastewater (at a rate of 25 Mm³ per year) is reused especially for the petrochemical industry on Jurong Island [33].

Replacing part of the activated sludge process (aeration and post-treatment) and RO pre-treatment process (microfiltration or ultrafiltration) in the NEWater production process with a membrane bioreactor (MBR) will reduce the energy requirement of wastewater treatment. Current research on ways to improve the wastewater system and sludge digestion process are also factors that will help the wastewater sector reduce its energy needs [34].

Within the scope of the NEWater project, water reuse in the country is to meet the water needs of the city by re-purifying the wastewater with membrane systems and to use it as drinking water in the form of bottled water and to reuse the recycled wastewater in industrial processes. With the NEWater project, which was commissioned in 2003, wastewater treatment in effluent quality in accordance with EPA and WHO standards can be realized at a level that can be used both indirectly and for direct use. While the water recovered in indirect use can be used as process water in silicon wafer production, power generation, petrochemical industry and cooling towers, treated water in direct use applications is discharged to reservoirs and rainwater channels and reaches drinking water treatment plants [25].

Utilizing a traction solution to naturally drive the osmotic process in the NEWater project, FO (Forward Osmosis) provides substantially lower energy consumption and contamination tendency

compared to RO (Reverse Osmosis); however, the FO product is not NEWater, but a diluted extraction solution that requires secondary treatment. This means that FO and RO may not be mutually exclusive and can be combined for energy optimization with RO concentrate, which is actually used as a draw solution for FO (Figure 4) [11].

When using equations, they should be numbered sequentially. The equation numbers should be enclosed by parentheses and located at the right-hand side of the page [8]. In addition, equations should be prepared with Word or other equation editors and should not be in picture format [9], [10].

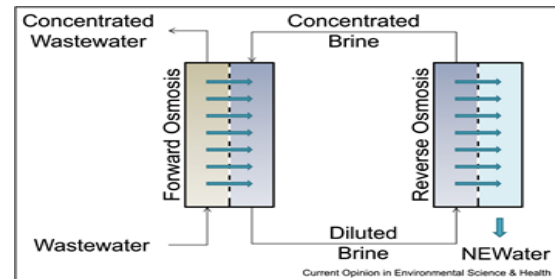


Figure 4. Integrating FO and RO methods for energy optimization. The RO brine would play the role of the draw solution in that NEWater production scheme.

The NEWater product meets the drinking water standard of both the World Health Organization and the US Environmental Protection Agency. The Health Effect Testing Program (HETP) has also shown no health effects from consuming NEWater. In fact, NEWater is cleaner and purer than a raw freshwater source (Figure 5) [35].

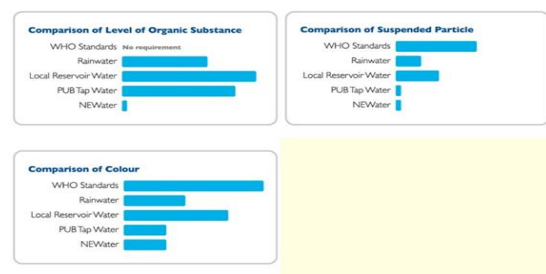


Figure 5. Organic Substance Comparison, Suspended Particle Comparison and Color Comparison.

4.1. NEWater Technology Stage

NEWater production process occurs a few stage. **Stage 1**–The first stage of the NEWater production process is known as Microfiltration (MF). In this process, the treated used water is passed through membranes to filter out and retained on the membrane surface suspended solids, colloidal particles, disease-causing bacteria, some viruses and protozoan cysts.

The filtered water that goes through the membrane contains only dissolved salts and organic molecules. **Stage 2–Reverse Osmosis** The second stage of the NEWater production process is known as Reverse Osmosis (RO). In RO, a semi-permeable membrane is used. The semi-permeable membrane has very small pores which only allow very small molecules like water molecules to pass through. Consequently, undesirable contaminants such as bacteria, viruses, heavy metals, nitrate, chloride, sulphate, disinfection by-products, aromatic hydrocarbons, pesticides etc, cannot pass through the membrane. Hence, NEWater is RO water and is free from viruses, bacteria and contains negligible amount of salts and organic matters. **Stage 3–UV Disinfection** At this stage, the water is already of a high grade water quality. The third stage of the NEWater production process really acts as a further safety back-up to the RO. In this stage, ultraviolet or UV disinfection is used to ensure that all organisms are inactivated and the purity of the product water guaranteed.

Before Storing NEWater in Water Tanks–Balance the pH in NEWater With the addition of some alkaline chemicals to restore the acid-alkali or pH balance, the NEWater is now ready to be piped off to its wide range of applications (Figure 6) [36].

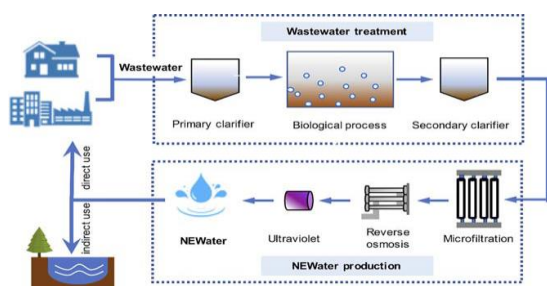


Figure 6. NEWater technology in Singapore

5. Conclusion and Suggestions

Water resources are depleted due to the rapidly increasing need for water in the world and the unconscious use of water in domestic, industrial and agricultural irrigation. It is beneficial in many factors, such as increasing the recycling and reuse of wastewater, reducing water scarcity and pollution, improving soil quality and reducing production costs. For this reason, most of the countries take measures for water and use the water treated in wastewater

References

- [1] Koyuncu, B. Zeytuncu, M. E. Pasaoglu, A. Yuksekdog, and B. Kose-Mutlu, "Resource recovery from waste, water and wastewaters with membrane technologies," *In Proceedings of the International Conference on Civil Infrastructure and Construction (CIC 2020)*, Doha, Qatar, pp. 634-639, 2020.

treatment plants in various areas as drinking water. Membrane technology is a system with significant potential in wastewater treatment. This technology stands out with its advantages over other treatment processes, especially in domestic and industrial wastewater treatment. Membrane systems are systems that can remove organic matter, pathogenic microorganisms and nutrients from wastewater with high efficiency. The number of treatment systems using this technology is increasing. Some of the obstacles to the implementation of these systems, which are advantageous for the treatment of wastewater of small settlements and factories, are the cost of membranes and the resulting operational pollution problems.

The use of wastewater as drinking water with the NEWater application in Singapore is a very important study in terms of preventing a possible water shortage in the world in the future. In addition, membrane technology will still occupy an important position in the future development trend. This article has attempted to summarize some membrane-related areas such as fouling and module structures, along with application examples, advantages and disadvantages. We hope this article will be useful in providing good information for further research on membrane technology applications in wastewater treatment.

Contributions of the Authors

In the study carried out, Author 1 in the formation of the idea, design, and literature review, compilation, and interpretation of the results; Author 2 contributed to the evaluation, presentation, and analysis of the results obtained, in the titles of spelling and checking the article in terms of content.

Conflict of Interest Statement

There is no conflict of interest between the authors.

Statement of Research and Publication Ethics

There is no need for an ethics committee approval in the prepared article.

- [2] M. F. García-Montoya, S. Gutiérrez-Granados, A. Alatorre-Ordaz, R. Galindo, R. Ornelas, and J. M. Peralta-Hernández, “Application of electrochemical/BDD process for the treatment wastewater effluents containing pharmaceutical compounds,” *J. Ind. Eng. Chem.*, vol. 31, pp. 238–243, 2015.
- [3] B. Şahin, “Küresel Bir Sorun: Su Kıtlığı ve Sanal Su Ticareti (Master Thesis, Sosyal Bilimler Enstitüsü)”. 2016.
- [4] L. Pintilie, C. M. Torres, C. Teodosiu, and F. Castells, “Urban wastewater reclamation for industrial reuse: An LCA case study,” *J. Clean. Prod.*, vol. 139, pp. 1–14, 2016.
- [5] Ö. Demir, M. Yıldız, Ü. Sercan, and C. Ş. Arzum, “Waste Water Recovery and Reuse,” pp. 1–14, 2017.
- [6] C. F. Bustillo-Lecompte and M. Mehrvar, “Slaughterhouse wastewater characteristics, treatment, and management in the meat processing industry: A review on trends and advances,” *J. Environ. Manage.*, vol. 161, pp. 287–302, 2015.
- [7] R. Ş. Taşdemir and İ. Koyuncu, “Membran Teknolojileri ile Alternatif Su Temini: Desalinasyon ve Atıksu Geri Kazanımı,” *Sürdürülebilir Çevre Dergisi*, vol. 1, no. 1, pp. 18–30, 2021.
- [8] A. F. Santos, P. Alvarenga, L. M. Gando-Ferreira, and M. J. Quina, “Urban wastewater as a source of reclaimed water for irrigation: Barriers and future possibilities,” *Environments*, vol. 10, no. 2, p. 17, 2023.
- [9] A. Lee, J. W. Elam, and S. B. Darling, “Membrane materials for water purification: design, development, and application,” *Environ. Sci. (Camb.)*, vol. 2, no. 1, pp. 17–42, 2016.
- [10] D. Ghernaout, N. Elboughdiri, and A. Alghamdi, “Direct potable reuse: The Singapore NEWater project as a role model,” *OALib*, vol. 06, no. 12, pp. 1–10, 2019.
- [11] O. Lefebvre, “Beyond NEWater: An insight into Singapore’s water reuse prospects,” *Curr. Opin. Environ. Sci. Health*, vol. 2, pp. 26–31, 2018.
- [12] H. Lee and T. P. Tan, “Singapore’s experience with reclaimed water: NEWater,” *Int. J. Water Resour. Dev.*, vol. 32, no. 4, pp. 611–621, 2016.
- [13] C. A. Quist-Jensen, F. Macedonio, and E. Drioli, “Membrane technology for water production in agriculture: Desalination and wastewater reuse,” *Desalination*, vol. 364, pp. 17–32, 2015.
- [14] N.P. Hankins, R. Singh (Eds.), *Emerging Membrane Technology for Sustainable Water Treatment*, Elsevier, Boston pp.15-52, 2016.
- [15] A. G. Fane, R. Wang, and Y. Jia, “Membrane technology: Past, present and future,” in *Membrane and Desalination Technologies*, Totowa, NJ: Humana Press, pp. 1–45, 2011
- [16] C. Stoquart, P. Servais, P. R. Bérubé, and B. Barbeau, “Hybrid Membrane Processes using activated carbon treatment for drinking water: A review,” *J. Memb. Sci.*, vol. 411–412, pp. 1–12, 2012.
- [17] A. K. Pabby, S. S. H. Rizvi, and A. M. S. (Eds.), *Handbook of Membrane Separations: Chemical, Pharmaceutical, Food, and Biotechnological Applications*, (1st ed.). CRC Press, 2015.
- [18] U. M. Aliyu, S. Rathilal, and Y. M. Isa, “Membrane desalination technologies in water treatment: A review,” *Water Pract. Technol.*, vol. 13, no. 4, pp. 738–752, 2018.
- [19] Lalia, B. S., Kochkodan, V., Hashaikeh, R., & Hilal, N., “A review on membrane fabrication: Structure, properties and performance relationship,” *Desalination*, vol. 326, pp. 77–95, 2013.
- [20] Jhaveri, J. H., & Murthy, Z. V. P., “A comprehensive review on anti-fouling nanocomposite membranes for pressure driven membrane separation processes,” *Desalination*, vol. 379, pp. 137–154, 2016.
- [21] M. Aslan, Membrane Technologies. *TÜÇEV*, 275 s., 9-13, 2016.
- [22] X. Liu, Z. Ren, H. H. Ngo, X. He, P. Desmond, and A. Ding, “Membrane technology for rainwater treatment and reuse: A mini review,” *Water Cycle*, vol. 2, pp. 51–63, 2021.
- [23] Z. Wang, J. Ma, C. Y. Tang, K. Kimura, Q. Wang, and X. Han, “Membrane cleaning in membrane bioreactors: A review,” *J. Memb. Sci.*, vol. 468, pp. 276–307, 2014.
- [24] A. Tolkou, A. Zouboulis, and P. Samaras, “The incorporation of ceramic membranes in MBR systems for wastewater treatment: Advantages and patented new developments,” *Recent Pat. Eng.*, vol. 8, no. 1, pp. 24–32, 2014.

- [25] D. İmer-Köseoğlu, S. Güçlü, and İ. Koyuncu, “Membrane Technologies and Applications in Water/Wastewater Treatment and Recovery,” *TÜÇEV*, 2018.
- [26] Suez, “Water tech and solutions technical paper Sulaibiya - world’s largest membrane water reuse Project”. [Online]. Available: https://www.gewater.com/kcpguest/documents/Technical%20Papers_Cust/Americas/English/TP1030EN.pdf, 2017. [Accessed: Apr. 20, 2023].
- [27] A. N. Angelakis and P. Gikas, “Water reuse: Overview of current practices and trends in the world with emphasis on EU states,” *Water Utility Journal*, vol. 8, no. 67, 2014.
- [28] J. K. Upadhyaya and G. Moore, “Sustainability indicators for wastewater reuse systems and their application to two small systems in rural Victoria, Australia,” *Can. J. Civ. Eng.*, vol. 39, no. 6, pp. 674–688, 2012.
- [29] B. Ekinci, “Example Country Practices for Efficient Use of Water Resources and Applicability of these Studies in Our Country. (Master Thesis, Republic of Turkey Ministry of Agriculture and Forestry)”. 2015.
- [30] C. Tortajada, Y. K. Joshi, and A. K. Biswas, *The Singapore water story: Sustainable development in an urban city-state*, Routledge, Oxon, 2013.
- [31] B. Harley, “Singapore’s marina barrage and reservoir-changing mindsets in urban solutions,” *Water Sensitive Cities*, C. Howe and C. Mitchell, Eds. London, England, IWA Publishing, pp. 147–154, 2011.
- [32] Global Water Intel. [Online]. Available: [https://www.globalwaterintel.com/client_media/uploaded/media/GWI%20Media%20pack%20A4%2013-14%20\(2\).pdf](https://www.globalwaterintel.com/client_media/uploaded/media/GWI%20Media%20pack%20A4%2013-14%20(2).pdf). [Accessed: Apr. 20, 2023].
- [33] V. Lazarova, T. Asano, A. Bahri, and J. Anderson, *Milestones in Water Reuse*. IWA Publishing, 2013.
- [34] M. F. Tay, C. Liu, E. R. Cornelissen, B. Wu, and T. H. Chong, “The feasibility of nanofiltration membrane bioreactor (NF-MBR)+ reverse osmosis (RO) process for water reclamation: Comparison with ultrafiltration membrane bioreactor (UF-MBR)+ RO process,” *Water research*, vol. 129, pp. 180–189, 2018.
- [35] Public Utilities Board. [Online]. Available: <https://www.pub.gov.sg/Documents/NEWater%20Technology.pdf>. [Accessed: Apr. 20, 2023].
- [36] Public Utilities Board. [Online]. Available: <https://www.pub.gov.sg/watersupply/waterquality/NEWater>. [Accessed: Apr. 20, 2023].



Lichens as Biomonitors of Air Pollutants Deposition: Strategically Important Element Pollution

E. Işıl ARSLAN TOPAL^{1*}, Murat TOPAL², Erdal ÖBEK³, Ali ASLAN⁴

¹Firat University, Department of Environmental Engineering, Elazığ/TURKEY

²Munzur University, Department of Chemistry and Chemical Processing Technologies, Tunceli/TURKEY

³Firat University, Department of Bioengineering, Elazığ/TURKEY

⁴Kyrgyz-Turkish Manas University, Department of Biology, Bishkek, KYRGYZSTAN

(ORCID: 0000-0003-0309-7787) (ORCID: 0000-0003-0222-5409)

(ORCID: 0000-0002-4595-572X) (ORCID: 0000-0002-5122-6646)



Keywords: Accumulation, Biomonitor, Elements, Environment, Lichen, Pollution.

Abstract

Investigation of various species of lichen as biomonitors of air pollutants deposition and evaluation of element pollution were aimed. Maximum accumulation was 43.9 ± 2.1 mg/kg in *X. somloensis*. Strontium in lichen species was quite high. Percentages of strontium for *L. pulmonaria*, *C. furcata*, *U. longissima*, *X. somloensis* and *F. caperata* were between 58% and 78% indicating the efficient accumulation of strontium. Lichens also accumulated strategically important elements. Maximum contamination factors in lichens were for strontium and tantalum. Maximum contamination factors of hafnium, niobium, lithium, gallium, and bismuth were for *L. pulmonaria* while maximum contamination factors of strontium, yttrium, scandium, and cerium were for *X. somloensis*. Maximum contamination factor of tantalum was for *F. caperata*. Enrichment factors for *L. pulmonaria*, *C. furcata*, and *F. caperata* were higher than 10, only for bismuth while lower than 10 for *U. longissima*. Enrichment factors for *X. somloensis* were higher than 10. Pollution load indexes for *L. pulmonaria* and *U. longissima* were higher than 1. The presence of strategically important elements in lichens showed that lichen species can be used as biomonitors of air pollutants.

1. Introduction

Environmental pollution threatens the ecosystem and health of humans because of toxicity. The major factors that contributed to the pollution of the environment are anthropogenic activities, industrialization, and development [1,2]. Nowadays, one of the main leading global problems is the presence of various pollutants in the environment. They not only affect the health of humans but also overshadow the life of other creatures [3]. Chemical pollution of the environment globally affects ecosystem function, services, and biodiversity [4,5].

The strategically important elements have various usage fields. As a result of the wide usage of these elements, they are released into the

environment. The strategically important elements have pollutant characteristics and strategic importance, at the same time. In the present paper hafnium (Hf), tantalum (Ta), niobium (Nb), strontium (Sr), lithium (Li), bismuth (Bi), cerium (Ce), yttrium (Y), gallium (Ga), and scandium (Sc) were investigated. Gallium has no known biological functions in living [6]. It is extensively used in the semiconductor industry. Ga arsenide is applied in different electronic components. Furthermore, gallium has been extensively used in medicine [7] because of its immunomodulating, anti-inflammatory, analgesic, and anti-hypercalcemic activities [6]. Bismuth is a rarely heavy metal. It has good chemical stability and peculiar physical and chemical properties [8]. The development in communication and

*Corresponding author: eiarslan@firat.edu.tr

Received: 27.01.2023, Accepted: 11.04.2023

microelectronics has been reflected in a concomitant increase in demand for Ta and Nb [9]. Lithium has strategic importance for various applications (e.g., lithium-ion batteries for mobile devices) [10,11]. Hafnium is a typical reactive element. Therefore, there is interest in using hafnium in nickel-based alloy systems [12]. Sr is a common trace element in the environment. It has commercial uses (e.g., glass, ceramics, and ferrite magnets). Strontium consumption via various ways can have adverse health effects (e.g., osteomalacia and abnormal bone development [13]. Yttrium is used in magnetic garnets [14]. It has the effect of refining grains of Mg alloys, can reduce the amount of Ca required in magnesium-based alloys, and may improve properties of them as well [15]. The high content of yttrium in different products results in accumulation in the body through food chain and endanger health by inhibiting the growth of pre-osteoblasts [16,17]. Cerium (Ce) is the most abundant rare earth metal found in the earth's crust [18]. Long-term ingestion of rare earth elements influences on activities of digestive enzymes [19,20]. Cerium minerals have been processed for industrial applications [18]. Scandium (Sc) is a valuable metal and used in production of high-strength and lightweight aluminum alloys and solid oxide fuel cells [21].

Different papers about the various applications of lichens were reported in the literature [22-25]. Apart from that papers, there are also some ones stating lichens as air pollution bioindicator/biomonitor [26-29]. Amount of elements accumulated in lichen thallus proportionally represents the presence of them in the atmosphere. When it comes to epiphytic species, thallus acts as a vehicle for transmitting particles by direct deposition from the air. Therefore, lichen serves as a valid instrument and proxy to assess air quality and potential contamination sources of elements [29-31]. Their prolonged exposure time to environmental factors, lack of cuticles or stomata and the absence of mechanisms of excretion make lichens behave like bioaccumulators of aerosol [29,32]. Lichens can accumulate even minor elements to measurable concentrations [33].

The aim of the present study is determination of accumulation of some strategically important elements in various lichens (*L. pulmonaria*, *C. furcata*, *U. longissima*, *X. somloensis* and *F. caperata*). When the literature is examined, there are few studies on accumulation of strategically important elements in lichens, and

therefore we focused on the following issues in our study; (1) We identified various lichens (*L. pulmonaria*, *C. furcata*, *U. longissima*, *X. somloensis* and *F. caperata*) in Artvin, Murgul (Turkey) (2) We determined the strategically important elements in lichens (3) We calculated the accumulation amounts and percentages of the strategic elements in lichen species (4) We assessed the element pollution by calculating enrichment factors, contamination factors, and pollution load indexes.

2. Material and Method

2.1. Sampling and Analysis

Lobaria pulmonaria, *Cladonia furcata*, *Usnea longissima*, *Xanthoparmelia somloensis* and *Flavoparmelia caperata* lichens investigated were collected from Murgul (Artvin, Turkey). The identification of lichen species was done by Prof. Dr. Ali Aslan. The lichens were dried and powdered. Analysis procedures are briefly given: samples were cold-leached with HNO₃. After cooling a modified Aqua Regia solution of equal parts concentrated HCl, HNO₃ and DI H₂O were added to sample for leaching in a heating block of the hot water bath. Samples were made up to volume with dilute HCl before filtered. Samples were analyzed by ICP/MS (ICP/MS-Perkin-Elmer ELAN 9000) for the evaluation of Hf, Ta, Nb, Li, Sr, Bi, Y, Sc, Ce, and Ga.

2.2. Pollution Status

Terrigenous or anthropogenic origin of elements in lichen species were evaluated by the calculated enrichment factor (EF) [29]. Enrichment factors for different lichen species were calculated by:

$$EF = \frac{[E_{lichen}/Al_{lichen}]}{[E_{crust}/Al_{crust}]} \quad (1)$$

where EF: enrichment factor, E_{lichen}: element value in lichen (mg/kg), Al_{lichen}: Al value in lichen (mg/kg), E_{crust}: element value in the Earth's crust (mg/kg) Al_{crust}: Al value in the Earth's crust (mg/kg).

Degree of contamination in Artvin (Murgul) region were evaluated by the calculated contamination factor (CF) [34]. Contamination factors were calculated by:

$$CF = C_i/C_b \quad (2)$$

where CF: contamination factor, C_i : element value in lichen (mg/kg), C_b : element value in control area (mg/kg). In this study, eastern Alps and northern Apennines were chosen as control [35] (for all elements, except elements Ta and Ga which do not exist in their study). Ta and Ga values were taken from Markert [36].

Pollution load index (PLI) indicating how much the sample exceeds metal concentrations of natural environments and also giving an indication of overall toxicity status for the sample is defined as the n th root of multiplication of CFs [37]. PLI was calculated by:

$$PLI = (CF_1 \times CF_2 \times CF_3 \times \dots \times CF_n)^{1/n} \quad (3)$$

where, CF_1 is the CF of the first element, CF_2 is the CF of the second element value, CF_3 is the CF of the third element value, CF_n is the CF of the n th element in the lichens species.

3. Results and Discussion

3.1. Accumulation by *Lobaria pulmonaria*

Strategically important elements accumulated by *Lobaria pulmonaria* are given in Figure 1.

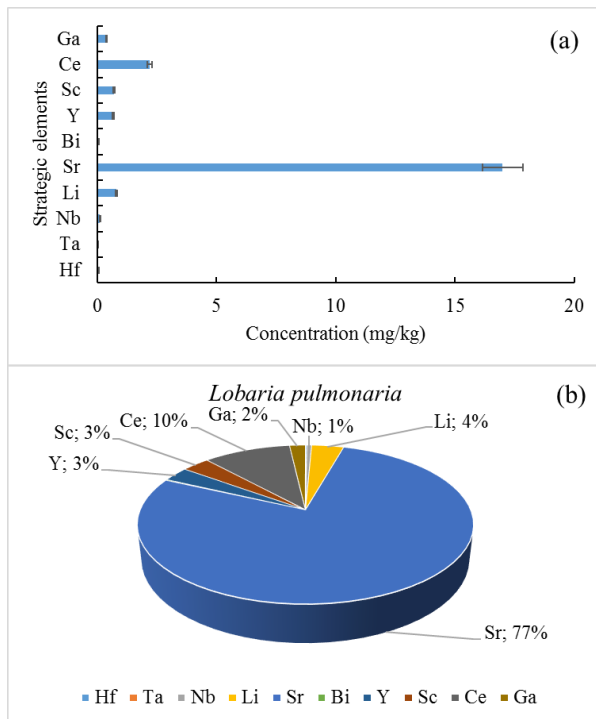


Figure 1. Strategically important elements accumulated by *Lobaria pulmonaria*

Figure 1(a) shows that the highest element concentration was 17 ± 0.8 mg/kg for Sr. In the literature, Rivera et al. [38] reported Sr concentration as $9 \mu\text{g/g}$ in lichen *Himantormia lugubris*. In our study, the lowest element concentration was 0.006 ± 0.001 mg/kg for Ta. Rivera et al. [38] reported Ta concentration as $0.00275 \mu\text{g/g}$ in lichen *Himantormia lugubris*. Parviainen et al. [28] reported Sr concentration of 14 mg/kg in lichens from Spain. Reported highest Sr concentration by Kousehlar and Widom [26] was 354.67 ppm in the lichens from Middletown, southwest Ohio. In our study, Hf, Bi, Nb, Ga, Y, Sc, Li, and Ce concentrations in *Lobaria pulmonaria* were 0.031 ± 0.001 , 0.04 ± 0.002 , 0.12 ± 0.006 , 0.4 ± 0.02 , 0.657 ± 0.03 , 0.7 ± 0.03 , 0.81 ± 0.04 , and $2.2 \pm 0.1 \text{ mg/kg}$, respectively. Rivera et al. [38] reported Hf and Sc concentrations as 0.0377 and $0.319 \mu\text{g/g}$ in lichen *Himantormia lugubris*, respectively. Parviainen et al. [28] reported Ce concentration of 3.8 mg/kg in lichens from Spain. Reported highest Ce and Ga concentration by Kousehlar and Widom [26] was 150.42 and 9.66 ppm in the lichens from Middletown, southwest Ohio, respectively. In our study, the strategic elements in *Lobaria pulmonaria* were $\text{Sr} > \text{Ce} > \text{Li} > \text{Sc} > \text{Y} > \text{Ga} > \text{Nb} > \text{Bi} > \text{Hf} > \text{Ta}$.

Considering these values, it can be said that the best accumulation by *Lobaria pulmonaria* is for Sr. The distribution percentages of the strategic elements accumulated by *Lobaria pulmonaria* are given in Figure 1(b). According to Figure 1(b), the highest element value was 77% for Sr, while the lowest element value 0.027% for Ta. Also, Bi and Hf values in *Lobaria pulmonaria* were below 1%. Y, Sc, Ce, Ga, Nb, and Li values were 3%, 3%, 10%, 2%, 1%, and 4%, respectively.

3.2. Accumulation by *Cladonia furcata*

Strategically important elements accumulated by *Cladonia furcata* are given in Figure 2.

According to Figure 2(a), the highest element concentration was $20 \pm 1.0 \text{ mg/kg}$ for Sr, while the lowest element concentration was $0.006 \pm 0.001 \text{ mg/kg}$ for Ta. In the literature, Rivera et al. [38] reported Sr and Ta concentrations as 36 and $0.0115 \mu\text{g/g}$ in lichen *Physconia muscigena*. In our study, the Hf, Bi, Nb, Ga, Sc, Li, Y, and Ce concentrations in *Cladonia furcata* were 0.038 ± 0.001 , 0.06 ± 0.003 , 0.16 ± 0.008 , 0.6 ± 0.03 , 1.2 ± 0.06 , 1.53 ± 0.07 , 1.95 ± 0.09 , and $4.6 \pm 0.23 \text{ mg/kg}$ respectively.

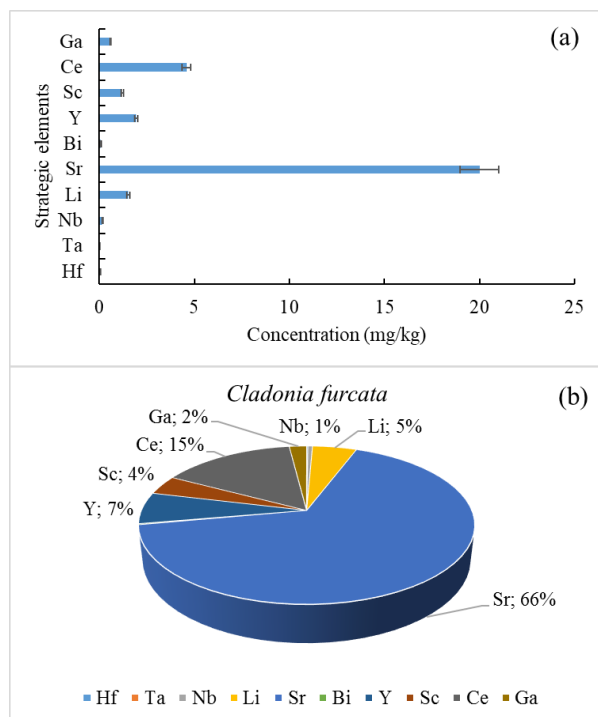


Figure 2. Strategically important elements accumulated by *Cladonia furcata*

Rivera et al. [38] reported Hf and Sc concentrations as 0.196 and 1.86 $\mu\text{g/g}$ in lichen *Physconia muscigena*. In our study, the strategic elements in *Cladonia furcata* were $\text{Sr} > \text{Ce} > \text{Y} > \text{Li} > \text{Sc} > \text{Ga} > \text{Nb} > \text{Bi} > \text{Hf} > \text{Ta}$. It can be said that the best accumulation by *Cladonia furcata* is for Sr. The distribution percentages of the strategic elements accumulated by *Cladonia furcata* are given in Figure 2(b). According to Figure 2(b), the highest element value was 66% for Sr, while the lowest element value 0.027% for Ta. Also, Bi and Hf values in *Cladonia furcata* were below 1%. Y, Sc, Ce, Ga, Nb, and Li values were 7%, 4%, 15%, 2%, 1%, and 5%, respectively.

3.3. Accumulation by *Usnea longissima*

Strategically important elements accumulated by *Usnea longissima* are given in Figure 3.

According to Figure 3(a), the highest element concentration was 26.8 ± 1.3 mg/kg for Sr, while the lowest element concentration was 0.006 ± 0.001 mg/kg for Ta. In the literature, Rivera et al. [38] reported Sr and Ta concentrations between 17 and 63 $\mu\text{g/g}$ and between <0.002 and 0.0044 $\mu\text{g/g}$ in lichen *Usnea antarctica*, respectively. Furthermore, the highest Sr and Ta concentrations in *Usnea aurantiacoatra* were reported as 51 and 0.0031 $\mu\text{g/g}$, respectively.

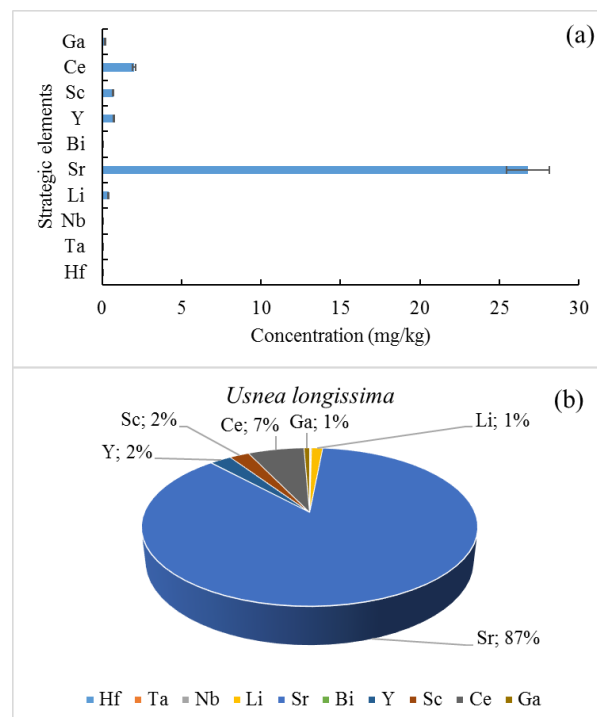


Figure 3. Strategically important elements accumulated by *Usnea longissima*

In the present study, Bi, Hf, Nb, Ga, Li, Sc, Y, and Ce concentrations in *Usnea longissima* were 0.02 ± 0.001 , 0.021 ± 0.001 , 0.04 ± 0.002 , 0.2 ± 0.01 , 0.4 ± 0.02 , 0.7 ± 0.03 , 0.757 ± 0.03 , and 2.0 ± 0.1 mg/kg respectively. In the literature, Rivera et al. [38] reported Hf and Sc concentrations between 0.0088 and 0.0447 $\mu\text{g/g}$ and between 0.158 and 1.051 $\mu\text{g/g}$ in lichen *Usnea antarctica*, respectively. Furthermore, the highest Hf and Sc concentrations in *Usnea aurantiacoatra* were reported as 0.0278 $\mu\text{g/g}$ and 0.576 $\mu\text{g/g}$, respectively. In the present study, the strategic elements in *Usnea longissima* were $\text{Sr} > \text{Ce} > \text{Y} > \text{Sc} > \text{Li} > \text{Ga} > \text{Nb} > \text{Hf} > \text{Bi} > \text{Ta}$. It can be said that the best accumulation by *Usnea longissima* is for Sr. The distribution percentages of the strategic elements accumulated by *Usnea longissima* are given in Figure 3(b). According to Figure 3(b), the highest element value was 87% for Sr, while the lowest element value 0.027% for Ta. Also, Bi, Nb, and Hf values in *Usnea longissima* were below 1%. Y, Sc, Ce, Ga, and Li values were 2%, 2%, 7%, 1%, and 1%, respectively.

3.4. Accumulation by *Xanthoparmelia somloensis*

Strategically important elements accumulated by *Xanthoparmelia somloensis* are given in Figure 4.

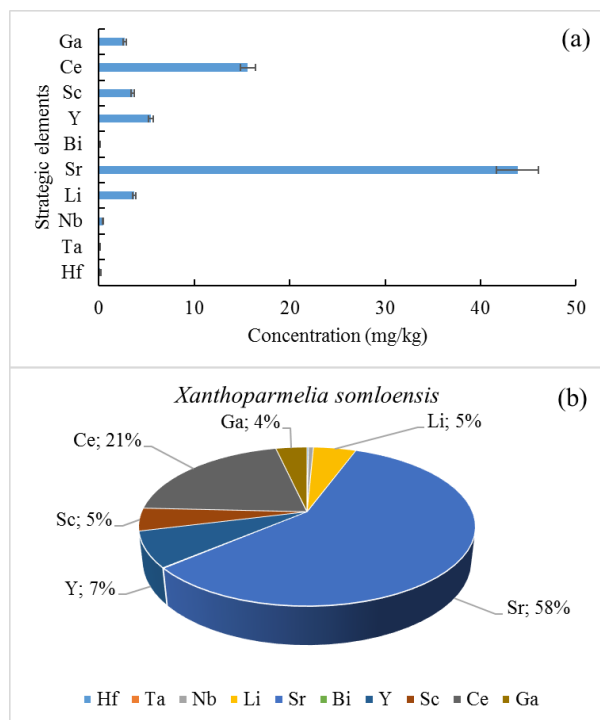


Figure 4. Strategically important elements accumulated by *Xanthoparmelia somloensis*

According to Figure 4(a), the highest element concentration was 43.9 ± 2.1 mg/kg for strontium, while the lowest element concentration was 0.002 ± 0.001 mg/kg for Ta. In the literature, Rivera et al. [38] reported Sr and Ta concentrations as 304 and $0.0655 \mu\text{g/g}$ in lichen *Rhizoplaca aspidophora*, respectively. In our study, the bismuth, hafnium, niobium, gallium, scandium, lithium, yttrium, and cesium concentrations in *Xanthoparmelia somloensis* were 0.08 ± 0.004 , 0.126 ± 0.006 , 0.43 ± 0.02 , 2.7 ± 0.13 , 3.5 ± 0.17 , 3.7 ± 0.18 , 5.457 ± 0.27 , and 15.6 ± 0.7 mg/kg respectively. Rivera et al. [38] reported Hf and Sc as 0.933 and $14 \mu\text{g/g}$ in lichen *Rhizoplaca aspidophora*, respectively. In our study, the strategic elements in *Xanthoparmelia somloensis* were $\text{Sr} > \text{Ce} > \text{Y} > \text{Li} > \text{Sc} > \text{Ga} > \text{Nb} > \text{Hf} > \text{Bi} > \text{Ta}$. It can be said that the best accumulation by *Xanthoparmelia somloensis* is for Sr. The distribution percentages of the strategic elements accumulated by *Xanthoparmelia somloensis* are given in Figure 4(b). According to Figure 4(b), the highest element value was 58% for Sr, while the lowest element value 0.0026% for Ta. Also, Bi and Nb values in *Xanthoparmelia somloensis* were below 1%. Y, Sc, Ce, Ga, and Li values were 7%, 5%, 21%, 4%, and 5%, respectively.

3.5. Accumulation by *Flavoparmelia caperata*

Strategically important elements accumulated by *Flavoparmelia caperata* were given in Figure 5.

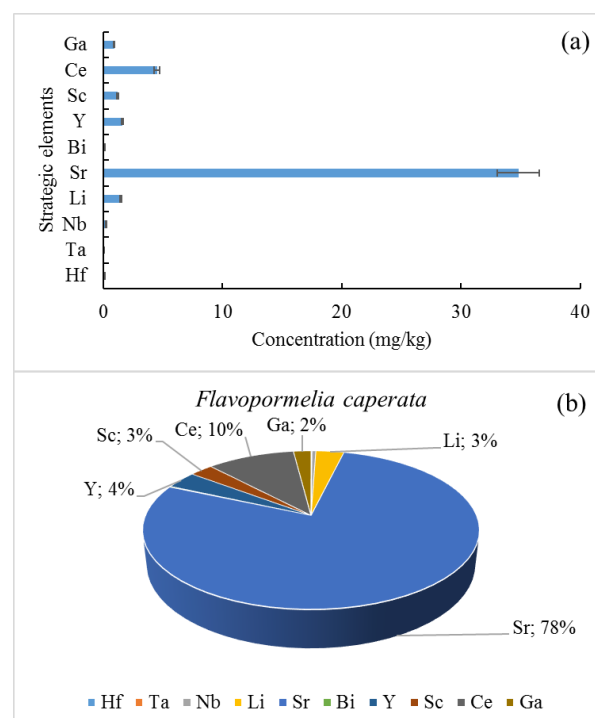


Figure 5. Strategically important elements accumulated by *Flavoparmelia caperata*

According to Fig. 5(a), the highest element concentration was 34.8 ± 1.7 mg/kg for Sr, while the lowest element concentration was 0.004 ± 0.002 mg/kg for Ta. In the literature, Rivera et al. [38] reported Sr and Ta concentrations as 57 and $0.0157 \mu\text{g/g}$ in lichen *Sphaerophorus globosus*, respectively. In our study, the Hf, Bi, Nb, Ga, Sc, Li, Y, and Ce concentrations in *Flavoparmelia caperata* were 0.045 ± 0.002 , 0.08 ± 0.004 , 0.2 ± 0.01 , 0.9 ± 0.04 , 1.2 ± 0.06 , 1.44 ± 0.07 , 1.595 ± 0.08 , and 4.5 ± 0.22 mg/kg respectively. Rivera et al. [38] reported Hf and Sc concentrations as 0.209 and $1.64 \mu\text{g/g}$ in lichen *Sphaerophorus globosus*, respectively. In our study, the strategic elements in *Flavoparmelia caperata* were $\text{Sr} > \text{Ce} > \text{Y} > \text{Li} > \text{Sc} > \text{Ga} > \text{Nb} > \text{Bi} > \text{Hf} > \text{Ta}$. It can be said that the best accumulation by *Flavoparmelia caperata* is for Sr. The distribution percentages of the strategic elements accumulated by *Flavoparmelia caperata* are given in Fig. 5(b). The highest element value was 78% for Sr, while the lowest element value 0.0089% for Ta. Also, Bi and Nb values in *Flavoparmelia caperata* were below 1%. Y, Sc, Ce, Ga, and Li values were 4%, 3%, 10%, 2%, and 3%, respectively.

The highest Hf concentration was 0.126 ± 0.006 mg/kg for *Xanthoparmelia*

somloensis, while the lowest Hf concentration was 0.021 ± 0.001 mg/kg for *Usnea longissima*. The Hf concentrations for *L. pulmonaria*, *C. furcata*, and *F. caperata* were 0.031 ± 0.001 , 0.038 ± 0.001 , and 0.1 ± 0.005 mg/kg, respectively. The Hf values of lichen species were *Xanthoparmelia somloensis* > *Flavoparmelia caperata* > *Cladonia furcata* > *Lobaria pulmonaria* > *Usnea longissima*. It was determined that Hf, one of the strategic elements, was well accumulated by *Xanthoparmelia somloensis*. The highest Ta concentration was 0.006 ± 0.001 mg/kg for *L. pulmonaria*, *C. furcata*, and *U. longissima* while the lowest Ta concentration was 0.002 ± 0.001 mg/kg for *Xanthoparmelia somloensis*. Ta values of lichens were *L. pulmonaria* = *C. furcata* = *U. longissima* > *F. caperata* > *X. somloensis*. The best Ta accumulation was determined for *L. pulmonaria*, *C. furcata*, and *U. longissima*. The highest Nb value was 0.43 ± 0.02 mg/kg for *Xanthoparmelia somloensis*, while the lowest Nb value was 0.04 ± 0.002 mg/kg for *Usnea longissima*. The Nb concentrations for *L. pulmonaria*, *C. furcata*, and *U. longissima* were 0.12 ± 0.006 , 0.16 ± 0.008 and 0.20 ± 0.01 mg/kg, respectively. The niobium values of lichen species were *Xanthoparmelia somloensis* > *Flavoparmelia caperata* > *Cladonia furcata* > *Lobaria pulmonaria* > *Usnea longissima*. The best Nb accumulation was determined for *Xanthoparmelia somloensis*. The highest Li concentration was 3.7 ± 0.18 mg/kg for *Xanthoparmelia somloensis*, while the lowest Li concentration was 0.4 ± 0.02 mg/kg for *Usnea longissima*. The Li concentrations for *L. pulmonaria*, *C. furcata*, and *U. longissima* were 0.81 ± 0.04 , 1.53 ± 0.07 , and 1.44 ± 0.07 mg/kg, respectively. The Li values of lichen species were *Xanthoparmelia somloensis* > *Cladonia furcata* > *Flavoparmelia caperata* > *Lobaria pulmonaria* > *Usnea longissima*. The best Li accumulation was determined for *Xanthoparmelia somloensis*. The highest Sr concentration was 43.9 ± 2.1 mg/kg for *X. somloensis*, while the lowest Sr concentration was 17 ± 0.8 mg/kg for *Lobaria pulmonaria*. The Sr concentrations for *Cladonia furcata*, *Usnea longissima*, and *Flavoparmelia caperata* were 20 ± 1.0 , 26.8 ± 1.3 , and 34.8 ± 1.7 mg/kg, respectively. The Sr values of lichen species were *Xanthoparmelia somloensis* > *Flavoparmelia caperata* > *Usnea longissima* > *Cladonia furcata* > *Lobaria pulmonaria*. The best Sr accumulation was determined as *Xanthoparmelia somloensis*. The highest Bi concentration was 0.08 ± 0.004 mg/kg for, *Xanthoparmelia somloensis* and

Flavoparmelia caperata, while the lowest Bi concentration was 0.02 ± 0.001 mg/kg for *Usnea longissima*. The Bi concentrations for *Lobaria pulmonaria* and *Cladonia furcata* were 0.04 ± 0.002 and 0.06 ± 0.003 mg/kg, respectively. The Bi values of lichen species were *Xanthoparmelia somloensis* = *Flavoparmelia caperata* > *Cladonia furcata* > *Lobaria pulmonaria* > *Usnea longissima*. The best Bi accumulation was determined as *Xanthoparmelia somloensis* and *Flavoparmelia caperata*. The highest Y concentration was 5.457 ± 0.27 mg/kg for *Xanthoparmelia somloensis*, while the lowest Y concentration was 0.657 ± 0.03 mg/kg for *Lobaria pulmonaria*. The Y concentrations for *C. furcata*, *U. longissima*, and *F. caperata* were 1.95 ± 0.09 , 0.757 ± 0.03 , and 1.595 ± 0.08 mg/kg, respectively. The Y values of lichen species were *Xanthoparmelia somloensis* > *Cladonia furcata* > *Flavoparmelia caperata* > *Usnea longissima* > *Lobaria pulmonaria*. The best Y accumulation was determined as *Xanthoparmelia somloensis*. The highest Sc concentration was 3.5 ± 0.17 mg/kg for *Xanthoparmelia somloensis*, while the lowest Sc concentration was 0.4 ± 0.02 mg/kg for *L. pulmonaria* and *U. longissima*. The Sc concentrations for *C. furcata* and *F. caperata* were 1.2 ± 0.06 . The Sc values of lichen species were *Xanthoparmelia somloensis* > *Cladonia furcata* = *Flavoparmelia caperata* > *Usnea longissima* = *Lobaria pulmonaria*. The best Sc accumulation was determined for *Xanthoparmelia somloensis*. The highest Ce concentration was 15.6 ± 0.7 mg/kg for *Xanthoparmelia somloensis*, while the lowest Ce concentration was 2.0 ± 0.1 mg/kg for *Usnea longissima*. The Ce concentrations for *L. pulmonaria*, *C. furcata*, and *F. caperata* were 2.2 ± 0.1 , 4.6 ± 0.23 , and 4.5 ± 0.22 mg/kg, respectively. The Ce values of lichen species were *Xanthoparmelia somloensis* > *Cladonia furcata* > *Flavoparmelia caperata* > *Lobaria pulmonaria* > *Usnea longissima*. The best Ce accumulation was determined as *Xanthoparmelia somloensis*. The highest Ga concentration was 2.71 ± 0.13 mg/kg for *Xanthoparmelia somloensis*, while the lowest Ga concentration was 0.2 ± 0.01 mg/kg for *Usnea longissima*. The Ga concentrations for *L. pulmonaria*, *C. furcata*, and *F. caperata* were 0.4 ± 0.02 , 0.6 ± 0.03 , and 0.9 ± 0.04 mg/kg, respectively. The Ga values of lichen species were *Xanthoparmelia somloensis* > *Cladonia furcata* > *Flavoparmelia caperata* > *Lobaria pulmonaria* > *Usnea longissima*. The best Ga accumulation was determined for *Xanthoparmelia somloensis*.

3.7. Assessment of pollution status

In this study, after the accumulation values of strategically important elements in different

lichens were determined, pollution status values were calculated. In this context, the enrichment factors are given in Table 1.

Table 1. Enrichment factors calculated for different lichen species

Lichens	Value									
<i>Lobaria pulmonaria</i>	0.27	0.30	0.50	2.04	2.44	15.83	1.50	2.59	1.73	1.18
<i>Cladonia furcata</i>	0.33	0.30	0.67	3.84	2.87	23.74	4.45	4.43	3.61	1.77
<i>Usnea longissima</i>	0.18	0.30	0.17	1.01	3.85	7.91	1.73	2.59	1.57	0.59
<i>Xanthoparmelia somloensis</i>	1.09	0.10	1.80	9.30	6.30	31.65	12.46	12.93	12.25	7.98
<i>Flavopormelia caperata</i>	0.39	0.20	0.84	3.62	5.00	31.65	3.64	4.43	3.53	2.66

When Table 1 was examined, the highest EF value in *Lobaria pulmonaria* was 15.83 for Bi, while the lowest was 0.27 for Hf. Maximum EF value in *Cladonia furcata* was 23.74 for Bi, while the lowest was 0.30 for Ta. Maximum EF value in *Usnea longissima* was 7.91 for Bi, while the lowest value was 0.17 for Nb. Maximum EF value in *Xanthoparmelia somloensis* was 31.65 for Bi, while the lowest value was 0.10 for Ta. The highest EF value in *Flavopormelia caperata* was 31.65 for Bi, while the lowest value was 0.20 for Ta. Enrichment factors lower than 10 are considered as

terrigenous and enrichment factors higher than 10 are considered to be impacted by anthropogenic activities [29]. According to Table 1, enrichment factors for *L.pulmonaria*, *C.furcata*, and *F.caperata* were higher than 10, only for Bi. Enrichment factors for *U.longissima* were lower than 10. Enrichment factors for *X.somloensis* were higher than 10 (Bi:31.65, Y:12.46, Sc:12.93, and Ce:12.25).

The contamination factors are given in Figure 6.

Lichen species

<i>Lobaria pulmonaria</i>	0.86	6.00	4.62	3.77	1.22	1.25	1.81	2.16	3.28	4.00
<i>Cladonia furcata</i>	0.04	0.00	0.03	0.41	16.35	0.05	1.08	0.56	1.40	0.15
<i>Usnea longissima</i>	0.48	6.00	1.15	0.98	1.64	0.42	0.70	1.26	1.43	1.33
<i>Xanthoparmelia somloensis</i>	0.26	0.00	0.37	3.76	26.79	0.19	7.77	2.78	10.93	2.03
<i>Flavopormelia caperata</i>	0.17	12.00	0.54	0.38	1.30	0.42	0.21	0.43	0.41	0.44

Value	Category	Value	Category	Value	Category
Cf<1.0	C1	1.0-2.0	C2	2.0-3.5	C3
3.5-8.0	C4	8.0-27.0	C5	>27.0	C6

Figure 6. The contamination factors

There are six categories corresponding to CF values [39]: Category 1 (C1) contamination factor < 1 no contamination; Category 2 (C2) 1 < contamination factor < 2 suspected contamination; Category 3 (C3) 2 < contamination factor < 3.5 slight contamination; Category 4 (C4) 3.5 < contamination factor < 8 moderate contamination; Category 5 (C5) 8 < contamination factor < 27 severe contamination;

Category 6 (C6) contamination factor > 27 extreme contamination. The highest CF value was determined for Ta (C4) in *Lobaria pulmonaria* while Nb (C4), Ga (C4), and Li (C4) followed it. These results indicated moderate contamination. The elements that indicated slight contamination were Ce (C3) and Sc (C3) while Y (C2), Bi (C2), and Sr (C2) indicated suspected contamination. Hf (C1) indicated no contamination.

CFs were calculated at the C4 category for three elements, C3 category for two elements, C2 category for three elements, and C1 category for one element. The highest CF value was determined for Sr (C5) in *Cladonia furcata* indicating severe contamination. As a result, it can be said that the source of Sr in the lichen *Cladonia furcata* is probably anthropogenic emissions. Ce and Y were at C2 category indicating suspected contamination. Sc (C1), Li (C1), Ga (C1), Bi (C1), Hf (C1), Nb (C1), and Ta (C1) indicated no contamination. CFs were calculated at the C1 category for seven elements, C2 category for two elements, and C5 category for one element. Most of the CFs were classified as C1. The highest CF value was determined for Ta (C4) in *Usnea longissima* indicating moderate contamination. Sr, Ce, Ga, Sc and Nb were at C2 category indicating suspected contamination. Li (C1), Y (C1), Hf (C1), and Bi (C1) indicated no contamination. CFs were calculated at the C1 category for four elements, C2 category for five elements, and C4 category for one element. The highest CF value was determined for Sr (C5) in *Xanthoparmelia somloensis* and Ce (C5) followed it. These results indicated severe contamination. Y and Li were at C4 category indicating moderate contamination. Sc and Ga were at C3 category indicating slight contamination. Nb (C1), Hf (C1), Bi (C1), and Ta (C1) indicated no contamination. CFs were calculated at the C5, C4, and C3 categories for two elements, C1 category for one element. As a result, it can be said that the source of Sr and Ce in the lichen *Xanthoparmelia somloensis* is probably anthropogenic emissions. The highest CF value was determined for Ta (C5) in *Flavopormelia caperata* indicating severe contamination. As a result, it can be said that the source of Ta in the lichen *Flavopormelia caperata* is probably anthropogenic emissions. Sr was at C2 category indicating suspected contamination. Nb (C1), Ga (C1), Sc (C1), Bi (C1), Ce (C1), Li (C1), Y (C1), and Hf (C1) indicated no contamination. CFs were calculated at the C1 category for eight elements, C5 and C2 category for one element. Most of the CFs were classified as C1.

As a result, the highest contamination factors in lichens investigated were determined for strontium and tantalum. Biological behaviours of Sr resemble those of calcium because of chemical similarity of them. The close relationship between calcium and strontium has been proven in studies with various plant systems, algae and yeasts. It has been shown that strontium may substitute for calcium in binding processes at biological cell surfaces as well as in active uptake via divalent cation transport systems [40]. Therefore, it is not surprising the high value of

Sr in lichen species. Near to the studied region, the copper flotation wastes from a mine are stored in the empty pit mine, the ore of which is finished. It is known that high concentrations of strontium are detected in drinking water in the area close to where these wastes are stored. Strontium is probably dispersed by atmospheric transport to near region of these flotation waste deposits and is subsequently deposited in lichens. The transportation and redeposition on Earth by dry or wet deposition of Sr released into the air from various activities is reported by WHO [41]. Main sources of Ta in the environment are geologic, mostly as a result of rock weathering, but a potential anthropogenic source of it is from coal combustion [42,43]. As a result of combustion of coal may caused high Ta in lichens investigated. Maximum contamination factors of Hf, Nb, Li, Ga, and Bi were for *L. pulmonaria* and maximum contamination factors of Sr, Y, Sc, and Ce were calculated for *X.somloensis*. Additionally, maximum contamination factor of Ta was calculated for *F.caperata*.

In this study, pollution load index (PLI) values were calculated within the scope of this study. PLI lower than 1 indicates that elemental load is near the background level, and higher than 1 indicates the extent of pollution. PLI indicates how much a sample exceeds the metal concentrations of natural environments and give an indication of the overall toxicity status for a sample [37]. According to obtained data, PLI values for *L.pulmonaria* and *U.longissima* were higher than 1. PLIs for *Lobaria pulmonaria* and *Usnea longissima* were 2.43 and 1.14, respectively. PLI values for *C.furcata*, *X.somloensis*, and *F.caperata* were 0.19, 0.89, and 0.57, respectively.

4. Conclusion and Suggestions

In this study, we identified *L.pulmonaria*, *C.furcata*, *U.longissima*, *X.somloensis*, and *F.caperata* lichens. The highest strategically important element accumulated by *Lobaria pulmonaria* (17 ± 0.8 mg/kg), *Cladonia furcata* (20 ± 1.0 mg/kg), *Usnea longissima* (26.8 ± 1.3 mg/kg), *Xanthoparmelia somloensis* (43.9 ± 2.1 mg/kg), and *Flavopormelia caperata* (34.8 ± 1.7 mg/kg) was determined as Sr. The best Sr accumulation was by *Xanthoparmelia somloensis*. Among the strategically important elements accumulated by lichens, the highest Sr percentage was found to be 78% in *Flavopormelia caperata*. The lowest strategic element accumulated by lichen species was determined as Ta. The lowest Ta

accumulation was determined as 0.002 ± 0.001 mg/kg for *Xanthoparmelia somloensis*. Maximum CF values were for Sr and Ta. Maximum CF values of Hf, Nb, Li, Ga, and Bi were for *L. pulmonaria* and maximum CF values of Sr, Y, Sc, and Ce were for *X. somloensis*. The maximum CF value of Ta was for *F. caperata*. In general, EF values were higher than 10. The PLIs for *L. pulmonaria* and *U. longissima* were greater than 1. As a result, lichens can be used as biomonitors of air pollutants.

There is no conflict of interest between the authors.

Statement of Research and Publication Ethics

The study is complied with research and publication ethics.

Conflict of Interest Statement

References

- [1] Y. Wang and Zhao, J, "Advances in Energy, Environment and Materials Science: Proceedings of the International Conference on Energy, Environment and Materials Science (EEMS 2015)", Guangzhou, PR China, August 25–26, 2015, CRC Press.
- [2] N. Maslamani, S. B. Khan, E. Y. Danish, E. M. Bakhsh, S. M. Zakeeruddin, and A. M. Asiri, "Carboxymethyl cellulose nanocomposite beads as super-efficient catalyst for the reduction of organic and inorganic pollutants", *International Journal of Biological Macromolecules*, vol. 167, pp. 101-116, 2021.
- [3] A. R. Bagheri, N. Aramesh, F. Sher, and M. Bilal, "Covalent organic frameworks as robust materials for mitigation of environmental pollutants", *Chemosphere*, vol. 270, 129523, 2021.
- [4] J. Rockström, W. Steffen, K. Noone, A. Persson, F. S. Chapin III, E. Lambin, and Foley, J, "Planetary boundaries: exploring the safe operating space for humanity", *Ecol. Soc.*, vol. 14, pp. 32, 2009.
- [5] E. F. Kean, R. F. Shore, G. Scholey, R. Strachan, and E. A. Chadwick, "Persistent pollutants exceed toxic thresholds in a freshwater top predator decades after legislative control", *Environmental Pollution*, vol. 272, 116415, 2021.
- [6] N. Kircheva and T. Dudev. "Competition between abiogenic and biogenic metal cations in biological systems: Mechanisms of gallium's anticancer and antibacterial effect", *Journal of Inorganic Biochemistry*, vol. 214, p.111309, 2021.
- [7] H. Asadian and A. Ahmadi, "The extraction of gallium from chloride solutions by emulsion liquid membrane: Optimization through response surface methodology", *Minerals Engineering*, vol. 148, no. 106207, p. 106207, 2020.
- [8] X. Wen, Q. Bao, L. Guo, and Z. Guo, "The introduction of super-gravity into optimization separation of bismuth and zinc from crude bismuth melt", *Chemical Engineering and Processing - Process Intensification*, vol. 160, 108266, 2021.
- [9] A. Shikika, M. Sethurajan, F. Muvundja, M. C. Mugumaoderha, and St. Gaydardzhiev, "A review on extractive metallurgy of tantalum and niobium", *Hydrometallurgy*, vol. 198, 105496, 2020.
- [10] WEF, 2019, World Economic Forum, A vision for a sustainable battery value chain in 2030. Unlocking the full potential to power sustainable development and climate change mitigation <https://www.weforum.org/reports/a-vision-for-a-sustainable-battery-value-chain-in-2030>
- [11] R. Millot and P. Négrel, "Lithium isotopes in the Loire River Basin (France): Hydrogeochemical characterizations at two complementary scales", *Applied Geochemistry*, vol. 125, 104831, 2021.
- [12] D. A. Yancheshmeh, M. Esmailian, and K. Shirvani, "Microstructural and oxidation behavior of NiCrAl super alloy containing hafnium at high temperature", *International Journal of Hydrogen Energy*, vol. 43, pp. 5365-5373, 2018.
- [13] M. Musgrove, "The occurrence and distribution of strontium in U.S. groundwater", *Applied Geochemistry*, vol. 126, 104867, 2021.
- [14] Y. Yang, T. Liu, L. Bi, and L. Deng, "Recent advances in development of magnetic garnet thin films for applications in spintronics and photonics", *Journal of Alloys and Compounds*, vol. 860, 158235, 2021.

- [15] X. Cheng, Y. Qu, C. Kang, M. Kang, R. Dong, and J. Zhao, Development of new medical Mg-Zn-Ca-Y alloy and in-vitro and in-vivo evaluations of its biological characteristics, *Materials Today Communications*, vol. 26, 102002, 2021.
- [16] V. Gonzalez, D. A. L. Vignati, M. N. Pons, E. Montarges-Pelletier, C. Bojic, and L. Giamberini, "Lanthanide ecotoxicity: First attempt to measure environmental risk for aquatic organisms", *Environ. Pollut.*, vol. 199, pp. 139-147, 2015.
- [17] J. Liu, L. Zeng, S. Liao, X. Liao, J. Liu, J. Mao, Y. Chen, T. Qiu, and S. Ren, "Highly efficient enrichment and adsorption of rare earth ions (yttrium(III)) by recyclable magnetic nitrogen functionalized mesoporous expanded perlite", *Chinese Chemical Letters*, vol. 31, pp. 2849-2853, 2021.
- [18] M. Kurian, "Cerium oxide based materials for water treatment – A review", *Journal of Environmental Chemical Engineering*, vol. 8, 104439, 2020.
- [19] W. F. Zhu, S. Q. Xu, P. Shao, H. Zhang, D. Wu, W. Yang, J. Feng, and L. Feng, "Investigation on liver function among population in high background of rare earth area in South China", *Biological Trace Element Research*, vol. 104, pp. 1-8, 2005.
- [20] Z. M. Migaszewski and A. Gałuszka, "The Characteristics, Occurrence, and Geochemical Behavior of Rare Earth Elements in the Environment: A Review", *Critical Reviews in Environmental Science and Technology*, vol. 45, pp. 429-471, 2015.
- [21] E. M. Peters, M. Svärd, and K. Forsberg, "Phase equilibria of ammonium scandium fluoride phases in aqueous alcohol mixtures for metal recovery by anti-solvent crystallization", *Separation and Purification Technology*, vol. 252, 117449, 2020.
- [22] M. Topal, E. I. Arslan Topal, E. Öbek, and A. Aslan, "Potential human health risks of toxic/harmful elements by consumption of *Pseudevernia furfuracea*", *International Journal of Environmental Health Research*, vol. 32, pp. 1889-1896, 2022.
- [23] B. Emsen, G. Sadi, A. Bostanci, N. Gursoy, A. Emsen, and A., Aslan, "Evaluation of the biological activities of olivetoric acid, a lichen-derived molecule, in human hepatocellular carcinoma cells" *Rend. Fis. Acc. Lincei*, vol. 32, pp. 135–148, 2021.
- [24] E. Sahin, S. Dabagoglu Psav, I. Avan, M. Candan, V. Sahinturk, and A. Tansu Koparal, "Lichen-derived physodic acid exerts cytotoxic and anti-invasive effects in human lung cancer", *Rend. Fis. Acc. Lincei*, vol. 32, pp. 511–520, 2021.
- [25] B. Çolak, D. Cansaran-Duman, G. Guney Eskiler, K. Földes, and S. Yangın, "Usnic acid-induced programmed cell death in ovarian cancer cells", *Rend. Fis. Acc. Lincei*, vol. 33, pp. 143–152, 2022.
- [26] M. Kousehlar and E. Widom, "Identifying the sources of air pollution in an urban-industrial setting by lichen biomonitoring - A multi-tracer approach", *Applied Geochemistry*, vol. 121, 104695, 2020.
- [27] T. Contardo, A. Vannini, K. Sharma, P. Giordani, and S. Loppi, "Disentangling sources of trace element air pollution in complex urban areas by lichen biomonitoring. A case study in Milan (Italy)", *Chemosphere*, vol. 256, 127155, 2020.
- [28] A. Parviainen, M. Casares-Porcel, C. Marchesi, and C. J. Garrido, "Lichens as a spatial record of metal air pollution in the industrialized city of Huelva (SW Spain)", *Environmental Pollution*, vol. 253, pp. 918-929, 2019.
- [29] A. Parviainen, E. M. Papaslioti, M. Casares-Porcel, and C. J. Garrido, "Antimony as a tracer of non-exhaust traffic emissions in air pollution in Granada (S Spain) using lichen bioindicators", *Environmental Pollution*, vol. 263, Part A, 114482, 2020.
- [30] M. E. Conti, and G. Cecchetti, "Biological monitoring: lichens as bioindicators of air pollution assessmentda review", *Environmental Pollution*, vol. 114, pp. 471-492, 2001.
- [31] G. Brunialti and L. Frati, "Bioaccumulation with lichens: the Italian experience", *Int. J. Environ. Stud.*, vol. 71, pp. 15-26, 2014.
- [32] M. E. Hale, "How to Know the Lichens", Wm. C. Brown Company Publishers, Dubuque, Iowa, p. 246, 1979.
- [33] Y. Gauslaa, T. Goward, and T. Pypker, "Canopy settings shape elemental composition of the epiphytic lichen *Lobaria pulmonaria* in unmanaged conifer forests", *Ecological Indicators*, vol. 113, 106294, 2020.
- [34] Y. Koroleva and V. Revunkov, "Air Pollution Monitoring in the South-East Baltic Using the Epiphytic Lichen *Hypogymnia physodes*", *Atmosphere*, vol. 8, pp. 119, 2007.

- [35] E. Cecconi, G. Incerti, F. Capozzi, P. Adamo, R. Bargagli, R. Benesperi, F. Candotto Carniel, S. E. Favero-Longo, S. Giordano, D. Puntillo, S. Ravera, V. Spagnuolo, and M. Tretiach, "Background element content of the lichen *Pseudevernia furfuracea*: a supra-national state of art implemented by novel field data from Italy", *Science of the Total Environment*, vol. 622, pp. 282–292, 2018.
- [36] B. Markert, "Establishing of Reference Plant for Inorganic Characterization of Different Plant Species By Chemical Fingerprinting", *Water Air Soil Pollution*, vol. 64, pp. 533-538, 1992.
- [37] H. Salo, M. S. Bućko, E. Vaahtovuori, J. Limo, J. Mäkinen, and L. J. Pesonen, "Biomonitoring of air pollution in SW Finland by magnetic and chemical measurements of moss bags and lichens", *J. Geochem. Explor.*, vol. 115, pp. 69–81, 2012.
- [38] M. S. Rivera, S. P. Catan, C. D. Fonzo, L. Dopchiz, M. A. Arribere, M. Ansaldo, M. I. Messuti, and D. F. Bubach, "Lichen as biomonitor of atmospheric elemental composition from Potter Peninsula, 25 de Mayo (King George) Island, Antarctica", *Ann Mar Sci.*, vol. 2, pp. 9-15, 2018.
- [39] A. Stojanowska J. Rybak M. Bożym, T. Olszowski, and J. S. Bihałowicz, "Spider Webs and Lichens as Bioindicators of Heavy Metals: A Comparison Study in the Vicinity of a Copper Smelter (Poland)", *Sustainability*, vol. 12, pp. 8066, 2020.
- [40] M. Anupama, K. Ashok Kumar, and J. Naveena Lavanya Latha, "Mechanism of strontium uptake and transport in *Neurospora crassa*", *European Journal of Pharmaceutical and Medical Research*, vol. 3, pp. 379-386, 2016.
- [41] WHO, Strontium and Strontium Compounds, Concise International Chemical Assessment Document 77, pp. 63, 2010.
- [42] K. K. Divine and P. L. Goering, Tantalum, chap. 21 of Merian, Ernest, Anke, Manfred, Ihnat, Milan, and Stoeppler, Markus, eds., *Elements and their compounds in the environment—Occurrence, analysis and biological relevance* (2d ed.): Weinheim, Germany, Wiley-VCH Verlag, GmbH, pp. 1087-1097, 2004..
- [43] P. L. Goering, and T. L. Ziegler, Niobium (Nb) (columbium), chap. 19 of Merian, Ernest, Anke, Manfred, Ihnat, Milan, and Stoeppler, Markus, eds., *Elements and their compounds in the environment—Occurrence, analysis and biological relevance* (2d ed.): Weinheim, Germany, WileyVCH Verlag GmbH, vol. 2, pp. 1039-1046, 2004.

Determination of MIC and MBC Values Using Different Extraction Methods in Plants of *Nigella Sativa*, *Cuminum Cyminum* and *Pimpinella Anisum L.* Samples from Kırıkkale Region

Eftal BÖKE^{1*}, Birgül KAÇMAZ², Aysun ERGENE³

¹Address (Kırıkkale University, Institute of Science, Department of Biology Kırıkkale, Turkey)

²Address (Kırıkkale University, department of infectious diseases and clinical microbiology Kırıkkale, Turkey)

³Address (Kırıkkale University, Faculty of Arts and Sciences, Department of Biology Kırıkkale, Turkey)

(ORCID: [0000-0002-7052-2790](https://orcid.org/0000-0002-7052-2790)) (ORCID: [0000-0002-5190-7249](https://orcid.org/0000-0002-5190-7249)) (ORCID: [0000-0003-4104-5697](https://orcid.org/0000-0003-4104-5697))



Keywords: *Nigella Sativa*, *Cuminum Cyminum*, *Pimpinella Anisum*, MIC, MBC, methanol

Abstract

The objective of our study was to investigate how 6 plant extracts derived from three plant species exhibit antimicrobial characteristics. The extraction process was conducted using methanol and employed both maceration and soxalet extraction methods. The liquid microdilution method was utilized to assess the ability of Black Cumin (*Nigella sativa*), Cumin (*Cuminum cuminum*), and Anise (*Pimpinella anisum*) cultivated in Kırıkkale province to combat *Staphylococcus aureus* (ATCC 25923) and *Escherichia coli* (ATCC 25922). All of the extracts of *Nigella sativa* (black cumin), *Cuminum cuminum* (Cuminum) and *Pimpinella anisum* (Anise) prepared by the maceration and soxalet extraction method showed antibacterial effects against both bacteria (inhibitory and bactericidal). it was determined that the antibacterial effect of the extracts obtained by the maceration method was higher than the extracts obtained by the soxalet extraction method.

1. Introduction

Herbal medicines have been employed for ages to treat different diseases. The practice of using plant extracts as medicine saw an increase in popularity during the late 1990s. Medicinal plants are important in the search for new drugs, especially in nations that are still developing [1]. There have been numerous efforts to discover new antimicrobial compounds from natural sources. As of recent, the issue of antibiotic-resistant organisms resulting from ineffective chemotherapy has become more prevalent. Stopping the spread of these organisms and enhancing treatment approaches is of utmost importance [2]. The search for more effective drugs and new targets for drug development is becoming increasingly imperative. Although there has been advancement in drug discovery through chemical

means such as molecular modeling, computational chemistry, and green synthesis, natural products have demonstrated the value of medicinal plants in terms of their potential to be used for human medicine [3]. A number of recent studies have shown that medicinal plants exhibit various pharmacological and biological properties [4]. Cultivation of medicinal and aromatic plants is a new alternative for producers in Kırıkkale Province. According to literature, three commonly grown plants in Kırıkkale province, namely Black Cumin (*Nigella sativa*), Cuminum (*Cuminum cuminum*), and Anise (*Pimpinella anisum*), have significant medicinal properties and have been traditionally used to treat various ailments throughout history [5-7]. The soil structure and climate of Kırıkkale province are very suitable for the continuous cultivation of these plants. These plants are used in traditional therapy, especially in liver

* Corresponding author: eftal_boke@hotmail.com

Received: 06.02.2023, Accepted: 06.08.2023

diseases, digestive system diseases such as diarrhea, as an appetite enhancer, analgesic and antibacterial. This research aimed to investigate the antimicrobial properties of plant samples in Kırıkkale region of Turkey, such as *Nigella sativa* (black cumin), *Cuminum cuminum* (cumin), and *Pimpinella anisum* (anise), taking into account the geographical conditions of the region.

2. Material and Method

2.1. Plant Examples

Nigella sativa (black cumin), *Cuminum cuminum* (cumin) and *Pimpinella anisum* (anise) plants grown in Keskin, Karakeçili and Delice districts of Kırıkkale province, respectively, were obtained from Kırıkkale Provincial Directorate of Food, Agriculture and Livestock. It was used in the study after species identification was made in Ankara University Faculty of Agriculture. The plants were cleansed using deionized water to get rid of any contaminants or dust and then air-dried in a shaded area at room temperature. The seeds, which are the most used part of the dried plants for consumption, were sieved after grinding with a grinding device and the powders with a particle size of 0.50–1.00 mm was used to obtain the plant extract.

2.2. Preparation of Plant Extracts

Plant extracts were obtained by using methanol as a solvent from seeds that were powdered by maceration method. For this purpose, 30 g of plant samples were weighed and 100 mL of methanol solvent was added and kept in a magnetic stirrer at a temperature suitable for the boiling point of the solvent for 24 hours. Plant extracts were obtained after filtration. In the Soxhlet extraction method, 30 g of the plant samples were weighed and 100 mL of solvent was added and they were kept in a Soxhlet device at a temperature suitable for the boiling point of the solvent. Plant extracts were obtained after filtration. Dry plant extracts were dissolved with 10% dimethylsulfoxide (DMSO) and sterilized with membrane filters (0.45 µm) and used for antimicrobial activity studies.

2.3. Evaluation of Antibacterial Activity

This study aimed to investigate the antibacterial activity of methanolic extracts obtained from the seeds of *Nigella sativa* (Black cumin), *Cuminum cuminum* (Cumin), and *Pimpinella anisum* (Anise)

using the liquid microdilution approach [8-9]. 100 mg of each extract was weighed and dissolved in 1000 µL of 10% dimethylsulfoxide (DMSO) in an Eppendorf tube. Nutrient broth was used to culture *Staphylococcus aureus* (ATCC 25923) and *Escherichia coli* (ATCC 25922) for a period of 24 hours at 37°C, then transferred to nutrient agar and incubated for another 24 hours. The liquid microdilution test was performed by adding 100 µL of Tryptic soy broth to each of the 96 wells on a microplate, followed by 100 µL of the plant extract. The extract concentrations were serially diluted twice to produce a range of values between 5 mg mL⁻¹ and 0.0098 mg mL⁻¹. The study involved the addition of 5 µL of bacterial suspensions to each well, which resulted in a final concentration of 5x10⁵ cfu mL⁻¹. To monitor the growth of bacteria, a well without any plant extract was designated as a positive control, and a separate well that only contained plant extract was used as a negative control to evaluate the impact of the plant extract by itself. In this study, the procedure was repeated 4 times for all samples. The microplates were kept in an incubator for a period of 24 hours, the temperature was maintained at 37°C. To identify the minimum inhibitory concentration, the quantity of plant extract that could prevent bacterial growth after the incubation period was determined, and the smallest amount was selected (MIC). A 10 µL sample was taken from the wells with MIC values and concentrations above it, and then inoculated into a blood medium. The inoculated blood medium was incubated at 37°C for another 24 hours. The quantity of bacterial colonies was assessed by counting them upon the completion of the incubation period, and the minimum bactericidal concentration (MBC) was determined, which refers to the concentration that can kill 99.9% of the first living bacteria.

3. Results and Discussion

The efficacy of antibacterial agents derived from *Nigella sativa* (Black cumin), *Cuminum cuminum* (Cumin), and *Pimpinella anisum* (Anise) seed extracts prepared using methanol by the maceration and Soxhlet techniques were evaluated for their effectiveness against both gram-positive bacteria, such as *Staphylococcus aureus*, and gram-negative bacteria, including *Escherichia coli*. The broth microdilution technique was used to determine the ability of the antibacterial agents to destroy the bacteria cells.

Table 1. MIC and MBC values of *Nigella sativa* (black cumin), *Cuminum cuminum* (Cuminum) and *Pimpinella anisum* (Anise) seed extracts prepared in methanol by maceration and soxhlet extraction method

Bacteria	Extraction Plants	Maceration		Soxhlet	
		MIC (mg/m L ⁻¹)	MBC (mg/m L ⁻¹)	MIC (mg/m L ⁻¹)	MBC (mg/m L ⁻¹)
<i>Staphylococcus aureus</i>	<i>Nigella sativa</i>	0.0625	0.0625	0.125	0.25
	<i>Cuminum cuminum</i>	0.125	0.5	0.25	0.5
	<i>Pimpinella anisum L.</i>	0.0625	0.125	0.0625	0.125
<i>Escherichia coli</i>	<i>Nigella sativa</i>	0.0625	0.0625	0.125	0.25
	<i>Cuminum cuminum</i>	0.125	0.25	0.5	0.5
	<i>Pimpinella anisum L.</i>	0.125	0.25	0.125	0.5

MIC and MBC values of *Nigella sativa* (Black cumin), *Cuminum cuminum* (Cuminum) and *Pimpinella anisum* (Anise) seed extracts prepared in methanol by maceration and Soxhlet method are given in Table 1. All of the seed extracts of *Nigella sativa* (black cumin), *Cuminum cuminum* (Cuminum) and *Pimpinella anisum* (Anise) prepared by the maceration and soxhlet extraction method exhibited an ability to counter the growth of both kinds of bacteria. (preventive and killing). In our study, when the antimicrobial effect was compared between plant species, it was determined that the maceration extract of *Nigella sativa*, which inhibited the microbial activity the most and stopped the microbial activity against *Staphylococcus aureus* and *E. coli* bacteria. *Pimpinella anisum* (Anise) prepared in methanol by the maceration and soxhlet extraction method showed more antibacterial effects against *Staphylococcus aureus* than *E. coli*. In addition, it was determined that the antibacterial effect of the extracts obtained by the maceration method was higher than the extracts obtained by the soxhlet extraction method.

In research on the make-up of plants, the crucial active elements found in *Nigella sativa* are composed of thymoquinone, thymohydroquinone, dithymoquinone, p-cymene, carvacrol, 4-terpineol, t-anethole, sesquiterpene, longifolene, α -pinene, and thymol [10]; The most important active components of *Cuminum cuminum* are alkaloid, anthraquinone, coumarin, flavonoid, glycoside,

protein, resin, saponin, tannin and steroid [11]; The most important active components of *Pimpinella anisum* are stated as trans-anetole, estragole, γ -hymachalen, para-anisaldehyde and methyl cavicol [12]. Previous studies have demonstrated that these substances possess antibacterial effects due to the active components in the plants causing damage to the cell wall and leading to cell death [13].

4. Conclusion and Suggestions

This study has an important meaning for the treatment of infections by compare the antibacterial properties of *Nigella sativa* (black cumin), *Cuminum cuminum* (Cuminum) and *Pimpinella anisum* (Anise) seed extracts prepared in methanol by maceration and soxhlet extraction method. All of the seed extracts have a broad spectrum of in vitro activity against *S. aureus* and *E. coli*. Determined antimicrobial activity of plant extracts prepared using different methods and different solvents; suggested that these plants grown in our country may be a source for newly synthesized chemotherapeutics.

Contributions of the authors

Corresponding author: writing (original draft, review & editing), investigation, in vitro studies and interpretation of experimental results.

Coauthor: Methodology, investigation, literature review, in vitro studies, and interpretation of experimental results.

Conflict of Interest Statement: There is no conflict of interest between the authors.

Statement of Research and Publication Ethics: Research and publication ethics compiled within the study.

Conflict of Interest Statement

There is no conflict of interest between the authors

Statement of Research and Publication Ethics

The study is complied with research and publication ethics

References

- [1] C. Cordeiro Marina, "Phytochemical and pharmacological investigations of *Bridelia retusa* Spreng," 2012.
- [2] A. G. Fankam, J. R. Kuate, and V. Kuete, "Antibacterial activities of *Beilschmiedia obscura* and six other Cameroonian medicinal plants against multi-drug resistant Gram-negative phenotypes," *BMC Complement. Altern. Med.*, vol. 14, no. 1, p. 241, 2014.
- [3] M. Lahlou, "The success of natural products in drug discovery," *Pharmacol. Pharm.*, vol. 04, no. 03, pp. 17–31, 2013.
- [4] M. Saxena , J. Saxena , R. Nema , D. Singh , A. Gupta *J.Eczacılık. fitokimya*, 1 (2013)
- [5] E. M. Abdallah, "Black seed (*Nigella sativa*) as antimicrobial drug: A mini-review," *Novel Approaches in Drug Designing & Development*, vol. 3, no. 2, pp. 9–13, 2017.
- [6] R. P. Singh, G. H.v., and M. K, "Cuminum cyminum – A popular spice: An updated review," *Pharmacogn. J.*, vol. 9, no. 3, pp. 292–301, 2017.
- [7] A. Amer and U. Aly, "Antioxidant and antibacterial properties of anise (*Pimpinella anisum* L.)," *Egypt. Pharm. J.*, vol. 18, no. 1, p. 68, 2019.
- [8] M. Azizi, H. K. Farshchi, F. Oroojalian, and H. Orafaee, "Green synthesis of silver nanoparticles using *Kelussia odoratissima* mozaff. Extract and evaluation of its antibacterial activity," *Journal of Agricultural Science and Technology*, vol. 19, no. 3, pp. 681–691, 2017.
- [9] F. Erci, R. Cakir-Koc, and I. Isildak, "Green synthesis of silver nanoparticles using *Thymbra spicata* L. var. *spicata* (zahter) aqueous leaf extract and evaluation of their morphology-dependent antibacterial and cytotoxic activity," *Artif. Cells Nanomed. Biotechnol.*, vol. 46, no. sup1, pp. 150–158, 2018.
- [10] S. Singh, S. S. Das, G. Singh, C. Schuff, M. P. de Lampasona, and C. A. N. Catalán, "Composition, in vitro antioxidant and antimicrobial activities of essential oil and oleoresins obtained from black cumin seeds (*Nigella sativa* L.)," *Biomed Res. Int.*, vol. 2014, p. 918209, 2014.

- [11] Q. Chen et al., “In vitro comparison of antioxidant capacity of cumin (*Cuminum cyminum* L.) oils and their main components,” *Lebenson. Wiss. Technol.*, vol. 55, no. 2, pp. 632–637, 2014.
- [12] A. Shojaii and M. Abdollahi Fard, “Review of Pharmacological Properties and Chemical Constituents of *Pimpinella anisum*,” *ISRN Pharm.*, vol. 2012, p. 510795, 2012.
- [13] K. O. Saygi, B. Kacmaz, and S. Gul, “Antimicrobial activities of coriander seed essential oil and silver nanoparticles,” *Dig. J. Nanomater. Biostructures*, vol. 16, no. 4, pp. 1527-1535, 2021.

Investigation of Post-weld Heat Treatment of Laser Welded Ti6Al4V Materials

Kadir AYDIN^{1*}, Mustafa KARAMOLLA²

¹Kütahya Dumlupınar University, Simav Vocational School, Kütahya/TÜRKİYE

²Manisa Celal Bayar University, Department of Mechanical Engineering, Faculty of Engineering, Manisa/TÜRKİYE

(ORCID: 0000-0001-5701-8058) (ORCID: 0000-0002-0196-9820)



Keywords: Laser welding, Ti6Al4V, Heat treatment.

Abstract
In this study, the changes in the internal structure and mechanical properties of laser-welded Ti6Al4V material after the heat treatment process were experimentally investigated. The transformation temperatures of the α and β phase structures of the Ti6Al4V material influenced the heat treatment temperatures. Optical microscopes, XRD, and SEM experiments were performed to detect the microstructural change. Tensile and hardness tests were also carried out to determine the change in mechanical values. The experimental study determined that the mechanical values of laser-welded Ti6Al4V material improved after the heat treatment process. It was determined that ductility and strength increased significantly at heat treatment temperatures above the β phase temperature value. It was observed that the Widmanstätten morphology visible in the weld area increased the hardness.

1. Introduction

Titanium alloys are widely preferred in chemistry, aerospace, medicine, and other industries. This situation is due to the high resistance of titanium material to corrosion, high fracture toughness, low density, and high strength/weight ratio [1]. One of the most widely preferred titanium alloys is Ti6Al4V. Ti6Al4V has α and β phases in its structure. These phases are one of the main factors in the change of microstructure and mechanical properties [2]-[4].

Laser welding is superior to other welding techniques with its high welding speed, narrow weld seam, low heat input, small heat-affected zone, automation compatibility, successful welding of different materials, and joining of different thicknesses [5]. Kashaev et al. took the material Ti6Al4V and fused it with Nd: YAG laser beam welding at the T weld position. At the end of the study, they obtained similar results with the base material in terms of elongation and tensile strength [6]. Xu et al. detected a high amount of α' phase in laser-welded Ti6Al4V material due to the sudden

cooling in the weld zone. In addition, they reported that dislocation clusters caused plastic deformation in the weld area [7]. Akman et al. reported that penetration decreases with increasing welding speed, and welding power is proportional to penetration [8]. In another study, Keskin determined that laser welding is efficient in titanium alloys and that the welded samples break from the base material in tensile tests [9]. Köse and Karaca applied heat treatment to Ti6Al4V material before and after welding. When the results were examined, it was determined that the ductility and toughness values of the aged samples increased, and the hardness and tensile strength of the unaged samples increased [10]. Köse and Karaca reported in another study that different heat inputs are also effective in changing the structure of the welded material. According to the material's microstructure joined with low heat input, it was determined that grain coarsening of the material joined with high heat input occurred in the weld metal, and the volumetric ratio of the primary α phase in the weld metal increased. It has been reported that the weld metal microstructure of the material,

* Corresponding author: kadir.aydin@dpu.edu.tr

Received: 14.02.2023, Accepted: 01.06.2023

combined with low heat input, consists of basket weave or acicular α' and primary β phases at the grain boundaries [11].

Heat treatment after laser welding is preferred to improve the material's mechanical properties. However, when the literature is examined, no study has been found on how the heat treatment performed at the transformation temperatures of the α and β phases in the Ti6Al4V structure affects the mechanical properties of the welded joint. This study applied heat treatment to the laser-welded Ti6Al4V part at the transformation temperatures of the α and β phases in its structure. The effects of this on the microstructure evolution and mechanical properties are discussed. It is the part that gives the purpose of the study and its place among the previous studies. The aim of this study should be clearly stated in the last paragraph of the introduction.

2. Material and Method

Butt welding was performed with the help of a laser welding machine, the IPG YLR-6000 laser welding machine. The laser power is 3000 watts, the welding speed is 2000 mm/sec, and the protective argon gas amount is 30 lt/min. In order to determine the optimum parameters in the laser welding process, experiments were carried out with different parameters, and smooth weld seams and good penetration were observed in the welding process with the above parameters. The chemical composition of the Ti6Al4V material is given in Table 1. The welding area is protected against oxidation with argon gas in the laser welding process. After laser welding, the test pieces were taken to the heat treatment process. The classification of test pieces is given in Table 2.

1) Heat treatment at 800 °C, below the α transformation (T_α) temperature of 880 °C;

2) Heat treatment at 950 °C, between T_α and T_β (β conversion temperature 990 °C);

3) Heat treatment at 1080 °C on T_β .

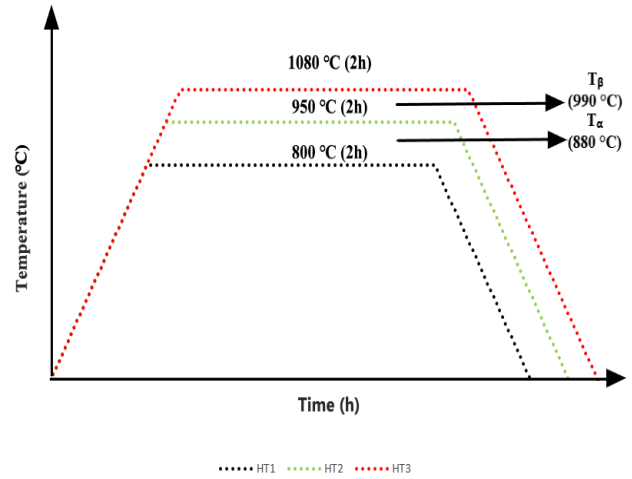


Figure 1. Heat treatment of laser welded Ti6Al4V materials.

Hardness, tensile and optical microscopy, SEM, and XRD tests were applied to the test specimens. Microhardness test was performed under 300 g load and 15 seconds load application parameters. The tensile test was performed in the form of uniaxial tension at room temperature and 0.5 mm/min speed in accordance with the ASTM E8/E8M-15a standard. Molded parts for the metallography experiment were sanded in the range of 200-2500 mesh, respectively. Then the pieces were polished on felt with the help of diamond paste. Then etching was done in Kroll solution for 20 seconds. Samples were viewed with a microscope. The internal structures of the samples were examined by scanning electron microscopy (SEM). The X-Ray Diffraction method (XRD) was performed by scanning in the range of 30-80 degrees. Figure 1 shows the tests and analyses performed on the test samples.

Table 1. Ti6Al4V chemical composition (%)

Al	V	Fe	C	O	N	H	Ti
5.5-6.5	3.5-4.5	0-0.25	0-0.08	0-0.13	0-0.05	0-0.012	Balance

Table 2. Classification of Ti-6Al-4V parts.

Code	Samples
As-received	Ti6Al4V specimen
LW	Laser welded Ti6Al4V
HT1	Laser welded followed by heat treatment (HT) at 800 °C for 2 hours, furnace cooling (FC)

HT2	Laser welded followed by HT at 950 °C for 2 hours, FC
HT3	Laser welded followed by HT at 1080 °C for 2 hours, FC

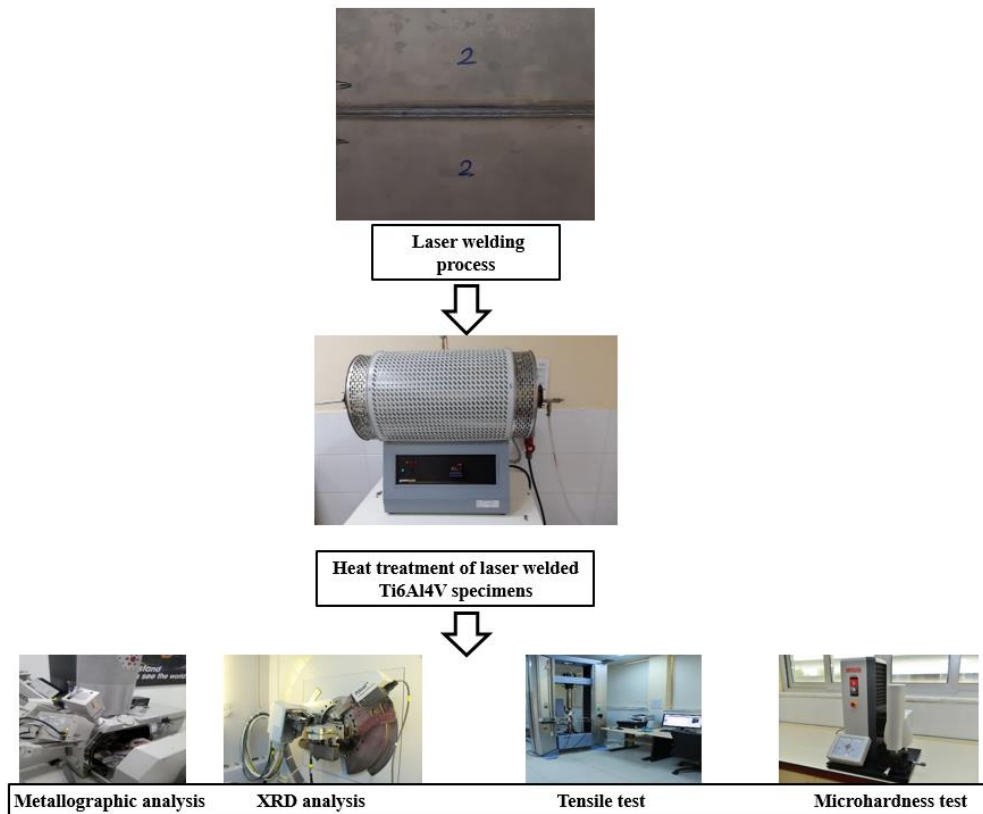


Figure 2. Test and analysis steps for Ti6Al4V.

3. Results and Discussion

An optical microscope view of laser-welded Ti6Al4V material is given in Figure 3. A needle-like martensitic structure was observed in the melting and heat-affected zones due to the sudden cooling after welding. In the base metal region, there is a coaxial spherical structure. This structure plays a role in increasing fracture toughness and supporting strength [12]. In the microstructure, light-colored sections represent the α phase with a tight-packed hexagonal lattice structure, and dark-colored sections represent the β -phase with a volume-centered cubic lattice structure. The change in the internal structures of the weld zone of the Ti6Al4V samples after heat treatment is given in Figure 3(d-f). After the 800 °C heat treatment, it is seen that the martensite structure begins to dissolve, although there are some needle-like structures (Figure 3(d)). Widmanstatten morphology was observed after heat treatments at 950 °C and 1080 °C. It was observed that the grain structure became coarser after the β transformation temperature in the heat treatment (1080 °C). In

addition, it was determined that a lamellar structure was formed in the weld area after the heat treatment processes.

Looking at the SEM images in Figure 4(a,b), it was determined that the laser-welded test specimens had micro-cracks in the weld area. It has been reported that this situation has a decreasing effect on mechanical property values [13]. Due to this micro-crack structure seen in the weld area, the welding efficiency of the welded joint was determined to be 75.3% compared to the base material. In addition, when the base material is examined, it is seen that α and β phases are together in the structure, but the α phase structure is more dominant. When the laser-welded sample is examined, there are α' peaks in the structure due to the sudden cooling (Figure 4(c)). Heat treatments were effective in increasing the peak levels. This is attributed to grain coarsening due to heat input.

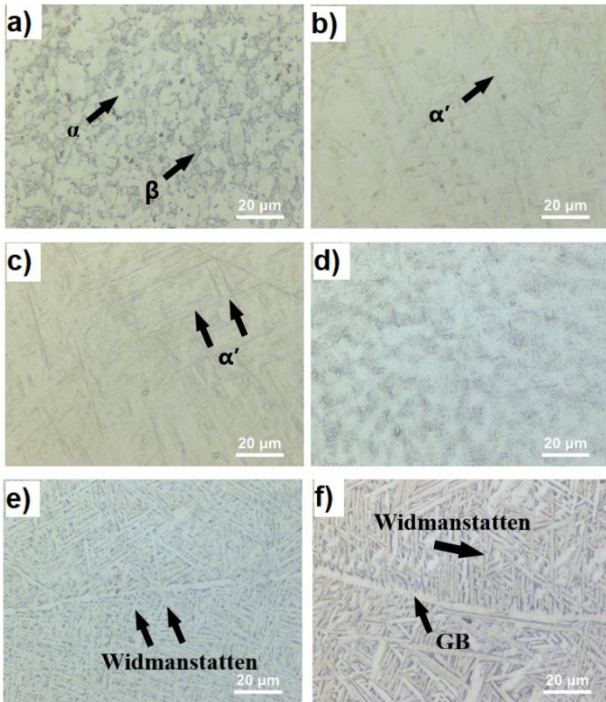


Figure 3. Microstructure of laser welded samples: a) base material, b) heat affected zone, c) weld zone, d) weld zone (HT1), e) weld zone (HT2), f) weld zone (HT3, GB: Grain boundary).

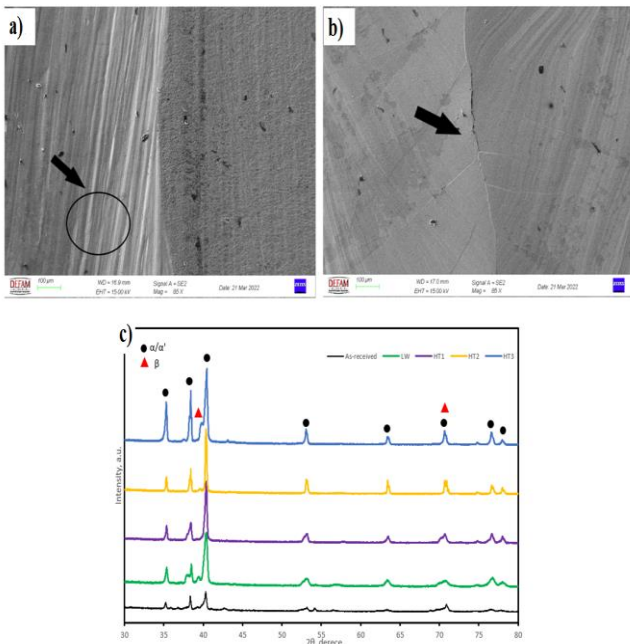


Figure 4. SEM view of the samples: a) General view, b) detail view, c) XRD analysis.

3.1. Mechanical Evolution

A view of the hardness distribution of the laser-welded Ti6Al4V part is given in Figure 5. The microhardness value of welded parts is related to the microstructure. The martensite structure in the weld

zone and the heat-affected zone are the reasons for the increase in hardness value. The hardness values of the rolled samples did not decrease when heat treatment was applied at 800 °C. On the contrary, there was some increase in hardness in the weld area (Fig. 5(b)). This is due to the presence of a certain amount of martensite phase in the structure of the parts after the heat treatment process. Even after three heat treatments, it is observed that the microhardness of the weld zone is higher than the welded sample without the heat treatment process. Researchers reported that with the decrease in β phase volume with post-weld heat treatment applications, hardness would increase, especially in the weld area [14]. In addition, a slight tendency to decrease hardness values after heat treatment was also observed at β transformation temperature. This is due to the increase in the β phase, which is more ductile than the α phase.

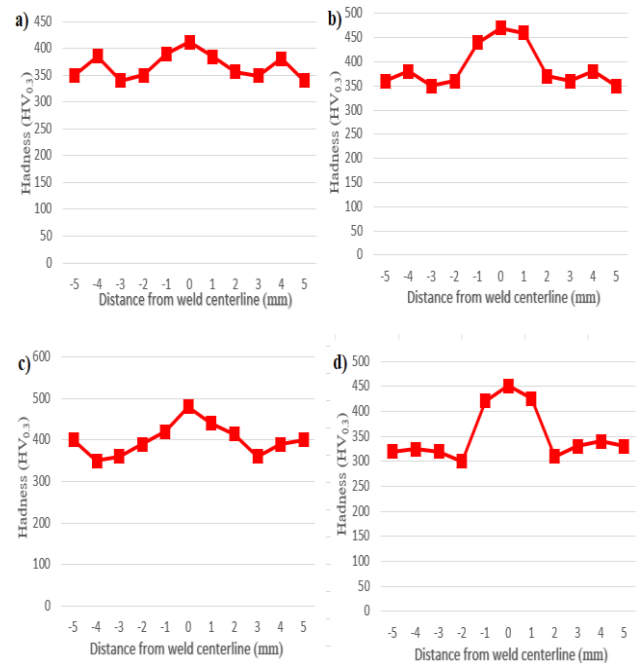


Figure 5. The hardness value of the samples: a) LW, b) HT1, c) HT2, d) HT3.

The tensile test results of laser welded Ti6Al4V material heat treated at different temperatures are given in Table 3. The welding efficiency of the laser welded (LW) sample was determined to be 75.3%. It is seen that the mechanical values of the laser welded sample are lower than the base material due to micro-cracks in the weld area. The best mechanical properties of the heat-treated and laser-welded Ti6Al4V parts were determined after the heat-treatment process at 1080 °C. After this heat treatment, the tensile strength value was determined

to be 853.6 MPa, and the elongation was determined to be 8.8%. The elongation value of the base material was determined to be 15.7%. When the heat-treated samples were examined, it was determined that the elongation value increased with the increase in temperature. It is estimated that this situation is caused by grain coarsening due to the increase in temperature [11].

The tensile strength and elongation values of laser welded rolled Ti6Al4V samples are given in

Figure 6. The elongation value of the base material was determined to be 15.7%. When the heat-treated samples were examined (HT1, HT2, and HT3), it was determined that the elongation value increased with the increase in the heat treatment temperature. It is estimated that this is due to grain coarsening due to increased heat treatment temperature [11].

Table 3. Ti6Al4V tensile test values.

	Yield strength [MPa]	Tensile strength [MPa]	Elongation [%]	Weld Efficiency (%)
As-received	933.5	1002.4	15.7	
LW	668.3	755.2	7.6	75.3
HT1	556.7	648.2	5.1	64.7
HT2	628.9	712.7	7.7	71.1
HT3	745.6	853.6	8.8	85.2

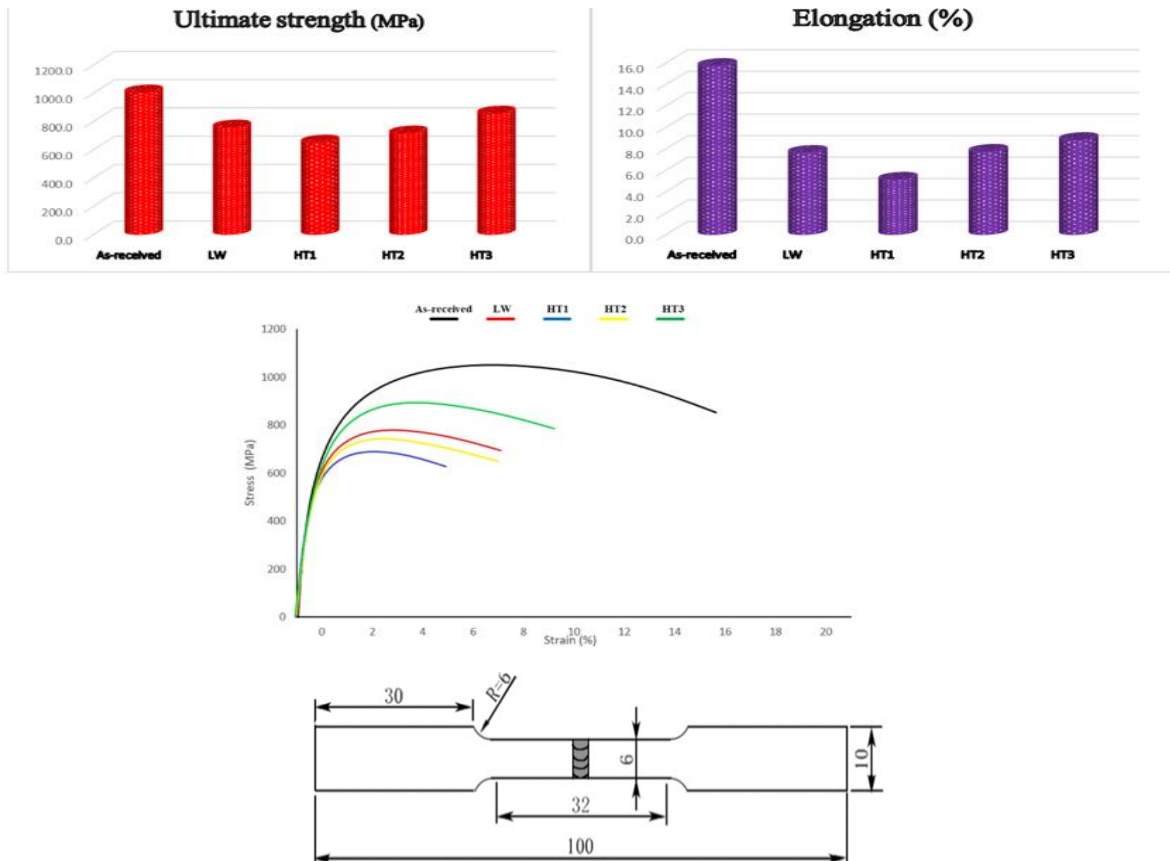


Figure 6. Tensile test results of parts.

4. Conclusion and Suggestions

The results of the microstructural changes and mechanical properties that occur in the material when heat treatment is applied to the laser-welded Ti6Al4V material are given below:

- When the microstructures of welded samples are examined, the weld area and the heat-affected zone are martensitic, while the base metal zone consists of equiaxed $\alpha + \beta$ phase structures. In addition, it was determined that the martensitic structure in the weld area was replaced by the lamella Widmanstätten morphology, especially after the heat treatments at 950 °C, and 1080 °C with the increase in temperature.
- The hardness of the welding zone of the materials joined by laser welding was higher than the base metal. It was determined that the hardness values decreased slightly after heat treatment at 1080 °C. This is thought to be due to grain coarsening.
- As a result of the tensile test, it has been observed that the strength of laser-welded parts is lower than

that of the base material. This is thought to be due to microcracks detected in the weld area. The best mechanical properties of welded parts were observed after heat treatment at 1080 °C.

Acknowledgment

We gratefully acknowledge support the of Manisa Celal Bayar University for financial support (BAP project number 2020/47).

Contributions of the authors

Writing, Experimental study: Kadir Aydın;
Supervising: Mustafa KARAMOLLA.

Conflict of Interest Statement

There is no conflict of interest between the authors.

Statement of Research and Publication Ethics

The study is complied with research and publication ethic.

References

- [1] N. K. Park, C. H. Lee, J. H. Kim, and J. K. Hong, "Characteristics of powder-rolled and sintered sheets made from HDH Ti powders," *Key Eng. Mater.*, vol. 520, pp. 281–288, 2012.
- [2] X. Xu, G. L. Nash, and P. Nash, "Sintering mechanisms of blended Ti6Al4V powder from diffusion path analysis," *J. Mater. Sci.*, vol. 49, no. 3, pp. 994–1008, 2014.
- [3] V. A. R. Henriques, H. R. Z. Sandim, G. C. Coelho, and C. R. M. da Silva, "Microstructural evolution during hot pressing of the blended elemental Ti–6%Al–7%Nb alloy," *Mater. Sci. Eng. A Struct. Mater.*, vol. 347, no. 1–2, pp. 315–324, 2003.
- [4] V. A. Joshi, Titanium alloys: An atlas of structures and fracture features. Boca Raton, FL: CRC Press, 2006.
- [5] K. Aydın and İ. Karaağaç, "Lazer kaynağı ve lazer kaynağının başlıca uygulamaları," *El-Cezeri Fen ve Mühendis. Derg.*, vol. 5, no. 2, pp. 693–705, 2018.
- [6] N. Kashaev, V. Ventzke, V. Fomichev, F. Fomin, and S. Riekehr, "Effect of Nd:YAG laser beam welding on weld morphology and mechanical properties of Ti–6Al–4V butt joints and T-joints," *Opt. Lasers Eng.*, vol. 86, pp. 172–180, 2016.
- [7] P.-Q. Xu, L. Li, and C. (sam) Zhang, "Microstructure characterization of laser welded Ti-6Al-4V fusion zones," *Mater. Charact.*, vol. 87, pp. 179–185, 2014.
- [8] E. Akman, A. Demir, T. Canel, and T. Sınmazçelik, "Laser welding of Ti6Al4V titanium alloys," *J. Mater. Process. Technol.*, vol. 209, no. 8, pp. 3705–3713, 2009.
- [9] "TİTANYUM (GRADE 1) - IATS'09 - Karabük Üniversitesi," yumpu.com. [Online]. Available: <https://www.yumpu.com/tr/document/view/2032910/titanyum-grade-1-iats09-karabuk-universitesi>. [Accessed: 14-Feb-2023].
- [10] C. Köse and E. Karaca, "Nd:YAG lazer kaynağı ile birleştirilen Ti6Al4V alaşımının mikroyapı ve mekanik özelliklerine ısı işlemlerinin etkileri," *Balıkesir Üniv. Fen Bilim. Enst. derg.*, vol. 21, no. 1, pp. 232–243, 2019.

- [11] C. Köse and E. Karaca, "Ti6Al4V alaşımının fiber lazer kaynak kabiliyeti," *NWSA-Eng. Sci.*, vol. 12, no. 3, pp. 140–152, 2017.
- [12] P. Fu, Z. Mao, C. Zuo, Y. Wang, and C. Wang, "Microstructures and fatigue properties of electron beam welds with beam oscillation for heavy section TC4-DT alloy," *Chin. J. Aeronaut.*, vol. 27, no. 4, pp. 1015–1021, 2014.
- [13] S. H. Wang, M. D. Wei, and L. W. Tsay, "Tensile properties of LBW welds in Ti–6Al–4V alloy at evaluated temperatures below 450 °C," *Mater. Lett.*, vol. 57, no. 12, pp. 1815–1823, 2003.
- [14] A. S. H. Kabir et al., "Effect of postweld heat treatment on microstructure, hardness, and tensile properties of laser-welded ti-6Al-4V," *Metall. Mater. Trans. A*, vol. 43, no. 11, pp. 4171–4184, 2012.

Bioecology and Systematic of Scorpions in Southwestern Anatolia Region (Arachnida: Scorpiones)

Fatih YEŞİLYURT^{1*}, İrfan ALBAYRAK²

¹*Yüksekova Vocational School, Hakkari University, Yüksekova, Hakkari, Turkey*

²*Kırkkale University*

(ORCID: [0000-0002-4181-6546](https://orcid.org/0000-0002-4181-6546))(ORCID: [0000-0002-0791-9584](https://orcid.org/0000-0002-0791-9584))



Keywords: Scorpion,
Zoogeography, Systematic,
Southwestern Anatolia, Turkey.

Abstract

In this study, scorpion fauna from six provinces in the Southwestern Anatolia Region (Antalya, Aydın, Burdur, Denizli, Isparta, and Muğla) of Turkey was studied, and 11 species in 6 genera belonging to 3 families were recorded. Examined specimens were collected between May 2006 and September 2011 from several provinces of the research field in the Southwestern Anatolia Region. As a result of field trips, 342 specimens were collected. Besides, some museum materials that were previously collected were used. At the end of the studies, it was determined that *Aegaeobuthus gibbosus*, *Anatoliurus kraepelini*, *Euscorpium arikani*, *E. avcii*, *E. gocmeni*, *E. honazicus*, *E. lycius*, *E. sultanensis*, *Iurus kinzelbachi*, *Metaiurus kadleci*, and *Neocalchas gruberi* species are distributed in the Southwestern Anatolia Region of Turkey. Among these samples, *Neocalchas gruberi* species was recorded from Isparta province, *Euscorpium arikani* was recorded from Muğla province, *E. honazicus* species was recorded from Burdur province, and *E. sultanensis* species was recorded from Isparta province, *Anatoliurus kraepelini* species was recorded from Isparta and Denizli provinces for the first time. In this study, the systematic, bioecologic, and faunistic information of the determined species were presented, besides ecological and biological field trip notes.

1. Introduction

Turkey's geographical location, climate, and flora have made rich faunal elements available. To determine the biodiversity values of our country, more detailed scientific studies will be required. In the scorpion of our country, which is a peninsula, when we look at the fauna, it is seen that some species are endemic and some of them are species originating from Central Asia, the Middle East, the Caucasus, and Europe.

Yağmur (2022) reported that 41 species belonging to 4 families (Buthidae, Euscorpidae, Iuridae, and Scorpionidae) live in Turkey [1]. Parmakelis et al. (2022), based on their findings, established three new genera of Iurinae (*Metaiurus*, *Anatoliurus*, and *Letoiurus*), and a new record of *Letoiurus rhodiensis* was given from Turkey [2]. Kovařík et al. (2022) revised the genus *Mesobuthus* Vachon (1950) and

described 14 new species [3]. Of these, *M. rahsena*, *M. Turcicus*, and *M. yagmuri* are included in the scorpion fauna of Turkey. In addition, it was stated in the same publication that the species known as *M. phillipsii* was *M. mesopotamicus*.

Von Ubisch (1922) described the *Iurus kraepelini* species from Finike (Antalya) [4]. Schenkel (1947) described the *Mesobuthus gibbosus anatolicus* subspecies from Sivas and Amasya [5]. *Aegaeobuthus gibbosus anatolicus* was described under the protonym *Buthus gibbosus* by Brullé in 1832 [6]. It was placed in the genus *Mesobuthus* by Vachon in 1950 [7], then in the genus *Aegaeobuthus* by Kovařík in 2019 [8]. Fet et al. (2009) made a revision on the genus *Calchas* and included *C. gruberi* and *C. birulai* [9]; Kovařík et al. (2010) re-examined the genus *Iurus* and described two new species, *Iurus kadleci* and *Iurus kinzelbachi*, in Turkey [10]. *Iurus kraepelini*, which is found in the south of Turkey and used as a

*Corresponding author fatihyesilyurt@hakkari.edu.tr

Received: 15.02.2023, Accepted: 07.06.2023

synonym of *Iurus asiaticus*, was used as a species, and it was stated that *Iurus asiaticus* was found in Eastern Anatolia. Soleglad et al. (2012), with the revision of *Iurus*, identified *Iurus* species found in Anatolia according to the angle of hemispermatothores and divided them into *Protoiurus* and *Iurus* [11]. Tropea et al. (2012) identified a new scorpion species named *Euscorpius* (*Euscorpius*) *avcii* in the Dilek Peninsula of Aydın province [12]. Yağmur et al. (2013a) described a new scorpion species, *E. lycius*, from Muğla and Antalya provinces [13]. Yağmur et al. (2013b) identified a new scorpion genus, *Neocalchas*, from Turkey [14]. Tropea et al. (2014) identified a new scorpion species, *Euscorpius gocmeni*, from Antalya province (Akseki district) [15]. Yağmur and Tropea (2015) identified a new scorpion species, *E. Arikani*, from Antalya province [16]. Yağmur et al. (2015a) described a new scorpion species, *Protoiurus kumlutasi*, from Antalya (Hidirellez Cave) [17]. Yağmur et al. (2015b) analyzed iurids, and new information is presented on the morphometric differences between adult and immature males of *Metaiurus kadleci* and the differences between *M. kadleci* and other *Protoiurus* species. An updated identification of *M. kadleci*, as well as an updated key to other species and a map showing all known settlements, are presented [18]. Tropea and Yağmur (2016a) identified a new scorpion species, *Euscorpius sultanensis*, from the Sultan Mountains [19]. Tropea and Yağmur (2016b) described a new scorpion species, *E. Hakani*, from Denizli [20]. Tropea et al. (2016a) identified a new scorpion species, *E. honazicus*, from Denizli province (Honaz Mountain) [21]. Tropea et al. (2016b) identified a new scorpion species, *E. Alanyaensis*, from Antalya province (Taurus Mountains Alanya side) [22]. The specimens collected by R. Kinzelbach in Turkey in the 1970s and found in the Mainz Naturhistorisches Museum (Germany) were analyzed by Yağmur (2021a). According to the current taxonomy, one “*Euscorpius carpathicus*” specimen from İzmir was identified as *E. avcii*; two “*E. carpathicus*” specimens from Mersin were identified as *E. koci* [23]. Cain et al. (2021) made a revision study on the genus *Buthacus* of Israel and surrounding regions and stated that the species known as *Buthacus macrocentrus* in Turkey is *Buthacus tadmorensis* [24].

As a result of all these studies, the scorpion fauna of Turkey is currently represented by 46 species: *Aegaeobuthus gibbosus anatolicus*, *A. nigrocinctus*, *Alpiscorpius mingrelicus*, *A. phrygius*, *A.*

uludagensis, *Anatoliurus kraepelini*, *A. kumlutasi*, *Androctonus turkiyensis*, *Buthacus tadmorensis*, *Calchas anlasi*, *C. birulai*, *C. kosswigi*, *C. nordmanni*, *Compsobuthus matthiesseni*, *C. schmiedeknechti*, *Euscorpius aladaglarenensis*, *E. alanyaensis*, *E. arikani*, *E. avcii*, *E. ciliciensis*, *E. eskisehirensis*, *E. gocmeni*, *E. hakani*, *E. honazicus*, *E. idaeus*, *E. italicus*, *E. koci*, *E. lesbiacus*, *E. lycius*, *E. sultanensis*, *E. tauricus*, *Hottentotta saulcyi*, *Iurus kinzelbachi*, *Leiurus abdullahbayrami*, *Letoiurus rhodiensis*, *Mesobuthus eupeus*, *M. mesopotamicus*, *M. rahsenae*, *M. turcicus*, *M. yagmuri*, *Metaiurus kadleci*, *Neocalchas gruberi*, *Olivierus caucasicus*, *Orthochirus fomichevi*, *Protoiurus asiaticus*, *Scorpio fuscus* (Cain et al., 2021; Yağmur, 2022; Kovařík et al., 2022; Parmakelis et al., 2022).

Of these species, *Aegaeobuthus gibbosus anatolicus*, *Anatoliurus kraepelini*, *A. kumlutasi*, *Euscorpius alanyaensis*, *E. arikani*, *E. avcii*, *E. gocmeni*, *E. hakani*, *E. honazicus*, *E. lycius*, *E. sultanensis*, *Iurus kinzelbachi*, *Metaiurus kadleci*, and *Neocalchas gruberi*, constitute the species found in the study area. The Southwestern Anatolia Region of Turkey (Antalya, Aydın, Burdur, Denizli, Isparta, and Muğla) is specifically investigated in this study. Therefore, the present study attempted to facilitate knowledge of the distribution of Turkish Scorpion fauna.

2. Material and Method

2.1. Location and characteristics of the research region

The sample collection area is between 27° 23' - 32° 27' east longitudes and 36° 06' - 38° 30' north latitudes in Southwest Anatolia. Within this selected region, there are the provinces of Antalya, Aydın, Burdur, Denizli, Isparta, and Muğla (Figure 3.1). Of these, Antalya, Burdur, and Isparta are located in the Mediterranean Region, while Aydın, Denizli, and Muğla are located in the Aegean Region.

2.2. Collection and evaluation of material

The majority of the samples examined in this study were collected from the Southwest Anatolia Region (Antalya, Aydın, Burdur, Denizli, Isparta, and Muğla) between May 2006 and September 2011. As a result of field studies, 259 samples from various localities were examined. However, with the samples collected by the author between 2003 and 2005 and collected by Dr. E. A. Yağmur from the same

Samples were collected during field studies conducted during the day and night between March and October. During the field studies carried out

during the daytime, the samples were generally found under the stones in March-May; in the night field studies, samples were searched with a UV lamp in the May-October periods, when the weather was completely dark.

Phillips TL-D18W/BLB UV installed in direct current luminaires lamp assembly is installed. Under UV light, scorpions give off a phosphorescent light. The setup was operated with 12 Volt, 5 Amh dry batteries; discharged batteries were filled with an Ataba brand charger. The animals were seen either at the entrance of their nests or in the rock cracks while they were wandering around hunting. The samples were collected with long collets and fixed in 70% ethyl alcohol.

The identifications of the species were made based on Birula (1917a, 1917b) [25]-[26], Kinzelbach (1975) [27], Fet et al. (2009) [9], Kovarik et al. (2010) [10], Kovarik (2019) [8], Soleglad et al. (2012) [11], Tropea et al. (2012) [12], Yağmur et al. (2013a) [13], Yağmur et al. (2013b) [14], Tropea et al. (2014) [15], Yağmur and Tropea (2015) [16], Yağmur et al. (2015a) [17], Yağmur et al. (2015b) [18], Tropea and Yağmur (2016a) [19], Tropea et al. (2016a) [21], Tropea et al. (2016b) [22], Parmakelis et al. (2022) [2]. For each examined species, the ventral and dorsal appearances of male and female individuals are given. The number of samples examined and their locality information were processed. The bioecological characteristics of the species and its geographical distribution in Turkey are given.

Carina, extremity, and trichobothrial terminology were based on Francke (1977) [28], Hjelle (1990) [29], and Vachon (1974) [30].

A Benq DCC1035 brand camera was used to capture the habitats of the collected specimens and their photographs. The samples were diagnosed with a Nikon SMZ800 brand stereo microscope, and their photographs were taken using a Stemi 2000-C brand Stereo Microscope, a Powershot G 10, and a Samsung ES 73 camera attached to this microscope. Garmin Etrex Vista branded GPS and Google Earth programs were used for locality determination.

The collected samples were stored in 15 ml, 50 ml plastic tubes and in 100 ml and 200 ml glass jars. The samples are preserved in the author's personal collection.

The samples used for this article were collected from 6 provinces in Southwest Anatolia between May 2006 and September 2011. It is also adapted from the author's thesis project.

3. Results and Discussion

Identification key for scorpions detected in Southwest Anatolia Region

1. Lateral eyes 5 pairs, sternum triangular, pedipalp tibia ventrally without trichobotria, metasoma thicker than chela, chela round in cross-section.....Buthidae, *Aegaeobuthus gibbosus*

— Sternum pentagonal, 2-3 pairs, chela flat in cross section.....(2)

2. Lateral eyes 2-3 pairs, pedipalp tibia with 1 trichobotria ventrally, longer than the width of the chela, strong carina on the metasomaJuridae (3)

— Lateral eyes 2 pairs, pedipalp tibia with 6-10 trichobotria ventrally; chela broad and flat, metasoma with very weak keel or without keel.. Euscorpiidae (6)

3. 3rd and 4th legs have tibial spurs, lateral eyes are two pairs Calchinae, *Neocalchas gruberi*

— 3rd and 4th legs lack tibial spurs, lateral eyes are three pairs Iurinae (4)

4. There are 1 or 2 trichobotria (ea) on the outside of the pedipalp patella, the space in the male chela is very narrow, the count of comb teeth is 9-11 in females and 10-11 in males*Jurus kinzelbachi*

— There are no ea trichobotries (ea) on the outside of the pedipalp patella, the space in the male chela is quite wide, the number of comb teeth is 11-14 in males and 10-12 in females..... (5)

5. The chela fingers are long, there are two arches on the mobile finger and these arches are quite prominent, the chela is elongated and narrow *Metaiurus kadleci*

— The chela fingers are short, there is only one arch in the mobile finger and this arch is not prominent, the chela is quite swollen..... *Anatoliurus kraepelini*

6. The trichobotria number on the external side of the pedipalp patella in the em series is 3 7

— The trichobotria number on the external side of the pedipalp patella in the em series is 4 9

7. The trichobotria number on the ventral side of the pedipalp patella pv series 5-7 and external series et 4-6 *Euscorpium arikani*
- The trichobotria number on the ventral side of the pedipalp patella pv series 5-6 or 6-7 and external series et 3-4 or 5-68
8. The trichobotria number on the ventral side of the pedipalp patella pv series 5-6 and external series et 3-4 *Euscorpium sultanensis*
- The trichobotria number on the ventral side of the pedipalp patella pv series 6-7 and external series et 5-6 *Euscorpium honazicus*
9. The trichobotria number on the ventral side of the pedipalp patella pv series 6-8 *Euscorpium avcii*
- The trichobotria number on the ventral side of the pedipalp patella pv series 8-13 10
10. The trichobotria number on the external series of the pedipalp patella et is 7-8..... *Euscorpium gocmeni*
- The trichobotria number on the external series of the pedipalp patella et is 5-7.....*Euscorpium lycius*

Muğla province, Fethiye, Yeşil Üzümlü Village, 1 (1♂, 16 May 2008); Antalya province, Alanya, Taşatan Plateau, 2 (2♂♂, 09 June 2009); Aydın province, Dilek Peninsula National Park, 1 km inside the canyon, 5 (5♂♂, 07 June 2009); Aydın province, Aytepe 1 (1♂, 01 September 2004); Isparta province, Aksu, Çayır yayla road, Anamas Mountain, 37° 48' 58" N, 31° 07' 24" E, 1315 m. 1 (1♂, 09 August 2010); Muğla province, Köyceğiz, 36° 55' 53.2" N, 28° 42' 28.1" E., 1 (1♀, 27 February 2010); Aydın province, Çine, Near Topçam Dam Lake, 37° 41' 11" N, 28° 00' 42" E, 108 m., 1 (1♀, 23 October 2009); Muğla province, Fethiye, Akdağlar 3rd Station 36° 45' 08.6" N, 29° 38.3' 08" E, 1628 m., 1 (1♀, 01 August 2008); Denizli province, Babadağ, 37° 47' 16" N, 28° 52' 09" E, 1720 m., 5 (1♂, 4♀♀, 02 August 2008); Muğla province, Fethiye, Çiçek Babadağ, 1 (1♀, 02 August 2008); Antalya province, 31 km ahead of Zeytintasi Cave, 1 (1♀, 13 May 2010); Antalya province, Korkuteli Road 35. km, 2 (2♂♂, 16 May 2010); Antalya province, Korkuteli-Elmalı road 10. km, 1 (1♂, 16 May 2010); Denizli province, Honaz, 37° 49' 20" N, 29° 16' 37" E, 435 m., 2 (2♂♂, 17 October 2009); Antalya province, Korkuteli-Elmalı road 10. km., 1 (1♀, 16 May 2010); Antalya province, Serik, Akbaş Village, Altıntaş Cave, 1 (1♂, 15 July 2005); Antalya province, Korkuteli road 35. km, 2 (2♀, 16 May 2010); Muğla province, Fethiye, Çiçek Babadağ, 1 (1♀, 02 August 2008); Aydın province, Around Paşayayla Hotel, 37° 56.9' 08.2" N, 27° 53.4' 08.1" E., 2 (2♂, 30 July 2008); Antalya province, Serik, Akbaş Village, Altıntaş Cave, 1 (1♀, 15 July 2005); Muğla province, Datça, Palamut Bükü, 1 (1♂, 15 July 2010); Aydın province, Didim, near Dilek Peninsula National Park, 2 (2♀♀, 12 July 2010); Denizli province, Cankurtaran, 5 (2♂♂, 3♀♀, 23 June 2010); Antalya province, Korkuteli road 35. km, 2 (2♀, 16 May 2010); Antalya province, Korkuteli, Datköy, 1 (1♀, 14 July 2005); Muğla province, Eski Datça Mevkii, 3 (2♂♂, 1♀, 12 August 2004); Muğla province, Fethiye, Üzümlü Village, 6 (6♂♂, 02 May 2006); Muğla province, Lake Bafa, 37° 29' 29.4" N, 27° 32' 21.8" E. 14 m., 1 (1♂, 24 October 2009); Muğla province, Fethiye, Yanıklar, 36° 41' 53" N, 29° 02' 54.7" E., 9 m., 1 (1♀, 15 September 2009); Antalya province, Manavgat, Oymapınar Village, Poyrazlı Mevkii, 16 (9♂♂, 7♀♀, 05 August 2005); Antalya province, Tilkiler Mevkii, 11 (5♀♀, 6♂♂, 02 August 2005); Aydın province, Dilek Peninsula National Park, 37° 41' 41" N, 27° 13' 55" E., 3 (2♂, 1♀, 07 May 2011); Aydın province, Dilek Peninsula National Park, 5 (4♂♂, 1♀, 13 July 2010); Aydın province, Dilek Peninsula National Park, 1 (1♂, 07 May 2011); Muğla province, Datça, Palamut Bükü, 2 (2♀, 15 July

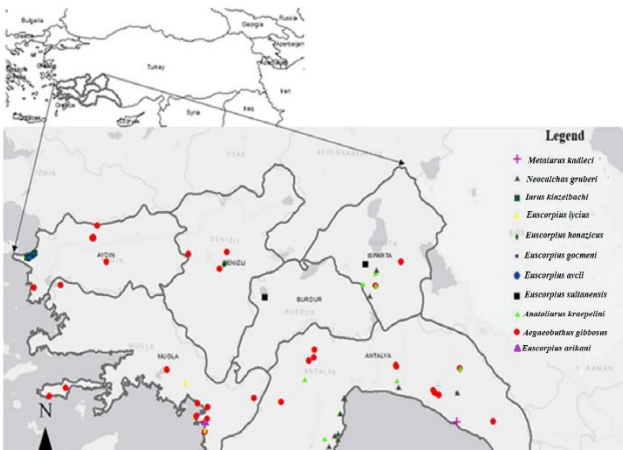


Figure 3. 1. Distribution Map of Detected Species

Family: Buthidae C.L. Koch, 1837 [31]

Genus: *Aegaobuthus* Kovarik, 2019 [8]

***Aegaobuthus gibbosus* (Brulle, 1832) [6]**

Material Examined: Aydın province, Kepez Location, 1 (1♂, 25 May 2004); Aydın province, Adnan Menderes University. campus, 1 (1♀, 31 July 2003); Aydın province, Söke, Dilek Peninsula National Park, 3 (1♂, 2♀, 17 April 2003); Antalya province, Manavgat, Oymapınar Canyon, 1 (1♀, 01 July 2004); Aydın: Center, 1 (1♂, July 23, 2003);

2010); Isparta province, 5 km south of Kovada Lake junction, 37° 38' 01" N, 30° 51' 41" E, 405 m., 1 (1♂, 11 May 2011); Muğla province, Fethiye, Faralya Village, 36° 29' 37" N, 29° 08' 07" E, 349 m., 1 (1♀, 30 May 2011); Aydın province, Kuşadası, Davutlar, Güzel Çamlı Village, 37° 41' 22" N, 27° 13' 31" E, 311 m., 14 (11♂♂, 3♀, 07 June 2011); Antalya province, 28 km north of Elmalı, 2 (1♂, 1♀, 08 July 2011); Antalya province, 12 km south of Akseki, 3 (1♂, 2♀♀, 09 July 2011).

Bioecological Notes: It is a species that prefers arid and warm environments. It has been determined that it spreads from sea level to 1800 m Yağmur 2005 [32]. In field studies, this species has been caught under stones in steppe habitats, in maquis, in pine forests, and along streams. Remains of insects that these scorpions were fed were also found under the stones where they were caught.

As a result of feeding a pregnant specimen caught in the field under laboratory conditions, it was determined that she gave birth to 42 puppies, but since the moment of birth could not be observed, it is possible that this number is higher. It has been observed that this species ate grasshoppers, spiders, flies, mantises, butterflies, and lizards while feeding in laboratory conditions. It has been determined that scorpions feed by using their pedipalps, just like humans use their hands and arms, after first poisoning and neutralizing their prey by stinging them with their sting. It has been observed that scorpions do not move much during the daytime, so it is thought that they aim to use their energy efficiently.

Distribution in Turkey: Mediterranean Region, Egean Region, Central Anatolia Region, south of the Black Sea Region.



Figure 3.2. A. Dorsal, B. Ventral View in Female, C. Dorsal, D. Ventral View in Male *Aegaeobuthus gibbosus*

Family: Euscorpiidae Laurie, 1896 [33]

Genus: *Euscorpius* Thorell, 1876 [34]

Euscorpius arikani, Yagmur & Tropea, 2015 [16]

Material Examined: E. Arikani Muğla: Köyceğiz, Çiçek Babadağ, 3 (2♂, 1♀, 02 August 2008).

Bioecological Notes: *Euscorpius arikani* was collected from under stones in the pine forest. In addition, it has been detected in the field studies carried out at night while waiting in rock cracks and cavities in the soil in rocky areas. It has been observed

that they are generally active during the cooler times of the year. In addition, their habitats are in regions that are constantly humid throughout the year. For this reason, they have been detected locally only in regions such as valleys, canyons, and high mountains.

Distribution in Turkey: Antalya, Muğla. This species was recorded from Muğla province for the first time.

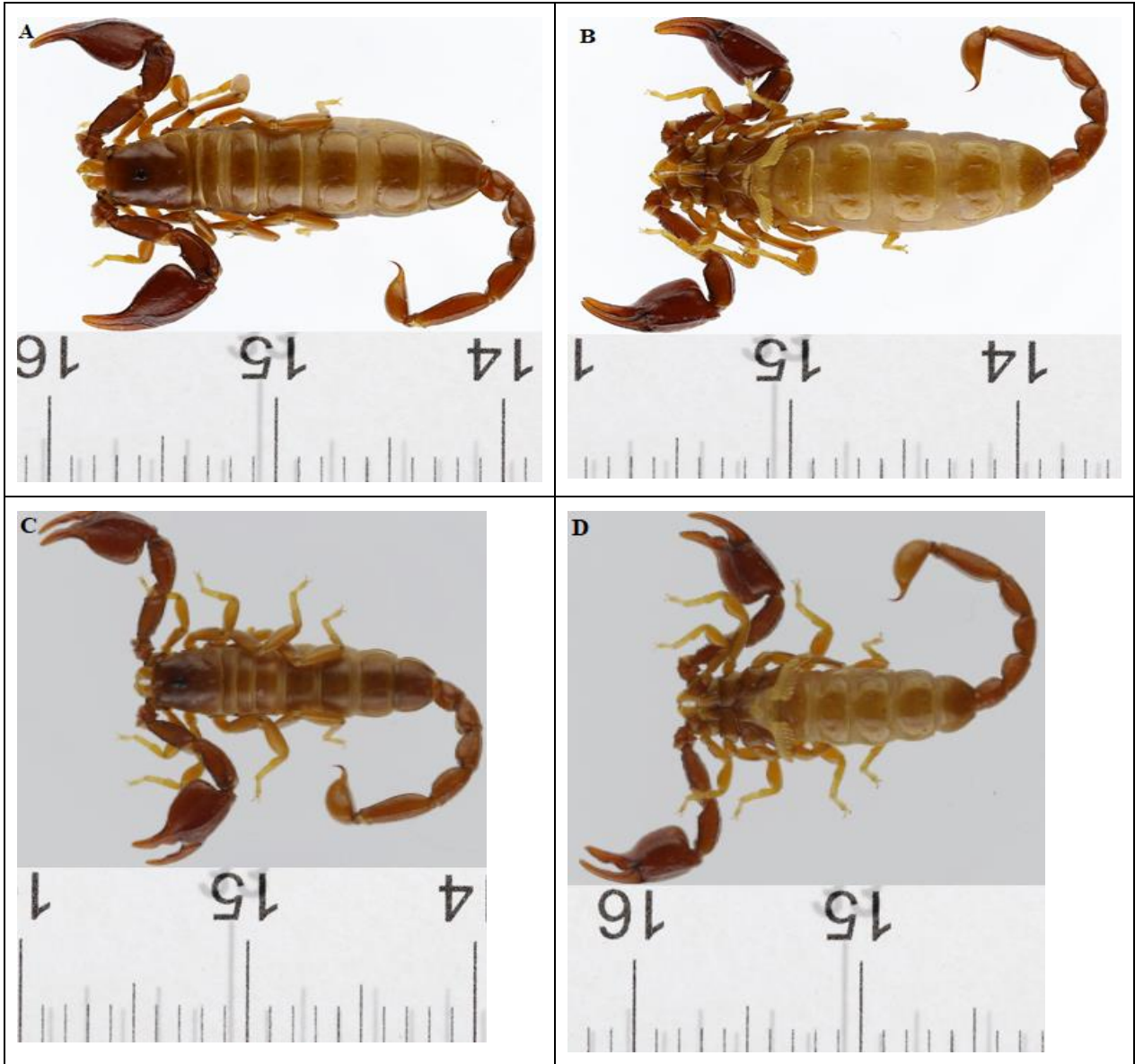


Figure 3.3. A. Dorsal, B. Ventral View in Female, C. Dorsal, D. Ventral View in Male *Euscorpilus arikani*

Euscorpilus avcii, Tropea, Yağmur, Koç, Yeşilyurt & Rossi, 2012 [12]

Material Examined: Aydın: Dilek Peninsula National Park, 22 (7♂♂, 15♀♀, 13 July 2010); Aydın: Dilek Peninsula National Park, 4 (2♂♂, 2♀♀, 07 May 2011); Aydın: Kuşadası, Davutlar, Güzel Çamlı N., 37° 41' 22" N, 27° 13' 31" E, 311 m. 15 (4♂♂, 11♀♀, 07 June 2011)

Bioecological Notes: *Euscorpilus avcii* was collected from under stones in the pine forest. In addition, it has been detected in the field studies carried out at night while waiting in rock cracks and cavities in the soil in rocky areas. It has been observed that they are

generally active during the cooler times of the year. In addition, their habitats are in regions that are constantly humid throughout the year. For this reason, they have been detected locally only in regions such as valleys, canyons, and high mountains.

Distribution in Turkey: Aydın.

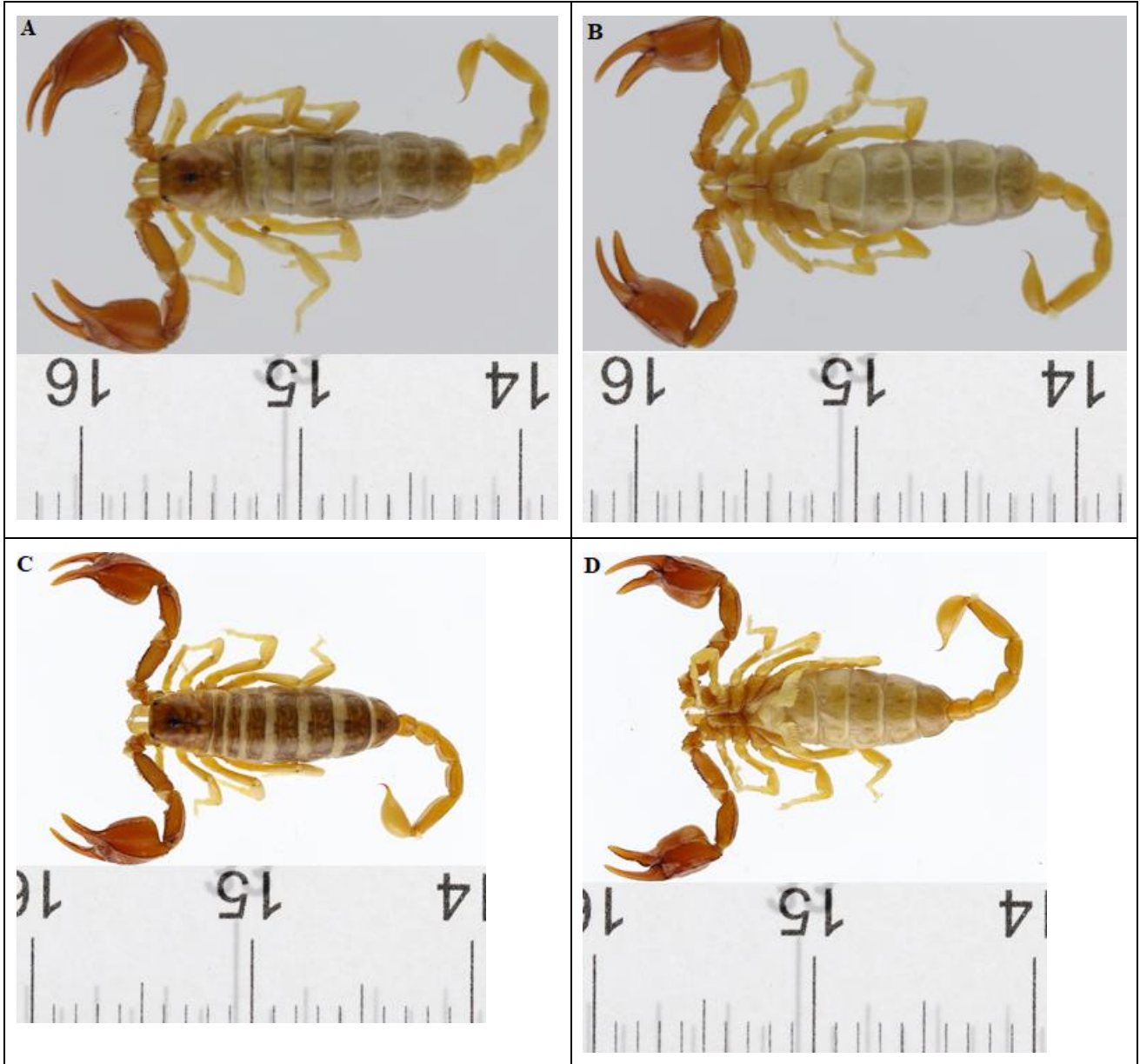


Figure 3.4. A. Dorsal, B. Ventral View in Female, C. Dorsal, D. Ventral View in Male *Euscorpium avcii*

Euscorpium gocmeni, Tropea, Yağmur and Yeşilyurt, 2014 [15]

Material Examined: Antalya: Akseki, Murtiçi, 36° 51' 54" N, 31° 45' 04" E. 493 m. 8 (6♂♂, 2♀♀, 01 September 2011).

Bioecological Notes: *Euscorpium gocmeni* was collected from under stones in the pine forest. In addition, it has been detected in the field studies carried out at night while waiting in rock cracks and cavities in the soil in rocky areas. It has been observed that they are generally active during the cooler times

of the year. In addition, their habitats are in regions that are constantly humid throughout the year. For this reason, they have been detected locally only in regions such as valleys, canyons and high mountains.

Distribution in Turkey: Antalya.



Figure 3.5. A. Dorsal, B. Ventral View in Female, C. Dorsal, D. Ventral View in Male *Euscorpium gocmeni*

E. honazicus, Tropea, Yağmur, Karampatsou, Parmakelis & Yeşilyurt, 2016a [21]

Material Examined: Denizli: Honaz Mountain, 37° 44' 16" N, 29° 15' 47" E, 871 m. 17 (5♂♂, 12♀♀, 17 October 2009); Denizli: Honaz Mountain Second Station, 37° 43' 50" N, 29° 14' 52" E, 1161 m. 3 (3♂♂, October 17, 2009); Burdur: Salda Lake Side, Yeşilova 5. km, 37° 30' 32.2" N, 29° 41' 58.4" E, 1168 m. 8 (7♂♂, 1♀, 16 October 2009)

Bioecological Notes: *Euscorpium honazicus* was collected from under stones in the pine forest. In addition, it has been detected in the field studies carried out at night while waiting in rock cracks and

cavities in the soil in rocky areas. It has been observed that they are generally active during the cooler times of the year. In addition, their habitats are in regions that are constantly humid throughout the year. For this reason, they have been detected locally only in regions such as valleys, canyons and high mountains.

Distribution in Turkey: Denizli and Burdur. This species was recorded from Burdur province for the first time.



Figure 3.6. A. Dorsal, B. Ventral View in Female, C. Dorsal, D. Ventral View in Male *Euscorpius honazicus*

Euscorpius lycius, Yağmur, Tropea and Yeşilyurt, 2013a [13]

Material Examined: Muğla: Fethiye, Faralya N., 36° 29' 37" N, 29° 08' 07" E, 349 m. 12 (5♂♂, 7♀♀, May 30, 2011)

Bioecological Notes: *Euscorpius lycius* was collected from under stones in the pine forest. In addition, it has been detected in the field studies carried out at night while waiting in rock cracks and cavities in the soil in

rocky areas. It has been observed that they are generally active during the cooler times of the year. In addition, their habitats are in regions that are constantly humid throughout the year. For this reason, they have been detected locally only in regions such as valleys, canyons and high mountains.

Distribution in Turkey: Antalya and Muğla.

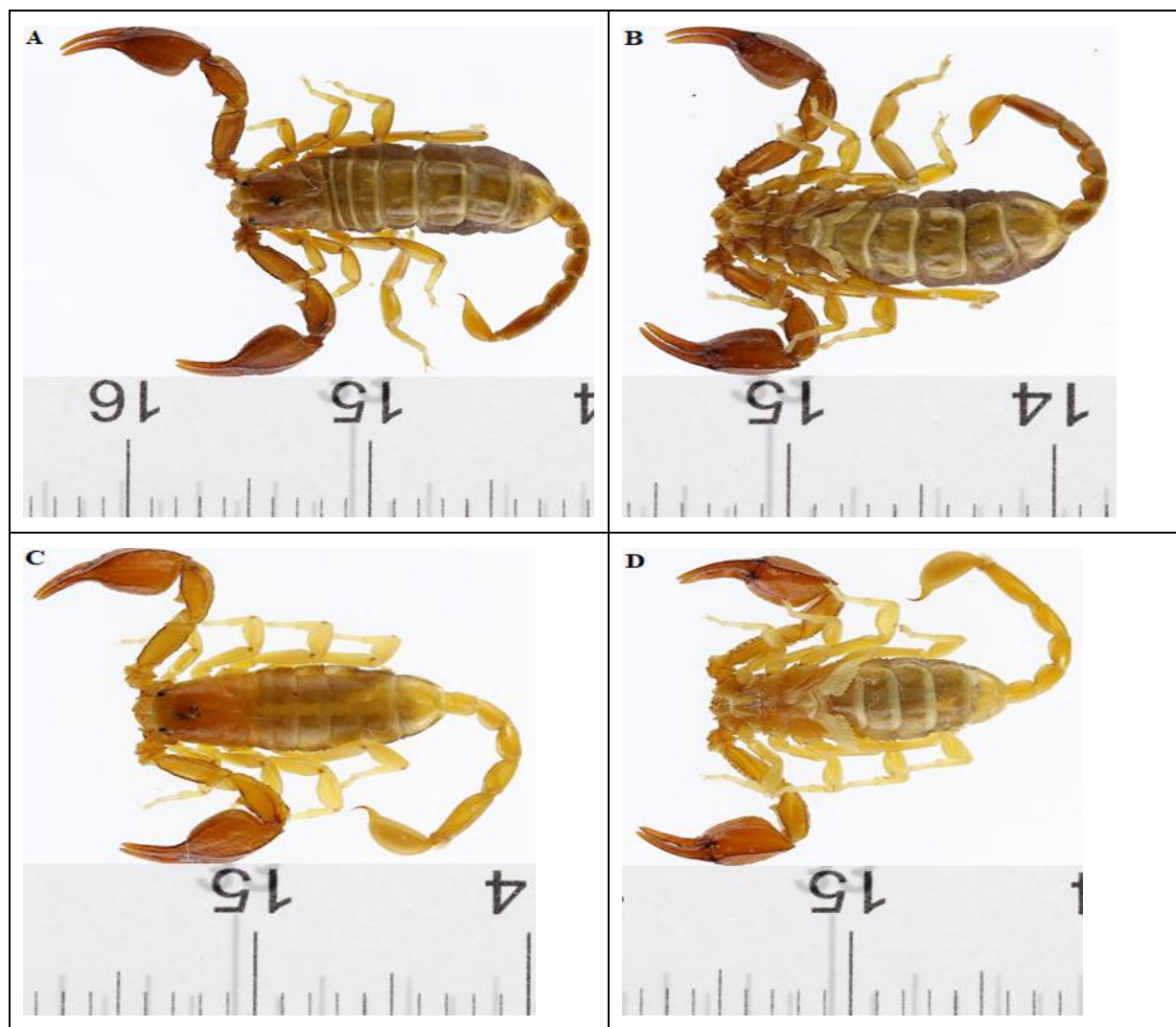


Figure 3.7. A. Dorsal, B. Ventral View in Female, C. Dorsal, D. Ventral View in Male *Euscorpium lycius*

Euscorpium sultanensis, Tropea and Yağmur, 2016a [19]

Material Examined: Isparta: Davraz Mountain, 37° 47' 14" N, 30° 44' 52" E, 44% humidity, 1838 m. 8 (6♂♂, 2♀♀, 09 August 2009)

Bioecological Notes: *Euscorpium sultanensis* was collected from under stones in the pine forest. In addition, it has been detected in the field studies carried out at night while waiting in rock cracks and cavities in the soil in rocky areas. It has been observed

that they are generally active during the cooler times of the year. In addition, their habitats are in regions that are constantly humid throughout the year. For this reason, they have been detected locally only in regions such as valleys, canyons and high mountains.

Distribution in Turkey: Sultan Mountains and Davraz Mountain, Isparta. This species was recorded from Isparta province for the first time.

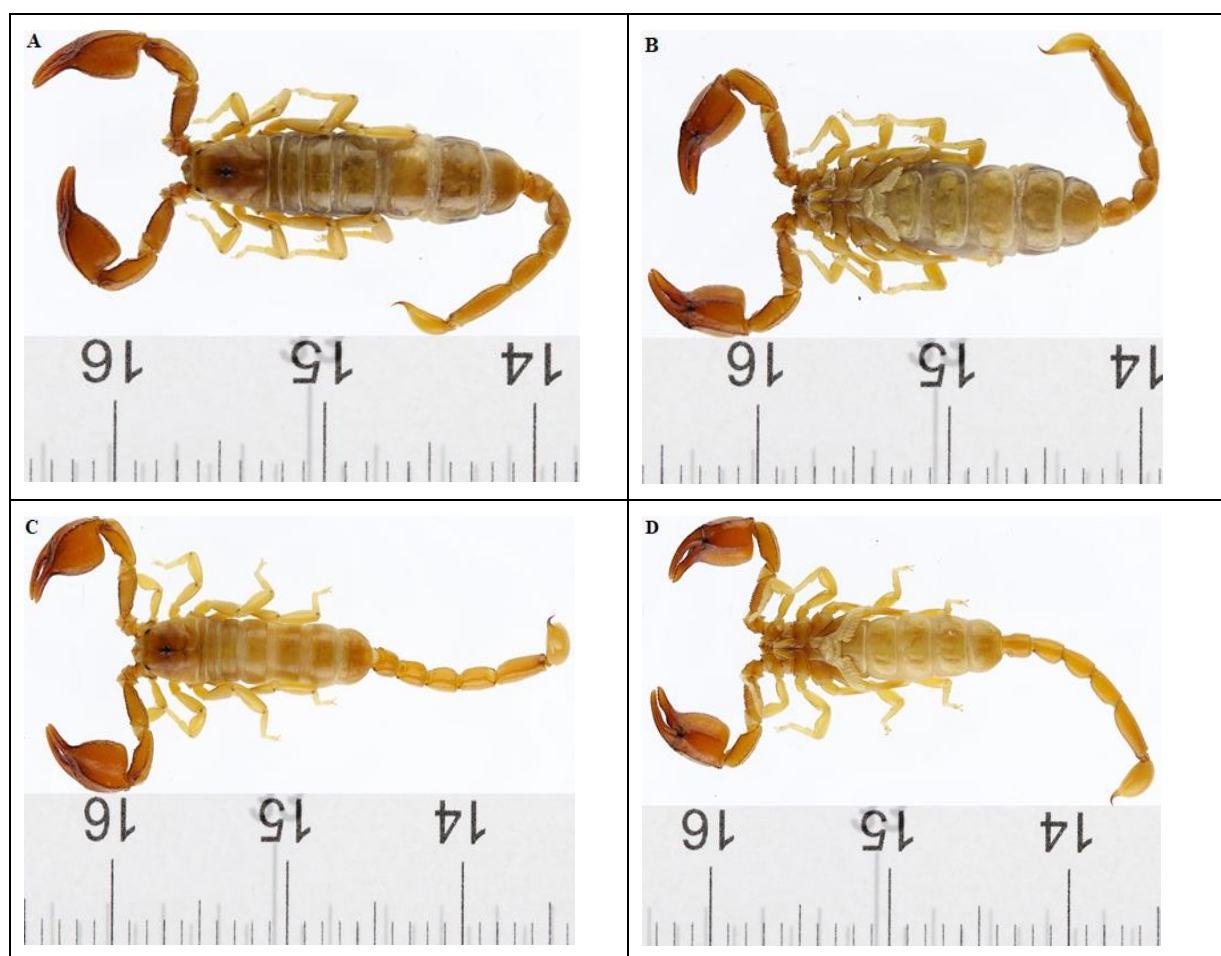


Figure 3.8. A. Dorsal, B. Ventral View in Female, C. Dorsal, D. Ventral View in Male *Euscorpis sultanensis*

Familiya: Iuridae Thorell, 1876 [34]

Genus: *Neocalchas* Yağmur et al. 2013b [14]

Neocalchas gruberi Fet, Soleglad et Kovařík, 2009 [9]

Material Examined: Antalya province, Kemer district, Botanik Restaurant, Tekirova, 1 (1♂, September 12, 2010); Isparta province, Eğirdir, Kırıntı, 1 (1♀, 14 May 2010); Antalya province, Kemer, Küçük Çaltıcak Beldibi, 36° 47' 42.8" N, 30° 34' 21.6" E, 62% humidity 7 m. 1 (1♀, 14 March 2009), Antalya province, Kesboğazi National Park, Forest Area 1 (1♀, 12 May 2010); Antalya province, Tekirova, Woodland 2 (1♀, 1♂, 12 May 2010); Isparta province, Eğirdir, Kırıntı, route to Antalya road 1 (1♂, 14 May 2010); Antalya province, 1.5 km west of Camyuva Town, 36° 31' 54.8" N, 30° 31' 14.4" E., 3 (3♂♂, 15 March 2009); Antalya province, Kemer, Küçük Çaltıcak, Beldibi, 36° 47' 42.8" N, 30°

34' 21.6" E, 62% humidity 7 m. 2 (2♀♀, March 14, 2009); Antalya province, Küçük Çaltıcak Center, 36° 47' 42.4" N, 30° 34' 21.3" E. 18 m. 2 (1♂, 1♀, April 30, 2011); Antalya province, Kemer, Olympos road junction 0.5 km 36° 26' 07.4" N, 30° 25' 42.3" E. 382 m. 1 (1♂, April 03, 2011); Antalya province, Küçük Çaltıcak, 4 (4♂♂, 02 May 2006); Antalya province, Kemer, Goynuk Canyon, 1 (1♂, 04 August 2011); Antalya province, Akseki, Murtiçi, 36° 51' 54" N, 31° 45' 04" E. 493 m. 5 (3♂♂, 2♀♀, 01 September 2011).

Bioecological Notes: *Neocalchas gruberi* was gathered from under rock and stones in pine forests and in bushes. It was also detected in the field studies carried out at night on limestone cliffs. It has been observed that they are generally active during the cooler times of the year. For this reason, it can be found mostly between March and June when the season is humid and the air temperature is low.

Distribution in Turkey: Antalya, Mersin and Isparta province. *Neocalchas gruberi* is recorded for the first time from Isparta.



Figure 3.9. A. Dorsal, B. Ventral View in Female, C. Dorsal, D. Ventral View in Male *Neocalchas gruberi*

Familya: Iuridae Thorell, 1876 [34]

Genus: *Metaiurus* Parmakelis, Dimitriadou, Gkigkiza, Karampatsou, Stathi, Fet, Yagmur & Kovarik, 2022 [2]

Metaiurus kadleci Kovarik, Fet, Soleglad et Yağmur, 2010 [10]

Material Examined: Antalya province, Alanya district, İncekum town, nameless little cave, 1 (1♀, 20 March 2009).

Bioecological Notes: The only specimen in this study was found inside the cave. Kovarik et al. (2010) reported this species from scrub areas near the pine forest. They also reported an example from inside the cave. Probably this species, like *Neocalchas gruberi*, prefers cool times and tends to hide in caves.

Distribution in Turkey: Antalya & Mersin.

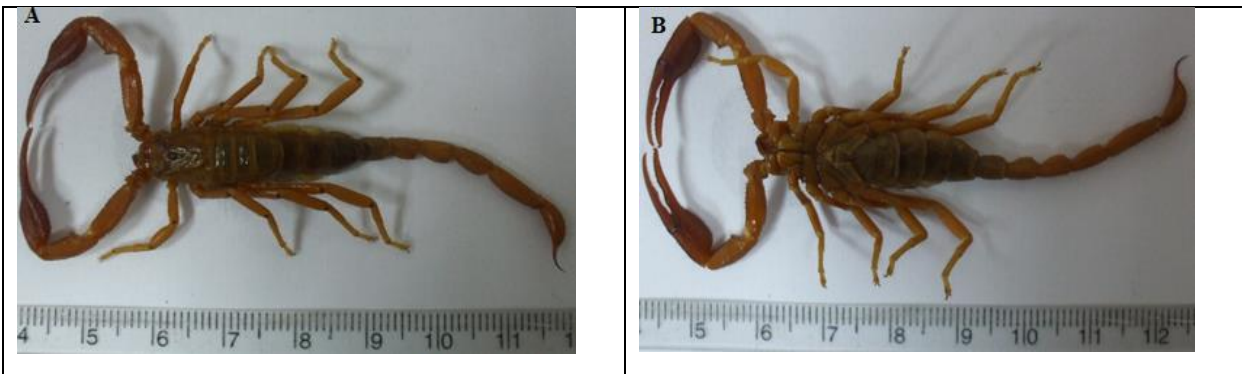


Figure 3.10. A. Dorsal View B. Ventral View in Female *Metaiurus kadleci*

Familya: Iuridae Thorell, 1876 [34]

Genus: *Iurus* Thorell, 1876 [34]

Iurus kinzelbachi Kovařík, Fet, Soleglad et Yağmur, 2010 [10]

Material examined: Aydın province, Dilek Peninsula National Park, 4 (2♂♂, 2♀♀, 13 July 2010); Aydın province, Kuşadası, Davutlar, 25 (17♀♀, 8♂♂, 1 June 2011).

Bioecological Notes: *Iurus kinzelbachi* specimens were collected from pine forest edges and limestone cliffs during nighttime fieldwork. As with other *Iurus* species, it has been observed that this species prefers warm seasons. In the field studies, it has been observed that this species tends to hide in crevices under large stones and in rock cracks.

Distribution in Turkey: Aydın.



Figure 3.11. A. Dorsal, B. Ventral View in Female, C. Dorsal, D. Ventral View in Male *Iurus kinzelbachi*

Familiya: Iuridae Thorell, 1876 [34]

Genus: *Anatoliurus* Parmakelis, Dimitriadou, Gkigkiza, Karamatsou, Stathi, Fet, Yagmur & Kovarik, 2022 [2]

Anatoliurus kraepelini von Ubisch, 1922 [4]

Material Examined: Antalya province, Kemer road, under the Botanic Restaurant, 3 (1♂, 2♀♀, 21 May 2006); Antalya province, Korkuteli road 35. km, 3 (3♀♀, 16 May 2010); Antalya province, Kemer, Botanic Restaurant, 1 (1♀, 12 May 2010); Antalya province, 3 km ahead of Serik, 1 (1♂, 12 May 2010); Antalya province, Kemer, Beldibi, 36° 47' 42.8" N, 30° 34' 21.6" E, 7 m Humidity 62.2 % 2 (2♀♀, 14 March 2009); Isparta province, Egirdir, Kırıntı Village, 1 (1♂, 14 May 2010); Isparta province, 5 km ahead of Isparta-Antalya Road Kazak 1 Tunnel, 1 (1♀, 14 May 2010); Muğla province, between Fethiye-Göcek 1 picnic area with daily diary, 35° 40' 65" N, 68° 05' 13" E., 1 (1♂, 10 April 2011); Antalya province, Kemer-Kumluca Road, 4 km inside the Tahtalı Mountain junction, 1 (1♂, 24 April 2011); Antalya province, Küçük Çaltıcak Center, 36° 47' 42.4" N, 30° 34' 21.3" E, 18 m., 1 (1♂, 30 April 2011); Antalya province, Kemer, Olympos Road junction 0.5 km, 36° 26' 07.4" N, 30° 25' 42.3" E, 382 m., 1 (1♂,

03 April 2011); Isparta province, 5 km south of Kovada Lake junction, 37° 38' 01" N, 30° 51' 41" E, 405 m. 18 (10♂♂, 8♀♀, 11 May 2011); Muğla province, Fethiye, Faralya N., 36° 29' 37" N, 29° 08' 07" E, 349 m., 2 (1♂, 1♀, 30 May 2011); Antalya province, Kemer, Lycian way, Göynük Canyon, 36° 41' 18" N, 30° 31' 33" E, 121 m., 22 (10♂, 12♀♀, 04 July 2011); Denizli province, Serinhisar, 3 km south of Altınyayla, 1 (1♀, 08 July 2011); Antalya province, Elmalı, 2 km south of Gömücü Village, 36° 24' 22" N, 29° 42' 02" E, 970 m., 2 (2♀♀, 09 July 2011); Antalya province, Akseki, 12 km south, 5 (5♀♀, 09 July 2011).

Bioecological Notes: *Anatoliurus kraepelini* was gathered from under rocks in pine forests and in bushes. It was also detected in the field studies carried out at night on limestone cliffs. It has been observed that they tend to hide in rock cracks and sometimes in some cavities in the soil during field studies carried out at night. They have been found to be intensely active during the warmer times of the year.

Distribution in Turkey: Antalya, Isparta, Konya, Mersin, Muğla, Denizli. This species is determined for the first time from Isparta and Denizli provinces.



Figure 3.12. A. Dorsal, B. Ventral View in Female, C. Dorsal, D. Ventral View in Male *Anatoliurus kraepelini*

4. Conclusion and Suggestions

In this article, specimens collected from 6 provinces in the Southwest of Turkey were examined, and 11 species were identified in 6 genera belonging to 3 families: *Aegeabuthus gibbosus*, *Anatoliurus kraepelini*, *Euscorpius arikani*, *E. avcii*, *E. gocmeni*, *E. honazicus*, *E. lycius*, *E. sultanensis*, *Iurus kinzelbachi*, *Metaiurus kadleci*, and *Neocalchas gruberi* are spread in the research area of Turkey.

Neocalchas gruberi was determined from Isparta province, *Euscorpius arikani* was recorded from Muğla province, *E. honazicus* species was determined from Burdur province, *E. sultanensis* species was determined from Isparta province, *Anatoliurus kraepelini* was determined from Isparta and Denizli provinces, for the first time.

Scorpions have a total of 2748 species, according to current data worldwide [35]. According to recent contributions, there are 46 scorpion species in Turkey and 14 in the research area. The research area covers approximately 30 percent of the number of scorpion species in Turkey.

The research area is rich in scorpion species diversity. It has been an important thesis study in terms of shedding light on future studies. This study

will make valuable contributions to the scorpion systematics in Turkey after more detailed analyses with studies in other regions.

Acknowledgment

This publication is produced from the author's thesis study. I would like to thank Kırıkkale University Scientific Research Unit for supporting the author's thesis study with the research project numbered 2009-36.

I would like to thank Dr. Erkan Azizoğlu for his contributions in the preparation of the map.

Contributions of the authors

All work was done by the corresponding author. Since the second author is the thesis advisor of the corresponding author, it is included in the article in terms of ethics.

Conflict of Interest Statement

There is no conflict of interest between the authors.

Statement of Research and Publication Ethics

The study is complied with research and publication ethics

References

- [1] H. Arıkan, E. Akçiçek. Akrepler “Yaşayan Fosiller”, İzmir: Ege Üniversitesi Yayınları, İzmir No: 222, ss. 9-34, 2022.
- [2] A. Parmakelis, D. Dimitriadou, E. Gkigkiza, L. Karampatsou, I. Stathi, V. Fet, E., A. Yagmur, F. Kovarik. “The evolutionary history of the relict scorpion family Iuridae of the eastern Mediterranean”. *Molecular Phylogenetics and Evolution*, 177: 1-15, 2022.
- [3] F. Kovarik, V. Fet, B. Gantenbein, M. R. Graham, E. A. Yağmur, F. Šťáhlavský, N. M. Poverennyi & N. E. Novruzov. “A revision of the genus *Mesobuthus* Vachon, 1950, with a description of 14 new species (Scorpiones: Buthidae)”. *Euscorpius*, vol.2022, no.348, pp. 1–189, 2022.
- [4] M. von, Ubisch, “Über eine neue Jurus-Art aus Kleinasien nebst einigen Bemerkungen über die Funktion der Kämmen der Skorpione,” *Zool. Jahrb., Abt. Syst.*, vol. 44, no. 1-2, pp. 503-515, 1922.
- [5] E. Schenkel, “Einige Mitteilungen über Spinnentiere,” *Rev. Suisse Zool.*, vol. 54, no.1, pp. 13-16, 1947.
- [6] A. Brullé. “Des Animaux articulés. Scorpionides. In: Baron J. B. G. M. Bory de Saint Vincent (ed.), Expédition scientifique de Morée,” *Section des sciences physiques. Zoologie. Paris*, vol.3 no. 1, pp. 57-60, 1832.
- [7] M. Vachon. “Etudes sur les Scorpions. III (suite). Description des Scorpions du Nord de l’Afrique,” *Arch. Institut Pasteur d’Algérie*, vol. 28, no.2, pp. 152-216, 1950.
- [8] F. Kovarik, “Taxonomic reassessment of the genera *Lychas*, *Mesobuthus*, and *Olivierus*, with descriptions of four new genera (Scorpiones: Buthidae),” *Euscorpius*, vol. 288, pp. 1–27, 2019.
- [9] V. Fet, M. E. Soleglad and F. Kovarik, “Etudes on iurids, II. Revision of genus *Calchas* Birula, 1899, with the description of two new species (Scorpiones: Iuridae),” *Euscorpius*, vol. 82, pp. 1–72, 2009.
- [10] F. Kovarik, V. Fet, M. E. Soleglad and E. A. Yağmur, “Etudes on iurids, III. Revision of the genus *Iurus* Thorell, 1876 (Scorpiones: Iuridae), with a description of two new species from Turkey”, *Euscorpius*, vol. 95, pp. 1–212, 2010.
- [11] M. E. Soleglad, V. Fet, F. Kovarik. and E. A. Yağmur, “Etudes on iurids, V. Further revision of *Iurus* Thorell, 1876 (Scorpiones: Iuridae), with a description of a new genus and two new species,” *Euscorpius*, vol. 143, pp. 1–70, 2012.
- [12] G. Tropea, E. A. Yağmur, H. Koç, F. Yeşilyurt & A. Rossi. “A new species of *Euscorpius* Thorell, 1876 (Scorpiones, Euscorpiidae) from Turkey,” *ZooKeys*. Vol. 219, pp. 63-80, 2012.
- [13] E. A. Yağmur, G. Tropea & F. Yeşilyurt. “A new species of *Euscorpius* Thorell, 1876 (Scorpiones, Euscorpiidae) from south western Turkey,” *ZooKeys*, vol. 348, pp. 29–45, 2013a.
- [14] E. A. Yağmur, M. E. Soleglad, V. Fet & F. Kovarik. “Etudes on iurids, VI. Further revision of *Calchas* Birula, 1899 (Scorpiones: Iuridae), with a description of a new genus and two new species,”. *Euscorpius*, vol. 159, pp. 1–37, 2013b.
- [15] G. Tropea, E. A. Yağmur & F. Yeşilyurt. “A new species of *Euscorpius* Thorell, 1876 (Scorpiones, Euscorpiidae) from the Antalya Province, Southern Turkey,” *Euscorpius*, vol.184, pp. 1–13, 2014.
- [16] E. A. Yağmur & G. Tropea. “A new species of *Euscorpius* Thorell, 1876 from southwestern Turkey (Scorpiones: Euscorpius).” *Arachnida*, vol. 3, pp. 14–26, 2015.
- [17] E. A. Yağmur, M. E. Soleglad, V. Fet & F. Kovarik. “Etudes on iurids, VIII. A new *Protoiurus* species from the Hidirellez Cave in Antalya, Turkey (Scorpiones: Iuridae),” *Euscorpius*, vol.200, pp. 1–25, 2015a.
- [18] E. A. Yağmur, F. Kovarik, V. Fet, M. E. Soleglad & F. Yeşilyurt. “Etudes on iurids, IX. Further analysis of a rare species *Protoiurus kadleci* (Scorpiones: Iuridae) from Turkey, based on adult males,” *Euscorpius*, vol. 201, pp. 1-18, 2015b.
- [19] G. Tropea & E. A. Yağmur. “A new species of *Euscorpius* Thorell, 1876 from the Sultan Mountains in western Turkey (Scorpiones: Euscorpiidae),” *Arachnida*, vol. 6, pp. 32–43, 2016a.
- [20] G. Tropea & E. A. Yağmur. “Two New Species of *Euscorpius* Thorell, 1876 from Southern Turkey (Scorpiones: Euscorpiidae),” *Euscorpius*, vol. 234, pp. 1-19, 2016b.
- [21] G. Tropea, E. A. Yağmur, L. Karampatsou, A. Parmakelis & F. Yeşilyurt. “A new species of *Euscorpius* Thorell, 1876 from Mount Honaz in southwestern Turkey (Scorpiones: Euscorpiidae),” *Euscorpius*, vol. 222, pp. 1–14, 2016a.

- [22] G. Tropea, E. A. Yağmur, A. Parmakelis & K. B. Kunt. “Another new species of *Euscorpius* Thorell, 1876 from the Taurus Mountains in Antalya Province, Southern Turkey (Scorpiones: Euscorpiidae),” *Euscorpius*, vol. 231, pp. 1–15, 2016b.
- [23] E. A. Yağmur. “On R. Kinzelbach’s euscorpiid specimens from Turkey deposited in the Naturhistorisches Museum Mainz, Germany (Scorpiones: Euscorpiidae),” *Euscorpius*, vol. 334, pp. 1-5, 2021a.
- [24] S. Cain, E. Gefen and L. Prendini. “Systematic Revision of the Sand Scorpions, Genus *Buthacus* Birula, 1908 (Buthidae C.L. Koch, 1837) of the Levant, with Redescription of *Buthacus arenicola* (Simon, 1885) from Algeria and Tunisia,” *Bulletin of the American Museum of Natural History*, vol. 450, p. 134, 2021.
- [25] A. A. Birula. Arthrogastric Arachnids of Caucasia, I: Scorpions, Ann. Caucasian Museum, Tiflis, A 5, 253 pp. [in Russian], English translated by J. Salkind, Edited by E. Rabinovitz, Israel Program for Scientific Translation, No. 1206, Jerusalem, 1964, v+170 pp, 1917a.
- [26] A. A. Birula. Fauna of Russia and Adjacent Countries: Arachnoidea, Vol. I, Scorpions, No. 1, in: Petrograd, xx+224 pp. [in Russian], English translated by B. Munitz, Edited by E. Rabinovitz, Israel Program for Scientific Translation, Jerusalem, 1965, xix+154 pp, 1917b.
- [27] R. Kinzelbach. “Die Skorpione der Ägäis: Beiträge zur Systematik, Phylogenie und Biogeographie, The Aegean Scorpions,” *Zool. Jb. Syst. Bd.*, vol.102, pp. 12-50, 1975.
- [28] O. F. Francke. “Scorpions of the genus *Diplocentrus* from Oaxaca, Mexico (Scorpionida, Diplocentridae),” *Journal of Arachnology*, vol. 4, pp. 145-200, 1977.
- [29] J. T. Hjelle. Anatomy and morphology. Pp. 9– 63 In: Polis G.A. (ed.). *The Biology of Scorpions*. Stanford, CA: Stanford University Press, 587 pp, 1990.
- [30] M. Vachon. “Etude des caractères utilisés pour classer les familles et les genres de scorpions (Arachnides). 1. La trichobothriotaxie en arachnologie. Sigles trichobothriaux et types de trichobothriotaxie chez les scorpions,” *Bulletin du Muséum National d’Histoire naturelle*, Paris. Vol. 140, pp. 859-958, 1974.
- [31] C. L. Koch. *Die Arachniden*. Nürnberg: C. H. Zeh’sche Buchhandlung, 4(1–5): 1–108, 1837.
- [32] E.A. Yağmur, *Scorpions of Gaziantep (Ordo: Scorpiones) and Their Zoogeographic Distributions*. Master Thesis, Gaziantep University, Gaziantep, 2005.
- [33] M. Laurie. Notes on the anatomy of some scorpions, and its bearing on the classification of the order. *Annals and Magazine of Natural History Ser.* Vol.6, no.17, pp. 185-194, 1896.
- [34] T. Thorell. “On the classification of scorpions,” *Annals and Magazine of Natural History*, vol. 4, no. 17, pp. 1–15, 1876.
- [35] J. O. Rein, “The Scorpion Files”, [www.ub.ntnu.no/scorpion-files/], Erişim tarihi: 28.12.2022.

Application of Intuitionistic Fuzzy Topological Operators in Spatial Objects Modeling

Sinem YILMAZ TARSUSLU^{1*}

¹ Department of Natural and Mathematical Sciences,
Faculty of Engineering, Tarsus University, 33400, Tarsus, Turkey.
(ORCID: 0000-0001-9192-7001)



Keywords: Intuitionistic Fuzzy Sets, Intuitionistic Fuzzy Topological Operators, Spatial Objects Modeling..

Abstract

The concept of topology is widely used in mathematical modeling of spatial objects and in GIS. One such application of fuzzy topological operators, detecting areas affected by Mikania micrantha, was studied by Shi and Liu. The precision of the results was evaluated by applying the intuitionistic fuzzy pre-interior and pre-clouser operators defined by the author to the data included in this study.

With this application example, it has been shown that the newly defined operators give results closer to the real bounds.

1. Introduction

The most important step for modeling real-world problems is to determine the topological relationships of spatial objects. Topological concepts are used in the analysis of spaces with uncertain boundaries, such as rivers, forests, oceans etc. The boundary determined by the crisp set topology are not suitable for the evaluation of problems involving uncertainty. On the other hand, fuzzy topology allows the definition of uncertainty in these spatial objects. Zadeh (1965) introduced the concept of the fuzzy set as an generalization of crisp set and the theory of fuzzy topology has been developed in following years. Some models have been developed by researchers to modelling the fuzzy relationship between spatial objects. Initially, the interior, boundary and exterior of spatial objects are determined. In the next step, fuzzy membership functions are defined to determine the membership degrees of these topological concepts. Since fuzzy topological concepts depend only on membership degrees, they are not sufficient to rank the hesitation relationships of objects. Intuitionistic fuzzy sets, introduced by Atanassov in 1983, allowed to modelling hesitation relationships of objects that contain uncertainty. Çoker defined the intuitionistic fuzzy topology in 1997[5]. Studies have been conducted by several authors to develop this concept.

The topology used in modeling real-world problems is based on identifying and using the common points of different spatial objects. The application of intuitionistic fuzzy topology on spatial objects was examined firstly by M.R. Malek[9]. In 2006, Saadati and Park examined properties of intuitionistic fuzzy metric spaces[12]. Singh and Srivastava studied the separation axioms[14]. In 2020, Marinov and Atanassov defined pre-interior and pre-clouser intuitionistic fuzzy topological operators and showed that these operators can be applied to determine the topological relations of spatial objects[10]. Marinov presented a software implementation of the framework of intuitionistic fuzzy sets[11]. In [16], author introduced $I_{\alpha,\beta}^{\gamma,\omega}$ and $C_{\alpha,\beta}^{\gamma,\omega}$ intuitionistic fuzzy topological operators. In this paper an application of these operators is examined.

Atanassov introduced the concept of Intuitionistic Fuzzy Sets, form an extension of fuzzy sets by expanding the truth value set to the $L^* = \{(x_1, x_2) \in [0, 1]^2 : x_1 + x_2 \leq 1\}$ is a lattice with $(x_1, x_2) \leq (y_1, y_2) : \Leftrightarrow "x_1 \leq y_1 \text{ and } x_2 \geq y_2"$. The operator theory have an important role in intuitionistic fuzzy sets. The concept of intuitionistic fuzzy modal operators was given in 1999 by K. Atanassov and then modal operators have been extensively studied in theoretical and application areas[2, 3, 6, 7]. First

*Corresponding author: sinemtarsuslu@tarsus.edu.tr

Received: 16.03.2023, Accepted: 25.05.2023

intuitionistic fuzzy topological operators were defined and new intuitionistic fuzzy topological operators were introduced in subsequent studies[3, 8, 16]. Fuzzy pre-topological/topological operators and intuitionistic fuzzy pre-topological/topological operators were applied to compute of the values of fuzzy relations of spatial objects with uncertainty in determining the boundaries such as forest area, lake, sea, etc [10, 13, 16].

2. Material and Method

Definition[2] An intuitionistic fuzzy set (IFS) on a set X is an object

$A = \{ \langle x, \mu_A(x), \nu_A(x) \rangle : x \in X \}$ where $\mu_A(x), (\mu_A : X \rightarrow [0,1])$ is called the degree of membership of x in $A, \nu_A(x), (\nu_A : X \rightarrow [0,1])$ is called the degree of non- membership of x in A , and where μ_A and ν_A satisfy the following condition:

$$\mu_A(x) + \nu_A(x) \leq 1, \text{ for all } x \in X.$$

The class of intuitionistic fuzzy sets on X is denoted by $IFS(X)$. The hesitation degree of x is defined by $\pi_A(x) = 1 - \mu_A(x) - \nu_A(x)$.

Definition[2] An IFS A is said to be contained in an IFS B ($A \hat{\subseteq} B$) if and only if, for all $x \in X : \mu_A(x) \leq \mu_B(x)$ and $\nu_A(x) \geq \nu_B(x)$.

It is clear that $A = B$ if and only if $A \hat{\subseteq} B$ and $B \hat{\subseteq} A$.

Definition[2] Let $A \in IFS$ and let $A^c = \{ \langle x, \mu_A(x), \nu_A(x) \rangle : x \in X \}$ then the above set is called the complement of A

$$A^c = \{ \langle x, \nu_A(x), \mu_A(x) \rangle : x \in X \}$$

The intersection and the union of two IFSs A and B on X is defined by

$$A \cap B = \{ \langle x, \mu_A(x) \wedge \mu_B(x), \nu_A(x) \vee \nu_B(x) \rangle : x \in X \}$$

$$A \cup B = \{ \langle x, \mu_A(x) \vee \mu_B(x), \nu_A(x) \wedge \nu_B(x) \rangle : x \in X \}$$

Some special Intuitionistic Fuzzy Sets on X are defined as following;

$$O^* = \{ \langle x, 0, 1 \rangle : x \in X \}$$

$$X^* = \{ \langle x, 1, 0 \rangle : x \in X \}$$

Definition[1] An *pre*-closure operator $\mathbf{c} : \mathbf{X} \rightarrow \mathbf{X}$ is a map which associates to each set $A \in \mathbf{X}$ a set $\mathbf{c}(A)$ such that;

- 1) $\mathbf{c}(\emptyset) = \emptyset$
- 2) $A \subseteq \mathbf{c}(A)$
- 3) $\mathbf{c}(A \cup B) = \mathbf{c}(A) \cup \mathbf{c}(B)$, for all $A, B \subset X$.

If in addition to above axioms the operator \mathbf{c} is idempotent, that is $\mathbf{c}(A) = \mathbf{c}(\mathbf{c}(A))$ then \mathbf{c} is called closure operator in \mathbf{X} . \mathbf{X} can be $\wp(X), FS(X)$ or $IFS(X)$.

Definition[1] For the *pre*-closure operator \mathbf{c} defined on \mathbf{X} we say that a set $A \in \mathbf{X}$ is closed iff $\mathbf{c}(A) = A$. Also,

$$\tau^c = \{ A : A \in \mathbf{X} \ \& \ \mathbf{c}(A) = A \}$$

is the topology generated by the *pre*-closure operator \mathbf{c} . If \mathbf{X} is $\wp(X), FS(X)$ or $IFS(X)$ then τ is called crisp topology, fuzzy topology or intuitionistic fuzzy topology, respectively.

Definition[1] An *pre*-interior operator $\mathbf{i} : \mathbf{X} \rightarrow \mathbf{X}$ is a map which associates to each set $A \in \mathbf{X}$ a set $\mathbf{i}(A)$ such that;

1. $\mathbf{i}(\mathbf{X}) = \mathbf{X}$
2. $\mathbf{i}(A) \subseteq A$
3. $\mathbf{i}(A \cap B) = \mathbf{i}(A) \cap \mathbf{i}(B)$, for all $A, B \subset X$.

If in addition to above axioms the operator \mathbf{i} is idempotent, that is $\mathbf{i}(A) = \mathbf{i}(\mathbf{i}(A))$ then \mathbf{i} is called interior operator in \mathbf{X} . \mathbf{X} can be $\wp(X), FS(X)$ or $IFS(X)$.

Definition[1] For the *pre*-interior operator \mathbf{i} defined on \mathbf{X} we say that a set $A \in \mathbf{X}$ is open iff

$\mathbf{i}(A) = A$. Also, $\tau_i = \{A : A \in \mathbf{X} \ \& \ \mathbf{i}(A) = A\}$ is the topology generated by the *pre* – interior operator \mathbf{i} . If \mathbf{X} is $\wp(X)$, $FS(X)$ or $IFS(X)$ then τ is called crisp topology, fuzzy topology or intuitionistic fuzzy topology, respectively.

If \mathbf{i} is *pre* – interior operator then $\mathbf{c}(A) = \mathbf{-i}(\mathbf{-}A)$ is its corresponding *pre* – closure. That is $(\mathbf{c}(A), \mathbf{-i}(\mathbf{-}A))$ is a pair of conjugate preclosure-preinterior operators.

Proposition[1] If \mathbf{i} and \mathbf{c} is a conjugate pair of preinterior and preclosure operators in \mathbf{X} , then

$$\tau^c = \{\mathbf{-}A : A \in \tau_i\} \text{ and } \tau_i = \{\mathbf{-}B : B \in \tau^c\}.$$

In [10], Marinov and Atanassov generalized the *pre* – interior and *pre* – closure operators to intuitionistic fuzzy sets and they introduced new intuitionistic fuzzy topological operators. In the same paper, they examined topological properties of these operators. Then, author defined new generalized intuitionistic fuzzy topological operators by considering the operators defined by Marinov and Atanassov in [16].

Definition[16] Let X be a set and $A \in IFS(X)$. For $\alpha, \beta, \gamma, \omega \in [0,1]$, the topological operator $I_{\alpha, \beta}^{\gamma, \omega}$ is defined as follow;

$$I_{\alpha, \beta}^{\gamma, \omega} : IFS(X) \rightarrow IFS(X)$$

such that

$$\mu_{I_{\alpha, \beta}^{\gamma, \omega}(A)}(x) = \begin{cases} \inf \mu_A(x), & 0 \leq \mu_A(x) < \alpha\gamma(1-\beta) \\ (1-\beta)\mu_A(x), & \alpha\gamma(1-\beta) \leq \mu_A(x) < \alpha\gamma \\ \frac{1}{1-\gamma}(\mu_A(x) - \alpha) + \alpha, & \alpha\gamma \leq \mu_A(x) < \alpha \\ \mu_A(x), & \alpha \leq \mu_A(x) \leq 1 \end{cases}$$

and

$$v_{I_{\alpha, \beta}^{\gamma, \omega}(A)}(x) = \begin{cases} v_A(x), & 0 \leq v_A(x) < \beta\omega \\ \min\{(1-\omega)v_A(x) + \beta\omega, 1 - \mu_{I_{\alpha, \beta}^{\gamma, \omega}(A)}(x)\}, & \beta\omega \leq v_A(x) < \beta \\ v_A(x), & \beta \leq v_A(x) \leq 1 \end{cases}$$

Proposition[16] Let X be a set and $A \in IFS(X)$.

For $\alpha, \beta, \gamma, \omega \in [0,1]$, the topological operator $I_{\alpha, \beta}^{\gamma, \omega}(A)$ is an intuitionistic fuzzy set.

Proposition[16] Let X be a set and $A \in IFS(X)$. For $\alpha, \beta, \gamma, \omega \in [0,1]$, the operator $I_{\alpha, \beta}^{\gamma, \omega}(A)$ is a *pre* – interior operator in $IFS(X)$.

Definition[16] Let X be a set and $A \in IFS(X)$. For $\alpha, \beta, \gamma, \omega \in [0,1]$, the topological operator $C_{\alpha, \beta}^{\gamma, \omega}$ is defined as follow;

$$C_{\alpha, \beta}^{\gamma, \omega} : IFS(X) \rightarrow IFS(X)$$

such that

$$\mu_{C_{\alpha, \beta}^{\gamma, \omega}(A)}(x) = \begin{cases} \mu_A(x), & 0 \leq \mu_A(x) < \beta\omega \\ \min\left\{\begin{matrix} (1-\omega)\mu_A(x) + \beta\omega, \\ 1 - v_{C_{\alpha, \beta}^{\gamma, \omega}(A)}(x) \end{matrix}\right\}, & \beta\omega \leq \mu_A(x) < \beta \\ \mu_A(x), & \beta \leq \mu_A(x) \leq 1 \end{cases}$$

and

$$v_{C_{\alpha, \beta}^{\gamma, \omega}(A)}(x) = \begin{cases} \inf v_A(x), & 0 \leq v_A(x) < \alpha\gamma(1-\beta) \\ (1-\beta)v_A(x), & \alpha\gamma(1-\beta) \leq v_A(x) < \alpha\gamma \\ \frac{1}{1-\gamma}(v_A(x) - \alpha) + \alpha, & \alpha\gamma \leq v_A(x) < \alpha \\ v_A(x), & \alpha \leq v_A(x) \leq 1 \end{cases}$$

Proposition[16] Let X be a set and $A \in IFS(X)$. For $\alpha, \beta, \gamma, \omega \in [0,1]$, the topological operator $C_{\alpha, \beta}^{\gamma, \omega}(A)$ is an intuitionistic fuzzy set.

Proposition[16] Let X be a set and $A \in IFS(X)$. For $\alpha, \beta, \gamma, \omega \in [0,1]$, the operator $C_{\alpha, \beta}^{\gamma, \omega}(A)$ is a *pre* – closure operator in $IFS(X)$.

Proposition[16] The operator $I_{\alpha, \beta}^{\gamma, \omega}$ is generalization of the operator I_μ and the operator $C_{\alpha, \beta}^{\gamma, \omega}$ is generalization of the operator C_ν .

Theorem[16] Let X be a set and $A \in IFS(X)$ then $(C_{\alpha, \beta}^{\gamma, \omega}(A), \mathbf{-}I_{\alpha, \beta}^{\gamma, \omega}(\mathbf{-}A))$, i.e $I_{\alpha, \beta}^{\gamma, \omega}$ and $C_{\alpha, \beta}^{\gamma, \omega}$ is a conjugate pair of *pre* – interior and *pre* – closure operators. They define the same topology

$$\tau_{I_{\alpha, \beta}^{\gamma, \omega}} = \left\{ \mathbf{-}B : B \in \tau_{C_{\alpha, \beta}^{\gamma, \omega}} \right\}.$$

The boundary of set A in the intuitionistic fuzzy topology defined by these operators is

$$\partial A = C_{\alpha, \beta}^{\gamma, \omega}(A) \cap (\mathbf{-}I_{\alpha, \beta}^{\gamma, \omega}(\mathbf{-}A)) \text{ according to the IF boundary definition given by Malek[9].}$$

Intuitionistic fuzzy generators are used to construct IFS and they are defined as a function:

Definition[4] A function $\phi : [0,1] \rightarrow [0,1]$ will be called intuitionistic fuzzy generator(IFG) if $\phi(x) \leq 1 - x$ for all $x \in X$.

3. Results and Discussion

In this study, the problem of detecting areas affected by Mikania micrantha, examined by Shi and Liu[13], is re-examined using intuitionistic fuzzy topological operators, *pre* – interior and *pre* – closure.

Methodology

- (i) Aerial photographs of the studied area are viewed as intuitionistic fuzzy spaces.
- (ii) Areas affected by Mikania micrantha in the aerial photo are viewed as intuitionistic fuzzy sets in each of intuitionistic fuzzy spaces.
- (iii) The membership and non-membership values of affected areas are calculated.
- (iv) The fuzzy value is defined by

$$\mu_A(x) = \begin{cases} \frac{\log(\text{Area of certain affected area})}{\log(\text{Total area of affected area})} & \text{if } \frac{\log(\bullet)}{\log(\ast)} > 0 \\ 0 & \text{otherwise} \end{cases}$$

(v) From Sugeno's generator, the intuitionistic fuzzy non-membership function is given as[15]:

$$\nu_A(x) = \frac{1 - \mu_A(x)}{1 + \lambda \mu_A(x)}, \quad \lambda \text{ is computed using}$$

intuitionistic fuzzy entropy(IFE) which is given as:

An important intuitionistic fuzzy generator is defined by Sugeno as following and implemented in the example examined in this study:

$$A_\lambda = \left\{ \left(x, \mu_A(x), \frac{1 - \mu_A(x)}{1 + \lambda \mu_A(x)} \right) : x \in X \right\}$$

$$IE(A) = \frac{1}{N} \sum_{j=1}^N \sum_{i=1}^N \pi_A(x_{ij}) e^{1 - \pi_A(x_{ij})},$$

and the optimum value of λ is computed as: $\lambda_{opt} = \max_\lambda (IE(A, \lambda))$. In this example, $h = 0.5$ was chosen.

Results and Analysis

Each Mikania micrantha area has an identity number and its boundary has been digitized on the aerial photos by Shi and Liu. Table 1 shows the size of each area affected by Mikania micrantha on an aerial photo[13].

In Table2, membership and non-membership degrees of areas were calculated, pre-interior, pre-closure and boundary values obtained: for

This method offers a suitable classification for modeling spatial objects that do not have clear boundaries. While fuzzy topological operators only make a classification over membership degrees, the operators used here provide a classification based on the non-membership degrees and hestigation degrees of spatial objects. Thus, an evaluation much closer to the real bounders is obtained. For different values of provide different values of interior, boundary, and exterior

Table 1. Size of Each Area Affected by Mikania Micrantha

ID	Area	ID	Area	ID	Area
1	7,97	19	60,5	37	195,46
2	8,17	20	61,97	38	265,48
3	8,8	21	63,86	39	293,35
4	10,23	22	73,64	40	312,6
5	10,37	23	73,83	41	315,02
6	15,32	24	76,67	42	343,49
7	17,09	25	77,1	43	349,76
8	17,52	26	82,68	44	388,28
9	24,75	27	85,58	45	401,55
10	25,12	28	87,16	46	403,61
11	28	29	93,8	47	498,05
12	31,69	30	104,38	48	564,57
13	31,92	31	105,35	49	629,68
14	36,75	32	135,05	50	774,58
15	37,83	33	142,95	51	786,1
16	42,46	34	155,6	52	855,94
17	53,36	35	184,86	53	1014,44
18	57,1	36	192,21		195,46
				Total	10713,58
				Average	202,14

Table 2. $\alpha = 0.6, \beta = 0.5, \gamma = 0.7$ and $\omega = 0,3$

ID	Area	μ_{Area}	ν_{Area}	$\mu_{C_{\alpha,\beta}^{\gamma,\omega}}$	$\nu_{C_{\alpha,\beta}^{\gamma,\omega}}$	$\mu_{C_{\alpha,\beta}^{\gamma,\omega}}$	$\nu_{C_{\alpha,\beta}^{\gamma,\omega}}$	μ_{β}	ν_{β}
1	7,97	0,223691	0,698217	0,111845	0,698217	0,301783	0,698217	0,301782849	0,698217151
2	8,17	0,226362	0,69498	0,113181	0,69498	0,30502	0,69498	0,305019876	0,694980124
3	8,8	0,234367	0,685325	0,117183	0,685325	0,314057	0,685325	0,314056724	0,685324606
4	10,23	0,250594	0,665963	0,125297	0,665963	0,325415	0,665963	0,325415487	0,665963382
5	10,37	0,252058	0,664229	0,126029	0,664229	0,326441	0,664229	0,32644086	0,664229345
6	15,32	0,294114	0,615389	0,147057	0,615389	0,35588	0,615389	0,355879553	0,615389176
7	17,09	0,305896	0,602025	0,152948	0,602025	0,364127	0,602025	0,364127406	0,602025085
8	17,52	0,308574	0,599007	0,154287	0,599007	0,366002	0,596689	0,366001984	0,596689036
9	24,75	0,345806	0,557756	0,172903	0,557756	0,392064	0,459188	0,392064136	0,459187891
10	25,12	0,347405	0,556014	0,173703	0,556014	0,393184	0,45338	0,393183535	0,453379758
11	28	0,359102	0,543341	0,179551	0,543341	0,401371	0,411135	0,401371478	0,411135078
12	31,69	0,372443	0,529038	0,186222	0,529038	0,41071	0,363461	0,410710326	0,363460961
13	31,92	0,373223	0,528208	0,186611	0,528208	0,411256	0,360693	0,411255856	0,360692641
14	36,75	0,388408	0,512134	0,194204	0,512134	0,421885	0,307113	0,421885339	0,307113324
15	37,83	0,391529	0,508855	0,195765	0,508855	0,42407	0,296184	0,424070312	0,296183984
16	42,46	0,403972	0,49587	0,201986	0,497109	0,43278	0,252898	0,432780268	0,252898438
17	53,36	0,428596	0,470563	0,208655	0,479394	0,450018	0,168542	0,450017541	0,168542478
18	57,1	0,435897	0,463158	0,05299	0,474211	0,455128	0,143861	0,455127848	0,143861371
19	60,5	0,44213	0,456872	0,073767	0,46981	0,459491	0,122905	0,459491066	0,122905233
20	61,97	0,444717	0,454272	0,082391	0,46799	0,461302	0,114238	0,461302085	0,114238461
21	63,86	0,447955	0,451026	0,093183	0,465718	0,463568	0,103419	0,463568422	0,10341853
22	73,64	0,463311	0,435746	0,144371	0,455022	0,474318	0,052486	0,455022097	0,144370614
23	73,83	0,463589	0,435471	0,145296	0,45483	0,474512	0,051571	0,454829908	0,145296621
24	76,67	0,467657	0,431457	0,158855	0,45202	0,47736	0,038189	0,452019651	0,158855285
25	77,1	0,468259	0,430863	0,160864	0,451604	0,477782	0,03621	0,451604039	0,160864346
26	82,68	0,475789	0,423469	0,185965	0,446429	0,483053	0,011565	0,446428572	0,18596491
27	85,58	0,479505	0,419838	0,198349	0,443887	0,485653	0,209919	0,443886738	0,209919099
28	87,16	0,481476	0,417916	0,20492	0,442541	0,487033	0,208958	0,442540981	0,208957843
29	93,8	0,489388	0,410231	0,231294	0,437161	0,492572	0,205115	0,437161463	0,231294323
30	104,38	0,500906	0,399131	0,269686	0,429392	0,500906	0,199565	0,429391578	0,269685726
31	105,35	0,501903	0,398175	0,273009	0,428722	0,501903	0,199087	0,428722445	0,273008566
32	135,05	0,528667	0,372791	0,362224	0,410954	0,528667	0,186396	0,410953984	0,36222428
33	142,95	0,534794	0,367056	0,382646	0,406939	0,534794	0,183528	0,406939493	0,382646093
34	155,6	0,543932	0,358554	0,413106	0,400988	0,543932	0,179277	0,400987656	0,413106002
35	184,86	0,562501	0,341462	0,475004	0,389024	0,562501	0,170731	0,38902364	0,47500391
36	192,21	0,566703	0,337629	0,48901	0,38634	0,566703	0,168815	0,386340482	0,489009952
37	195,46	0,56851	0,335985	0,495033	0,385189	0,56851	0,167992	0,38518931	0,495033139
38	265,48	0,601506	0,306356	0,601506	0,364449	0,601506	0,153178	0,364449175	0,601506486
39	293,35	0,612265	0,296858	0,612265	0,3578	0,612265	0,148429	0,357800406	0,612264547
40	312,6	0,619114	0,290851	0,619114	0,353596	0,619114	0,145426	0,353595715	0,619114008
41	315,02	0,619945	0,290124	0,619945	0,353087	0,619945	0,145062	0,35308704	0,619945077
42	343,49	0,629269	0,282003	0,629269	0,347402	0,629269	0,141001	0,347401991	0,629269291
43	349,76	0,631219	0,280312	0,631219	0,346219	0,631219	0,140156	0,346218505	0,631218712
44	388,28	0,642478	0,270596	0,642478	0,339417	0,642478	0,135298	0,339417103	0,642478171
45	401,55	0,6461	0,267488	0,6461	0,337242	0,6461	0,133744	0,337241768	0,646099721
46	403,61	0,646651	0,267016	0,646651	0,336911	0,646651	0,133508	0,336911057	0,646651166
47	498,05	0,669309	0,247772	0,669309	0,323441	0,669309	0,123886	0,323440707	0,669309356
48	564,57	0,682819	0,236453	0,682819	0,315517	0,682819	0,118227	0,315517194	0,682819464
49	629,68	0,694582	0,22669	0,694582	0,305418	0,694582	0,113345	0,305418036	0,694581964
50	774,58	0,716902	0,208398	0,716902	0,283098	0,716902	0,185017	0,283098473	0,716901527
51	786,1	0,718492	0,207106	0,718492	0,281508	0,718492	0,185017	0,2815075	0,7184925
52	855,94	0,727665	0,199683	0,727665	0,272335	0,727665	0,185017	0,272334764	0,727665236
53	1014,44	0,745974	0,185017	0,745974	0,254026	0,745974	0,185017	0,25402602	0,74597398

Table 3. $\alpha = 0.8, \beta = 0.2, \gamma = 0.3$ and $\omega = 0,6$

ID	Area	μ_{Area}	ν_{Area}	$\mu_{Y,\omega}_{\alpha,\beta}$	$\nu_{Y,\omega}_{\alpha,\beta}$	$\mu_{C,Y,\omega}_{\alpha,\beta}$	$\nu_{C,Y,\omega}_{\alpha,\beta}$	μ_a	ν_a
1	7,97	0,223691	0,698217	0,178952	0,698217	0,223691	0,654596	0,223690558	0,654595929
2	8,17	0,226362	0,69498	0,181089	0,69498	0,226362	0,649972	0,226361503	0,649971606
3	8,8	0,234367	0,685325	0,187493	0,685325	0,234367	0,636178	0,234366748	0,636178003
4	10,23	0,250594	0,665963	0,015134	0,665963	0,250594	0,608519	0,250593553	0,608519117
5	10,37	0,252058	0,664229	0,017226	0,664229	0,252058	0,606042	0,252058371	0,606041922
6	15,32	0,294114	0,615389	0,077305	0,615389	0,294114	0,53627	0,294113646	0,536270252
7	17,09	0,305896	0,602025	0,094138	0,602025	0,305896	0,517179	0,305896294	0,517178693
8	17,52	0,308574	0,599007	0,097963	0,599007	0,308574	0,512867	0,308574262	0,51286673
9	24,75	0,345806	0,557756	0,151151	0,557756	0,345806	0,453938	0,345805909	0,453937668
10	25,12	0,347405	0,556014	0,153436	0,556014	0,347405	0,451448	0,347405049	0,451448468
11	28	0,359102	0,543341	0,170146	0,543341	0,359102	0,433344	0,359102112	0,433343605
12	31,69	0,372443	0,529038	0,189205	0,529038	0,372443	0,412912	0,372443323	0,41291184
13	31,92	0,373223	0,528208	0,190318	0,528208	0,373223	0,411725	0,373222651	0,411725417
14	36,75	0,388408	0,512134	0,212011	0,512134	0,388408	0,388763	0,388407627	0,388762853
15	37,83	0,391529	0,508855	0,21647	0,508855	0,391529	0,384079	0,391529018	0,38407885
16	42,46	0,403972	0,49587	0,234245	0,49587	0,403972	0,365528	0,403971812	0,365527902
17	53,36	0,428596	0,470563	0,269424	0,470563	0,428596	0,329375	0,428596487	0,329375348
18	57,1	0,435897	0,463158	0,279853	0,463158	0,435897	0,318798	0,435896925	0,31879773
19	60,5	0,44213	0,456872	0,288757	0,456872	0,44213	0,309817	0,442130095	0,309816528
20	61,97	0,444717	0,454272	0,292453	0,454272	0,444717	0,306102	0,444717264	0,306102198
21	63,86	0,447955	0,451026	0,297078	0,451026	0,447955	0,301465	0,447954889	0,301465084
22	73,64	0,463311	0,435746	0,319016	0,435746	0,463311	0,279637	0,435745852	0,319015978
23	73,83	0,463589	0,435471	0,319413	0,435471	0,463589	0,279245	0,435471297	0,319412683
24	76,67	0,467657	0,431457	0,325224	0,431457	0,467657	0,273509	0,431456644	0,325223694
25	77,1	0,468259	0,430863	0,326085	0,430863	0,468259	0,272661	0,430862912	0,32608472
26	82,68	0,475789	0,423469	0,336842	0,423469	0,475789	0,262099	0,423469388	0,336842104
27	85,58	0,479505	0,419838	0,342149	0,419838	0,479505	0,256912	0,419838198	0,342149462
28	87,16	0,481476	0,417916	0,344966	0,417916	0,481476	0,254165	0,417915687	0,344965864
29	93,8	0,489388	0,410231	0,356269	0,410231	0,489388	0,243187	0,410230661	0,356268995
30	104,38	0,500906	0,399131	0,372722	0,399131	0,500906	0,22733	0,399130826	0,372722454
31	105,35	0,501903	0,398175	0,374147	0,398175	0,501903	0,225964	0,398174922	0,374146528
32	135,05	0,528667	0,372791	0,412382	0,372791	0,528667	0,189702	0,372791406	0,412381834
33	142,95	0,534794	0,367056	0,421134	0,367056	0,534794	0,181509	0,367056419	0,42113404
34	155,6	0,543932	0,358554	0,434188	0,358554	0,543932	0,169363	0,358553794	0,434188287
35	184,86	0,562501	0,341462	0,460716	0,341462	0,562501	0,144946	0,341462343	0,460715961
36	192,21	0,566703	0,337629	0,466719	0,337629	0,566703	0,13947	0,33762926	0,466718551
37	195,46	0,56851	0,335985	0,4693	0,335985	0,56851	0,137121	0,335984729	0,469299917
38	265,48	0,601506	0,306356	0,516438	0,306356	0,601506	0,094794	0,306355965	0,516437837
39	293,35	0,612265	0,296858	0,531806	0,296858	0,612265	0,081225	0,296857723	0,531806496
40	312,6	0,619114	0,290851	0,541591	0,290851	0,619114	0,072644	0,290851021	0,54159144
41	315,02	0,619945	0,290124	0,542779	0,290124	0,619945	0,071606	0,290124344	0,542778682
42	343,49	0,629269	0,282003	0,556099	0,282003	0,629269	0,060004	0,282002844	0,556098987
43	349,76	0,631219	0,280312	0,558884	0,280312	0,631219	0,057589	0,28031215	0,558883875
44	388,28	0,642478	0,270596	0,574969	0,270596	0,642478	0,043708	0,270595862	0,574968815
45	401,55	0,6461	0,267488	0,580142	0,267488	0,6461	0,039269	0,267488241	0,580142458
46	403,61	0,646651	0,267016	0,58093	0,267016	0,646651	0,038594	0,267015796	0,580930237
47	498,05	0,669309	0,247772	0,613299	0,247772	0,669309	0,011103	0,247772438	0,61329908
48	564,57	0,682819	0,236453	0,632599	0,236453	0,682819	0,189163	0,236453134	0,632599235
49	629,68	0,694582	0,22669	0,649403	0,22669	0,694582	0,181352	0,226690478	0,649402805
50	774,58	0,716902	0,208398	0,681288	0,208398	0,716902	0,166718	0,208398038	0,681287895
51	786,1	0,718492	0,207106	0,683561	0,207106	0,718492	0,165684	0,207105593	0,683560714
52	855,94	0,727665	0,199683	0,696665	0,199873	0,727665	0,159747	0,199873369	0,696664622
53	1014,44	0,745974	0,185017	0,72282	0,194007	0,745974	0,185017	0,194006825	0,722819971

Table 3. $\alpha = 0.8, \beta = 0.2, \gamma = 0.3$ and $\omega = 0,6$

The optimal $\alpha, \beta, \gamma, \omega$ values can be obtained for the spatial object examined. Also operators studied by Shi and Liu give more zero values for chosen alpha values. In the intuitionistic fuzzy topological operators

examined in this study, the number of non-zero values obtained is larger. This allows us to obtain more realistic results in modeling objects with uncertain boundaries.

4. Conclusion and Suggestions

In this paper, $I_{\alpha,\beta}^{\gamma,\omega}$ and $C_{\alpha,\beta}^{\gamma,\omega}$ intuitionistic fuzzy topological operators studied on a spatial object example. For optimal $\alpha, \beta, \gamma, \omega$ values topological interior, closure and boundary values were obtained. Table 2 and Table 3 shows that the topological values obtained here are more sensitive than those obtained with fuzzy topological operators and crisp topology.

This classification of topological relations offers a new way of modeling spatial object problems with uncertain boundaries.

Acknowledgment

This study has been supported by the Research Fund of Tarsus University in Turkey with Project Number: MF.20.006.

References

- [1] A. Arkhangel'skii, V. Fedorchuk, *General Topology I*, Springer-Verlag, Berlin, 1990
- [2] K. Atanassov, *Intuitionistic Fuzzy Sets*, VII ITKR.s Session, Sofia, June, 1983.
- [3] K. Atanassov K., *Studies in Fuzziness and Soft Computing-On Intuitionistic Fuzzy Sets Theory*, ISBN 978-3-642-29126-5, Springer Heidelberg, New York, 2012.
- [4] H. Bustince, J. Kacprzyk and V. Mohedano, "Intuitionistic Fuzzy Generators-Application to Intuitionistic Fuzzy Complementation," *Fuzzy Sets Syst.*, vol. 114, no. 3, pp. 485-504, 2000.
- [5] D. Çoker, "An Introduction to Intuitionistic Fuzzy Topological Spaces", *Fuzzy Sets and Systems*, vol. 88, no. 1, pp. 81-89, 1997.
- [6] G. Çuvalcoğlu, *New Tools Based on Intuitionistic Fuzzy Sets and Generalized Nets*, ISBN 978-3-319-26301-4, Springer International Publishing Switzerland, 55-71, 2016.
- [7] G. Çuvalcoğlu, E. Aykut, "An application of some intuitionistic fuzzy modal operators to agriculture" *Notes on IFS*, vol. 21, no. 2, pp. 140-149, 2015.
- [8] F.G. Lupianez, "Intuitionistic fuzzy Topological Operators and Topology," *International Journal of Pure and Applied Mathematics*, vol. 17, no. 1, pp. 35-40, 2004.
- [9] M.R. Malek, *Spatial Object Modeling in Intuitionistic Fuzzy Topological Spaces*. In: Tsumoto S., Słowiński R., Komorowski J., Grzymała-Busse J.W. (eds) *Rough Sets and Current Trends in Computing*. RSCCTC 2004. Lecture Notes in Computer Science, 3066. Springer, Berlin, Heidelberg, 2004.
- [10] E. Marinov, K.T: Atanassov, "Partially Continuous Pretopological and Topological Operators for Intuitionistic Fuzzy Sets," *Iranian Journal of Fuzzy Systems*, vol. 17, no. 2, pp. 1-15, 2020.
- [11] E. Marinov, "Software Implementation of Intuitionistic Fuzzy Sets and Some Operators," *Notes on IFS*, vol. 28, no. 1, 51-85, 2022.
- [12] R. Saadati, J.H. Park, "On Intuitionistic Fuzzy Topological Spaces", *Kybernetes*, vol.35, no. 5, pp. 743-747, 2006.
- [13] W. Shi, K. Liu, "A Fuzzy Topology for Computing the Interior, Boundary and Exterior of Spatial Objects Quantitatively in GIS," *Computers & Geosciences*, vol. 33, no. 7, pp. 898-915, 2007.
- [14] A. K. Singh, and R. Srivastava, "Separation Axioms in Intuitionistic Fuzzy Topological Spaces," *Advances in Fuzzy Systems*, vol. 2012, pp. 1-7, 2012. Article ID 604396, 7 pages, doi:10.1155/2012/604396
- [15] M. Sugeno, T. Terano, "A Model of Learning Based on Fuzzy Information," *Kybernetes*, vol. 6, no. 3, pp. 157-166, 1977.
- [16] S. Tarsuslu (Yılmaz), "A Study on Intuitionistic Fuzzy Topological Operators," *Italian Journal of Pure And Applied Mathematics*, vol. 49, pp. 863-875, 2023.
- [17] L.A. Zadeh, *Fuzzy Sets*, Information and Control, 8, 338-353, 1965.
- [18] L.A. Zadeh, "The concept of linguistic variable and its application to approximate reasoning," *Inform. Sci.*, vol. 8, pp. 133-139, 1975.

Identification of Walnut Variety from The Leaves Using Deep Learning Algorithms

Alper Talha KARADENİZ^{1*}, Erdal BAŞARAN², Yüksel ÇELİK³

¹ Digital transformation and software department, Trabzon University, Trabzon, Turkey

² Department of Computer Engineering, Karabuk University, Karabuk, Turkey

³ Department of Computer Technology, Agri Ibrahim Cecen University, Agri, Turkey

(ORCID ID [0000-0003-4165-3932](https://orcid.org/0000-0003-4165-3932)) (ORCID ID: [0000-0001-8569-2998](https://orcid.org/0000-0001-8569-2998)) (ORCID ID: [0000-0002-7117-9736](https://orcid.org/0000-0002-7117-9736))



Keywords: Walnut Dataset, CNN, Machine learning, Deep Learning

Abstract

In order to determine the variety from walnut leaves, each leaf must be examined in detail. Species that are very similar in color and shape to each other are very difficult to distinguish with the human eye. Examining and classifying plant leaves belonging to many classes one by one is not appropriate in terms of time and cost. Studies on walnut varieties in the literature are generally classified as a result of experimental studies in the laboratory environment. There are two or three different classes in studies using walnut leaf images. In this study, firstly, a unique walnut dataset obtained from 1751 walnut leaf images obtained from 18 different walnut varieties was created. Classification was made using deep learning methods on the original walnut dataset. It has been tested with CNN models, which are widely used in the literature, and some performance metrics are recorded and the results are compared. The images were first preprocessed for cropping, denoising and resizing. Classification was made using CNN models on the original dataset and augmented dataset with data augmentation method. It was seen that the VGG16 CNN model gave the best results both in the original dataset and the augmented dataset. In this model, the accuracy result found with the original data set was 0.8552, while the accuracy result in the enhanced data set was 0.9055. When the accuracy values are examined, it is seen that walnut varieties are classified successfully.

1. Introduction

Plants are one of the essential resources for our world, and these resources need to be transported to the future healthily [1]. Demand for food crops is increasing due to the increasing global population and the challenges posed by climate change. However, as the need for agricultural nutrients increases, the costs must be minimal. Plants with the appropriate genotype should be selected to use the resources effectively. This will help increase productivity and efficiency. The automatic and correct recognition of walnut varieties is important for agricultural engineers and walnut growers.

The diagnosis of plant leaves is utilized by a detailed examination of each leaf. It isn't easy to distinguish species similar in color and shape from each other with the human eye. Examining and

classifying one by one plant leaves belonging to many classes is not appropriate in terms of time and cost. Therefore, taking leaf images and automatically diagnosing and classifying them in the computer environment provides a lot of convenience in terms of time and cost [2]. By using artificial intelligence techniques, software studies have been carried out to provide faster and more accurate results than the functions performed by the human eye [3].

Feature extraction is a difficult process for machine learning. However, it is necessary for the classification process and affects the classification performance [4]. With the developing technology, the speeds and capacities of Central Processing Units (CPUs) and Graphics Processing Units (GPUs) have increased. With these developments, serious performances have been achieved in the data processing stage, leading to the emergence of

* Corresponding author: alperkaradeniz@trabzon.edu.tr

Received: 10.03.2023, Accepted: 09.05.2023

deep learning architectures [5]. On the other hand, deep learning-based studies for the detection and classification of plant leaf diseases have been studied to evaluate their deep learning potential [6].

Considering the mentioned reasons and examining the classification studies carried out in recent years, it is seen that deep neural networks, especially convolutional neural networks (CNN), delivered better results compared to traditional machine learning [7]. One of the most important reasons for the widespread use of CNN algorithms is automatic feature extraction [8]. Furthermore, a matrix (raw image) is used as input to the model, not a vector (feature vector) [9].

Vasif Nabiye et al. developed a method for plant identification using CNN and Transfer Learning. In the Oxford Flowers Dataset study, a fine-tuning approach was used to transfer learning from the ImageNet domain. MobileNetV2 trained on the ImageNet database was used as a pre-trained network, and an accuracy of 0.9897 was achieved. In addition, positive results were obtained by writing a mobile application [10]. Ibtesam M. Dheir et al. The dataset consisting of 2868 images and five different nut species was classified. In the model, there are 4 convolution layers and these layers use the ReLU activation function. After the convolution layers, there is the Max Pooling layer and then the smoothing layer. The first of the last two layers consists of 512 hidden layers and a total of 2,603,205 parameters that can be trained by the network. The last layer is the output layer and Softmax is used as the activation function. A success of 0.98 was achieved in the study [11]. Yixue Liu et al. conducted a study classifying 21 types of grape leaves. After working with preprocessing and CNN algorithms, they developed the Grad-CAM algorithm to analyze the effect of image complementary preprocessing on the classification results and obtained very successful outcomes. As a result of the tests performed using the Googlenet model, the success rate was 0.974 [8]. Daniel Nkemelu et al. worked on classifying 12 different types of plant seedlings. Tests were conducted with K-Nearest Neighbor (KNN), Support Vector Machine (SVM), and a CNN model they created. As a result of tests with several preprocessing and CNN algorithms, the highest accuracy rate of 0.926 was reached [12]. Yu Sun et al designed a 26-layer deep learning model for classification with large-scale data obtained from the natural environment. The

proposed model was tested on the BJFU100 dataset and achieved a success rate of 91.78%. Considering the results, it seems that the model is promising for smart forestry [13]. In the first study with the original walnut data set, a new ResNet-based model was proposed. In the proposed model, ResNet architecture was used for feature extraction, Atom Search Optimization algorithm was used for feature selection and SVM was used for classification. As a result of the experimental tests, a success rate of 81.77% was achieved [14].

In addition to plant identification in the literature, disease diagnosis studies from leaf images have become very popular in recent years. Umit Atila et al. proposed the EfficientNet deep learning architecture by using the Plant Village dataset to classify plant leaf diseases and compared the performance of this model with other state-of-the-art deep learning models. The EfficientNet architecture and other deep learning models are trained using the transfer learning approach, and all layers of the models are set to be trainable in transfer learning. As a result of the tests performed, an accuracy of 0.999 was obtained [4]. Rakesh Chandra Joshi et al. suggested an automatic recognition system for the viral infection of Vignamungo, a legume variety usually grown in the Indian subcontinent. This proposed automated system is based on deep learning and is named VirLeafNet. Data used for system training were obtained from images of healthy, mildly infected, and severely infected leaves obtained over multiple periods. Test results of the proposed models; VirLeafNet-1 was found to be 0.912, VirLeafNet-2 0.964 and VirLeafNet-3 0.974 [15]. Lucas M. Tassis et al. proposed an automatic CNN-based model for the detection of lesioned images from coffee trees. In the first stage of the proposed model, Mask R-CNN network was used for segmentation. In the second stage, UNet and PSPNet networks were used for segmentation. In the final stage, ResNet was applied for the classification process. As a result of the experimental tests, the success rate was found to be 942% [16]. A. Anagnostis et al. has created an accurate and fast object detection system that can identify anthracnose leaves in walnut trees for use in real agricultural environments and has achieved a 0.87 verification. It has been concluded that this system is a viable solution for real-time discovery, monitoring, and decision-making [17] [18].

The producers must buy the right walnut saplings to grow walnuts. It is challenging even for experts to distinguish the walnut variety from the leaves. It takes 3-5 years to see fruits in walnut. Therefore, during this period, the producer spends on an undesired walnut variety or cannot be produced in the region. In this case, the producer tries to change the variety by top-working or has to reestablish the walnut orchard. Saplings that are not namely true have been brought to the courts in many places, causing disagreements between the grower and the nursery. Every year, many legal cases are filed between the nursery and the producers who purchased saplings that do not belong to the desired walnut variety.

In this study, classification with CNN models was utilized to identify walnut varieties from walnut leaves. Before giving the data set input to the CNN models, preprocessing methods were applied, and experimental test results were compared. To improve the model, the data augmentation process was applied to the data set, experimental tests were performed again, and the comparison process was utilized.

With this study, many undesirable issues can be prevented, such as the purchase and planting of wrong saplings, time loss until fruiting, loss of

seedlings not planted in a suitable climate, and court processes. Thus, more successful establishment and finalization of walnut orchards will be possible.

2. Generating Original Dataset

2.1. Dataset

Our data set was created by sampling from the walnut orchard in the Application Garden of Yalova Atatürk Horticultural Central Research Institute. A total of 1751 leaves from 18 different cultivars were photographed one by one. The nomenclature in the data set is registered by the institute.

Walnut varieties were determined in advance, their leaves were cut from their branches and displayed on a white background. Images were created using the Canon EOS 100D camera, in daylight, close-up and automatically. All leaf images were taken from trees of a predetermined variety on the same day and within a few hours. Imaging is applied the same for each leaf, but there may be differences in the person's posture, sun, shade and angle when taking the photo.

Examples of 18 types of walnuts are shown in Figure 1.



Figure 1. Leaf image examples of walnut species.

The number of leaf images of walnut cultivars in the original walnut dataset is shown in Table 1.

Table 1. Leaf image numbers of walnut species.

Number	Name	Data Count
1	Bilecik	96
2	Chandler	82
3	Fernette	89
4	Fernor	104
5	Frenquette	126

6	Hardley	95
7	Howard	85
8	Kaman1	98
9	Kaplan86	84
10	Lara	63
11	Maya1	74
12	Mitland	147
13	Oguzlar77	59
14	Pedro	77
15	Sebin	88
16	Sen	157
17	Ser	119
18	Yalova3	108
		Total : 1751

2.2. Preprocessing

Before experimental tests with CNN models, preprocessing was applied to the images in the dataset to improve the images. There are errors and noises in the images due to shooting. In order to make a better classification from the raw images taken for the data set, only the area with the leaf was determined. The leaves were cut from the edge lines and preprocessed with the help of image processing methods.

In these preprocesses, in order to convert the first image to black and white, the Localrange of image filter 7.7 neighborhood was applied to the images, and the local ranges of the images were obtained. The most appropriate black and white images were obtained based on these local range values and 20 threshold values.

As a second step, morphological methods were used to eliminate noise in the image. The morphological operations used are erosion, dilation, and closing, respectively. The morphological structuring element is created as a parameter in the erosion and dilation processes. This element is a neighborhood matrix with two-dimensional or multidimensional binary values in

which actual pixels are included in the morphological calculation, and false pixels are not. In the Erosion process, a square configuration element with a width of 10 pixels is created. At the same time, the bright regions surrounded by dark-toned regions in the image are narrowed, while the dark-toned regions covered by bright regions are enlarged. After this process, dilation is applied with a square element width of 75 pixels. In the dilation process, while the bright regions surrounded by dark-toned regions in the image expand, the dark-toned regions surrounded by bright regions weaken and even disappear depending on the size of the building element and the dark-toned region. The disk method is applied for the closing process instead of the configuration element. With this method, morphological operations are provided to work faster. The noise on the image is minimized by applying the closing, dilation, and erosion operations to the binary image sequentially.

Objects on the image are labeled and determined on the 2-d binary image (Label connected components in 2-D binary image). Finally, only the leaf region dataset images were obtained by taking the outer frame of the leaf, which is the largest of the objects. Data preprocessing steps are shown in Figure 3.

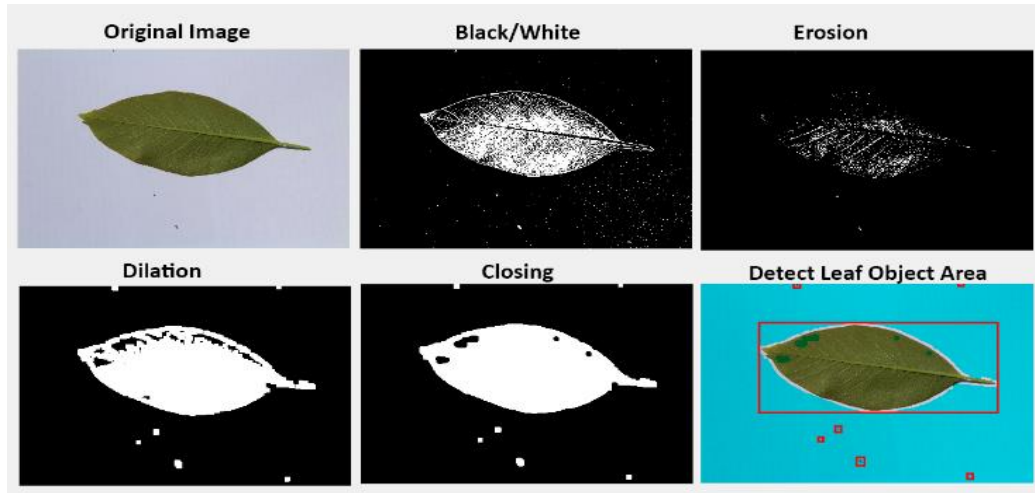


Figure 3. Data preprocessing steps.

After the pre-processing processes were completed, the images were scaled to 600 x 600 dimensions for the experimental tests to run more efficiently.

2.3. Data Augmentation

Data augmentation techniques are a widely used method in deep learning to increase the generalization ability of the model [19]. Data augmentation techniques were applied to our data set consisting of walnut leaf images. These techniques are applied between 0-30 degrees brightness, shift, zoom and flip operations and 1-1.5 degrees rotation. As a result of the data augmentation processes, the number of images in the augmented data set has been increased by approximately 4 times and consists of 6606 images.

3. Material and Method

3.1. CNN Models

CNN models consist of multiple deep layers that do different tasks. CNN models basically consist of 3 layers: convolution, pooling and fully connected layer [18]. In other words, CNNs consist of trainable sections placed one after the other. After receiving the input data in CNN, the training process is carried out by making layer-by-layer operations. Finally, it gives an output to compare the expected value with the generated value. Error occurs as much as the difference between the output and the expected result. This error is transferred to the weights in the network with the back propagation algorithm. The weights are updated at each iteration to reduce the error [5]. The general CNN architecture is shown in Figure 2.

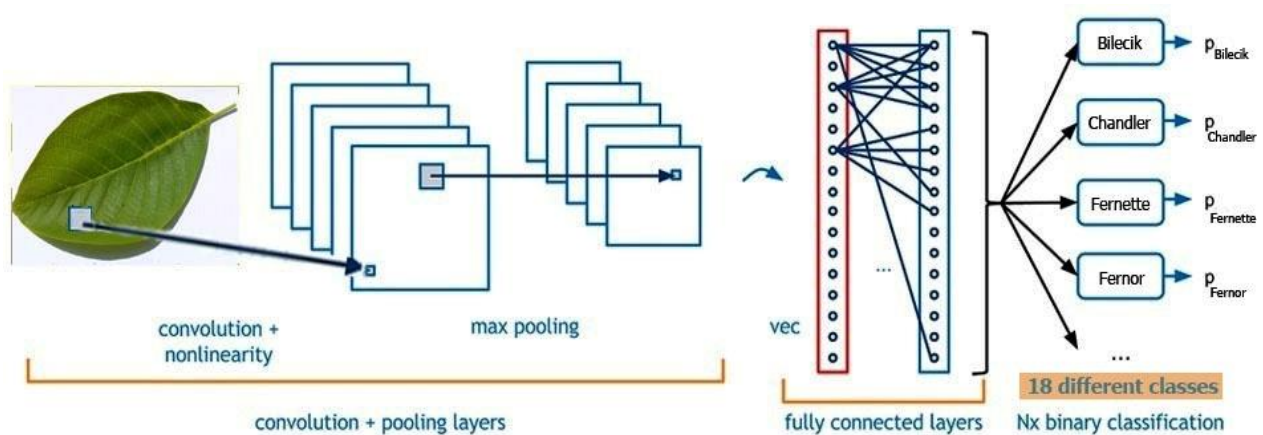


Figure 2. CNN's general architecture.

In the study, Alexnet, InceptionNetV3, VGG16, VGG19, ResNet50, ResNet101, EfficientNet, Darknet19 and GoogleNet CNN models were used for experimental tests.

3.1.1. AlexNet

The AlexNet model is a CNN architecture consisting of 10 layers and approximately 61 million parameters. This CNN architecture was first introduced in the ImageNet competition held in 2012. The first layer of AlexNet is the input layer with an image size of 227 x 227. Then there are 5 convolution layers. After the convolution layer comes 3 fully connected layers. As the last layer, there is the output layer, the Softmax layer. In AlexNet architecture, ReLu activation function is used to increase efficiency between convolution layers and fully connected layer. The Softmax layer is used as the output layer and each output value represents a class value [20] [21].

3.1.2. InceptionV3

InceptionV3 was developed by Google. In addition to previous versions, batch normalization and factorization have been added. The first aim is to reduce the number of parameters and connections to reduce costs, while not reducing the efficiency of the network. Softmax is used in the last layer, the output layer. The Inception V3 architecture consists of 42 layers, including the input layer, which takes a 299x299 pixel image [22].

3.1.3. VGG16

VGG-16 is a CNN architecture with approximately 138 million parameters proposed in 2014. Instead of using many hyper-parameters, this architecture applies 3 x 3 filters and 2 x 2 pooling at each step. There are three layers in the full connection layer, the first two of which are ReLU and the last one is Softmax. VGG-16 contains 16 layers, and the input layer works by taking images of 224 x 224 pixels [23].

3.1.4. VGG19

VGG network architecture was introduced by Simonyan et al. [22]. The VGG19 architecture starts with five block convolutional layers and is

configured with three fully connected layers. Convolutional layers are 3 x 3, and ReLU activation is performed after each convolution layer, followed by 2 x 2 pooling. One thousand fully connected layers are used, and the Softmax activation function is used for the output [24].

3.1.5. ResNet50

ResNet50 consists of a network architecture based on a large number of stacked residual volumes. These residual units are used as building blocks to form the ResNet50 network. Each residual unit consists of convolution and pooling layers. ResNet50 CNN architecture, consisting of 224 x 224 pixel input images, was defined in 2015. It is a CNN architecture that is recommended to prevent distortions in inputs with a large number of dimensions [25].

3.1.6. ResNet101

The difference between Resnet101 and Resnet50 is that it has 17 more redundant blocks in the Conv4 layer [26].

3.1.7. EfficientNet

CNN architectures are generally developed with a fixed resource and more resources are used to improve accuracy as needed. This model can identify factors that carefully balance network depth, width, and resolution and perform better by systematically examining scaling. This observation proposes a new scaling method that equally scales all depth/width/resolution dimensions using a simple but highly effective composite coefficient. The model was 8.4 times smaller than the best CNN and 6.1 times faster at inference, while in ImageNet, it found 97.1% accuracy. EfficientNet also achieved an accuracy of 91.7% in the CIFAR-100 dataset and 98.8% in the Flowers dataset [27].

3.1.8. DarkNet19

DarkNet19 is a CNN algorithm capable of clustering up to 1000 clusters. There are 64 layers on the DarkNet19 CNN architecture. These layers are the input layer, Convolution Layer, Batch Normalization (BN), LeakyReLU, maximum pooling, overall average pooling, Softmax, and

output layers. The LeakyRelu function, an improved version of the traditional ReLU type, is used for activation [28].

3.1.9. GoogleNet

The size of the receiving area in the GoogleNet network is 224×224, taking RGB color channels with average subtraction. The total number of layers used for the construction of the network is about 100. In GoogleNet architecture, a pooling layer with a filter size of 5 x 5, a 1 x 1 convolution layer with 128 filters, a fully connected layer with 1024 units and ReLU, and Softmax for the classifier are used [29].

4. Experiment Test

4.1. Performance Metrics

There are 18 different types in our data set. Therefore, multiple classifications were made. The confusion matrix is used to measure the performance of this type of classification. Values such as True Positive (TP), True Negative (TN), False Positive (FP), False Negative (FN) are obtained from the confusion matrix.

Here, TP represents the number of correctly classified images for each category, and TN represents the sum of correctly classified images outside of the category they should be. FN is the number of misclassified images from the

$$Rec = \frac{TP}{TP+FN} \tag{5}$$

$$F1 - Score = 2 * \frac{Pre*Rec}{Pre+Rec} \tag{6}$$

4.2. Training

Our study's original and expanded walnut data sets were randomly divided into 70% training and 30% test sets. The learning rate for all optimization methods was decided as 0.001.

Before starting the training, the images were set with CNN input sizes as 227 × 227 pixels for AlexNet, 224 × 224 pixels for ResNet50, ResNet101, GoogleNet, EfficientNetB0, VGG16 and VGG19, 299 × 299 pixels for Inception V3, and 256 x 256 pixels for DarkNet19.

In experimental studies, the mini-batch size is set to 16. Table 2 shows the hyper-parameters used in all experiments in our research.

appropriate category. FP is the number of images misclassified outside of the intended category.

Performance criteria used in our study; Accuracy (Acc), Precision (Sen), Specificity (Spe), Precision (Pre) and F-Score.

Sensitivity is the ratio of the number of correctly predicted positive images to the total number of positive images. Specificity is the ratio of the number of correctly predicted negative images to the total number of negative images. Accuracy is the ratio of the number of correctly classified samples to the total number of samples. Precision is the ratio of correctly predicted positive outcomes to all positive outcomes. In addition, Recall (Rec) is a metric that shows how many of the transactions we should predict positively are positively predicted. It has the same formula as Recall Sensitivity. The F1-Score value shows us the harmonic mean of the Preve Rec values.

The necessary calculations for the mentioned performance metrics are shown in equations 1-6 [30] [31].

$$Spe = \frac{TN}{TN+FP} \tag{1}$$

$$Sen = \frac{TP}{TP+FN} \tag{2}$$

$$Acc = \frac{TP+TN}{TP+FN+TN+FP} \tag{3}$$

$$Pre = \frac{TP}{TP+FP} \tag{4}$$

Table 2. Hyperparameters used in experimental CNN tests.

CNN Name	Image Size	Learning Rate	Epoch
AlexNet	227 x 227		
VGG16	224 x 224		
VGG19	224 x 224	0.0001	32
DarkNet19	256 x 256		
Inception V3	229 x 229		
EfficientNetB0	224 x 224		
Googlenet	224 x 224		
Resnet101	224 x 224		
Resnet50	224 x 224		

5. Results and Discussions

Our study aims to examine the classification success of the walnut data set we created by using the most popular CNN models in the literature and comparing the CNN models' success rates.

Experimental studies were carried out with all the CNN models mentioned, on both

the original and augmented datasets. As a result of these studies, Accuracy, Sensitivity, Specificity, Precision and F1-Score results were found. The values obtained from tests with the original dataset are shown in Table 3. The accuracy rates of the CNN models according to the test results are given in Figure 4.

Table 3. Experimental test results of CNNs

CNN Model	Accuracy	Sensitivity	Specificity	Precision	F1-Score
AlexNet	0.7771	0.7514	0.9869	0.7757	0.7584
DarkNet19	0.7695	0.7362	0.9865	0.7448	0.7377
GoogleNet	0.7524	0.7251	0.9855	0.7330	0.7264
InceptionV3	0.6439	0.6112	0.9790	0.6309	0.6131
ResNet50	0.7695	0.7362	0.9865	0.7575	0.7425
ResNet101	0.7524	0.7197	0.9855	0.7411	0.7272
VGG16	0.8552	0.8315	0.9915	0.8300	0.8363
VGG19	0.8400	0.8137	0.9906	0.8220	0.8157
EfficientNet	0.7467	0.7230	0.9851	0.7334	0.7245

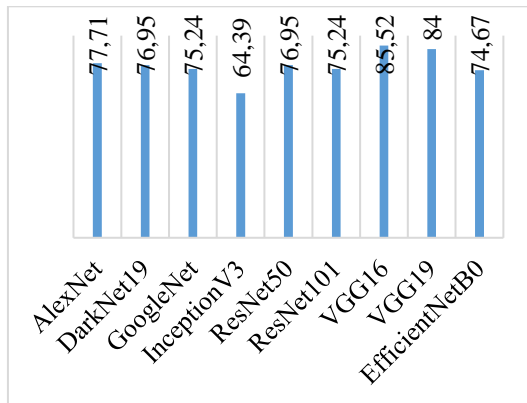


Figure 4. Accuracy rates of CNN models.

As seen in Table 3, VGG16 achieved the highest success with an accuracy rate of 85.52%.

Figure 5 shows the confusion matrix of the highest performing model, VGG16.

DaTa Type	Frenquett	Bilecik	Chandler	Fernette	Fernor	Hardley	Howard	Kaman1	Kaplan86	Lara	Maya1	Mithland	Oguzlar77	Pedro	Sebin	Sen	Serr	Yalova3
Frenquette	33	4	0	0	1	0	0	0	0	0	0	0	0	0	0	0	4	0
Bilecik	0	21	0	0	0	1	0	0	0	0	0	0	5	0	0	2	0	0
Chandler	0	0	19	0	0	1	1	0	1	4	5	0	0	1	0	0	0	0
Fernette	3	0	1	27	4	0	0	1	4	1	0	1	1	1	0	1	6	0
Fernor	0	0	1	0	12	1	1	0	0	1	0	0	1	0	2	0	0	0
Hardley	0	2	1	0	5	23	2	0	0	0	0	0	2	3	2	5	5	1
Howard	0	0	0	0	2	0	13	0	0	0	0	0	0	0	0	0	0	0
Kaman1	0	0	2	0	7	1	5	28	2	4	3	0	0	1	0	0	1	0
Kaplan86	0	0	0	0	0	0	0	0	4	0	8	0	0	0	0	0	0	0
Lara	0	0	0	0	0	0	4	0	1	9	1	0	0	0	0	0	0	0
Maya1	0	0	0	0	0	0	0	0	13	0	5	1	0	0	0	0	0	0
Mithland	2	0	1	0	0	0	0	0	0	0	0	42	2	1	0	1	3	0
Oguzlar77	0	0	0	0	0	0	0	0	0	0	0	0	2	0	0	0	0	0
Pedro	0	0	0	0	0	1	0	0	0	0	0	0	0	16	0	0	0	0
Sebin	0	0	0	0	0	0	0	0	0	0	0	0	0	0	22	0	0	0
Sen	0	2	0	0	0	0	0	0	0	0	0	0	2	0	0	38	2	6
Serr	0	0	0	0	0	0	0	0	0	0	0	0	3	0	0	0	15	0
Yalova3	0	0	0	0	0	0	0	0	0	0	0	0	0	0	0	0	0	25

Figure 5. Confusion Matrix obtained with the VGG16.

Table 4. Experimental test results of CNNs with Augmented Dataset

CNN Model	Accuracy	Sensitivity	Specificity	Precision	F1-Score
AlexNet	0.8631	0.8504	0.9920	0.8543	0.8518
DarkNet19	0.8992	0.8872	0.9941	0.8878	0.8870
GoogleNet	0.8675	0.8512	0.9922	0.8605	0.8532
InceptionNetV3	0.8061	0.7919	0.9886	0.7968	0.7928
ResNet50	0.8704	0.8547	0.9924	0.8634	0.8577
ResNet101	0.8583	0.8424	0.9917	0.8520	0.8460
VGG16	0.9055	0.8900	0.9945	0.8894	0.8891
VGG19	0.9045	0.8918	0.9944	0.8941	0.8924
EfficientNetB0	0.8505	0.8341	0.9912	0.8408	0.8365

The graphs of the accuracy rates of the test results of the augmented dataset and CNN models are given in Figure 6. As seen in Table 4, as a result of the experimental tests performed with the augmented data set, VGG16 granted the highest success with an accuracy rate of 90.55%, as in the original data set. However, VGG19 achieved better results on some performance metrics having the best results in Sensitivity and F1-Score. In addition, VGG16 and VGG19 produced very close results in almost all metrics. DarkNet19 also performs quite well relative to VGG models.

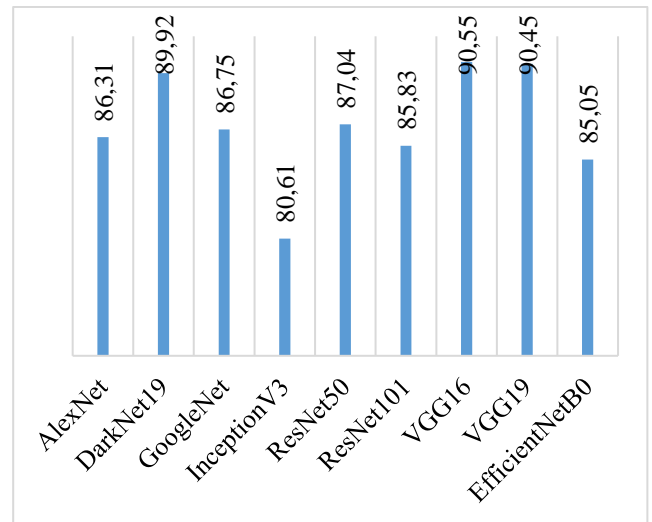
**Figure 6.** Accuracy rates of CNN models with the augmented dataset.

Figure 7 shows the confusion matrix of VGG16, which delivered the highest performance in the experimental test results in the augmented data set.

DaTa Type	Frenquette	Bilecik	Chandler	Fernette	Fernor	Hardley	Howard	Kaman1	Kaplan86	Lara	Maya1	Mithland	Oguzlar77	Pedro	Sebin	Sen	Serr	Yalova3
Frenquette	144	0	0	0	0	0	0	0	1	1	0	1	0	0	0	0	0	0
Bilecik	0	106	0	0	1	0	0	0	0	0	0	0	0	0	0	2	1	3
Chandler	0	1	92	0	1	0	0	0	1	1	0	0	0	0	0	0	0	0
Fernette	0	0	0	104	1	0	0	0	0	0	0	0	0	0	0	0	0	0
Fernor	0	1	0	4	109	0	2	2	2	3	0	0	0	0	0	0	0	0
Hardley	0	0	3	0	0	103	0	2	0	0	0	0	2	1	0	1	0	0
Howard	0	0	0	1	3	0	94	1	0	1	0	0	0	0	0	0	0	0
Kaman1	0	0	0	0	0	0	1	113	0	0	0	0	0	1	0	0	0	0
Kaplan86	0	0	2	0	0	1	0	0	49	3	43	0	0	1	0	0	0	0
Lara	0	0	1	2	1	0	4	1	0	62	1	0	0	0	1	0	0	2
Maya1	0	0	2	0	0	0	1	0	44	1	40	0	0	0	0	0	0	0
Mithland	1	0	0	0	0	0	0	0	0	0	0	169	0	0	0	0	0	0
Oguzlar77	0	0	0	0	0	0	0	0	0	0	0	0	67	0	0	1	0	2
Pedro	0	1	4	1	0	3	1	0	1	0	0	0	0	79	1	0	0	0
Sebin	0	0	0	0	0	0	0	1	0	0	0	0	6	0	95	0	2	0
Sen	1	0	0	0	0	0	0	0	0	0	0	0	0	0	0	177	1	2
Serr	0	0	1	0	0	0	0	0	0	0	0	0	0	0	0	0	136	1
Yalova3	0	4	0	0	0	0	0	0	0	0	0	0	1	0	0	1	0	120

Figure 7. Confusion matrix of VGG16 according to augment dataset.

As can be seen in Tables 3 and 4, the performance of the augmented dataset is better in all CNN models than in the original dataset. In addition, VGG19 Sensitivity and F1-Score performance metrics in the augmented data set offered better results than VGG16 indicating the importance of the number of images in the data set for CNN models.

6. Conclusions

Identification of the walnut variety from the leaves can be utilized as a result of a detailed examination of each leaf. Since these leaves are very similar in color, shape, and texture, it is difficult to distinguish them by traditional methods. Within the scope of this study, a unique walnut dataset containing 18 different classes and 1751 walnut leaf images has been brought to the literature. The original and augmented version of the data set were

classified separately using nine different CNN models in the literature. The performance results were compared. Looking at all performance calculation metrics in both datasets, VGG16 was the best performing CNN model. While the accuracy result of VGG16 found with the original data set was 0.8552, the accuracy in the augmented data set was 0.9055. Considering the success rates, walnut varieties were classified successfully with the deep learning methods.

In the future, in addition to the existing CNN models, developing a different and more successful deep learning model is aimed to use as a mobile application for nurseries and walnut growers.

Dataset availability Link to access the data set: <https://github.com/TechResearchLab/Walnut-Leaves-Dataset>

Acknowledgment

I would like to thank my father Prof. Dr. Turan KARADENİZ, my sister, I know Dr. Instructor Tuba BAK, Director of the Institute, who allowed us to take the walnut images from the application garden of Yalova Atatürk Horticultural Central Research Institute. We would like to thank Yılmaz BOZ and the staff of the Institute.

Contributions of the authors

This article was produced from a PhD thesis.

Conflict of Interest Statement

This article was produced from the thesis work of the first author and second and third authors are thesis advisors.

The authors declare that there is no conflict to interest related to this paper.

Ethics committee approval is not required for the prepared article.

References

- [1] K. Kulkarni, Z. Zhang, L. Chang, J. Yang, P. C. A. da Fonseca, and D. Barford, "Building a pseudo-atomic model of the anaphase-promoting complex," *Acta Crystallogr. Sect. D Biol. Crystallogr.*, vol. 69, no. 11, pp. 2236–2243, 2013.
- [2] F. Doğan and İ. Türkoğlu, "Derin öğrenme algoritmalarının yaprak sınıflandırma başarımlarının karşılaştırılması," *Sak. Univ. J. Comput. Inf. Sci.*, vol. 1, no. 1, pp. 10–21, 2018.
- [3] S. Solak and U. Altınışık, "Görüntü işleme teknikleri ve kümeleme yöntemleri kullanılarak fındık meyvesinin tespit ve sınıflandırılması," *Sak. Univ. J. Sci.*, vol. 22, no. 1, pp. 56–65, 2018.
- [4] Ü. Atıla, M. Uçar, K. Akyol, and E. Uçar, "Plant leaf disease classification using EfficientNet deep learning model," *Ecol. Inform.*, vol. 61, p. 101182, 2021.
- [5] Y. LeCun, Y. Bengio, and G. Hinton, "Deep learning," *Nature*, vol. 521, no. 7553, pp. 436–444, 2015.
- [6] M. H. Saleem, J. Potgieter, and K. M. Arif, "Plant disease detection and classification by deep learning," *Plants*, vol. 8, no. 11, p. 468, 2019.
- [7] B. Yanıkoğlu and E. Aptoula, "İçeriğe Dayalı İmge Erişim Yöntemleri ile Bitki Tanıma," 2016.
- [8] Y. Liu, J. Su, G. Xu, Y. Fang, F. Liu, and B. Su, "Identification of grapevine (*Vitis vinifera* L.) cultivars by vine leaf image via deep learning and mobile devices," 2020.
- [9] M. Reichstein, G. Camps-Valls, B. Stevens, M. Jung, J. Denzler, and N. Carvalhais, "Deep learning and process understanding for data-driven Earth system science," *Nature*, vol. 566, no. 7743, pp. 195–204, 2019.
- [10] T. Karahan and V. Nabyev, "Plant identification with convolutional neural networks and transfer learning," *Pamukkale Üniversitesi Mühendislik Bilim. Derg.*, vol. 27, no. 5, pp. 638–645, 2021.
- [11] I. M. Dheir, A. Soliman, A. Mettleq, and A. A. Elsharif, "Nuts Types Classification Using Deep learning," *Int. J. Acad. Inf. Syst. Res.*, vol. 3, no. 12, pp. 12–17, 2019.
- [12] D. K. Nkemelu, D. Omeiza, and N. Lubalo, "Deep convolutional neural network for plant seedlings classification," *arXiv Prepr. arXiv1811.08404*, 2018.
- [13] Y. Sun, Y. Liu, G. Wang, and H. Zhang, "Deep learning for plant identification in natural environment," *Comput. Intell. Neurosci.*, vol. 2017, 2017.
- [14] A. T. Karadeniz, Y. Çelik, and E. Başaran, "Classification of walnut varieties obtained from walnut leaf images by the recommended residual block based CNN model," *Eur. Food Res. Technol.*, vol. 249, no. 3, pp. 727–738, 2023.
- [15] R. C. Joshi, M. Kaushik, M. K. Dutta, A. Srivastava, and N. Choudhary, "VirLeafNet: Automatic analysis and viral disease diagnosis using deep-learning in *Vigna mungo* plant," *Ecol. Inform.*, vol. 61, p. 101197, 2021.
- [16] L. M. Tassis, J. E. T. de Souza, and R. A. Krohling, "A deep learning approach combining instance and semantic segmentation to identify diseases and pests of coffee leaves from in-field images," *Comput. Electron. Agric.*, vol. 186, p. 106191, 2021.
- [17] A. Anagnostis *et al.*, "A deep learning approach for anthracnose infected trees classification in walnut

- orchards,” *Comput. Electron. Agric.*, vol. 182, p. 105998, 2021.
- [18] A. Anagnostis, G. Asiminari, E. Papageorgiou, and D. Bochtis, “A convolutional neural networks based method for anthracnose infected walnut tree leaves identification,” *Appl. Sci.*, vol. 10, no. 2, p. 469, 2020.
- [19] A. Dobrescu, M. V. Giuffrida, and S. A. Tsaftaris, “Doing more with less: a multitask deep learning approach in plant phenotyping,” *Front. Plant Sci.*, vol. 11, p. 141, 2020.
- [20] A. Krizhevsky, I. Sutskever, and G. E. Hinton, “Imagenet classification with deep convolutional neural networks,” *Adv. Neural Inf. Process. Syst.*, vol. 25, pp. 1097–1105, 2012.
- [21] A. Krizhevsky, I. Sutskever, and G. E. Hinton, “Imagenet classification with deep convolutional neural networks,” *Commun. ACM*, vol. 60, no. 6, pp. 84–90, 2017.
- [22] C. Szegedy, V. Vanhoucke, S. Ioffe, J. Shlens, and Z. Wojna, “Rethinking the inception architecture for computer vision,” in *Proceedings of the IEEE conference on computer vision and pattern recognition*, pp. 2818–2826, 2016.
- [23] K. Simonyan and A. Zisserman, “Very deep convolutional networks for large-scale image recognition,” *arXiv Prepr. arXiv1409.1556*, 2014.
- [24] T. Carvalho, E. R. S. De Rezende, M. T. P. Alves, F. K. C. Balieiro, and R. B. Sovat, “Exposing computer generated images by eye’s region classification via transfer learning of VGG19 CNN,” in *2017 16th IEEE International Conference on Machine Learning and Applications (ICMLA)*, pp. 866–870, 2017.
- [25] K. He, X. Zhang, S. Ren, and J. Sun, “Deep residual learning for image recognition,” in *Proceedings of the IEEE conference on computer vision and pattern recognition*, pp. 770–778, 2016.
- [26] Y. Dong, H. Zhang, C. Wang, and Y. Wang, “Fine-grained ship classification based on deep residual learning for high-resolution SAR images,” *Remote Sens. Lett.*, vol. 10, no. 11, pp. 1095–1104, 2019.
- [27] M. Tan and Q. Le, “Efficientnet: Rethinking model scaling for convolutional neural networks,” in *International Conference on Machine Learning*, pp. 6105–6114, 2019.
- [28] W. Setiawan and A. Purnama, “Tobacco Leaf Images Clustering using DarkNet19 and K-Means,” in *2020 6th Information Technology International Seminar (ITIS)*, pp. 269–273, 2020.
- [29] C. Szegedy *et al.*, “Going deeper with convolutions,” in *Proceedings of the IEEE conference on computer vision and pattern recognition*, pp. 1–9, 2015.
- [30] M. Sokolova and G. Lapalme, “A systematic analysis of performance measures for classification tasks,” *Inf. Process. Manag.*, vol. 45, no. 4, pp. 427–437, 2009.
- [31] E. Başaran, “Classification of white blood cells with SVM by selecting SqueezeNet and LIME properties by mRMR method,” *Signal, Image Video Process.*, pp. 1–9, 2022.

Assessing Seismic Crack Performance of Diyarbakır Çüngüş Masonry Stone Bridge Considering 2023 Kahramanmaraş, Hatay, Malatya, Gaziantep Earthquakes

Murat CAVUSLU^{1*}

¹Zonguldak Bülent Ecevit University, Department of Civil Engineering, Zonguldak, Türkiye
(ORCID: [0000-0002-2285-8513](https://orcid.org/0000-0002-2285-8513))



Keywords: Earthquake, Masonry Stone Arch Bridge, Non-Reflecting Boundary Condition, 2023 Kahramanmaraş Earthquakes, Seismic Analysis.

Abstract

Examination of the creep behavior of historical structures and the correct assessment of seismic failures in historical structures are of great importance for the safety and future of these important structures. In this study, time-dependent settlement and three-dimensional (3D) seismic analyses of a historical stone bridge were investigated using the 3D discrete element modeling technique. For the settlement and seismic analyses, the historical single-span Çüngüş bridge which was built in the 18th century in Diyarbakır, Türkiye by Ottoman Empire was used. Since Diyarbakır is in a dangerous zone according to the Türkiye seismic map, the examination of this structure is very critical for the history of Türkiye. The 3D model of the bridge was created using the FLAC3D program based on the finite-difference method and all the stone elements in the historical bridge were modeled separately as blocks. Special interaction elements were defined between the discretely modeled stones. For settlement creep analyses, the Burger-creep material model, which was not used for the creep behavior of historical buildings in the past, was utilized. Firstly, the 500-year long-term creep behavior of the bridge was examined by considering the fix boundary condition and full reservoir condition. According to the creep analyses, it was seen that the most deformation and failure section of the bridge is the arch section. Then, for the seismic analyses of the bridge, free-field and quiet non-reflecting boundary conditions were defined in the model. Furthermore, hysteresis damping coefficients were taken into account in seismic analyses with the help of special FLAC3D code. 10 different earthquakes were considered for the seismic analyses. According to the earthquake analyses, the earthquake behavior of the Çüngüş historical bridge was assessed by considering the full reservoir condition and it was understood that the 2023 Kahramanmaraş, Hatay, Malatya, Gaziantep earthquakes significantly changed the seismic safety behavior of Çüngüş single-span historical bridge.

1. Introduction

Historical buildings can provide important information about the past of countries, and the preservation of these structures is of great importance for the history of countries. For these structures to serve humanity more, the time-dependent failure behavior of the stone elements should be examined and restored. In addition, examining the earthquake

behavior of historical buildings in seismic regions and taking precautions is very critical for the safety of these structures. Bridges are one of the most important examples of historical structures built in the past. There are many studies on the seismic analyses of historical bridges in the literature. Aydin and Özkaya [1] performed the structural analyses of the Sarpdere historical stone bridge. Firstly, a three-dimensional finite element model of the bridge was

*Corresponding author: murat.cavusli@beun.edu.tr

Received: 11.03.2023, Accepted: 25.05.2023

generated by using ANSYS software. The total maximum load-carrying capacity behavior of the bridge was evaluated and it was seen from numerical analyses that the maximum cracks occurred on the arch section of the bridge. The location of the arch section of a masonry bridge can vary depending on the specific design and construction of the bridge. However, typically, the arch section is located in the middle or center of the bridge span, as this is where the greatest weight and pressure from the weight of the bridge and any vehicles or loads crossing it are concentrated. The arch section is designed to distribute this weight and pressure evenly across the entire span of the bridge, providing support and stability to the structure. Bayraktar and Hokelekli [2] assessed the structural behavior of brick and stone historical bridges considering nonlinear soil deformability effects. Bridges were modeled as three-dimensional using brick and wedge elements. According to seismic analyses, it was seen that the most critical section of the bridge during an earthquake is the arch section. Furthermore, the seismic behaviors of the brick and stone bridges are very different from each other. Bergamo et al. [3] investigated the stress and deformed behavior of historical stone bridges. Firstly, the mechanical properties of the bridge were acquired from experimental tests. Then, static experimental tests were performed to obtain the static behavior of the bridge. The three-dimensional finite element model of the bridge was created and maximum deformations occurred on the arch section of the bridge. Conde et al. [4] evaluated the influences of material properties and geometry of the arch section of the bridge on the structural behavior of the Monforte de Lemos historical stone bridge. According to four different arch types, it was seen that arch types have enormous effects on the structural behavior of bridges. Moreover, arch types have significant static effects on the collapse behavior of bridges. Conde et al. [5] investigated the probabilistic analyses of the stone arch bridges using the finite element model and limit analysis model. According to numerical analyses, the maximum failure damages occurred on the arch section of the bridge. Moreover, very different reliability indexes were observed for EN 1990, ISO 2394, ISO 13822, JCSS, and fib standards. Gönen and Soyöz [6] examined the three-dimensional earthquake behavior of the historical stone bridges using the finite element macro-modeling approach. The bridge was modeled as three-dimensional using ANSYS software and nonlinear earthquake analyses were performed under 14 various strong ground motions. It was proposed that future studies should aim at determining the performance criteria for historical

stone bridges. Güllü and Jaf [7] evaluated the three-dimensional earthquake behavior of the Mataracı historical stone bridge. After the three-dimensional model of the bridge was created, 5 different modes of the bridge were examined by considering the soil-structure interaction and fix base. Besides, the seismic behavior of the bridge was evaluated considering a strong earthquake. According to seismic analyses, it has been understood that modeling historical bridges by considering the soil-structure interaction and fix base significantly changes the seismic behavior of these structures. Naderi and Zekavati [8] evaluated the earthquake behavior of historical stone bridges using the finite element method and discrete element method. The first five modes of the bridge were assessed in detail and it was seen that the first mode of the bridge is 4.985 Hz. Then, the seismic deformation behavior of the bridge was evaluated and it was understood that the maximum deformations occurred on the arch section of the bridge during the earthquakes. Rovithis and Pitilakis [9] examined the static behavior of a historical stone bridge. The three-dimensional model of the bridge was created considering the fixed-base model, the flexible-base model, and the flexible-base rehabilitated model. According to these models, the frequency for Mode 1 is 11.27 Hz, 1.62 Hz, and 2.058 Hz for the fixed-base model, the flexible-base model, and the flexible-base rehabilitated model, respectively. Moreover, the response spectrum behavior of the bridge was assessed considering the free-field ground response analyses. Saygılı and Lemos [10] evaluated the earthquake damage performance of the masonry bridges. Historical Kazan and Şenyuva bridges were utilized for the numerical analyses. Firstly, three-dimensional models of the bridges were created using SAP2000 and 3DEC software, and the first five modes of the bridges were assessed in detail. According to numerical analyses, it was seen that the maximum relative X displacements during the earthquake occurred on Point 5, and the maximum relative traversal displacements were observed on Point 4. Sayin [11] assessed the nonlinear earthquake behavior of the historical Nadir Bridge. The bridge was modeled as three-dimensional and it was understood that strong ground motions strongly affect the seismic behavior of historical bridges. Simos et al. [12] investigated the effects of near-fault and far-fault earthquakes on the seismic behavior of the Konitsa historical stone bridges. Surface contact was defined in the model. Firstly, a three-dimensional finite element model of the bridge was created and seismic analyses were performed considering a near-fault and a far-fault earthquake. 5 Modes of the bridge were evaluated and it was seen that the first mode of the

bridge is 2.3136 Hz. Then, the crack behavior of the bridge was assessed in detail and it was understood that maximum cracks occurred on the arch of the bridge. Zani et al. [13] examined the effects of soil compressibility on the structural behavior of historical stone bridges. Firstly, the structural behavior of the bridge was checked using load tests and the Italian Technical Regulations. Then, the bridge was modeled as three-dimensional and the deformation behavior of the bridge was assessed in detail. According to three various models of the bridge, it was seen that the maximum principal stress is 3.1×10^5 MPa for Model A. Karalar and Çavuşlu [14] examined the structural performance of a historical building considering 2018 TBEC. Furthermore, there are many studies about static and seismic analyses of historical stone bridges in the literature [15-16], [22-26]. It was seen from these studies that the Burger-creep material model, free-field non-reflecting boundary condition, quiet non-reflecting boundary condition, three-dimensional discrete modeling, and special interaction parameters (k_n and k_s) were not used to perform the creep and seismic analyses of the historical stone arch bridges in the past studies. For this reason, this study is very important to fill these deficiencies in the literature. In this study, the creep and seismic behaviors of the Çüngüş historical stone arch bridge built in the 18th century in Diyarbakır, Türkiye were investigated in detail. Firstly, the three-dimensional creep model and the three-dimensional seismic model of the bridge were created. While creating the three-dimensional creep model, each stone element in the arch section of the bridge was modeled separately. This modeling process was done with the help of FLAC3D code based on the finite-difference method. This method is a numerical technique for solving differential equations by approximating derivatives with finite differences and it converts differential equations, which may be nonlinear, into a system of linear equations that can be solved by matrix algebra techniques. Special interaction parameters (k_n and k_s) were defined between the stone elements modeled separately. When the literature is examined, it is seen that there are very limited studies in which the creep and seismic analyzes of historical stone bridges are examined by modeling discrete stone elements and by assigning special k_n and k_s interaction elements between each stone element. Therefore, the first aim of this study is to examine how discrete element modeling and specific interaction elements change the creep settlement and seismic behavior of historical bridges. The Burger-Creep material model, which was not used in the past to examine the creep settlement behavior of historical bridges, was used in

the creep settlement analyses. The Burgers-Creep material model is a visco-plastic model combining the Burgers model and the Mohr-Coulomb model [18]. The second aim of this study is to fill this gap in the literature and observe how the Burger-Creep material model changes the long-term creep behavior of historical bridges. Then, special free-field and quiet boundary conditions were utilized for the seismic analyses of the bridge. The other purpose of this study is to examine the effects of free-field and quiet boundary conditions on the seismic behavior of historical arch-stone bridges. A total of 10 different near-fault earthquakes were used in seismic analyses, and one of the most important purposes of this study is to reveal the effects of near-fault earthquakes on the seismic behavior of historical stone bridges. This study is of great importance in terms of eliminating the deficiencies in the literature.

INDEX OF ABBREVIATIONS	
M_w	<i>Moment Magnitude</i>
PGA	<i>Peak Ground Acceleration</i>
PGV	<i>Peak Ground Velocity</i>
PGD	<i>Peak Ground Displacement</i>
k_n	<i>Normal Stiffness</i>
k_s	<i>Shear Stiffness</i>
E	<i>Modulus of Elasticity</i>
f_c	<i>Compressive Strength</i>
μ	<i>Poisson's Ratio</i>

2. Çüngüş Historical Arch Bridge and Seismic Hazard Map of Diyarbakır-Türkiye

Diyarbakır Çüngüş stone bridge is one of the most important historical structures in Türkiye (Fig. 1). In the literature, there is no information about its period and builder. However, it is estimated that the bridge was built in the 18th (1743) century in terms of plan and architecture. The main construction material of the bridge, which has one span and a pointed arch, is yellow limestone obtained from the region. The arch thickness is 0.53 m and the spandrel wall thickness is 0.41 m. The feet of the bridge are set on natural rocks. The bridge has 34.74 m long, 5 m wide, and 16.42 m high. The span of the arch is 9.32 m at the ends where the feet sit on the rocks. The tissue, which deteriorated over time, was not repaired with the same technique

but was replaced with rubble material that requires less labor. The upper section of the bridge was also recently covered with interlocking cobblestone. Signs of different periods have been detected on the upstream surface. Besides, stone remains were found about 10 m away from the upstream face of the bridge.

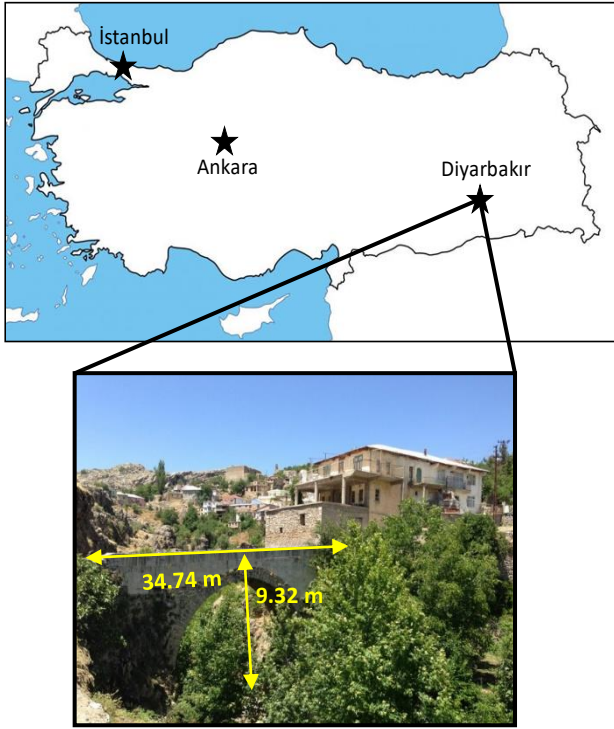


Figure 1. General view of the Çüngüş stone arch bridge.

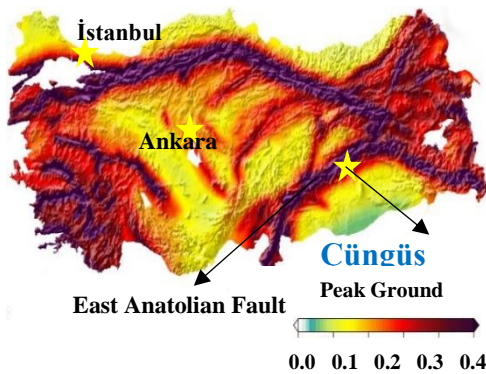


Figure 2. The fault map of Türkiye [17].

Çüngüş stone arch bridge is a historical building built on seismic active earthquake zones in Diyarbakır, Türkiye. This bridge is located on the East Anatolian Fault and this fault is in constant motion. Türkiye's seismic map was shown in detail in Fig. 2. According to Fig. 2, it was seen that the Çüngüş bridge has been exposed to many important earthquakes from the past to the present, and

examining the seismic behavior of this structure is of great importance for the future of this structure. As a result of the earthquakes that took place in Diyarbakır in the past, it was determined that there was no structural damage to the Çüngüş bridge. However, due to time, significant abrasions were observed on the stone elements of the bridge. Besides, according to the observation results, visible displacements and seismic failures occurred in the body and arch parts of the bridge as a result of the 2023 Kahramanmaraş earthquake. The region where the Çüngüş bridge is located was exposed to major earthquakes in 2023. The East Anatolian Fault (EAF) produced very large earthquakes in the Kahramanmaraş, Hatay, Malatya, and Gaziantep in 2023 and as a result of these earthquakes, great destructions occurred. Besides, these earthquakes have caused the death of thousands of people in these provinces. It is of vital importance to examine these current and severe earthquakes and to model our structures according to these earthquakes. In this study, the earthquake behavior of the Çüngüş bridge, which is located on the EAF, was investigated by considering the 2023 Kahramanmaraş, Hatay, Malatya, and Gaziantep earthquakes. The characteristics of the earthquakes used in seismic analyses were summarized in Table 1 in detail.

Table 1. Characteristic properties of strong ground motions [19].

Case	Earthquake	Year	M_w	Distance (km)	PGA (cm/s^2)	PGV (cm/s)
1	Pazarcık1 (K.maraş)		7.7	8.6	2178.71 (E-W)	186.78 (E-W)
2	Elbistan (K.maraş)		7.6	7	635.45 (N-S)	170.79 (N-S)
3	Nurdağı1 (Gaziantep)		6.6	6.2	454.15 (N-S)	44.60 (U-D)
4	Yayladağı (Hatay)		6.4	21.7	775.40 (N-S)	75.79 (E-W)
5	İslahiye (Gaziantep)		5.7	11.19	363.52 (E-W)	13.85 (E-W)
6	Yeşilyurt (Malatya)	2023	5.6	6.15	25.23 (E-W)	2.36 (N-S)
7	Doğanşehir (Malatya)		5.6	10.23	47.28 (E-W)	2.90 (E-W)
8	Nurdağı2 (Gaziantep)		5.6	6.98	44.15 (E-W)	2.91 (E-W)
9	Pazarcık2 (K.maraş)		5.5	5.96	49.84 (U-D)	2.84 (N-S)
10	Ekinözü (K.maraş)		5.5	10.93	79.35 (E-W)	4.26 (E-W)

3. Three-Dimensional Finite Difference Model of Bridge

In this study, it was aimed to examine the creep and seismic behaviors of the historical Çüngüş stone bridge built in the 18th century in Diyarbakır,

Türkiye. For this purpose, the three-dimensional model of the bridge was modeled with the help of the FLAC3D program. The discrete element method was used for modeling the bridge. Firstly, the arch of the bridge was formed. Then, each stone element in the arch part was modeled separately and interaction stiffness coefficients were defined between the interface surfaces of the stone elements by considering the k_n and k_s coefficients [18]. A total of 2672 stone elements were used in the arch part of the bridge. In addition, a total of 94883 and 297529 stone elements were utilized in the rockfill and foundation of the bridge, respectively. In the FLAC3D program, "kn" and "ks" are stiffness interface parameters that are used to define the behavior of the material constitutive model for the simulation of geological and geotechnical processes. "kn" refers to the normal stiffness interface parameter, which represents the resistance to compression and extension of the material. It determines the response of the material to normal stresses or strains, perpendicular to the surface. Then, "ks" refers to the shear stiffness interface parameter, which represents the resistance to shearing of the material. It determines the response of the material to shear stresses or strains, parallel to the surface. In FLAC3D, these parameters are often used in the definition of contact models between different materials or between the material and the boundaries or the loads in the simulation. Then, rockfill elements were separately modeled on the arch, and all rockfill elements built on the arch were defined to the program with the help of special FLAC3D codes. All dimensions of the stones were modeled following the survey project of the bridge (Fig. 3).

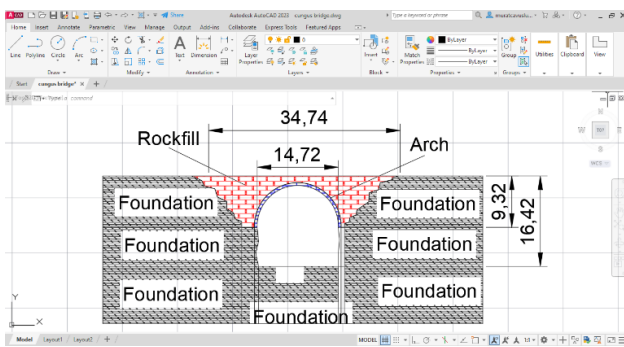


Figure 3. Survey AutoCAD project of Çüngüş bridge.

Finally, the foundation section of the bridge was created. While creating the foundation section of the bridge, it was extended to the sides as the height of the arch. For the upstream and downstream sections of the bridge, it was extended as three times the height of the arch [20-21]. Furthermore, the foundation section was extended towards the underside of the arch as five times the height of the arch. After the

three-dimensional model of the bridge was created, the fix (reflecting) boundary condition was defined in the z-direction at the base of the bridge for creep settlement analyses. On the lateral parts of the bridge, the fix boundary condition was defined in the x and y directions. Besides, for seismic analyses, quiet (non-reflecting) boundary condition was defined at the base of the model. The free-field boundary condition was taken into account for the lateral parts of the model. These non-reflective boundary conditions ensure that seismic waves are not reflected in the model and provide realistic analyses for seismic analyses [20-21]. The Burger-creep material model was taken into account for creep analyses. The burger-creep material model is one of the important material models derived to examine the failure behavior of elements such as stones, and this model has not been used to examine the creep settlement behavior of historic bridges in the past [18]. The Burger creep model is a viscoelastic-plastic model used to simulate the deformation behavior of rocks and soils under sustained loading conditions. It is based on power-law rheology, which describes the deformation rate as a function of stress and temperature. The model takes into account three components of deformation: elastic, viscoelastic, and plastic. The elastic component is characterized by the linear relationship between stress and strain, while the viscoelastic component is characterized by the power-law relationship between stress and time-dependent strain rate. The plastic component is characterized by the power-law relationship between stress and strain. While performing the long-term creep analyses, time intervals were defined using special fish codes. Moreover, special hysteresis damping elements were defined for seismic analyses. The three-dimensional finite-difference model of the bridge was shown in Fig. 4. Moreover, the material properties of the Çüngüş bridge were summarized in Table 2.

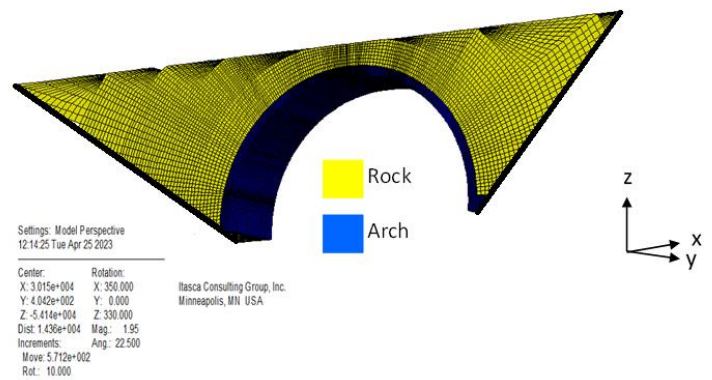


Figure 4. Three-dimensional finite-difference model of the Çüngüş bridge.

Table 2. Summary of the material properties of the Çüngüş bridge [20-21].

Material Property	Arch	Rockfill Material	Foundation
E	8.8 (GPa)	8.1 (GPa)	9.8 (GPa)
fc	7.7 (MPa)	6.9 (MPa)	10.1 (MPa)
μ	0.28	0.25	0.36

4. Three-Dimensional Creep and Seismic Analysis Results

In this section, time-dependent creep settlement and nonlinear seismic analysis results of the historical Çüngüş arch bridge were shown in detail. The Burger-Creep material model, which was not previously used for time-dependent creep analysis of historical arch bridges in the past, was utilized in the creep and failure analyses. Creep settlement analyses were performed for the 500-year failure behavior of the Çüngüş bridge. In Fig. 5, the first five modes of the bridge obtained as a result of creep analyses were presented in detail. According to Fig. 5, the first mode is 1.89 Hz and this value allows us to gain significant information about the modal behavior of the historical bridges. Moreover, the second mode of the bridge is 3.34 Hz. As a result of the modal analyses, the 3rd mode, the 4th mode, and 5th mode of the Çüngüş bridge are 3.98 Hz, 4.31 Hz, and 4.85 Hz, respectively (Fig. 5). These values are of great importance for observing the modal behaviors of historical bridges. Besides, the 5 different modes of the bridge obtained using the Burger-creep material model provide researchers with important information about how this material model affects the modal behavior of historical bridges (Fig. 5). In Fig. 6, the 500-year creep settlement behavior of the Çüngüş bridge was shown in detail. As Fig. 6 was investigated in detail, it was seen that the changing rate in the settlement behavior of the Çüngüş bridge increased continuously from 1773 to 2173. However, after a certain time, the changing rate in the failure behavior of the bridge decreased. As Fig. 6 was assessed in detail, between 1773 and 1873, no large displacement changes were observed in the bridge body. However, significant displacement increases occurred in the arch section of the bridge after 1973. From 1973 to 2173, about 5 mm of settlement took place in the middle section of the bridge. This result shows how much displacement increase will occur in the body of the Çüngüş bridge in the future. Between 2173 and 2273, significant displacement increases were not observed in the bridge body. As of 2173, settlement values in the bridge body will become stable. These results will guide researchers to estimate the displacement values

that will occur in the future in the bodies of historical bridges (Fig. 6).

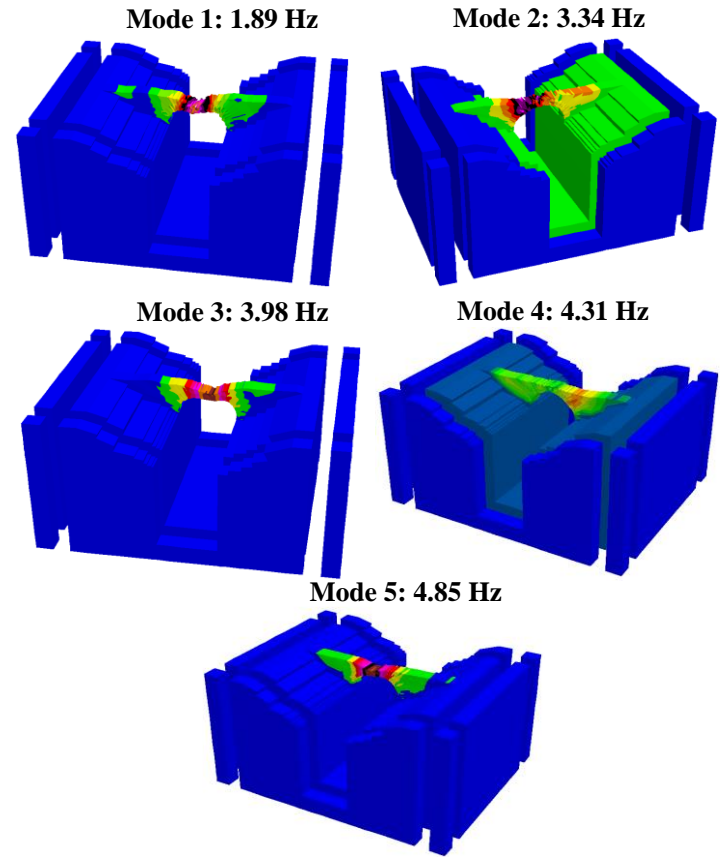


Figure 5. Modal analysis results of the Çüngüş bridge.

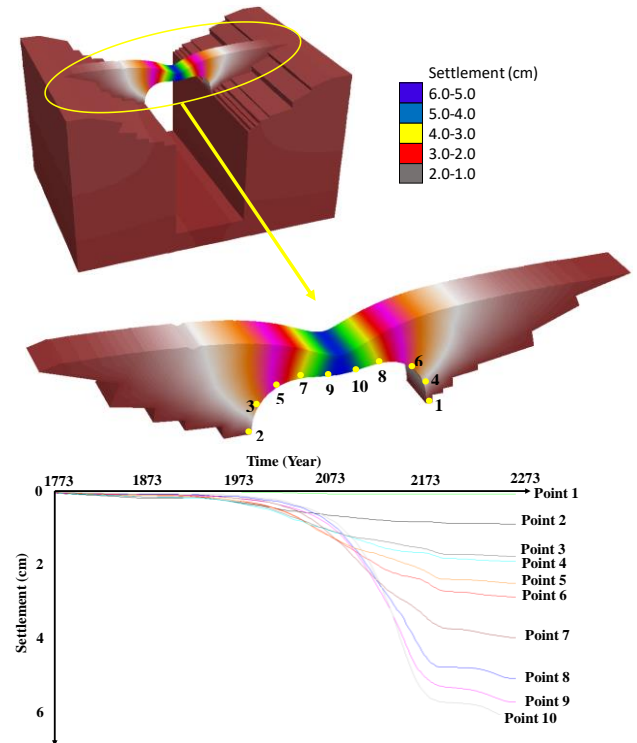


Figure 6. Long-term creep settlement analysis results of the Çüngüş bridge.

Furthermore, during 500 years, the largest displacements occurred on Point 9 and Point 10. Moreover, it was understood that the smallest displacements took place on Point 1 and Point 2. In Figs. 7-16, the seismic analysis results performed by considering the creep analysis results of the bridge were presented in detail. Earthquake accelerations were applied to the 3D model of the bridge in x, y, and z directions and seismic cracks that took place in the arch section of the bridge were also shown in detail. The seismic displacement results from the bridge are shown only for the vertical direction. In Fig. 7, the nonlinear earthquake analysis results of the bridge were shown for Case 1 (Pazarcık1 earthquake). For Case 1, it was seen that the greatest vertical displacements in the bridge occurred in the arch section of the bridge. However, significant displacements were not observed in the foundation section of the bridge (Fig. 7a). As the cracks that occurred in the arch and rockfill material parts of the bridge were examined in detail, it was understood that maximum cracks were observed in the middle parts of the arch section (Fig. 7b). Furthermore, it was seen that the maximum vertical displacements were obtained in the middle parts of the arch section, and the greatest displacement value in the middle parts of the arch section is 25.604 mm (Fig. 7c). As Fig. 8 was evaluated in detail, it was understood that the most critical section of the bridge is the arch section. Besides, for Case 2 (Elbistan earthquake) it was seen that the greatest displacement value in the arch section of the bridge is 24.382 mm. Moreover, significant deformations were observed in the arch section of the bridge for Case 2 (Fig. 8a). Fig. 8b shows the seismic cracks in the rockfill material section of the bridge. The largest cracks on the bridge were observed at the middle sections of the arch (Fig. 8b). In Fig. 9, the seismic analysis results of the bridge were shown for Case 3 (Nurdağı1 earthquake). According to Fig. 9a, it was concluded that the largest displacements (23.30 mm) on the bridge took place in the middle parts of the bridge. In addition, it was seen that the lowest displacements occurred in the feet sections of the bridge (Fig. 9a). In Fig. 9c, it was observed that the maximum displacements for Case 3 occurred in the middle parts of the arch section of the bridge. In Fig. 10, the earthquake behavior of the Çüngüş bridge was shown for Case 4 (Yayladağı earthquake) in detail. For Case 4, it was seen that the largest displacements took place in the arch part of the bridge. Moreover, it was understood that the smallest displacements took place in the foundation section of the bridge. 20.103 mm maximum displacement was observed in the middle of the arch section of the bridge.

Approximately 4 mm maximum displacements were observed at the feet of the arch section (Fig. 10a). Besides, it was observed that significant cracks occurred in the middle of the arch part. These cracks may threaten the seismic safety of the bridge during the earthquake. For this reason, it was suggested that the earthquake safety of historical bridges should be interpreted by considering these seismic cracks (Fig. 10b). In Fig. 11, the earthquake analysis results of the Çüngüş bridge were presented for Case 5 (İslahiye earthquake). According to Case 5, the greatest displacement value in the arch part of the bridge is 19.067 mm (Fig. 11a). Moreover, it was seen that significant cracks occurred in the arch part of the bridge. It was observed that significant vertical bending took place in the arch section of the bridge during the earthquake (Fig. 11c).

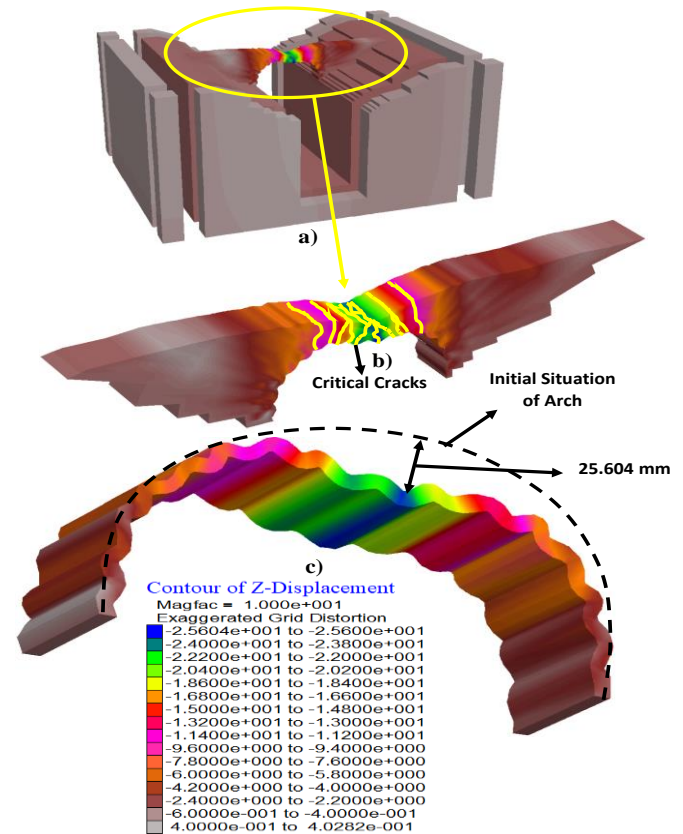


Figure 7. Seismic analysis results (mm) of the Çüngüş bridge for Case 1 (Pazarcık1 earthquake).

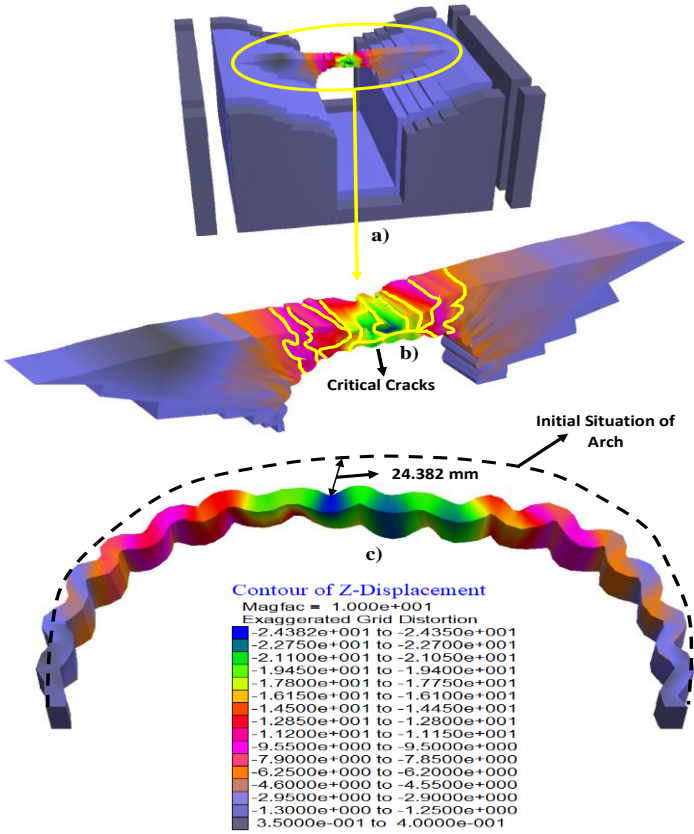


Figure 8. Seismic analysis results (mm) of the Çüngüş bridge for Case 2 (Elbistan earthquake).

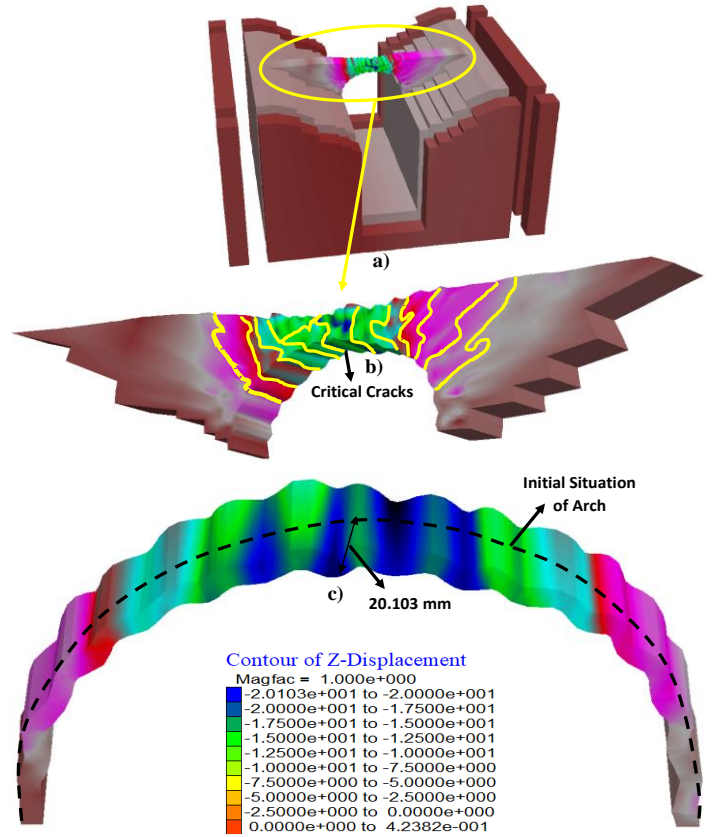


Figure 10. Seismic analysis results (mm) of the Çüngüş bridge for Case 4 (Yayladağı earthquake).

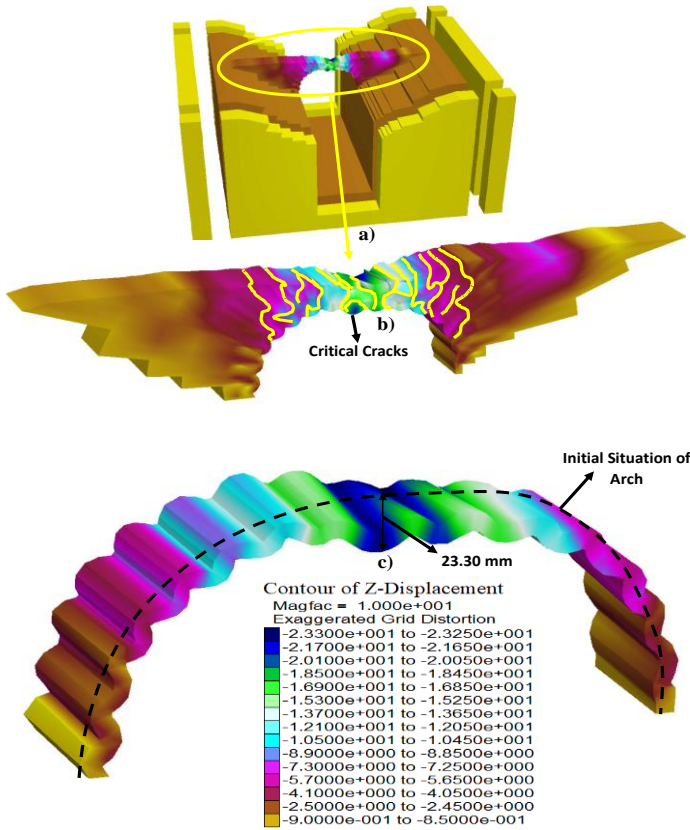


Figure 9. Seismic analysis results (mm) of the Çüngüş bridge for Case 3 (Nurdağı1 earthquake).

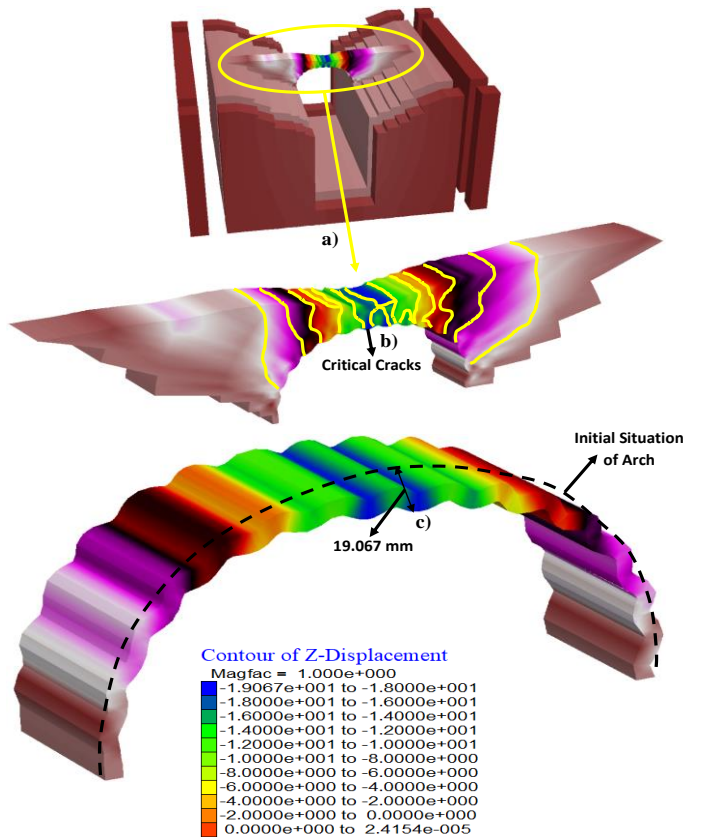


Figure 11. Seismic analysis results (mm) of the Çüngüş bridge for Case 5 (İslahiye earthquake).

In Fig. 12, the earthquake analysis of the Çüngüş arch stone bridge was examined for Case 6 (Yeşilyurt earthquake). As Fig. 12 was evaluated, it was understood that the vertical displacements and cracks in the arch section of the bridge are at serious levels. According to Fig. 12a, it was seen that the maximum vertical displacement value on the Çüngüş bridge is 16.07 mm. This maximum displacement value occurred at the edges of the arch section. Furthermore, it was understood that the smallest displacements observed in the bridge during the earthquake took place in the foundation. When Fig. 12b was assessed in detail, it was seen that the most critical cracks observed in the bridge during the earthquake occurred at the edges of the arch section. In Fig. 12c, only the seismic behavior of the arch section was investigated and it was seen that serious bending was acquired at the edges of the arch section. In Fig. 13, the nonlinear earthquake results and crack analysis results of the Çüngüş bridge were presented for Case 7 (Doğanşehir earthquake). For Case 7, it was seen that the most critical section of the bridge during the earthquake is the arch section. It was observed that the greatest vertical displacements took place in the middle sections of the Çüngüş bridge. It was understood that the greatest seismic vertical displacement value in the arch part is 14.322 mm (Fig. 13a). In Fig. 13b, it was concluded that the cracks that took place in the middle sections of the bridge are larger than the other parts of the bridge. In Fig. 13c, only the seismic behavior of the arch part was assessed and it was seen that the bending in the middle parts of the arch section is much larger than the other sections. From this result, it was understood that the most critical section of the Çüngüş bridge during the Doğanşehir earthquake is the middle parts of the arch section. In Fig. 14, the nonlinear seismic and crack behaviors of the Çüngüş bridge were evaluated for Case 8 (Nurdağı2 earthquake) in detail. According to Fig. 14, it was seen that the largest displacement value on the bridge is 13.04 mm. This value is very important for the seismic safety of historical bridges. Because even very small displacements on historical bridges can cause damage to these important structures. For this reason, it is strongly recommended to use the maximum seismic displacements obtained in this study for the restoration of historical arch bridges. In Fig. 15, the seismic analysis results of the historical Çüngüş bridge were presented for Case 9 (Pazarcık2 earthquake). According to Fig. 15, it was seen that the largest displacement value that took place in the Çüngüş bridge is 12.056 mm. It was observed that this numerical value occurred in the middle sections of the historical bridge. Fig. 15b shows the seismic cracks on the bridge for Case 9, and it was seen that the most

critical cracks that occurred in the bridge during the earthquake took place in the middle sections of the bridge. Moreover, there are no significant seismic cracks in the edge parts of the bridge when compared to the middle sections of the bridge. In Fig. 15c, the seismic behavior of the arch section of the Çüngüş bridge was investigated and it was observed that serious bending took place in the middle parts of the arch section. In Fig. 16, the seismic analysis results of the Çüngüş bridge were presented for Case 10 (Ekinözü earthquake). According to Fig. 16a, the greatest vertical displacement value that occurred in the middle parts of the bridge during the earthquake is 8.849 mm. Smaller vertical displacements were acquired at the feet of the bridge (Fig. 16b).

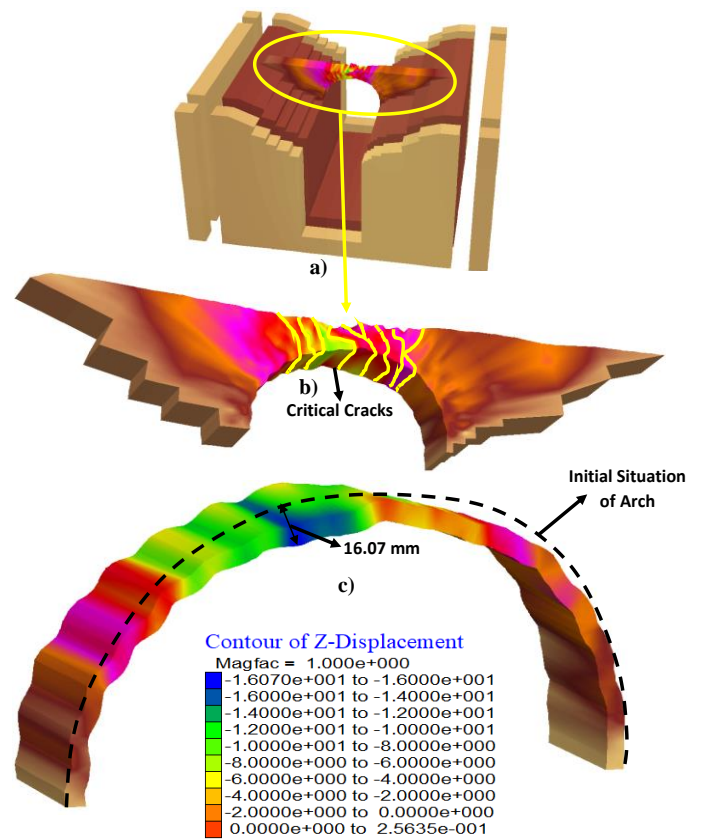


Figure 12. Seismic analysis results (mm) of the Çüngüş bridge for Case 6 (Yeşilyurt earthquake).

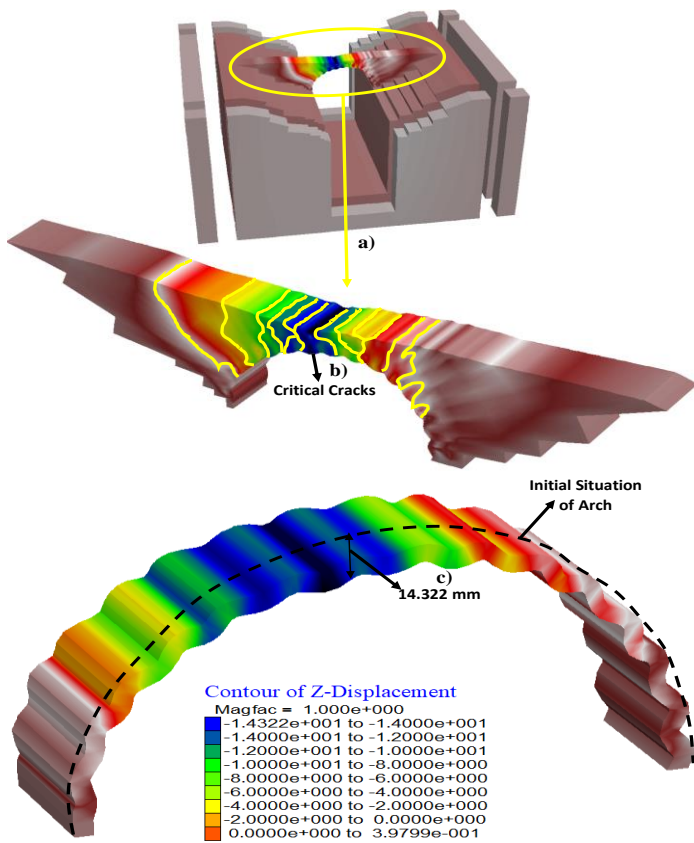


Figure 13. Seismic analysis results (mm) of the Çüngüş bridge for Case 7 (Doğanşehir earthquake).

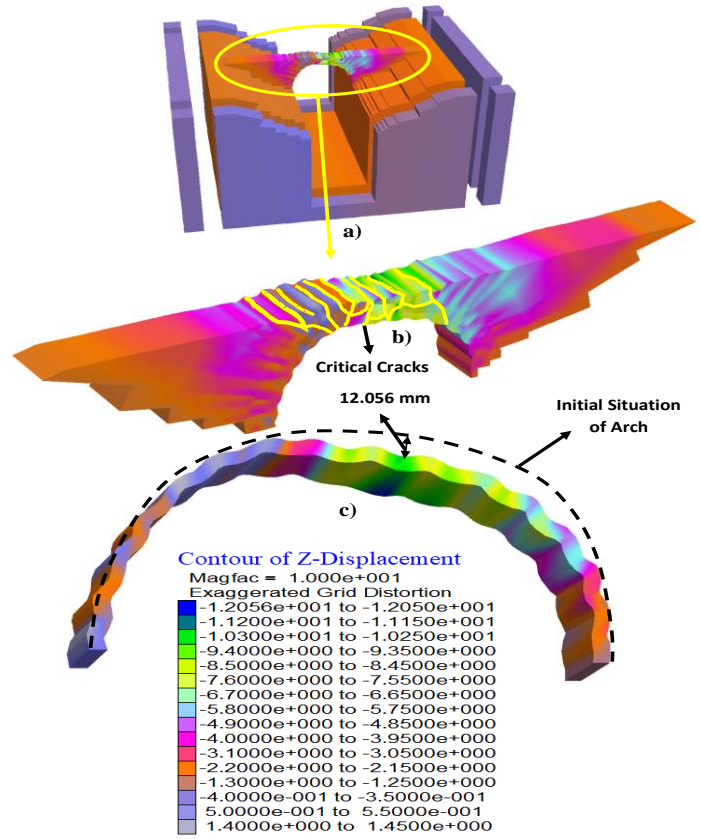


Figure 15. Seismic analysis results (mm) of the Çüngüş bridge for Case 9 (Pazarcık2 earthquake).

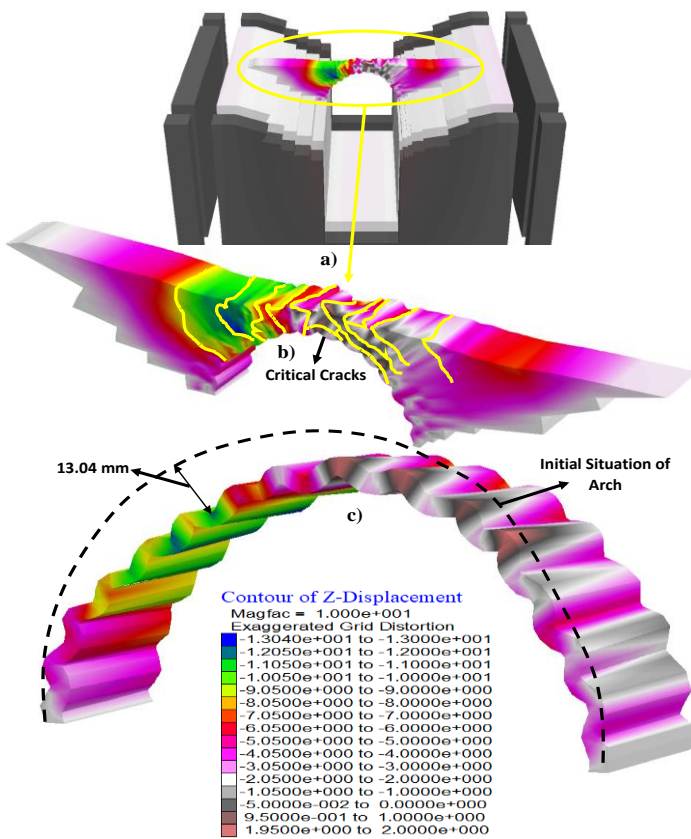


Figure 14. Seismic analysis results (mm) of the Çüngüş bridge for Case 8 (Nurdağı2 earthquake).

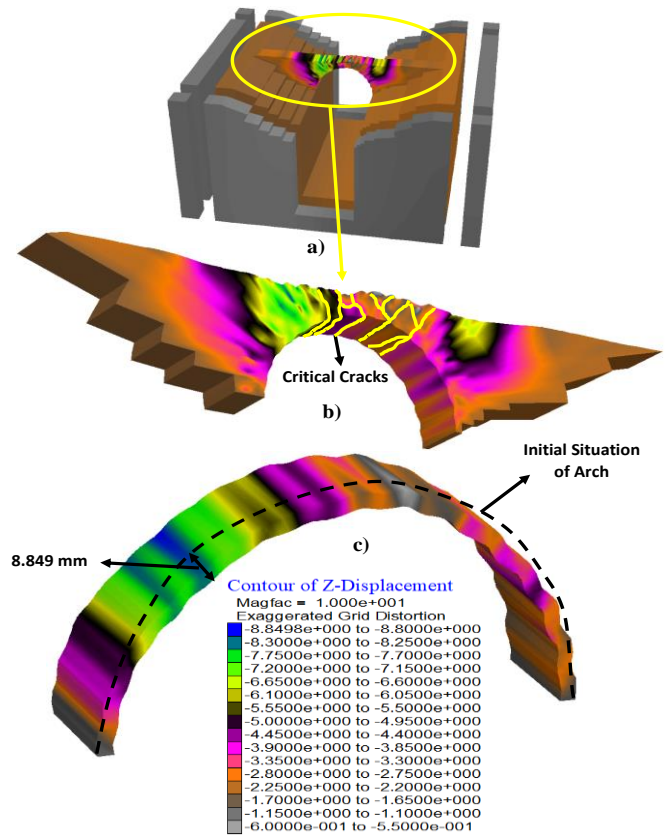


Figure 16. Seismic analysis results (mm) of the Çüngüş bridge for Case 10 (Ekinözü earthquake).

5. Conclusion and Suggestions

In this study, both the long-term creep settlement and earthquake behavior of the historical Çüngüş arch bridge built in the 18th century in Diyarbakır, Türkiye were investigated in detail. The three-dimensional discrete element modeling technique was used while modeling the bridge. Moreover, free field and quiet boundary conditions were applied to the three-dimensional finite-difference model of the bridge, and the seismic behavior of the bridge was investigated under 10 different near-fault earthquakes for the full reservoir situation of the bridge. This study provides new and special contributions to the literature on the examination of creep and seismic behavior of historical bridges. As a result of this study, the following critical results were obtained.

- According to the time-depending creep settlement analyses of the historical Çüngüş stone bridge, it was concluded that the arch (Fig. 4) is the most deformed section of the bridge. During 500 years of creep analysis, the most vertical displacements were obtained in the middle of the arch section of the bridge. Furthermore, the largest vertical displacement values on Point 9 and Point 10 are approximately 6 mm.

- According to the creep settlement analysis results of the Çüngüş stone bridge, it was seen that the changing rate of vertical displacements in the bridge during the first 200 years is very low, and the changing rate in the vertical displacements in the bridge increased between 1973 and 2173. From this result, it was concluded that the changing rate in the vertical displacements of the historical bridge is very low during the first 200 years.

- According to the seismic analysis results, it was understood that the most critical section of the bridge is the arch section (Fig. 4). It was concluded that the seismic vertical displacements in the arch section are higher than the other sections of the bridge. Besides, it was observed that the greatest bending occurred in the middle sections of the arch. According to this result, it has been understood that the arch section of the bridge is the part that needs the most attention for the earthquake strength of historical buildings built on earthquake faults.

- According to the 10 various earthquake analyses, it was observed that the largest displacements and seismic cracks on the bridge occurred in the 2023 Kahramanmaraş (Pazarcık) earthquake. The greatest displacement value that occurred in the middle parts of the bridge during the Kahramanmaraş (Pazarcık) earthquake is 25.604 mm.

This value is of great importance for the future and survival of the Çüngüş Bridge.

- It was seen that the most critical cracks that occurred during the earthquake were obtained in the arch section (Fig. 4) of the bridge. According to 10 different earthquakes, it has been observed that there are very large cracks in the middle sections of the arch section of the bridge and smaller seismic cracks at the edges of the bridge. From this result, it was understood that the most critical sections for the crack behavior of historical stone bridges are the arch sections (Fig. 4).

Acknowledgment

The author wishes to express their thanks to the authors of the literature for the supplied scientific aspects and ideas for this study.

Conflict of Interest Statement

There is no conflict of interest between the authors.

Statement of Research and Publication Ethics

The study is complied with research and publication ethics.

References

- [1] A.C. Aydın, S.G. Özkaya, "The finite element analysis of collapse loads of single-spanned historic masonry arch bridges (Ordu, Sarpdere Bridge)," *Engineering Failure Analysis*, vol. 84, pp. 131-138, 2018.
- [2] A. Bayraktar, E. Hökelekli, "Nonlinear soil deformability effects on the seismic damage mechanisms of brick and stone masonry arch bridges," *International Journal of Damage Mechanics*, vol. 30, no. 3, pp. 431-452, 2021.
- [3] O. Bergamo, G. Campione, C. Cucchiara, G. Russo, "Structural behavior of the old masonry bridge in the Gulf of Castellammare," *Engineering Failure Analysis*, vol. 62, pp. 188-198, 2016.
- [4] B. Conde, L. Díaz-Vilariño, S. Lagüela, P. Arias, "Structural analysis of Monforte de Lemos masonry arch bridge considering the influence of the geometry of the arches and fill material on the collapse load estimation," *Construction and Building Materials*, vol. 120, pp. 630-642, 2016.
- [5] B. Conde, J.C. Matos, D.V. Oliveira, B. Riveiro, "Probabilistic-based structural assessment of a historic stone arch bridge," *Structure and Infrastructure Engineering*, vol. 17, no. 3, pp. 379-391, 2021.
- [6] S. Gönen, S. Soyöz, "Seismic analysis of a masonry arch bridge using multiple methodologies," *Environmental Earth Sciences*, vol. 226, 111354, 2021.
- [7] H. Güllü, H.S. Jaf, "Full 3D nonlinear time history analysis of dynamic soil–structure interaction for a historical masonry arch bridge," *Environmental Earth Sciences*, vol. 75, 1421, 2016.
- [8] M. Naderi, M. Zekavati, "Assessment of seismic behavior stone bridge using a finite element method and discrete element method," *Earthquakes and Structures*, vol. 14, no. 4, pp. 297-303, 2018.
- [9] E.N. Rovithis, K.D. Pitilakis, "Seismic assessment and retrofitting measures of a historic stone masonry bridge," *Earthquakes and Structures*, vol. 10, no. 3, pp. 645-667, 2016.
- [10] Ö. Saygılı, J.V. Lemos, "Seismic vulnerability assessment of masonry arch bridges," *Structures*, vol. 33, pp. 3311-3323, 2021.
- [11] E. Sayin, "Nonlinear seismic response of a masonry arch bridge," *Earthquakes and Structures*, vol. 10, no. 2, pp. 483-494, 2016.
- [12] N. Simos, G.C. Manos, E. Kozikopoulos, "Near- and far-field earthquake damage study of the Konitsa stone arch bridge," *Engineering Structures*, vol. 177, pp. 256-267, 2018.
- [13] G. Zani, P. Martinelli, A. Galli, M.d. Prisco, "Three-dimensional modelling of a multi-span masonry arch bridge: Influence of soil compressibility on the structural response under vertical static loads," *Engineering Structures*, vol. 221, 110998, 2020.
- [14] M. Karalar, M. Çavuşlu, "Performance Evaluation of Historical Rombaki Masonry Building," *Bitlis Eren Üniversitesi Fen Bilimleri Dergisi*, vol. 9, no. 1, pp. 226-247, 2020.
- [15] M. Karaton, H.S. Aksoy, E. Sayın, Y. Calayır, "Nonlinear seismic performance of a 12th century historical masonry bridge under different earthquake levels," *Engineering Failure Analysis*, vol. 79, pp. 408-421, 2017.
- [16] A. Rafiee, M. Vinches, "Mechanical behaviour of a stone masonry bridge assessed using an implicit discrete element method," *Engineering Structures*, vol. 48, pp. 739-749, 2013.
- [17] S. Akkar, T. Azak, T. Çan, U. Çeken, M.B. Demircioğlu, T.Y. Duman, M. Erdik, F.T. Ergintav, S. Kadirioğlu, D. Kalafat, Ö. Kale, R.F. Kartal, K. Kekovalı, T. Kılıç, S. Özalp, S. Poyraz Altuncu, K. Şeşetyan, S. Tekin, A. Yakut, M.T. Yılmaz, M.S. Yücemem, Ö. Zülfikar, "Updated Probabilistic Seismic Hazard Maps for Türkiye," PSHA Workshop, Future directions for probabilistic seismic hazard

assessment at a local, national and transnational scale 5 to 7 September 2017, Lenzburg Switzerland, 2017.

- [18] Itasca, Inc. FLAC version 5 user manual. Minneapolis, USA: Itasca Consulting Group, Inc.: 2002.
- [19] AFAD, Disaster and Emergency Management Presidency. Retrieved from <https://deprem.afad.gov.tr/event-catalog>, 2023.
- [20] M. Cavuslu, "Evaluating effects of various water levels on long-term creep and earthquake performance of masonry arch bridges using finite difference method," *Geomechanics and Engineering*, vol. 31, pp. 31-52, 2022.
- [21] M. Cavuslu, "3D seismic assessment of historical stone arch bridges considering effects of normal-shear directions of stiffness parameters between discrete stone elements," *Structural Engineering and Mechanics*, vol. 83, pp. 207-227, 2022.
- [22] Ö. F. Nemutlu, İ. Güzel, B. Balun, M. Öztürk and A. Sarı, "Nonlinear Seismic Assessment of Historical Masonry Karaz Bridge Under Different Ground Motion Records", *Bitlis Eren Üniversitesi Fen Bilimleri Dergisi*, vol. 12, no. 1, pp. 247-260, 2023.
- [23] G. B. Sakçalı, A. Gönül, M. B. Bağbancı, İ. Yüksel, "Linear/Nonlinear Dynamic Analysis and Prediction of Failure Mechanism of Irgandi Bridge", *Periodica Polytechnica Civil Engineering*, vol. 66, no. 4, pp. 1248-1261, 2022.
- [24] E. G. Yılmaz, E. Sayın, A. Özmen, "Dynamic Analysis of Historical Masonry Arch Bridges under Different Earthquakes: The Case of Murat Bey Bridge", *Turkish Journal of Science and Technology*, vol. 17, pp. 461-473, 2022.
- [25] B. Şeker, M. Özkaynak, "Investigation of Structural Performance of Historical Amasya Hundi Hatun Bridge", *Architecture, Civil Engineering, Environment*, vol. 15, no. 2, pp. 109-120, 2022.
- [26] S. Şeker, H. Şahin, "Evaluation of the Seismic Behavior of the Historic Clandras Bridge" *Usak University Journal of Engineering Sciences*, vol. 5, no. 1, pp. 1-12, 2022.

An Application of an (R, S) Inventory Management Model for a Construction Materials Manufacturing Company by Using Simulation

Durdu Hakan UTKU^{1*}

¹University of Turkish Aeronautical Association, Department of Industrial Engineering,
Ankara 06700, Turkey
(ORCID: 0000-0002-5755-6101)



Keywords: (R, S) Inventory Control Modeling, Simulation, Inventory Management, Production Control.

Abstract

Globalization has motivated companies to develop competitive strategies in today's business environment. In this context, they lead them to review their costs. When the cost items are analyzed, the most critical point that will give an advantage to companies in terms of cost is that companies healthily manage their inventory. Inventory management is of vital importance as the companies have a significant percentage in terms of cost and ensure that the customer demands are met in a timely and sufficient manner. This study focuses on the problems of the company's inventory control decisions that ensure balanced and minimum costs through effective inventory management. In this study, one-year data on demand, consumption, and inventory of a company that uses traditional methods including semi-finished products are considered. Since the demand is not known precisely and it is probabilistic, we apply the (R, S) inventory control model. We use simulation as a stochastic methodology to determine the inventory level of the construction materials manufacturing company under consideration. As a result of the study, after comparing the actual data in the current system with the developed model we apply, it is observed that the cost reduction and its use provided additional benefits to the company.

1. Introduction

Inventory is the quantities of items that the enterprises hold to meet customers' expectations. Determining and managing the right inventory model plays a critical role in the prevention of problems that may arise in the future. Any mistake that may accrue in this regard may cause financial damages to the companies together with the loss of reputation. The companies may hold more inventory on hand than they need. This situation causes waste and loss of money due to the becoming obsolete of the product over time. Also, it will increase the risk of investing in high quantities of the items, the cost of workers, insurance, security, and storage.

On the other hand, having a high inventory level is a problem as well as having a too-low level of inventory that may increase the costs and the effectiveness of

the companies. A small quantity of shortage of inventory for the company may lead to high-level costs, a decrease in customer satisfaction, and a loss of commercial reputation. Effective inventory management ensures the elimination of disruptions caused by production and keeps the product ready at the time of purchase by the customer. If the companies have appropriate systems to manage their inventory effectively, they may control their operating costs and increase profitability. Hence, the most appropriate inventory management policy should be selected and implemented.

Multi-stage inventory systems are modeled as either deterministic or stochastic. In real life, because some variables, like demand and lead time, are not likely to be known in advance, it is necessary to consider inventory management in a stochastic way. Thus, in this study, we use simulation as a stochastic

*Corresponding author: hakanutku.thk@gmail.com

Received:31.03.2023, Accepted:05.06.2023

methodology to determine the inventory level of the construction company under consideration.

Inventory is the physical goods that enterprises store to meet the requirements that may occur in future periods or to prevent problems that may accrue in the production process. The determination of the suitable inventory management method counts on the capacity, organizational structure, production type, and financial situation of the company. In order to use the resources effectively in inventory management, companies should use appropriate methodologies.

There are different studies carried out by different sectors for inventory management with different methods. In this part, the research studies using ABC analysis and the Analytical Hierarchy Process (AHP) method, the Just in Time (JIT) philosophy and system, and the stochastic stock control method in the literature are investigated. In the literature, the most common inventory control systems are (R, s) , (s, Q) , (s, S) , (R, S, S) , and (r, s, nQ) systems. In the (R, s) system, the inventory status is checked in each R period and if S is at or below the reorder point, the inventory position is raised to the S level. It includes a periodic review feature, which gives companies an advantage in reducing shipping costs. It is generally preferred by companies that purchase the material from the same supplier. Rabta and Aïssani [1] investigate the steadiness in an (R, S, s) inventory modeling and apply a strong stability method to consider quantitative estimates. Poisson distributed demand pattern is used in the numerical experiments for the (R, s, S) modeling. The effect of the strong v -stability of the Markov chain is observed in the study. Babiloni et al. [2] study estimating the fill rate in an (R, S) system. An approach to estimate the exact fill rate is proposed when the demand behavior fits a discrete probability distribution. A simulation methodology is proposed to test and show the effectiveness of the study. Janssen et al. [3] propose a method to find the reorder point and mean inventory level including service level constraints for the (R, s, Q) inventory model. The proposed approach covers the discrete demand process. Gökçen et al. [4] develop a heuristic to find optimal inventory control parameters of Optimization via Simulation (OvS) for the (R, s, S) policy and supplier selection in a two-stage supply chain taking into account the lost sales. They aim to show how the OvS model can be applied effectively with the lost sales taking into account the supply chain cost. Rodrigues and Yoneyama [5] present a new inventory control model for non-repaired products that are periodically checked. They propose an (R, s, S) model that minimizes the total cost of inventory with a fill rate constraint.

Tarim and Smith [6] develop a constraint programming (CP) model for an (R, s, S) system including service level constraints. To improve the performance of the algorithms, domain reduction methods are made use of. It is found that the proposed CP model performs better in mixed-integer programming modeling. Moors and Strijbosch [7] introduce a formula for the average shortage of an (R, s, S) inventory control system in which demand data fit the gamma distribution. The Delphi software is used to simulate the proposed (R, s, S) system for gamma distributions. Ekren and Arslan [8] aim to compare different lateral transfer policies in an (S, s) inventory control problem for a supply chain network system. Simulation models are developed in ARENA 14.5. Using the OptQuest tool, the total cost is minimized by taking the fill rate into account and the performances of the models are compared. They show that the proposed supply chain design produces efficient results compared to the supply chain without a lateral transfer policy. Moors and Strijbosch [9] develop a fast and effective algorithm to simulate an (R, s, S) model in which both the demand and lead time are stochastic. They emphasize that the proposed algorithm can be used to calculate fill rate performance measurements and find parameter values leading to a projected service level. Aytekin [10] aims to eliminate the management difficulties that may arise due to the usual increase in product diversity and applies the Just in Time (JIT) method by using the data obtained from a hospital material and service management unit. Inventory control model alternatives are evaluated by using the priority matrices method.

Another application is carried out on the raw material inventory control at the cement factory by Karahan and Aslan [11]. Since the orders made by the factory are given at certain intervals during the year, it is found appropriate to use the inventory model from the stochastic inventory control models (R, S) in this application. A simulation model is designed by using the ARENA simulation software to see the changes that may be obtained in the operations and costs of the company's current model and the developed (R, S) inventory model. Fisher and Raman [12] study determining the minimum order quantity on the stochastic inventory control model. In the proposed stochastic programming model, they try to estimate the probability distributions of the demand. The model increases the profit by 60% compared to the current system. Madduri [13] develops inventory policies for foods based on continuous and periodic inspections. Review policies are evaluated using simulation models. Considering the perishability of the product from the results of the simulations, EOQ

order policies are examined. The periodic review policy is stated to be ideal.

Yalçınkaya and Karataş [14] use ABC analysis to identify critical items in the inventory. To analyze the company's current inventory management policy for the specified items in the inventory, ARENA is used as software. The criticality of the materials needed in hospitals and their continuity has created the necessity of taking advantage of stock management policies. Wang et al. [15] aim not to be in stock out occurrence for hospital materials and to keep the costs of the inventory to a minimum as much as possible. Additionally, the study enables overcoming the disadvantages of existing reorder point approaches. Aslantaş [16] performs an ABC analysis for the products used in the production of distribution transformers in a transformer factory. A simulation-optimization approach is implemented for the periodic review inventory policy (R, s, nQ). A

significant cost reduction is observed with the policy implemented. Kasımoğlu et al. [17] develop a mixed-integer programming model to solve the excess buffer inventory problems for a white goods production company with sequence-dependent setup times. Utku [18] proposes an optimization model and a simulation model to evaluate the bottlenecks and improve production procedures by investigating different alternatives at an automobile industry company. Pınar et al. [20] perform an ABC analysis for a textile company and propose a management strategy for the company.

Table 1 summarizes the literature about the (R, s, Q) stochastic inventory models and enables us to compare and see the differences between the proposed model. The proposed model contributes to the literature by using the simulation as a solution and diagnostic tool for stochastic inventory modeling.

Table 1. Some of the related studies in which (R, S) inventory management is considered in the literature.

Authors	Subject	Method
Rabta & Aïssani (2004) [1]	Investigating the steadiness in an (R, S, s) modeling and applying a strong stability method to consider quantitative estimates	Markov Chain
Babiloni et al. (2012) [2]	Estimating the fill rate in the (R, S) system	Simulation
Janssen et al. (1996) [3]	Determining the reorder point and average inventory level for the (R, s, Q) inventory modeling.	Compound Bernoulli Process (CBM)
Gökçen et al. (2015) [4]	Showing how the Optimization via Simulation (OvS) model can be applied effectively with the lost sales system considering the supply chain cost	Optimization via Simulation (OvS)
Rodrigues & Yoneyama (2020) [5]	Minimizing the total cost of inventory with a fill rate constraint	Prognostics and Health Monitoring (PHM)
Tarim & Smith (2007) [6]	A Constraint Programming (CP) model for a nonstationary (R, s, S) system including service-level constraints	Constraint Programming (CP)
Moors & Strijbosch (2017) [7]	A model for the average shortage of an (R, s, S) model in which demand fits the gamma distribution	Delphi Program
Ekren & Arslan (2019) [8]	The comparison of different lateral transfer policies in an (S, s) inventory control problem for a supply chain network system	Simulation modeling
Moors & Strijbosch (2002) [9]	A simulation model for an (R, s, S) inventory system in which both demand and lead time are stochastic	Delphi Program
Aytekin (2009) [10]	An application of just-in-time inventory management (Hospital)	Just in Time (JIT) inventory management
Karahan & Aslan (2016) [11]	An application on inventory control (Cement Factory)	Stochastic stock control modeling (R, S).
Fisher & Raman (1996) [12]	Cost reduction in case of the demand uncertainty	Stochastic modeling
Madduri (2009) [13]	Inventory policies for perishable products with fixed shelf-lives	Simulation modeling
Yalçınkaya & Karataş (2020) [14]	Simulation modeling of ABC inventory control process for spare parts in an automotive company	Simulation modeling

Wang et al. (2015) [15]	An inventory management problem	
Aslantaş (2019) [16]	Simulation optimization for the inventory control in a transformer production company	An (R, s, nQ) model and a simulation-based optimization approach are used.
Kasimoğlu et al. (2021)	Optimization for the prevention of excess buffer inventory	Mixed-integer programming

In this study, we consider the inventory management of two types of final products of exterior materials manufacturing with the stochastic behavior of the real demand data. Different from the literature, as a contribution, the (R, S) inventory management of the manufacturing system is modeled by using discrete event simulation regarding the cost and inventory level of the products.

In the remainder of the study, the material and methodology are stated in the second section including simulation modeling and input data analysis; results are discussed, and an output analysis is carried out in the third section finally, the

conclusion and the suggestions are mentioned in the fourth section.

2. Material and Method

An inventory management model for the “Betopan” and “Yalipan” items in a construction material manufacturing company is developed and real data are used for the application. The demand, consumption, and inventory data for the factory's products in the past years are shown in Table 2, Table 3, and Table 4, respectively.

Table 2. One-Year Purchasing, Consumption, and Inventory for Betopan product.

Months	J.	F.	M.	A.	Ma.	J.	Ju.	Au.	S.	O.	N.	D.
Betopan Purch.	5.23	760	503	418	29	4.74	148	43	127	3.17	5.43	3.99
Betopan Cons.	2.32	2.16	2.34	5.87	7.21	5.56	4.13	2.80	5.98	4.64	3.47	2.80
Betopan Inv.	28.32	26.47	23.24	21.19	15.21	15.14	10.12	7.23	1.10	1.115	3.12	4.90

Table 3. One-Year Purchasing, Consumption, and Inventory for Yalipan product.

Months	J.	F.	M.	A.	Ma.	J.	Ju.	Au.	S.	O.	N.	D.
Yalipan Purch.	0	0	0	0	29	4.74	0	0	0	0	0	0
Yalipan Cons.	570	1.148	2.96	2.31	1.90	289	80	1.81	464	501	1.27	2.13
Yalipan Inv.	15.28	14.56	11.01	9.62	9.19	10.50	10.21	7.74	7.32	7.48	6.38	4.62

Table 4. Inventory Statistics for the Past Year.

One year total Betopan consumption	49,313	One year total Yalipan consumption	15,444
Average monthly Betopan consumption	4,109,417	Average monthly Yalipan consumption	1,287
One-year total Betopan inventory	157,174	One-year total Yalipan inventory	113,944
One year Betopan inventory cost (TL)	3,245,780	One year Yalipan inventory cost (TL)	2,783,120

The quantity of Betopan consumed by the factory is 49,313, while the actual amount of Betopan kept in inventory in the factory is 157,174 (Table 4). That is, the inventory held is about 3 times the amount consumed. The quantity of Yalipan consumed in the

company is 15,444 and the actual quantity of Yalipan inventory held is 113,944. Accordingly, the quantity of inventory held is approximately 7 times the quantity consumed. As shown in Table 4, the

quantity held in inventory is much greater than the quantity consumed.

2.1. Simulation Modeling

Simulation is a suitable methodology that we can be used for analyzing the behavior of real systems by mirroring the components and relevant processes to evaluate and foster measurements to improve the systems. Designing the model and necessary experiments are the major two phases in the implementation of the simulation. Simulation is used for various types of supply chains and their management because of the opportunities that it assures a wide spectrum of benefits. Accomplishing the appropriate level of inventory for every component of the supply chain, determining the desired service levels that stand for an efficient struggle for the uncertainties, and helping an efficient production planning, scheduling, and implementation of them in the supply chains are some of these opportunities [19]. Simulation enables us to foresee the system's efficiency, compare different alternatives, and decide on the best alternative. The discrete-event system simulation modeling is used for the simplified imitation of real-world systems which are generated to understand their performance over time and to identify different behaviors of systems.

In this model, since the demand is unknown and probabilistic, we use simulation as a suitable method to apply the (R, S) inventory control model for a construction materials manufacturing company. The inventory control policy of Betopan and Yalipan products is modeled with the simulation method and the safety inventory and order quantities are determined as a result of the simulation study. Using the outputs obtained, the current situation and results of the proposed model are compared considering the costs. For the application, the necessary monthly consumption data are analyzed, and the probabilistic behavior of the data is mirrored in the simulation model by determining the distribution of the past data via input data analysis.

In this study, the assumptions considered for the developed model are as follows:

- (1) (R, S) inventory policy is applied.
- (2) Production is a continuous activity.
- (3) The order cost is independent of the number of orders.

(4) The simulation model is accepted to be initiated from the initial condition.

The distribution functions of the consumption amount of the semi-finished products of the company are analyzed by using ARENA software and its Input Analyzer module.

2.2. Input Data Analysis

In order to establish the simulation model, the probability distributions of the product groups are to be examined, and the quantity of demand is required. Input data analysis is essential for the simulation model to reflect the real system. The data that is used in the model include the data of "Betopan" and "Yalipan" inventory records obtained in the previous year of the company. The minimum, maximum, and standard deviation values of the product groups are determined in accordance with the data obtained. Also, information on demand distributions and lead time of products are stated in this section.

ARENA Input Analyzer is used to analyze the distribution of the data observed, and it provides the histogram graphics of the data to use for the diagnosis of the family of the distribution that fits the data. In this way, the probabilistic behavior of the system is simulated in the simulation model generated. For the Betopan consumption, the most appropriate distribution is found as $2 + 5.73 * BETA (0.58, 0.996)$ by the ARENA Input Analyzer. Accordingly, the P-value is found as 0.15 for the distribution which proves that the data fit the Beta distribution. In addition, the minimum value of the product group is 2.16, the maximum value is 7.22, the standard deviation is 1.72 and the average is 4.11. For the Yalipan consumption, according to the input analysis, the data fit $1 + WEIB(43.5, 0.351)$. The P-value is found as 0.15 for the distribution that supports that the data fit the Weibull distribution. The company waits for a certain time to supply products from the same supplier. In this case, they try to prevent this situation by keeping extra inventory. In order to determine the behavior of the system, we use past data as stated in Table 5. Accordingly, the distribution of the data is determined by using real lead time data.

Table 5. The sample data for finding the distribution of the lead time.

Order Number	Lead Time (days)	Order Number	Lead Time (days)
1	4	16	5
2	3,7	17	4,8

3	4,2	18	3,6
4	3,3	19	4,1
5	4,9	20	4,7
6	4,9	21	3,8
7	3,2	22	3,5
8	4,7	23	4,3
9	3,8	24	3,1
10	4,1	25	4,9
11	4,1	26	3,6
12	3,6	27	3
13	3,1	28	4,2
14	3,3	29	3,6
15	4,5	30	3,1

In Figure 1 the autocorrelation (AC) and partial correlation (PAC) in the first lag are not within the limits but have about 5% off the limits which is acceptable since there is a very small difference considering the limit. Since the sample of data is independent of each other, they are random and can be used to generate a distribution of delivery times. Using the ARENA Input Analyzer, we fit the lead time values and get the fitted distribution result as $2 + 3 * BETA(0.722,0.788)$. The beta distribution is a distribution used for continuous unbiased variables limited to values between 0 and 1 but is defined by shape and scale as two parameters. The P-value is 0.16 which supports the good fit to the Beta distribution.

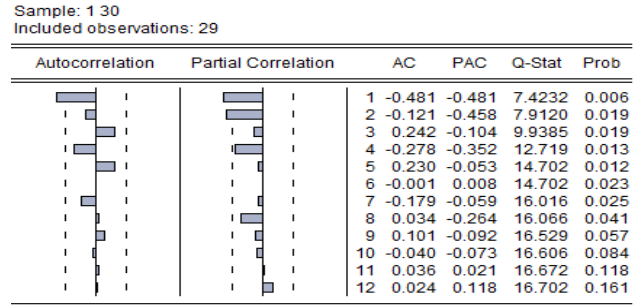


Figure 1. Autocorrelation and Partial Correlation.

2.3. Simulation Model

In this section, a simulation model is developed for the production and inventory system of the company by using ARENA software. As shown in Figure 2, the model includes two components. In the first part, the model simulates customer demand generation. This component starts with the creation of the customers and the demand associated with them. The entity is the customer. There are two decision modules available to indicate whether the customer demands can be met from the inventory or the production will start to maintain the inventory level. Thus, it checks the inventory level and initiates the production when the level of the inventory reaches reorder point. Additionally, it also monitors the demand that is lost when the customers are not satisfied.

The entities in the production component of the simulation are the production units. In this section, incoming raw materials accumulate in the in-process queues and they are processed and eventually added to the variable that we define with the name "inventory". In addition to the inventory, there are two decision modules to check whether adequate production has been done.

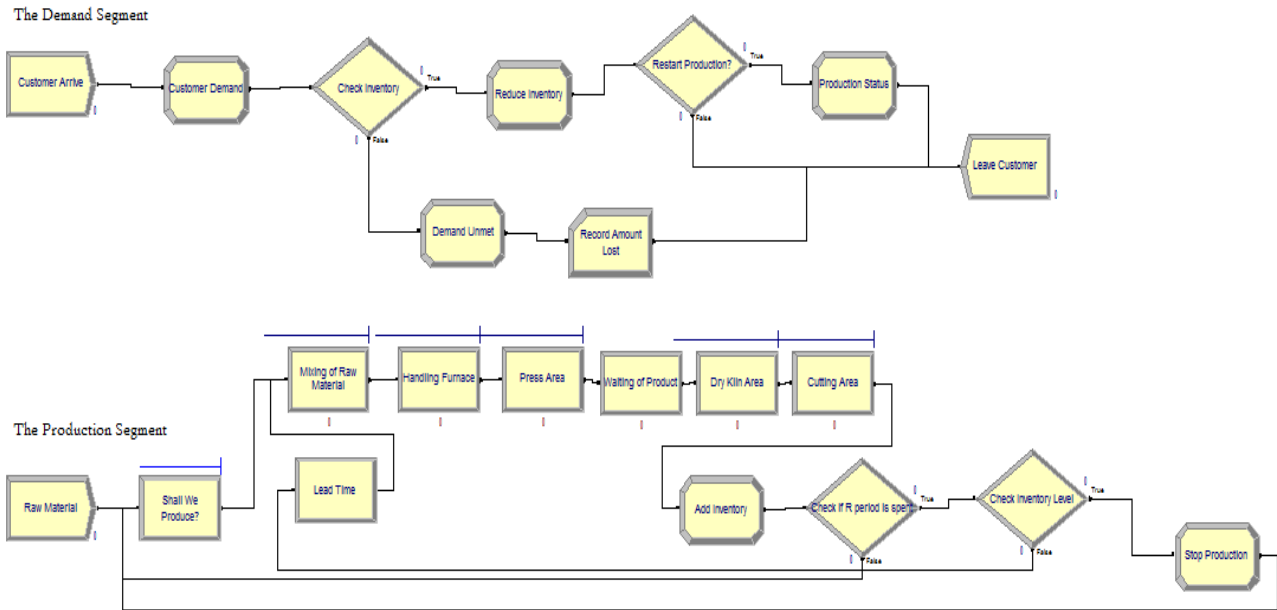


Figure 1. Arena Interface for the Simulation Model.

Accordingly, the major subcomponents including the input data and output data transformation procedures are also included in both of the model components in Figure 2. These procedures include all of the necessary elements like variables, resources, and statistics that set the relevant input variables, calculate the necessary statistics and produce the related report.

The source of the customer demand is generated by using the “create” module that is defined as “Customer Arrive” in the demand component of the model. The customer arrivals are determined as random behavior with a random variable that is found that fits the uniform distribution with parameters (2, 7). Besides, the customer demand is found that fits a beta distribution with parameters (0.58, 0.996) by using the Input Analyzer tool in ARENA by applying the real data obtained from the company. Thus, the customer entity enters this module and is assigned a random value within this distribution range. Then the customer entity comes to “Check Inventory” as a decision module to decide if the customer demand can be satisfied from the inventory. The control module may follow two ways: (1) If the variable “Inventory” has a value that is equal to or greater than the value of the “Demand”, this means that the demand is to be satisfied. Accordingly, the entity named “customer” gets the “True” statement from the module named “Assign”. Then, “Reduce Inventory” decreases the onhand inventory considering the demand. Then switches to the decision module that is named “Restart Production?”, to control if the variable named “Reorder Point” is “Inventory \leq Reorder Point”. In case that is true, the constraint defined in our “Assign” module named production status (Production = 1) enables the connection to the second

segment in case of production needs. This will enable the product that is held in the “Hold” module named (Shall we Produce?). In general, the work completed in this segment is to create customers and demands and to adjust the changing inventory level with customer arrivals. (2) In case the value of the “Inventory” variable has a smaller value than the demand value, it means that the current demand is not satisfied or partially satisfied. In both ways, the customer entity moves to the “Update Shortage module, which is an “Assign” module, where the Inventory variable is set to 0. At the same time, the “Lost” variable is followed by the customers whose demand could not be satisfied. In addition to this, the variable “Amount Lost” states the demand lost. The entity related to the customer then goes through the module named “Record”, that records the amount lost, to keep track of the quantity that is lost for each of the customer (unsatisfied customer) by using “Tally”. Then, by using the module named “Leave Customer”, the entity moves in order to be disposed of.

The production segment starts with the “Raw Material” module which is a “Create” module. Entities defined in this part represent the production units. The product entity moves in the model repeatedly, with each cycle representing a production cycle. The “Shall We Produce?” which is a “Hold” module controls the process modules that come after themselves and carry out the production. The “Hold” module helps the user to monitor an entity by searching for the true or false logic condition. If the “Production = 1” condition is correct, it moves to the other modules, otherwise, it continues to wait in the queue “Shall We Produce?”. When the condition is

satisfied, the entities go through a six-stage production process including mixing raw material, handling furnace, pres area, waiting of product, dry kiln area, and cutting area. All of these operations are provided by the module named "Process" by using the ARENA software interface. All these processes have their unique processing time values, for example, mixing raw materials takes 10 to 20 minutes.

The level of inventory in the warehouse is kept by the "Inventory" variable that is at the beginning determined and stated to be 502. At the end of operations, the product entity in circulation comes to the "Assign" module named "Add Inventory". The "Add Inventory" module adds a group of 20 of the final products to the inventory. Then the product entity has to go through two decide modules. The first one is "Check if the R period is spent", which allows us to check whether the elapsed time is up to the "r"

period. Using the information obtained from the company, R represents 3-month periods and since the "TNOW" expression refers to the current time in the arena program, this indicates the time corresponding to 3 months (TNOW = 2160). The second is the "Check Inventory Level" module, which checks whether the updated inventory level is greater than or equal to the s level (Inventory > = S Level). If the entities do not meet the requirements, they must return to the beginning of production and repeat the processes. The entities that meet these two conditions come to the "Stop Production", which is an "Assign" module, where the production is updated as "0" and the production stops.

By using the "Variable" module, the defined variables in the model can be examined and evaluated. Figure 3 shows the defined "Variables".

Variable - Basic Process									
	Name	Comment	Rows	Columns	Data Type	Clear Option	File Name	Initial Values	Report Statistics
1	Inventory				Real	System		1 rows	<input checked="" type="checkbox"/>
2	S Level				Real	System		1 rows	<input checked="" type="checkbox"/>
3	Batch Size				Real	System		1 rows	<input checked="" type="checkbox"/>
4	Reorder Point				Real	System		1 rows	<input checked="" type="checkbox"/>
5	Demand				Real	System		0 rows	<input checked="" type="checkbox"/>
6	Total Customers				Real	System		0 rows	<input checked="" type="checkbox"/>
7	Lost				Real	System		0 rows	<input checked="" type="checkbox"/>
8	Demand Met				Real	System		0 rows	<input checked="" type="checkbox"/>
9	Production				Real	System		0 rows	<input checked="" type="checkbox"/>
10	Specific Production Cost				Real	System		1 rows	<input checked="" type="checkbox"/>
11	Specific Shortage Cost				Real	System		1 rows	<input checked="" type="checkbox"/>
12	Specific Holding Cost				Real	System		1 rows	<input checked="" type="checkbox"/>
13	Amount Production				Real	System		0 rows	<input checked="" type="checkbox"/>
14	Number of Setup				Real	System		0 rows	<input type="checkbox"/>
15	Set Up Cost per Unit				Real	System		1 rows	<input type="checkbox"/>

Figure 3. The "Variables" in the model.

By using the module named "Statistic", it is possible to obtain the added statistics by the modeler that are collected throughout the simulation run and it

makes it available to specify the output data files by the user. Figure 4 shows the "Statistic" module (spreadsheet) that helps us to see the information kept in the Inventory Model.

Statistic - Advanced Process			
	Name	Type	Expression
1	Average Inventory Level	Time-Persistent	Inventory
2	Production On	Time-Persistent	Production == 1
3	Lost Rate	Output	Lost Customer / Total Customers
4	Holding Cost	Output	Specific Holding Cost * Inventory
5	Shortage Cost	Output	Amount Lost per Customer * Specific Shortage Cost
6	Production Cost	Output	Amount Production
7	Total Inventory Cost	Output	OVALUE(Holding Cost) + OVALUE(Production Cost) + OVALUE(Shortage Cost) + OVALUE(Set Up Cost per Unit)
8	Set Up Cost	Output	Set Up Cost per Unit * Number of Setup

Figure 4. Spreadsheet of the Statistic Module.

In Figure 4, there are two (DSTAT) Time-Persistent statistics, which are stated as "Average Inventory Level", for the "Inventory" variable and "Production On", for the expression "Production=1".

The outputs which are kept in the "Time-Persistent" statistics include the mean value, minimum and maximum values of the variables, and the 95% confidence interval that is observed during any run.

Additionally, the list includes six outputs: holding cost, shortage cost, production cost, set-up cost, total inventory cost, and loss rate. This help cost calculation while finding (near to) optimal results.

3. Results and Discussion

In this section, we implement validation and verification to check whether the simulation model established will work as a real system and investigate

whether the results of the simulation are realistic together with the output analysis.

We determine the inventory level that will result in the lowest expected cost from the designed model. The “Process Analyzer” in ARENA is used and the trials are conducted to find the Betopan product inventory level. New values for the desired parameters are found over the revised values (reorder point, batch size, and s level).

Table 5. Results for the Betopan Product.

	Total Inventory Cost	Inventory (Level)	Production On
Base Model	3,712,768.073	30,961.059	0.978
Alternative 1	3,186,992.582	26,578.997	0.977
Alternative 2	2,839,193.154	23,680.026	0.976
Alternative 3	2,665,893.154	22,235.026	0.976
Alternative 4	2,695,084.744	22,473.056	0.979

In Table 5 it is seen that the inventory cost for the “Alternative 3” trial is less than the others. The inventory level corresponding to this cost for the Betopan product is 22,235. This alternative also provides a 97 percent utilization. We consider

“Alternative 3” since the primary goal is repeated in the same way for the “Yalipan” product and the results are reported in Table 6.

Table 6. Summary Results for the Yalipan Product

	Total Inv. Cost (TL)	Inventory (Level)	Production On
Base Model	2,750,312.010	26,059.365	0.977
Alternative 1	2,126,540.063	19,468.001	0.975
Alternative 2	1,737,863.190	14,680.746	0.976
Alternative 3	2,003,769.157	16,996.219	0.977
Alternative 4	1,557,862.139	11,330.086	0.978

As shown in Table 6, after 4 trials for the Yalipan product, the optimal “s” level is found. The fourth alternative result is the lowest in terms of cost

and the highest utilization when compared to other values. Thus, Alternative 4 is selected.

Table 7. Summary Results for Both of the Products.

	Total Inventory Cost (TL) After Simulation Application	Total Inventory Cost (TL) of The Current System
Betopan	2,665,893.154	3,245,780
Yalipan	1,577,862.139	2,783,120
Total	4,243,755.293	6,028,900

Table 8. Results for the Betopan and Yalipan Products.

	Total Inv. Cost (TL)	Inventory (Level)	Production On
Betopan	2,665,893.154	22,235.026	0.976
Yalipan	1,557,862.139	11,330.086	0.978

As seen from Tables 5-8 Betopan values are higher than Yalipan because it is more preferred by the customers.

For the validation purpose, after the simulation results are obtained as in Table 5 – 8, the comparison of the results from the (R, S) stochastic inventory control model developed and proposed in the study with the current inventory control performed by traditional methods are implemented. For both products, the factory has calculated the total annual inventory cost as 6,028,900 TL with their classical method. The total cost of holding inventory is calculated by the developed stochastic (R, S) model as 4,243,755.293 TL for the following year. In other words, even if the proposed inventory control model is used for only two products, it is seen that it reduces the inventory cost by 1,785,144.707 TL annually.

4. Conclusion and Suggestions

In this study, the inventory status of two types of final products belonging to the factory which is a manufacturer of exterior materials is considered. An application is implemented according to the data obtained from the production facility of the siding factory. In order to reflect the stochastic nature of the demand data, the (R, S) inventory management system is modeled by using discrete event simulation regarding the cost and inventory level of the products.

In the model, two types of product groups are considered: “Betopan” and Yalipan” products. The simulation model developed aims at the inventory control of the “Betopan” and “Yalipan” products of the company. With the developed model, (R, S) parameters that make the total cost minimum is found. In line with the results obtained, it is observed that total inventory cost decreases by about 30 percent. Additionally, the cost reduction and its use provide additional benefits to the company. The study can be extended and applied to all end products and inventory levels that make the total cost minimum can be determined. As a future study, the simulation model can be used for the implementation and comparison of different inventory policies for the companies.

Acknowledgment

I would like to thank Irem Unal and Irem Bugdaycı for their support during some phases of this study.

Conflict of Interest Statement

There is no conflict of interest.

Statement of Research and Publication Ethics

The study complies with research and publication ethics.

References

- [1] B. Rabta and D. Aïssani, “Strong stability in an (R, s, S) inventory model”, *International Journal of Production Economics*, vol. 97, no.2 , pp. 159-171, 2005.
- [2] E. Babiloni, E. Guijarro, M. Cardos, and S. Estelles, “Exact Fill Rates for the (R, S) Inventory Control with Discrete Distributed Demands for the Backordering Case”, *Informatica Economica*, vol. 16, no. 3, pp.19-26, 2012.
- [3] F. Janssen, R. Heuts, and T. de Kok, “On the (R,s, Q) inventory model when demand is modeled as a compound Bernoulli process”, *European Journal of Operational Research*, vol. 104, no. 1998, pp. 423-436, 1996.
- [4] M. Gökçen, A. Boru, A. T. Dosdogru, and F. Geyik, “(R, S, S) Inventory Control Policy and Supplier Selection in A Two Echelon Supply Chain: An Optimization via Simulation Approach”, *Proceedings of the 2015 Winter Simulation Conference (WSC)*, pp. 2057-2067, IEEE, December 2015.

- [5] L.R., Rodrigues, and T. Yoneyama, "A spare parts inventory control model based on Prognostics and Health monitoring data under a fill rate constraint", *Computers & Industrial Engineering*, vol. 148, pp. 106724, 2020.
- [6] S.A. Tarim, S, and B. M. Smith, "Constraint programming for computing non-stationary (R, S) inventory policies", *European Journal of Operational Research*, vol. 189, no. 3, pp. 1004–1021, 2008.
- [7] J.J.A. Moors, and L. W. G. Strijbosch, "Exact fill rates for (R, s, S) inventory control with gamma distributed demand", *Journal of the Operational Research Society*, vol. 53, no. 11, pp. 268-1274, 2017
- [8] B.Y. Ekren, and B. Arslan, "Simulation-based lateral transshipment policy optimization for s, S inventory control problem in a single-echelon supply chain network", *An International Journal of Optimization and Control: Theories & Applications*, vol. 10, pp. 9-16, 2019.
- [9] J.J.A. Moors, and L. W. G. Strijbosch, "Simulating an (R, s, S) Inventory System", *Econometrics, CentER Discussion Paper*, Vol. 2002-94, 2002.
- [10] S. Aytakin, "Tam Zamanında Stok Yönetimi (Just-in-Time) Felsefesinin Hastane İşletmelerine Uygulanabilirliği ve Bir Üniversite Hastanesi Örneği", *Balıkesir Üniversitesi Sosyal Bilimler Enstitüsü Dergisi*, vol. 12, no. 21, pp. 102–115, 2009.
- [11] M. Karahan, and Ş. Aslan, "Bir Çimento Fabrikasında Hammadde Stok Kontrolü Uygulaması". *Süleyman Demirel Üniversitesi İktisadi ve İdari Bilimler Fakültesi Dergisi*, vol. 21, no. 3, pp. 773–783, 2016.
- [12] M. Fisher, and A. Raman, "Reducing the Cost of Demand Uncertainty through Accurate Response to Early Sales", *Operations Research*, vol. 44, no. 1, pp. 87-99, 1996.
- [13] V.S.R. Madduri, "Inventory Policies for perishable products with fixed Shelf Lives", *The Pennsylvania State University, Harold and Inge Marcus Department of Industrial and Manufacturing Engineering*, Pennsylvania, (2009).
- [14] Ö. Yalçınkaya, and Y. Karadaş, "Bir Otomotiv Yedek Parça Şirketinde ABC Analizi ve Sipariş Sürecinin Simülasyonla Modellenmesi", *DEU Muhendislik Fakültesi Fen ve Muhendislik Dergisi*. Vol. 22., pp. 287-300, 2020.
- [15] L.C., Wang, C. Y. Cheng, Y. T. Tseng, and Y. F. Liu, "Demand-pull replenishment model for hospital inventory management: a dynamic buffer-adjustment approach", *International Journal of Production Research*, vol. 53, no. 24, 7pp. 533-7546, 2015.
- [16] M. Aslantaş, "Bir transformatör firmasında stok kontrol parametrelerinin simülasyon tabanlı optimizasyonu", *Master's thesis*, Balıkesir Üniversitesi Fen Bilimleri Enstitüsü. (2019).
- [17] S. Kasımoğlu, G. Demir, B. P. Yaz, and D. H. Utku, "An Application: A Model with Sequence Dependent Setup Times for Parallel Machines for the Die House Station in a White Goods Manufacturing Company", *Osmaniye Korkut Ata Üniversitesi Fen Bilimleri Enstitüsü Dergisi*, vol. 4, no. 1, pp. 33-44, 2021.
- [18] D.H. Utku, "The Evaluation and Improvement of the Production Processes of an Automotive Industry Company via Simulation and Optimization", *Sustainability*, vol.15, no. 3, pp. 2331, 2023.
- [19] J. Banks, J.S. Carson, B.L. Nelson, and D.M. Nicol, "Discrete-event system simulation", *Pearson new international edition*, Pearson Higher Ed. 2013.
- [20] A. Pınar, D.H. Utku, and F. Kasımoğlu, "An Inventory Optimization Model for a Textile Manufacturing Company". *Journal of Turkish Operations Management*, vol. 6, no. 2, pp. 1252-1262, 2022.

Synthesis, Solvatochromic Analysis and Theoretical Studies of 3-((1H-benzo[d][1,2,3]triazole-1-yl)methyl)-4-phenylethyl-1H-1,2,4-triazole-5(4H)-thione

Zuhal KARAGÖZ GENÇ¹, Umut İbrahim OĞUZ², Murat GENÇ^{2*}

¹Adiyaman University Faculty of Pharmacy

²Adiyaman University Faculty of Arts and Sciences

(ORCID: 0000-0002-8847-9129) (ORCID: 0000-0003-1993-8819) (ORCID: 0000-0003-1224-4128)



Keywords: Benzotriazole, 1,2,4-triazole, DFT, Microwave irradiation, Docking

Abstract

The novel 2-(2-(1H-benzo[d][1,2,3]triazole-1-yl)acetyl)-N-phenylethyl hydrazinecarbothioamide (1) was synthesized by reaction of 2-(1H-benzo[d][1,2,3]triazole-1-yl)acetohydrazide and 2-phenylethylisothiocyanate. The condensation of compound 1 in presence of sodium hydroxide gave 3-((1H-benzo[d][1,2,3]triazole-1-yl)methyl)-4-phenylethyl-1H-1,2,4-triazole-5(4H)-thione (BPT). Theoretical calculations of BPT have been studied. The 6-311G+ (d,p) basis set was used for the DFT computations. The calculated spectra matched up with what was observed; hence the findings were confirmed. The same theoretical calculation procedure was used to examine BPT's LUMO, HOMO, and other associated energy values. To find out whether solute-solvent interactions were peculiar to BPT, the Catalán–Kamlet–Taft solvent parameter was used. Molecular docking studies were performed and identified the active sites of BPT with four anti-microbial receptors like *Aspergillus niger* (3EQA), *Hordeum vulgare* (1CNS), and *Candida Albicans* (4HOE) *Streptomyces* sp. (1CHK).

1. Introduction

In recent years, drug resistance has become a significant problem in the world, and in previous decades, multi-drug resistant gram-negative and gram-positive pathogenic bacteria caused lethal contagious diseases that affected the human population. Since the 1940s, penicillin has been used in human therapeutics; besides, various antibiotics have been used for 60 years. Firstly, antibiotics were not only developed to treat human infections but also used in veterinary, plant aquaculture, and agriculture [1, 2]. The extensive use of antibiotics caused a robust discerning burden that incommutably resulted in resistant bacteria spreading. The multifaceted mechanism for the advent of resistance has occurred: the resistance gene spread across the bacterial demesne with deceptive disregard for species barrier. However, the acquisition of resistance of genetic

factors has not been limited by the bacterial evolutionary response. Consequently, drug resistance has been developed as a global issue for human health that attracts the attention of scientists towards new antibacterial drug design and development. In this direction, heterocyclic compounds demonstrate their vital position because of varied biological activities [3, 4].

One of the heterocyclic compounds is 1,2,4-triazoles that contain three nitrogen atoms and two carbon atoms in a five-membered di-unsaturated ring structure [5].

Chemically speaking, 1,2,4-triazoles are a diverse group of molecules with numerous beneficial pharmacological properties. Some 1,2,4-triazole-based compounds have been shown to induce chemotherapeutic effects in cancer cells [6-10]. When it comes to drug design, N-heterocyclic molecules are critical [11-14]. triazoleMany classes of biologically

* Corresponding author: mgenç23@gmail.com

Received:08.04.2023, Accepted: 18.04.2023

active chemicals contain the molecule 1,2,4-triazole. 1,2,4-triazoles and their derivatives, in particular, are of great interest due to the vast range of biological activity they exhibit, such as anticancer [15], fungicidal [16-18], bactericidal [19-21], antioxidant [22], analgesic [23] and antidepressant [24] for these reasons, it was interesting to study 1,2,4-triazoles' vibrational spectra, electronic properties and molecular structure with the expectation that the results would be the helpful guide for future synthesis of more potent compounds and the prediction of their biological activity mechanism.

Due to our increased interest in search of new biological active agents having a 1,2,4-triazole ring, here we report an easy one-pot one component synthesis of the novel 1,2,4-triazole molecule, using NaOH, in good yield, and the present work also reports theoretical results of the synthesized compound to find structural characteristics by using DFT 6-311G+(d,p) methods..

2. Material and Method

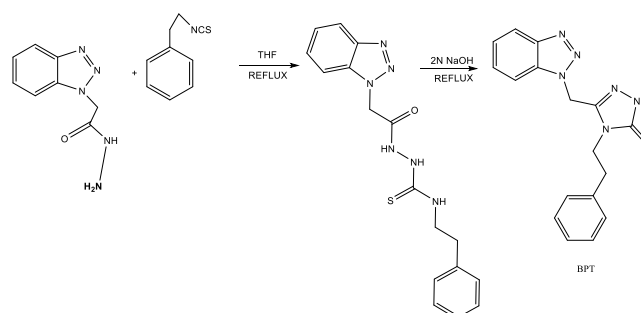
To produce compounds 1 and 2-(1H-benzo[d][1,2,3]triazole-1-yl)acetohydrazide (2), we followed the procedure outlined in the literature [25]. All chemicals were acquired from Merck and Sigma Aldrich and used without further purification.

2.1. Physical measurement

We used Perkin-Elmer FT-IR (ATR) to record the infrared spectra, a Stuart SMP 30 melting point apparatus to record the melting point, and an uncorrected analysis of both TMS (=0.0 ppm) was used as an internal standard to record 1H and 13C-NMR spectra on the Bruker (300 MHz).

Synthesis of 3-((1H-triazolebenzotriazole-1-yl)methyl)-4-phenylethyl-1H-1,2,4-triazole-5(4H)-thione(BPT)

2-{2-(1H-benzotriazole-1-yl-acetyl)}-N-(3-phenylmethyl) hydrazincarbothioamid (CAS Registry Number 502869-56-9) (1g) was added to a 10 mL (2 N) solution of NaOH, and the combination was kept at reflux for 5 hours. After that, it was acidified with 37% conc. HCl and the pure product were produced by recrystallization in ethanol (Scheme 1).



Scheme.1. Synthetic pathway of 3-((1H-triazolebenzotriazole-1-yl)methyl)-4-phenylethyl-1H-1,2,4-triazole-5(4H)-thione(BPT)

M.p:188-190°C; FT-IR(ATR):3148(N-H), 3096-3037(CAr-H), 2851-2981(C-H), 1604(C=C), 758(C=S); 1H-NMR(400MHz, DMSO-d₆) 12.50 (s, 1H, NH), 8.10 (s, 1H, Ar-H), 7.52 (s, 1H, Ar-H), 7.33(s, 1H, Ar-H), 7.40 (m, 4H, Ar-H), 7.24 (m, 2H, Ar-H), 5.12 (s, 2H, CH₂), 3.32 (t, 2H, CH₂, J=8Hz), 3.00 (t, 2H, CH₂, J=8Hz).. 13C-NMR(75MHz, DMSO-d₆): 168, 146, 137, 132, 129, 128, 127, 124, 120, 109, 46,41, 33. Anal. calcd for C₁₇H₁₆N₆S (336.41): C 60.69; H 4.79; N 24.98; S 9.53; found C 60.72; H 4.81; N 24.96; S 9.61. yield: 88%

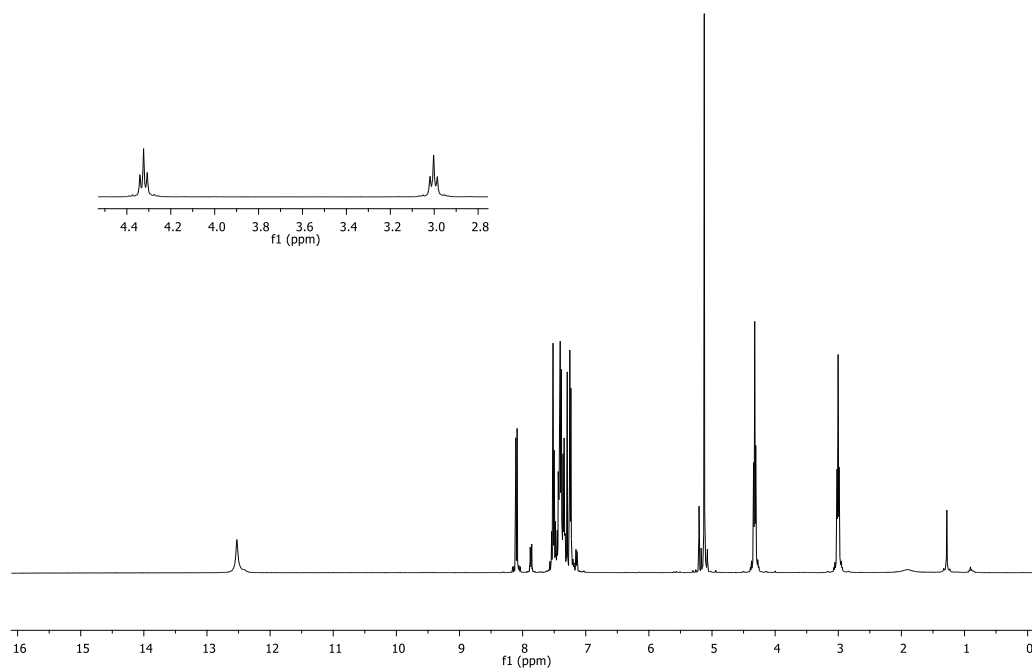


Figure 1. $^1\text{H-NMR}$ spectrum of (BPT)

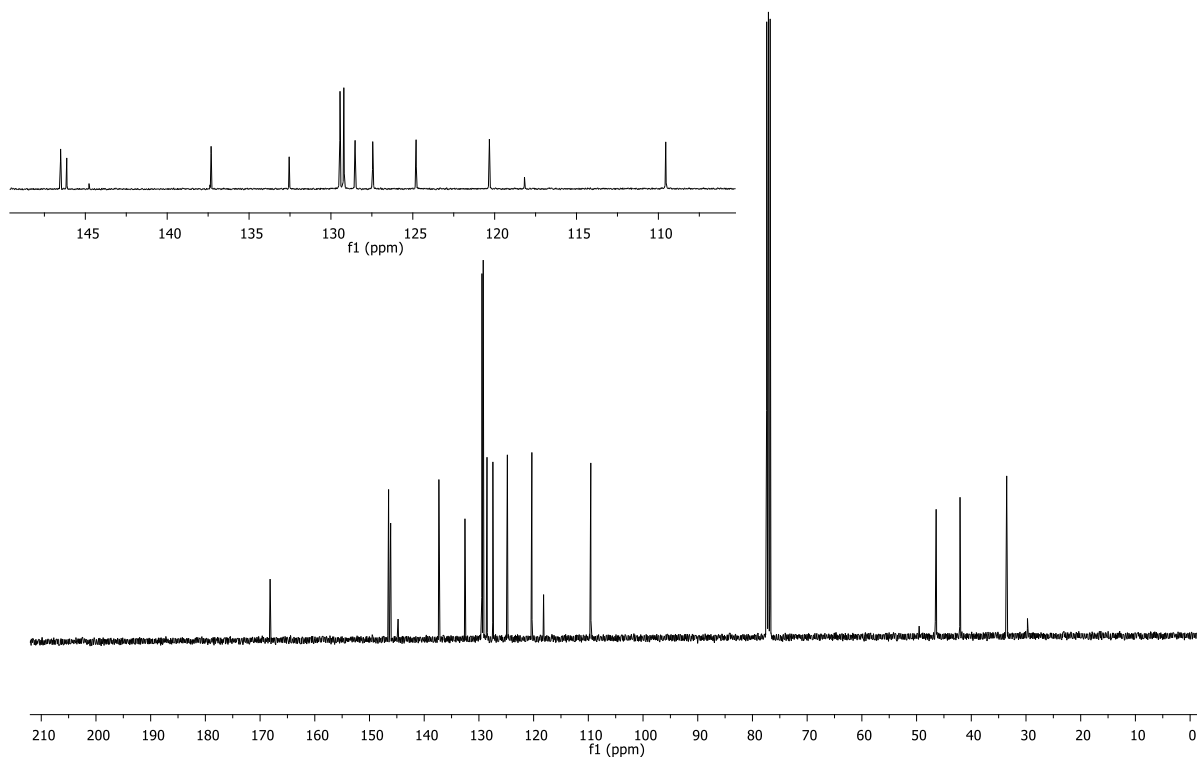


Figure 2. $^{13}\text{C-NMR}$ spectrum of (BPT)

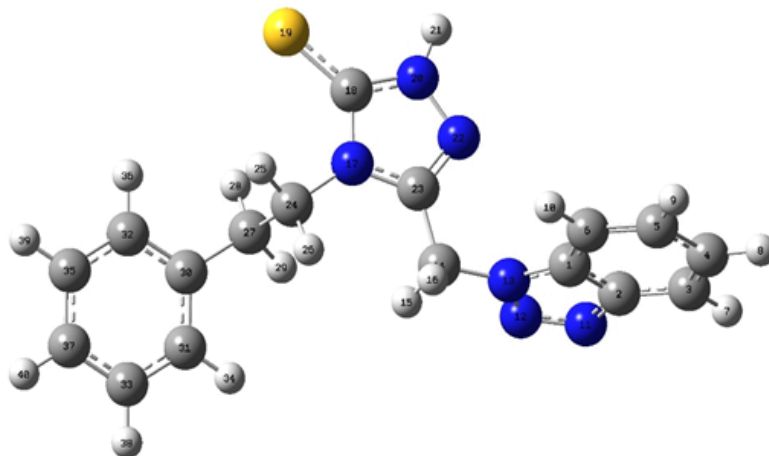


Figure 3. Optimized structure of BPT at B3LYP/6-311+(d,p) level

3. Theoretical study

The calculations for the molecular modelling were done with the Gaussian 09 software suite. Based on 6-311+G(d,p), the calculations were performed at the (DFT/B3LYP) technique. The molecule's vibrational frequencies were computed using the same quantum chemistry model's gas-phase equilibrium geometry. The Becke3-Lee-Yang-Parr (B3LYP) technique was used to include electron correlations [25]. Becke's gradient exchange corrections, Lee, Yang, and Parr correlation functional, and/or Vosko, Wilk, and Nusair correlation functional are all included in this [26].

3.1. Molecular geometry

The geometrical structure and atomic labelling of 3-((1H-benzo[d][1,2,3]triazole-1-yl)methyl)-4-phenylethyl-1H-1,2,4-triazole-5(4H)-thione have been computed and illustrated at Figure 3. the BPT's structural parameters have been optimized. Tables are given supplementary data. A partial double bond character has been discovered for all BPT ring bonds in the phenyl ring (S.Table 1) [27] that most of the phenyl ring's optimal bond lengths are similar in magnitude and lying between bond length ~ 1.40 Å to ~ 1.38 Å. Similarly, bond lengths of 1,2,4- triazole rings are between ~ 1.38 Å to ~ 1.29 Å.

Additionally, the smallest \angle (C24-N17-C14) and largest angle value (N17-C14-N13) of the molecule was computed at 98.50 and 140.

3.2. Atomic charge

Atomic charges perform a key role in a molecular system as electronic structure, molecular polarizability, dipole moment, atomic charge effect,

and the other molecular system properties. In addition, the asymmetric distribution of electrons in the chemical bond brings about certain charges. The calculated Mulliken atomic charges of BPT are shown in Fig.4.(S.Table 2) The charge distributions of molecules show the N atoms that bonded to a Substituent. The influence of the electron effect proceeds from hyperconjugation, and the inductive effect of Substituent groups in aromatic rings induces a particular negatively charged value in the aromatic carbon atoms. For the NBO, the natural atomic charges of BPT illustrate a similar tendency as Mulliken's atomic charges.

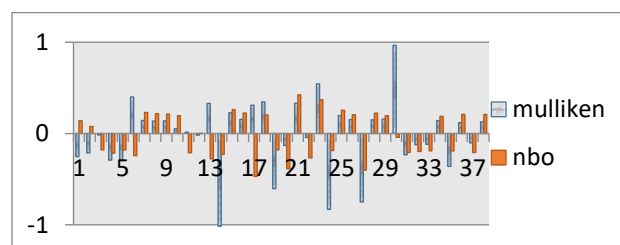


Figure 4. Graphical representations of atomic charges on the atoms of BPT

3.3. Frontier molecular orbital analysis

In terms of the BPT, the most critical molecular orbitals are HOMO-1, HOMO, LUMO, and LUMO+1. Using the B3LYP/6-311+ (d,p) technique, these orbital energies were figured out and delineated in Fig 5. The calculation showed that the charge distribution of the HOMOs level of BPT is highly delocalized on the 1,2,4-triazole (Fig 5). The charge density of the LUMO level is delocalized on the benzotriazole ring. It was concluded from the above

discussion that there is an electron flow from the 1,2,4-triazole to the Benzotriazole. The energy separation between the LUMO-HOMO orbital value is 4.32 eV.

Besides the absolute hardness (η), chemical potentials (μ), absolute electronegativities LUMO-HOMO energy gap (ΔE), global softness (S), global electrophilicity (ω), electronegativity (χ), absolute softness (σ), additional electronic charges (ΔN_{max}), have been calculated according to the following equations (S.Table 3) [28]

$$\eta = (|E_{LUMO} - E_{HOMO}|) / 2 \quad (1)$$

$$\chi = -(E_{LUMO} + E_{HOMO}) / 2 \quad (2)$$

$$\mu = -\chi \quad (3)$$

$$\sigma = 1/\eta \quad (4)$$

$$\omega = \mu^2 / 2\eta \quad (5)$$

$$\Delta N_{max} = -\mu / 2\eta \quad (6)$$

$$S = 1/2\eta \quad (7)$$

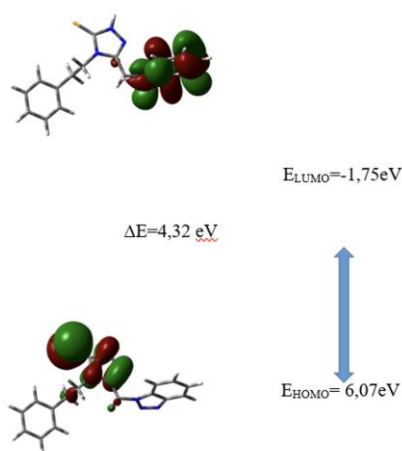


Figure 5. Calculated Frontier molecular orbitals of the title compound with DFT/B3LYP-G(d,p++)

3.4. NMR chemical shift analysis

The NMR spectroscopy is an essential technique for analyses of organic compounds. Geometry optimizations of BPT were performed with the DFT/B3LYP/semiempirical method/PM3 level basis set. After optimization, stage 1H and ^{13}C - NMR calculations of BPT were calculated GIAO [29-30] and 6-311+G (d,p) basis set in DMSO. Theoretical 1H and ^{13}C - NMR chemical shifts results of BPT

generally agree with the experimental chemical shift data.

The experimental and theoretical 1H and ^{13}C -NMR R2 values are 0.93 and 0.99, respectively and the atom positions, chemical shifts are generated in S.Table 4.

3.5. NBO Analysis

For investigating charge transfer or conjugative contact in molecular systems, NBO analysis guarantees an efficient method and ensures the research of intra- and intermolecular bonding and interaction in molecular systems [31]. There will be a more significant amount of giving tendencies from electron donors to electron acceptors, resulting in a longer E(2) value and, as a result, a more significant amount of conjugation throughout the entire system. There is a stable donor-acceptor interaction when electron density delocalization occurs between Lewis-type (bond or lone pair) Lewis NBO orbitals and formally empty non-Lewis NBO orbitals (anti-bond or Rydberg). NBO analysis used the second-order Fock matrix to look at intermolecular interactions. The stabilization energy associated with $I \rightarrow j$ delocalization is approximated as follows for each donor NBO (I) and acceptor NBO (j):

$$E(2) = \Delta E_{ij} = q_i = \frac{F(i,j)^2}{\epsilon_i \epsilon_j}$$

F_{ij} is the diagonal NBO fock matrix element of ϵ_i , ϵ_j , where q is the donor orbital occupied (orbital energies). DFT/B3LYP/6-311+(d,p) level NBO analyses have been undertaken, and the interaction LP (1) C2 \rightarrow π^* C1-N13 has the most excellent E(2) value around as shown in S.Table 5.

3.6. Molecular Electrostatic Potential (MEP) Analysis

To find out the net electrostatic effect caused by the entire charge distribution of the molecular and to correlate it with chemical reactivity, partial charges, dipole moments, and electro-negativity, we calculate the molecular electrostatic potential (MEP). It also makes it possible to understand the relative polarity using a visual approach [32,33]. The charge distribution of the molecule is shown in three dimensions in Figure 6 (below). There are three different electrostatic potential values in Fig 6: blue represents areas with the highest electrostatic potential, green indicates areas with zero potential, and red denotes areas with the lowest electrostatic

potential (see Fig 5). Red, orange, yellow, green, blue: these are the possible increments. The most vital repellent color is red, while the most robust attractive color is blue. An electronegative atom pair is frequently seen in regions of negative potential where there is a single atom. When looking at the MEP map of BPT, both the NH and the $-CH_2$ groups that joined the 1,2,4-triazole ring can be found in the positive zone. A look at Fig. 6 shows that a map of MEP values shows that negative potential exists over the benzotriazole group's N12 and N13 bonding atoms.

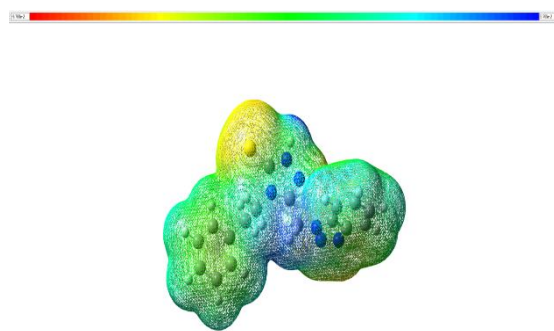


Figure 6. Molecular Electrostatic Potential (MEP) Analysis of BPT

3.7. Infrared Spectroscopy

In order to calculate the vibrational frequencies of BPT, the DFT/B3LYP method with the 6-311G+(d,p) basis set was utilized, as was the Gauss-View molecular visualization tool for the vibrational band assignments.

S.Table 6 shows theoretical computed IR spectra of the molecule's peaks. The measured and computed wave numbers agree very well. For two reasons, there could be a discrepancy between estimated and observed values. The first is that experimental data are in the solid phase, whereas theoretical calculations are in the gaseous phase. In addition, contrary to calculations, experimental values have been reported in the presence of intermolecular interactions.

The NH vibrations are the strong characteristic band for organic molecules [33,34]. NH stretching was observed at 3230 cm^{-1} in Raman and 3146 cm^{-1} in the IR spectrum while computed at 3668 cm^{-1} . Besides, NH in-plane bending vibration was observed at 1510, 1454 and 1205 cm^{-1} in Raman and 1495 and 1177 cm^{-1} in IR spectrum of the BPT while computed at 1496, 1550 and 1249 cm^{-1} . (Fig 7)

C-H stretching computed at 3203, 3185, 3173 cm^{-1} while was observed 3064, 3052 cm^{-1} in raman, 3093, 3037 cm^{-1} in IR spectrum. C-H bending was

observed 1485, 1324, 1152 cm^{-1} in IR, 1387, 1369, 1168 cm^{-1} in Raman spectrum.

C=N vibrations are also the other strong characteristic peaks of biomolecules. This peak vibration was observed 1625, 1591, 1590, IR, Raman, Theoretical spectrum, respectively.

In the case of N-N, vibrations were observed 1451, 1303 cm^{-1} in IR, 1454, 1348 in Raman spectrum while computed 1485, 1378 and 1359 cm^{-1} . (Fig 7)

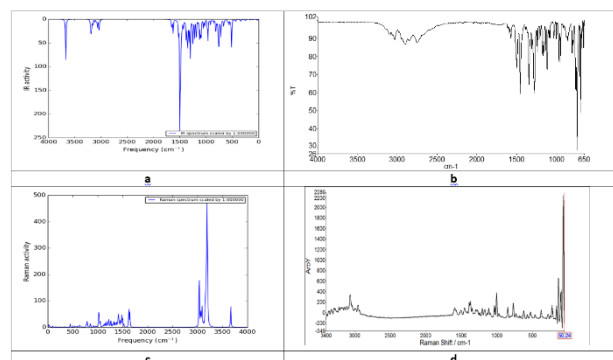


Figure 7. Experimental and theoretical vibration spectra of BPT (a= experimental FTIR spectrum, b= theoretical IR spectrum, c= experimental raman spectrum, d= theoretical raman spectrum)

3.8. Thermodynamic parameters

Rotation, vibration, and translation are all part of thermodynamics; hence they all matter. BPT's thermodynamic functional characteristics have been calculated using density functional theory (DFT). S.Table 7 contains estimated values that are useful for calculating biomolecular thermodynamic energy and predicting chemical reaction directions. To be clear, all of these thermodynamic calculations were done in the gas phase and could not be applied to the solution. Researchers looked examined BPT's thermodynamic characteristics between 100 and 1000 Kelvin. [36]. It was observed that enthalpy, entropy and heat capacity values increased depending on the temperature. The relevant equations are shown in Figure 8 and S.Table 7.

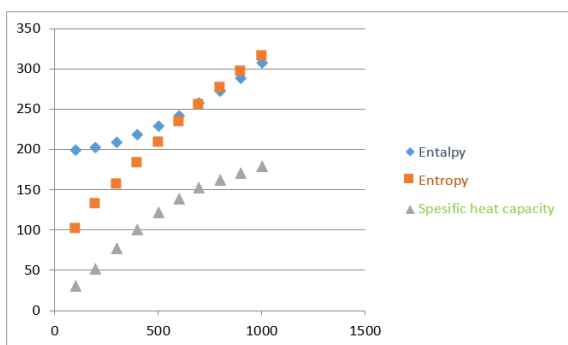


Figure 8. Thermodynamic Parameters of BPT

$$H^0_m = 73,40893 + 0,304215 T - 6,1 \cdot 10^{-5} T^2, \quad (R^2 = 0,9999)$$

$$S = 194,0431 + 0,029679T + 8,44 \times 10^{-5} T^2, \quad (R^2 = 0,9995)$$

$$CV = -085211 + 0,306056 T - 1,3 \times 10^{-4} T^2, \quad (R^2 = 0,9991)$$

3.9. Catalan and Kamlet-Taft solvatochromic parameters

UV spectra of BPT were taken in different solvents. The parameters affecting the absorbance bands of BPT were determined by the Catalan and Kamlet-Taft equations [36,37].

Catalan equation is given below.

$$V = aSA + bSB + cSp + dSdP$$

Catalan parameters are defined as solvent acidity (SA), solvent basicity (SB), solvent polarizability (SP) and solvent dipolarity (SdP).

Catalan equation was calculated as

$$V = 12.07 + 81.80SA + 12.44SB + 343.32SP + 25.38SdP$$

and $R^2 = 0.66$.

According to this equation, absorb and band is controlled SP ability.

The Kamlet-Taft equation is $V = V_0 + a\alpha + b\beta + c\pi^*$

The Kamlet-Taft solvent parameters are defined as the hydrogen bond donation ability (α), the hydrogen bond acceptor ability (β), the dipolarity-polarizability (π^*)

The Kamlet-Taft equation was calculated as $V = 231.60 + 50.62\alpha + 2.40\beta + 3.74\pi^*$ $R^2 = 0.24$. In regards to The Kamlet-Taft equation was found the most parameter as the hydrogen bond donation ability.

UV-Vis Spectrums of BPT were recorded with solvents of different polarities such as chloroform, THF, Ethanol, Pyridine, Formic acid. The experimental UV-Vis spectrum of BPT was observed a strong band of about 260 nm because of

$\pi \rightarrow \pi^*$ electronic transition. The computed wavelengths were recorded at about 315, 290, 281 nm, respectively. Hence, the electronic transition of $H \rightarrow L$ that is the most intense value was obtained at about 315 nm. The UV-Vis. parameters of BPT in different solvents are given in S. Table 8.

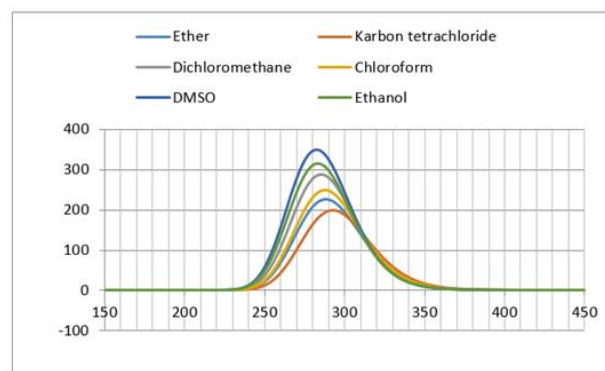


Figure 9. Theoretical UV Spectrum in Different solvents of BPT

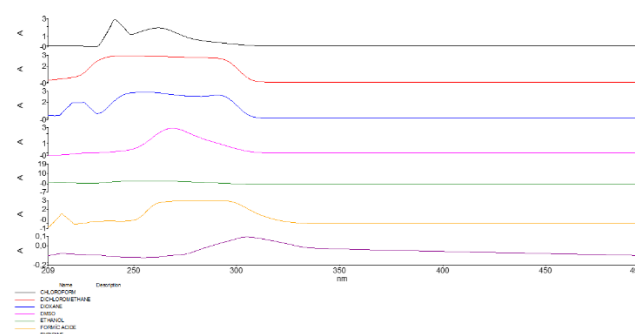


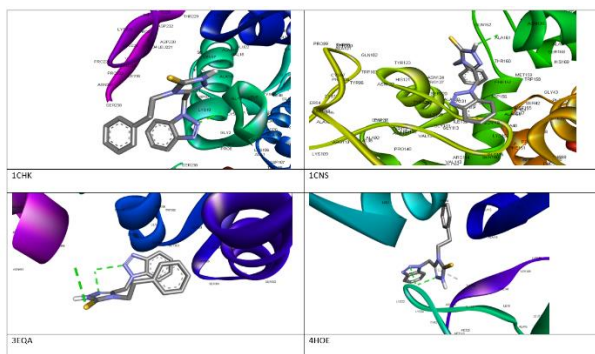
Figure 10. Experimental UV Spectrum in Different solvents of BPT

3.10. Molecular Docking

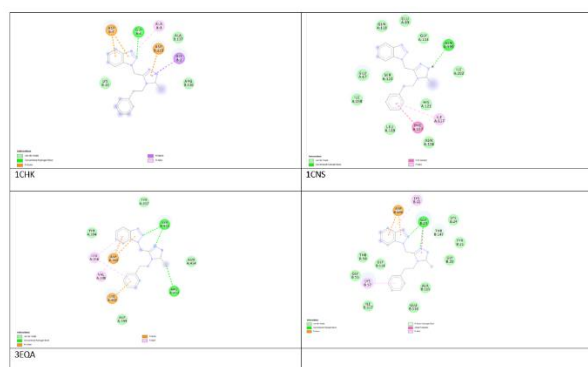
Molecular docking studies were performed by Autodock 4.2. We identified the active sites of BPT with four anti-microbial receptors like *Aspergillus niger* (3EQA), *Hordeum vulgare* (1CNS), and *Candida Albicans* (4HOE) *Streptomyces sp.* (1CHK) [38]. S. Table 9 summarizes the interactions and binding free energy in Kcal/mol between synthesized BPT and receptors. The binding energy of (1CHK), (1CNS), (3EQA) and (4HOE) are found to be 4.7, 7.3, 6.2 and 7.6 Kcal/mol, respectively.

Hybridizing benzotriazoles scaffold with 1,2,4-triazole ring moieties proved to be a favourable strategy in building up new molecules with good ability of the binding into the receptors binding site as triazole ring showed hydrogen bonding interactions

with ASN199 (1CNS), Er455, ARG453(3EQA), GLY23 (4HOE).



Figures 11. 3D Binding orientation of BPT with different proteins



Figures 12. 2D Binding orientation of BPT with different proteins.

4. Conclusion and Suggestions

Benzotriazole substitute 1,2,4-triazole was synthesized, FT-IR and NMR spectrums are studied both experimentally and theoretically. DFT (B3LYP) method using 6-311+G(d,p) basis set was used to compute the geometric parameters, vibrational frequencies, and chemical shifts of BPT's normal modes. Determine the charge transfer by performing a HOMO/LUMO study. The 1,2,4-triazole delocalizes the HOMO, while the benzotriazole delocalizes the LUMO. For ^1H and ^{13}C NMR, the chemical shifts agreed well with the DMSO solution's experimental results. By using NBO studies to explain molecular interaction and stability and the second-order perturbation for transactions, we have

References

- [1] S. Rachakonda and L. Cartee, "Challenges in antimicrobial drug discovery and the potential of nucleoside antibiotics," *Curr. Med. Chem.*, vol. 11, no. 6, pp. 775–793, 2004
- [2] C. Nathan, "Antibiotics at the crossroads," *Nature*, vol. 431, no. 7011, pp. 899–902, 2004

been able to stabilize the structure. Based on these findings, we believe BPT is a viable candidate for further pharmacological and biochemical research. Clinical drugs containing triazole nucleus are being used in treating several ailments. The progress of resistance in *Candida* spp against fluconazole, the most effective anticandidal commercial drug, prompted the pharmacologist to synthesize triazole alcohols as fluconazole analogues to treat fluconazole-resistant fungal strains. 1,2,4-Triazole moiety via hydrogen bonding and dipole interaction can improve the solubility and affinity of the compounds with bimolecular targets. Among the broad spectrum of bioactivities, we comprehensively reviewed the advances in anticancer, anticonvulsant, antifungal, antibacterial, antiparasitic, analgesic antituberculosis anti-inflammatory and, antiviral, activities of 1,2,4-triazole derivatives particularly reported over the past decade. In according to the our study results; hybridizing benzotriazoles scaffold with 1,2,4-triazole ring moieties proved to be a favourable strategy in building up new molecules with good ability of the binding into the receptors binding site as triazole ring showed hydrogen bonding interactions.

Acknowledgment

The Adiyaman University Research Foundation (FEFYL/2012-0006) generously funded this research project, and we are grateful for their assistance

Contributions of the authors

The authors confirm that the contribution is equally for this paper.

Conflict of Interest Statement

There is no conflict of interest between the authors.

Statement of Research and Publication Ethics

The study is complied with research and publication ethics

- [3] K. Cheng, Q.-Z. Zheng, Y. Qian, L. Shi, J. Zhao, and H.-L. Zhu, "Synthesis, antibacterial activities and molecular docking studies of peptide and Schiff bases as targeted antibiotics," *Bioorg. Med. Chem.*, vol. 17, no. 23, pp. 7861–7871, 2009.
- [4] T. M. Barbosa and S. B. Levy, "The impact of antibiotic use on resistance development and persistence," *Drug Resist. Updat.*, vol. 3, no. 5, pp. 303–311, 2000.
- [5] K. S. Kiran, M. K. Kokila, Guruprasad, and Niranjana, "Crystal structure determination and molecular docking studies of 4-(5-Phenyl pyrazin-2-yl)-4h-1,2,4 Triazole-3-thiol with focal adhesion kinase inhibitors," *Open Chem. J.*, vol. 3, no. 1, pp. 69–74, 2016
- [6] Y. Sert, A. A. El-Emam, E. S. Al-Abdullah, A.-M. S. Al-Tamimi, C. Cırak, and F. Ucun, "Use of vibrational spectroscopy to study 4-benzyl-3-(thiophen-2-yl)-4,5-dihydro-1H-1,2,4-triazole-5-thione: A combined theoretical and experimental approach," *Spectrochim. Acta A Mol. Biomol. Spectrosc.*, vol. 126, pp. 280–290, 2014.
- [7] Y.-P. Hou et al., "Synthesis and antitumor activity of 1,2,4-triazoles having 1,4-benzodioxan fragment as a novel class of potent methionine aminopeptidase type II inhibitors," *Bioorg. Med. Chem.*, vol. 19, no. 20, pp. 5948–5954, 2011
- [8] A. Šermukšnytė, K. Kantminienė, I. Jonuškienė, I. Tumosienė, and V. Petrikaitė, "The effect of 1,2,4-triazole-3-thiol derivatives bearing hydrazone moiety on cancer cell migration and growth of melanoma, breast, and pancreatic cancer spheroids," *Pharmaceuticals (Basel)*, vol. 15, no. 8, p. 1026, 2022.
- [9] H. Alsaad, A. Kubba, L. H. Tahtamouni, and A. H. Hamzah, "Synthesis, docking study, and structure activity relationship of novel anti-tumor 1, 2, 4 triazole derivatives incorporating 2-(2, 3- dimethyl aminobenzoic acid) moiety," *Farmatsiia (Sofia)*, vol. 69, no. 2, pp. 415–428, 2022.
- [10] D. C. Kahraman, E. Bilget Guven, P. S. Aytac, G. Aykut, B. Tozkoparan, and R. Cetin Atalay, "A new triazolothiadiazine derivative inhibits stemness and induces cell death in HCC by oxidative stress dependent JNK pathway activation," *Sci. Rep.*, vol. 12, no. 1, p. 15139, 2022.
- [11] L. B. de O. Freitas et al., "Synthesis and antiproliferative activity of 8-hydroxyquinoline derivatives containing a 1,2,3-triazole moiety," *Eur. J. Med. Chem.*, vol. 84, pp. 595–604, 2014
- [12] V. Spanò et al., "Synthesis of a new class of pyrrolo[3,4-h]quinazolines with antimitotic activity," *Eur. J. Med. Chem.*, vol. 74, pp. 340–357, 2014.
- [13] R. Marulasiddaiah, R. G. Kalkhambkar, and M. V. Kulkarni, "Synthesis and biological evaluation of cyclic imides with coumarins and azacoumarins," *Open J. Med. Chem.*, vol. 02, no. 03, pp. 89–97, 2012.
- [14] P. Diana et al., "Synthesis and antitumor activity of 3-(2-phenyl-1,3-thiazol-4-yl)-1H-indoles and 3-(2-phenyl-1,3-thiazol-4-yl)-1H-7-azaindoles," *ChemMedChem*, vol. 6, no. 7, pp. 1300–1309, 2011.
- [15] Y.-P. Hou et al., "Synthesis and antitumor activity of 1,2,4-triazoles having 1,4-benzodioxan fragment as a novel class of potent methionine aminopeptidase type II inhibitors," *Bioorg. Med. Chem.*, vol. 19, no. 20, pp. 5948–5954, 2011.
- [16] A. C. Pasqualotto, K. O. Thiele, and L. Z. Goldani, "Novel triazole antifungal drugs: focus on isavuconazole, ravuconazole and albaconazole," *Curr. Opin. Investig. Drugs*, vol. 11, no. 2, pp. 165–174, 2010
- [17] J. Xu et al., "Design, synthesis and antifungal activities of novel 1,2,4-triazole derivatives," *Eur. J. Med. Chem.*, vol. 46, no. 7, pp. 3142–3148, 2011
- [18] C. Tratat et al., "Design, synthesis and biological evaluation of new substituted 5-benzylideno- 2-adamantylthiazol[3,2-b][1,2,4]triazol-6(5H)ones. Pharmacophore models for antifungal activity" *Arabian Journal of Chemistry*, vol.11, no. 4, pp. 573-590, 2018
- [19] G. V. Suresh Kumar, Y. Rajendraprasad, B. P. Mallikarjuna, S. M. Chandrashekar, and C. Kistayya, "Synthesis of some novel 2-substituted-5-[isopropylthiazole] clubbed 1,2,4-triazole and 1,3,4-oxadiazoles as potential antimicrobial and antitubercular agents," *Eur. J. Med. Chem.*, vol. 45, no. 5, pp. 2063–2074, 2010.
- [20] M. Strzelecka and P. Świątek, "1,2,4-triazoles as important antibacterial agents," *Pharmaceuticals (Basel)*, vol. 14, no. 3, p. 224, 2021.

- [21] A. A. El-Emam, A.-M. S. Al-Tamimi, M. A. Al-Omar, K. A. Alrashood, and E. E. Habib, "Synthesis and antimicrobial activity of novel 5-(1-adamantyl)-2-aminomethyl-4-substituted-1,2,4-triazoline-3-thiones," *Eur. J. Med. Chem.*, vol. 68, pp. 96–102, 2013.
- [22] A. Pachuta-Stec, "Antioxidant Activity of 1,2,4-Triazole and its Derivatives: A Mini-Review," *Mini Rev. Med. Chem.*, vol. 22, no. 7, pp. 1081–1094, 2022.
- [23] J. K. Sugden and T. O. Yoloje, "Medicinal applications of indole derivatives," *Pharm. Acta Helv.*, vol. 53, no. 3–4, pp. 65–92, 1978
- [24] "SciFinder® Login," Cas.org. [Online]. Available: <https://scifinder.cas.org/scifinder/view/scifinder/scifinderExplore.jsf>. [Accessed: 16-Jun-2023].
- [25] A. D. Becke, "Density-functional thermochemistry. III. The role of exact exchange," *J. Chem. Phys.*, vol. 98, no. 7, pp. 5648–5652, 1993
- [26] C. Lee, W. Yang, and R. G. Parr, "Development of the Colle-Salvetti correlation-energy formula into a functional of the electron density," *Phys. Rev. B Condens. Matter*, vol. 37, no. 2, pp. 785–789, 1988.
- [27] K. Wolinski, J. F. Hinton, and P. Pulay, "Efficient implementation of the gauge-independent atomic orbital method for NMR chemical shift calculations," *J. Am. Chem. Soc.*, vol. 112, no. 23, pp. 8251–8260, 1990.
- [28] K. Bahgat and S. Fraihat, "Normal coordinate analysis, molecular structure, vibrational, electronic spectra and NMR investigation of 4-Amino-3-phenyl-1H-1,2,4-triazole-5(4H)-thione by ab initio HF and DFT method," *Spectrochim. Acta A Mol. Biomol. Spectrosc.*, vol. 135, pp. 1145–1155, 2015
- [29] S. Muthu, T. Rajamani, M. Karabacak, and A. M. Asiri, "Vibrational and UV spectra, first order hyperpolarizability, NBO and HOMO-LUMO analysis of 4-chloro-N-(2-methyl-2,3-dihydroindol-1-yl)-3-sulfamoyl-benzamide," *Spectrochim. Acta A Mol. Biomol. Spectrosc.*, vol. 122, pp. 1–14, 2014
- [30] K. Bahgat and S. Fraihat, "Normal coordinate analysis, molecular structure, vibrational, electronic spectra and NMR investigation of 4-Amino-3-phenyl-1H-1,2,4-triazole-5(4H)-thione by ab initio HF and DFT method," *Spectrochim. Acta A Mol. Biomol. Spectrosc.*, vol. 135, pp. 1145–1155, 2015.
- [31] M. D. Diener and J. M. Alford, "Isolation and properties of small-bandgap fullerenes," *Nature*, vol. 393, no. 6686, pp. 668–671, 1998.
- [32] J.B. Foresman, E. Frisch Gaussian, Pittsburgh, PA, 1993. NIST Chemistry Webbook, IR database, <http://srdata.nist.gov/cccbdb>.
- [33] H.M. Jamroz, Vibrational energy distribution analysis: VEDA 4 program, Warsaw, 2004
- [34] A. Lakshmi and V. Balachandran, "Rotational isomers, NBO and spectral analyses of N-(2-hydroxyethyl) phthalimide based on quantum chemical calculations," *J. Mol. Struct.*, vol. 1033, pp. 40–50, 2013.
- [35] M. Genç, "Solvatochromic analysis and DFT computational study of N-(hexyl)-N-(5-(3-hydroxynaphthyl-2-yl)-1,3,4-oxadiazol-2-yl)amine," *Appl. Phys. A Mater. Sci. Process.*, vol. 125, no. 6, 2019.
- [36] J. Catalán and H. Hopf, "Empirical treatment of the inductive and dispersive components of Solute–Solvent interactions: The solvent polarizability (SP) scale: Inductive and dispersive components of Solute–Solvent interactions," *European J. Org. Chem.*, vol. 2004, no. 22, pp. 4694–4702, 2004
- [37] M. J. Kamlet, J. L. M. Abboud, M. H. Abraham, and R. W. Taft, "Linear solvation energy relationships. 23. A comprehensive collection of the solvatochromic parameters, .pi.*, .alpha., and .beta., and some methods for simplifying the generalized solvatochromic equation," *J. Org. Chem.*, vol. 48, no. 17, pp. 2877–2887, 1983.
- [38] S. M. Hiremath et al., "Synthesis of 5-(5-methyl-benzofuran-3-ylmethyl)-3H-[1, 3, 4] oxadiazole-2-thione and investigation of its spectroscopic, reactivity, optoelectronic and drug likeness properties by combined computational and experimental approach," *Spectrochim. Acta A Mol. Biomol. Spectrosc.*, vol. 205, pp. 95–110, 2018.

Estimating The Location of a Buried Body from Magnetic Anomaly Through Normalized Full Gradient: A Case Study from The Sapinuwa Ancient City, Turkey

Şenol ÖZYALIN^{1*}, Zafer AKÇIĞ¹

¹Dokuz Eylül University Faculty Of Engineering Department Of Geophysical Engineering

²Address

(ORCID: 0000-0002-1401-9453) (ORCID: 0000-0002-9978-1681)



Keywords: Geophysics, Normalized Full Gradient, NFG, Magnetic anomaly, Sapinuwa ancient city.

Abstract

In geophysics, magnetic data can be used to obtain information about the depth and location of the structure, whether it is near the surface or deeper. This study is an example of applying the Normalized Full Gradient (NFG) method to an archeological site to determine the depth and location of structures that cause magnetic anomalies at the archeological site. One of the parameters that affects the shape and size of the magnetic anomaly is the depth of the source causing the anomaly. For this reason, it is important to correctly determine the location of the source. One of the methods of determining the depth of the structure using magnetic field data is the NFG technique. When using the downward analytical continuation, bias occurs due to the transition of the depth of mass, which is invalidated by this method. The NFG technique has been tested on anomalies caused by prismatic synthetic models. Test studies with synthetic models using the NFG technique have yielded satisfactory results. Based on these results, the NFG technique was applied to the real magnetic anomaly collected from the ancient city of Sapinuwa. The results were compared with the building remains found during the proposed excavations. The results obtained were satisfactory..

1. Introduction

Potential field data has a wide place among various methods in applied geophysics. This stage is the result of the long-term development of applied geophysics. It has been applied to a significant extent, especially in oil and gas reserves and mineral explorations. Since the 1960s, thanks to the important developments in computer techniques, many successful applications have been realized in potential areas with the development of existing evaluation theories for the solution of geophysical problems.

It is a fact that geophysical methods are used extensively in hydrocarbon and mineral explorations, which are accepted as natural riches in many parts of the world until today. In recent years, it has been used intensively in the examination of the properties of

structures very close to the surface or just below the surface, as well as in deep welded structures.

The aim of this study is to reveal the geophysical properties of such areas by using geophysical methods in archaeological areas. For this reason, the magnetic method, which is included in the group of potential field methods within the geophysical research methods, was used.

In this study, one of the geophysical evaluation methods, the NFG technique, which is based on the downward analytical continuation of the gradient field, was used. It is a method in which the relationship between the potential field and the source that creates the field can be re-established (for example, the analytic continuation method). This is the conversion of the measured magnetic field to the magnetic field in another, more understandable plane.

* Corresponding author: senol.ozyalin@deu.edu.tr

Received: 11.05.2023, Accepted: 22.06.2023

Such a process is based on a very simple relationship between the determined singular points of the structures constituting the anomaly and the geometric shape of the structures (center of gravity, vertices of the polygonal section).

The analytical continuation distinguishes some indistinguishable structural anomalies in the observed magnetic field. Analytical properties are lost at singular points of the boundaries of the mass, leading to an anomaly in its magnetic potentials and derivatives. The shape of the source and the location of the source causing the anomaly can be determined from the knowledge of the source and the singular points at its boundaries. The downward analytical continuation values of the observed magnetic field data show irregular changes during the passage of the source causing the anomaly. The normalized Full Gradient method is one of the most successful methods used in the determination of the singular points of the potential fields. These methods are often called singular points method and were first introduced by Strakhov (1962) and Golizdra (1962) [1,2].

The NFG technique has been rapidly adopted since the 1960s, and this method has been used by researchers. In particular, it can be applied to identify singular points of potential areas [3-14]. In addition, this technique has been successfully applied to seismic methods [15] and electromagnetic methods [16]. Magnetic and gravity have been often used to model subsurface geology. The magnetic survey is widely used to estimate the geometric parameters of simple models. These models can be in the form of a sphere, cylinder, dyke, or thin plate [17-20].

Magnetic imaging (especially gradiometer), ground-penetrating radar (GPR), and Electrical resistivity tomography (ERT) methods have widespread usage in archaeological sites. In the past years, some of the applications of these methods are presented by Ekinci and Kaya (2006)[21], Balkaya et al. (2012)[22], and Büyüksaraç et al. (2014)[23]. In addition, in particular, some examples of archaeogeophysical studies in ancient cities of Anatolia are given as Amorium [24], Baris [25], Commagene [26], Dedemezari Nekropolü [27, 28], Kılıç[29], Malos [30,31], Parion, [32, 33], Pisidia Antioch [34], Side [35], Satala [36], Sardis [37], Smyrna Höyük [38, 39], Tepecik and Norşun [40], Zeugma [41]. In this study, the NFG technique was performed using field datasets containing magnetic profile anomalies caused by buried structures in the ancient city of Sapinuwa (Çorum, Turkey) and noiseless synthetically produced data.

2. Sapinuwa Ancient City

The ancient city of Sapinuwa is an ancient city dating back to the Bronze Age, located in the Ortaköy district of Çorum province. It is known as the second-largest city of the Hittite kingdom. The city, which had great strategic importance, was also important politically and economically. Our study area is located in the north of Central Anatolia, 55 km southeast of Çorum city center, and 60 km northeast of Boğazköy in Ortaköy District. Today's Ortaköy District, with the Alan Mountains in the south and Karadağlar in the north, is on a plateau formed by terraces descending from west to east in the valley where Özderesi, a branch of the Çekerek River, is located.

The Hittite city of Sapinuwa is located about 3 km southwest of the Ortaköy District center, and appears as a widespread settlement on this plateau extending as terraces on the northern slopes of the Özderesi Valley, a branch of the Çekerek River. The city covers an area of 3 km in the east-west direction and 2.5 km in the south-north direction, including the lower and upper city (Figure 1).

Boğazköy was the most important center where the Hittites ruled in Anatolia. In addition, centers such as Maşat mound, Kültepe, Alaca mound and Sapinuwa also have an important place. In Sapinuwa, there are large religious and administrative structures that also served as administrative centers from time to time. Due to its location, it has an extremely important strategic position. The city is located at a key point on an important passage connecting Göynücek-Amasya Plain to its east and Kelkit Valley, which is its continuation, to Alaca-Sungurlu Plains to its west and Boğazköy located here.

The city is located at a key point on an important passage connecting Göynücek-Amasya Plain to its east and Kelkit Valley, which is its continuation, to Alaca-Sungurlu Plains to its west and Boğazköy located here. There is a 20 km long corridor in which the Çekerek River flows, extending to the Göynücek Plain in the east of the city. On this corridor, front defense facilities were built by selecting key points. It is accepted that the city has adopted a highly effective defense strategy by using these front defense facilities.

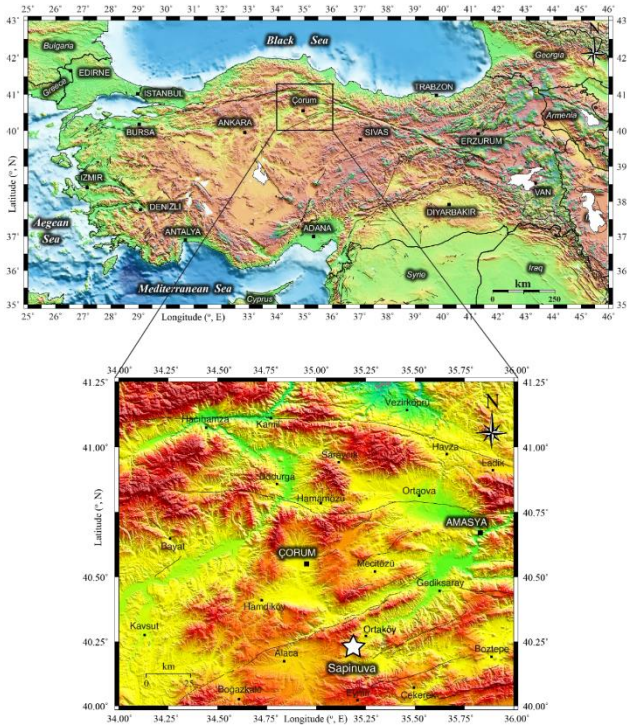


Figure 1. Location map of Sapinuwa ancient city. The map was generated using Generic Mapping Tools (GMT) [42].

3. Material and Method

3.1. Definition of the Magnetic Anomaly

Figure 2 shows the prism model. The vertical and horizontal magnetic field components are defined in [43] with equations (1) and (2), respectively.

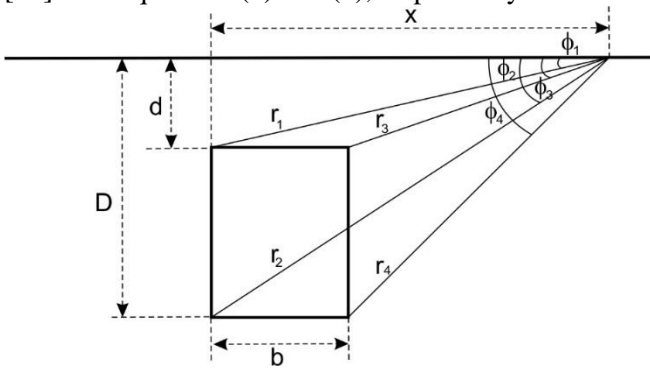


Figure 2. Vertical prism model

$$Z = 2k \left\{ H_0 \sin \beta \ln \left(\frac{r_2 r_3}{r_1 r_4} \right) - Z_0 (\phi_1 - \phi_2 - \phi_3 + \phi_4) \right\} \quad (1)$$

and

$$H = 2k \left\{ Z_0 \ln \left(\frac{r_2 r_3}{r_1 r_4} \right) - H_0 \sin \beta (\phi_1 - \phi_2 - \phi_3 + \phi_4) \right\} \quad (2)$$

where Z is the vertical magnetic field, H is the horizontal magnetic field, H is the azimuth angle, I is the inclination angle.

$$\begin{aligned} r_1^2 &= d^2 + (x + d \cot \alpha)^2 \\ r_2^2 &= D^2 + (x + D \cot \alpha)^2 \\ r_3^2 &= d^2 + (x + d \cot \alpha - b)^2 \\ r_4^2 &= D^2 + (x + D \cot \alpha - b)^2 \end{aligned} \quad (3)$$

$$\begin{aligned} \phi_1 &= \tan^{-1} [d / (x + d \cot \alpha)] \\ \phi_2 &= \tan^{-1} [D / (x + D \cot \alpha)] \\ \phi_3 &= \tan^{-1} [d / (x + d \cot \alpha - b)] \\ \phi_4 &= \tan^{-1} [D / (x + D \cot \alpha - b)] \end{aligned} \quad (4)$$

Here, a prism with top depth d , bottom depth D , width b , distances from each vertex to the observation point r_1, r_2, r_3, r_4 and tangent angle $\phi_1, \phi_2, \phi_3, \phi_4$ for each vertex. The total magnetic field is given by the equation (5)

$$F = 2k \{ H \sin \beta \cos I + Z \cos I \} \quad (5)$$

3.2. Normalized Full Gradient Method (NFG)

The NFG technique is based on the downward analytical continuation of potential field data and analytical signal amplitude. As is known, all potential sources are located below the measuring plane. Potential field data recorded in a given plane can theoretically be calculated on a plane above or below the measurement plane if there is no source. In a potential field data, although it is possible to make an analytical continuation upwards (outside the mass) to the desired height, it is not possible to make an analytical continuation downwards as much as desired in the environment of the mass causing the anomaly.

The extension can be applied to the data up to the closest point of the source, in other words, up to its top surface. Because after this point, some singular points are encountered. So downward analytical continuation is only made up to this maximum depth where the singular point is. From this point of view, the downward analytical continuation values of the potential field data show irregular changes while passing the body, which causes an anomaly. The initial value of these irregular variations indicates the depth to the upper surface of the body causing the anomaly. The downward analytical continuation is a

useful assessment method for identifying shallow sources.

Nabighian (1972) [44] showed that the amplitude of potential field data can be described by the following equation.

$$G(x) = \sqrt{F_x^2(x) + F_z^2(x)} \tag{6}$$

Here, $F(x)$ represents the potential field data, and, $F_x(x)$ and $F_z(x)$ represent the horizontal and vertical derivatives of the magnetic anomaly, respectively. The mathematical basis of the NFG technique is the $G_T(x,z)$ operator. In general, the NFG amplitude at a given point is expressed by the following equation [3, 45].

$$G_T(x_i, z_j) = \frac{\sqrt{[F_x^2(x_i, z_j) + F_z^2(x_i, z_j)]^v}}{\frac{1}{M} \sum_{i=1}^M \sqrt{[F_x^2(x_i, z_j) + F_z^2(x_i, z_j)]^v}} \tag{7}$$

Where $G_T(x,z)$ is the NFG's amplitude at a specific point (x_i, z_j) , z_j is the downward continuation level, $(i = 0, 1, 2, 3, \dots, M; j = 0, 1, 2, 3, \dots, z)$. The function $F(x,z)$ expresses the magnetic field along the x-axis and analytical continuation is made along the z-axis at Δz intervals. M is the number of points in the profile, and the functions $F_x(x)$ and $F_z(x)$ are derivatives of $F(x,z)$ along the x and z axes. v is the degree of the NFG operator. The full gradient term is expressed as the sum of the horizontal gradient $F_x(x,z)$ and the vertical gradient $F_z(x,z)$. The term NFG, on the other hand, refers to the division of the full gradient of equation 6 by the arithmetic mean value.

In order to protect small frequency components in potential field data, the subharmonic value is usually taken as 1. The upper harmonic limit value is usually found by trial and error. For this purpose, $N=10, 20, 30,$ and 40 values were used within the scope of the study. For each harmonic value, the appearance of NFG cross-sections was observed. It is desirable that there are no sharp transitions between the maximum and minimum contour closures in NFG sections and the absence of multiple local minimum closures. If the NFG contour values are greater than 1, they are taken to be the maxima. On the contrary, if those are smaller than 1 represent the minima [16]. Sındırgı and Özyalın (2019) [12] developed a new criterion instead of trial and error method to determine the most appropriate harmonic number. In their article, they obtained the optimum harmonic number by calculating the minimum error values corresponding to different harmonic numbers.

3.3. Calculation of the NFG operator

The calculation of the NFG operator can be performed using a Fourier series approximation of the function $F(x,z)$ along the x-axis in the range $(-L,L)$ given by Bracewell (1984) [46] and Blakely (1995) [47].

$$F(x, z) = \sum_{n=0}^{\infty} \left[A_n \cos\left(\frac{\pi nx}{L}\right) + B_n \sin\left(\frac{\pi nx}{L}\right) \right] e^{\frac{\pi nz}{L}} \tag{8}$$

The basis of this method is the use of Fourier series. Analytical continuation operation for any z-plane of a harmonic function given in the interval $[0,L]$ can be written as a Fourier sine series.

$$F(x, z) = \sum_{n=1}^N B_n \sin\left(\frac{\pi nx}{L}\right) e^{\frac{\pi nz}{L}} \tag{9}$$

Here; B_n is the Fourier sine coefficient, n is the harmonic number, L is the length of the profile, z is the plane on which the analytical continuation is made. With the help of equation 9, it is possible to calculate the $F(x)$ function above or below a given plane.

When the first-order derivatives of the $F(x,z)$ function defined in equation 9 are taken in the x and z directions, $F_x(x,z)$ and $F_z(x,z)$ are defined by the following equation.

$$F_x(x, z) = \frac{\pi}{L} \sum_{n=1}^N n B_n \cos\left(\frac{\pi nx}{L}\right) e^{\frac{\pi nz}{L}} \tag{10}$$

$$F_z(x, z) = \frac{\pi}{L} \sum_{n=1}^N n B_n \sin\left(\frac{\pi nx}{L}\right) e^{\frac{\pi nz}{L}} \tag{11}$$

The B_n sine coefficients in equation (11) can be found with the help of the following equation.

$$B_n = \sum_{n=1}^N F(x, z) \sin\left(\frac{\pi nx}{L}\right) \tag{12}$$

To eliminate the Gibbs effect resulting from downward continuation process, a smoothing factor (q) can be defined as follows. This term is called the Lanczos smoothing operator.

$$q = \left[\frac{\sin\left(\frac{\pi n}{N}\right)}{\frac{\pi n}{N}} \right]^\mu \tag{13}$$

where μ is any integer number and the degree of smoothing.

4. Experimental Results

In this section, the NFG technique was applied to synthetic magnetic data generated from prismatic-shaped models mostly used in magnetic methodology to investigate the effectiveness of the method. A synthetic prism model was calculated to test the effect of the suggested technique on the determination of location parameters such as the depth of the structure center and its distance from the origin. The synthetic models were calculated by the method of Telford et al. (1976)[43] for a prismatic-shaped 2D body. Trials were made on three different models to examine the NFG field depending on the width and thickness variation of a magnetic prism. For all of the four prismatic-shaped synthetic models, the profile length was chosen as 40 m. Likewise, inclination, declination, azimuth angle, and magnetization intensity values were defined for all four prismatic-shaped synthetic models. These values were taken as 60° , 0° , 0° , and 1 A/m [SI] , respectively.

4.1. Synthetic Model #1

The parameters of synthetic Model #1 and the model parameters obtained from the NFG technique are shown in Table 1. Synthetically generated $\Delta T(x,0)$ curves and NFG sections are given in Figure 3. NFG technique with different harmonic numbers is applied to the synthetic anomalies of a prismatic model. It is observed that the NFG technique produces closed contours around the anomalous body for all harmonic intervals. They are the depths of the maximum singular points in the NFG sections calculated for various harmonics. The center of the completely closed contours of the NFG harmonics corresponds to the actual burial depth of the structure. In Table 1, the structural parameters of this model and largest singular point value (LSPV) of the NFG field, the depth in the z-axis, and the horizontal distance in the x-axis for the $N=10, 20, 30,$ and 40 harmonics are given. Figure 3 shows that the NFG technique precisely determines the surface projection point of the structure ($x = 20.5 \text{ m}$) at various harmonic numbers. In addition, the structure depth was obtained exactly ($h=1.5\text{m}$) at the 40th harmonic number

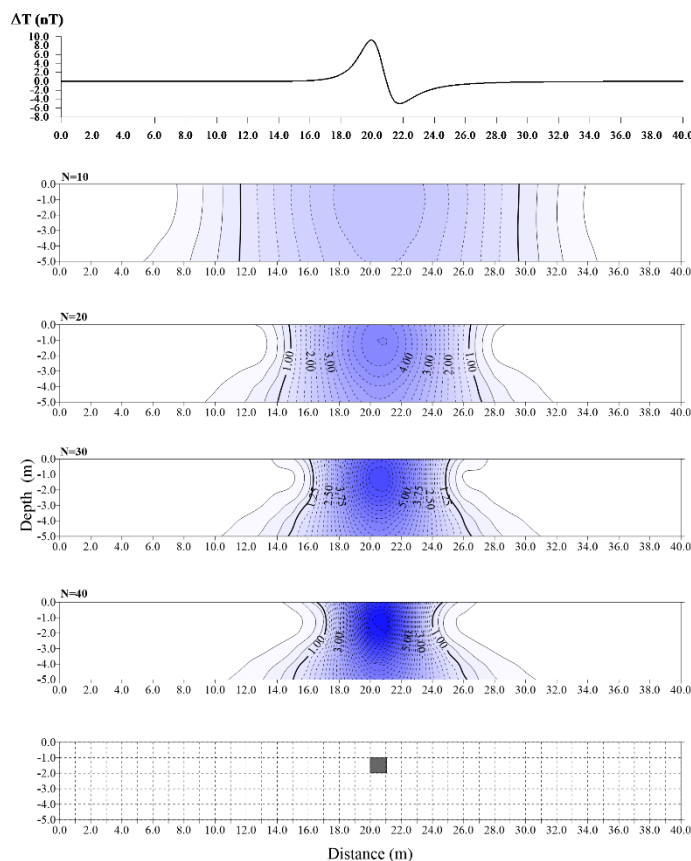


Figure 3. Synthetic anomaly and NFG sections for a single 2D synthetic prism model #1 for various harmonics

4.2. Synthetic Model #2

Model#2 was created to see the effect of the NFG technique on the solution with the increase of the structure width. The parameters of synthetic Model #2 and the model parameters obtained from the NFG technique are shown in Table 2. In this application, the top surface depth, thickness, and distance to the origin parameters of the structure in Model #1 are used exactly. In Model #2, only the width of the structure has been increased. In Model #2, the prism width is defined as 11.0 m . The magnetic anomaly and NFG sections of the model are shown in Figure 4. Due to the increase in model width in all NFG sections with different harmonic numbers, positive closures are observed completely independently of each other at horizontal distances corresponding to the boundaries at both ends of the structure. There are negative closures in the direction of the extension of the structure. This detail is clearly observed in the 40th harmonics. The depth of the

structure and their distance from the origin were found clearly on both sides.

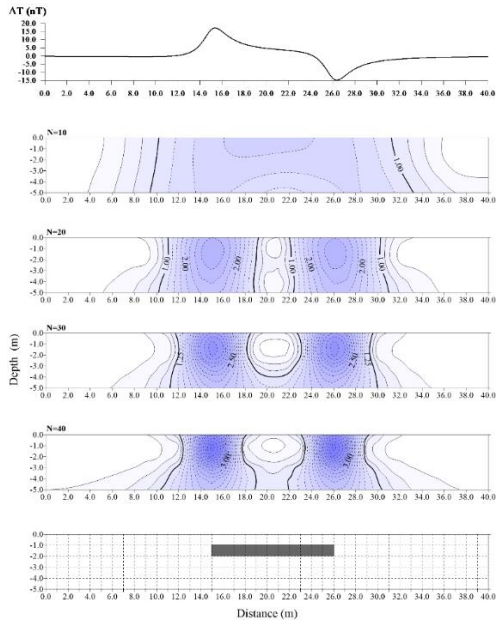


Figure 4. Synthetic anomaly and NFG sections for a single 2D synthetic prism Model #2 for various harmonics

4.3. Synthetic Model #3

In this section, we wanted to see the effect of the structure thickness on the solution in the NFG solution. Model #3 was generated to see the effect of the NFG technique on the solution with the increase of the structure thickness. The parameters of synthetic Model #3 and the model parameters obtained from the NFG technique are shown in Table 3. In this section, the top surface depth, width, and distance to the origin parameters of the structure in Model #2 are used exactly. In Model #3, only the thickness of the structure has been increased. There are negative closures in the direction of the extension of the structure (Figure 5). While in the previous Model #1 and Model #2 studies, the singular point values corresponded to the center of the structure, it is observed that the singular points in the NFG sections for different harmonics are concentrated towards the upper surface of the structure with the increase in thickness in Model #3.

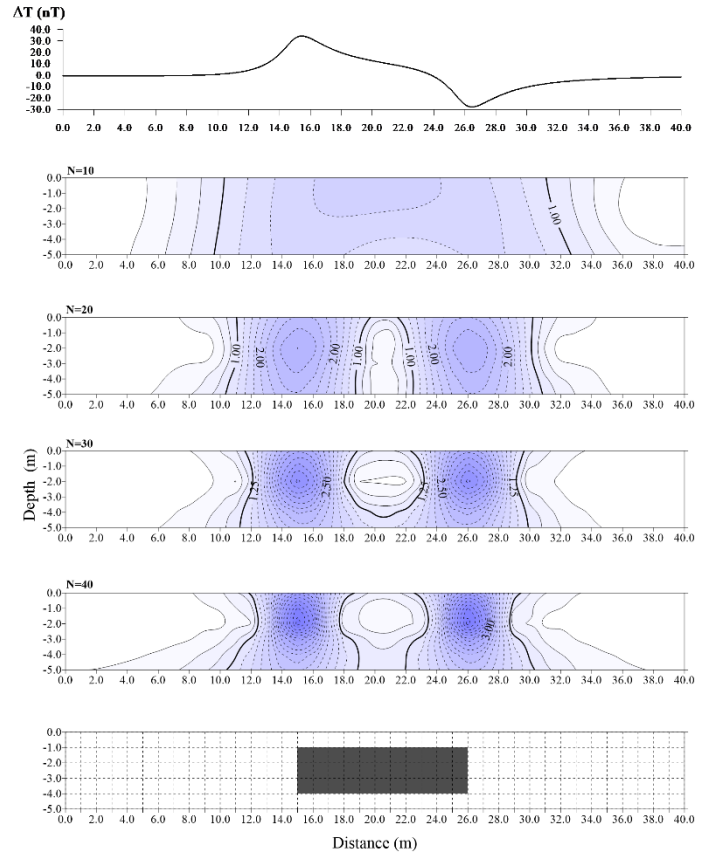


Figure 5. Synthetic anomaly and NFG sections for a single 2D synthetic prism model #3 for various harmonics

4.1. Synthetic Model #4

The model under consideration is three magnetic prisms in contact with each other at the same depth (Fig. 6). The angles of inclination, declination, and azimuth used in the previous three models are also used in Model #4. However, while the magnetization intensity of Prism #1 and Prism #3 is 1 A/m [SI] in the calculations, the magnetization intensity of Prism #2 in the middle is 1.5 A/m [SI]. The purpose of choosing the model is to examine NFG solutions by comparing them to geological structures in contact with different magnetization intensities. NFG sections for the magnetic anomaly of this model and different harmonics calculated from this anomaly are shown in Figure 6. The structural parameters of this model are given in Table 4. When the NFG cross-section at the 40th harmonic in Figure 6 is examined, positive closures are observed in the horizontal distances corresponding to the borders at the two ends of the structures, due to the wide increase in the width of the model compared to its thickness. There are negative closures in the direction of the extension of

the structure. This detail is clearly observed in the 40th harmonics.

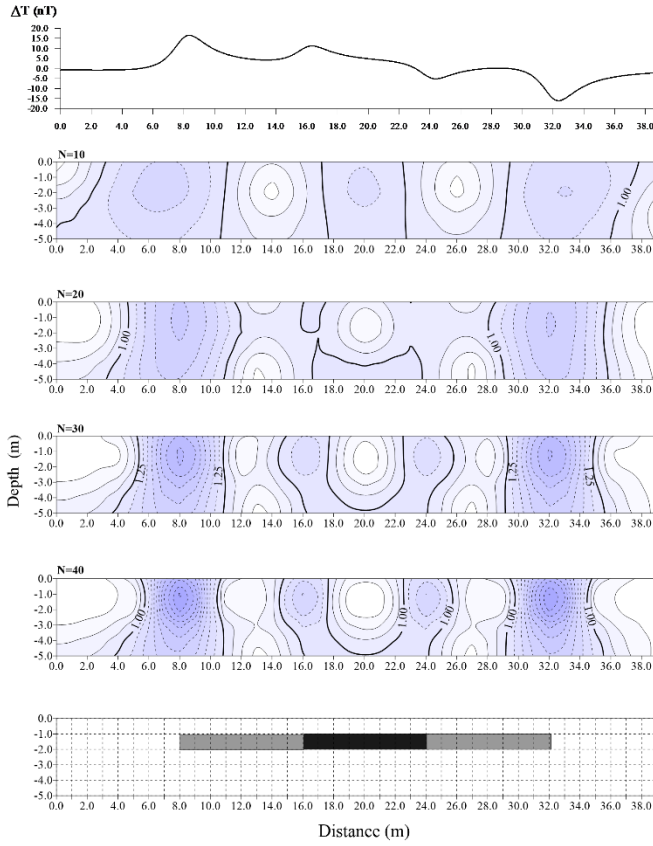


Figure 6. Synthetic anomaly and NFG sections for multi-body 2D synthetic prism Model #4 for various harmonics

Table 1. The best model parameters obtained from the NFG for synthetic Model #1

MODEL 1	Depth (m)	Thickness (m)	Width (m)	Distance (m)
	1.0	1.0	1.0	20.5
Harmonic Number (N)				
	10	20	30	40
LSPV	2.45	4.86	7.27	9.96
Distance (m)	20.5	20.5	20.5	20.5
Depth (m)	1.1	1.4	1.4	1.5

Table 2. The best model parameters obtained from the NFG for synthetic Model #2

MODEL 2	Depth (m)	Thickness (m)	Width (m)	Distance (m)
	1.0	1.0	11.0	20.5
Harmonic Number (N)				
	10	20	30	40
LSPV	1.85	2.98	4.40	5.60
Distance (m)	15.0-26.1	15.0-26.1	15.0-26.1	15.0-26.1
Depth (m)	1.1	1.4	1.4	1.5

Table 3. The best model parameters obtained from the NFG for synthetic Model #3

MODEL 3	Depth (m)	Thickness (m)	Width (m)	Distance (m)
	1.0	3.0	11.0	20.5
	Harmonic Number (N)			
	10	20	30	40
LSPV	1.86	3.00	4.48	5.70
Distance (m)	15.0-26.1	15.0-26.1	15.0-26.1	15.0-26.1
Depth (m)	4.1	2.0	1.8	1.3

Table 4. The best model parameters obtained from the NFG for synthetic Model #4

MODEL #4	Prism #1	Prism #2	Prism #3
Depth (m)	1.0	1.0	1.0
Thickness (m)	1.0	1.0	1.0
Width (m)	8.0	8.0	8.0
Distance (m)	12.0	20.0	28.0

5. Field Examples

In the Hittite city of Sapinuwa, the first search started in 1998 with resistivity studies. Since the study area has suffered a great fire several times in history, magnetic measurements were carried out with the thought that the magnetic method could yield more appropriate results here. Total magnetic field data was collected using Scintrex Smartmag brand magnetometer. The orientation of each profile was chosen from south to north and the direction of the sensor was oriented towards north. The sensor height was chosen as 0.50 m. In order to define the study area, measurements were carried out by selecting small independent areas, and in later studies, measurements were carried out in a large area consisting of adjacent areas.

5.1. Site #1

In this area with dimensions of 15*15 m, the profile spacing is 1.0 m and the measuring spacing in each profile is 1.0 m. When the total magnetic field anomaly obtained is examined, the first point that draws attention is a difference of approximately 130 nT between the positive and negative closures in the W-E direction in the middle of the field, and similarly

a difference of approximately 160 nT in the N-S direction (Figure 7).

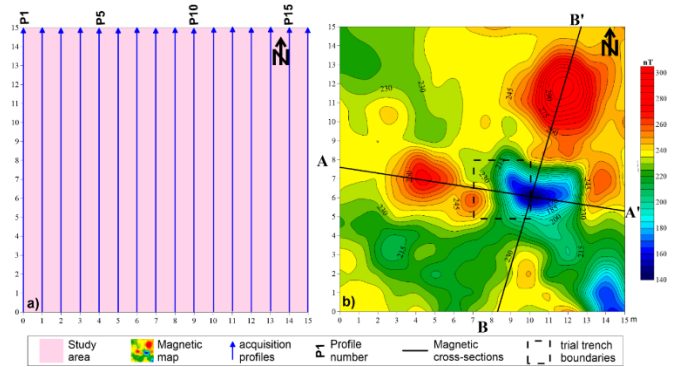


Figure 7. (a) Magnetic survey area and data acquisition profiles, (b) Magnetic anomaly map of the studied Site #1 and NFG sections

In this study area, firstly, a 15 m long AA' section in the W-D direction to cut the closures and a 15 m BB' section in approximately S-N direction were taken. NFG technique was applied to the data obtained from AA' and BB' sections (Figures 8). When both figures were examined, an average depth of approximately 1.0 m was found. As a result of the evaluation of the magnetic anomaly

map of the area with the NFG technique, LSPV locations are shown in Figure 8.

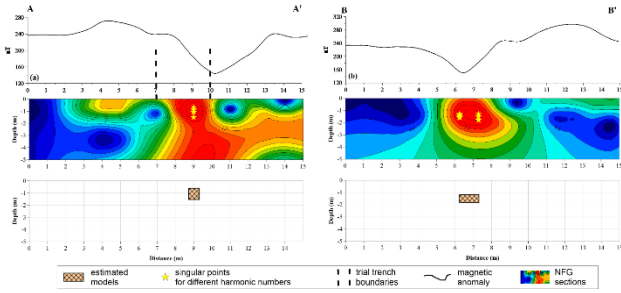


Figure 8. An application of the NFG technique to the magnetic anomalies obtained from Site #1

A trial trench is proposed in the 3*3 m area indicated by the black dashed line in Figure 7. Successful geophysical results were obtained at the end of the excavations at the proposed site. During the excavation, wall ruins were found 0.70 m below the surface extending approximately SW-NE in the western part of the trench. At the later stage of the excavation, these ruins were cleared and the foundation part of the wall was reached at approximately 1.0 m. Likewise, in the NFG section in Figure 8, the proposed trench boundaries are shown with a black dashed line. The foundations of the building obtained at the end of this trench are shown in Figure 9.



Figure 9. The wall remains unearthed in the proposed trial trench at Site #1.

5.2. Site #2

The dimensions of the Site #2 search area are 14*26 m. The distance between the profiles is 1.0 m and the measuring range in each profile is 1.0 m. When the total magnetic field map obtained in Site #2 is examined, positive and negative closures extending in

the S-N direction are observed (Figure 10). The dimensions of our working area are 14*26 m, 1.0 m between profiles, and the measuring range in each profile is 1.0 m. For this reason, firstly, a 25 m long AA' section was taken in the S-N direction to cut the closures. NFG technique was applied to the magnetic anomaly of the AA' section (Figure 11).

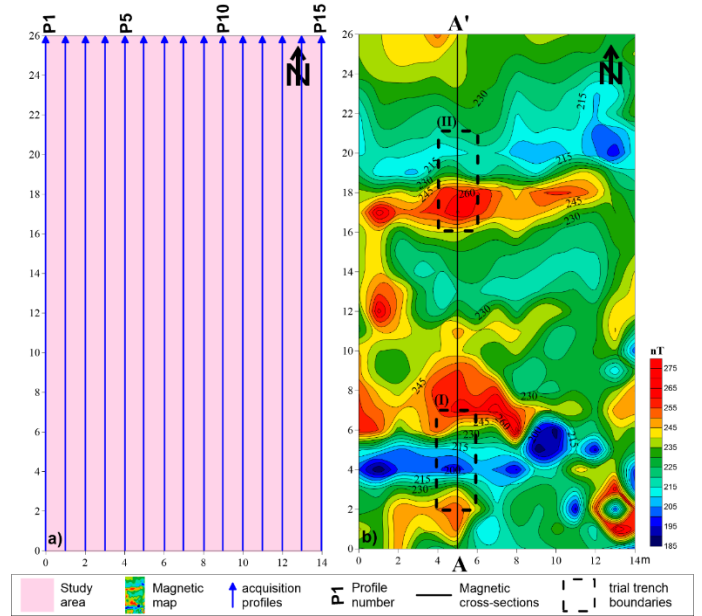


Figure 10. Magnetic survey area and data acquisition profiles, (b) Magnetic anomaly map of the studied Site #2 and NFG sections

When the NFG section was examined, it was observed that there were two separate structures. Symbols with yellow asterisks show singular point values for different harmonic numbers. It starts from about 1.0 m and reaches up to 1.7 m. A trial trench is proposed in two separate areas of 2*5 m, indicated by the black dashed line in Figure 10. The foundations of the building obtained at the end of this trench are shown in Figure 12.

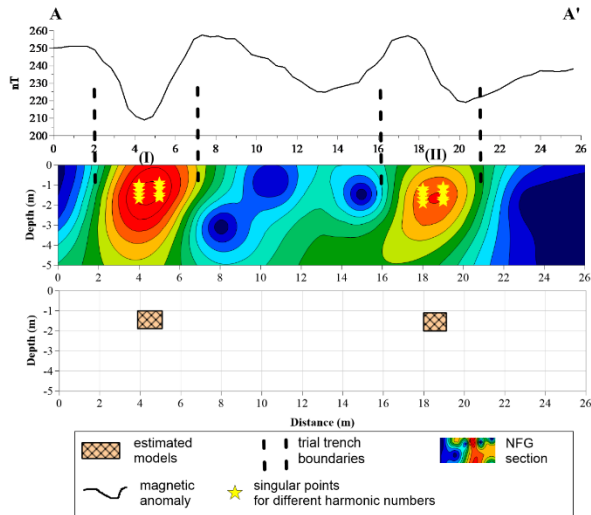


Figure 11. An application of the NFG technique to the magnetic anomalies obtained from Site #2



Figure 12. The wall remains unearthed in the proposed trial trench at Site #2.

6. Results and Discussion

The NFG technique is based on downward analytical continuation, and the NFG technique applied to magnetic field data gives direct information about the location and depth of buried structures in archaeological sites.

NFG cross sections were calculated for harmonics $N = 10, 20, 30$ and 40 (Figure 3). In the middle part of the profile, inclusions start to appear, although they are not obvious around the singular point value (2.45) at the $N=10$ harmonic. Contour inclusions become more frequent at $N = 20$ and 30 harmonic. The maximum singular point value (9.96) becomes the most prominent at the $N=40$ harmonic. In case of an increase in the width of the structure, no significant inclusion is observed in the $N=10$ harmonic (Figure 4). With the increase of the

harmonic number, the maximum inclusions are concentrated on the two sides of the structure, while the minimum inclusions are observed in the middle part of the structure. In case of an increase in the thickness of the structure, no significant inclusion is observed in the $N=10$ harmonic, similar to the previous model (Figure 5). In $N=30$ and 40 harmonics, while the maximum inclusions are concentrated on the two sides of the structure, minimum inclusions are observed in the middle part of the structure. In three different structure models, while maximum inclusions are concentrated at the edges of the structures in all harmonics, minimum inclusions are observed in the middle of the structures (Figure 6).

Two NFG applications were performed by taking sections AA' and BB' from the Site #1 magnetic map (Figure 8a and b). In both NFG applications, singular point values for different harmonic values are shown with yellow asterisks. While the singular point values for the AA' section are positioned at approximately 9m in the horizontal position, it is observed that they vary between 0.7-1.5m in the vertical axis. The fact that it does not change in the horizontal axis indicates that the width of the structure is narrow (figure 8a). On the other hand, it is possible to say that the structure is slightly wider and deeper in the distribution of individual point values in section BB' (Figure 8b)

NFG was applied by taking a section from the Site #2 magnetic map (Figure 11). The observation of a maximum closure between the two minimums in the left and right parts of the NFG section from the NFG application indicates that there are two different structures. It is observed that structure depth starts from about 1.0 m and reaches up to 1.7 m.

Singular points were detected with better precision at higher harmonics than at lower harmonics for shallow depths. When synthetic model studies are examined, as the structure width increases according to structure thickness, the singular values shift towards the structure boundaries instead of the structure center.

7. Conclusion and Suggestions

In the present study, 2D NFG technique was used to detect the location of a 2D prismatic-shaped. The method was applied to both synthetic and field datasets. The performance and reliability of the NFG technique were tested on the synthetic magnetic data. The solution efficiency of this method was investigated according to different structure properties (e.g. width, thickness). Especially, the NFG technique has been applied to multiple structure models. As a result of the evaluation, the method can define the structures correctly (location and depth). In archaeological sites, this finding helps overcome the problem of locating buried multi-structures.

The field data used in the present study are also acquired at Sapinuwa ancient site in Çorum, Turkey. The NFG technique was applied to three magnetic profiles obtained from the magnetic maps of two separate areas at Sapinuwa ancient site. After evaluation of the NFG technique of three magnetic profiles obtained from the two sites, search trenches were proposed. When the location parameters of the ruined structures obtained by the proposed method in this study are compared with the results of the archaeological excavations, they show a good agreement with each other. For these data sets, the

estimated depths are very close to the depths measured from archaeological excavations. It can be said that this method, applied to the magnetic data set collected from archaeological sites, produces successful and effective results.

Acknowledgment

This study is part of the PhD thesis named “Potansiyel alanlarda Otomatik Değerlendirme Teknikleri ve Arkeolojik Alanlara Uygulanması, (2003)” of Şenol Özyalın. I would like to thank Prof. Dr. Aygül Süel and Dr. Mustafa R. Süel, who directed the excavation of the ancient city of Sapinuwa for providing valuable support during the collection of magnetic data. Thanks are due to Prof. Dr. Rahmi Pınar for helping. We also owe special thanks to three anonymous referees.

Conflict of Interest Statement

There is no conflict of interest between the authors.

Statement of Research and Publication Ethics

The study is complied with research and publication ethics

References

- [1] V. N. Strakhov, “On methods of mathematical theory construction in interpretation of magnetic and gravity anomalies,” *Applied Geophysics*, vol. 25, pp. 125–133, 1962.
- [2] G. Y. Golizdra, “On relationship between singular points of gravity potential and form anomalous masses”. In: 2nd Conference of Young Geologists of Ukraine Proceedings, Kyiv, 1962.
- [3] V. M. Berezkin, “Application of the total vertical gradient of gravity for determination of the depths to the sources of gravity anomalies,” *Exploration Geophysics*, vol. 18, pp. 69-79, 1967.
- [4] V.M. Berezkin, “Full Gradient Method in Geophysical Prospecting,” Moscow, USSR: Nedra Publishing House, 1988.
- [5] R. Pašteka, “2D semi-automated and environmental methods in gravimetry and magnetometry,” *Acta Geologica Universitatis Comenianae*, Vol: 55, pp: 5-50, 2000.
- [6] Ş. Özyalın, “Automated interpretation methods in potential fields and application to the archeological sites,” PhD Thesis, Dokuz Eylül University, İzmir, Turkey, 2003.
- [7] A. Aydın, “Interpretation of gravity anomalies with the normalized full gradient (NFG) method and an example,” *Pure and Applied Geophysics*, V.164, pp. 2329-2344, 2007.
- [8] A. Aydın, “Application of the normalized full gradient (NFG) method to resistivity data,” *Turkish Journal of Earth Sciences*, Vol. 19, pp. 513-526, 2010.
- [9] P. Sındırgı, O. Pamukçu, Ş. Özyalın, “Application of normalized full gradient method to self potential (SP) data”, *Pure and Applied Geophysics*, V. 165, pp. 409-427, 2008.
- [10] B. Oruç, A. Keskinsezer, “Detection of causative bodies by normalized full gradient of aeromagnetic anomalies from east Marmara region, NW Turkey,” *Journal of Applied Geophysics*, V.65, pp. 39-49, 2008.

- [11] H. Aghajani, A. Moradzadeh, H. Zeng, "Detection of high potential oil and gas fields using normalized full gradient of gravity anomalies: a case study in the Tabas Basin, Eastern Iran," *Pure and Applied Geophysics*, V. 168, pp. 1851-1863, 2011.
- [12] P. Sındırgı, Ş. Özyalın, "Estimating the location of a causative body from a self-potential anomaly using 2D and 3D normalized full gradient and Euler deconvolution" *Turkish Journal of Earth Sciences*, Vol. 28: No. 4, pp. 640-659, 2019.
- [13] Y.L. Ekinçi, Ş. Özyalın, P. Sındırgı, Ç. Balkaya, G. Göktürkler, "Amplitude inversion of 2D analytic signal of magnetic anomalies through differential evolution algorithm," *Journal of Geophysics and Engineering*, Vol. 14(6), pp. 1492-1508, 2017.
- [14] Y.L. Ekinçi, A. Büyüksaraç, Ö. Bektaş, C. Ertekin "Geophysical Investigation of Mount Nemrut Stratovolcano (Bitlis, Eastern Turkey) Through Aeromagnetic Anomaly Analyses," *Pure Appl. Geophys.* Vol. 177, pp. 3243–3264, 2020. <https://doi.org/10.1007/s00024-020-02432-0>
- [15] H. Karşlı, "The Usage of Normalized Full Gradient Method in Seismic Data Analysis and a Comparison to Complex Envelope Curves," PhD Thesis, Karadeniz Technical University, Trabzon, Turkey, 2001.
- [16] D. Dondurur, "Depth estimates for Slingram electromagnetic anomalies from dipping sheet-like bodies by the normalized full gradient method," *Pure and Applied Geophysics*, Vol. 161, pp. 2179-2196, 2005.
- [17] S. Srivastava, B.N.P. Agarwal, "Inversion of the amplitude of the two-dimensional analytic signal of the magnetic anomaly by the particle swarm optimization technique", *Geophys J Int* Vol. 182, pp. 652–662, 2010. <https://doi.org/10.1111/j.1365-246X.2010.04631.x>
- [18] E.S.M. Abdelrahman, E.R. Abo-Ezz, K.S. Essa, "Parametric inversion of residual magnetic anomalies due to simple geometric bodies", *Explor Geophys* Vol. 43, pp.178–189, 2012. <https://doi.org/10.1071/EG11026>
- [19] K.S. Essa, M. Elhussein, "A new approach for the interpretation of self-potential data by 2-D inclined plate", *J Appl Geophys*, Vol. 136, pp. 455–461, 2017. <https://doi.org/10.1016/j.jappgeo.2016.11.019>
- [20] A. Biswas, M.P. Parija, S. Kumar, "Global nonlinear optimization for the interpretation of source parameters from total gradient of gravity and magnetic anomalies caused by thin dyke", *Ann Geophys*, 2017. <https://doi.org/10.4401/ag-7129>
- [21] Y.L. Ekinçi, M.A. Kaya, "Manyetik verilerde sınır analizi yöntemi kullanarak gömülü arkeolojik yapı sınırlarının tanımlanması", *Yerbilimleri*, Vol. 27(2), pp. 97-107, 2006.
- [22] Ç. Balkaya, G. Göktürkler, Z. Erhan, Y.L. Ekinçi, "Exploration for a cave by magnetic and electrical resistivity surveys: Ayvacık Sinkhole example, Bozdağ, İzmir (western Turkey)," *Geophys.* Vol. 77, pp. B135-B146, (2012). <https://doi.org/10.1190/geo2011-0290.1>
- [23] A. Büyüksaraç, C.Ç. Yalçiner, Y.L. Ekinçi, A. Demirci, M.A. Yücel, "Geophysical investigations at Agadere Cemetery, Gallipoli Peninsular, NW Turkey", *Australian Journal of Forensic Sciences*, Vol. 46(1), pp. 111–123, 2014. <http://dx.doi.org/10.1080/00450618.2013.804948>.
- [24] Y.L. Ekinçi, Ç. Balkaya, A. Şeren, M.A. Kaya, C. Lightfoot, 2014. "Geomagnetic and Geoelectrical Prospection for Buried Archaeological Remains on the Upper City of Amorium, a Byzantine City in Midwestern Anatolia, Turkey". *Journal of Geophysics and Engineering*, Vol.11 (1), 015012, 2014.
- [25] S. Yılmaz, Ç. Balkaya, O. Çakmak, E. Oksum, "GPR and ERT Explorations at the Archaeological Site of Kılıç Village (Isparta, SW Turkey)", *Journal of Applied Geophysics*, Vol. 170: 103859, 2019.
- [26] Ç. Balkaya, Y.L. Ekinçi, O. Çakmak, M. Blömer, J. Arnkens, M.A. Kaya, "A challenging archaeo-geophysical exploration through GPR and ERT surveys on the Keber Tepe, City Hill of Doliche, Commagene (Gaziantep, SE Turkey)", *Journal of Applied Geophysics*, Vol. 186,104272, 2021.
- [27] M.Ö. Arısoy, Ö. Koçak, A. Büyüksaraç, F. Bilim, "Images of Buried Graves in Bayat, Afyon (Turkey) from High-resolution Magnetic Data and Their Comparison with Preliminary Excavations", *Journal of Archaeological Science*, Vol. 34 (9): pp.1473-1484, 2007.
- [28] A. Büyüksaraç, M.Ö. Arısoy, Ö. Bektaş, Ö. Koçak, T. Çay, "Determination of Grave Locations in Dedemezari Necropolis (Western Turkey) using Magnetic Field Derivatives", *Archaeological Prospection*, Vol. 15 (4), pp. 267-283, 2008.
- [29] S. Yılmaz, Ç. Balkaya, O. Çakmak, E. Oksum, "GPR and ERT explorations at the archaeological site of Kılıç village (Isparta, SW Turkey)", *Journal of Applied Geophysics*, Vol. 170,103859, 2019. <https://doi.org/10.1016/j.jappgeo.2019.103859>

- [30] M.A Kaya, Ş. Özyalın, “Malos Antik Kentinin Manyetik Yöntemle Araştırılması”, Workshop: Arkeoloji ve Jeofizik, İzmir, 1999.
- [31] Ç. Balkaya , A. Sever , O. Çakmak, F. Özcan, "Arkeolojik Alanlarda Jeofizik Prospeksiyon: Pisidia Mallos Örneği", Bitlis Eren Üniversitesi Fen Bilimleri Dergisi, Vol. 9(2), pp. 958-966, 2020. doi:10.17798/bitlisfen.624678
- [32] Y.L. Ekinci, M.A. Kaya, “3D Resistivity Imaging of Buried Tombs at the Parion Necropolis (NW Turkey)”, Journal of the Balkan Geophysical Society, Vol. 10 (2), pp.1-8. 2007.
- [33] Y.L. Ekinci, M.A. Kaya, C. Başaran, H. Kasapoğlu, A. Demirci, C., Durgut, “Geophysical Imaging Survey in the South Necropolis at the Ancient City of Parion (Kemer-Biga), Northwestern Anatolia, Turkey: Preliminary Results”, Mediterranean Archaeology and Archaeometry, Vol. 12 (2), pp. 145-157, 2012.
- [34] Ç. Balkaya, Ü.Y. Kalyoncuoğlu, M. Özhanlı, G. Merter, O. Çakmak, İ.T. Güven, “Ground penetrating Radar and Electrical Resistivity Tomography Studies in the Biblical Pisidian Antioch City, SW Anatolia”, Archaeological Prospection, Vol. 25 (4), pp. 285-300, 2018.
- [35] İ. Akca, Ç. Balkaya, A. Pülz, H.S. Alanyalı, M.A. Kaya, “Integrated Geophysical Investigations to Reconstruct the Archaeological Features in the Episcopal District of Side (Antalya, Southern Turkey)”, Journal of Applied Geophysics, Vol. 163, pp. 22-30, 2019.
- [36] M.G. Drahor, T.Ö. Kurtulmuş, M.A. Berge, M. Hartmann, M.A. Speidel, “Magnetic Imaging and Electrical Resistivity Tomography Studies in a Roman Military Installation found in Satala Archaeological Site, Northeastern Anatolia, Turkey”, Journal of Archaeological Science, Vol. 35 (2), pp. 259-271, 2008.
- [37] M.G. Drahor, “Integrated Geophysical Studies in the Upper part of Sardis Archaeological Site, Turkey”, Journal of Applied Geophysics, Vol. 59 (3), pp. 205-223, 2006.
- [38] M.A. Berge, M.G. Drahor, “Electrical Resistivity Tomography Investigations of Multi Layered Archaeological Settlements: Part I – Modelling”, Archaeological Prospection, Vol. 18 (3), pp. 159-171, 2011.
- [39] M.A. Berge, M.G. Drahor, “Electrical Resistivity Tomography Investigations of MultiLayered Archaeological Settlements: Part II – A Case from Old Smyrna Höyük, Turkey”, Archaeological Prospection, Vol. 18 (4), pp. 291-302, 2011.
- [40] M.A. Kaya, Ç. Balkaya, Y.L. Ekinci, A. Demirci, “Kültür Mirasımız, Torunlarımızın Emaneti için Arkeojeofizik, Neden, Nereye?”, Jeofizik Bülteni, Vol. 72, pp. 29-45, 2013.
- [41] M.A. Berge, M.G. Drahor, T.Ö. Kurtulmuş, M. Hartmann, M.A. Speidel, “Magnetic and Electrical Resistivity Tomography Investigations in a Roman Legionary Camp Site (Legio IV Scythica) in Zeugma, Southeastern Anatolia, Turkey”, Archaeological Prospection, Vol. 15 (3), pp. 159- 186, 2008.
- [42] P. Wessel, W.H.F. Smith, “New version of the Generic Mapping Tools (GMT)”, EOS Transactions 76, 329, 1995. doi: 10.1029/95EO00198
- [43] W.M., Telford, L.P. Geldart, D.A. Keys, “Applied Geophysics,” Cambridge University Press, Cambridge, 860 p., 1976.
- [44] M. N. Nabighian, “The analytic signal of two-dimensional magnetic bodies with polygonal cross-section: its properties and use for automated anomaly interpretation,” Geophysics, Vol. 37, pp. 507–17, 1972.
- [45] V. M. Berezkin, “Using in Oil-Gas Exploration of Gravity Method,” Moscow, Nedra, 1973.
- [46] R. Bracewell, “The Fourier Transform and Its Applications,” McGraw-Hill Book Co., New York, 1984.
- [47] R.J. Blakely, “Potential Theory in Gravity and Magnetic Applications,” Cambridge University Press, New York, 1995.